Modern Electric, Hybrid Electric, and Fuel Cell Vehicles

Fundamentals, Theory, and Design

Mehrdad Ehsani
Yimin Gao
Sebastien E. Gay
Ali Emadi

CRC PRESS

Modern Electric, Hybrid Electric, and Fuel Cell Vehicles

Fundamentals, Theory, and Design

POWER ELECTRONICS AND APPLICATIONS SERIES

Muhammad H. Rashid, Series Editor
University of West Florida

PUBLISHED TITLES

Complex Behavior of Switching Power Converters
Chi Kong Tse

DSP-Based Electromechanical Motion Control
Hamid A.Toliyat and Steven Campbell

Advanced DC/DC Converters
Fang Lin Luo and Hong Ye

Renewable Energy Systems: Design and Analysis with Induction Generators
M. Godoy Simões and Felix A. Farret

Uninterruptible Power Supplies and Active Filters
Ali Emadi, Abdolhosein Nasiri, and Stoyan B. Bekiarov

Electric Energy: An Introduction
Mohamed El-Sharkawi

Modern Electric, Hybrid Electric, and Fuel Cell Vehicles

Fundamentals, Theory, and Design

Mehrdad Ehsani, Texas A&M University

Yimin Gao, Texas A&M University

Sebastien E. Gay, Texas A&M University

Ali Emadi, Illinois Institute of Technology

CRC PRESS

Boca Raton London New York Washington, D.C.

Library of Congress Cataloging-in-Publication Data

Modern electric, hybrid electric, and fuel cell vehicles: fundamentals, theory, and design/Mehrdad Ehsani ... [et al.].
p. cm. – (Power electronics and applications series)
Includes bibliographical references and index.
ISBN 0-8493-3154-4 (alk. paper)
1. Hybrid electric vehicles. 2. Fuel cells. I. Ehsani, Mehrdad. II. Title. III. Series.

TL221.15.G39 2004
629.22'93—dc22 2004054249

Visit the CRC Press Web site at www.crcpress.com

International Standard Book Number 0-8493-3154-4
Library of Congress Card Number 2004054249
Printed in the United States of America 1 2 3 4 5 6 7 8 9 0
Printed on acid-free paper

To my wife, Zohreh, for her love and support
Mehrdad Ehsani

To my wife, Anni Liu, and my daughter, Yuan Gao
Yimin Gao

To my parents, professors, and mentors
Sebastien E. Gay

To my family, parents, and sister
Ali Emadi

Preface

The development of automobiles with heat engines is one of the greatest achievements of modern technology. However, the highly developed automotive industry and the large number of automobiles in use around the world have caused and are still causing serious problems for society and human life. Deterioration in air quality, global warming, and a decrease in petroleum resources are becoming the major threats to human beings. More and more stringent emissions and fuel consumption regulations are stimulating an interest in the development of safe, clean, and high-efficiency transportation. It has been well recognized that electric, hybrid electric, and fuel cell-powered drive train technologies are the most promising solutions to the problem of land transportation in the future.

To meet the revolutionary challenge, an increasing number of North American and other engineering schools have started the academic discipline of advanced vehicle technologies in both undergraduate and graduate programs. In 1998, the principal author of this book shared his first lecture on "Advanced Vehicle Technologies — Design Methodology of Electric and Hybrid Electric Vehicles" with graduate students in mechanical and electrical engineering at Texas A&M University. While preparing the lecture, it was found that although there is a wealth of information in technical papers and reports, there is as yet no comprehensive and integrated textbook or reference for students. Furthermore, practicing engineers also need a systematically integrated reference to understand the essentials of this new technology. This book aims to fill this gap.

The book deals with the fundamentals, theory, and design of conventional cars with internal combustion engines (ICEs), electric vehicles (EVs), hybrid electric vehicles (HEVs), and fuel cell vehicles (FCVs). It comprehensively presents vehicle performance, configuration, control strategy, design methodology, modeling, and simulation for different conventional and modern vehicles based on mathematical equations.

This book includes vehicle system analysis, ICE-based drive trains, EV design, HEV configurations, electric propulsion systems, series/parallel/mild hybrid electric drive train design methodologies, energy storage systems, regenerative braking, fuel cells and their applications in vehicles, and fuel cell hybrid electric drive train design. It emphasizes the overall drive train system and not just specific components. The design methodology is described by step-by-step mathematical equations. Furthermore, in explaining the design methodology of each drive train, design examples are presented with simulation results.

This book consists of 13 chapters. In Chapter 1, the social and environmental import of modern transportation is discussed. This mainly includes air pollution, global warming, and petroleum resource depletion associated with the development of modern transportation. In this chapter, the impact of future vehicle technologies on the oil supplies is analyzed. The results are helpful for the future development strategy of the next-generation vehicles. In addition, the development history of EV, HEV, and FCV is briefly reviewed.

In Chapter 2, the basic understanding of vehicle performance, power source characteristics, transmission characteristics, and equations used to describe vehicle performance are provided. The main purpose of this chapter is to provide the basic knowledge that is necessary for understanding vehicular drive train design.

In Chapter 3, the major operating characteristics of different heat engines are introduced. As the primary power source, the engine is the most important subsystem in conventional and hybrid drive train systems. A complete understanding of the characteristics of an engine is necessary for the design and control of conventional cars and HEVs.

In Chapter 4, EVs are introduced. This chapter mainly addresses the design of electric propulsion systems and energy storage devices, the design of traction motor and transmission, the prediction of vehicle performance, and simulation.

In Chapter 5, the basic concept of hybrid traction is established. Various configurations of HEVs are discussed, such as series hybrid, parallel hybrid, torque-coupling and speed-coupling hybrids, and other configurations. The major operating characteristics of these configurations are presented.

In Chapter 6, several electric propulsion systems are introduced, including DC, AC, permanent magnet brushless DC, and switched reluctance motor drives. Their basic construction, operating principles, and control and operating characteristics are described from the traction application point of view.

In Chapter 7, the design methodology of series hybrid electric drive trains is presented. This chapter focuses on the power design of engine and energy storage, design of traction motor, transmission characteristics, and control strategy. A design example is also provided.

In Chapter 8, the design methodology of parallel hybrid electric drive trains is provided. This chapter includes driving pattern and mode analysis, control strategy, design of the major components (engine, energy storage, and transmission), and vehicle performance simulation.

In Chapter 9, the design methodology of mild hybrid drive trains is introduced with two major configurations of parallel torque coupling and series–parallel, torque–speed coupling. This chapter focuses on operation analysis, control development, and simulation.

In Chapter 10, different energy storage technologies are introduced including batteries, ultracapacitors, and flywheels. The discussion focuses

on power and energy capacities. The concept of hybrid energy storage is also introduced in this chapter.

In Chapter 11, vehicular regenerative braking is introduced. In this chapter, different controls of regenerative braking are analyzed, including braking force distribution on the front and rear wheels, amount of braking energy in various driving cycles, and the amount of energy that can be recovered by regenerative braking.

In Chapter 12, different fuel cell systems are described, mainly focusing on their operation principles and characteristics, technologies, and fuel supplies. Vehicular applications of fuel cells are also explained.

In Chapter 13, the systematic design of fuel cell hybrid drive trains is introduced. First, the concept of fuel cell hybrid vehicles is established. Then, its operating principles and control of the drive train are analyzed. Lastly, the design methodology is described, focusing on the power design of the fuel cell system, electric propulsion, and the energy storage system. A design example and its corresponding simulation verification are also provided.

The material in this book is recommended for a graduate or senior-level undergraduate course. Depending on the background of the students in different disciplines such as mechanical and electrical engineering, course instructors have the flexibility to choose the material or skip the introductory sections/chapters from the book for their lectures. This text has been taught at Texas A&M University as a graduate-level course. An earlier version of this text has been revised several times based on the comments and feedback received from the students in this course. We are grateful to our students for their help.

This book is also an in-depth source and a comprehensive reference in modern automotive systems for engineers, practitioners, graduate and senior undergraduate students, researchers, and managers who are working in automotive-related industries, government, and academia.

In addition to the work by others, many of the technologies and advances presented in this book are the collection of many years of research and development by the authors and other members of the Advanced Vehicle Systems Research Program at Texas A&M University. We are grateful to all members of the Advanced Vehicle Systems Research group as well as the Power Electronics and Motor Drives group, especially Dr. Hyung-Woo Lee and Mr. Peymen Asadi, who made great contributions to the brushless DC and switched reluctance motor drive sections, respectively. Switched reluctance motor vibration, acoustic noise, and design sections draw heavily from the Ph.D. dissertation of Prof. Babak Fahimi, which is gratefully acknowledged. In addition, we would like to express our sincere gratitude to Prof. Hassan Moghbelli, who thoroughly reviewed the earlier version of the manuscript and provided his valuable suggestions to improve the quality of the book.

We would also like to express our sincere thanks to Mr. Glenn C. Krell, whose proofreading and corrections have improved this text. In addition,

we would like to acknowledge the efforts and assistance of the staff of CRC Press, especially Nora Konopka and Jeff Hall. Last but not least, we thank our families for their unconditional support and absolute understanding during the writing of this book.

Mehrdad Ehsani
Yimin Gao
Sebastien E. Gay
Ali Emadi

Biography

Short Biography of the Principal Author, Prof. Mehrdad Ehsani

Mehrdad (Mark) Ehsani received his B.S. and M.S. degrees from the University of Texas at Austin in 1973 and 1974, respectively, and his Ph.D. degree from the University of Wisconsin-Madison in 1981, all in electrical engineering.

From 1974 to 1977, he was with the Fusion Research Center, University of Texas, as a Research Engineer. From 1977 to 1981, he was with Argonne National Laboratory, Argonne, Illinois, as a Resident Research Associate, while simultaneously doing his doctoral work at the University of Wisconsin-Madison in energy systems and control systems. Since 1981, he has been at Texas A&M University, College Station, TX, where he is now a Professor of electrical engineering and Director of Texas Applied Power Electronics Center (TAPC). He is the author of over 200 publications in pulsed-power supplies, high-voltage engineering, power electronics and motor drives, and is the recipient of the Prize Paper Awards in Static Power Converters and motor drives at the IEEE-Industry Applications Society 1985, 1987, and 1992 Annual Meetings, in addition to numerous other honors and recognitions. In 1984, he was named the Outstanding Young Engineer of the Year by the Brazos chapter of the Texas Society of Professional Engineers. In 1992, he was named the Halliburton Professor in the College of Engineering at Texas A&M. In 1994, he was also named the Dresser Industries Professor in the same college. In 2001, he was selected for Ruth & William Neely/Dow Chemical Faculty Fellow of the College of Engineering for 2001 to 2002, for "contributions to the Engineering Program at Texas A&M, including classroom instruction, scholarly activities, and professional service." He was also selected for the IEEE Vehicular Society 2001 Avant Garde Award for "contributions to the theory and design of hybrid electric vehicles." He is the coauthor of a book on converter circuits for superconductive magnetic energy storage and a contributor to an IEEE Guide for Self-Commutated Converters and other monographs. He has 13 granted or pending U.S. and EC patents. His current research work is in power electronics, motor drives, hybrid vehicles, and their control systems.

Dr. Ehsani has been a member of the IEEE Power Electronics Society (PELS) AdCom, past Chairman of the PELS Educational Affairs Committee, past Chairman of the IEEE-IAS Industrial Power Converter Committee, and past chairman of the IEEE Myron Zucker Student-Faculty Grant program. He was the General Chair of the IEEE Power Electronics Specialist Conference in 1990. He is the chairman of the IEEE VTS Vehicle Power and Propulsion and Convergence Fellowship Committees. In 2002, he was elected to the Board of Governors of VTS. He also serves on the editorial board of several technical journals and is the associate editor of *IEEE Transactions on Industrial Electronics* and *IEEE Transactions on Vehicular Technology*. He is a Fellow of IEEE, an IEEE Industrial Electronics Society and Vehicular Technology Society Distinguished Speaker, and an IEEE Industry Applications Society and Power Engineering Society Distinguished Lecturer. He is also a registered professional engineer in the State of Texas.

Short Biography of Dr. Yimin Gao

Yimin Gao received his B.S., M.S., and Ph.D. degrees in mechanical engineering (major in development, design, and manufacturing of automotive systems) in 1982, 1986, and 1991, respectively, all from Jilin University of Technology, Changchun, Jilin, China. From 1982 to 1983, he worked as a vehicle design engineer in DongFeng Motor Company, Shiyan, Hubei, China. He finished a layout design of a 5 ton truck (EQ144) and participated in prototyping and testing. From 1983 to 1986, he was a graduate student in the Automotive Engineering College of Jilin University of Technology, Changchun, Jilin, China. His working field was improvement of vehicle fuel economy by optimal matching of engine and transmission.

From 1987 to 1992, he was a Ph.D. student in the Automotive Engineering College of Jilin University of Technology, Changchun, Jilin, China. In this period, he worked on the research and development of legged vehicles, which can potentially operate in harsh environments where mobility is difficult for wheeled vehicles. From 1991 to 1995, he was an associate professor and automotive design engineer in the Automotive Engineering College of Jilin University of Technology. In this period, he taught undergraduate students the course of Automotive Theory and Design (several rounds) and graduate students the course of Automotive Experiment Technique (two rounds). Meanwhile, he also conducted vehicle performance, chassis, and components analysis, and conducted automotive design including chassis design, power train design, suspension design, steering system design, and brake design.

He joined the Advanced Vehicle Systems Research Program at Texas A&M University in 1995 as a research associate. Since then, he has been working in this program on the research and development of electric and hybrid electric vehicles. His research areas are mainly the fundamentals, architecture, control, modeling, and design of electric and hybrid electric drive trains, and major components. He is a member of SAE.

Short Biography of Sebastien E. Gay

Sebastien E. Gay received his M.S. in electrical engineering from Texas A&M University in 2001. Before this, he obtained his "Diplôme d'Ingénieur" from the "Institut National Polytechnique de Grenoble," (France) in 2000, and bachelor's degrees in mechanical and electrical engineering from the "Institut Universitaire de Technologie," Grenoble, (France) in 1996 and 1997, respectively. He is currently working toward his Ph.D., specializing in eddy current brakes. His research interests include hybrid electric and electric road and rail vehicles, vehicle systems advanced components, fuel cells, and oscillating electric machines. He is the co-author of a book on DSP-based control of electromechanical motion devices and two invention disclosures including one that received a "Spirit of Innovation Award" in May 2003 from the Texas A&M University Technology Licensing Office.

Short Biography of Dr. Ali Emadi

Ali Emadi received his B.S. and M.S. degrees in electrical engineering with highest distinction from the Sharif University of Technology, Tehran, Iran. He also received his Ph.D. degree in electrical engineering specializing in power electronics and motor drives from Texas A&M University, College Station, TX, where he was awarded the Electric Power and Power Electronics Institute (EPPEI) fellowship for his graduate studies. In 1997, he was a lecturer at the Electrical Engineering Department of Sharif University of Technology. Dr. Emadi joined the Electrical and Computer Engineering (ECE) Department of the Illinois Institute of Technology (IIT) in August 2000.

Dr. Emadi is the director of Grainger Power Electronics and Motor Drives Laboratories at IIT, where he has established research and teaching laboratories

as well as courses in power electronics, motor drives, and vehicular power systems. He is also the co-founder and co-director of the IIT Consortium on Advanced Automotive Systems (ICAAS). His main research interests include modeling, analysis, design, and control of power electronic converters/systems and motor drives. His areas of interest also include integrated converters, vehicular power systems, and hybrid electric and fuel cell vehicles.

Dr. Emadi has been named the Eta Kappa Nu Outstanding Young Electrical Engineer for 2003 by virtue of his outstanding contributions to hybrid electric vehicle conversion, for excellence in teaching, and for his involvement in student activities by the Eta Kappa Nu Association, the Electrical Engineering Honor Society. He is the recipient of the 2002 University Excellence in Teaching Award from IIT as well as the 2004 Sigma Xi/IIT Award for Excellence in University Research. He directed a team of students to design and build a novel low-cost brushless DC motor drive for residential applications, which won the First Place Overall Award of the 2003 IEEE/DOE/DOD International Future Energy Challenge for Motor Competition. He is an Associate Editor of *IEEE Transactions on Power Electronics*, an Associate Editor of *IEEE Transactions on Industrial Electronics*, and a member of the editorial board of the *Journal of Electric Power Components and Systems*. Dr. Emadi is the principal author of over 120 journal and conference papers as well as three books including *Vehicular Electric Power Systems: Land, Sea, Air, and Space Vehicles* (New York: Marcel Dekker, 2003), *Energy Efficient Electric Motors: Selection and Applications* (New York: Marcel Dekker, 2004), and *Uninterruptible Power Supplies and Active Filters* (Boca Raton: CRC Press, 2004). Dr. Emadi is also the editor of the *Handbook of Automotive Power Electronics and Motor Drives* (New York: Marcel Dekker, 2005). He is a senior member of IEEE and a member of SAE. He is also listed in the International Who's Who of Professionals and Who's Who in Engineering Academia.

Contents

1. Environmental Impact and History of Modern Transportation 1
   - 1.1 Air Pollution 2
     - 1.1.1 Nitrogen Oxides 2
     - 1.1.2 Carbon Monoxide 3
     - 1.1.3 Unburned Hydrocarbons 3
     - 1.1.4 Other Pollutants 3
   - 1.2 Global Warming 4
   - 1.3 Petroleum Resources 5
   - 1.4 Induced Costs 7
   - 1.5 Importance of Different Transportation Development Strategies to Future Oil Supply 9
   - 1.6 History of Electric Vehicles 13
   - 1.7 History of Hybrid Electric Vehicles 15
   - 1.8 History of Fuel Cell Vehicles 17

   References 19

2. Vehicle Fundamentals 21
   - 2.1 General Description of Vehicle Movement 22
   - 2.2 Vehicle Resistance 23
     - 2.2.1 Rolling Resistance 23
     - 2.2.2 Aerodynamic Drag 25
     - 2.2.3 Grading Resistance 26
   - 2.3 Dynamic Equation 27
   - 2.4 Tire–Ground Adhesion and Maximum Tractive Effort 29
   - 2.5 Power Train Tractive Effort and Vehicle Speed 31
   - 2.6 Vehicle Power Plant and Transmission Characteristics 33
     - 2.6.1 Power Plant Characteristics 34
     - 2.6.2 Transmission Characteristics 36
       - 2.6.2.1 Gear Transmission 37
       - 2.6.2.2 Hydrodynamic Transmission 39
       - 2.6.2.3 Continuously Variable Transmission 43
   - 2.7 Vehicle Performance 44
     - 2.7.1 Maximum Speed of a Vehicle 45
     - 2.7.2 Gradeability 46
     - 2.7.3 Acceleration Performance 46

2.8 Operating Fuel Economy 49
2.8.1 Fuel Economy Characteristics of Internal Combustion Engines 49
2.8.2 Calculation of Vehicle Fuel Economy 50
2.8.3 Basic Techniques to Improve Vehicle Fuel Economy 52
2.9 Braking Performance 54
2.9.1 Braking Force 54
2.9.2 Braking Distribution on Front and Rear Axles 55
References 60

3. Internal Combustion Engines 61
3.1 4S, Spark-Ignited IC Engines 62
3.1.1 Operating Principles 62
3.1.2 Operation Parameters 64
3.1.2.1 Rating Values of Engines 64
3.1.2.2 Indicated Work per Cycles and Mean Effective Pressure 64
3.1.2.3 Mechanical Efficiency 66
3.1.2.4 Specific Fuel Consumption and Efficiency 67
3.1.2.5 Specific Emissions 68
3.1.2.6 Fuel/Air and Air/Fuel Ratio 68
3.1.2.7 Volumetric Efficiency 69
3.1.3 Relationships between Operation and Performance Parameters 69
3.1.4 Engine Operation Characteristics 70
3.1.4.1 Engine Performance Parameters 70
3.1.4.2 Indicated and Brake Power and Torque 71
3.1.4.3 Fuel Consumption Characteristics 72
3.1.5 Operating Variables Affecting SI Engine Performance, Efficiency, and Emissions Characteristics 74
3.1.5.1 Spark Timing 74
3.1.5.2 Fuel/Air Equivalent Ratio 74
3.1.6 Emission Control 77
3.1.7 Basic Technique to Improve Performance, Efficiency, and Emission Characteristics 78
3.2 4S, Compression-Ignition IC Engines 81
3.3 Two-Stroke Engines 82
3.4 Wankel Rotary Engines 86
3.5 Stirling Engines 89
3.6 Gas Turbine Engines 94
3.7 Quasi-Isothermal Brayton Cycle Engines 97
References 98

4. Electric Vehicles 99
4.1 Configurations of Electric Vehicles 99

4.2 Performance of Electric Vehicles 102
4.2.1 Traction Motor Characteristics 103
4.2.2 Tractive Effort and Transmission Requirement 104
4.2.3 Vehicle Performance 105
4.3 Tractive Effort in Normal Driving 109
4.4 Energy Consumption 114
References 116

5. Hybrid Electric Vehicles 117
5.1 Concept of Hybrid Electric Drive Trains 118
5.2 Architectures of Hybrid Electric Drive Trains 120
5.2.1 Series Hybrid Electric Drive Trains 121
5.2.2 Parallel Hybrid Electric Drive Trains 123
5.2.2.1 Torque-Coupling Parallel Hybrid Electric Drive Trains 124
5.2.2.2 Speed-Coupling Parallel Hybrid Electric Drive Trains 130
5.2.2.3 Torque-Coupling and Speed-Coupling Parallel Hybrid Electric Drive Trains 133
References 136

6. Electric Propulsion Systems 137
6.1 DC Motor Drives 142
6.1.1 Principle of Operation and Performance 142
6.1.2 Combined Armature Voltage and Field Control 146
6.1.3 Chopper Control of DC Motors 146
6.1.4 Multiquadrant Control of Chopper-Fed DC Motor Drives 151
6.1.4.1 Two-Quadrant Control of Forward Motoring and Regenerative Braking 151
6.1.4.1.1 Single Chopper with a Reverse Switch 151
6.1.4.1.2 Class C Two-Quadrant Chopper 152
6.1.4.2 Four-Quadrant Operation 154
6.2 Induction Motor Drives 155
6.2.1 Basic Operation Principles of Induction Motors 156
6.2.2 Steady-State Performance 159
6.2.3 Constant Volt/Hertz Control 162
6.2.4 Power Electronic Control 163
6.2.5 Field Orientation Control 166
6.2.5.1 Field Orientation Principles 166
6.2.5.2 Control 173
6.2.5.3 Direction Rotor Flux Orientation Scheme 175
6.2.5.4 Indirect Rotor Flux Orientation Scheme 178

6.2.6 Voltage Source Inverter for FOC 180
6.2.6.1 Voltage Control in Voltage Source Inverter 182
6.2.6.2 Current Control in Voltage Source Inverter 185
6.3 Permanent Magnetic Brush-Less DC Motor Drives 187
6.3.1 Basic Principles of BLDC Motor Drives 190
6.3.2 BLDC Machine Construction and Classification 190
6.3.3 Properties of PM Materials 193
6.3.3.1 Alnico 194
6.3.3.2 Ferrites 195
6.3.3.3 Rare-Earth PMs 195
6.3.4 Performance Analysis and Control of BLDC Machines 196
6.3.4.1 Performance Analysis 196
6.3.4.2 Control of BLDC Motor Drives 198
6.3.5 Extension of Speed Technology 199
6.3.6 Sensorless Techniques 200
6.3.6.1 Methods Using Measurables and Math 201
6.3.6.2 Methods Using Observers 201
6.3.6.3 Methods Using Back EMF Sensing 202
6.3.6.4 Unique Sensorless Techniques 203
6.4 Switched Reluctance Motor Drives 204
6.4.1 Basic Magnetic Structure 204
6.4.2 Torque Production 207
6.4.3 SRM Drive Converter 210
6.4.4 Modes of Operation 213
6.4.5 Generating Mode of Operation (Regenerative Braking) 214
6.4.6 Sensorless Control 216
6.4.6.1 Phase Flux Linkage-Based Method 218
6.4.6.2 Phase Inductance-Based Method 218
6.4.6.2.1 Sensorless Control Based on Phase Bulk Inductance 218
6.4.6.2.2 Sensorless Control Based on Phase Incremental Inductance 219
6.4.6.3 Modulated Signal Injection Methods 220
6.4.6.3.1 Frequency Modulation Method 220
6.4.6.3.2 AM and PM Methods 221
6.4.6.3.3 Diagnostic Pulse-Based Method 221
6.4.6.4 Mutually Induced Voltage-Based Method 222
6.4.6.5 Observer-Based Methods 222
6.4.7 Self-Tuning Techniques of SRM Drives 222
6.4.7.1 Self-Tuning with the Arithmetic Method 223
6.4.7.1.1 Optimization with Balanced Inductance Profiles 223
6.4.7.1.2 Optimization in the Presence of Parameter Variations 224
6.4.7.2 Self-Tuning Using an Artificial Neural Network 224

6.4.8 Vibration and Acoustic Noise in SRM 226
6.4.9 SRM Design 228
6.4.9.1 Number of Stator and Rotor Poles 228
6.4.9.2 Stator Outer Diameter 229
6.4.9.3 Rotor Outer Diameter 230
6.4.9.4 Air gap 230
6.4.9.5 Stator Arc 231
6.4.9.6 Stator Back-Iron 231
6.4.9.7 Performance Prediction 231
References 232

7. Series Hybrid Electric Drive Train Design 239
7.1 Operation Patterns 240
7.2 Control Strategies 242
7.2.1 Max. SOC-of-PPS Control Strategy 243
7.2.2 Thermostat Control Strategy (Engine-On–Off) 244
7.3 Sizing of the Major Components 246
7.3.1 Power Rating Design of the Traction Motor 246
7.3.2 Power Rating Design of the Engine/Generator 247
7.3.3 Design of PPS 249
7.3.3.1 Power Capacity of PPS 249
7.3.3.2 Energy Capacity of PPS 250
7.4 Design Example 251
7.4.1 Design of Traction Motor Size 251
7.4.2 Design of the Gear Ratio 251
7.4.3 Verification of Acceleration Performance 252
7.4.4 Verification of Gradeability 253
7.4.5 Design of Engine/Generator Size 254
7.4.6 Design of the Power Capacity of PPS 255
7.4.7 Design of the Energy Capacity of PPS 255
7.4.8 Fuel Consumption 256
References 257

8. Parallel Hybrid Electric Drive Train Design 259
8.1 Control Strategies of Parallel Hybrid Drive Train 261
8.1.1 Maximum State-of-Charge of Peaking Power Source (Max. SOC-of-PPS) Control Strategy 262
8.1.2 Engine Turn-On and Turn-Off (Engine-On–Off) Control Strategy 265
8.2 Design of Drive Train Parameters 266
8.2.1 Design of Engine Power Capacity 266
8.2.2 Design of Electric Motor Drive Power Capacity 268
8.2.3 Transmission Design 271
8.2.4 Energy Storage Design 272

8.3 Simulations 274
References 276

9. Mild Hybrid Electric Drive Train Design 277
9.1 Energy Consumed in Braking and Transmission 278
9.2 Parallel Mild Hybrid Electric Drive Train 280
9.2.1 Configuration 280
9.2.2 Operating Modes and Control Strategy 281
9.2.3 Drive Train Design 283
9.2.4 Performance 285
9.3 Series–Parallel Mild Hybrid Electric Drive Train 287
9.3.1 Configuration of the Drive Train with a Planetary Gear Unit 287
9.3.2 Operating Modes and Control 291
9.3.2.1 Speed-Coupling Operating Mode 291
9.3.2.2 Torque-Coupling Operating Mode 293
9.3.2.3 Engine-Alone Traction Mode 294
9.3.2.4 Regenerative Braking Mode 294
9.3.2.5 Engine Starting 295
9.3.3 Control Strategy 295
9.3.4 Drive Train with Floating-Stator Motor 296
References 298

10. Energy Storages 299
10.1 Electrochemical Batteries 300
10.1.1 Electrochemical Reactions 302
10.1.2 Thermodynamic Voltage 304
10.1.3 Specific Energy 304
10.1.4 Specific Power 306
10.1.5 Energy Efficiency 309
10.1.6 Battery Technologies 309
10.1.6.1 Lead-Acid Batteries 310
10.1.6.2 Nickel-based Batteries 311
10.1.6.2.1 Nickel/Iron System 311
10.1.6.2.2 Nickel/Cadmium System 311
10.1.6.2.3 Nickel–Metal Hydride (Ni–MH) Battery 312
10.1.6.3 Lithium-Based Batteries 313
10.1.6.3.1 Lithium–Polymer (Li–P) Battery 313
10.1.6.3.2 Lithium-Ion (Li-Ion) Battery 313
10.2 Ultracapacitors 314
10.2.1 Features of Ultracapacitors 315
10.2.2 Basic Principles of Ultracapacitors 315

10.2.3 Performance of Ultracapacitors 317
10.2.4 Ultracapacitor Technologies 320
10.3 Ultrahigh-Speed Flywheels....322
10.3.1 Operation Principles of Flywheels....322
10.3.2 Power Capacity of Flywheel Systems 324
10.3.3 Flywheel Technologies....326
10.4 Hybridization of Energy Storages 328
References....332

11. Fundamentals of Regenerative Braking 333
11.1 Energy Consumption in Braking....334
11.2 Braking Power and Energy on Front and Rear Wheels 334
11.3 Brake System of EVs and HEVs....338
11.3.1 Series Brake — Optimal Feel 338
11.3.2 Series Brake — Optimal Energy Recovery 339
11.3.3 Parallel Brake....341
11.4 Antilock Brake System (ABS) 343
References....345

12. Fuel Cell Vehicles 347
12.1 Operating Principles of Fuel Cells....348
12.2 Electrode Potential and Current–Voltage Curve 350
12.3 Fuel and Oxidant Consumption 354
12.4 Fuel Cell System Characteristics 355
12.5 Fuel Cell Technologies....357
12.5.1 Proton Exchange Membrane Fuel Cells 357
12.5.2 Alkaline Fuel Cells 359
12.5.3 Phosphoric Acid Fuel Cells1 361
12.5.4 Molten Carbonate Fuel Cells 361
12.5.5 Solid Oxide Fuel Cells 362
12.5.6 Direct Methanol Fuel Cells 363
12.6 Fuel Supply 364
12.6.1 Hydrogen Storage....364
12.6.1.1 Compressed Hydrogen....364
12.6.1.2 Cryogenic Liquid Hydrogen 366
12.6.1.3 Metal Hydrides 367
12.6.2 Hydrogen Production 368
12.6.2.1 Steam Reforming 369
12.6.2.2 POX Reforming 370
12.6.2.3 Autothermal Reforming 370
12.6.3 Ammonia as Hydrogen Carrier 371
12.7 Nonhydrogen Fuel Cells 371
References....372

13. Fuel Cell Hybrid Electric Drive Train Design....375
13.1 Configuration....376
13.2 Control Strategy....377
13.3 Parametric Design....379
13.3.1 Motor Power Design....379
13.3.2 Power Design of the Fuel Cell System....381
13.3.3 Design of the Power and Energy Capacity of the PPS....381
13.3.3.1 Power Capacity of the PPS....381
13.3.3.2 Energy Capacity of the PPS....381
13.4 Design Example....383
References....385

Index....387

1

Environmental Impact and History of Modern Transportation

CONTENTS

1.1 Air Pollution 2
1.1.1 Nitrogen Oxides 2
1.1.2 Carbon Monoxide 3
1.1.3 Unburned Hydrocarbons 3
1.1.4 Other Pollutants 3
1.2 Global Warming 4
1.3 Petroleum Resources 5
1.4 Induced Costs 7
1.5 Importance of Different Transportation Development Strategies to Future Oil Supply 9
1.6 History of Electric Vehicles 13
1.7 History of Hybrid Electric Vehicles 15
1.8 History of Fuel Cell Vehicles 17
References 18

The development of internal combustion engine vehicles, especially automobiles, is one of the greatest achievements of modern technology. Automobiles have made great contributions to the growth of modern society by satisfying many of its needs for mobility in everyday life. The rapid development of the automotive industry, unlike that of any other industry, has prompted the progress of human society from a primitive one to a highly developed industrial society. The automotive industry and the other industries that serve it constitute the backbone of the word's economy and employ the greatest share of the working population.

However, the large number of automobiles in use around the world has caused and continues to cause serious problems for the environment and human life. Air pollution, global warming, and the rapid depletion of the Earth's petroleum resources are now problems of paramount concern.

In recent decades, the research and development activities related to transportation have emphasized the development of high efficiency, clean, and

safe transportation. Electric vehicles, hybrid electric vehicles, and fuel cell vehicles have been typically proposed to replace conventional vehicles in the near future.

This chapter reviews the problems of air pollution, gas emissions causing global warming, and petroleum resource depletion. It also gives a brief review of the development of electric vehicles, hybrid electric vehicles, and fuel cell technology.

1.1 Air Pollution

At present, all vehicles rely on the combustion of hydrocarbon fuels to derive the energy necessary for their propulsion. Combustion is a reaction between the fuel and the air that releases heat and combustion products. The heat is converted to mechanical power by an engine and the combustion products are released into the atmosphere. A hydrocarbon is a chemical compound with molecules made up of carbon and hydrogen atoms. Ideally, the combustion of a hydrocarbon yields only carbon dioxide and water, which do not harm the environment. Indeed, green plants "digest" carbon dioxide by photosynthesis. Carbon dioxide is a necessary ingredient in vegetal life. Animals do not suffer from breathing carbon dioxide unless its concentration in air is such that oxygen is almost absent.

Actually, the combustion of hydrocarbon fuel in combustion engines is never ideal. Besides carbon dioxide and water, the combustion products contain a certain amount of nitrogen oxides (NO_x), carbon monoxides (CO), and unburned hydrocarbons (HC), all of which are toxic to human health.

1.1.1 Nitrogen Oxides

Nitrogen oxides (NO_x) result from the reaction between nitrogen in the air and oxygen. Theoretically, nitrogen is an inert gas. However, the high temperatures and pressures in engines create favorable conditions for the formation of nitrogen oxides. Temperature is by far the most important parameter in nitrogen oxide formation. The most commonly found nitrogen oxide is nitric oxide (NO), although small amounts of nitrogen dioxide (NO_2) and traces of nitrous oxide (N_2O) are also present. Once released into the atmosphere, NO reacts with oxygen to form NO_2. This is later decomposed by the Sun's ultraviolet radiation back to NO and highly reactive oxygen atoms that attack the membranes of living cells. Nitrogen dioxide is partly responsible for smog; its brownish color makes smog visible. It also reacts with atmospheric water to form nitric acid (HNO_3), which dilutes in rain. This phenomenon is referred to as "acid rain" and is responsible for the destruction of forests in industrialized countries.[1] Acid rain also contributes to the degradation of historical monuments made of marble.[1]

1.1.2 Carbon Monoxide

Carbon monoxide results from the incomplete combustion of hydrocarbons due to a lack of oxygen.[1] It is a poison to human and animal beings that breathe it. Once carbon monoxide reaches the blood cells, it fixes to the hemoglobin in place of oxygen, thus diminishing the quantity of oxygen that reaches the organs and reducing[2] the physical and mental abilities of affected living beings. Dizziness is the first symptom of carbon monoxide poisoning, which can rapidly lead to death. Carbon monoxide binds more strongly to hemoglobin than oxygen. The bonds are so strong that normal body functions cannot break them. Persons intoxicated by carbon monoxide must be treated in pressurized chambers, where the pressure makes the carbon monoxide–hemoglobin bonds easier to break.

1.1.3 Unburned Hydrocarbons

Unburned hydrocarbons are a result of the incomplete combustion of hydrocarbons.[1, 2] Depending on their nature, unburned hydrocarbons may be harmful to living beings.[2] Some of these unburned hydrocarbons may be direct poisons or carcinogenic chemicals such as particulates, benzene, or others. Unburned hydrocarbons are also responsible for smog: the Sun's ultraviolet radiations interact with unburned hydrocarbons and NO in the atmosphere to form ozone and other products. Ozone is a molecule formed of three oxygen atoms. It is colorless but very dangerous, and poisons as it attacks the membranes of living cells, thus causing them to age prematurely or to die. Toddlers, older people, and asthmatic humans suffer greatly from exposure to high ozone concentrations. Annually, deaths from high ozone peaks in polluted cities are reported.[3]

1.1.4 Other Pollutants

Impurities in fuels result in the emission of pollutants. The major impurity is sulfur, which is mostly found in diesel and jet fuel and also in gasoline and natural gas.[1] The combustion of sulfur (or sulfur compounds such as hydrogen sulfide) with oxygen releases sulfur oxides (SO_x). Sulfur dioxide (SO_2) is the major product of this combustion. Upon contact with air, it forms sulfur trioxide, which later reacts with water to form sulfuric acid, a major component of acid rain. It should be noted that sulfur oxide emissions originate from transportation sources, but also largely from the combustion of coal in power plants and steel factories. In addition, there is debate over the exact contribution of natural sources such as volcanoes.

Petroleum companies add chemical compounds to their fuels in order to improve the performance or lifetime of engines.[1] Tetraethyl lead, often referred to simply as "lead," was used to improve the knock resistance of gasoline and therefore allow for better engine performance. However, the

combustion of this chemical releases lead metal, which is responsible for a neurological disease called "saturnism." Its use is now forbidden in most developed countries and it has been replaced by other chemicals.[1]

1.2 Global Warming

Global warming is a result of the "greenhouse effect" induced by the presence of carbon dioxide and other gases, such as methane, in the atmosphere. These gases trap the Sun's infrared radiation reflected by the ground, thus retaining the energy in the atmosphere and increasing the temperature. An increased Earth temperature results in major ecological damages to its ecosystems and in many natural disasters that affect human populations.[2]

Among the ecological damages induced by global warming, the disappearance of some endangered species is a concern because it destabilizes the natural resources that feed some populations. There are also concerns about the migration of some species from warm seas to previously colder northern seas, where they can potentially destroy indigenous species and the economies that live off those species. This may be happening in the Mediterranean Sea, where barracudas from the Red Sea have been observed.

Natural disasters command our attention more than ecological disasters because of the amplitude of the damage they cause. Global warming is believed to have induced meteorological phenomena such as "El Niño," which disturbs the South-Pacific region and regularly causes tornadoes, inundations, and dryness. The melting of the polar icecaps, another major result of global warming, raises the sea level and can cause the permanent inundation of coastal regions, and sometimes of entire countries.

Carbon dioxide is the result of the combustion of hydrocarbons and coal. Transportation accounts for a large share (32% from 1980 to 1999) of carbon dioxide emissions. The distribution of carbon dioxide emissions is shown in Figure 1.1.[4]

Figure 1.2 shows the trend in carbon dioxide emissions. The transportation sector is clearly now the major contributor of carbon dioxide emissions. It should be noted that developing countries are rapidly increasing their transportation sector, and these countries represent a very large share of the world's population. Further discussion is provided in the next subsection.

The large amounts of carbon dioxide released in the atmosphere by human activities are believed to be largely responsible for the increase in global Earth temperature observed during recent decades (Figure 1.3). It is important to note that carbon dioxide is indeed digested by plants and sequestrated by the oceans in the form of carbonates. However, these natural assimilation processes are limited and cannot assimilate all of the emitted carbon dioxide, resulting in an accumulation of carbon dioxide in the atmosphere.

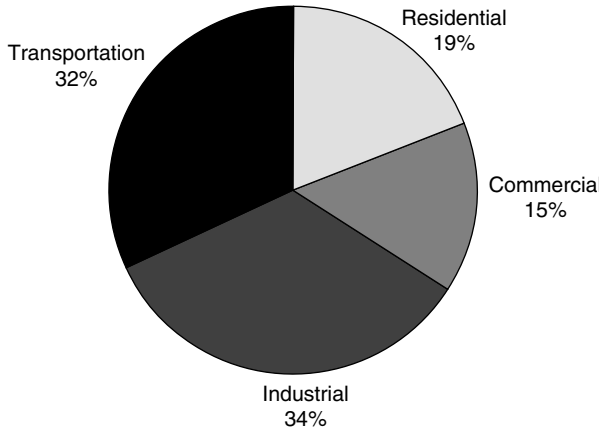

FIGURE 1.1
Carbon dioxide emission distribution from 1980 to 1999

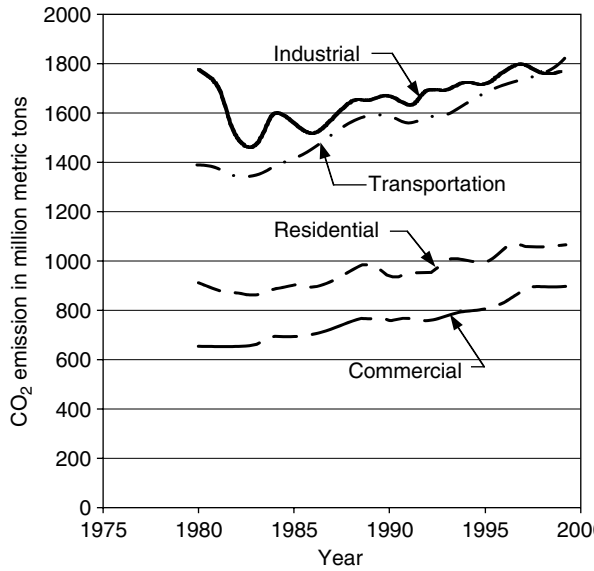

FIGURE 1.2
Evolution of carbon dioxide emission

1.3 Petroleum Resources

The vast majority of fuels used for transportation are liquid fuels originating from petroleum. Petroleum is a fossil fuel, resulting from the decomposition of living matters that were imprisoned millions of years ago (Ordovician,

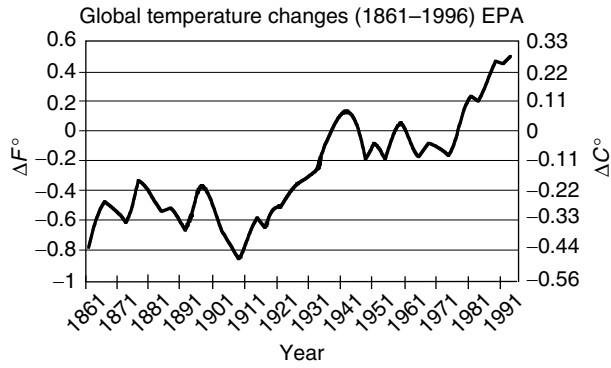

FIGURE 1.3
Global Earth atmospheric temperature. (*Source*: IPCC (1995) updated.)

600 to 400 million years ago) in geologically stable layers. The process is roughly the following: living matters (mostly plants) die and are slowly covered by sediments. Over time, these accumulating sediments form thick layers, and transform to rock. The living matters are trapped in a closed space, where they encounter high pressures and temperatures, and slowly transform into either hydrocarbons or coal, depending on their nature. This process took millions of years to accomplish. This is what makes the Earth's resources in fossil fuels finite.

The proved reserves are "those quantities that geological and engineering information indicates with reasonable certainty can be recovered in the future from known reservoirs under existing economic and operating conditions".[5] Therefore, they do not constitute an indicator of the Earth's total reserves. The proved reserves, as they are given in the British Petroleum 2001 estimate,[5] are given in billion tons in Table 1.1. The R/P ratio is the number of years that the proved reserves would last if the production were to continue at its current level. This ratio is also given in Table 1.1 for each region.[5]

The oil extracted nowadays is the easily extractable oil that lies close to the surface, in regions where the climate does not pose major problems. It is believed that far more oil lies underneath the crust of the Earth in such regions like Siberia, and the American and Canadian Arctic. In these regions, the climate and ecological concerns are major obstacles to extracting or prospecting for oil. The estimation of the Earth's total reserves is a difficult task for political and technical reasons. A 2000 estimation of undiscovered oil resources by the U.S. Geological Survey is given in Table 1.2.[6]

Although the R/P ratio does not include future discoveries, it is significant. Indeed, it is based on proved reserves, which are easily accessible to this day. The amount of future oil discoveries is hypothetical, and the newly discovered oil will not be easily accessible. The R/P ratio is also based on the hypothesis that production will remain constant. It is obvious, however, that consumption (and therefore production) is increasing yearly to keep up with the growth of

TABLE 1.1

Proved Petroleum Reserves in 2000

Region	Proved Reserves in 2000 in Billion Tons	R/P ratio
North America	8.5	13.8
South and Central America	13.6	39.1
Europe	2.5	7.7
Africa	10	26.8
Middle East	92.5	83.2
Former USSR	9.0	22.7
Asia Pacific	6.0	15.6
Total world	142.1	39.9

TABLE 1.2

U.S. Geological Survey Estimate of Undiscovered Oil in 2000

Region	Undiscovered Oil in 2000 in Billion Tons
North America	19.8
South and Central America	14.3
Europe	3.0
Sub-Saharan Africa and Antarctica	9.7
Middle East and North Africa	31.2
Former USSR	15.7
Asia Pacific	4.0
World (potential growth)	98.3 (91.5)

developed and developing economies. Consumption is likely to increase in gigantic proportions with the rapid development of some largely populated countries, particularly in the Asia-Pacific region. The plot of Figure 1.4 shows the trend in oil consumption over the last 20 years.[7] Oil consumption is given in thousand barrels per day (1 barrel is about 8 metric tons).

Despite the drop in oil consumption for Eastern Europe and the former USSR, the world trend is clearly increasing, as shown in Figure 1.5. The fastest growing region is Asia-Pacific, where most of the world's population lives. An explosion in oil consumption is to be expected, with a proportional increase in pollutant emissions and carbon dioxide emissions.

1.4 Induced Costs

The problems associated with the frenetic combustion of fossil fuels are many: pollution, global warming, and the foreseeable exhaustion of resources, among others. Although difficult to estimate, the costs associated with these problems are huge and indirect,[8] and may be financial, human, or both.

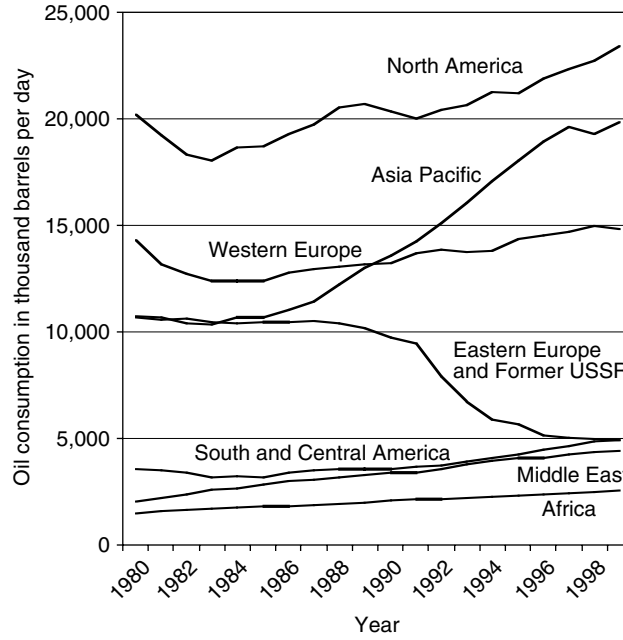

FIGURE 1.4
Oil consumption per region

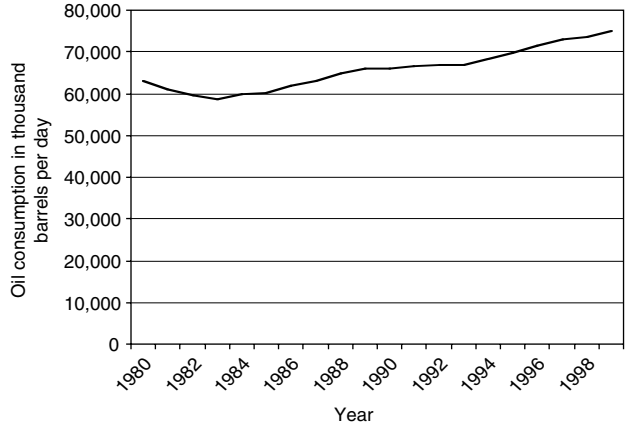

FIGURE 1.5
World oil consumption

Costs induced by pollution include, but are not limited to, health expenses, the cost of replanting forests devastated by acid rain, and the cost of cleaning and fixing monuments corroded by acid rain. Health expenses probably represent the largest share of these costs, especially in developed countries with socialized medicine or health-insured populations.

Costs associated with global warming are difficult to assess. They may include the cost of the damages caused by hurricanes, lost crops due to dryness, damaged properties due to floods, and international aid to relieve the affected populations. The amount is potentially huge.

Most of the petroleum-producing countries are not the largest petroleum-consuming countries. Most of the production is located in the Middle East, while most of the consumption is located in Europe, North America, and Asia-Pacific. As a result, consumers have to import their oil and depend on the producing countries. This issue is particularly sensitive in the Middle East, where political turmoil affected the oil delivery to Western countries in 1973 and 1977. The Gulf War, Iran–Iraq war, and the constant surveillance of the area by the U.S. and allied forces come at a cost that is both human and financial. The dependency of Western economies upon a fluctuating oil supply is potentially expensive. Indeed, a shortage in oil supply causes a serious slowing down of the economy, resulting in damaged perishable goods, lost business opportunities, and the eventual impossibility of running businesses.

In searching for a solution to the problems associated with oil consumption, one has to take into account those induced costs. This is difficult because the cost is not necessarily asserted where it is generated. Many of the induced costs cannot be counted in asserting the benefits of an eventual solution. The solution to these problems will have to be economically sustainable and commercially viable without government subsidies in order to sustain itself in the long run. Nevertheless, it remains clear that any solution to these problems — even if it is only a partial solution — will indeed result in cost savings and will benefit the payers.

1.5 Importance of Different Transportation Development Strategies to Future Oil Supply

The number of years that the oil resources of the Earth can support our oil supply completely depends on the discovery of new oil reserves and cumulative oil production (as well as cumulative oil consumption). Historical data show that the new discovery of oil reserves occurs slowly. On the other hand, the consumption shows a high growth rate, as shown in Figure 1.6. If oil discovery and consumption follow current trends, the world oil resource will be used by about 2038.[9,10]

It is becoming more and more difficult to discover new reserves of petroleum under the Earth. The cost of exploring new oil fields is becoming higher and higher. It is believed that the scenario of the oil supply will not change much if the consumption rate cannot be significantly reduced.

As shown in Figure 1.7, the transportation sector is the primary user of petroleum, consuming 49% of the oil used in the world in 1997. The patterns of consumption of industrialized and developing countries are quite different,

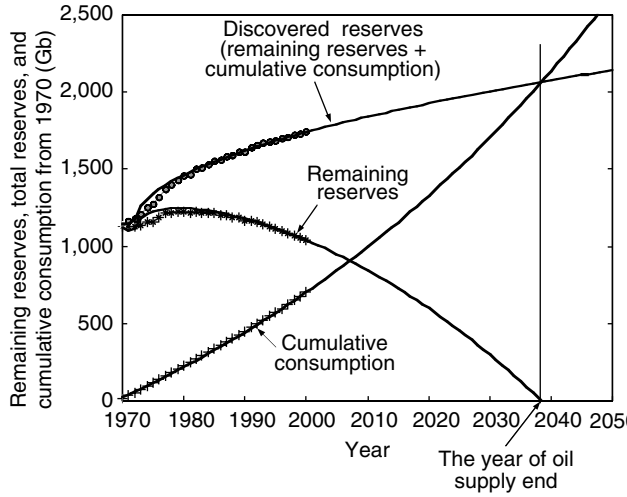

FIGURE 1.6
World oil discovery, remaining reserves, and cumulative consumption

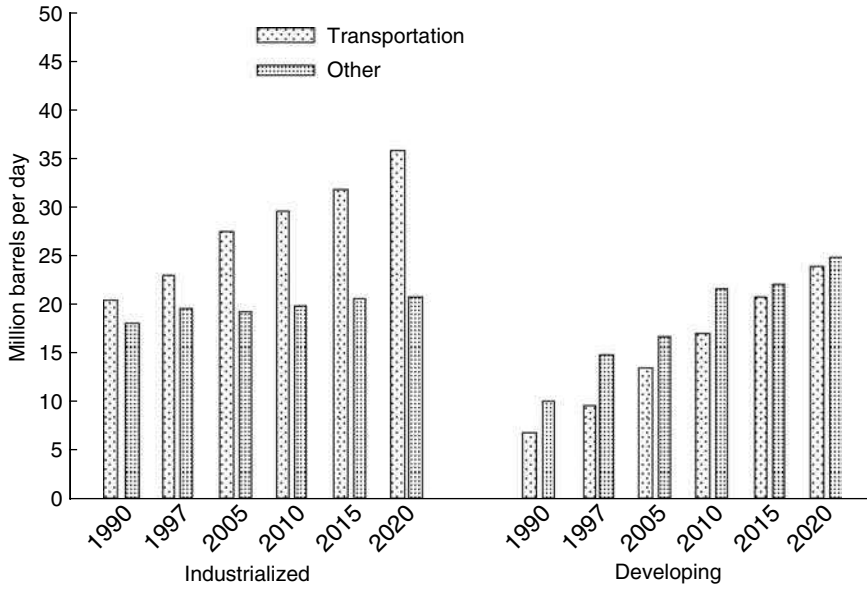

FIGURE 1.7
World oil consumption

however. In the heat and power segments of the markets in industrialized countries, nonpetroleum energy sources were able to compete with and substitute for oil throughout the 1980s, and by 1990, oil consumption in other sectors was less than in the transportation sector.

Most of the gains in worldwide oil use occur in the transportation sector. Of the total increase (11.4 million barrels per day) projected for industrialized countries from 1997 to 2020, 10.7 million barrels per day are attributed to the transportation sector, where few alternatives are economical until late in the forecast.

In developing countries, the transportation sector shows the fastest projected growth in petroleum consumption, promising to rise nearly to the level of nontransportation energy use by 2020. In the developing world, however, unlike in industrialized countries, oil use for purposes other than transportation is projected to contribute 42% of the total increase in petroleum consumption. The growth in nontransportation petroleum consumption in developing countries is caused in part by the substitution of petroleum products for noncommercial fuels (such as wood burning for home heating and cooking).

Improving the fuel economy of vehicles has a crucial impact on oil supply. So far, the most promising technologies are hybrid electric vehicles and fuel cell vehicles. Hybrid vehicles, using current internal combustion engines (ICEs) as their primary power source and batteries/electric motors as the peaking power source, have a much higher operation efficiency than those powered by ICEs alone. The hardware and software of this technology are almost ready for industrial manufacturing. On the other hand, fuel cell vehicles, which are potentially more efficient and cleaner than hybrid electric vehicles, are still in the laboratory stage and it will take a long time to overcome technical hurdles for commercialization.

Figure 1.8 shows the generalized annual fuel consumptions of different development strategies of next-generation vehicles. Curve a–b–c represents the annual fuel consumption trend of current vehicles, which is assumed to have a 1.3% annual growth rate. This annual growth rate is assumed to be the annual growth rate of the total vehicle number. Curve a–d–e represents a development strategy in which conventional vehicles gradually become hybrid vehicles during the first 20 years, and after 20 years all the vehicles will be hybrid vehicles. In this strategy, it is assumed that the hybrid vehicle is 25% more efficient than a current conventional vehicle (25% less fuel consumption). Curve a–b–f–g represents a strategy in which, in the first 20 years, fuel cell vehicles are in a developing stage while current conventional vehicles are still on the market. In the second 20 years, fuel cell vehicles will gradually go to market, starting from point b and becoming totally fuel cell powered at point f. In this strategy, it is assumed that 50% less fuel will be consumed by fuel cell vehicles than that by current conventional vehicles. Curve a–d–f–g represents the strategy by which the vehicles become hybrid in the first 20 years, and fuel cell powered in the second 20 years.

Cumulative oil consumption is more meaningful because it involves annual consumption and the time effect, and is directly associated with the reduction of oil reserves, as shown in Figure 1.6. Figure 1.9 shows the scenario of generalized cumulative oil consumptions of the development strategies mentioned above. Although fuel cell vehicles are more efficient than

hybrid vehicles, the cumulative fuel consumption by strategy a–b–f–g (a fuel cell vehicle in the second 20 years) is higher than strategy a–d–e (a hybrid vehicle in the first 20 years) within 45 years, due to the time effect. From Figure 1.8, it is clear that strategy a–d–f–g (a hybrid vehicle in the first 20 years and a fuel cell vehicle in the second 20 years) is the best. Figure 1.6 and Figure 1.9 reveal another important fact: that fuel cell vehicles should not rely on oil products because of the difficulty of future oil supply 45 years

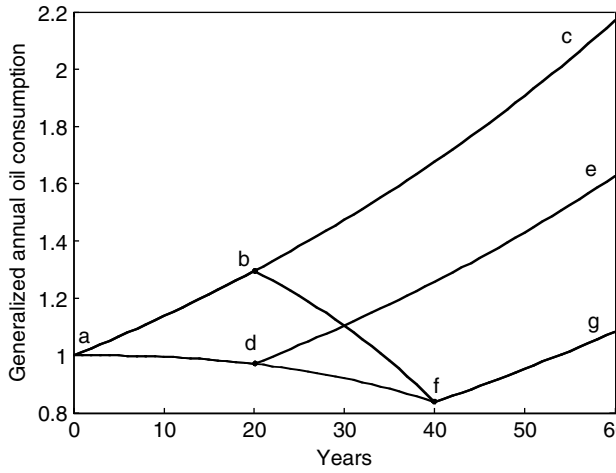

FIGURE 1.8
Comparison of the annual fuel consumption between different development strategies of the next-generation vehicles

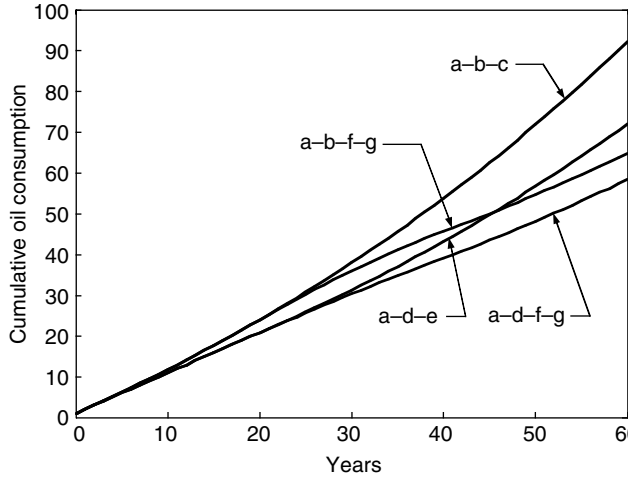

FIGURE 1.9
Comparison of the cumulative fuel consumption between different development strategies of next-generation vehicles

later. Thus, the best development strategy of next-generation transportation would be to commercialize hybrid electric vehicles immediately and, at the same time, do the best to commercialize nonpetroleum fuel cell vehicles as soon as possible.

1.6 History of Electric Vehicles

The first electric vehicle was built by Frenchman Gustave Trouvé in 1881. It was a tricycle powered by a 0.1 hp DC motor fed by lead–acid batteries. The whole vehicle and its driver weighed approximately 160 kg. A vehicle similar to this was built in 1883 by two British professors.[11] These early realizations did not attract much attention from the public because the technology was not mature enough to compete with horse carriages. Speeds of 15 km/h and a range of 16 km were not exciting for potential customers. The 1864 Paris to Rouen race changed it all: the 1135 km were run in 48 h and 53 min at an average speed of 23.3 km/h. This speed was by far superior to that possible with horse-drawn carriages. The general public became interested in horseless carriages or automobiles, as these vehicles were now called.

The following 20 years were an era during which electric vehicles competed with their gasoline counterparts. This was particularly true in America, where there were not many paved roads outside a few cities. The limited range of electric vehicles was not a problem. However, in Europe, the rapidly increasing number of paved roads called for extended ranges, thus favoring gasoline vehicles.[11]

The first commercial electric vehicle was Morris and Salom's Electroboat. This vehicle was operated as a taxi in New York City by a company created by its inventors. The Electroboat proved to be more profitable than horse cabs despite a higher purchase price (around $3000 vs. $1200). It could be used for three shifts of 4 h with 90-min recharging periods in between. It was powered by two 1.5 hp motors that allowed a maximum speed of 32 km/h and a 40-km range.[11]

The most significant technical advance of that era was the invention of regenerative braking by Frenchman M.A. Darracq on his 1897 coupe. This method allows recuperating the vehicle's kinetic energy while braking and recharging the batteries, which greatly enhances the driving range. It is one of the most significant contributions to electric and hybrid electric vehicle technology as it contributes to energy efficiency more than anything else in urban driving.

In addition, among the most significant electric vehicles of that era was the first vehicle ever to reach 100 km/h. It was "La Jamais Contente" built by Frenchman Camille Jenatzy. Note that Studebaker and Oldsmobile first started in business by building electric vehicles.

As gasoline automobiles became more powerful, more flexible, and, above all, easier to handle, electric vehicles started to disappear. Their high cost did

not help, but it is their limited driving range and performance that really impaired them vs. their gasoline counterparts. The last commercially significant electric vehicles were released around 1905. During nearly 60 years, the only electric vehicles sold were common golf carts and delivery vehicles.

In 1945, three researchers at Bell Laboratories invented a device that was meant to revolutionize the world of electronics and electricity: the transistor. It quickly replaced vacuum tubes for signal electronics and soon the thyristor was invented, which allowed switching high currents at high voltages. This made it possible to regulate the power fed to an electric motor without the very inefficient rheostats, and allowed the running of AC motors at variable frequency. In 1966, General Motors (GM) built the Electrovan, which was propelled by induction motors that were fed by inverters built with thyristors.

The most significant electric vehicle of that era was the Lunar Roving Vehicle, which the Apollo astronauts used on the Moon. The vehicle itself weighed 209 kg and could carry a payload of 490 kg. The range was around 65 km. The design of this extraterrestrial vehicle, however, has very little significance down on Earth. The absence of air and the lower gravity on the Moon, and the low speed made it easier for engineers to reach an extended range with limited technology.

During the 1960s and 1970s, concerns about the environment triggered some research on electric vehicles. However, despite advances in battery technology and power electronics, their range and performance were still obstacles.

The modern electric vehicle era culminated during the 1980s and early 1990s with the release of a few realistic vehicles by firms such as GM with the EV1 and PSA with the 106 Electric. Although these vehicles represented a real achievement, especially when compared with early realizations, it became clear during the early 1990s that electric automobiles could never compete with gasoline automobiles for range and performance. The reason is that in batteries the energy is stored in the metal of electrodes, which weigh far more than gasoline for the same energy content. The automotive industry abandoned the electric vehicle to conduct research on hybrid electric vehicles. After a few years of development, these are far closer to the assembly line for mass production than electric vehicles have ever been.

In the context of the development of the electric vehicle, it is battery technology that is the weakest, blocking the way of electric vehicles to market. Great effort and investment have been put into battery research, with the intention of improving performance to meet the electric vehicle's requirement. Unfortunately, progress has been very limited. Performance is far behind the requirement, especially energy storage capacity per unit weight and volume. This poor energy storage capability of batteries limits electric vehicles only to some specific applications, such as at airports and railroad stations, on mail delivery routes, and on golfcourses, etc. In fact, basic study[12] shows that electric vehicles will never be able to challenge liquid-fueled vehicles even with the optimistic value of battery energy capacity.

Thus, in recent years, advanced vehicle technology research has turned to hybrid electric vehicles as well as fuel cell vehicles.

1.7 History of Hybrid Electric Vehicles

Surprisingly, the concept of a hybrid electric vehicle is almost as old as the automobile itself. The primary purpose, however, was not so much to lower the fuel consumption but rather to assist the ICE to provide an acceptable level of performance. Indeed, in the early days, ICE engineering was less advanced than electric motor engineering.

The first hybrid vehicles reported were shown at the Paris Salon of 1899.[13] These were built by the Pieper establishments of Liège, Belgium and by the Vendovelli and Priestly Electric Carriage Company, France. The Pieper vehicle was a parallel hybrid with a small air-cooled gasoline engine assisted by an electric motor and lead–acid batteries. It is reported that the batteries were charged by the engine when the vehicle coasted or was at a standstill. When the driving power required was greater than the engine rating, the electric motor provided additional power. In addition to being one of the two first hybrid vehicles, and being the first parallel hybrid vehicle, the Pieper was undoubtedly the first electric starter.

The other hybrid vehicle introduced at the Paris Salon of 1899 was the first series hybrid electric vehicle and was derived from a pure electric vehicle commercially built by the French firm Vendovelli and Priestly [13]. This vehicle was a tricycle, with the two rear wheels powered by independent motors. An additional 3/4 hp gasoline engine coupled to a 1.1 kW generator was mounted on a trailer and could be towed behind the vehicle to extend its range by recharging the batteries. In the French case, the hybrid design was used to extend the range of an electric vehicle, and not to supply additional power to a weak ICE.

Frenchman Camille Jenatzy presented a parallel hybrid vehicle at the Paris Salon of 1903. This vehicle combined a 6 hp gasoline engine with a 14 hp electric machine that could either charge the batteries from the engine or assist them later. Another Frenchman, H. Krieger, built the second reported series hybrid vehicle in 1902. His design used two independent DC motors driving the front wheels. They drew their energy from 44 lead–acid cells that were recharged by a 4.5 hp alcohol spark-ignited engine coupled to a shunt DC generator.

Other hybrid vehicles, both of the parallel and series type, were built during a period ranging from 1899 until 1914. Although electric braking has been used in these early designs, there is no mention of regenerative braking. It is likely that most, possibly even all, designs used dynamic braking by short circuiting or by placing a resistance in the armature of the traction motors. The Lohner-Porsche vehicle of 1903 is a typical example of this

approach.[13] The frequent use of magnetic clutches and magnetic couplings should be noted.

Early hybrid vehicles were built in order to assist the weak ICEs of that time or to improve the range of electric vehicles. They made use of the basic electric technologies that were then available. In spite of the great creativity that presided in their design, these early hybrid vehicles could no longer compete with the greatly improved gasoline engines that came into use after World War I. The gasoline engine made tremendous improvements in terms of power density, the engines became smaller and more efficient, and there was no longer a need to assist them with electric motors. The supplementary cost of having an electric motor and the hazards associated with the –acid batteries were key factors in the disappearance of hybrid vehicles from the market after World War I.

However, the greatest problem that these early designs had to cope with was the difficulty of controlling the electric machine. Power electronics did not become available until the mid-1960s and early electric motors were controlled by mechanical switches and resistors. They had a limited operating range that was incompatible with efficient operation. Only with great difficulty could they be made compatible with the operation of a hybrid vehicle.

Dr. Victor Wouk is recognized as the modern investigator of the hybrid electric vehicle movement.[13] In 1975, along with his colleagues, he built a parallel hybrid version of a Buick Skylark.[13] The engine was a Mazda rotary engine, coupled to a manual transmission. It was assisted by a 15 hp separately excited DC machine, located in front of the transmission. Eight 12 V automotive batteries were used for energy storage. A top speed of 80 mph (129 km/h) was achieved with acceleration from 0 to 60 mph in 16 sec.

The series hybrid design was revived by Dr. Ernest H. Wakefield in 1967, when working for Linear Alpha Inc. A small engine-AC generator, with an output of 3 kW, was used to keep a battery pack charged. However, the experiments were quickly stopped because of technical problems. Other approaches studied during the 1970s and early 1980s used range extenders, similar in concept to the French Vendovelli and Priestly 1899 design. These range extenders were intended to improve a range of electric vehicles that never reached the market. Other prototypes of hybrid vehicles were built by the Electric Auto Corporation in 1982 and by the Briggs & Stratton Corporation in 1980. Both of these were parallel hybrid vehicles.

Despite the two oil crises of 1973 and 1977, and despite growing environmental concerns, no hybrid electric vehicle made it to the market. The researchers' focus was drawn by the electric vehicle, of which many prototypes were built during the 1980s. The lack of interest in hybrid electric vehicles during this period may be attributed to the lack of practical power electronics, modern electric motors, and battery technologies. The 1980s witnessed a reduction in conventional ICE-powered vehicle sizes, the introduction of catalytic converters, and the generalization of fuel injection.

The hybrid electric vehicle concept drew great interest during the 1990s when it became clear that electric vehicles would never achieve the objective

of saving energy. The Ford Motor Corporation initiated the Ford Hybrid Electric Vehicle Challenge, which drew efforts from universities to develop hybrid versions of production automobiles.

Automobile manufacturers around the world built prototypes that achieved tremendous improvements in fuel economy over their ICE-powered counterparts. In the U.S., Dodge built the Intrepid ESX 1, 2, and 3. The ESX-1 was a series hybrid vehicle, powered by a small turbocharged three-cylinder diesel engine and a battery pack. Two 100 hp electric motors were located in the rear wheels. The U.S. government launched the Partnership for a New Generation of Vehicles (PNGV), which included the goal of a mid-size sedan that could achieve 80 mpg. The Ford Prodigy and GM Precept resulted from this effort. The Prodigy and Precept vehicles were parallel hybrid electric vehicles powered by small turbocharged diesel engines coupled to dry clutch manual transmissions. Both of them achieved the objective but production did not follow.

Efforts in Europe are represented by the French Renault Next, a small parallel hybrid vehicle using a 750 cc spark-ignited engine and two electric motors. This prototype achieved 29.4 km/l (70 mpg) with maximum speed and acceleration performance comparable to conventional vehicles. Volkswagen also built a prototype, the Chico. The base was a small electric vehicle, with a nickel–metal hydride battery pack and a three-phase induction motor. A small two-cylinder gasoline engine was used to recharge the batteries and provide additional power for high-speed cruising.

The most significant effort in the development and commercialization of hybrid electric vehicles was made by Japanese manufacturers. In 1997, Toyota released the Prius sedan in Japan. Honda also released its Insight and Civic Hybrid. These vehicles are now available throughout the world. They achieve excellent figures of fuel consumption. Toyota Prius and Honda Insight vehicles have a historical value in that they are the first hybrid vehicles commercialized in the modern era to respond to the problem of personal vehicle fuel consumption.

1.8 History of Fuel Cell Vehicles

As early as 1839, Sir William Grove (often referred to as the "Father of the Fuel Cell") discovered that it might be possible to generate electricity by reversing the electrolysis of water. It was not until 1889 that two researchers, Charles Langer and Ludwig Mond, coined the term "fuel cell" as they were trying to engineer the first practical fuel cell using air and coal gas. While further attempts were made in the early 1900s to develop fuel cells that could convert coal or carbon into electricity, the advent of the ICE temporarily quashed any hopes of further development of the fledgling technology.

Francis Bacon developed what was perhaps the first successful fuel cell device in 1932, with a hydrogen–oxygen cell using alkaline electrolytes and nickel electrodes — inexpensive alternatives to the catalysts used by Mond and Langer. Due to a substantial number of technical hurdles, it was not until 1959 that Bacon and company first demonstrated a practical 5-kW fuel cell system. Harry Karl Ihrig presented his now-famous 20-hp fuel cell-powered tractor that same year.

NASA also began building compact electric generators for use on space missions in the late 1950s. NASA soon came to fund hundreds of research contracts involving fuel cell technology. Fuel cells now have a proven role in space programs, after supplying electricity to several space missions.

In more recent decades, a number of manufacturers — including major automakers — and various federal agencies have supported ongoing research into the development of fuel cell technology for use in fuel cell vehicles and other applications.[14] Hydrogen production, storage, and distribution are the biggest challenges. Truly, fuel cell-powered vehicles still have a long way to go before they can be introduced in the market.

References

[1] C.R. Ferguson and A.T. Kirkpatrick, *Internal Combustion Engines — Applied Thermo-Sciences*, 2nd ed., John Wiley & Sons, New York 2001.

[2] U.S. Environmental Protection Agency (EPA), Automobile emissions: an overview, *EPA 400-F-92-007*, Fact Sheet OMS-5, August 1994.

[3] U.S. Environmental Protection Agency (EPA), Automobiles and ozone, *EPA 400-F-92-006*, Fact Sheet OMS-4, January 1993.

[4] Carbon dioxide emissions from energy consumption by sector, 1980–1999, Energy Information Administration, U.S. Department of Energy, http://www.eia.doe.gov/emeu/aer/txt/tab1202.htm.

[5] BP statistical review of world energy — oil, 2001, http://www.bp.com/downloads/837/global_oil_section.pdf.

[6] USGS World Energy Assessment Team, World undiscovered assessment results summary, *U.S. Geological Survey Digital Data Series 60*, http://greenwood.cr.usgs.gov/energy/WorldEnergy/DDS-60/sum1.html#TOP.

[7] World petroleum consumption, 1980–1999, International Energy Database, Energy Information Administration, U.S. Department of Energy, January 2001.

[8] D. Doniger, D. Friedman, R. Hwang, D. Lashof, and J. Mark, Dangerous addiction: ending America's oil dependence, *National Resources Defense Council and Union of Concerned Scientists*, 2002.

[9] M. Ehsani et al., Impact of hybrid electric vehicles on the world's petroleum consumption and supply, *Society of Automotive Engineers (SAE) Future Transportation Technology Conference*, Paper no. 2003-01-2310, 2003.

[10] J.E. Hake, International energy outlook — 2000 with projection to 2020, http://tonto.eia.doe.gov/FTPROOT/presentations/ieo2000/sld008.htm.

[11] E.H. Wakefield, *History of the Electric Automobile: Battery-Only Powered Cars*, Society of Automotive Engineers (SAE), Warrendale, PA, 1994.
[12] Y. Gao and M. Ehsani, An investigation of battery technologies for the Army's hybrid vehicle application, in *Proceedings of the IEEE 56th Vehicular Technology Conference*, Vancouver, British Columbia, Canada, Sept. 2002.
[13] E.H. Wakefield, *History of the Electric Automobile: Hybrid Electric Vehicles*, Society of Automotive Engineers (SAE), 1998.
[14] California Fuel Cell Partnership, http://www.fuelcellpartnership.org/.

2

Vehicle Fundamentals

CONTENTS

2.1 General Description of Vehicle Movement 22
2.2 Vehicle Resistance 23
2.2.1 Rolling Resistance 23
2.2.2 Aerodynamic Drag 25
2.2.3 Grading Resistance 26
2.3 Dynamic Equation 27
2.4 Tire–Ground Adhesion and Maximum Tractive Effort 29
2.5 Power Train Tractive Effort and Vehicle Speed 31
2.6 Vehicle Power Plant and Transmission Characteristics 33
2.6.1 Power Plant Characteristics 34
2.6.2 Transmission Characteristics 36
2.6.2.1 Gear Transmission 37
2.6.2.2 Hydrodynamic Transmission 39
2.6.2.3 Continuously Variable Transmission 43
2.7 Vehicle Performance 44
2.7.1 Maximum Speed of a Vehicle 45
2.7.2 Gradeability 46
2.7.3 Acceleration Performance 46
2.8 Operating Fuel Economy 49
2.8.1 Fuel Economy Characteristics of Internal Combustion Engines 49
2.8.2 Calculation of Vehicle Fuel Economy 50
2.8.3 Basic Techniques to Improve Vehicle Fuel Economy 52
2.9 Braking Performance 54
2.9.1 Braking Force 54
2.9.2 Braking Distribution on Front and Rear Axles 55
References 60

Vehicle operation fundamentals mathematically describe vehicle behavior based on the general principles of mechanics. A vehicle, consisting of thousands of components, is a complex system. To describe its behavior fully, sophisticated mechanical and mathematical knowledge is needed. A great

amount of literature of this kind already exists. Since this book proposes to discuss electric and hybrid electric power trains, the discussion of vehicle fundamentals will be restricted to one-dimensional movement. This chapter will therefore focus on vehicle performance speed, gradeability, acceleration, fuel consumption, and braking performance.

2.1 General Description of Vehicle Movement

Figure 2.1 shows the forces acting on a vehicle moving up a grade. The tractive effort, F_t, in the contact area between tires of the driven wheels and the road surface propels the vehicle forward. It is produced by the power plant torque and is transferred through transmission and final drive to the drive wheels. While the vehicle is moving, there is resistance that tries to stop its movement. The resistance usually includes tire rolling resistance, aerodynamic drag, and uphill resistance. According to Newton's second law, vehicle acceleration can be written as

$$\frac{dV}{dt} = \frac{\Sigma F_t - \Sigma F_{tr}}{\delta M_v}, \tag{2.1}$$

where V is vehicle speed, ΣF_t is the total tractive effort of the vehicle, ΣF_{tr} is the total resistance, M_v is the total mass of the vehicle, and δ is the mass factor, which is an effect of rotating components in the power train. Equation

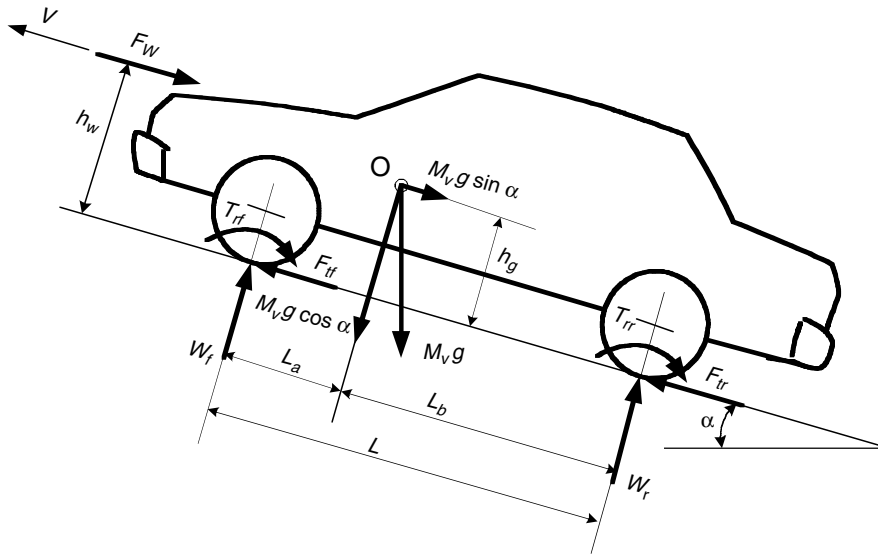

FIGURE 2.1
Forces acting on a vehicle

(2.1) indicates that speed and acceleration depend on tractive effort, resistance, and vehicle mass.

2.2 Vehicle Resistance

As shown in Figure 2.1, vehicle resistance opposing its movement includes rolling resistance of the tires, appearing in Figure 2.1 as rolling resistance torque T_{rf} and T_{rr}, aerodynamic drag, F_w, and grading resistance (the term $M_v g \sin \alpha$ in Figure 2.1). All of the resistances will be discussed in detail in the following sections.

2.2.1 Rolling Resistance

The rolling resistance of tires on hard surfaces is primarily caused by hysteresis in the tire materials. This is due to the deflection of the carcass while the tire is rolling. The hysteresis causes an asymmetric distribution of ground reaction forces. The pressure in the leading half of the contact area is larger than that in the trailing half, as shown in Figure 2.2(a). This phenomenon results in the ground reaction force shifting forward. This forwardly shifted ground reaction force, with the normal load acting on the wheel center, creates a moment, that opposes the rolling of the wheel. On soft surfaces, the rolling resistance is primarily caused by deformation of the ground surface as shown in Figure 2.2(b). The ground reaction force almost completely shifts to the leading half.

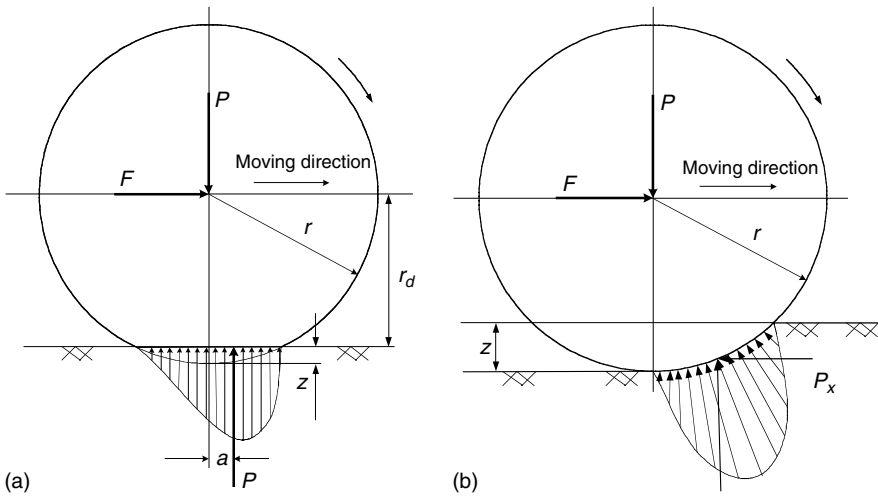

FIGURE 2.2
Tire deflection and rolling resistance on a (a) hard and (b) soft road surface

The moment produced by the forward shift of the resultant ground reaction force is called the rolling resistant moment, as shown in Figure 2.2(a), and can be expressed as

$$T_r = Pa. \tag{2.2}$$

To keep the wheel rolling, a force F, acting on the center of the wheels, is required to balance this rolling resistant moment. This force is expressed as

$$F = \frac{T_r}{r_d} = \frac{Pa}{r_d} = Pf_r, \tag{2.3}$$

where r_d is the effective radius of the tire and $f_r = a/r_d$ is called the rolling resistance coefficient. In this way, the rolling resistant moment can be replaced equivalently by a horizontal force acting on the wheel center in the opposite direction of the movement of the wheel. This equivalent force is called rolling resistance with a magnitude of

$$F_r = Pf_r, \tag{2.4}$$

where P is the normal load, acting on the center of the rolling wheel. When a vehicle is operated on a slope road, the normal load, P, should be replaced by the component, which is perpendicular to the road surface. That is,

$$F_r = Pf_r \cos\alpha, \tag{2.5}$$

where α is the road angle (refer to Figure 2.1).

The rolling resistance coefficient, f_r, is a function of the tire material, tire structure, tire temperature, tire inflation pressure, tread geometry, road roughness, road material, and the presence or absence of liquids on the road. The typical values of rolling resistance coefficients on various roads are given in Table 2.1.[2] For fuel saving in recent years, low-resistance tires for passenger cars have been developed. Their rolling resistance coefficient is less than 0.01.

The values given in Table 2.1 do not take into account their variations with speed. Based on experimental results, many empirical formulae have been proposed for calculating the rolling resistance on a hard surface. For example,

TABLE 2.1

Rolling Resistance Coefficients

Conditions	Rolling resistance coefficient
Car tires on concrete or asphalt	0.013
Car tires on rolled gravel	0.02
Tar macadam	0.025
Unpaved road	0.05
Field	0.1–0.35
Truck tires on concrete or asphalt	0.006–0.01
Wheels on rail	0.001–0.002

the rolling resistance coefficient of passenger cars on concrete road may be calculated from the following equation:

$$f_r = f_0 + f_s\left(\frac{V}{100}\right)^{2.5}, \tag{2.6}$$

where V is vehicle speed in km/h, and f_0 and f_s depend on inflation pressure of the tire.[1]

In vehicle performance calculation, it is sufficient to consider the rolling resistance coefficient as a linear function of speed. For the most common range of inflation pressure, the following equation can be used for a passenger car on concrete road:[1]

$$f_r = 0.01\left(1 + \frac{V}{100}\right). \tag{2.7}$$

This equation predicts the values of f_r with acceptable accuracy for speeds up to 128 km/h.

2.2.2 Aerodynamic Drag

A vehicle traveling at a particular speed in air encounters a force resisting its motion. This force is referred to as aerodynamic drag. It mainly results from two components: shape drag and skin friction.

Shape drag: The forward motion of the vehicle pushes the air in front of it. However, the air cannot instantaneously move out of the way and its pressure is thus increased, resulting in high air pressure. In addition, the air behind the vehicle cannot instantaneously fill the space left by the forward motion of the vehicle. This creates a zone of low air pressure. The motion has therefore created two zones of pressure that oppose the motion of a vehicle by pushing it forward (high pressure in front) and pulling it backward (low pressure in the back) as shown in Figure 2.3. The resulting force on the vehicle is the shape drag.

Skin friction: Air close to the skin of the vehicle moves almost at the speed of the vehicle while air far from the vehicle remains still. In between, air

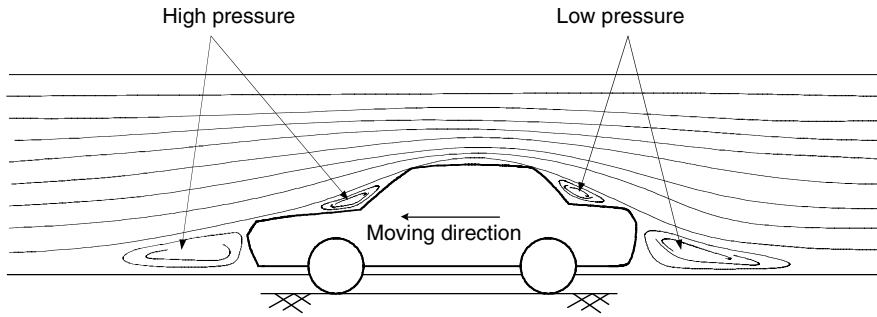

FIGURE 2.3
Shape drag

molecules move at a wide range of speeds. The difference in speed between two air molecules produces a friction that results in the second component of aerodynamic drag.

Aerodynamic drag is a function of vehicle speed V, vehicle frontal area A_f, shape of the vehicle, and air density ρ. Aerodynamic drag is expressed as

$$F_w = \frac{1}{2}\rho A_f C_D (V + V_w)^2, \tag{2.8}$$

where C_D is the aerodynamic drag coefficient that characterizes the shape of the vehicle and V_w is the component of wind speed on the vehicle's moving direction, which has a positive sign when this component is opposite to the vehicle speed and a negative sign when it is in the same direction as vehicle speed. The aerodynamic drag coefficients for a few types of vehicle body shapes are shown in Figure 2.4.

2.2.3 Grading Resistance

When a vehicle goes up or down a slope, its weight produces a component, which is always directed to the downward direction, as shown in Figure 2.5. This component either opposes the forward motion (grade climbing) or

Vehicle Type	Coefficient of Aerodymanic Resistance
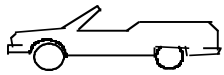 Open convertible	0.5–0.7
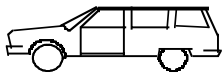 Van body	0.5–0.7
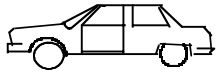 Ponton body	0.4–0.55
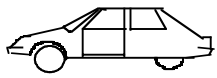 Wedge-shaped body; headlamps and bumpers are integrated into the body, covered underbody, optimized cooling air flow	0.3–0.4
 Headlamp and all wheels in body, covered underbody	0.2–0.25
 K-shaped (small breakway section)	0.23
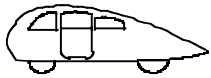 Optimum streamlined design	0.15–0.20
Trucks, road trains	0.8–1.5
Buses	0.6–0.7
Streamlined buses	0.3–0.4
Motorcycles	0.6–0.7

FIGURE 2.4
Indicative drag coefficients for different body shapes

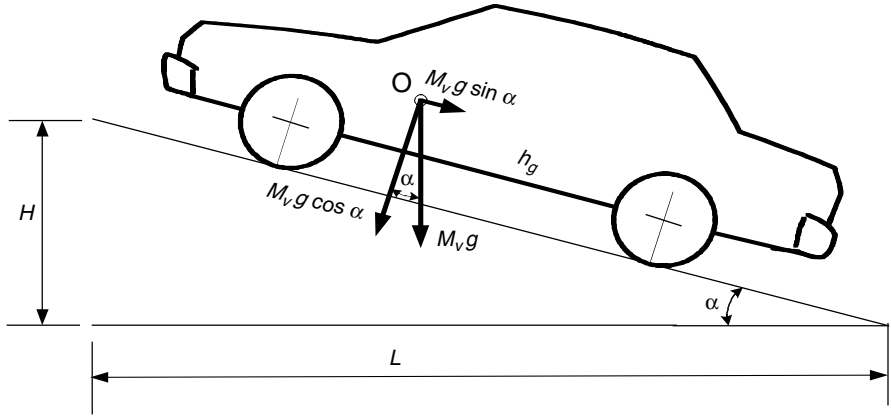

FIGURE 2.5
Automobile climbing a grade

helps the forward motion (grade descending). In vehicle performance analysis, only uphill operation is considered. This grading force is usually called grading resistance.

The grading resistance, from Figure 2.5, can be expressed as

$$F_g = M_v g \sin\alpha. \tag{2.9}$$

To simplify the calculation, the road angle, α, is usually replaced by grade value when the road angle is small. As shown in Figure 2.5, the grade is defined as

$$i = \frac{H}{L} = \tan\alpha \approx \sin\alpha. \tag{2.10}$$

In some literature, the tire rolling resistance and grading resistance together are called road resistance, which is expressed as

$$F_{rd} = F_f + F_g = M_v g(f_r \cos\alpha + \sin\alpha). \tag{2.11}$$

When the road angle is small, the road resistance can be simplified as

$$F_{rd} = F_f + F_g = M_v g(f_r + i). \tag{2.12}$$

2.3 Dynamic Equation

In the longitudinal direction, the major external forces acting on a two-axle vehicle, as shown in Figure 2.1, include the rolling resistance of front and rear tires F_{rf} and F_{rr}, which are represented by rolling resistance moment T_{rf} and T_{rr}, aerodynamic drag F_w, grading resistance F_g ($M_v g \sin\alpha$), and tractive

effort of the front and rear tires, F_{tf} and F_{tr}. F_{tf} is zero for a rear-wheel-driven vehicle, whereas F_{tr} is zero for a front-wheel-driven vehicle.

The dynamic equation of vehicle motion along the longitudinal direction is expressed by

$$M_v \frac{dV}{dt} = (F_{tf} + F_{tr}) - (F_{rf} + F_{rr} + F_w + F_g), \tag{2.13}$$

where dV/dt is the linear acceleration of the vehicle along the longitudinal direction and M_v is the vehicle mass. The first term on the right-hand side of (2.13) is the total tractive effort and the second term is the resistance.

To predict the maximum tractive effort that the tire–ground contact can support, the normal loads on the front and rear axles have to be determined. By summing the moments of all the forces about point R (center of the tire–ground area), the normal load on the front axle W_f can be determined as

$$W_f = \frac{M_v g L_b \cos\alpha - (T_{rf} + T_{rr} + F_w h_w + M_v g h_g \sin\alpha + M h_g dV/dt)}{L}. \tag{2.14}$$

Similarly, the normal load acting on the rear axle can be expressed as

$$W_r = \frac{M_v g L_a \cos\alpha - (T_{rf} + T_{rr} + R_w h_w + M_v g h_g \sin\alpha + M_v h_g dV/dt)}{L}. \tag{2.15}$$

For passenger cars, the height of the center of application of aerodynamic resistance, h_w, is assumed to be near the height of the center of gravity of the vehicle, h_g. Equations (2.14) and (2.15) can be simplified as

$$W_f = \frac{L_b}{L} M_v g \cos\alpha - \frac{h_g}{L}\left(F_w + F_g + M_v g f_r \frac{r_d}{h_g}\cos\alpha + M_v \frac{dV}{dt}\right) \tag{2.16}$$

and

$$W_r = \frac{L_a}{L} M_v g \cos\alpha + \frac{h_g}{L}\left(F_w + F_g + M_v g f_r \frac{r_d}{h_g}\cos\alpha + M_v \frac{dV}{dt}\right), \tag{2.17}$$

where r_d is the effective radius of the wheel. Referring to (2.5) and (2.13), (2.16) and (2.17) can be rewritten as

$$W_f = \frac{L_b}{L} M_v g \cos\alpha - \frac{h_g}{L}\left(F_t - F_r\left(1 - \frac{r_d}{h_g}\right)\right) \tag{2.18}$$

and

$$W_r = \frac{L_a}{L} M_v g \cos\alpha + \frac{h_g}{L}\left(F_t - F_r\left(1 - \frac{r_d}{h_g}\right)\right), \tag{2.19}$$

where $F_t = F_{tf} + F_{tr}$ is the total tractive effort of the vehicle and F_r is the total rolling resistance of the vehicle. The first term on the right-hand side of (2.18) and (2.19) is the static load on the front and rear axle when the vehicle is at rest on level ground. The second term is the dynamic component of the normal load.

The maximum tractive effort that the tire–ground contact can support (any small amount over this maximum tractive effort will cause the tire to spin on

the ground) is usually described by the product of the normal load and coefficient of road adhesion μ or referred to as frictional coefficient in some literatures (more details in Section 2.4). For a front-wheel-driven vehicle,

$$F_{t\max} = \mu W_f = \mu\left[\frac{L_b}{L}M_v g\cos\alpha - \frac{h_g}{L}\left(F_{t\max} - F_r\left(1-\frac{r_d}{h_g}\right)\right)\right] \tag{2.20}$$

and

$$F_{t\max} = \frac{\mu M_v g\cos\alpha[L_b + f_r(h_g - r_d)]/L}{1+\mu h_g/L}, \tag{2.21}$$

where f_r is the coefficient of the rolling resistance. For a rear-wheel-driven vehicle,

$$F_{t\max} = \mu W_r = \mu\left[\frac{L_a}{L}M_v g\cos\alpha - \frac{h_g}{L}\left(F_{t\max} - F_r\left(1-\frac{r_d}{h_g}\right)\right)\right] \tag{2.22}$$

and

$$F_{t\max} = \frac{\mu M_v g\cos\alpha[L_a + f_r(h_g - r_d)]/L}{1+\mu h_g/L}. \tag{2.23}$$

In vehicle operation, the maximum tractive effort on the driven wheels, transferred from the power plant through transmission, should not exceed the maximum values that are limited by the tire–ground cohesion in (2.21) and (2.23). Otherwise, the driven wheels will spin on the ground, leading to vehicle instability.

2.4 Tire–Ground Adhesion and Maximum Tractive Effort

When the tractive effort of a vehicle exceeds the limitation of the maximum tractive effort due to the adhesive capability between the tire and the ground, the drive wheels will spin on the ground. Actually, the adhesive capability between the tire and the ground is sometimes the main limitation of vehicle performance. This is especially true when the vehicle drives on wet, icy, snow-covered, or soft soil roads. In this case, a tractive torque on the drive wheel would cause the wheel to have significant slipping on the ground. The maximum tractive effort on the driven wheel depends on the longitudinal force that the adhesive capability between the tire and ground can supply, rather than the maximum torque that the engine can supply.

Experimental results show that, on various types of ground, the maximum tractive effort of the drive wheel closely relates to the slipping of the running wheel. This is also true on a good paved, dry road where the slipping is very small due to the elasticity of the tire. The slip, s, of a tire is usually defined as

$$s = \left(1-\frac{V}{r\omega}\right)\times 100\% = \left(1-\frac{r_e}{r}\right)\times 100\%, \tag{2.24}$$

where V is the translatory speed of the tire center, ω is the angular speed of the tire, r is the rolling radius of the free rolling tire, and r_e is the effective rolling radius of the tire, defined as the ratio of the translatory speed of the tire center to the angular speed of the tire. In traction, the speed V is less than $r\omega$, therefore, the slip of the tire has a positive value between 0 and 1.0. During braking, however, the tire slip would be defined as

$$s = \left(1 - \frac{r\omega}{V}\right) \times 100\% = \left(1 - \frac{r}{r_e}\right) \times 100\%, \tag{2.25}$$

which has a positive value between 0 and 1.0, similar to traction. The maximum traction effort of a tire corresponding to a certain tire slip is usually expressed as

$$F_x = P\mu, \tag{2.26}$$

where P is the vertical load of the tire and μ is the tractive effort coefficient, which is a function of tire slip. The tractive effort coefficient and tire slip always have a relationship as shown in Figure 2.6.

In the small slip range (section OA in Figure 2.6), the tractive effort is almost linearly proportional to the slip value. This small slip is caused by the elasticity of the tire rather than the relative slipping between the tire and the ground at the contact patch, as shown in Figure 2.7. When a tractive torque is applied to the tire, a tractive force is developed at the tire–ground contact patch. At the same time, the tire tread in front and within the contact patch is subjected to compression. A corresponding shear deformation of the side wall of the tire is also developed. As tread elements are compressed before entering the contact region, the distance that the tire travels will be less than the distance in a free rolling tire. Because of the nearly linear elastic property of the tire, the tractive effort–slip curve is almost linear. A further increase in wheel torque and tractive force results in part of the tire tread sliding on the ground. Under these circumstances, the relationship between tractive force and slip is nonlinear. This corresponds to section AB of the curve as shown in Figure 2.6. The peak tractive effort is reached at a slip of 15–20%. A further increase in slip beyond this

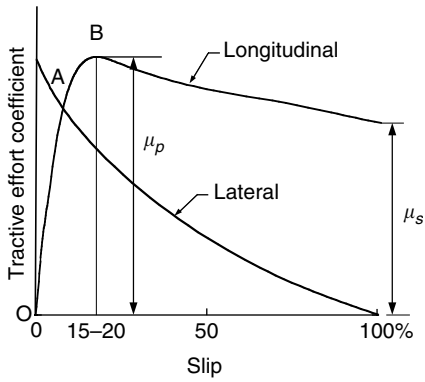

FIGURE 2.6
Variation of tractive effort coefficient with longitudinal slip of a tire

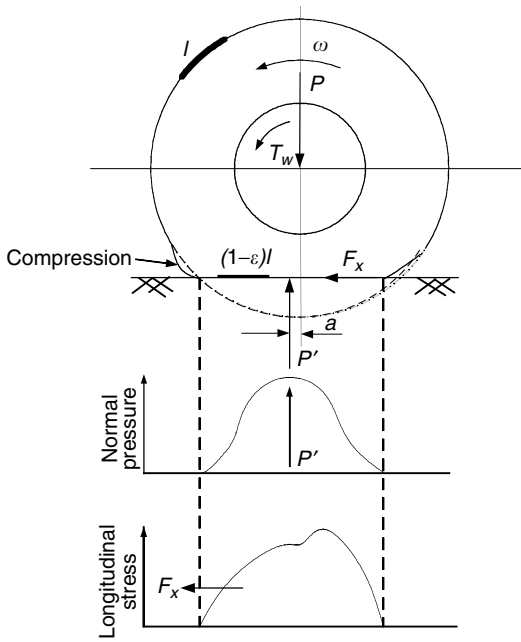

FIGURE 2.7
Behavior of a tire under the action of driving torque

TABLE 2.2

Average Values of Tractive Effort Coefficient on Various Roads

Surface	Peak Values, μ_p	Sliding Values, μ_s
Asphalt and concrete (dry)	0.8–0.9	0.75
Concrete (wet)	0.8	0.7
Asphalt (wet)	0.5–0.7	0.45–0.6
Grave	0.6	0.55
Earth road (dry)	0.68	0.65
Earth road (wet)	0.55	0.4–0.5
Snow (hard packed)	0.2	0.15
Ice	0.1	0.07

results in an unstable condition. The tractive effort coefficient falls rapidly from the peak value to the purely sliding value as shown in Figure 2.6. For normal driving, the slip of the tire must be limited in a range less than 15–20%. Table 2.2 shows the average values of tractive effort coefficients on various roads.

2.5 Power Train Tractive Effort and Vehicle Speed

An automotive power train, as shown in Figure 2.8, consists of a power plant (engine or electric motor), a clutch in manual transmission or a torque converter in automatic transmission, a gearbox (transmission), final drive,

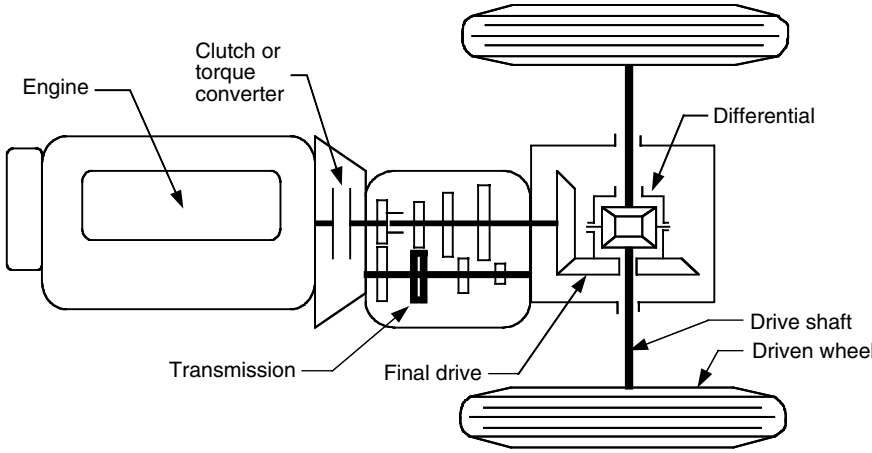

FIGURE 2.8
Conceptual illustration of an automobile power train

differential, drive shaft, and driven wheels. The torque and rotating speed of the power plant output shaft are transmitted to the drive wheels through the clutch or torque converter, gearbox, final drive, differential, and drive shaft. The clutch is used in manual transmission to couple the gearbox to or decouple it from the power plant. The torque converter in automatic transmission is a hydrodynamic device, functioning as the clutch in manual transmission with a continuously variable gear ratio (for more details, see Section 2.6). The gearbox supplies a few gear ratios from its input shaft to its output shaft for the power plant torque–speed profile to match the requirements of the load. The final drive is usually a pair of gears that supply a further speed reduction and distribute the torque to each wheel through the differential.

The torque on the driven wheels, transmitted from the power plant, is expressed as

$$T_w = i_g i_0 \eta_t T_p \tag{2.27}$$

where i_g is the gear ratio of the transmission defined as $i_g = N_{in}/N_{out}$ (N_{in} — input rotating speed, N_{out} — output rotating speed), i_0 is the gear ratio of the final drive, η_t is the efficiency of the driveline from the power plant to the driven wheels, and T_p is the torque output from the power plant.

The tractive effort on the driven wheels, as shown in Figure 2.9, can be expressed as

$$F_t = \frac{T_w}{r_d}. \tag{2.28}$$

Substituting (2.27) into (2.28) yields the following result:

$$F_t = \frac{T_p i_g i_0 \eta_t}{r_d}. \tag{2.29}$$

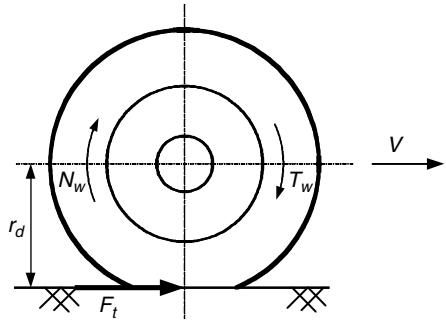

FIGURE 2.9
Tractive effort and torque on a driven wheel

The friction in the gear teeth and the friction in the bearings create losses in mechanical gear transmission. The following are representative values of the mechanical efficiency of various components:

Clutch: 99%
Each pair of gears: 95–97%
Bearing and joint: 98–99%

The total mechanical efficiency of the transmission between the engine output shaft and drive wheels or sprocket is the product of the efficiencies of all the components in the driveline. As a first approximation, the following average values of the overall mechanical efficiency of a manual gear-shift transmission may be used:

Direct gear: 90%
Other gear: 85%
Transmission with a very high reduction ratio: 75–80%

The rotating speed (rpm) of the driven wheel can be expressed as

$$N_w = \frac{N_p}{i_g i_0}, \tag{2.30}$$

where N_p is the output rotating speed (rpm). The translational speed of the wheel center (vehicle speed) can be expressed as

$$V = \frac{\pi N_w r_d}{30} \text{(m/s)}. \tag{2.31}$$

Substituting (2.30) into (2.31) yields

$$V = \frac{\pi N_p r_d}{30 i_g i_0} \text{(m/s)}. \tag{2.32}$$

2.6 Vehicle Power Plant and Transmission Characteristics

There are two limiting factors to the maximum tractive effort of a vehicle. One is the maximum tractive effort that the tire–ground contact can support (equation [2.21] or [2.23]) and the other is the tractive effort that the power plant

torque with given driveline gear ratios can provide (equation [2.29]). The smaller of these two factors will determine the performance potential of the vehicle. For on-road vehicles, the performance is usually limited by the second factor. In order to predict the overall performance of a vehicle, its power plant and transmission characteristics must be taken into consideration.

2.6.1 Power Plant Characteristics

For vehicular applications, the ideal performance characteristic of a power plant is the constant power output over the full speed range. Consequently, the torque varies with speed hyperbolically as shown in Figure 2.10. At low speeds, the torque is constrained to be constant so as not to be over the maxima limited by the adhesion between the tire–ground contact area. This constant power characteristic will provide the vehicle with a high tractive effort at low speeds, where demands for acceleration, drawbar pull, or grade climbing capability are high.

Since the internal combustion engine and electric motor are the most commonly used power plants for automotive vehicles to date, it is appropriate to review the basic features of the characteristics that are essential to predicating vehicle performance and driveline design. Representative characteristics of a gasoline engine in full throttle and an electric motor at full load are shown in Figure 2.11 and Figure 2.12, respectively. The internal combustion engine usually has torque–speed characteristics far from the ideal performance characteristic required by traction. It starts operating smoothly at idle speed. Good combustion quality and maximum engine torque are reached at an intermediate engine speed. As the speed increases further, the mean effective pressure decreases because of the growing losses in the air-induction manifold and a decline in engine torque. Power output, however, increases to its maximum at a certain high speed. Beyond this point, the engine torque decreases more rapidly with increasing speed. This results in the decline of engine power output. In vehicular applications, the maximum permissible

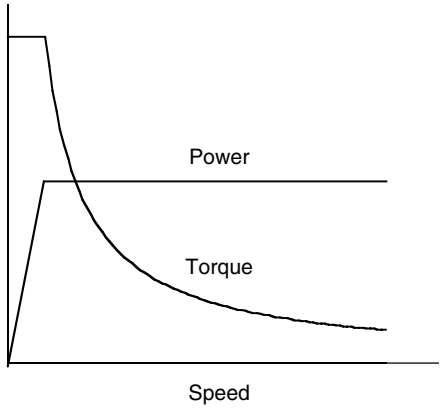

FIGURE 2.10
Ideal performance characteristics for a vehicle traction power plant

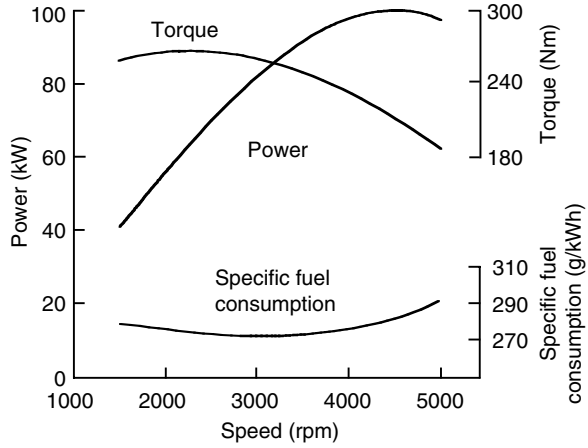

FIGURE 2.11
Typical performance characteristics of gasoline engines

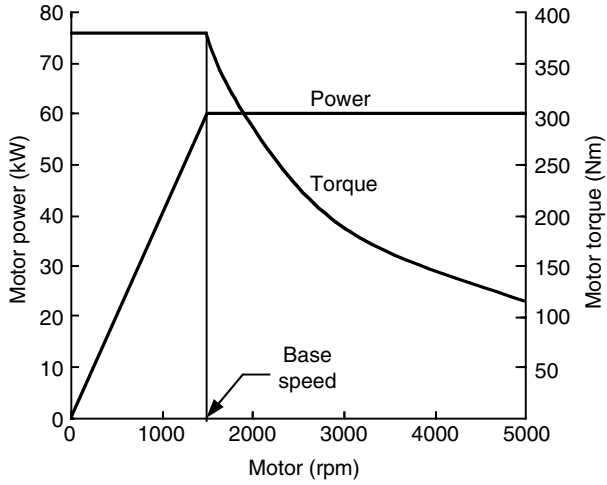

FIGURE 2.12
Typical performance characteristics of electric motors for traction

speed of the engine is usually set just a little above the speed of the maximum power output. The internal combustion engine has a relatively flat torque–speed profile (compared with an ideal one), as shown in Figure 2.11. Consequently, a multigear transmission is usually employed to modify it, as shown in Figure 2.13.

Electric motors, however, usually have a speed–torque characteristic that is much closer to the ideal, as shown in Figure 2.12. Generally, the electric motor starts from zero speed. As it increases to its base speed, the voltage increases to its rated value while the flux remains constant. Beyond the base speed, the

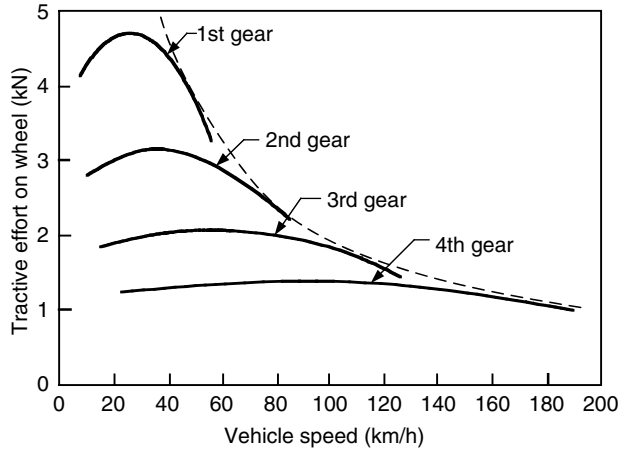

FIGURE 2.13
Tractive effort of internal combustion engine and a multigear transmission vehicle vs. vehicle speed

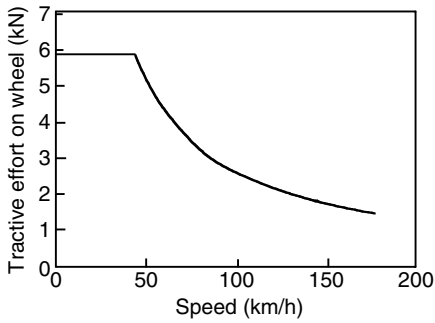

FIGURE 2.14
Tractive effort of a single-gear electric vehicle vs. vehicle speed

voltage remains constant and the flux is weakened. This results in constant output power while the torque declines hyperbolically with speed. Since the speed–torque profile of an electric motor is close to the ideal, a single-gear or double-gear transmission is usually employed, as shown in Figure 2.14.

2.6.2 Transmission Characteristics

The transmission requirements of a vehicle depend on the characteristics of the power plant and the performance requirements of the vehicle. As mentioned previously, a well-controlled electric machine such as the power plant of an electric vehicle will not need a multigear transmission. However, an internal combustion engine must have a multigear or continuously varying transmission to multiply its torque at low speed. The term transmission here includes all those systems employed for transmitting engine power to the drive wheels. For automobile applications, there are usually two basic types of transmission: manual gear transmission and hydrodynamic transmission.

2.6.2.1 Manual Gear Transmission

Manual gear transmission consists of a clutch, gearbox, final drive, and drive shaft as shown in Figure 2.8. The final drive has a constant gear reduction ratio or a differential gear ratio. The common practice of requiring direct drive (nonreducing) in the gearbox to be in the highest gear determines this ratio. The gearbox provides a number of gear reduction ratios ranging from three to five for passenger cars and more for heavy commercial vehicles that are powered with gasoline or diesel engines.

The maximum speed requirement of the vehicle determines the gear ratio of the highest gear (i.e., the smallest ratio). On the other hand, the gear ratio of the lowest gear (i.e., the maximum ratio) is determined by the requirement of the maximum tractive effort or the gradeability. Ratios between them should be spaced in such a way that they will provide the tractive effort–speed characteristics as close to the ideal as possible, as shown in Figure 2.15. In the first iteration, gear ratios between the highest and the lowest gear may be selected in such a way that the engine can operate in the same speed range for all the gears. This approach would benefit the fuel economy and performance of the vehicle. For instance, in normal driving, the proper gear can be selected according to vehicle speed to operate the engine in its optimum speed range for fuel-saving purposes. In fast acceleration, the engine can be operated in its speed range with high power output. This approach is depicted in Figure 2.16.

For a four-speed gearbox, the following relationship can be established (see Figure 2.16):

$$\frac{i_{g1}}{i_{g2}} = \frac{i_{g2}}{i_{g3}} = \frac{i_{g3}}{i_{g4}} = K_g \tag{2.33}$$

and

$$K_g = \sqrt[3]{\frac{i_{g1}}{i_{gg4}}}, \tag{2.34}$$

where i_{g1}, i_{g2}, i_{g3}, and i_{g4} are the gear ratios for the first, second, third, and fourth gear, respectively. In a more general case, if the ratio of the highest

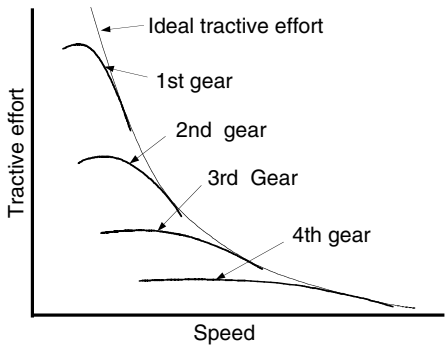

FIGURE 2.15
Tractive effort characteristics of a gasoline engine-powered vehicle

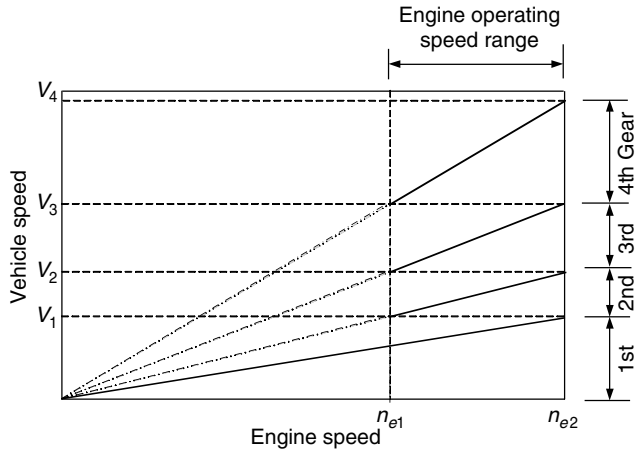

FIGURE 2.16
Demonstration of vehicle speed range and engine speed range for each gear

gear, i_{gn} (smaller gear ratio), and the ratio of the lowest gear, i_{g1} (largest gear ratio), have been determined and the number of the gear n_g is known, the factor K_g can be determined as

$$K_g = \left(\frac{i_{g1}}{i_{gn}}\right)^{(n_g-1)}, \tag{2.35}$$

and each gear ratio can be obtained by

$$\begin{aligned} i_{gn-1} &= K_g i_{gn} \\ i_{gn-2} &= K_g^2 i_{gn} \\ &\vdots \\ i_{g2} &= K_g^{n_g-1} i_{gn}. \end{aligned} \tag{2.36}$$

For passenger cars, to suit changing traffic conditions, the step between the ratios of the upper two gears is often a little closer than that based on (2.36). That is,

$$\frac{i_{g1}}{i_{g2}} > \frac{i_{g2}}{i_{g3}} > \frac{i_{g3}}{i_{g4}}. \tag{2.37}$$

This, in turn, affects the selection of the ratios of the lower gears. For commercial vehicles, however, the gear ratios in the gearbox are often arranged based on (2.37).

Figure 2.17 shows the tractive effort of a gasoline engine vehicle with four-gear transmission and that of an electric vehicle with single-gear transmission. It is clear that electric machines with favorable torque–speed characteristics can satisfy tractive effort with simple single-gear transmission.

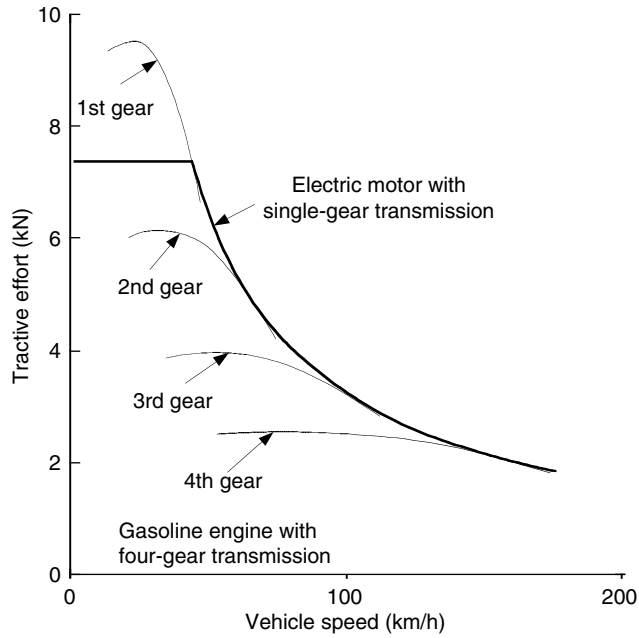

FIGURE 2.17
Tractive efforts of a gasoline engine vehicle with four-gear transmission and an electric vehicle with single-gear transmission

2.6.2.2 Hydrodynamic Transmission

Hydrodynamic transmissions use fluid to transmit power in the form of torque and speed and are widely used in passenger cars. They consist of a torque converter and an automatic gearbox. The torque converter consists of at least three rotary elements known as the impeller (pump), the turbine, and the reactor, as shown in Figure 2.18. The impeller is connected to the engine shaft and the turbine is connected to the output shaft of the converter, which in turn is coupled to the input shaft of the multispeed gearbox. The reactor is coupled to external housing to provide a reaction on the fluid circulating in the converter. The function of the reactor is to enable the turbine to develop an output torque higher than the input torque of the converter, thus producing torque multiplication. The reactor is usually mounted on a free wheel (one-way clutch) so that when the starting period has been completed and the turbine speed is approaching that of the pump, the reactor is in free rotation. At this point, the converter operates as a fluid coupled with a ratio of output torque to input torque that is equal to 1.0.

The major advantages of hydrodynamic transmission may be summarized as follows:

- When properly matched, the engine will not stall.
- It provides flexible coupling between the engine and the driven wheels.

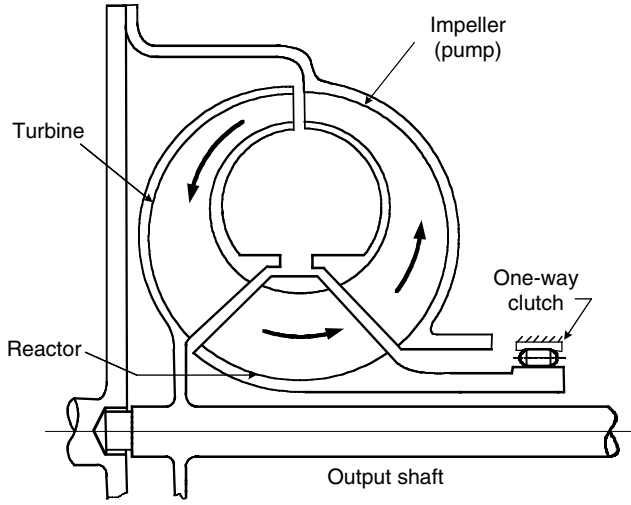

FIGURE 2.18
Schematic view of a torque converter

- Together with a suitably selected multispeed gearbox, it provides torque–speed characteristics that approach the ideal.

The major disadvantages of hydrodynamic transmission are its low efficiency in a stop–go driving pattern and its complex construction.

The performance characteristics of a torque converter are described in terms of the following four parameters:

1. *Speed ratio*

$$C_{sr} = \frac{output\_speed}{input\_speed}, \tag{2.38}$$

which is the reciprocal of the gear ratio mentioned before.

2. *Torque ratio*

$$C_{tr} = \frac{output\_torque}{input\_torque}. \tag{2.39}$$

3. *Efficiency*

$$\eta_c = \frac{output\_speed \times output\_torque}{input\_speed \times input\_torque} = C_{sr}C_{tr}. \tag{2.40}$$

4. *Capacity factor* (*size factor*)

$$K_{tc} = \frac{speed}{\sqrt{torque}}. \tag{2.41}$$

The capacity factor, K_c, is an indicator of the ability of the converter to absorb or transmit torque, which is proportional to the square of the rotary speed.

Typical performance characteristics of the torque converter are shown in Figure 2.19, in which torque ratio, efficiency, and input capacity factor — that is the ratio of input speed to the square root of input torque — are plotted against speed ratio. The torque ratio has the maximum value at stall condition, where the output speed is zero. The torque ratio decreases as the speed ratio increases (gear ratio decreases) and the converter eventually acts as a hydraulic coupling with a torque ratio of 1.0. At this point, a small difference between the input and output speed exists because of the slip between the impeller (pump) and the turbine. The efficiency of the torque converter is zero at stall condition and increases with increasing speed ratio (decrease in the gear ratio). It reaches the maximum when the converter acts as a fluid coupling (torque ratio equal to 1.0).

To determine the actual operating condition of the torque converter, the engine operating point has to be specified because the engine drives the torque converter. To characterize the engine operating condition for the purpose of determining the combined performance of the engine and the converter, an engine capacity factor, K_e, is introduced and defined as

$$K_e = \frac{n_e}{\sqrt{T_e}}, \tag{2.42}$$

where n_e and T_e are engine speed and torque, respectively. The variation of the capacity factor with speed for a typical engine is shown in Figure 2.20. To achieve proper matching, the engine and the torque converter should have a similar range in the capacity factor.

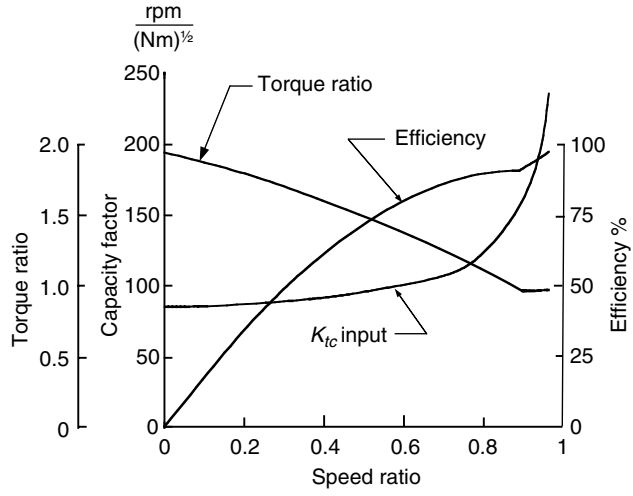

FIGURE 2.19
Performance characteristics of a torque converter

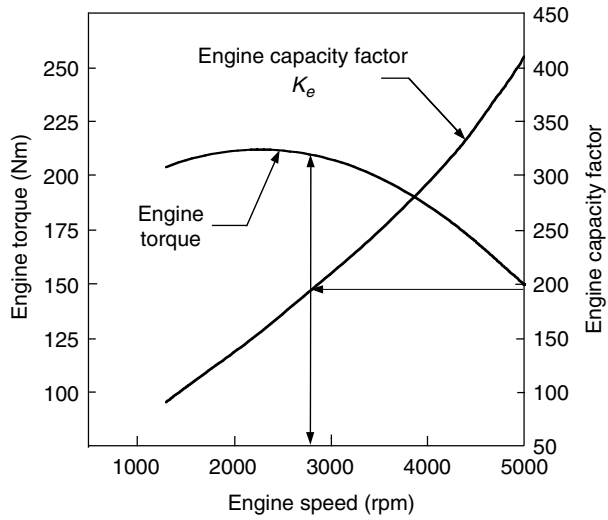

FIGURE 2.20
Capacity factor of a typical engine

The engine shaft is usually connected to the input shaft of the torque converter, as mentioned above. That is,

$$K_e = K_c. \tag{2.43}$$

The matching procedure begins with specifying the engine speed and engine torque. Knowing the engine operating point, one can determine the engine capacity factor, K_e (see Figure 2.21). Since $K_e = K_c$, the input capacity factor of the torque converter corresponding to the specific engine operating point is then known. As shown in Figure 2.20, for a particular value of the input capacity factor of the torque converter, K_{tc}, the converter speed ratio, C_{sr}, and torque ratio, C_{tr}, can be determined from the torque converter performance characteristics. The output torque and output speed of the converter are then given by

$$T_{tc} = T_e C_{tr} \tag{2.44}$$

and

$$n_{tc} = n_e C_{sr}, \tag{2.45}$$

where T_{tc} and n_{tc} are the output torque and output speed of the converter, respectively.

Since the torque converter has a limited torque ratio range (usually less than 2), a multispeed gearbox is usually connected to it. The gearbox comprises several planetary gear sets and is automatically shifted. With the gear

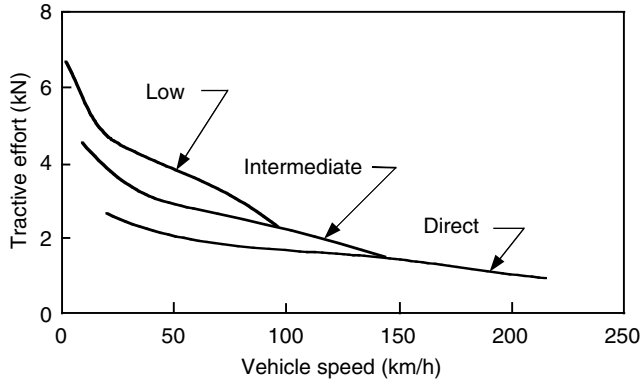

FIGURE 2.21
Tractive effort–speed characteristics of a passenger car with automatic transmission

ratios of the gearbox, the tractive effort and speed of the vehicle can be calculated (see [2.27] and [2.32]) by

$$F_t = \frac{T_e C_{tr} i_g i_0 \eta_t}{r} \tag{2.46}$$

and

$$V = \frac{\pi n_e C_{sr} r}{30 i_g i_0} (\text{m/s}) = 0.377 \frac{n_e C_{sr} r}{i_t} (\text{km/h}). \tag{2.47}$$

Figure 2.21 shows the variation of the tractive effort with speed for a passenger car equipped with a torque converter and a three-speed gearbox.

2.6.2.3 Continuously Variable Transmission

A continuously variable transmission (CVT) has a gear ratio that can be varied continuously within a certain range, thus providing an infinity of gear ratios. This continuous variation allows for the matching of virtually any engine speed and torque to any wheel speed and torque. It is therefore possible to achieve an ideal torque–speed profile (constant power profile) because any engine power output to the transmission can be applied at any speed to the wheels.

The commonly used CVT in automobiles uses a pulley and belt assembly. One pulley is connected to the engine shaft, while the other is connected to the output shaft. The belt links the two pulleys. The distance between the two half pulleys can be varied, thus varying the effective diameter on which the belt grips. The transmission ratio is a function of the two effective diameters:

$$i_g = \frac{D_2}{D_1}, \tag{2.48}$$

where D_1 and D_2 are the effective diameters of the output pulley and input pulley, respectively.

Until recently, this implementation was affected by the limited belt–pulley adhesive contact. The design has been improved by the use of metallic belts that provide better solidity and improved contact. Furthermore, an interesting concept has been developed and is being used by Nissan. This concept uses three friction gears: one is connected to the engine shaft, another to the output shaft, while the third gear grips on the particular profile of the other two gears. It can be rotated to grip on different effective diameters, therefore achieving a variable gear ratio.

2.7 Vehicle Performance

The performance of a vehicle is usually described by its maximum cruising speed, gradeability, and acceleration. The predication of vehicle performance is based on the relationship between tractive effort and vehicle speed discussed in Sections 2.5 and 2.6. For on-road vehicles, it is assumed that the maximum tractive effort is limited by the maximum torque of the power plant rather than the road adhesion capability. Depicted tractive effort (equation [2.29] or [2.46]) and resistance ($F_r + F_w + F_g$) on a diagram are helpful for vehicle performance analysis as shown in Figure 2.22 and

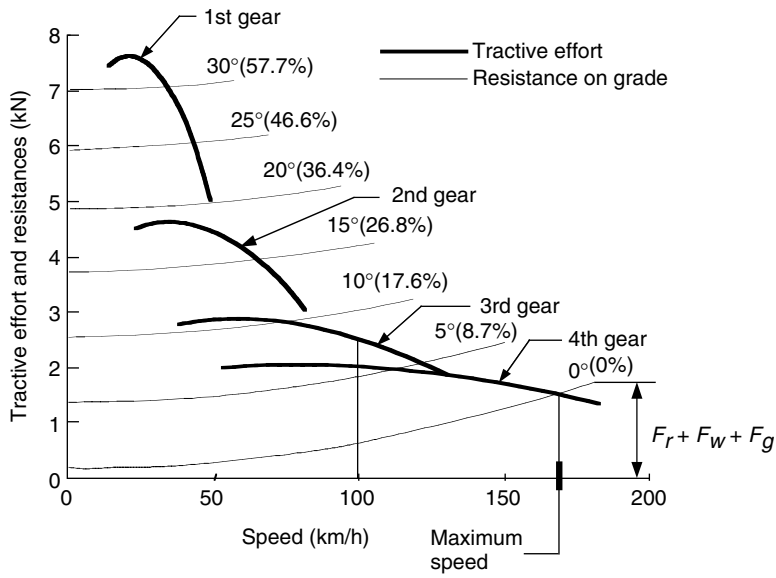

FIGURE 2.22
Tractive effort of a gasoline engine-powered vehicle with multispeed transmission and its resistance

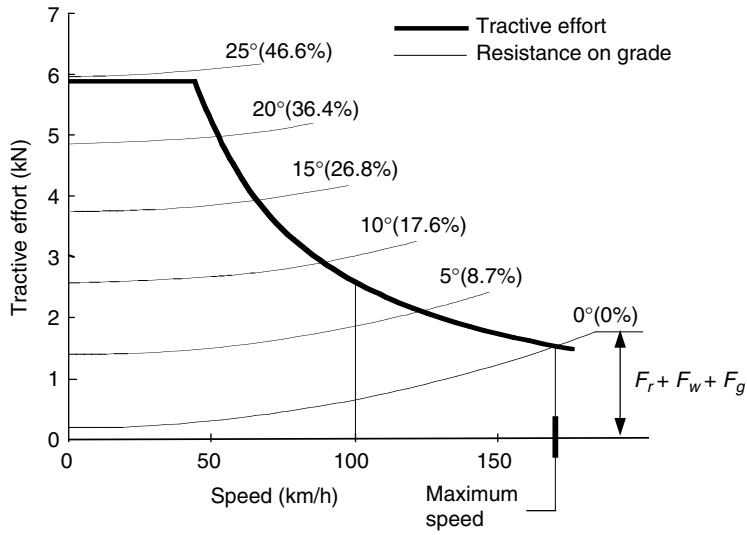

FIGURE 2.23
Tractive effort of an electric motor-powered vehicle with single-speed transmission and its resistance

Figure 2.23 for a gasoline engine-powered, four-gear manual transmission vehicle and an electric motor-powered, single-gear transmission vehicle, respectively.

2.7.1 Maximum Speed of a Vehicle

The maximum speed of a vehicle is defined as the constant cruising speed that the vehicle can develop with full power plant load (full throttle of the engine or full power of the motor) on a flat road. The maximum speed of a vehicle is determined by the equilibrium between the tractive effort of the vehicle and the resistance or the maximum speed of the power plant and gear ratios of the transmission. The tractive effort and resistance equilibrium can be expressed as

$$\frac{T_p i_g i_0 \eta_t}{r_d} = M_v g f_r \cos\alpha + \frac{1}{2} \rho_a C_D A_f V^2. \tag{2.49}$$

This equation indicates that the vehicle reaches its maximum speed when the tractive effort, represented by the left-hand-side term in (2.49), equals the resistance, represented by the right-hand-side terms. The intersection of the tractive effort curve and the resistance curve represents the maximum speed of the vehicle, as shown in Figure 2.22 and Figure 2.23.

It should be noted that for some vehicles, no intersection exists between the effort curve and the resistance curve, because of a large power plant or large gear ratio. In this case, the maximum speed of the vehicle can be

determined by the maximum speed of the power plant. Using (2.32) or (2.47), the maximum speed of the vehicle can be written as

$$V_{max} = \frac{\pi n_{p\,max} r_d}{30 i_0 i_{g\,min}} (\text{m/s}), \tag{2.50}$$

where $n_{p\,\max}$ and $i_{g\,\min}$ are the maximum speed of the engine (electric motor) and the minimum gear ratio of the transmission, respectively.

2.7.2 Gradeability

Gradeability is usually defined as the grade (or grade angle) that the vehicle can overcome at a certain constant speed, for instance, the grade at a speed of 100 km/h (60 mph). For heavy commercial vehicles or off-road vehicles, the gradeability is usually defined as the maximum grade or grade angle in the whole speed range.

When the vehicle drives on a road with relative small grade and constant speed, the tractive effort and resistance equilibrium can be written as

$$\frac{T_p i_0 i_g \eta_t}{r_d} = M_v g f_r + \tfrac{1}{2} \rho_a C_D A_f V^2 + M_v g\, i. \tag{2.51}$$

Thus,

$$i = \frac{(T_p i_0 i_g \eta_t / r_d) - M_v g f_r - (1/2)\rho_a C_D A_f V^2}{M_v g} = d - f_r, \tag{2.52}$$

where

$$d = \frac{F_t - F_w}{M_v g} = \frac{(T_p i_0 i_g \eta_t / r_d) - (1/2)\rho_a C_D A_f V^2}{M_v g} \tag{2.53}$$

is called the performance factor. While the vehicle drives on a road with a large grade, the gradeability of the vehicle can be calculated as

$$\sin\alpha = \frac{d - f_r \sqrt{1 - d^2 + f_r^2}}{1 + f_r^2}. \tag{2.54}$$

The gradeability of the vehicle can also be obtained from the diagram in Figure 2.22 or Figure 2.23, in which the tractive effort and resistance are plotted.

2.7.3 Acceleration Performance

The acceleration performance of a vehicle is usually described by its acceleration time and the distance covered from zero speed to a certain high speed (zero to 96 km/h or 60 mph, for example) on level ground. Using Newton's second law (equation [2.13]), the acceleration of the vehicle can be written as

$$a = \frac{dV}{dt} = \frac{F_t - F_f - F_w}{M_v \delta} = \frac{(T_p i_0 i_g \eta_t / r_d) - M_v g f_r - (1/2)\rho_a C_D A_f V^2}{M_v \delta} = \frac{g}{\delta}(d - f_r), \tag{2.55}$$

where δ is called the mass factor, considering the equivalent mass increase due to the angular moments of the rotating components. The mass factor can be written as

$$\delta = 1 + \frac{I_w}{M_v r_d^2} = \frac{i_0^2 \, i_g^2 \, I_p}{M_v r^2}, \tag{2.56}$$

where I_w is the total angular moment of the wheels and I_p is the total angular moment of the rotating components associated with the power plant. Calculation of the mass factor, δ, requires knowing the values of the mass moments of inertia of all the rotating parts. In the case where these values are not known, the mass factor, δ, for a passenger car would be estimated using the following empirical relation:

$$\delta = 1 + \delta_1 + \delta_2 i_g^2 \, i_0^2, \tag{2.57}$$

where δ_1 represents the second term on the right-hand side of equation (2.56), with a reasonable estimate value of 0.04, and δ_2 represents the effect of the power plant-associated rotating parts, and has a reasonable estimate value of 0.0025.

Figure 2.24 and Figure 2.25 show the acceleration along with vehicle speed for a gasoline engine-powered vehicle with four-gear transmission and an electric motor-powered vehicle with single-gear transmission.

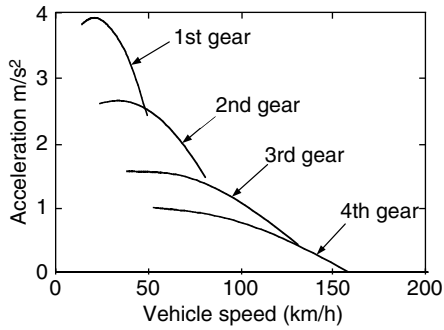

FIGURE 2.24
Acceleration of a gasoline engine-powered vehicle with four-gear transmission

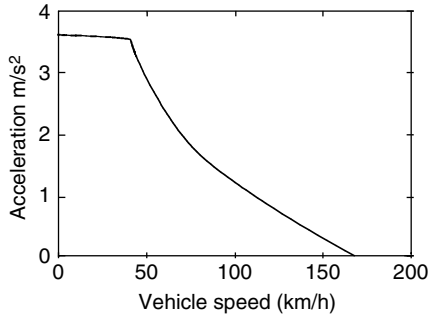

FIGURE 2.25
Acceleration of an electric machine-powered vehicle with single-gear transmission

From (2.55), the acceleration time, t_a, and distance, S_a, from low speed V_1 to high speed V_2 can be written, respectively, as

$$t_a = \int_{V_1}^{V_2} \frac{M_v \delta V}{(T_p i_g i_0 \eta_t / r_d) - M_v g f_r - (1/2)\rho_a C_D A_f V^2}\, dV \tag{2.58}$$

and

$$S_a = \int_{V_1}^{V_2} \frac{M_v \delta}{(T_p i_g i_0 \eta_t / r_d) - M_v g f_r - (1/2)\rho_a C_D A_f V^2}\, dV. \tag{2.59}$$

In (2.58) and (2.59), the torque of the power plant, T_p, is a function of speed (see Figure 2.11 and Figure 2.12), which in turn is a function of vehicle speed (see [2.23] and [2.37]) and gear ratio of the transmission. This makes it difficult to solve (2.58) and (2.59) analytically; therefore, numeral methods are usually used. Figure 2.26 and Figure 2.27 show the acceleration time and

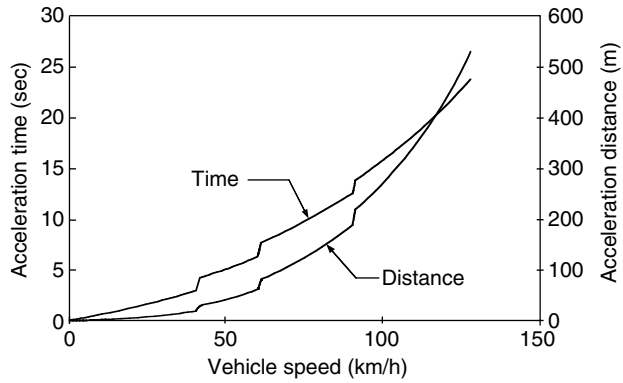

FIGURE 2.26
Acceleration time and distance along with vehicle speed for a gasoline engine-powered passenger car with four-gear transmission

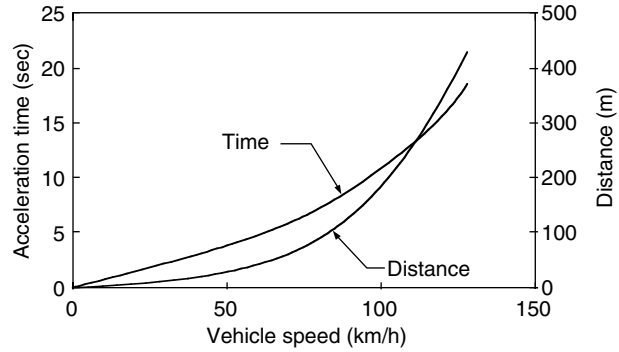

FIGURE 2.27
Acceleration time and distance along with vehicle speed for an electric machine-powered passenger car with single-gear transmission

distance along with vehicle speed for a gasoline engine-powered and an electric machine-powered electric vehicle, respectively.

2.8 Operating Fuel Economy

The fuel economy of a vehicle is evaluated by the amount of fuel consumption per 100 km traveling distance (liters/100 km) or mileage per gallon fuel consumption (miles/gallon), which is currently used in the U.S. The operating fuel economy of a vehicle depends on a number of factors, including fuel consumption characteristics of the engine, gear number and ratios, vehicle resistance, vehicle speed, and operating conditions.

2.8.1 Fuel Economy Characteristics of Internal Combustion Engines

The fuel economy characteristic of an internal combustion engine is usually evaluated by the amount of fuel per kWh energy output, which is referred to as the specific fuel consumption (g/kWh). The typical fuel economy characteristic of a gasoline engine is shown in Figure 2.28. The fuel consumption is quite different from one operating point to another. The optimum operating points are close to the points of full load (wide-opened throttle). The speed of the engine also has a significant influence on fuel economy. With a given power output, the fuel consumption is usually lower at low speed than at high speed. For instance, when the engine shown in Figure 2.28 has a power output of 40 kW, its minimum specific fuel consumption would be 270 g/kWh at a speed of 2080 rpm.

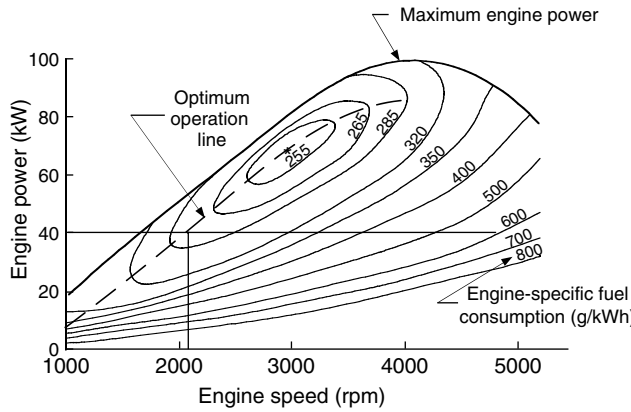

FIGURE 2.28
Fuel economy characteristics of a typical gasoline engine

For a given power output at a given vehicle speed, the engine operating point is determined by the gear ratio of the transmission (refer to [2.32] and [2.47]). Ideally, a continuous variable transmission can choose the gear ratio, in a given driving condition, to operate the engine at its optimum operating point. This advantage has stimulated the development of a variety of continuous variable transmissions, including frictional drive, hydrodynamic drives, hydrostatic drives, and hydromechanical variable drive.

2.8.2 Calculation of Vehicle Fuel Economy

Vehicle fuel economy can be calculated by finding the load power and the specific fuel consumption of the engine. The engine power output is always equal to the resistance power of the vehicle, that is,

$$P_e = \frac{V}{\eta_t}\left(F_f + F_w + F_g + M_v \delta \frac{dV}{dt}\right). \tag{2.60}$$

Equation (2.60) can be written as

$$P_e = \frac{V}{1000\eta_t}\left(M_v g f_r \cos\alpha + \tfrac{1}{2}\rho_a C_D A_f V^2 + M_v g \sin\alpha + M_v \delta \frac{dV}{dt}\right)(\text{kW}). \tag{2.61}$$

The engine speed, related to vehicle speed and gear ratio, can be expressed as

$$N_e = \frac{30 V i_g i_0}{\pi r_d}. \tag{2.62}$$

After determination of the engine power and speed by (2.60) and (2.61), the value of the specific fuel consumption, g_e, can be found in the graph of the engine fuel economy characteristics as shown in Figure 2.28. The time rate of fuel consumption can be calculated by

$$Q_{fr} = \frac{P_e g_e}{1000\gamma_f}\ (\text{l/h}), \tag{2.63}$$

where g_e is the specific fuel consumption of the engine in g/kWh and γ_f is the mass density of the fuel in kg/l. The total fuel consumption within a total distance, S, at a constant cruising speed, V, is obtained by

$$Q_s = \frac{P_e g_e}{1000\gamma_f}\frac{S}{V}. \tag{2.64}$$

Figure 2.29 shows an example of the fuel economy characteristics of a gasoline vehicle at constant cruising speed on level ground. This figure indicates that at high speeds, the fuel consumption increases because the aerodynamic resistance power increases with the speed cubed. This figure also indicates that with a high-speed gear (small gear ratio), the fuel economy of the vehicle can be enhanced due to the reduced engine speed at a given vehicle speed and increased gear ratio.

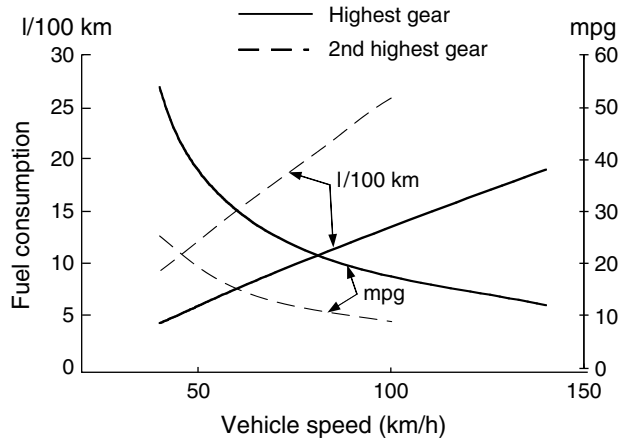

FIGURE 2.29
Fuel economy characteristics of a typical vehicle at constant speed

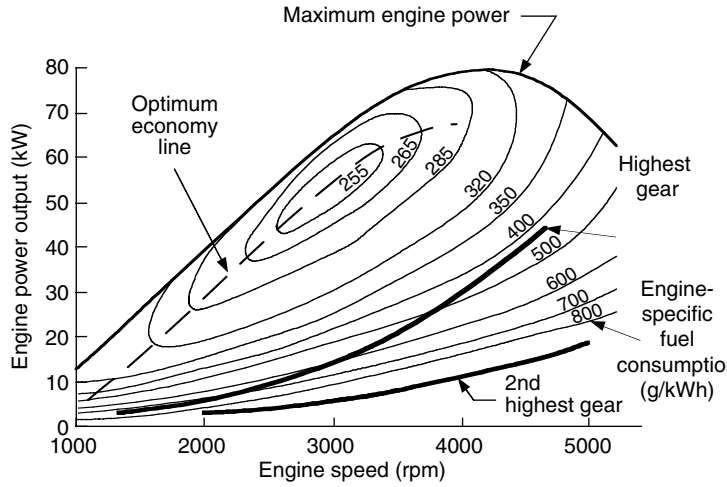

FIGURE 2.30
Operating point of an engine at constant speed with highest gear and second highest gear

Figure 2.30 shows the operating points of an engine at constant vehicle speed, with the highest gear and the second highest gear. It indicates that the engine has a much lower operating efficiency in low gear than in high gear. This is the reason why the fuel economy of a vehicle can be improved with more gear transmission and continuous variable transmission.

It should be noted that because of the complexity of vehicle operation in the real world, fuel consumption at constant speed (as shown in Figure 2.29) cannot accurately represent fuel consumption for a vehicle under real driving conditions. Thus, various drive cycles have been developed to simulate

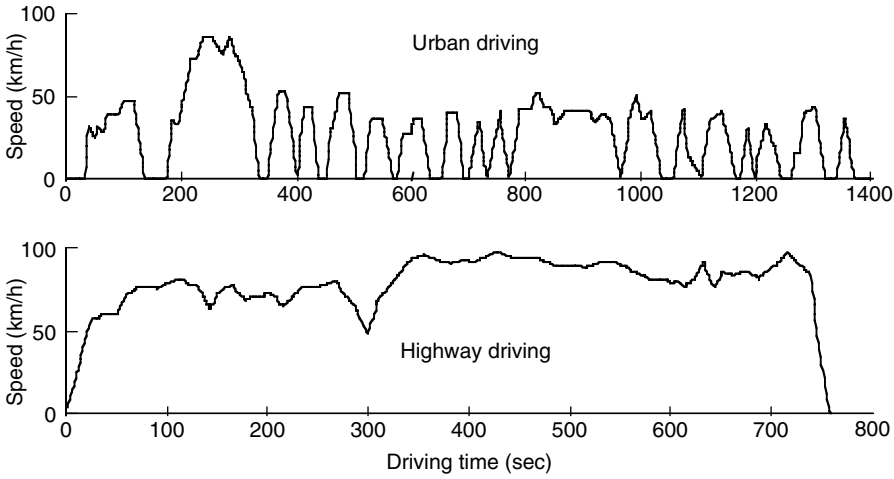

FIGURE 2.31
EPA FTP75 urban and highway drive cycles

real driving conditions. The drive cycles are usually represented by the speed of the vehicle along with the relative driving time. Figure 2.31 shows the urban and highway drive cycles of EAP FTP75 used in the U.S.

To calculate fuel consumption in a drive cycle, the total fuel consumption can be obtained by the summation of fuel consumption in each time interval, Δt_i,

$$Q_{tc} = \sum_i \frac{P_{ei}\, g_{ei}}{1000\gamma_f} \Delta t_i, \tag{2.65}$$

where P_{ei} is the average power of the engine in the ith time interval in kW, g_{ei} is the average specific fuel consumption of the engine in the ith time interval in g/kWh, and Δt_i is the ith time interval in h. This calculation can be performed by a numerical method using a suitable computer program. Figure 2.32 and Figure 2.33 show examples of the fuel economy and engine operating points in EPA FTP75 urban and highway drive cycles, respectively.

2.8.3 Basic Techniques to Improve Vehicle Fuel Economy

The effort to improve the fuel economy of vehicles has been an ongoing process in the automobile industry. Fundamentally, the techniques used include the following aspects:

(1) *Reducing vehicle resistance*: Using light materials, advanced manufacturing technologies can reduce the weight of vehicles, in turn reducing the rolling resistance and inertial resistance in acceleration and therefore reducing the demanded power on the engine. The use of advanced technologies in tire production is another

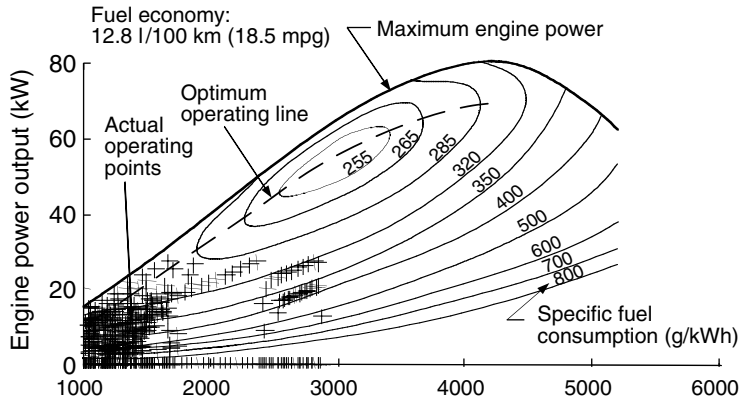

FIGURE 2.32
Fuel economy and engine operating points in EPA FTP75 urban drive cycle overlapped on engine fuel consumption characteristics map

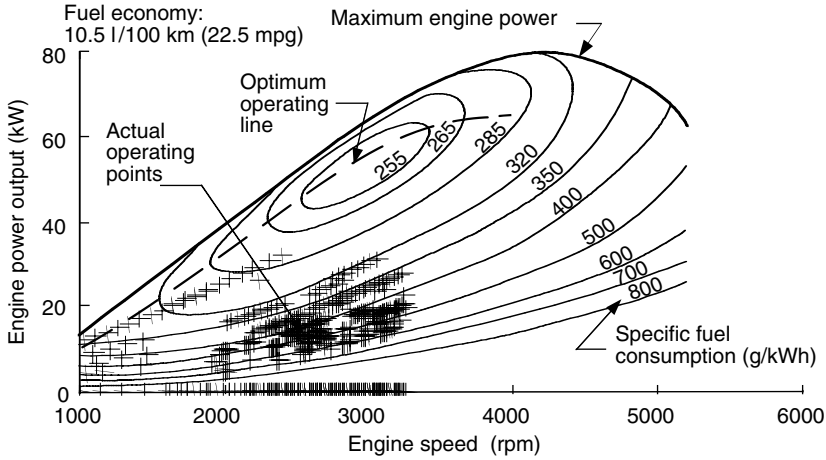

FIGURE 2.33
Fuel economy and engine operating points in EPA FTP75 highway drive cycle overlapped on engine fuel consumption characteristics map

important method of reducing the rolling resistance of vehicles. For instance, steel wire plied radial tires have a much lower rolling resistance coefficient than conventional bias ply tires. Reducing aerodynamic resistance is also quite important for improving the fuel economy at high speeds. This can be achieved by using a flow shaped body style, a smooth body surface, and other techniques. Furthermore, improving transmission efficiency can reduce energy losses in the transmission. Proper transmission construction, good lubrication, proper adjustment and tightening of moving parts in the transmission, and so on will achieve this purpose.

(2) *Improving engine operation efficiency*: Improving engine operation efficiency has the potential to contribute to the improvement of vehicle fuel economy. There are many effective advanced techniques, such as accurate air/fuel ratio control with computer-controlled fuel injection, high thermal isolated materials for reducing thermal loss, varying ignition-timing techniques, active controlled valve and port, etc.
(3) *Properly matched transmission*: The parameters of the transmission, especially gear number and gear ratios, have considerable influence on the operating fuel economy as described previously. In the design of the transmission, the parameters should be constructed such that the engine will operate close to its fuel optimum region.
(4) *Advanced drive trains*: Advanced drive trains developed in recent years, such as new power plants, various hybrid drive trains, etc., may greatly improve the fuel economy of vehicles. Fuel cells have higher efficiency and lower emissions than conventional internal combustion engines. Hybridization of a conventional combustion engine with an advanced electric motor drive may greatly enhance the overall efficiency of vehicles.

2.9 Braking Performance

The braking performance of a vehicle is undoubtedly one of the most important characteristics that affect vehicle safety. In urban driving, a significant amount of energy is consumed in braking. In recent years, more and more electric drives have been involved in vehicle traction, such as electric vehicles, hybrid electric vehicles, and fuel cell-powered vehicles. The electrification of the vehicle drive train makes it feasible to recover some of the energy lost in braking. This technology is usually referred to as regenerative braking. A well-designed regenerative braking system not only improves vehicle efficiency but also potentially improves braking performance. In this section, a method of approach to the analysis of braking performance will be presented, which aims to help the designing of regenerative braking systems.

2.9.1 Braking Force

Figure 2.34(a) shows a wheel during braking. The brake pad is pressed against the brake plate, thus developing a frictional torque on the brake plate. This braking torque results in a braking force in the tire–ground contact area. It is just this braking force that tries to stop the vehicle. The braking force can be expressed as

$$F_b = \frac{T_b}{r_d}. \tag{2.66}$$

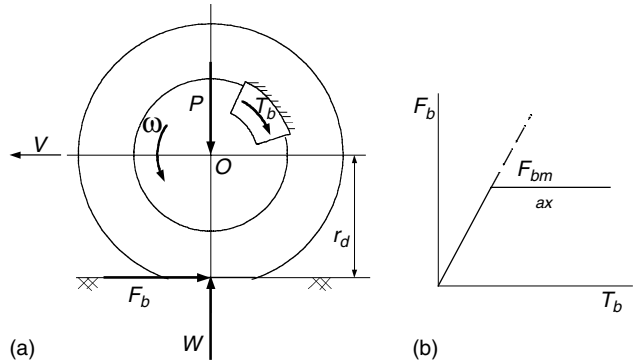

FIGURE 2.34
(a) Braking torque and braking force, and (b) relationship between braking torque and braking force

The braking force increases with an increase in braking torque. However, when the braking force reaches the maximum braking force that the tire–ground adhesion can support, it will not increase further, although the braking torque may still increase as shown in Figure 2.34(b). This maximum braking force limited by the adhesive capability can be expressed as

$$F_{b\max} = \mu_b W, \tag{2.67}$$

where μ_b is the adhesive coefficient of the tire–ground contact. Similar to the traction case (Figure 2.8), the adhesive coefficient varies with the slipping of the tire. There exists a maximum value in the slip range of 15–20%, declining somewhat at 100% slip.

2.9.2 Braking Distribution on Front and Rear Axles

Figure 2.35 shows the forces acting on a vehicle during braking on a flat road. Rolling resistance and aerodynamic drag are ignored in this figure, because they are quite small compared to the braking forces. j is the deceleration of the vehicle during braking, which can be easily expressed as

$$j = \frac{F_{bf} + F_{br}}{M_v}, \tag{2.68}$$

where F_{bf} and F_{br} are the braking forces acting on front and rear wheels, respectively.

The maximum braking force is limited by the tire–ground adhesion and is proportional to the normal load acting on the tire. Thus, the actual braking force developed by the brake torque should also be proportional to the normal load so that both the front and the rear wheels obtain their maximum braking force at the same time. During braking, there is load transfer from the rear axle to the front axle. By considering the equilibrium of moments

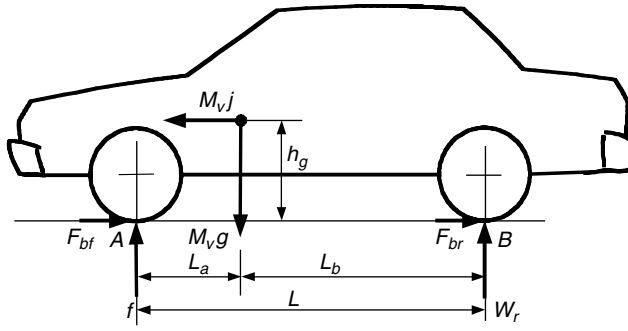

FIGURE 2.35
Force acting on a vehicle during braking on a flat road

about the front and rear tire–ground contact points A and B, the normal loads on the front and rear axles, W_f and W_r, can be expressed as

$$W_f = \frac{M_v g}{L}\left(L_b + h_g \frac{j}{g}\right) \tag{2.69}$$

and

$$W_r = \frac{M_v g}{L}\left(L_a - h_g \frac{j}{g}\right), \tag{2.70}$$

where j is the deceleration of the vehicle.

The braking forces of the front and rear axle should be proportional to their normal load, respectively; thus, one obtains

$$\frac{F_{bf}}{F_{br}} = \frac{W_f}{W_r} = \frac{L_b + h_g j/g}{L_a - h_g j/g}. \tag{2.71}$$

Combining (2.68) and (2.71), the ideal braking forces on the front and rear axle can be obtained as shown in Figure 2.36, where j represents the maximum acceleration that a vehicle can obtain on the road with an adhesive coefficient μ. The ideal braking force distribution curve (simply, I curve) is a nonlinear hyperbolic curve. If it is desired for the front and rear wheels to lock up at the same time on any road, the braking force on the front and rear axle must closely follow this curve.

In vehicle design, the actual braking forces on the front and rear axle are usually designed to have a fixed linear proportion. This proportion is represented by the ratio of the front axle braking force to the total braking force of the vehicle, that is

$$\beta = \frac{F_{bf}}{F_b}, \tag{2.72}$$

where F_b is the total braking force of the vehicle ($F_b = F_{bf} + F_{br}$). With β being the actual braking force on the front and rear axle, this can be expressed as

$$F_{bf} = \beta F_b. \tag{2.73}$$

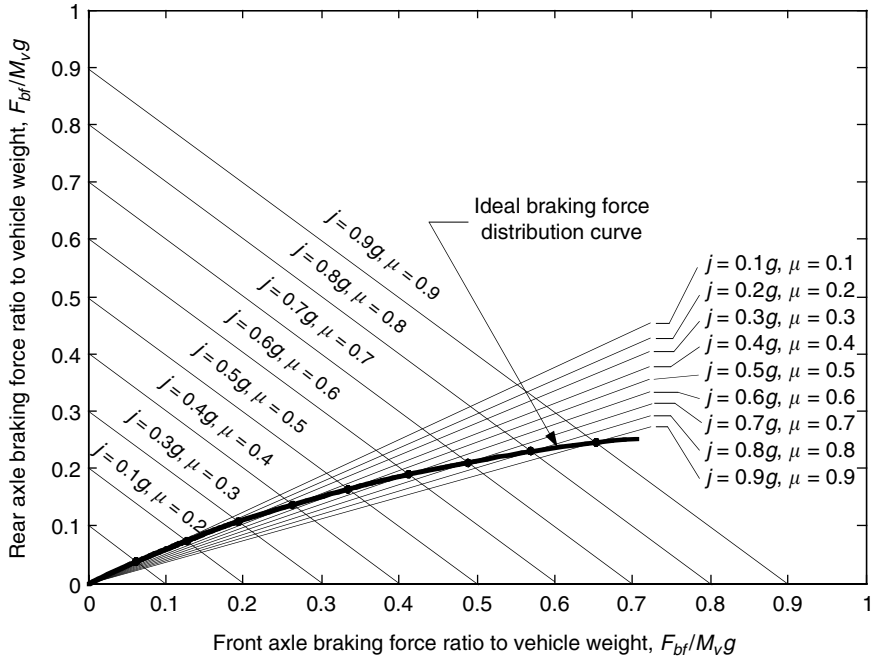

FIGURE 2.36
Ideal braking force distribution curve on the front and rear axles

and

$$F_{br} = (1-\beta)F_b. \tag{2.74}$$

Thus, one obtains

$$\frac{F_{bf}}{F_{br}} = \frac{\beta}{1-\beta}. \tag{2.75}$$

Figure 2.37 shows the ideal and actual braking force distribution curves (labeled I and β curves). It is clear that only one intersection point exists, at which the front and rear axles lock up at the same time. This point represents one specific road adhesive coefficient, μ_0. Referring to (2.71), in which j/g is replaced by μ_0, and (2.75), one can obtain

$$\frac{\beta}{1-\beta} = \frac{L_b + \mu_0 h_g}{L_a - \mu_0 h_g}. \tag{2.76}$$

From (2.75), one can obtain μ_0 or β by

$$\mu_0 = \frac{L\beta - L_b}{h_g} \tag{2.77}$$

and

$$\beta = \frac{\mu_0 h_g + L_b}{L}. \tag{2.78}$$

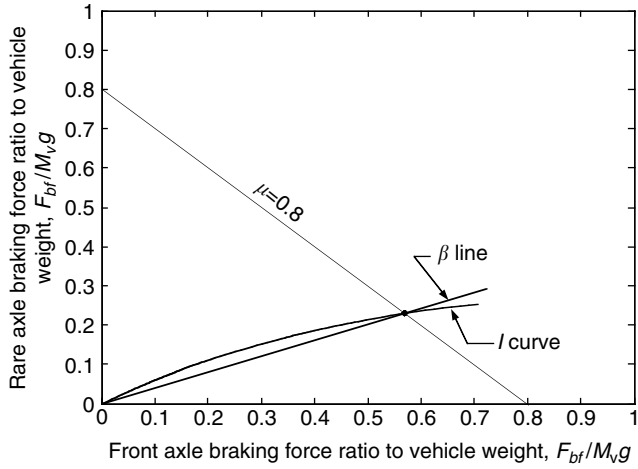

FIGURE 2.37
Ideal and actual braking force distribution curves

During braking on roads with an adhesive coefficient that is less than μ_0 (the region in which the β curve is below the I curve), the front wheels lock up first, whereas when the road adhesive coefficient is larger than μ_0 (the region in which the β curve is above the I curve), the rear wheels lock up first.

When the rear wheels lock up first, the vehicle will lose directional stability, as shown in Figure 2.38. The figure shows the top view of a two-axle vehicle acted upon by the braking force and the inertia force. When the rear wheels lock, the capability of the rear tires to resist lateral forces is reduced to zero (refer to Figure 2.7). If some slight lateral movement of the rear wheels is initiated by side wind, road camber, or centrifugal force, a yawing moment due to the inertia force about the yaw center of the front axle will develop. As the yaw motion progresses, the moment arm of the inertia force increases, resulting in an increase in yaw acceleration. As the rear end of the vehicle swings around 90°, the moment arm gradually decreases and eventually the vehicle rotates 180° with the rear end leading the front end.

The lockup of front wheels will cause a loss of directional control, and the driver will no longer be able to exercise effective steering. It should be pointed out, however, that front wheel lockup does not cause directional instability. This is because whenever the lateral movement of the front wheels occurs, a self-correcting moment due to the inertial force of the vehicle about the yaw center of the rear axle develops. Consequently, it tends to bring the vehicle back to a straight-line path. Figure 2.39 shows the measured angular deviation of a vehicle when the front and rear wheels do not lock at the same instant.[1]

Loss of steering control may be detected more readily by the driver and control may be regained by the release or partial release of the brakes. Contrary to the case of front wheel lockup, when rear wheels lock and the

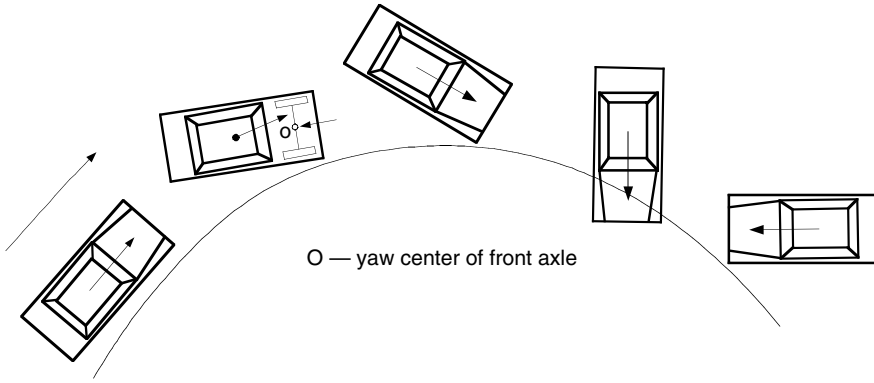

FIGURE 2.38
Loss of directional stability due to the lockup of rear wheels

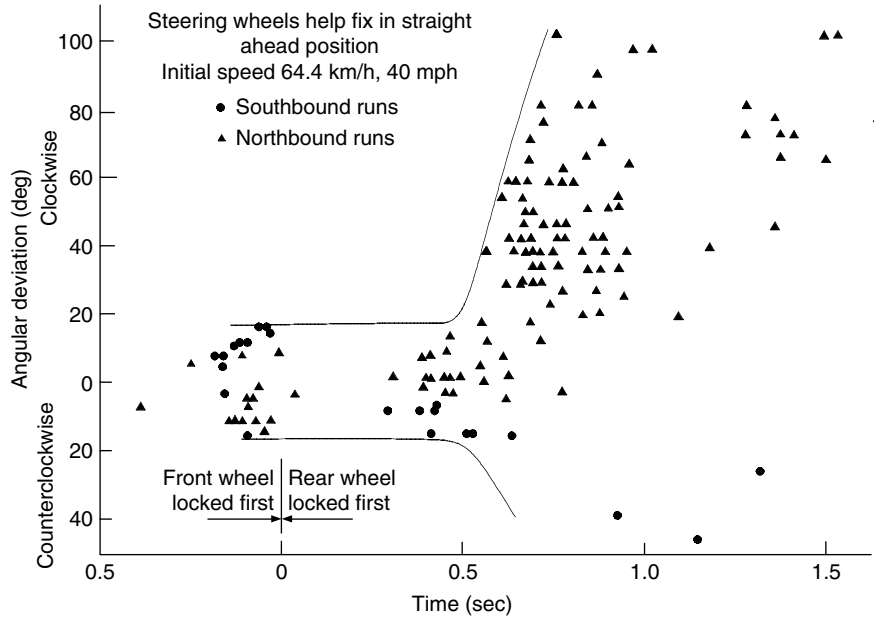

FIGURE 2.39
Angular deviation of a car when all four wheels do not lock at the same instant

angular deviation of the vehicle exceeds a certain level, control cannot be regained even by complete release of the brakes and by the most skilful driving. This suggests that rear wheel lockup is a more critical situation, particularly on a road with a low adhesive coefficient. Since on slippery surfaces the value of the braking force is low, the kinetic energy of the vehicle will dissipate at a low rate and the vehicle will experience a serious loss of

directional stability over a considerable distance. Therefore, designers of vehicle brake systems must ensure that rear wheels do not lock up first.

The antilock braking system (ABS), developed in recent years, can effectively prevent wheels from locking up. This system employs speed sensors to detect the wheel rotating speed. When a wheel lockup is detected, the braking pressure control system reduces the pressure and brings the wheel back to its rotation.[3]

References

[1] J.Y. Wong, *Theory of Ground Vehicles*, John Wiley & Sons, New York, 1978.
[2] Bosch, *Automotive Handbook*, by Robert Bosch GmbH, Stuttgart, 2000.
[3] S. Mizutani, *Car Electronics*, Sankaido Co., Warrendale, PA, 1992.

3

Internal Combustion Engines

CONTENTS

3.1 4S, Spark-Ignited IC Engines 62
3.1.1 Operating Principles 62
3.1.2 Operation Parameters 64
3.1.2.1 Rating Values of Engines 64
3.1.2.2 Indicated Work per Cycles and Mean Effective Pressure 64
3.1.2.3 Mechanical Efficiency 66
3.1.2.4 Specific Fuel Consumption and Efficiency 67
3.1.2.5 Specific Emissions 68
3.1.2.6 Fuel/Air and Air/Fuel Ratio 68
3.1.2.7 Volumetric Efficiency 69
3.1.3 Relationships between Operation and Performance Parameters 69
3.1.4 Engine Operation Characteristics 70
3.1.4.1 Engine Performance Parameters 70
3.1.4.2 Indicated and Brake Power and Torque 71
3.1.4.3 Fuel Consumption Characteristics 72
3.1.5 Operating Variables Affecting SI Engine Performance, Efficiency, and Emissions Characteristics 74
3.1.5.1 Spark Timing 74
3.1.5.2 Fuel/Air Equivalent Ratio 74
3.1.6 Emission Control 77
3.1.7 Basic Technique to Improve Performance, Efficiency, and Emission Characteristics 78
3.2 4S, Compression-Ignition IC Engines 81
3.3 Two-Stroke Engines 82
3.4 Wankel Rotary Engines 86
3.5 Stirling Engines 89
3.6 Gas Turbine Engines 94
3.7 Quasi-Isothermal Brayton Cycle Engines 97
References 98

The internal combustion (IC) engine is the most popular powerplant for motor vehicles. In the foreseeable future, it promises to become the dominant vehicular powerplant. In hybrid electric vehicles, the IC engine will also be the first selection as a primary power source. However, the operation of a hybrid electric vehicle differs from that of a conventional motor vehicle. The engine in a hybrid electric vehicle runs for a longer time at high power and does not require its power to be changed frequently. A specifically designed and controlled engine for hybrid vehicle applications has not been fully developed. In this chapter, the commonly used four-stroke (4S) IC engine and other types of engines, which can be possibly used in hybrid vehicles, such as two-stroke engines, rotary engines, Stirling engines, and gas turbine engines, are reviewed. For more details, readers may consult the relevant literature.

3.1 4S, Spark-Ignited IC Engines

3.1.1 Operating Principles

A 4S, spark-ignited (SI), internal combustion engine is illustrated in Figure 3.1. It consists of subsystems including powering (crankshaft, connection rod, pistons, and cylinders), intake and exhaust (air filter, throttle, inlet and exhaust manifolds, inlet and exhaust valves, and valve control cams), fuel supply (fuel tank [not shown], fuel pump [not shown], and fuel injectors), ignition (battery [not shown], ignition coils [not shown], distributor [not shown], and spark plugs), cooling (coolant, water pump [not shown], radiator [not shown]), and lubricating (not shown).

The combustion of the air/fuel mixture formed within the inlet manifold and trapped in the cylinder produces heat, so that the temperature and pressure in the cylinder increase quickly. Thus, the piston is forced to move down. The connection rod transfers the linear movement of the piston into the rotary motion of the crankshaft.

A 4S, SI engine has four distinctive processes corresponding to the four strokes of each piston[1,2] (Figure 3.2).

1. Induction stroke (cylinder-filling process): The inlet valve is open, the exhaust valve is closed, and the piston travels down the cylinder, drawing in charge from the air/fuel mixture formed within the inlet manifold.
2. Compression stroke: Both inlet and exhaust valves are closed, and the piston goes up the cylinder. As the piston approaches the top dead center (TDC), the spark plug produces a spark to ignite the air/fuel mixture.
3. Expansion stroke (power producing, or working process): Combustion propagation through the charge raises the temperature and

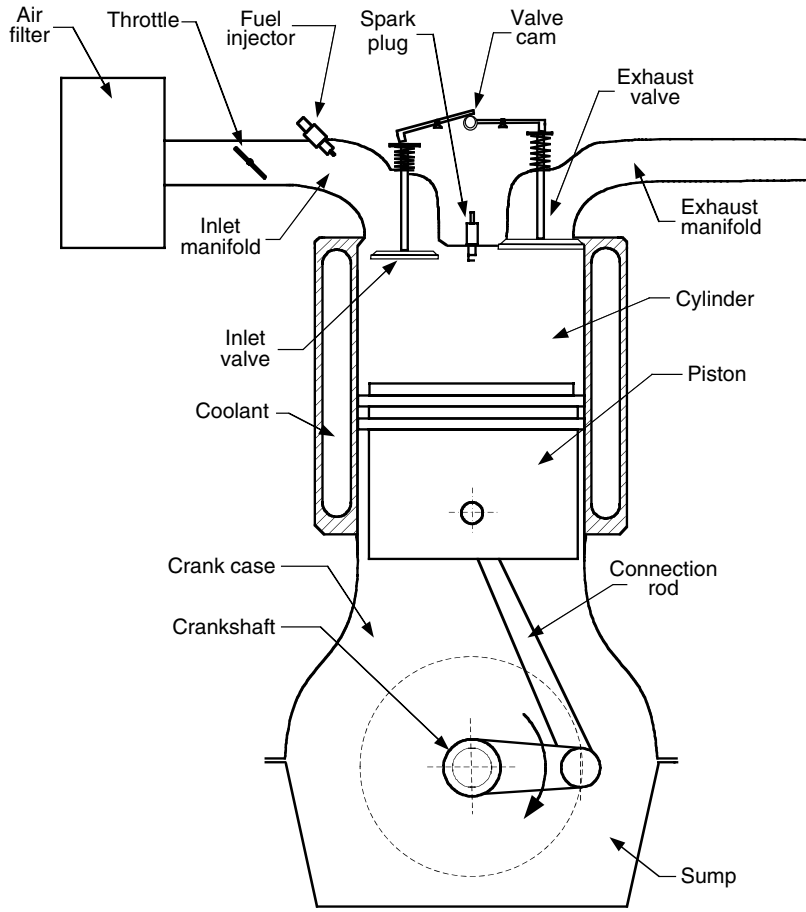

FIGURE 3.1
4S, SI gasoline engine

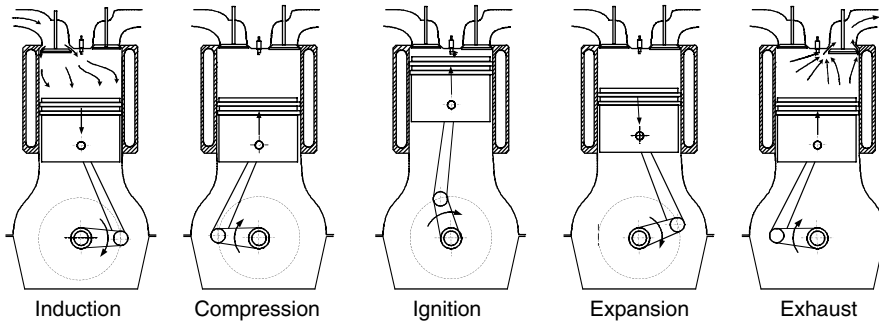

FIGURE 3.2
Four strokes of a spark ignition engine

pressure in the cylinder, moving the piston down. At the end of the expansion stroke, the exhaust valve opens and an irreversible expansion of the exhaust gases blows out the exhaust valve. This is termed "blow-down."

4. Exhaust stroke: The exhaust valve remains open, and as the piston travels up the cylinder, the remaining gases in the cylinder are expelled. At end of the exhaust stroke, the exhaust valve closes. However, some residual exhaust gases will remain. This exhaust dilutes the next charge. Following this stroke, the induction stroke of the next cycle starts.

Since the cycle is completed only once every two revolutions of the crankshaft, the gear driver camshaft (for opening and closing the valves) has to be driven by the mechanism operating at half crankshaft speed (engine speed). Some of the power from the expansion stroke is stored in the flywheel to provide the energy for another three strokes.

3.1.2 Operation Parameters

3.1.2.1 Rating Values of Engines

The most common parameters for engine performance are:
Maximum rated power: The highest power that an engine is allowed to develop for a short period of operation.
Normal rated power: The highest power that an engine is allowed to develop in continuous operation.
Rated speed: The rotational speed of the crankshaft, at which the rated power is developed.
For vehicle application, engine performance is more precisely defined by:

1. The maximum power (or maximum torque) available at each speed within a useful engine operating range.
2. The range of speed and the power over which engine operation is satisfactory.

3.1.2.2 Indicated Work per Cycle and Mean Effective Pressure

The torque performance of the 4S SI engine is determined by the pressure within the cylinder, as shown in Figure 3.3. In induction stroke (g–h–a), the pressure in the cylinder is usually lower than the atmospheric pressure because of the resistance of the airflow into the cylinder. In compression stroke (a–b–c), the pressure increases with the up movement of the piston. When the piston approaches the TDC, the spark plug produces a spark to ignite the air/fuel mixture trapped in the cylinder, and the pressure increases quickly. In expansion stroke (c–d–e), the high-pressure gases in the cylinder push the piston downward, producing torque on the crankshaft. In

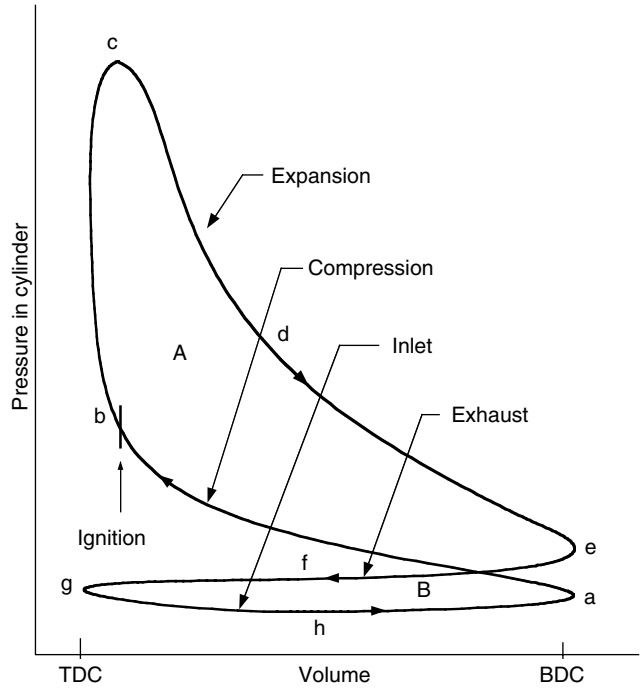

FIGURE 3.3
Diagram of pressure vs. volume

exhaust stroke (e–f–g), the gases in the cylinder are propelled out of the cylinder at a higher pressure than in induction stroke.

The torque performance is usually evaluated by the gross work done in one cycle, usually called gross indicated work, $W_{c,in}$. The gross indicated work can be calculated by

$$W_{c,in} = \int_{\text{area } A} p\, dV - \int_{\text{area } B} p\, dV, \tag{3.1}$$

where p is the pressure in the cylinder and V is the volume. The work done in the area B is negative, because the pressure in induction stroke is lower than the pressure in exhaust stroke. In order to achieve the maximum work in one cycle, area A should be made as large as possible by increasing the pressure in expansion stroke, and area B should be made as small as possible by increasing the pressure in induction stroke and decreasing in exhaust stroke. When the pressure in induction stroke is greater than the pressure in exhaust stroke, the work in this area will become positive. This is the case of the supercharged engine.

The torque of an engine depends on the engine size (engine displacement, which is defined as the volume that the piston sweeps from TDC to bottom dead center [BDC]). A more useful relative performance measure is the mean

effective pressure (*mep*), which is defined as the work per cycle per displacement:

$$mep = \frac{work\ per\ cycle}{displacement\ of\ cylinder}. \tag{3.2}$$

The mean effective pressure can be expressed in terms of torque as

$$mep\ (\text{kPa}) = \frac{2\pi\ n_R\ T\ (\text{Nm})}{V_d\ (\text{dm}^3)}, \tag{3.3}$$

where n_R *is* the number of revolutions of crankshaft for each power stroke per cylinder ($n_R = 2$ for 4S engines and $n_R = 1$ for two-stroke engines), T is the torque in Nm, and V_d is the displacement of the engine. The torque of an engine depends only on the mean effective pressure in the cylinder and the engine displacement V_d. For a given engine size, increasing the *mep* is the only method of increasing the engine torque. It should be noted that when dealing with *mep*, one must clearly tell whether it is indicated *mep* (*imep*), which is measured within the cylinder, or brake *mep* (*bmep*), which is measured on the crankshaft. The difference between them is that the *imep* includes the engine mechanical loss (it is gross), and *bmep* does not include the engine mechanical loss (it is net). Mechanical loss is discussed in the following section.

3.1.2.3 Mechanical Efficiency

Not all the power produced in the cylinder (indicated power) is available on the crankshaft. Part of it is used to drive engine accessories and overcome the friction inside the engine. All of these power requirements are grouped together and called friction power P_f. Thus,

$$P_{ig} = P_b + P_f, \tag{3.4}$$

where P_b is the brake power (useful power on the crankshaft). It is quite difficult to determine friction accurately. In practice, one common approach for automotive engines is to drive or motor the engine on a dynamometer (operate the engine without firing it) and measure the power supplied by the dynamometer.

The ratio of the brake power (useful power on the crankshaft) to the indicated power is called the mechanical efficiency, η_m:

$$\eta_m = \frac{P_b}{P_{ig}} = 1 - \frac{P_f}{P_{ig}}. \tag{3.5}$$

The mechanical efficiency of an engine depends on the throttle position as well as the design and engine speed. Typical values for modern automotive engines with wide-open characteristics are 90% at a speed below about 1800 to 2400 rpm, decreasing to 75% at the maximum rated speed. As the engine is throttled, the mechanical efficiency decreases eventually to zero at idle operation.

By removing the engine mechanical loss from the indicated work or indicated mean effective pressure, one can obtain the net work or brake mean effective pressure that is measured on the crankshaft. The maximum brake mean effective pressure of good engine designs is well established, and is essentially constant over a large range of engine sizes. Typical values for *bmep* are as follows. For naturally aspirated SI engines, maximum values are in the range 850 to 1059 kPa (125 to 150 psi) at the engine speed where maximum torque is produced. At the maximum rated power, *bmep* values are 10 to 15% lower. For turbocharged automotive SI engines, the maximum *bmep* is in the range 1250 to 1700 kPa (180 to 250 psi). At the maximum rated power, *bmep* is in the range of 900 to 1400 kPa (130 to 200 psi).

3.1.2.4 Specific Fuel Consumption and Efficiency

In engine tests, fuel consumption is measured as a flow rate — mass flow per unit time, $\dot{m}_f$. A more useful parameter is the *specific fuel consumption (sfc)* — the fuel flow rate per useful power output. It measures how efficiently an engine is using the fuel supplied to produce work:

$$sfc = \frac{\dot{m}_f}{P}, \tag{3.6}$$

where $\dot{m}_f$ is the fuel flow rate and P is the engine power. If the engine power P is measured as the net power from the crankshaft, the specific fuel consumption is called *brake-specific fuel consumption (bsfc)*. The *sfc* or *bsfc* is usually measured in SI units by the gram numbers of fuel consumed per kW power output per hour (g/kWh). Low values of *sfc* (*bsfc*) are obviously desirable. For SI engines, typical best values of *bsfc* are about 250 to 270 g/kWh.

Normally, a dimensionless parameter that related the desirable engine output (work per cycle or power) to the necessary input (fuel flow) would have more fundamental value. The ratio of the work produced per cycle to the amount of fuel energy supplied per cycle that can be released in the combustion process is commonly used for this purpose. It is a measure of the engine efficiency (fuel conversion efficiency) as shown below:

$$\eta_f = \frac{W_c}{m_f \; Q_{HV}} = \frac{P}{\dot{m}_f \; Q_{HV}}, \tag{3.7}$$

where W_c is the work done in one cycle, m_f is the fuel mass consumed per cycle, and Q_{HV} is the heating value of the fuel, which is defined as the heat released from unit fuel with complete combusting at standard conditions and the combustion products cooling down to their original temperature. The typical heating values for the commercial hydrocarbon fuels used in engines are in the range of 42 to 44 MJ/kg (11.7 to 12.2 kWh/kg). Dimensionless efficiency can be expressed by *sfc* as

$$\eta_f = \frac{1}{sf_c \; Q_{HV}}. \tag{3.8}$$

3.1.2.5 Specific Emissions

The levels of emission of oxides of nitrogen (nitric oxide [NO] and nitrogen dioxide [NO_2] usually found together as NO_x), carbon monoxide, unburned hydrocarbons (HCs), and particulars are important engine operating characteristics. The concentrations of gaseous emissions in the engine exhaust are usually measured in parts per million or percent by volume (mole fraction). Specific emissions are the flow rate of pollutant per power output.

$$s\mathrm{NO}_x = \frac{\dot{m}_{\mathrm{NO}_x}}{P}, \tag{3.9}$$

$$s\mathrm{CO} = \frac{\dot{m}_{\mathrm{CO}}}{P}, \tag{3.10}$$

$$s\mathrm{HC} = \frac{\dot{m}_{\mathrm{HC}}}{P}, \tag{3.11}$$

$$spart = \frac{\dot{m}_{part}}{P}. \tag{3.12}$$

Alternatively, emission rates can be normalized by the fuel flow rate; an emissions index (EI) is commonly used as

$$EI_{\mathrm{NO}_x} = \frac{\dot{m}_{\mathrm{NO}_x}(\mathrm{g/sec})}{\dot{m}_f(\mathrm{kg/sec})}, \tag{3.13}$$

with similar expressions for CO, HA, and particulates.

3.1.2.6 Fuel/Air and Air/Fuel Ratio

In engine testing, both the air mass flow ratio, $\dot{m}_a$, and the fuel mass flow rate, $\dot{m}_f$, are normally measured. The ratio of these flow rates is useful in defining engine operating conditions.

$$\textit{fuel/air ratio } (F/A) = \frac{\dot{m}_f}{\dot{m}_a} \quad \textit{and} \quad \textit{air/fuel ratio } (A/F) = \frac{\dot{m}_a}{\dot{m}_f}. \tag{3.14}$$

The stoichiometric fuel/air ratio is defined as the mass ratio of fuel to air such that, with this mass ratio, the combustion can be chemically completed. For gasoline, the stoichiometric fuel/air ratio is 0.0685 (air/fuel ratio: 14.6). More conveniently, fuel/air equivalent ratio, ϕ, air/fuel equivalent ratio, λ, are commonly used. The fuel/air equivalent ratio is defined as

$$\phi = \frac{(F/A)_{actual}}{(F/A)_s} \tag{3.15}$$

and

$$\lambda = \frac{(A/F)_{actual}}{(A/F)_s}. \tag{3.16}$$

For fuel-rich mixtures: $\phi > 1$, $\lambda < 1$.
For stoichiometric mixtures: $\phi = \lambda = 1$.
For fuel-lean mixtures: $\phi < 1$, $\lambda > 1$.

The normal operating range for a conventional SI engine using gasoline is $0.82 \leq \phi \leq 1.23$, or $0.056 \leq F/A \leq 0.083$.

3.1.2.7 Volumetric Efficiency

The intake system — the air filter, intake manifold, throttle plate, intake port, intake valve — restricts the amount of air that an engine of given displacement can induct. The parameter used to measure the effectiveness of an engine's induction process is the volumetric efficiency, η_v. The volumetric efficiency is defined as the volume flow rate of air into the intake system divided by the rate at which volume is displaced by the piston:

$$\eta_v = \frac{2\dot{m}_a}{\rho_{a,i} V_d N}, \tag{3.17}$$

where $\rho_{a,i}$ is the inlet air density and N is the rpm of the engine. An alternative equivalent definition for volumetric efficiency is

$$\eta_v = \frac{m_a}{\rho_{a,i} V_d}, \tag{3.18}$$

where m_a is the mass of air induced into the cylinder per cycle.

The inlet density may either be taken as the atmospheric air density (in which case, η_v measures the pumping performance of the entire inlet system) or may be taken as the density in the inlet manifold (in which case, η_v measures the pumping performance of the inlet port and valve only). Typical maximum values of η_v for naturally aspirated engines are in the range of 80 to 90%. The volumetric efficiency for diesel is somewhat higher than for SI engines.

3.1.3 Relationships between Operation and Performance Parameters

The importance of the parameters discussed above to engine performance becomes evident when power, torque, and mean effective pressure are expressed in terms of these parameters. For power P,

$$P = \frac{\eta_f m_a N Q_{HV} (F/A)}{n_R}. \tag{3.19}$$

For a 4S engine, volumetric efficacy can be introduced, and (3.19) can be expressed as

$$P = \frac{\eta_f \eta_v N V_d Q_{HV} \rho_{a,i} (F/A)}{n_R}. \tag{3.20}$$

For torque T,

$$T = \frac{\eta_f \eta_v V_d Q_{HV} \rho_{a,i} (F/A)}{4\pi}. \tag{3.21}$$

For mean effective pressure,

$$mep = \eta_f \, \eta_v \, Q_{HV} \, \rho_{a,i} \, (F/A). \tag{3.22}$$

The power per unit piston area, often called the specific power, is a measure of the engine designer's success in using the available piston area regardless of the cylinder size. From equation (3.20), the specific power is

$$\frac{P}{A_p} = \frac{\eta_f \eta_v NLQ_{HV} \rho_{a,i}(F/A)}{2}. \tag{3.23}$$

The mean piston speed can be introduced with equation (3.23):

$$\frac{P}{A_p} = \frac{\eta_f \eta_v \overline{S}_p Q_{HV} \rho_{a,i}(F/A)}{4}, \tag{3.24}$$

where $\overline{S}_p$ is the mean piston speed.
These relationships illustrate the direct importance to engine performance of:

1. High fuel conversion efficiency
2. High volumetric efficiency
3. Increasing the output of a given displacement engine by increasing the inlet air density
4. Maximum fuel/air ratio that can be usefully burned in the engine
5. High mean piston speed

3.1.4 Engine Operation Characteristics

3.1.4.1 Engine Performance Parameters

The practical engine performance parameters of interest are power, torque, specific fuel consumption, and specific emissions. The power of the 4S engine can be expressed as

$$P = \frac{mepA_p\overline{S}_p}{4}, \tag{3.25}$$

where *mep* is mean effective pressure, A_p is area of piston head, and $\overline{S}_p$ is mean piston speed. The torque, T, is given by

$$T = \frac{mepV_d}{4\pi}. \tag{3.26}$$

Thus for well-designed engines, the maximum values of mean effective pressure and piston speed are either flow limited (in naturally aspirated engines) or stress limited (in turbocharged engines). Power is proportional to piston area and torque to displaced volume. For 4S engines, the mean effective pressure can be expressed as

$$mep = \eta_f \eta_v Q_{LHV} \rho_{a,i} \left(\frac{F}{A} \right). \tag{3.27}$$

The importance of high fuel conversion efficiency, volumetric efficiency (breathing capacity), and inlet air density is clear. Specific fuel consumption is related to the fuel conversion efficiency by

$$sfc = \frac{1}{\eta_f Q_{LHV}}. \tag{3.28}$$

These parameters have both brake and indicated values. The difference between these two quantities is the engine's friction (and pumping) requirements and their ratio is the mechanical efficiency [see equation (3.5)].

The relative importance of these parameters varies over an engine's operation speed and load range. The maximum rated or normal rated brake power and the quantities such as *bmep* define an engine's full potential. The maximum brake torque (and *bmep* derived from it) over the full speed range indicates the engine's ability to obtain a high airflow through itself over the full speed range and to use that air effectively. Over the whole operating range — particularly in those parts of the range where the engine operates for a long period of time — engine fuel consumption, efficiency, and engine emissions are important.

3.1.4.2 Indicated and Brake Power and Torque

The wide-open throttle operating characteristics of an SI engine are shown in Figure 3.4. The indicated power is the average rate of work transfer from the gases in the cylinders to the piston during the compression and expansion

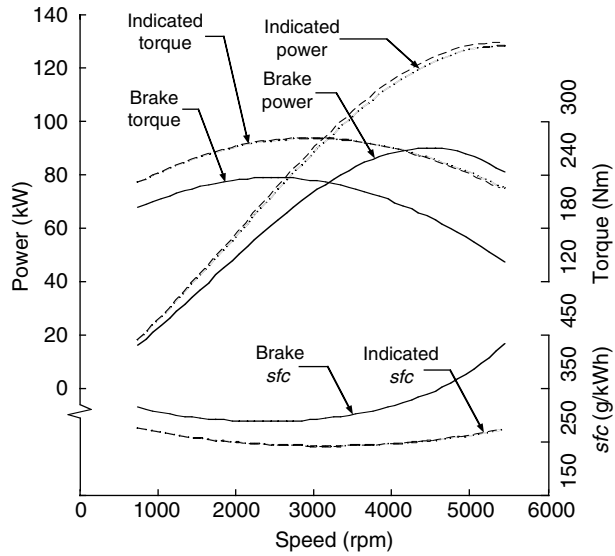

FIGURE 3.4
Indicated and brake powers, torques, and specific fuel consumptions varying with engine speed

strokes. The brake torque is obtained by subtracting the friction power from the indicated power. The brake power shows a maximum value at about a speed slightly less than the maximum speed of the engine. The indicated torque shows a maximum value in the mid-speed range, which approximately corresponds to the speed at which the volumetric efficiency has the maximum value. The brake torque decreases more than the indicated torque at high speed because of more friction.

At partial load and fixed throttle position, these parameters behave similarly; however, at high speeds, torque decreases more rapidly than at full load as shown in Figure 3.5. The partially opened throttle causes more resistance to air flowing at a higher speed, and the volumetric efficiency decreases. The pumping components of total friction also increase as the engine is throttled.

3.1.4.3 Fuel Consumption Characteristics

The fuel consumption characteristics (brake-specific fuel consumption) of an engine vary widely with engine speed and load, as shown in Figure 3.6. Generally, an engine has an optimal operating region in which fuel consumption is minimal. This region is usually located at the middle of the speed range, corresponding to the maximum torque, where the losses in induction and exhaust strokes are minimized. On the other hand, this region is close to the full load operation (wide open throttle), where the percentage of losses to the total indicated power is small. In vehicle design, the operating points of the engine should be close to this region in order to achieve high operating fuel economy.

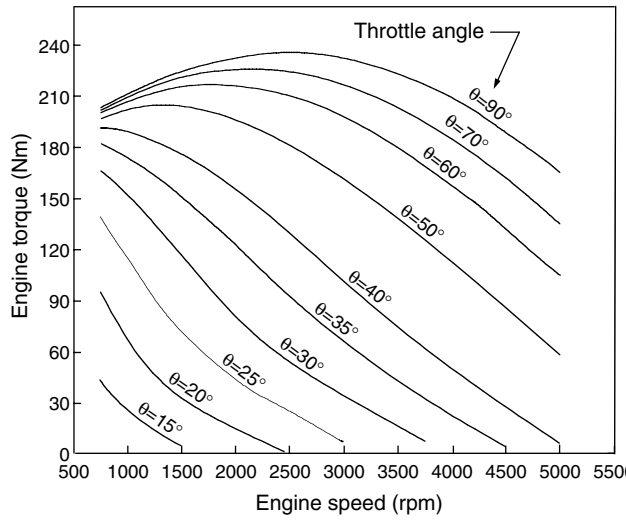

FIGURE 3.5
Torque characteristics with engine throttle opening and engine speed

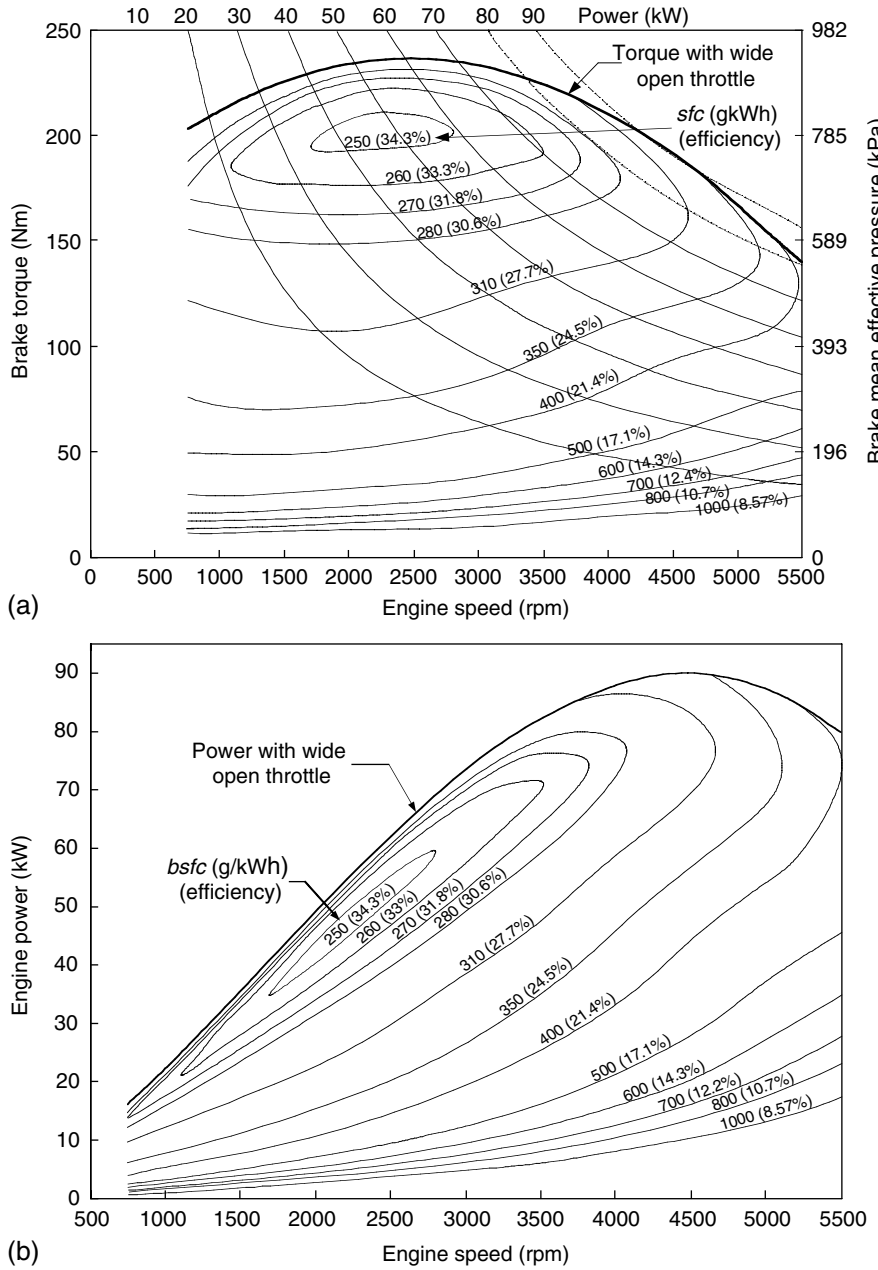

FIGURE 3.6
Fuel consumption characteristics of a typical SI engine

3.1.5 Operating Variables Affecting SI Engine Performance, Efficiency, and Emissions Characteristics

The major operating variables that affect SI engine performance, efficiency, and emissions characteristics are spark timing, valve timing, air/fuel ratio, the fraction of exhaust gases that are recycled for NO_x emission control, etc.

3.1.5.1 Spark Timing

For SI engines under normal operating conditions, toward the end of the compression stroke, a spark plug produces a spark to ignite the mixture in the cylinder and combustion is initiated. Because the propagation of the flame in the cylinder needs time, ignition must start before the end of the compression stroke. The degree of the crankshaft angle, from the starting of the ignition to the end of the compression stroke, is called *spark advance* in degrees of crankshaft. Spark timing has a considerable effect on engine performance, efficiency, and exhaust emission.

Figure 3.7(a) shows the gas pressure in the cylinder with the crankshaft angle at different spark timings. Starting the ignition too soon (50° before TDC in Figure 3.7[a]) results in a high gas pressure acting on the piston in the compression stroke. Consequently, the negative work in the compression stroke increases and positive work in the expansion stroke decreases, resulting in low average torque. Sometimes, too-early ignition causes abnormal combustion in the cylinder, which usually causes piston "knocking." Knocking is the most serious abnormal combustion phenomenon, which usually causes damage to the mechanical parts, such as the crankshaft, bearings, and connection rods. Too-late ignition (10° before TDC in Figure 3.7[a]) results in low gas pressure in the cylinder, and thus low effective work. There exists an optimal spark timing at which the average engine torque reaches its maximum value. This optimal spark timing is called maximum brake torque (MBT) timing as shown in Figure 3.7(b). Spark timing, which is advanced or retarded from MBT timing, gives lower average torque. MBT timing is associated with the rate of flame development and propagation, the length of the flame travel path across the combustion chamber, and the details of the flame termination process after it reaches the wall. These depend on engine design, operating conditions, properties of fuel, air, burned gas mixture, etc. With a given design, engine speed exerts a considerable influence on MBT timing, therefore the sparking timing should be adjusted with engine speed.

The time from ignition starting to reaching the maximum gas pressure in the cylinder changes slightly. Thus, with increasing engine speed, the sparking advance should be increased as shown in Figure 3.7(c). Correct spark timing is important because NO and HC emissions vary significantly with spark timing.

3.1.5.2 Fuel/Air Equivalent Ratio

Proper fuel/air (or air/fuel) ratio in the fuel/air mixture is a crucial factor that affects the performance, efficiency, and emission characteristics of an

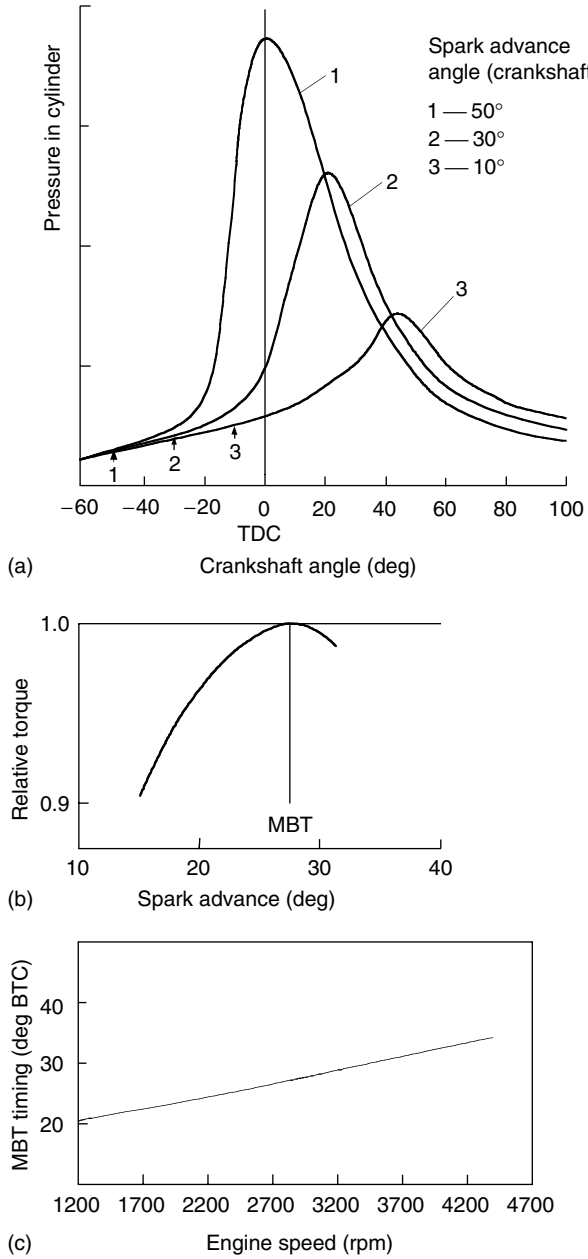

FIGURE 3.7
Effect of spark advance on engine performance: (a) cylinder pressure, (b) torque, and (c) MBT timing with engine speed

engine as shown in Figure 3.8. The mean effective pressure peaks at slightly rich stoichiometry (between $\phi = 1$ and 1.2). However, the fuel conversion efficiency decreases as the mixture is enriched above the stoichiometry ($\phi > 1$) because part of the fuel is left after combustion. When ϕ decreases, the fuel conversion efficiency increases because sufficient oxygen exists in the cylinder to oxidize the fuel and the energy of the fuel is almost released as thermal energy. In SI engines, a very lean mixture will cause losing fire (fail to ignite the mixture). $\phi = 0.8$ would be the bottom limit. With a lean mixture, the combustion produces lower temperature in the cylinder, thus resulting in a low mean effective pressure.

Fuel/air ratio has a dominant effect on emissions of SI engines as shown in Figure 3.9. Leaner mixtures produce lower emissions (NO_x, CO, and HC) until combustion quantity becomes poor (and eventually misfire occurs). When the fuel/air ratio is lower than a certain point (0.85 in Figure 3.9), HC emissions rise sharply and engine operation becomes erratic. The NO_x emissions have a curve shape different than those of CO and HC. It has a peak value close to the stoichiometric mixture, because NO_x tends to form at high temperature and pressure, which is the case in stoichiometric combustion.

Figure 3.9 indicates the complexities of emission control. In a cold engine with slow fuel vaporization, fuel flow is increased to provide an easily combustible fuel-rich mixture in the cylinder until the engine warms up and the enrichment is removed. At part-load conditions, a lean mixture in the cylinder which would produce lower HC and CO emissions and moderate NO_x emissions could be used. The use of recycled exhaust to dilute the engine intake mixture lowers the NO_x level (decreasing the temperature in the cylinder) and combustion quality also deteriorates. In practice, the fuel/air ratio varies with engine speed and intake mass flow rate as shown in Figure 3.10. At a low mass flow rate (small throttle opening), the mixture is close to

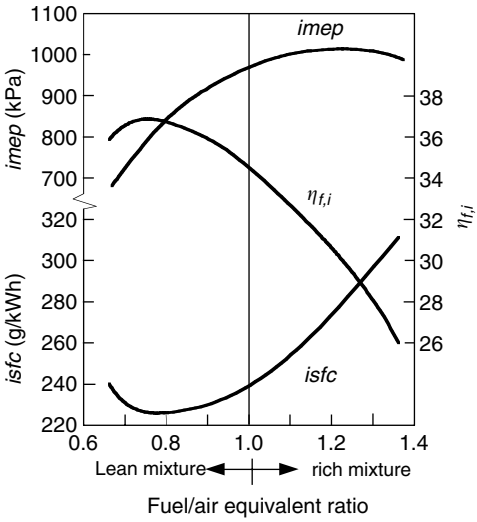

FIGURE 3.8
Fuel/air ratio effect on *imep*, fuel conversion efficiency, and *isfc*

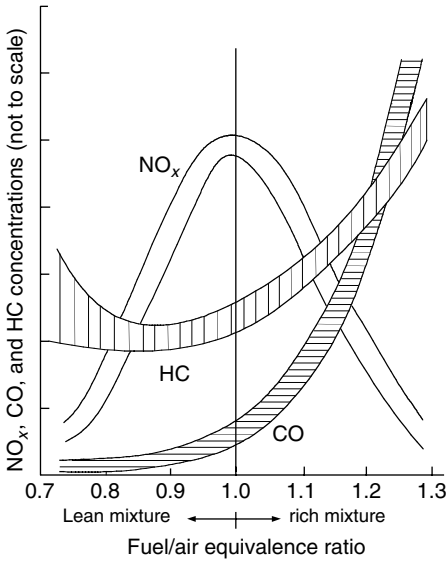

FIGURE 3.9
Fuel/air ratio effect on emissions

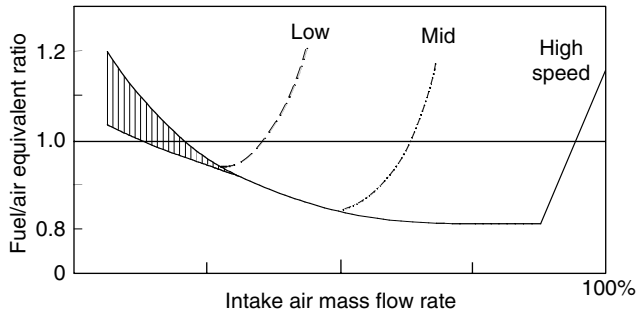

FIGURE 3.10
Fuel/air ratio varies with engine speed and intake mass flow

stoichiometric or richer, especially in an engine with carburetor fuel metering (the upper curve in Figure 3.10), due to less fuel atomization in the mixture and smooth engine operation. With a fuel injection system, fuel atomization is better than with a carburetor. With a high intake mass flow rate, the mixture becomes richer for high torque output. In the middle, the mixture is lean for better efficiency and emissions.

3.1.6 Emission Control

Today, emissions are treated in three points: fuel, engine, and exhaust (after-treatment). Gasoline is modified by means of additives and refining processes to adapt its composition in order to reduce the formation of pollutant species and facilitate the after-treatment. For example, a reformulated

gasoline may contain methyl tertiary-butyl ether (MTBE), which increases the fuel octane ratio in replacement of lead. MTBE is less harmful to the atmosphere than the lead compounds used previously; however, it is no longer used because of its danger to water sources in case of spill. Gasoline is also treated for its sulfur content. Some after-treatment techniques can only tolerate very small amounts of sulfur compounds in the gases.

A good example of engine design techniques that limit the formation of pollutant species is the exterior air intake. Previously, the engine would breathe air from underneath the hood. This air is much hotter than ambient air, thus resulting in higher temperatures during the compression and combustion and therefore resulting in high nitric oxide formation. Nowadays, the air intake is from the outside, which is much cooler and therefore results in lower nitric oxide formation. Other design or operation parameters that affect the formation of pollutant species include high-pressure fuel injection and turbulent intake flows that improve the homogeneity of the mixture; combustion chamber design; aluminum engine blocks that allow running the engine cooler; sodium-filled exhaust valves that can be cooled more easily; exhaust gas oxygen sensing that informs the engine controller what the air/fuel ratio actually is, etc.

The most powerful means of controlling the emission of pollutant species is the exhaust after-treatment. The most widespread technique, which is now mandatory in most Western countries, is the catalytic converter. It is composed of a mesh of catalytic materials such as platinum and rhodium. These catalysts react with the pollutant species and transform them to harmless species. Nitric oxides are reduced to oxygen and air, carbon monoxide is oxidized to carbon dioxide, and unburned hydrocarbons are combusted to carbon dioxide and water. A catalytic converter that can take care of all three species at the same time is referred to as a three-way catalytic converter.

Catalytic converters need a slight excess of oxygen in order to oxidize CO and HC species. Therefore, the air/fuel ratio must be precisely controlled in order to maintain a constant oxygen concentration in the exhaust. This is done by means of exhaust oxygen sensing and fuel injection. Catalytic converters are the primary reason for the replacement of carburetors by fuel injections. The catalysts operate efficiently only at high temperatures. They do not work for about 1 min when the engine is cold-started. It is during this lapse of time that the engine emits most of its pollutants. It should be noted that some emission control techniques do impair fuel consumption. This is especially true for the catalytic converter, which acts as a restriction in the exhaust flow.

3.1.7 Basic Technique to Improve Performance, Efficiency, and Emission Characteristics

Forced induction: The amount of torque produced in an internal combustion engine depends on the amount of air induced in the cylinder. An easy way to increase the amount of air induced is to increase the pressure in the intake

manifold. This can be done by three means: variable intake manifold, supercharging, or turbocharging.

The intake manifold is like a wind instrument: it has resonant frequencies. A variable intake manifold tunes itself according to the engine speed in order to exploit those resonant frequencies. If the tuning is proper, the amount of air induced in the cylinder can be optimized because the pressure in the intake manifold is increased. This technique improves the "breathing" of the engine but does not result in a very large increase of torque output.

A supercharger is an air compressor turned by the engine crankshaft. The air thus compressed is fed to the intake manifold. The advantage of a supercharger is that it can significantly increase the pressure in the intake manifold, even at low speed. The most significant disadvantage is that the supercharging power is taken from the engine crankshaft. This reduces the engine output and harms the fuel consumption.

A turbocharger consists of a turbine driven by exhaust gases and of a compressor turned by the turbine. A turbocharger has the great advantage of taking its energy from exhaust gases, which are normally wasted. Therefore, the efficiency of the engine does not suffer from the addition of the turbocharger. Turbocharging can tremendously increase the power output of the engine, especially if coupled to a charge cooling system. It also significantly improves the efficiency because the higher intake pressure reduces the negative work associated with the induction stroke. The disadvantages of turbocharging include slow response time, little or no effectiveness at low engine speed, and high rotational speed for the turbo-charger, which increases the cost of forced induction.

Supercharging and turbocharging both suffer from two inconveniences: knock and emissions. Compressing the intake air increases its temperature. An increased temperature means a greater risk of auto-ignition and knock for the mixture, and increased nitric oxide emissions. The remedy to this problem consists in cooling down the intake air after compression. This is done by means of an intercooler or heat exchanger. The compressed air is passed through a radiator, while ambient air or water is passed over the exterior of the radiator, removing the heat from the charge. The temperature of the induced air can be reduced sufficiently to avoid auto-ignition and knock. The nitric oxide emissions are also reduced. It should be noted that an engine designed for forced induction has a lower compression ratio than an engine that is designed for normal induction. Cooling the induced air is also beneficial for torque production, because cooler air is denser air. Therefore, more air can be induced in the cylinder if it is colder.

Gasoline direct injection and lean-burn engines: HC and CO emissions can be reduced if the engine burns a lean mixture. If an SI engine could run on extremely lean mixtures, then the emissions would be very significantly reduced. However, ultralean mixtures pose problems because the flame has trouble propagating. (The design of the engine needs to adapt to this condition by providing very efficient mixing.)

Gasoline direct injection is one means of achieving very efficient mixing. Because the injector is located in the cylinder, it must inject fuel at high pressure, which reduces the size of the fuel droplets. The fuel can be injected close to the spark plug, thus enriching locally the mixture and allowing better ignition. An additional advantage of gasoline direct injection includes the cooling of the intake air, which reduces knock and allows operating at a higher compression ratio. This further improves engine efficiency. Besides the cost increase, gasoline direct injection results in higher NO_x emissions.

Multivalve and variable valve timing: While many engines use only two valves, high-performance engines use three, four, or five valves in order to increase the intake flow area. Multiple valves provide a significant increase of torque at high engine speed, but sacrifice the low speed torque because the larger intake flow area results in slower flows at low speed. Multiple valves imply multiple camshafts, which increase the cost and complexity of the engine.

It has been previously exposed that valve timing needs to be optimized for each engine but also for specific operating conditions in order to avoid reverse flows. While conventional engines use a fixed, compromise valve timing, some advanced engines use a variable valve timing. This allows a better control of the amount of mixture and therefore helps in reducing the fuel consumption and emissions. The major drawbacks are the cost and complexity of variable valve systems.

Throttle-less torque control: Because most of the losses at partial torque output result from the throttle, eliminating the throttle eliminates these losses and improves the partial torque fuel consumption. Torque control is achieved by means of variable valve timing or by varying the fuel ratio in lean-burn engines.

Variable compression ratio: A variable compression ratio allows operating a forced induction engine at optimal compression ratio at any intake pressure. If the charging mechanism does not provide a maximum intake pressure, then the compression ratio of the engine can be increased without risking auto-ignition or knock. The increased compression ratio results in an improved fuel economy at partial torque output.

Exhaust gas recirculation: Exhaust gas recirculation (EGR) consists in readmitting some of the exhaust gases into the combustion chamber in order to reduce the effective displacement of the engine. This technique is used in conventional vehicles to decrease the fuel consumption at partial torque output, while preserving the acceleration capabilities of the engine. The greatest benefit of EGR is in emissions because it reduces the amount of fuel burned in the chamber and therefore the temperature of the exhaust gases. The nitric oxide emissions are greatly reduced.

Intelligent ignition: Intelligent ignition systems can set the spark advances at their optimum valve at any operating speed and load for optimum performance, efficiency, and exhaust emissions. High-power ignition systems can prevent losing fire in any cylinder, especially for engines with a lean mixture combination.

New engine materials: New materials developed for engine components will contribute to better fuel economy in two ways. Firstly, ceramic materials can be expected to offer better thermal insulation than metallic ones, with corresponding lower heat transfer (and therefore lower heat loss) and hence higher thermal efficiency. Secondly, lightweight materials such as fiber-reinforced plastics with high tensile strength can save considerable weight.

3.2 4S, Compression-Ignition IC Engines

Compression-ignition engines normally use diesel as their fuel. The 4S, compression-ignition IC engine has operation principles similar to the 4S SI engine. It also has four distinguished strokes — induction, compression, expansion, and exhaust. However, in compression-ignition engines, air alone is induced into the cylinder. The fuel is injected directly into the cylinder just before the piston moves up to the TDC. High temperature in the compressed air ignites the fuel. Air flow at a given engine speed is essentially unchanged and load control is achieved by varying the amount of fuel injected in each cycle. Compared with spark-ignition engines, a compression-ignition engine works differently because:

1. The compression ratio is higher
2. During the initial part of compression, only air is present
3. The fuel/air mixture is always stoichiometrically weak.

These operation characteristics result in a better fuel efficiency than an SI engine. Furthermore, the compression-ignition engine is, in general, designed to operate at lower speeds, and consequently the friction losses are smaller.

Since the fuel/air ratio in a compression-ignition engine is always lean, CO emission is much lower than in SI engines, and can be negligible. Unburned HCs in a properly regulated diesel engine come from two sources. Firstly, around the perimeters of the reaction zone there will a mixture that is too lean to burn, and the longer the delay period, the greater the amount of HC emissions from this source. However, there is a delay period below which no further reductions in HC emissions are obtained. Under these conditions, the HC emissions mostly originate from a second source: the fuel retained in the nozzle sac (the space between the nozzle seat and the spray holes) and the spray holes. Fuel from these sources can enter the combustion chamber late in the cycle, thereby producing HC emissions.

The formation of NO_x is strongly dependent on temperature, the local concentration of oxygen, and the duration of combustion. Thus, in diesel engines, NO_x is formed during the diffusion combustion phase on the weak side of the reaction zone. Reducing the diffusion-controlled combustion duration by increasing the rate of injection leads to a reduction in NO_x emissions.

Retarding the injection timing also reduces the NO_x emissions, since the later injection leads to lower temperature. However, injection retarding will reduce the fuel efficiency of the engine.

The black smoke from diesel engines originates from the fuel-rich side of the reaction zone in the diffusion-controlled combustion phase. After the rapid combustion at the end of the delay period, the subsequent combustion of the fuel is controlled by the rates of diffusion of air into the fuel vapor and vice versa, and the diffusion of the combustion products away from the reaction zone. Carbon particles form by the thermal decomposition (cracking) of large hydrocarbon molecules, and soot particles form by agglomeration. The soot particles can be oxidized when they enter the lean side of the reaction zone and further oxidation occurs during the expansion stroke, after the end of the diffusion combustion phase.

Smoke generation is increased by high temperature in the fuel-rich zone during diffusion combustion. Smoke emission can be reduced by shortening the diffusion combustion phase, because this gives less time for soot formation and more time for soot oxidation. The diffusion phase can be shortened by increased swirl, more rapid rejection, and a finer fuel spray. Advancing the injection timing can also reduce the smoke.

3.3 Two-Stroke Engines

The two-stroke cycle combines the necessary processes of induction, exhaust, compression, and expansion in a single crankshaft rotation, unlike a four-stroke cycle that requires two rotations.[3] A basic two-stroke cycle is shown in Figure 3.11. Two-stroke engines eliminate the separate induction and exhaust strokes. The basic operation principle is illustrated in Figure 3.11 and explained below.

1. In Figure 3.11(a), the piston is approaching the top center. Above the piston, the trapped air and fuel charge are being ignited by the spark plug, producing a rapid rise in temperature and pressure that will drive the piston down on the power stroke. Below the piston, the opened inlet port induces air from the atmosphere into the crankcase due to the increasing volume of the crankcase lowering the pressure below the atmospheric value. To induce fuel into the engine, various options exist of either placing a carburetor in the inlet tract, injecting fuel into the inlet tract, injecting fuel into the crankcase transfer ducts, or injecting fuel directly into the cylinder before or after the closure of the exhaust port. If operating the engine as a diesel power unit, the latter is the only option.
2. In Figure 3.11(b), the exhaust port above the piston has been opened. It is often called the “release” point in the cycle and this allows the

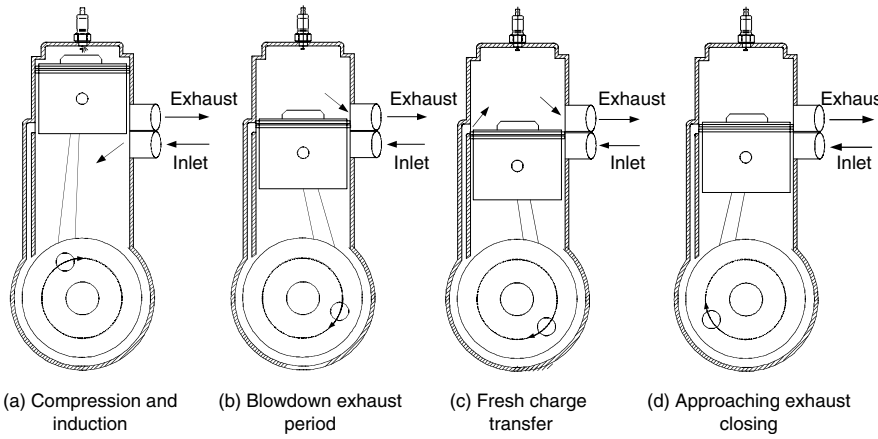

FIGURE 3.11
Basic two-stroke cycle

transmission of a pulse of hot, high-pressure exhaust gas from the combustion process into the exhaust duct. As the area of the port increases with crankshaft angle, and the cylinder pressure falls with time, it is clear that the exhaust duct pressure profile with time is one that increases to a maximum value and then decays. Such a flow process is described as unsteady gas flow and such a pulse can be reflected from all pipe area changes, or at the pipe end termination to the atmosphere. These reflections have a dramatic influence on engine performance. Below the piston, the compression of the fresh charge is taking place. The pressure and temperature achieved will be a function of the proportion of reduction of the crankcase volume, that is, the crankcase compression ratio.

3. In Figure 3.11(c), above the piston, the initial exhaust process referred to as "blowdown" is nearing completion. The piston uncovers the transfer ports and connects the cylinder directly to the crankcase through the transfer ducts. If the crankcase pressure exceeds the cylinder pressure, then the fresh charge enters the cylinder in what is known as the "scavenge process." Clearly, if the transfer ports are badly directed, then the fresh charge can exit directly out of the exhaust port and be totally lost from the cylinder. Such a process, referred to as "short-circuiting," would result in the cylinder being filled only with exhaust gas at the onset of the next combustion process, and no pressure rise or power output would ensue. Worse, all of the fuel in a carbureted configuration would be lost to the exhaust — a consequentially monstrous emission of unburned HC. This is the main reason why a conventional two-stroke engine has a lower efficiency and bad emissions.

4. In Figure 3.11(d), the piston in the cylinder is approaching what is known as the "trapping" point. The scavenge process has been completed and the cylinder is now filled with a mix of air, fuel if a carbureted design, and exhaust gas. As the piston rises, the cylinder pressure also rises, but the exhaust port is still open and, barring the intervention of some unsteady gas-dynamic effects generated in the exhaust pipe, the piston will spill fresh charge into the exhaust duct, to the detriment of resulting power output, fuel consumption, and pollutant emissions.

The simplest method of allowing fresh charge access into, and exhaust gas discharge from, the two-stroke engine is by the movement of the piston exposing port in the cylinder wall as shown in Figure 3.11. This means that all port timing events are symmetrical with respect to TDC and BDC. It is possible to produce asymmetrical inlet and exhaust timing events by the use of disc valves, reed valves, and poppet valves.

The use of poppet valves for both inlet and exhaust timing control is sketched in Figure 3.12 as an example of uniflow scavenging. This design is commonly used in 4S engines. Generally, the poppet valves' design is considered to be difficult to design so as to adequately flow sufficient charge into a two-stroke engine, compared with using the port in a cylinder wall with the same access area.[4]

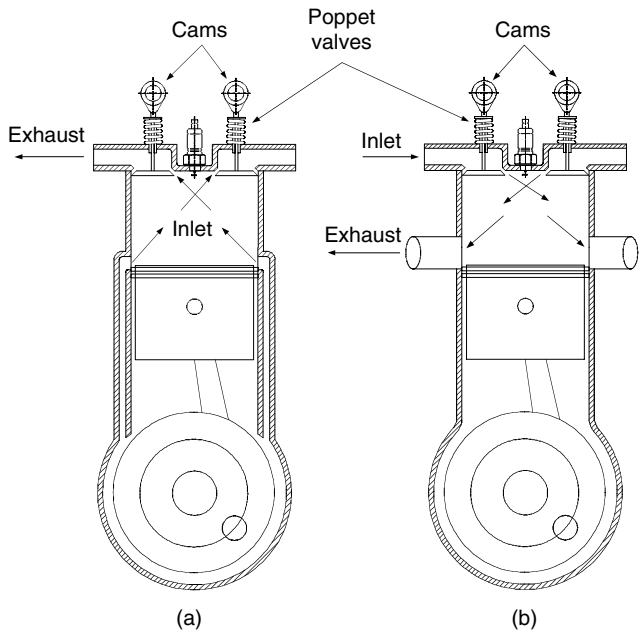

FIGURE 3.12
Uniflow scavenged with crankcase compression

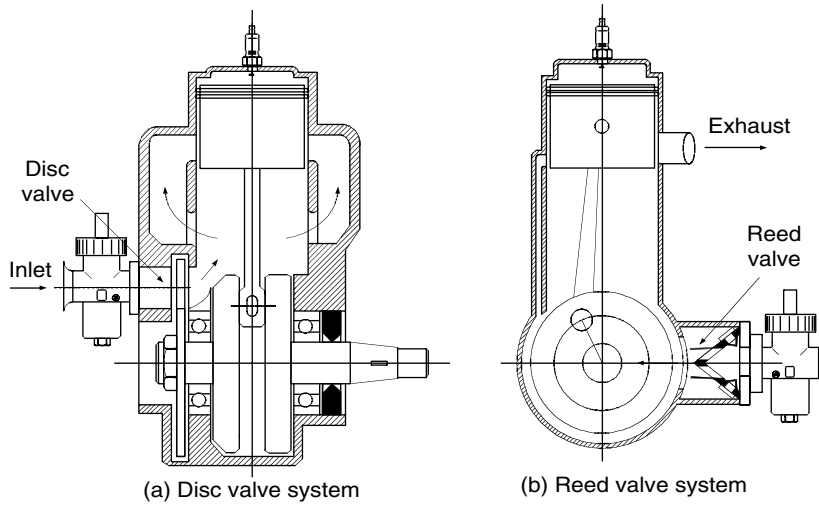

FIGURE 3.13
Disc valve and reed valve with crankcase compression

The disc valves and reed valves are the other two valves for two-stroke engines, as shown in Figure 3.13. The disc valve can provide asymmetric porting timing by designing the disc. However, the porting timing can be varied with engine speed. Consequently, the porting timing is optimized only at a specified speed, and at other speeds the engine performance will be as good as at this speed. Reed valves have always been popular as they provide an effective automatic valve whose timings vary with both engine load and engine speed. The high-performance outboard racing engine demonstrated that high specific power output was possible with reed valves.[4] Racing motorcycle organizations developed this further. Today, most reed valves are designed as V-blocks (refer to Figure 3.13[b]).

The essential element of the original two-stroke engines was the use of crankcase as the air pumping device. The conventional lubrication method has been to mix the lubricant with the gasoline and supply it through the carburetor in ratios of gasoline to lubricant from 25:1 to 100:1, depending on the application. Combined with some fuel charge being short-circuited to the exhaust duct along with the air, the resulting exhaust is rich in unburned hydrocarbons and lubricants, some partially burned and some totally unburned. It is consequently visible as smoke. This is ecologically unacceptable. By definition, an external air pump can be utilized to replace the crankcase air-pumping. This can be either a positive displacement blower of a Roots type, or a centrifugal blower driven from the crankshaft. Clearly, it would be more efficient thermodynamically to use a turbocharger, where the exhaust energy to the exhaust turbine is available to drive the air compressor. This arrangement is shown in Figure 3.14, where the engine has both a blower and a turbocharger. The blower would be used as a starting aid and

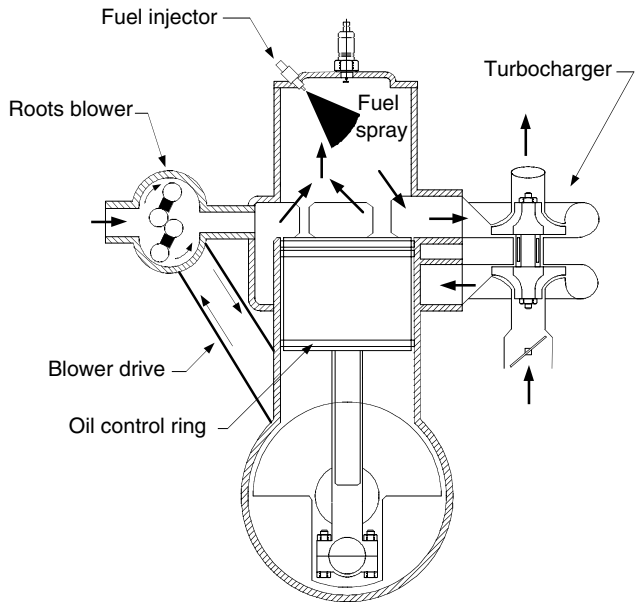

FIGURE 3.14
A supercharged and turbocharged fuel-injection two-stroke engine

as an air supplementary device at low loads and speeds, with the turbocharger used as the main air supply unit at the higher torque and power levels at any speed. To prevent any short-circuiting of fuel to the exhaust, a fuel injector would be used to supply fuel directly to the cylinder, after the exhaust port is closed and not in the position shown in Figure 3.14, at BDC. Such an engine type has already demonstrated excellent fuel economy behavior, good exhaust emission characteristics of unburned hydrocarbons and carbon monoxide, and superior emission characteristics of oxides of nitrogen, in comparison with an equivalent four-stroke engine.

3.4 Wankel Rotary Engines

The rotary-piston engine (or Wankel engine, named by its inventor) generates power by the compression, ignition, and expansion of gasoline/air mixture in a 4S cycle in the same way as conventional internal combustion engines. The completely different mechanical design allows all moving parts to have a continuous rotary motion instead of a reciprocating movement. The rotor (or piston) is roughly triangular shaped and rotates on an eccentric on the output shaft within a housing of epitrochoid shape. The term is given to the path described by a point within a circle rolling around another circle.

The two-lobe epitrochoid of the Wankel is generated when the interior circle is twice the radius of the rolling circle.

The four strokes of the cycle occur in the spaces formed between the three sides of the rotor and two-lobed trochoidal chamber or housing; the spaces are expanded and contracted as the rotor turns. Figure 3.15 illustrates the operating cycle. The three separate working chambers are labeled A, B, and C. As the intake port is uncovered, volume A expands and draws a fresh fuel/air charge into the engine (Figure 3.15a). Next the trailing apex seal isolates volume A from the intake port and the charge is compressed as volume A steadily decreases with rotation of the rotor, reaching the minimum shown at the point of ignition (Figure 3.15b and c). During this sequence of events, the other two faces of the rotor define volumes B and C, which experience exactly the same sequence, each offset by one-third of a rotation.

Unlike the piston in a conventional engine, which requires a connecting rod to transmit power to the crankshaft, the rotor (or "rotary piston") runs directly on an eccentric shaft, from which torque output is derived. The Wankel also differs from the conventional automobile engine in having no valves. The fuel/air inlet port and the exhaust port are opened and closed at the appropriate time in the combustion cycle by the passage of the rotor itself.

The advantages of the Wankel engine are as follows:

Because the engine delivers one power stroke for each full crankshaft rotation, the Wankel uses its displacement volume twice as often as the 4S engine does. One immediate advantage is that for equivalent power output, a Wankel engine is only about half the size and weight of a conventional engine.

Another advantage of the rotary engine is the reduced number of parts — typically 40% of the number of moving parts in a V-8 engine, although the advantage over a four-cylinder engine would be less. This has certain implications for the easier and faster manufacturing of the engine.

Since the Wankel engine possesses only rotary motion, all the unbalanced forces are simple harmonic and can be fully canceled with rotating counterweights to produce very little vibration as compared with one quarter of a

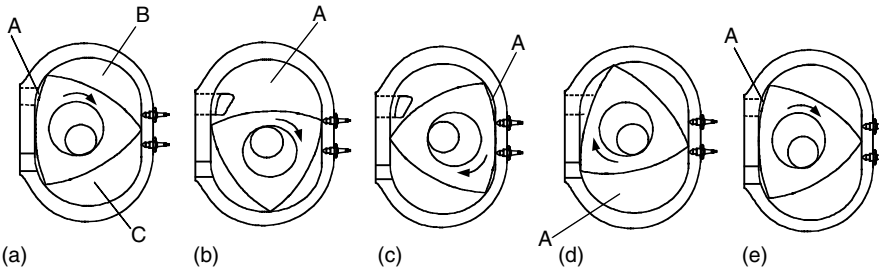

FIGURE 3.15
The Wankel rotary engine cycle

revolution in the 4S engine. This dispersed application of torque adds to the basic smoothness of the Wankel with consequent lower noise (aided by the absence of a valve train). A single-rotor Wankel is as smooth as a three-cylinder piston engine. Most rotary engines developed for automotive use have two rotors.

The engine is capable of burning fuel of a lower octane rating than a conventional piston engine with a slightly better performance gained from unleaded petrol. It can run at the stoichiometric fuel/air ratio allowing NO_x control (raw NO_x emissions are generally lower than a conventional petrol engine due to the slower combustion) with a combination of EGR and a reduction catalyst, and HC and CO control with an oxidation catalyst.

The Wankel engine breathes well because of a greater length (crank degrees) of induction period and because of a relatively unrestricted flow path for the incoming mixture and exhaust gases. Volumetric efficiency in excess of 100% has been claimed for some designs. In the one- and two-rotor versions, the induction system is simple, reducing problems associated with bad distribution of the fuel/air mixture. Also, the speed range of the engine is broad (i.e., higher than a conventional reciprocating engine) due to the better breathing characteristics, potentially lower mechanical friction, no limitations imposed by valve train dynamics, and the absence of reciprocating parts.

Perhaps the most far-reaching economic significance of the Wankel lies outside the engine itself in the potential it offers for the redesign of the passenger car. The engine's comparatively small size and light weight would permit vehicle aerodynamic improvements by way of lower hood lines and weight reduction because of the lower engine mass and the requirement for a smaller engine compartment.

The Wankel engine's main disadvantages are reported to be its expensive construction materials, its requirement of high-precision manufacturing techniques, poor fuel economy, and high emissions of unburned HCs. The high HC emissions came about because of poor sealing between the rotor and housing. The apex seal especially suffered from reliability and durability problems and has been unable to match conventional piston rings. But newly developed sealing materials are expected to provide a much higher level of service. The apex seal in current rotary engines is composed of a single piece of carbon impregnated with an aluminum alloy.

The high HC emissions have also contributed to a generally poor fuel economy. The other main factor is that combustion in the Wankel engine tends to be slower and hence less efficient than it is in the conventional piston engine. In most new designs, combustion is accelerated by using two spark plugs in each combustion chamber. Continuing efforts to improve engine efficiency via direct injection and stratified charge have been reported. Stratification of the charge can readily be accomplished by injecting the fuel and creating a rich mixture in the vicinity of the TDC position of the rotor. This will substantially reduce the peak temperature and therefore decrease the NO_x produced. A lean mixture in the leading section of the chamber will enhance the oxidation of CO and HCs.

3.5 Stirling Engines

The Stirling engine is a reciprocate, continuous external combustion engine that has a piston and cylinder similar to a conventional internal combustion engine as shown in Figure 3.16.[6] However, inside the engine, the working fluid (usually hydrogen or helium) is sealed. Alternately, heating and cooling the working fluid causes a pressure fluctuation that acts on the piston to produce power. A Stirling engine has a high-temperature heat source and a low-temperature heat sink. The heat source sounds the compression space and the heat sink sounds the expansion space. Both heat source and heat sink are separated by a regenerator (thermodynamics sponge), as shown in Figure 3.17.

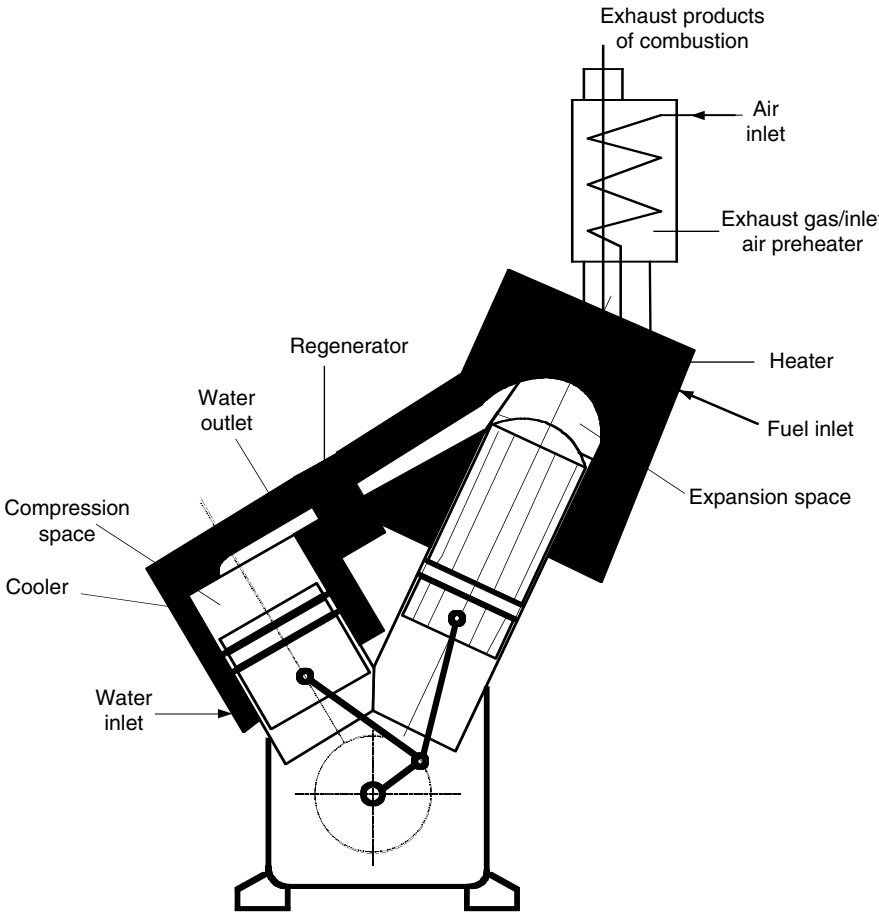

FIGURE 3.16
Diagram of a practical opposed-piston Stirling engine

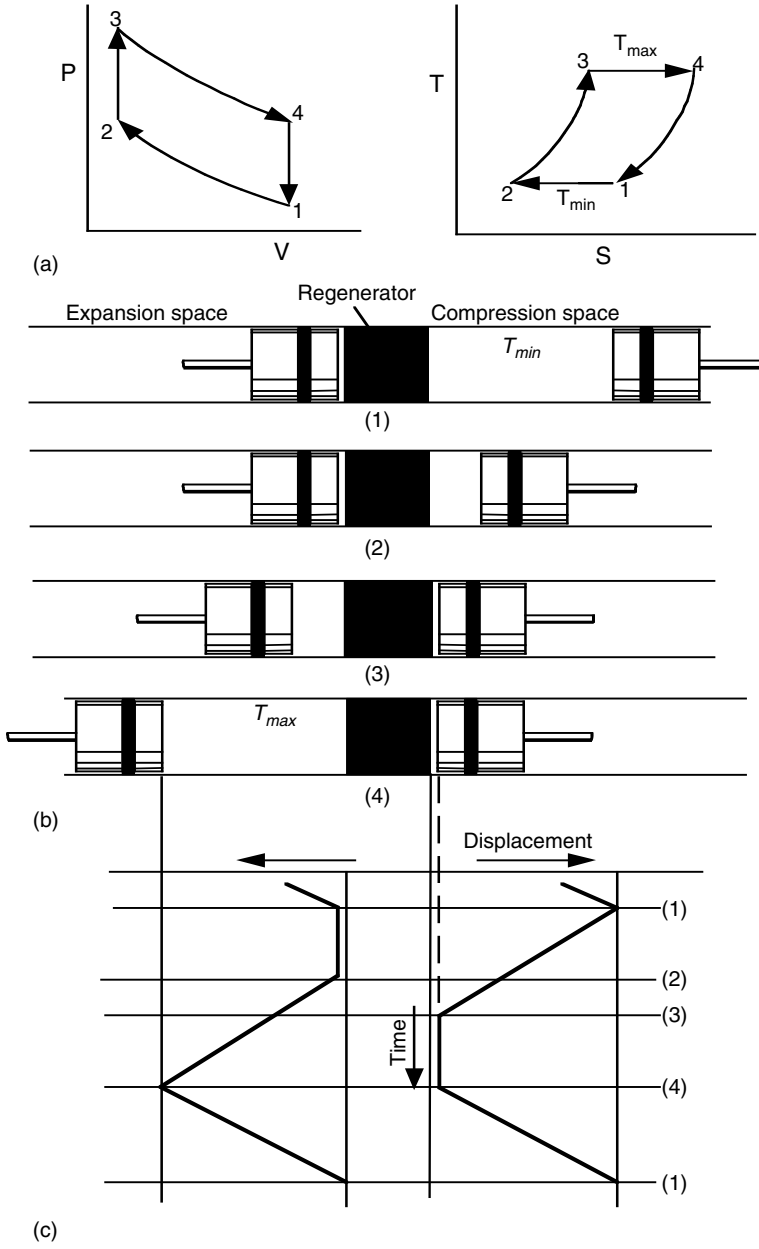

FIGURE 3.17
The ideal Stirling cycle: (a) P–V and T–S diagram, (b) piston arrangement at the terminal points of the cycle, and (c) time–displacement diagram

The Stirling engine works based on the Stirling thermodynamic cycle. The ideal Stirling cycle is illustrated in Figure 3.17,[6,7] which consists of a cylinder containing two opposed pistons, with a regenerator between the pistons. The regenerator, a thermodynamic sponge, is usually a matrix of finely divided metal in the form of wires or strips. One of the two volumes between the regenerator and the pistons is the expansion space, in which high temperature, T_{max}, is maintained by a heat source surrounding it. The other volume is the compression space, in which low temperature, T_{min}, is maintained by the heat sink surrounding it. Therefore, there is a temperature gradient ($T_{max} - T_{min}$) across the transverse faces of the regenerator. It is usually assumed that there is no thermal conduction in the longitudinal direction.

To start the cycle, we assume that the compression-space piston is at the outer dead point, and the expansion-space piston is at the inner dead point, close to the face of the regenerator. All the working fluid is then in the cold compression space. The volume is maximum, so that the pressure and temperature are at their minimum values, represented as 1 on the P–V and T–S diagrams as shown in Figure 3.17(a). During compression (process 1–2), the compression piston moves toward the inner dead point, and the expansion-space piston remains stationary. The working fluid is compressed in the compression space, and the pressure increases. The temperature is maintained constant because heat Q_c is abstracted from the compression-space cylinder to the surroundings (heat sink).

In the transfer process 2–3, both pistons move simultaneously, the compression piston toward (and the expansion piston away from) the regenerator, so that the volume between them remains constant. Therefore, the working fluid is transferred, through the porous metallic matrix of the regenerator, from the compression space to the expansion space. In its passage through the regenerator, the working fluid is heated from T_{min} to T_{max} by heat transfer from the matrix, and emerges from the regenerator into the expansion space at temperature T_{max}. The gradual increase in temperature passing through the matrix, at constant volume, causes an increase in pressure.

In the expansion process 3–4, the expansion piston continues to move away from the regenerator toward the outer dead center point; the compression piston remains stationary at the inner dead center point, adjacent to the regenerator. As expansion progresses, the pressure decreases as the volume increases; the temperature remains constant because heat Q_E is added to the system from an external heat source.

The final process in the cycle is the transfer process 4–1, during which both pistons move simultaneously to transfer the working fluid (at constant volume) back through the regenerative matrix, so that the working fluid decreases in temperature and emerges at T_{min} into the compression space. Heat transferred in the process is contained in the matrix, for transfer to the gas in process 2–3 of the subsequence cycle.

The cycle is composed of heat transfer. Therefore, there are four heat-transfer processes:

1. Process 1–2: isothermal compression; heat transfer from the working fluid at T_{min} to the external heat sink.
2. Process 2–3: constant volume; heat transfer to the working fluid from the regenerative matrix.
3. Process 3–4: isothermal expansion; heat transfer to the working fluid at T_{max} from an external heat source.
4. Process 4–1: constant volume; heat transfer from the working fluid to the regenerative matrix.

If the heat transferred in process 2–3 has the same magnitude as in process 4–1, then the only heat transfer between the engine and its surroundings are (a) heat supply at T_{max} and (b) heat rejection at T_{min}. This heat supply and heat rejection at constant temperature satisfies the requirement of the second law of thermodynamics for maximum thermal efficiency, so that the efficiency of the Stirling engine is the same as the Carnot cycle, that is, $\eta = (T_{max} - T_{min})/T_{max}$. The principal advantage of the Stirling cycle over the Carnot cycle lies in the replacement of two isentropic processes by two constant-volume processes, which greatly increases the area of the P–V diagram. Therefore, to obtain a reasonable amount of work from the Stirling cycle, it is not necessary to resort to the impractically high pressures and swept volumes, as in the Carnot cycle.

The torque/speed characteristics of a Stirling engine are relatively flat as shown in Figure 3.18. This is particularly favorable for automotive applications where high torque at low speed is advantageous to achieve good acceleration.

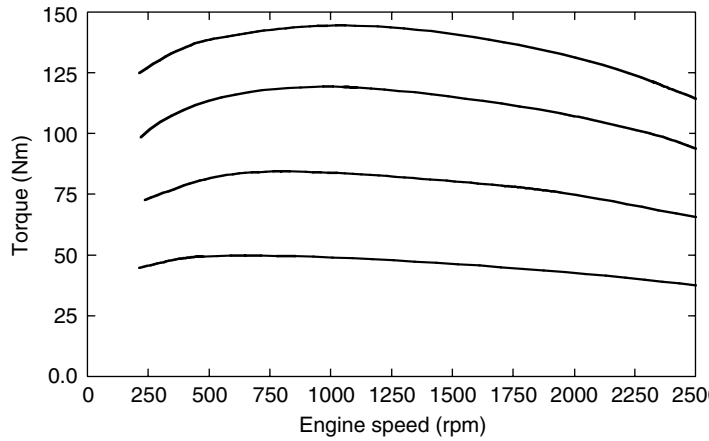

FIGURE 3.18
Torque/speed characteristics of typical Stirling engines

The inherent low torque at low speeds allows the use of a relatively simple transmission system for vehicle use.

The performance and fuel consumption characteristics map for a Stirling engine is shown in Figure 3.19.[6] Compared with combustion engines, the outstanding feature of the Stirling engine is that the fuel consumption at part load increases, compared to its optimum fuel consumption operating point, much less than that of internal combustion engines. This outstanding characteristic will lead to a good fuel economy for a vehicle that most of the time operates in part load.

The exhaust emissions are low and easy to control because combustion is isolated from the cycle changes in pressure and temperature experienced by the working fluid. An excess of air of between 20 and 80%, continuous combustion, and no "quench" of flame by a "cold" metal surface also help to ensure almost complete combustion. Because continuous combustion replaces the intermittent explosive nature of combustion in other piston engines, the Stirling engine usually has low noise.

Another important advantage of the Stirling engine in its application to vehicles is the multifuel and self-starting characteristics. Because combustion

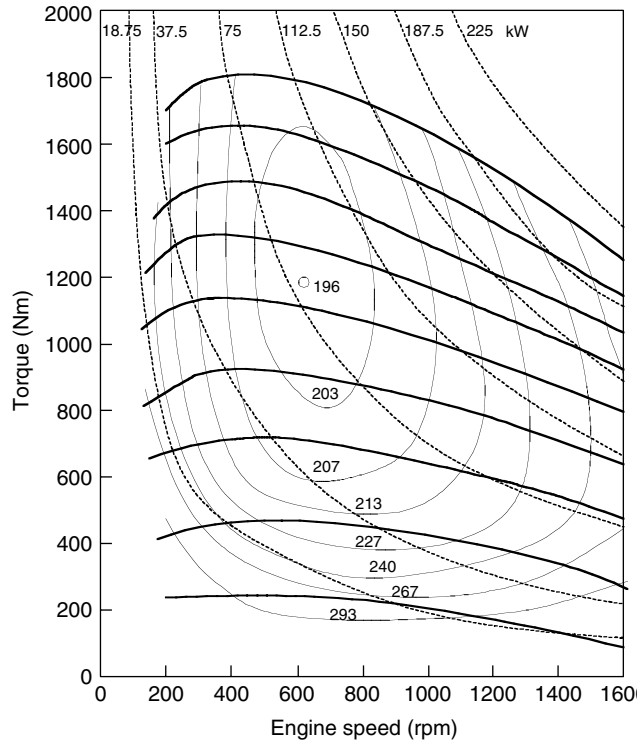

FIGURE 3.19
Performance and fuel consumption map for a four-cylinder Stirling engine for traction applications

is isolated from its working fluid, and only heat is transferred to the working fluid from a heat source, a variety of fuels can be used.

However, the Stirling engines also have some disadvantages. The main disadvantages have traditionally been a high manufacture cost, a heavy and bulky end result, and difficulty in controlling the power output accurately. Also, it has so far proven impossible to hold the leakage rate of hydrogen or helium from the system down to a level that would be acceptable. The durability of piston seals has been as much of a problem as the effectiveness of the seals to prevent leakage.

In practical everyday automotive operation, there are some additional shortcomings. First, external combustion prolongs the start-up time. Power cannot be drawn from a cold engine until the heater head reaches a reasonable operating temperature. Second, fuel energy is spent in raising the heater head to operating temperature, and when the engine is shut down, that stored energy is dissipated without performing useful work.

3.6 Gas Turbine Engines

The gas turbine engine is a rotary, continuous IC engine where the fuel is supplied to a burner and burned with an excess of compressed air (lean-burn). The hot combustion gases then expand and pass through a turbine, generating power that is transferred to the output shaft by gearing, as shown in Figure 3.20.[5]

The gas turbine engine operates in accordance with the principles described below:

1. Compression: Air enters the gas turbine and is compressed.
2. Heat exchange: Heat is drawn from the exhaust gases and communicated to the compressed air. There is a recuperation of the exhaust gases' energy that is otherwise lost.
3. Combustion: Fuel is mixed with hot air and ignited. The pressure increases.
4. Expansion: The hot exhaust gases drive the turbine, thus releasing their energy. The turbine turns the compressor and the output shaft.

Figure 3.21 and Figure 3.22 show the *bsfc* map for a complete range of output power and speed. The shape of the *bsfc* map of the turbine engine is quite different than that of SI and CI engines. The speed of a turbine engine can start from zero speed, and extend to its maximum. The drop in fuel economy at partial load from the full load of a turbine engine is much smaller than that of the SI and CI engine. The *bsfc* values are more sensitive to speed than to power. Therefore, turbine engine favors running with constant speed, and load variations have less influence on the fuel economy.

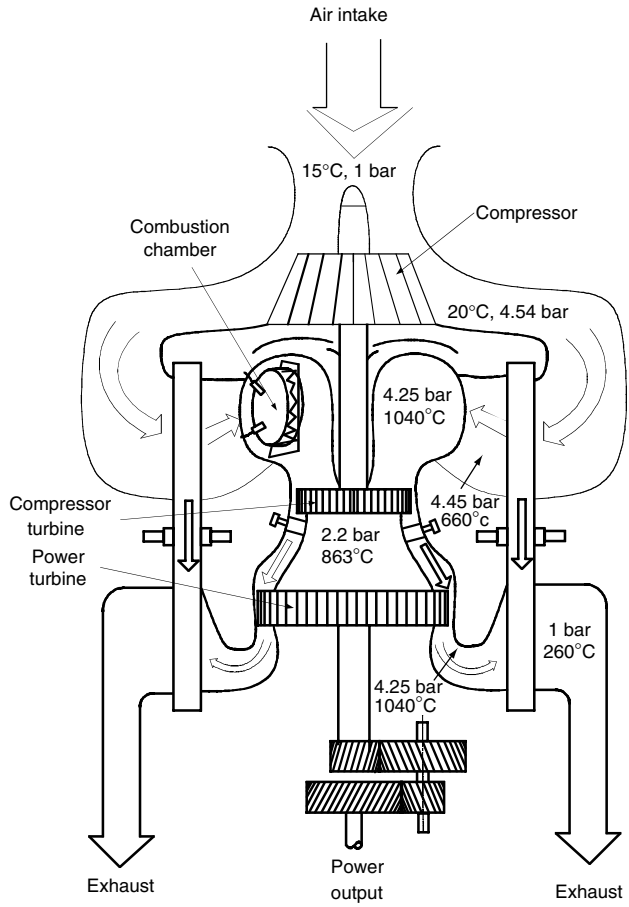

FIGURE 3.20
Gas turbine engine with heat exchanger

The advantages of gas turbines include:

1. A very compact engine because of its high rotational speed
2. Vibration-free operation due to the rotating movement
3. The ability to operate on a wide variety of fuels
4. Reduced HC and CO emissions compared to internal combustion engines because the combustion is continuous and therefore easier to control

However, gas turbines suffer from some major disadvantages for automotive applications:

1. High noise levels due to the quenching of the gases by the turbine and compressor.

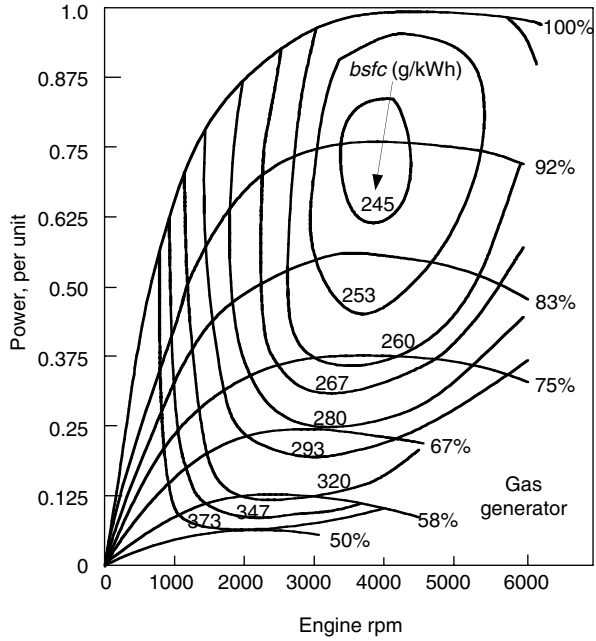

FIGURE 3.21
Fuel consumption characteristics of the Kronograd KTT gas turbine

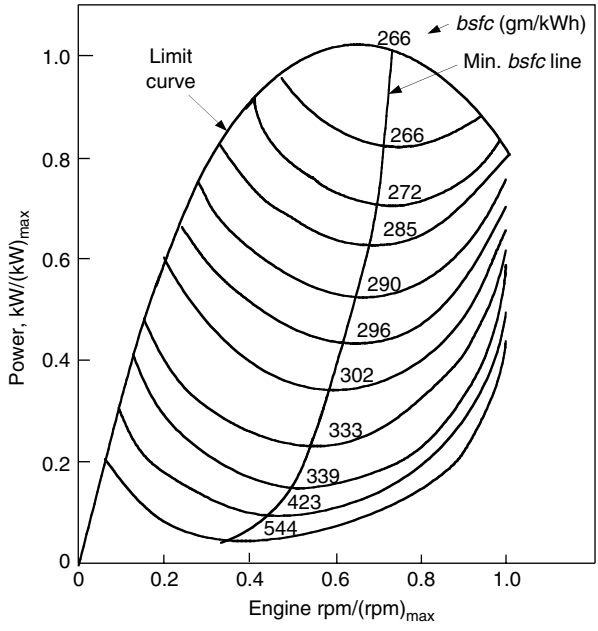

FIGURE 3.22
Fuel consumption characteristics of the Chrysler upgraded turbine

2. High fuel consumption because the gas turbine does not scale down efficiently: the efficiency of a dynamic compressor and turbine is low for small sizes (below a few hundred kilowatts).
3. High rotating speeds are required for small (below a few hundred kilowatts) turbines to operate at their maximum efficiency. This requires sophisticated materials to withstand the mechanical constraints.
4. The high temperatures continuously encountered by the turbine require expensive materials that also have to withstand high rotational speeds.
5. The efficiency is extremely speed dependent, thus requiring a speed decoupling.
6. No torque output at low speed.
7. High cost of the heat exchanger.

3.7 Quasi-Isothermal Brayton Cycle Engines

The Quasi-Isothermal Brayton Cycle Engine (QIBCE) is an invention of Prof. Mark Holtzapple at Texas A&M University. It is a variation of the gas turbine with two major differences intended to improve on the most crippling disadvantages of the gas turbine.

The most significant improvement is the compressor and turbine principle. Instead of being of the dynamic type, and therefore bound to operate at a very high speed, these elements are of the positive displacement type that operate effectively and efficiently at low speeds. The principle is that of a gear pump, of the kind used in automobiles for oil.

The second improvement is the quasi-isothermal compression, which requires less energy than the adiabatic compression in conventional Brayton cycles. This is achieved by spraying water in the compressor. The liquid water "captures" the heat resulting from the compression, while it remains in a liquid or slightly vaporized state. This keeps the overall flow temperature from rising, therefore reducing the energy necessary for compression.

The claimed advantages of the QIBCE engine are:

1. Potential for very high efficiency
2. Compactness
3. Continuous combustion that results in low HC and CO emissions
4. Reduced noise emissions compared to a gas turbine because the quenching of the gases does not occur
5. Simplicity due to a reduced number of parts

The disadvantages would be:

1. Specialized and potentially expensive materials for the turbine because it is permanently exposed to high temperatures. However, these materials should be less stressed than in a gas turbine because of the lower operating speeds.
2. High cost of the heat exchanger.

To this day, this engine is only a concept and a prototype must be implemented to verify the claimed advantages.

References

[1] J.B. Heywood, *Internal Combustion Engine Fundamentals*, McGraw-Hill Inc., New York, 1988.
[2] R. Stone, *Introduction to Combustion Engines*, 2nd ed., Society of Automotive Engineers (SAE), Warrendale, PA, 1992.
[3] P. Duret, *A New Generation of Two-Stroke Engines for The Future*? Edison's Technip, Paris, 1993.
[4] G.P. Blair, *Design and Simulation of Two Stroke Engines*, Society of Automotive Engineers (SAE), Warrendale, PA, 1996.
[5] J.P. O'brien, *Gas Turbines for Automotive Use*, Noyes, Data Corporation, Park Ridge, NJ, 1980.
[6] G. Walker, G. Reader, O.R. Fauvel, and E.R. Bingham, *The Stirling Alternative — Power System, Refrigerants and Heat Pump*s, Gordon and Breach Science Publishers, London, 1994.
[7] M.J. Collie, *Stirling Engine Design and Feasibility for Automotive Use*, Noyes, Data Corporation, Park Ridge, NJ, 1979.

4

Electric Vehicles

CONTENTS

4.1 Configurations of Electric Vehicles 99
4.2 Performance of Electric Vehicles 102
4.2.1 Traction Motor Characteristics.....103
4.2.2 Tractive Effort and Transmission Requirement.....104
4.2.3 Vehicle Performance 105
4.3 Tractive Effort in Normal Driving 109
4.4 Energy Consumption 114
References 116

Electric vehicles (EVs) use an electric motor for traction, and chemical batteries, fuel cells, ultracapacitors, and/or flywheels for their corresponding energy sources. The electric vehicle has many advantages over the conventional internal combustion engine vehicle (ICEV), such as an absence of emissions, high efficiency, independence from petroleum, and quiet and smooth operation. The operational and fundamental principles in EVs and ICEVs are similar, as described in Chapter 2. There are, however, some differences between ICEVs and EVs, such as the use of gasoline tanks vs. batteries, ICE vs. electric motor, and different transmission requirements. This chapter will focus on the methodology of power train design and will investigate the key components including traction motor and energy storages.

4.1 Configurations of Electric Vehicles

Previously, the EV was mainly converted from the existing ICEV by replacing the internal combustion engine and fuel tank with an electric motor drive and battery pack while retaining all the other components, as shown in Figure 4.1. Drawbacks such as its heavy weight, lower flexibility, and performance degradation have caused the use of this type of EV to fade out.

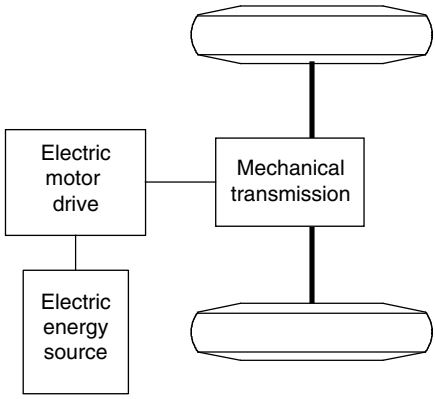

FIGURE 4.1
Primary electric vehicle power train

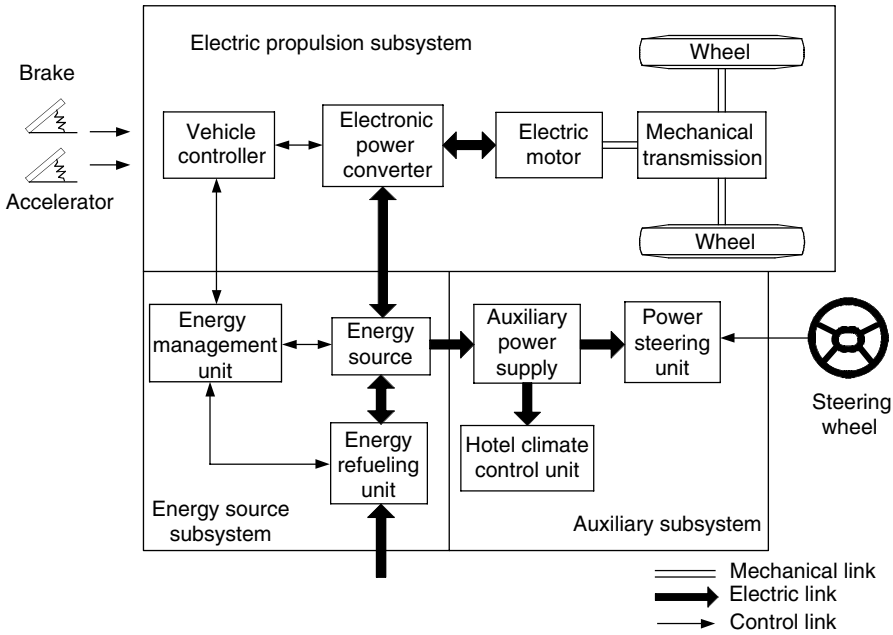

FIGURE 4.2
Conceptual illustration of general EV configuration

In its place, the modern EV is built based on original body and frame designs. This satisfies the structure requirements unique to EVs and makes use of the greater flexibility of electric propulsion.

A modern electric drive train is conceptually illustrated in Figure 4.2.[1] The drive train consists of three major subsystems: electric motor propulsion, energy source, and auxiliary. The electric propulsion subsystem is comprised of a vehicle controller, power electronic converter, electric motor, mechanical transmission, and driving wheels. The energy source subsystem involves the

energy source, the energy management unit, and the energy refueling unit. The auxiliary subsystem consists of the power steering unit, the hotel climate control unit, and the auxiliary supply unit.

Based on the control inputs from the accelerator and brake pedals, the vehicle controller provides proper control signals to the electronic power converter, which functions to regulate the power flow between the electric motor and energy source. The backward power flow is due to the regenerative braking of the EV and this regenerated energy can be restored to the energy source, provided the energy source is receptive. Most EV batteries as well as ultracapacitors and flywheels readily possess the ability to accept regenerated energy. The energy management unit cooperates with the vehicle controller to control the regenerative braking and its energy recovery. It also works with the energy refueling unit to control the refueling unit, and to monitor the usability of the energy source. The auxiliary power supply provides the necessary power at different voltage levels for all the EV auxiliaries, especially the hotel climate control and power steering units.

There are a variety of possible EV configurations due to the variations in electric propulsion characteristics and energy sources, as shown in Figure 4.3.[1]

(a) Figure 4.3(a) shows the configuration of the first alternative, in which an electric propulsion replaces the IC engine of a conventional vehicle drive train. It consists of an electric motor, a clutch, a gearbox, and a differential. The clutch and gearbox may be replaced by automatic transmission. The clutch is used to connect or disconnect the power of the electric motor from the driven wheels. The gearbox provides a set of gear ratios to modify the speed-power (torque) profile to match the load requirement (refer to Chapter 2). The differential is a mechanical device (usually a set of planetary gears), which enables the wheels of both sides to be driven at different speeds when the vehicle runs along a curved path.

(b) With an electric motor that has constant power in a long speed range (refer to Chapter 2), a fixed gearing can replace the multispeed gearbox and reduce the need for a clutch. This configuration not only reduces the size and weight of the mechanical transmission, but also simplifies the drive train control because gear shifting is not needed.

(c) Similar to the drive train in (b), the electric motor, the fixed gearing, and the differential can be further integrated into a single assembly while both axles point at both driving wheels. The whole drive train is further simplified and compacted.

(d) In Figure 4.3(d), the mechanical differential is replaced by using two traction motors. Each of them drives one side wheel and operates at a different speed when the vehicle is running along a curved path.

(e) In order to further simplify the drive train, the traction motor can be placed inside a wheel. This arrangement is the so-called in-wheel drive. A thin planetary gear set may be used to reduce the motor speed and enhance the motor torque. The thin planetary

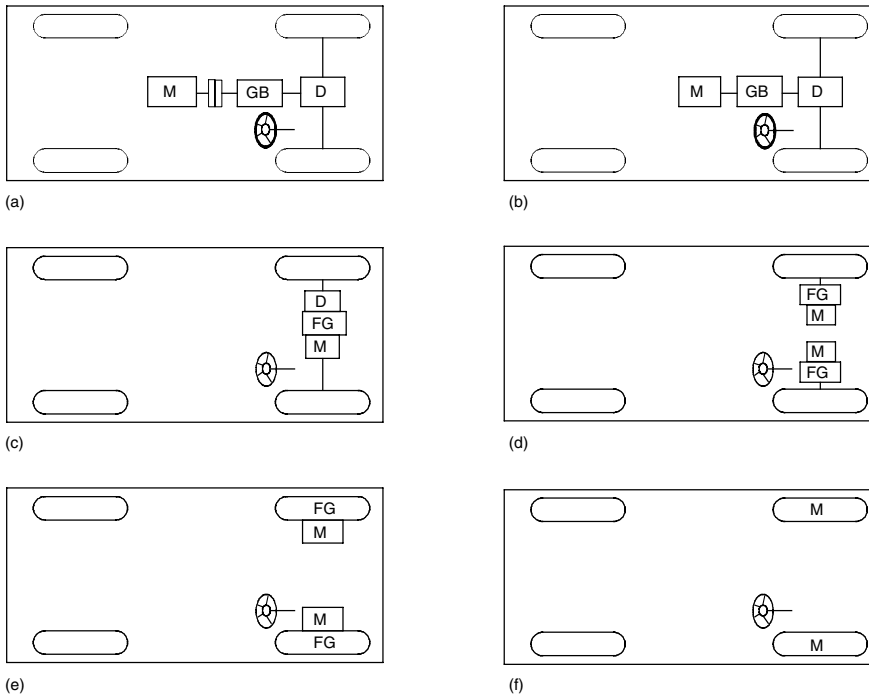

FIGURE 4.3
Possible EV configurations

gear set offers the advantage of a high-speed reduction ratio as well as an inline arrangement of the input and output shaft.

(f) By fully abandoning any mechanical gearing between the electric motor and the driving wheel, the out-rotor of a low-speed electric motor in the in-wheel drive can be directly connected to the driving wheel. The speed control of the electric motor is equivalent to the control of the wheel speed and hence the vehicle speed. However, this arrangement requires the electric motor to have a higher torque to start and accelerate the vehicle.

4.2 Performance of Electric Vehicles

A vehicle's driving performance is usually evaluated by its acceleration time, maximum speed, and gradeability. In EV drive train design, proper motor

power rating and transmission parameters are the primary considerations to meet the performance specification. The design of all these parameters depends mostly on the speed–power (torque) characteristics of the traction motor, as mentioned in Chapter 2, and will be discussed in this chapter.

4.2.1 Traction Motor Characteristics

Variable-speed electric motor drives usually have the characteristics shown in Figure 4.4. At the low-speed region (less than the base speed as marked in Figure 4.4), the motor has a constant torque. In the high-speed region (higher than the base speed), the motor has a constant power. This characteristic is usually represented by a speed ratio x, defined as the ratio of its maximum speed to its base speed. In low-speed operations, voltage supply to the motor increases with the increase of the speed through the electronic converter while the flux is kept constant. At the point of base speed, the voltage of the motor reaches the source voltage. After the base speed, the motor voltage is kept constant and the flux is weakened, dropping hyperbolically with increasing speed. Hence, its torque also drops hyperbolically with increasing speed.[3,4,5]

Figure 4.5 shows the torque–speed profiles of a 60 kW motor with different speed ratios x (x=2, 4, and 6). It is clear that with a long constant power region, the maximum torque of the motor can be significantly increased, and hence vehicle acceleration and gradeability performance can be improved and the transmission can be simplified. However, each type of motor inherently has its

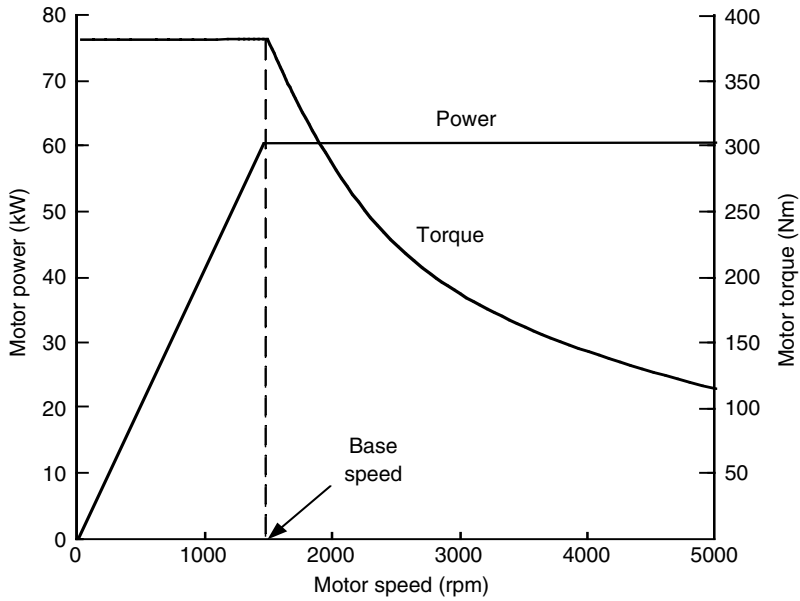

FIGURE 4.4
Typical variable-speed electric motor characteristics

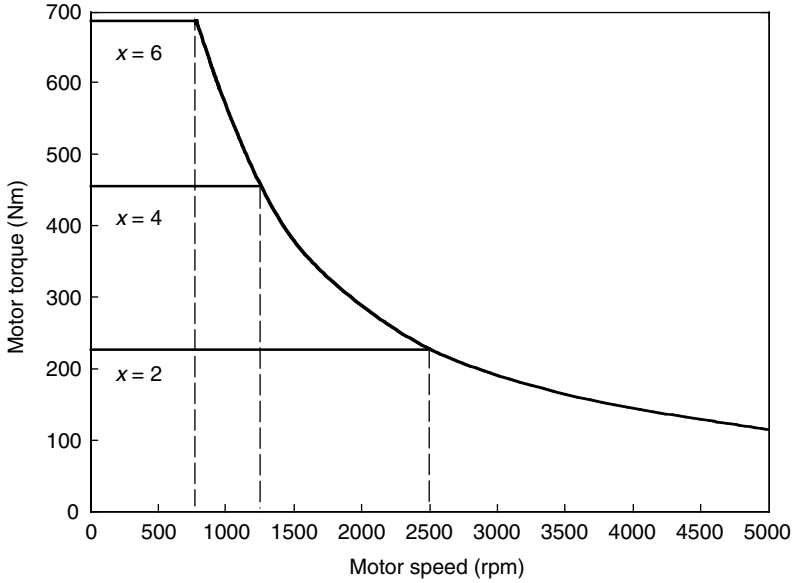

FIGURE 4.5
Speed–torque profile of a 60 kW electric motor with $x = 2$, 4, and 6

limited maximum speed ratio. For example, a permanent magnet motor has a small x (<2) because of the difficulty of field weakening due to the presence of the permanent magnet. Switched reluctance motors may achieve $x>6$ and induction motors about $x=4$.[2,3]

4.2.2 Tractive Effort and Transmission Requirement

The tractive effort developed by a traction motor on driven wheels and the vehicle speed are expressed as

$$F_t = \frac{T_m i_g i_0 \eta_t}{r_d} \tag{4.1}$$

and

$$V = \frac{\pi N_m r_d}{30 i_g i_0} (\text{m/s}), \tag{4.2}$$

where T_m and N_m are the motor torque output and speed in rpm, respectively, i_g is the gear ratio of transmission, i_0 is the gear ratio of final drive, η_t is the efficiency of the whole driveline from the motor to the driven wheels, and r_d is the radius of the drive wheels.

The use of a multigear or single-gear transmission depends mostly on the motor speed–torque characteristics. That is, at a given rated motor power, if the motor has a long constant power region, a single-gear transmission

would be sufficient for a high tractive effort at low speeds. Otherwise, a multigear (more than two gears) transmission has to be used. Figure 4.6 shows the tractive effort of an EV, along with the vehicle speed with a traction motor of $x = 2$ and a three-gear transmission. The first gear covers the speed region of a–b–c, the second gear covers d–e–f, and the third gear covers g–f–h. Figure 4.7 shows the tractive effort with a traction motor of $x = 6$ and a two-gear transmission. The first gear covers the speed region of a–b–c and the second gear d–e–f. Figure 4.8 shows the tractive effort with a traction motor of $x = 6$ and a single-gear transmission. These three designs have the same tractive effort vs. vehicle speed profiles. Therefore, the vehicles will have the same acceleration and gradeability performance.

4.2.3 Vehicle Performance

Basic vehicle performance includes maximum cruising speed, gradeability, and acceleration. The maximum speed of a vehicle can be easily found by the intersection point of the tractive effort curve with the resistance curve (rolling resistance plus aerodynamic drag), in the tractive effort vs. vehicle speed diagram shown in Figures 4.6–4.8. It should be noted that such an intersection point does not exist in some designs, which usually use a larger traction motor or a large gear ratio. In this case, the maximum vehicle speed is determined by the maximum speed of the traction motor as

$$V_{max} = \frac{\pi N_{m\,max} r_d}{30 i_{g\,min} i_0} (\text{m/s}), \tag{4.3}$$

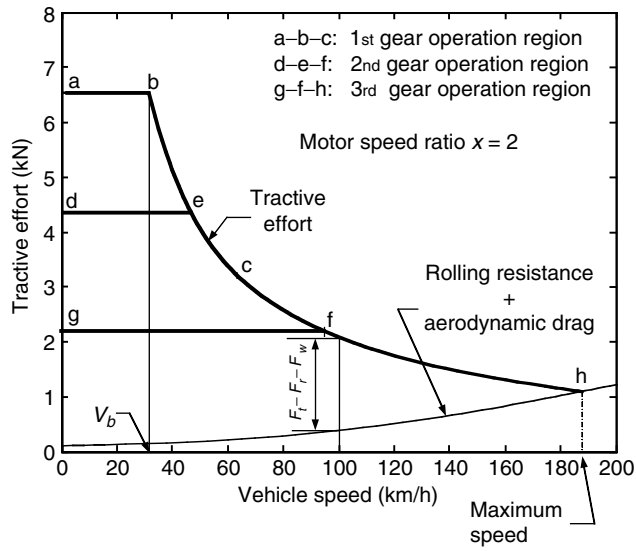

FIGURE 4.6
Tractive effort vs. vehicle speed with a traction motor of $x = 2$ and three-gear transmission

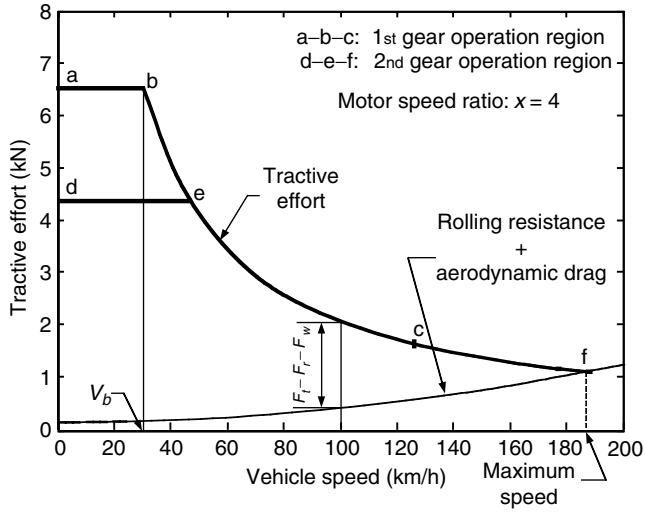

FIGURE 4.7
Tractive effort vs. vehicle speed with a traction motor of $x = 4$ and two-gear transmission

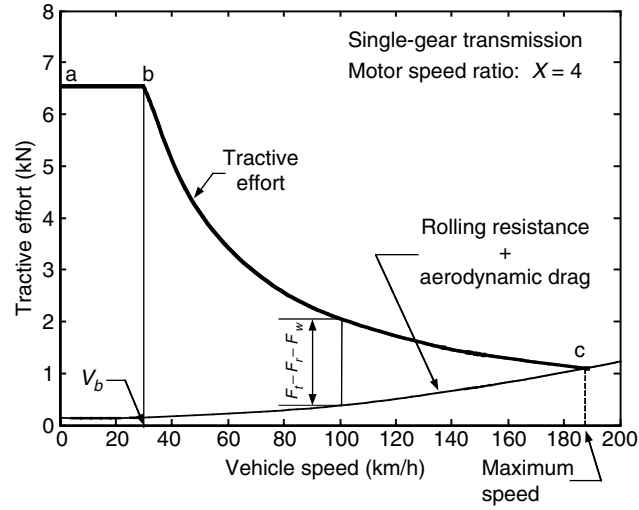

FIGURE 4.8
Tractive effort vs. vehicle speed with a traction motor of $x = 6$ and single-gear transmission

where $N_{m\ max}$ is the allowed maximum rpm of the traction motor and $i_{g\ min}$ is the minimum gear ratio of the transmission (highest gear).

Gradeability is determined by the net tractive effort of the vehicle, $F_{t\text{-}net}$ ($F_{t\text{-}net} = F_t - F_r - F_w$), as shown in Figures 4.6–4.8. At mid- and high speeds, the gradeability is smaller than the gradeability at low speeds. The

maximum grade that the vehicle can overcome at the given speed can be calculated by

$$i = \frac{F_{t\text{-}net}}{M_v g} = \frac{F_t - (F_r + F_w)}{M_v g}, \tag{4.4}$$

where F_t is the tractive effort on the driven wheels, F_r is the tire rolling resistance, and F_w is the aerodynamic drag. However, at low speeds, the gradeability is much larger. Calculations based on (4.4) will cause significance error; instead, equation (4.5) should be used:

$$\sin \alpha = \frac{d - f_r\sqrt{1 - d^2 + f_r^2}}{1 + f_r^2}, \tag{4.5}$$

where $d = (F_t - F_w)/M_v g$, which is called the vehicle performance factor (refer to Chapter 2), and f_r is the tire rolling resistance coefficient.

Acceleration performance of a vehicle is evaluated by the time used to accelerate the vehicle from a low-speed V_1 (usually zero) to a higher speed (100 km/h for passenger cars). For passenger cars, acceleration performance is more important than maximum cruising speed and gradeability, since it is the acceleration requirement, rather than the maximum cruising speed or the gradeability, that dictates the power rating of the motor drive. Referring to (2.58) and Figures 2.36–2.38, the acceleration time for an EV can be expressed as

$$t_a = \int_0^{V_b} \frac{M_v \delta}{P_t/V_b - M_v g f_r - (1/2)\rho_a C_D A_f V^2}\, dV + \int_{V_b}^{V_f} \frac{M_v \delta}{P_t/V - M_v g f_r - (1/2)\rho_a C_D A_f V^2}\, dV, \tag{4.6}$$

where V_b and V_f are the vehicle base speed as shown in Figures 4.6–4.8, and the final acceleration speed, respectively, and P_t is the tractive power on the driven wheels transmitted from the traction motor corresponding to the vehicle base speed. The first term on the right-hand side of (4.6) is in correspondence with the speed region lower than the vehicle base speed; the second term is in correspondence with the speed region beyond the vehicle base speed.

It is difficult to obtain the analytical solution from equation (4.6). For initial evaluation of the acceleration time vs. the tractive power, one can ignore the rolling resistance and the aerodynamic drag and obtain

$$t_a = \frac{\delta M_v}{2P_t}(V_f^2 + V_b^2), \tag{4.7}$$

where the vehicle mass factor, δ, is a constant. The tractive power, P_t, can then be expressed as

$$P_t + \frac{\delta M_v}{2t_a}(V_f^2 + V_b^2). \tag{4.8}$$

To determine the tractive power rating accurately, the power consumed in overcoming the rolling resistance and dynamic drag should be considered.

The average drag power during acceleration can be expressed as

$$\overline{P}_{drag} = \frac{1}{t_a}\int_0^{t_a}\left(M_v g f_r V + \frac{1}{2}\rho_a C_D A_f V^3\right)dt. \tag{4.9}$$

Referring to Figure 2.28 and Figure 2.29, the vehicle speed V can be expressed using time t, as

$$V = V_f\sqrt{\frac{t}{t_a}}. \tag{4.10}$$

Substituting (4.10) into (4.9) and integrating, one obtains

$$\overline{P}_{drag} = \frac{2}{3}M_v g f_r V_f + \frac{1}{5}\rho_a C_D A_f V_f^3. \tag{4.11}$$

The total tractive power for accelerating the vehicle from zero to speed V_f in t_a seconds can be finally obtained as

$$P_t = \frac{\delta M_v}{2t_a}(V_f^2 + V_b^2) + \frac{2}{3}M_v g f_r V_f + \frac{1}{5}\rho_a C_D A_f V_f^3. \tag{4.12}$$

Equation (4.12) indicates that for a given acceleration performance, low vehicle base speed will result in small motor power rating. However, the power rating decline rate to the vehicle base speed reduction is not identical. Differentiating equation (4.12) with respect to the vehicle speed V_b, one can obtain

$$\frac{dP_t}{dV_b} = \frac{\delta M_v}{t_a}V_b. \tag{4.13}$$

Figure 4.9 shows an example of the tractive power rating and the power rating decline rate to the vehicle speed reduction (dP_t/dV_b) vs. the speed fact x.

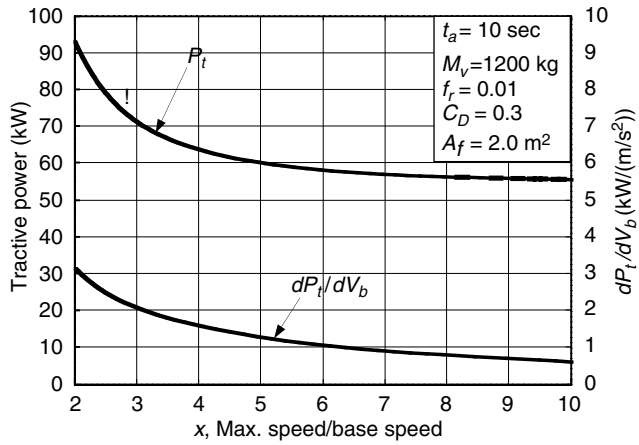

FIGURE 4.9
Power rating vs. speed factor

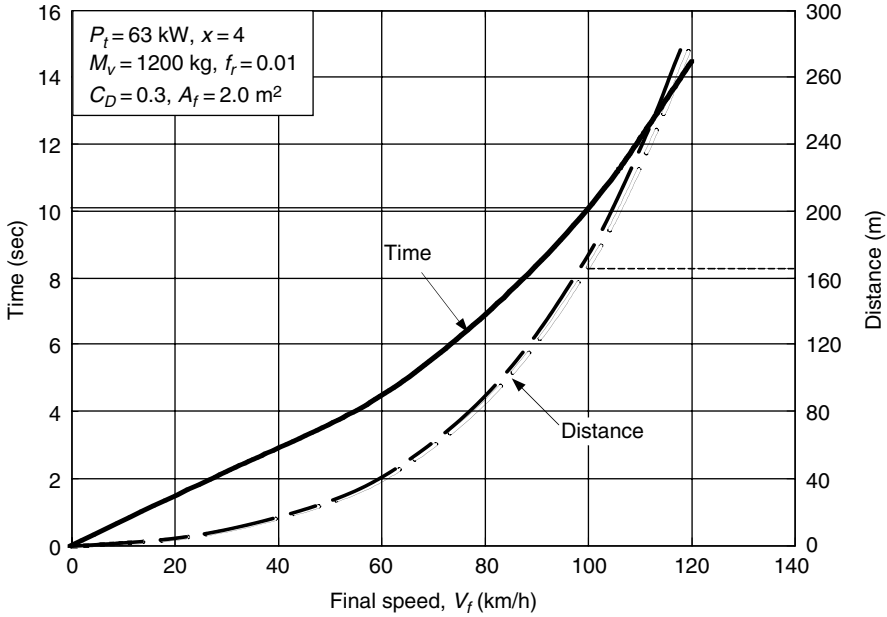

FIGURE 4.10
Acceleration time and distance vs. final speed

In this example, acceleration time is 10 sec, the vehicle mass is 1200 kg, the rolling resistance coefficient is 0.01, the aerodynamic drag coefficient is 0.3, and the front area is 2 m^2. This figure clearly indicates that a low x (high V_b) reduction in V_b will result in a significant decline in the power rating requirement. But with a high x (low V_b), $x > 5$ for example, it is not so effective. Figure 4.10 gives an example of the acceleration time and the distance vs. the vehicle speed, using equation (4.6) and numerical methods.

4.3 Tractive Effort in Normal Driving

The vehicle performance described in the previous section dictates vehicle capabilities with respect to speed, gradeability, and acceleration, thus dictating the power capacity of the power train. However, in normal driving conditions these maximum capabilities are rarely used. During most of the operation time, the power train operates with partial load. Actual tractive effort (power) and vehicle speed vary widely with operating conditions, such as acceleration or deceleration, uphill or downhill motion, etc. These variations are associated with the traffic environment as well as the type of vehicles. City and highway traffic conditions vary greatly, as do the different

missions of the vehicles, such as a universal passenger car and vehicles with regular operation routes and schedules.

It is difficult to describe the tractive effort and vehicle speed variations in all actual traffic environments accurately and quantitatively. However, some representative drive cycles (driving schedules) have been developed to emulate typical traffic environments. These drive cycles are represented by the vehicle speeds vs. the operating time while driving on a flat road. Some typical drive cycles are illustrated in Figure 4.12, which include (a) FTP75 urban cycle, (b) FTP75 highway cycle, (c) US06 cycle, which is a high-speed and high-acceleration drive cycle, (d) J227a schedule B, (e) J227a schedule C, and (f) J227a schedule D. The J227a series is recommended by the Society of Automotive Engineers in the U.S.A.[6] and is applied in the evaluation of EVs and batteries.

In a specific drive cycle, the tractive effort of a vehicle can be expressed as

$$F_t = M_v g f_r \cos\alpha + \frac{1}{2}\rho_a C_D A_f V^2 + M_v \delta \frac{dV}{dt}. \tag{4.14}$$

In a short time period, the speed is assumed to be linear with time, and acceleration is constant as shown in Figure 4.11. The acceleration, dV/dt in a drive cycle, can be obtained by

$$\frac{dV}{dt} = \frac{V_{k+1} - V_k}{t_{k+1} - t_k} (k = 1, 2, \ldots n;\ n \text{ — total number of points}). \tag{4.15}$$

By using (4.13), the tractive efforts in any instant in a drive cycle can be calculated, as shown in Figure 4.12. The operating points of the tractive effort vs. the vehicle speed scatter over the plane, and they clearly show the operating area in which the power train operates most of the time. Furthermore, the time distribution of the vehicle speed and tractive effort can be generated as shown in Figure 4.13. This time distribution information is very helpful for power train design, in which the most efficient region of the power train is designed to overlap with the greatest operation time area.

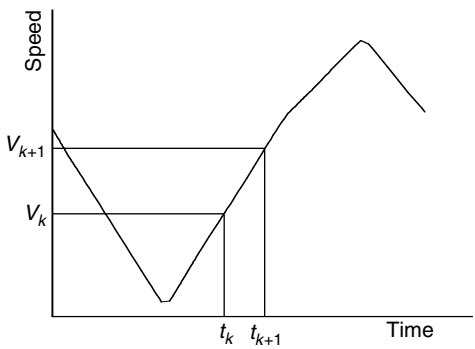

FIGURE 4.11
Acceleration being consumed constant with a short time period

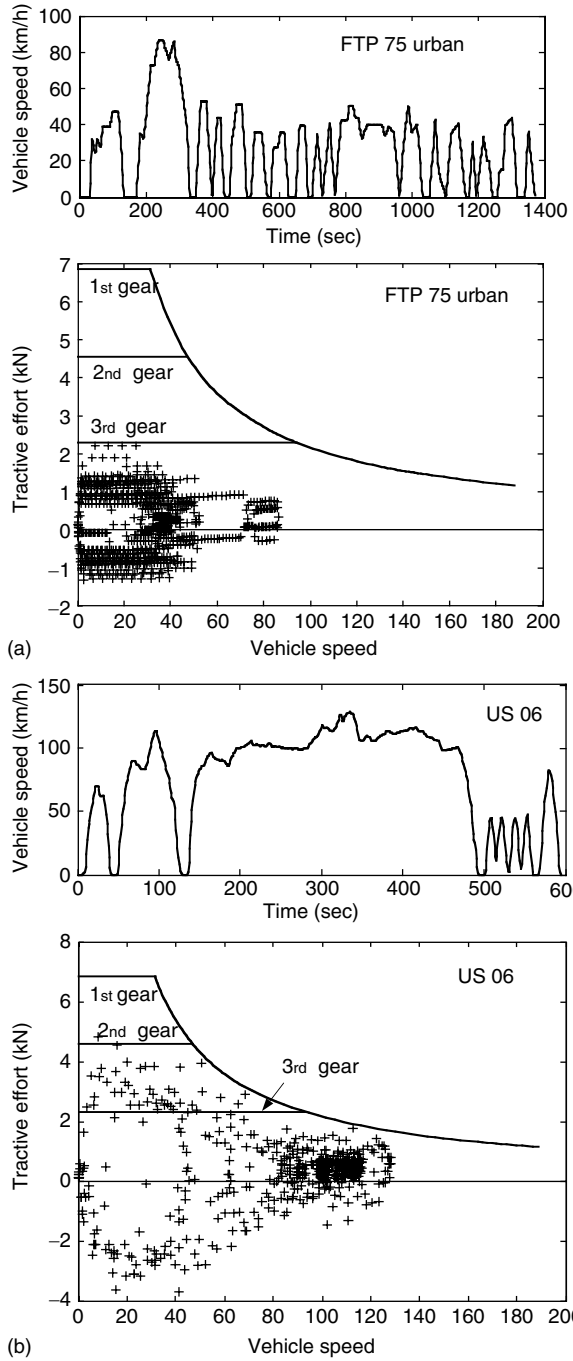

FIGURE 4.12
Speed profile and tractive effort in different representative drive cycles; operating points are marked by '+', (a) FTP 75 urban, (b) FTP 75 highway, (c) US06, (d) J227a schedule B, (e) J227a schedule C, and (f) J227a schedule D

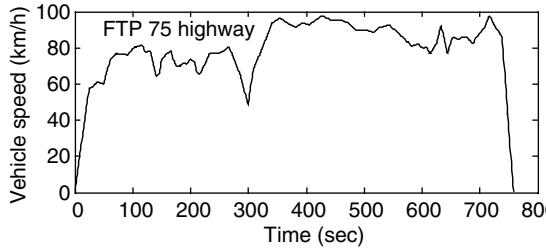

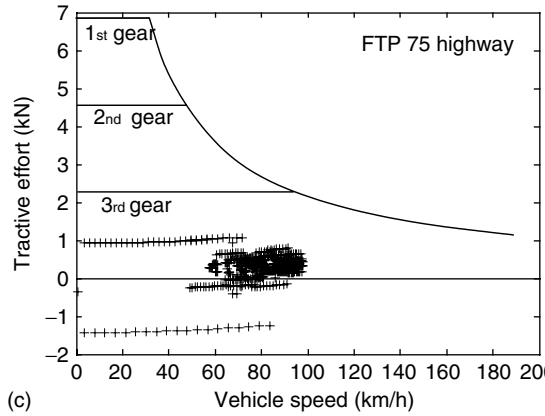

(c)

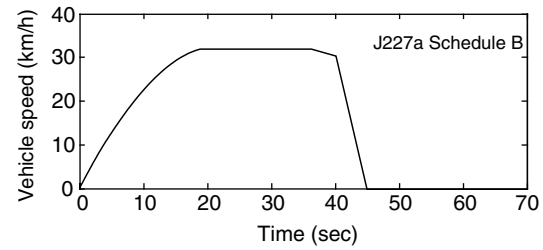

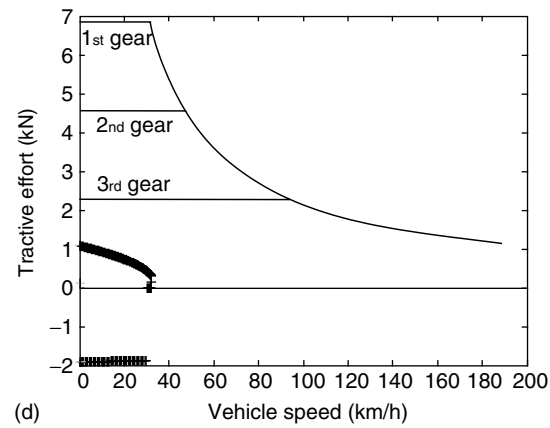

(d)

FIGURE 4.12 *(Continued)*

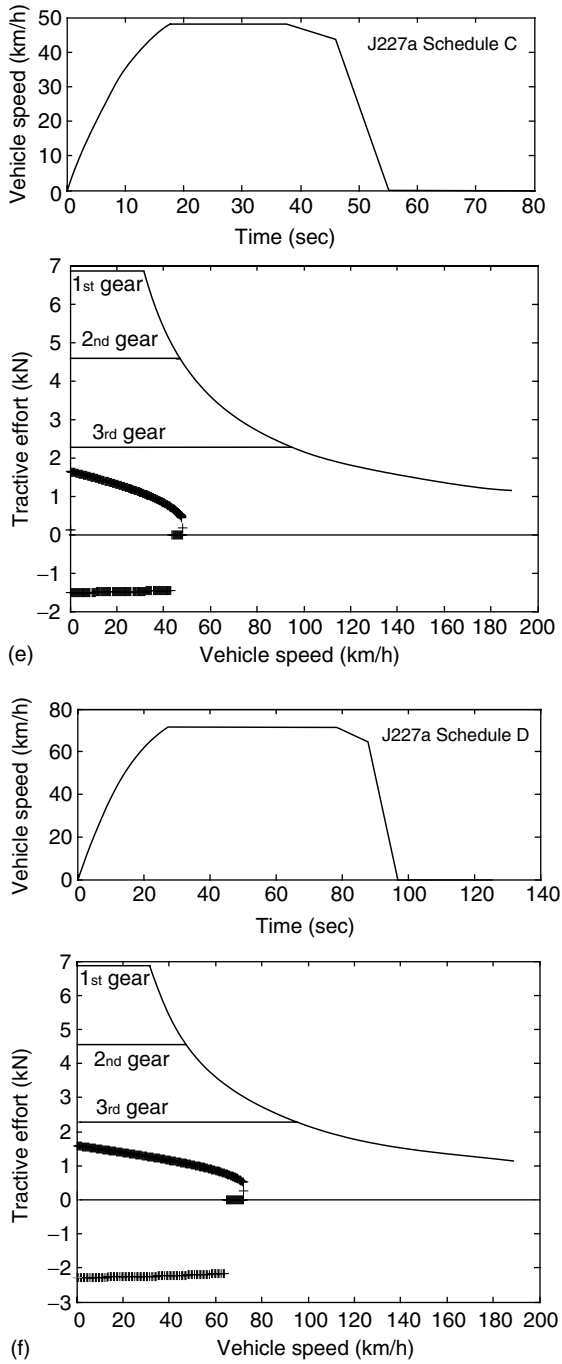

FIGURE 4.12 *(Continued)*

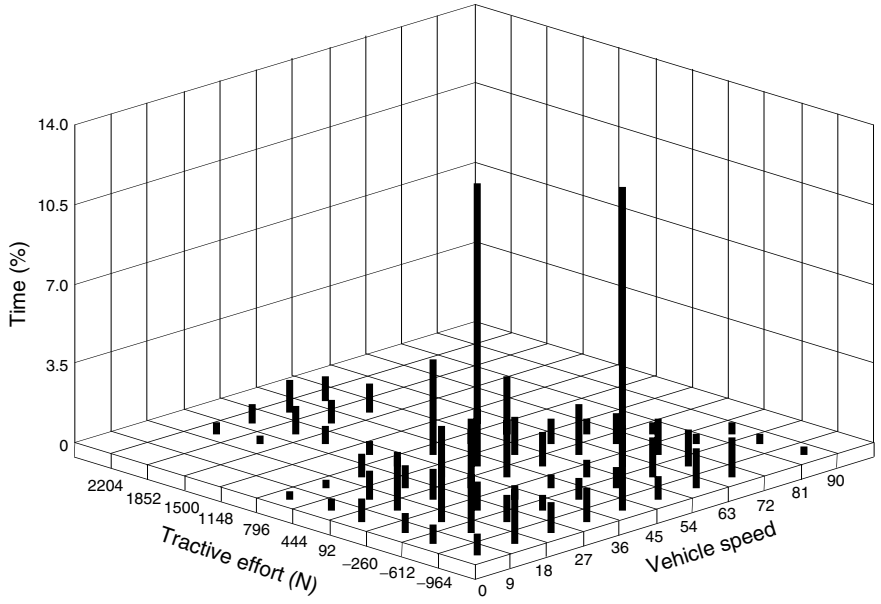

FIGURE 4.13
Time distribution on vehicle speed and tractive effort in an FTP 75 urban cycle

4.4 Energy Consumption

In transportation, the unit of energy is usually kilowatt-hour (kWh) rather than joule or kilojoule (J or kJ). The energy consumption per unit distance in kWh/km is generally used to evaluate the vehicle energy consumption. However, for ICE vehicles the commonly used unit is a physical unit of fuel volume per unit distance, such as liters per 100 km (l/100 km). In the U.S., the distance per unit volume of fuel is usually used; this is expressed as miles per gallon (mpg). On the other hand, for battery-powered EVs, the original energy consumption unit in kWh, measured at the battery terminals, is more suitable. The battery energy capacity is usually measured in kWh and the driving range per battery charge can be easily calculated. Similar to ICE vehicles, l/100 km (for liquid fuels) or kg/100 km (for gas fuels, such as hydrogen) or mpg, or miles per kilogram is a more suitable unit of measurement for vehicles that use gaseous fuels.

Energy consumption is an integration of the power output at the battery terminals. For propelling, the battery power output is equal to resistance power and any power losses in the transmission and the motor drive, including power losses in electronics. The power losses in transmission and motor drive are represented by their efficiencies η_t and η_m, respectively. Thus, the battery power output can be expressed as

$$P_{b\text{-}out} = \frac{V}{\eta_t \eta_m}\left(M_v g\,(f_r + i) + \frac{1}{2}\rho_a C_D A_f V^2 + M\delta\frac{dV}{dt}\right). \tag{4.16}$$

Here, the nontraction load (auxiliary load) is not included. In some cases, the auxiliary loads may be too significant to be ignored and should be added to the traction load. When regenerative braking is effective on an EV, a part of that braking energy — wasted in conventional vehicles — can be recovered by operating the motor drive as a generator and restoring it into the batteries. The regenerative braking power at the battery terminals can also be expressed as

$$P_{b\text{-}in} = \frac{\alpha V}{\eta_t \eta_m}\left(M_v g\,(f_r + i) + \frac{1}{2}\rho_a C_D A_f V^2 + M\delta\frac{dV}{dt}\right), \tag{4.17}$$

where road grade i or acceleration dV/dt or both of them are negative, and α $(0 < \alpha < 1)$ is the percentage of the total braking energy that can be applied by the electric motor, called the regenerative braking factor. The regenerative braking factor α is a function of the applied braking strength and the design of the power train, which will be discussed in detail in the later chapters. The net energy consumption from the batteries is

$$E_{out} = \int_{traction} P_{b\text{-}out}\,dt + \int_{braking} P_{b\text{-}in}\,dt. \tag{4.18}$$

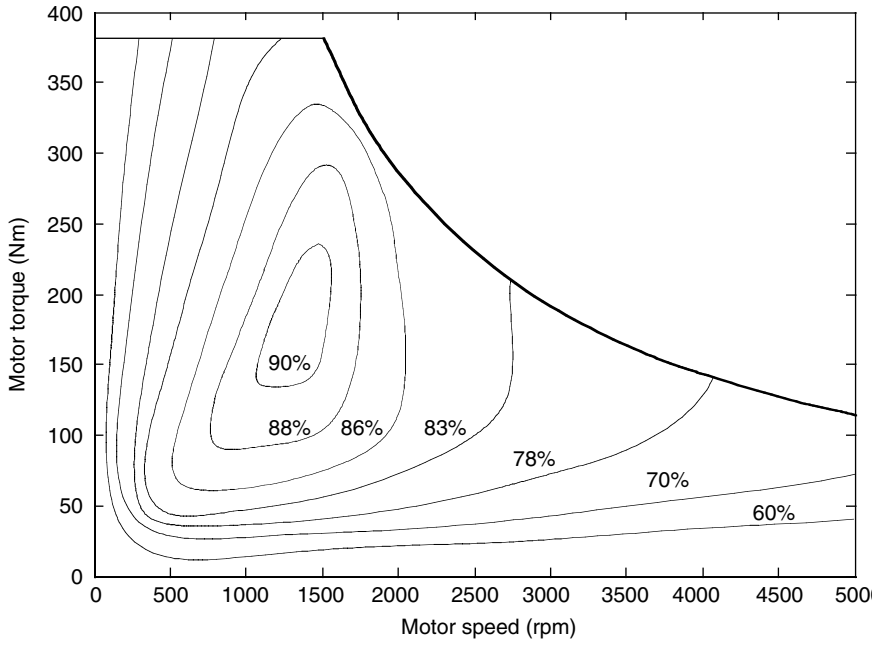

FIGURE 4.14
Typical electric motor efficiency characteristics

It should be noted that the braking power in (4.17) has a negative sign. When the net battery energy consumption reaches the total energy in the batteries, measured at their terminal, the batteries are empty and need to be charged. The traveling distance between two charges (usually called effective travel range) is determined by the total energy carried by the batteries, the resistance power, and the effectiveness of the regenerative braking (α).

The efficiency of a traction motor varies with its operating points on the speed–torque (speed–power) plane as shown in Figure 4.14, where the most efficient operating area exists. In power train design, this area should overlap with or at least be as close as possible to the area of the greatest operation, as mentioned in the previous section.

References

[1] C.C. Chan and K.T. Chau, *Modern Electric Vehicle Technology*, Oxford University Press, New York, 2001.

[2] K.M. Rahman and M. Ehsani, Performance analysis of electric motor drives for electric and hybrid electric vehicle application, *IEEE Power Electronic in Transportation*, 49–56, 1996.

[3] Y. Gao, H. Maghbelli, M. Ehsani, et al., Investigation of proper motor drive characteristics for military vehicle propulsion, *Society of Automotive Engineers (SAE) Journal*, Paper No. 2003-01-2296, Warrendale, PA, 2003.

[4] Z. Rahman. M. Ehsani, and K. Butler, An investigation of electric motor drive characteristics for EV and HEV propulsion systems, *Society of Automotive Engineers (SAE) Journal*, Paper No. 2000–01–3062, Warrendale, PA, 2003.

[5] Z. Rahman, M. Ehsani, and K. Butler, Effect of extended-speed, constant-power operation of electric drives on the design and performance of EV-HEV propulsion system, *Society of Automotive Engineers (SAE) Journal*, Paper No. 2000–01–1557, Warrendale, PA, 2003.

[6] D.A.J. Rand, R. Woods, and R.M. Dell, *Batteries for Electric Vehicles*, Research Studies Press, Ltd., Baldock, Hertfordshire, United Kingdom, 1998.

5

Hybrid Electric Vehicles

CONTENTS

5.1 Concept of Hybrid Electric Drive Trains 118
5.2 Architectures of Hybrid Electric Drive Trains 120
5.2.1 Series Hybrid Electric Drive Trains 121
5.2.2 Parallel Hybrid Electric Drive Trains 123
5.2.2.1 Torque-Coupling Parallel Hybrid Electric Drive Trains 124
5.2.2.2 Speed-Coupling Parallel Hybrid Electric Drive Trains 130
5.2.2.3 Torque-Coupling and Speed-Coupling Parallel Hybrid Electric Drive Trains 133
References 136

Conventional vehicles with internal combustion engines (ICE) provide good performance and long operating range by utilizing the high energy-density advantages of petroleum fuels. However, conventional ICE vehicles bear the disadvantages of poor fuel economy and environmental pollution. The main reasons for their poor fuel economy are (1) engine fuel efficiency characteristics are mismatched with the real operation requirements (refer to Figure 2.34 and Figure 2.35), (2) dissipation of vehicle kinetic energy during braking, especially while operating in urban areas, and (3) low efficiency of hydraulic transmission in current automobiles in stop-and-go driving patterns (refer to Figure 2.20). Battery-powered electric vehicles (EV), on the other hand, possess some advantages over conventional ICE vehicles, such as high energy efficiency and zero environmental pollution. However, the performance, especially the operation range per battery charge, is far less competitive than ICE vehicles, due to the lower energy content of the batteries vs. the energy content of gasoline. Hybrid electric vehicles (HEV), which use two power sources — a primary power source and a secondary power source — have the advantages of both ICE vehicles and EV and overcome their disadvantages.[1,2] In this chapter, the basic concept and operation principles of the HEV power trains are discussed.

5.1 Concept of Hybrid Electric Drive Trains

Basically, any vehicle power train is required to (1) develop sufficient power to meet the demands of vehicle performance, (2) carry sufficient energy onboard to support vehicle driving in the given range, (3) demonstrate high efficiency, and (4) emit few environmental pollutants. Broadly, a vehicle may have more than one energy source and energy converter (power source), such as a gasoline (or diesel) heat engine system, hydrogen–fuel cell–electric motor system, chemical battery–electric motor system, etc. A vehicle that has two or more energy sources and energy converters is called a hybrid vehicle. A hybrid vehicle with an electrical power train (energy source energy converters) is called an HEV.

A hybrid vehicle drive train usually consists of no more than two power trains. More than two power train configurations will complicate the system. For the purpose of recapturing part of the braking energy[8] that is dissipated in the form of heat in conventional ICE vehicles, a hybrid drive train usually has a bidirectional energy source and converter. The other one is either bidirectional or unidirectional. Figure 5.1 shows the concept of a hybrid drive train and the possible different power flow routes.

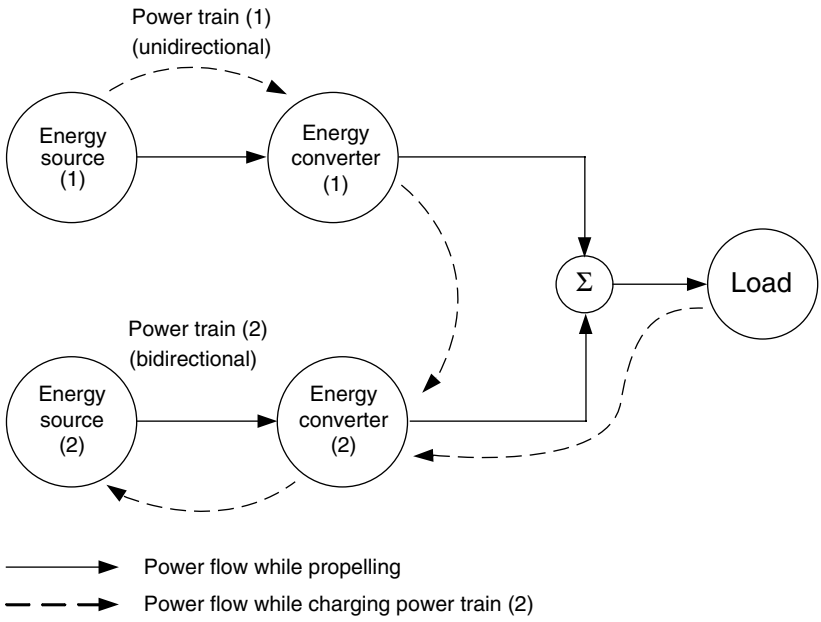

FIGURE 5.1
Conceptual illustration of a hybrid electric drive train

Hybrid drive trains supply the required power by an adapted power train. There are many available patterns of combining the power flows to meet load requirements as described below:

1. Power train 1 alone delivers power to the load
2. Power train 2 alone delivers power to the load
3. Both power train 1 and 2 deliver power to load at the same time
4. Power train 2 obtains power from load (regenerative braking)
5. Power train 2 obtains power from power train 1
6. Power train 2 obtains power from power train 1 and load at the same time
7. Power train 1 delivers power to load and to power train 2 at the same time
8. Power train 1 delivers power to power train 2, and power train 2 delivers power to load
9. Power train 1 delivers power to load, and load delivers power to power train 2.

In the case of hybridization with a liquid fuel-IC engine (power train 1) and a battery-electric machine (power train 2), pattern (1) is the engine-alone propelling mode. This may be used when the batteries are almost completely depleted and the engine has no remaining power to charge the batteries, or when the batteries have been fully charged and the engine is able to supply sufficient power to meet the power demands of the vehicle. Pattern (2) is the pure electric propelling mode, in which the engine is shut off. This pattern may be used in situations where the engine cannot operate effectively, such as very low speed, or in areas where emissions are strictly prohibited. Pattern (3) is the hybrid traction mode and may be used when a large amount of power is needed, such as during sharp acceleration or steep hill climbing. Pattern (4) is the regenerative braking mode, by which the kinetic or potential energy of the vehicle is recovered through the electric motor functioning as a generator. The recovered energy is stored in the batteries and reused later on. Pattern (5) is the mode in which the engine charges the batteries while the vehicle is at a standstill, coasting, or descending a slight grade, in which no power goes into or comes from the load. Pattern (6) is the mode in which both regenerative braking and the IC engine charge the batteries simultaneously. Pattern (7) is the mode in which the engine propels the vehicle and charges the batteries simultaneously. Pattern (8) is the mode in which the engine charges the batteries, and the batteries supply power to the load. Pattern (9) is the mode in which the power flows into the batteries from the heat engine through the vehicle mass. The typical configuration of this mode is two power trains separately mounted on the front and the rear axle of the vehicle.

The varied operation modes in a hybrid vehicle create more flexibility over a single power train vehicle. With proper configuration and control, applying the specific mode for each special operating condition can optimize overall performance, efficiency, and emissions. However, in a practical

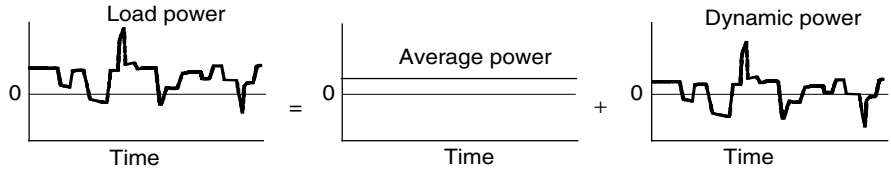

FIGURE 5.2
A load power is decomposed into steady and dynamic components

design, deciding which mode should be implemented depends on many factors, such as the physical configuration of the drive train, the power train efficiency characteristics, load characteristics, etc.

Operating each power train in its optimal efficiency region is essential for the overall efficiency of the vehicle. An IC engine generally has the best efficiency operating region with a wide throttle opening. Operating away from this region will cause the efficiency to suffer a lot (refer to Figures 2.30, 2.32, 2.34, and 2.35). On the other hand, efficiency suffering in an electric motor is not as detrimental when compared to an IC engine that operates away from its optimal region (refer to Figure 3.14).

The load power of a vehicle varies randomly in real operation due to frequent acceleration, deceleration, and climbing up and down grades, as shown in Figure 5.2. Actually, the load power is composed of two components: one is steady (average) power, which has a constant value, and the other is dynamic power, which has a zero average. In hybrid vehicle strategy, one power train that favors steady-state operation, such as an IC engine fuel cell, can be used to supply the average power. On the other hand, other power trains such as an electric motor can be used to supply the dynamic power. The total energy output from the dynamic power train will be zero in a whole driving cycle. This implies that the energy source of the dynamic power train does not lose energy capacity at the end of the driving cycle. It functions only as a power damper.

In a hybrid vehicle, steady power may be provided by an IC engine, a Stirling engine, a fuel cell, etc. The IC engine or the fuel cell can be much smaller than that in a single power train design because the dynamic power is taken by the dynamic power source, and can then operate steadily in its most efficient region. The dynamic power may be provided by an electric motor powered by electrochemical batteries, ultracapacitors, flywheels (mechanical batteries), and their combinations.[1–3]

5.2 Architectures of Hybrid Electric Drive Trains

The architecture of a hybrid vehicle is loosely defined as the connection between the components that define the energy flow routes and control ports. Traditionally, HEVs were classified into two basic types: series and

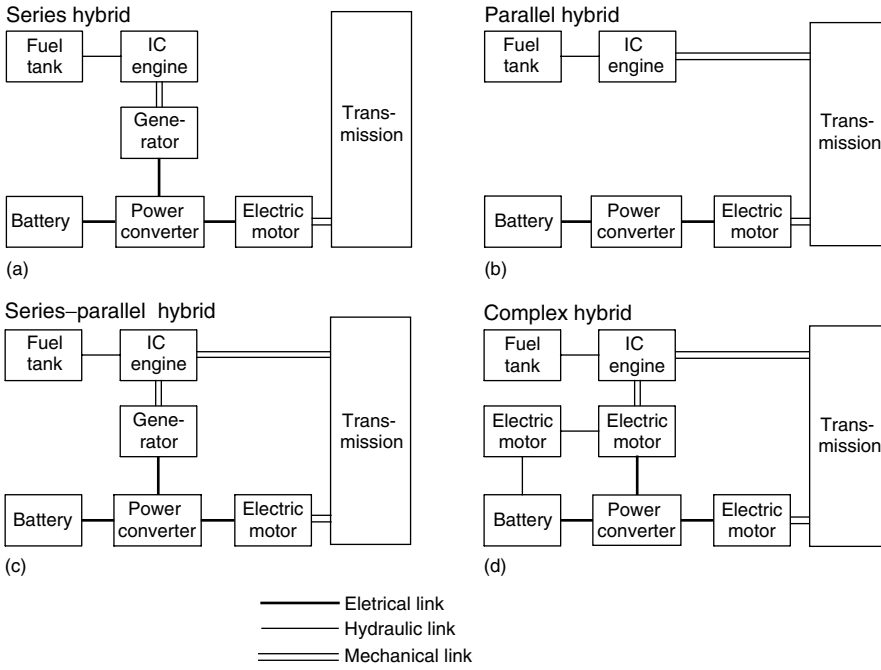

FIGURE 5.3
Classification of hybrid electric vehicles

parallel. It is interesting to note that, in 2000, some newly introduced HEVs could not be classified into these kinds.[5] Therefore, HEVs are now classified into four kinds: series hybrid, parallel hybrid, series–parallel hybrid, and complex hybrid, which are functionally shown in Figure 5.3.[4] In Figure 5.3, a fuel tank-IC engine and a battery-electric motor are taken, respectively, as examples of the primary power source (steady power source) and secondary power source (dynamic power source). Of course, the IC engine can be replaced by other types of power sources, such as fuel cells. Similarly, the batteries can be replaced by ultracapacitors or by flywheels and their combinations, which will be discussed in detail in the following chapters.

5.2.1 Series Hybrid Electric Drive Trains

A series hybrid drive train is a drive train where two power sources feed a single powerplant (electric motor) that propels the vehicle. The most commonly found series hybrid drive train is the series hybrid electric drive train shown in Figure 5.4. The unidirectional energy source is a fuel tank and the unidirectional energy converter is an engine coupled to an electric generator. The output of the electric generator is connected to an electric power bus through an electronic converter (rectifier). The bidirectional energy source is an electrochemical battery pack, connected to the bus by means of a power

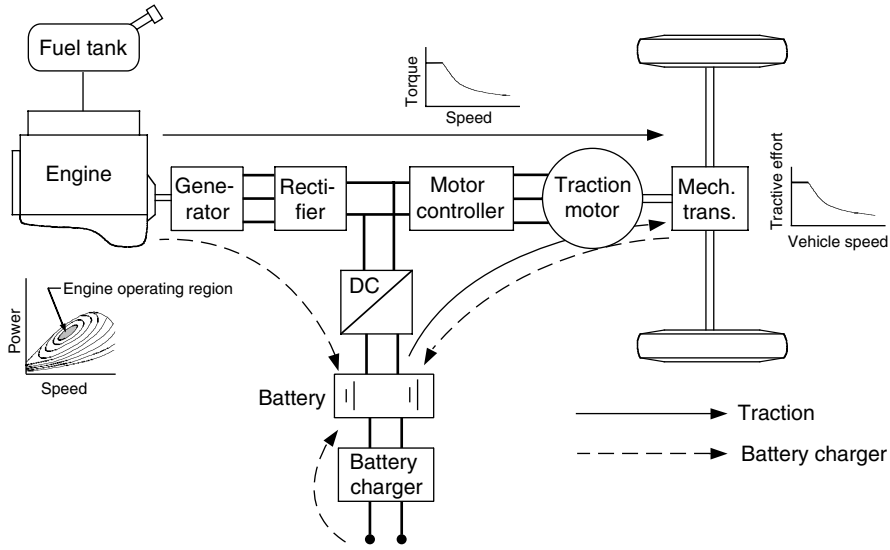

FIGURE 5.4
Configuration of a series hybrid electric drive train

electronics converter (DC/DC converter). The electric power bus is also connected to the controller of the electric traction motor. The traction motor can be controlled either as a motor or a generator, and in forward or reverse motion. This drive train may need a battery charger to charge the batteries by a wall plug-in from the power network.

Series hybrid electric drive trains potentially have the following operation modes:

1. Pure electric mode: The engine is turned off and the vehicle is propelled only by the batteries.
2. Pure engine mode: The vehicle traction power only comes from the engine-generator, while the batteries neither supply nor draw any power from the drive train. The electric machines serve as an electric transmission from the engine to the driven wheels.
3. Hybrid mode: The traction power is drawn from both the engine-generator and the batteries.
4. Engine traction and battery charging mode: The engine-generator supplies power to charge the batteries and to propel the vehicle.
5. Regenerative braking mode: The engine-generator is turned off and the traction motor is operated as a generator. The power generated is used to charge the batteries.
6. Battery charging mode: The traction motor receives no power and the engine-generator charges the batteries.
7. Hybrid battery charging mode: Both the engine-generator and the traction motor operate as generators to charge the batteries.

Series hybrid drive trains offer several advantages:

1. The engine is fully mechanical when decoupled from the driven wheels. Therefore, it can be operated at any point on its speed–torque characteristic map, and can potentially be operated solely within its maximum efficiency region as shown in Figure 5.4. The efficiency and emissions of the engine can be further improved by optimal design and control in this narrow region. A narrow region allows greater improvements than an optimization across the entire range. Furthermore, the mechanical decoupling of the engine from the driven wheels allows the use of a high-speed engine. This makes it difficult to power the wheels directly through a mechanical link, such as gas turbines or powerplants, with slow dynamics like the Stirling engine.
2. Because electric motors have near-ideal torque–speed characteristics, they do not need multigear transmissions as discussed in Chapter 3. Therefore, their construction is greatly simplified and the cost is reduced. Furthermore, instead of using one motor and a differential gear, two motors may be used, each powering a single wheel. This provides speed decoupling between the two wheels like a differential but also acts as a limited slip differential for traction control purposes. The ultimate refinement would use four motors, thus making the vehicle an all-wheel-drive without the expense and complexity of differentials and drive shafts running through the frame.
3. Simple control strategies may be used as a result of the mechanical decoupling provided by the electrical transmission.

However, series hybrid electric drive trains have some disadvantages:

1. The energy from the engine is converted twice (mechanical to electrical in the generator and electrical to mechanical in the traction motor). The inefficiencies of the generator and traction motor add up and the losses may be significant.
2. The generator adds additional weight and cost.
3. The traction motor must be sized to meet maximum requirements since it is the only powerplant propelling the vehicle.

5.2.2 Parallel Hybrid Electric Drive Trains

A parallel hybrid drive train is a drive train in which the engine supplies its power mechanically to the wheels like in a conventional ICE-powered vehicle. It is assisted by an electric motor that is mechanically coupled to the transmission. The powers of the engine and electric motor are coupled together by mechanical coupling, as shown in Figure 5.5. The mechanical

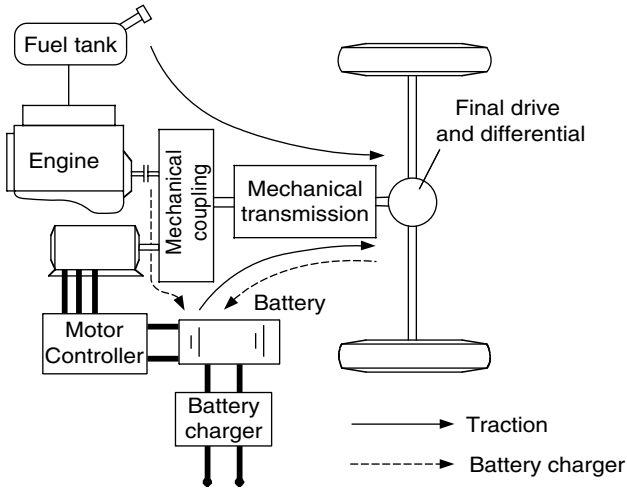

FIGURE 5.5
Configuration of a parallel hybrid electric drive train

combination of the engine and electric motor power leaves room for several different configurations, detailed hereafter.

5.2.2.1 Torque-Coupling Parallel Hybrid Electric Drive Trains

The mechanical coupling in Figure 5.5 may be a torque or speed coupling. The torque coupling adds the torques of the engine and the electric motor together or splits the engine torque into two parts: propelling and battery charging. Figure 5.6 conceptually shows a mechanical torque coupling, which has two inputs. One is from the engine and one is from the electric motor. The mechanical torque coupling outputs to the mechanical transmission.

If loss is ignored, the output torque and speed can be described by

$$T_{out} = k_1 T_{in1} + k_2 T_{in2} \tag{5.1}$$

and

$$\omega_{out} = \frac{\omega_{in1}}{k_1} = \frac{\omega_{in2}}{k_2}, \tag{5.2}$$

where k_1 and k_2 are the constants determined by the parameters of torque coupling. Figure 5.7 lists some typically used mechanical torque-coupling devices.

There are a variety of configurations in torque coupling hybrid drive trains. They are classified into two-shaft and one-shaft designs. In each category, the transmission can be placed in different positions and designed with different gears, resulting in different tractive characteristics. An optimum design will depend mostly on the tractive

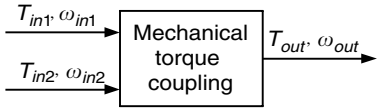

FIGURE 5.6
Torque coupling device

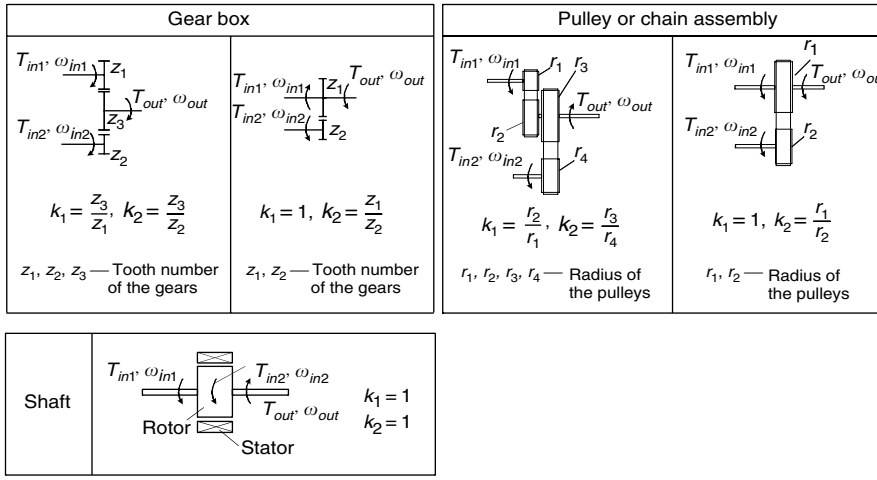

FIGURE 5.7
Commonly used mechanical torque coupling devices

requirements, engine size and engine characteristics, motor size and motor characteristics, etc.

Figure 5.8 shows a two-shaft configuration design, in which two transmissions are used: one is placed between the engine and the torque coupling and other is placed between the motor and torque coupling. Both transmissions may be single or multigear. Figure 5.9 shows the tractive effort–speed profiles of a vehicle with different transmission parameters. It is clear that two multigear transmissions produce many tractive effort profiles. The performance and overall efficiency of the drive train may be superior to other designs, because two multigear transmissions provide more opportunities for both the engine and electric traction system (electric machine and batteries) to operate in their optimum region. This design also provides great flexibility in the design of the engine and electric motor characteristics. However, two multigear transmissions will significantly complicate the drive train.[6,7]

In Figure 5.8, the single-gear transmission 1 and the multigear transmission 2 may be used. The tractive effort–speed profiles are shown in Figure 5.9(b). In actual hybrid drive train design, the maximum tractive effort with this transmission arrangement may be sufficient for the hill-climbing performance of the vehicle; greater tractive effort would not be necessary due to the limitation of the tire–ground contact adhesion. The use of a single-gear transmission takes inherent advantage of the high torque characteristic of

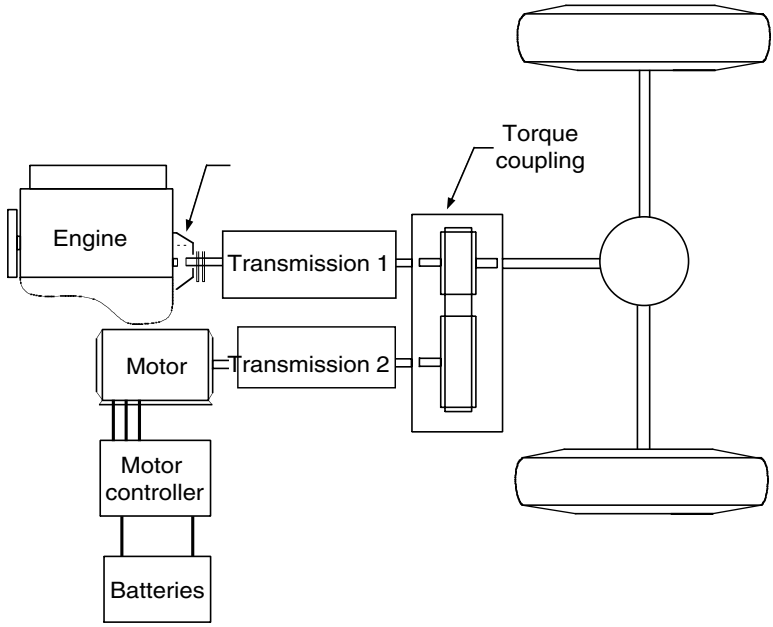

FIGURE 5.8
Two-axle configuration

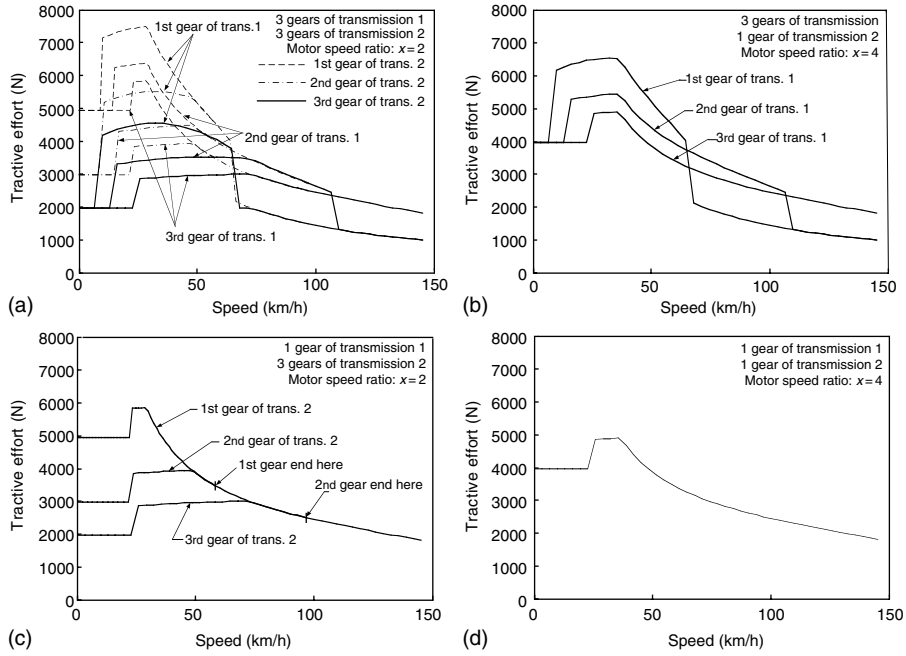

FIGURE 5.9
Tractive effort along with vehicle speed with different transmission schemes

electric machines at low speeds. The multigear transmission 2 is used to overcome the disadvantages of the IC engine speed–torque characteristics (flat torque output along speed). The multispeed transmission 2 also tends to improve the efficiency of the engine and reduces the speed range of the vehicle — in which an electric machine alone must propel the vehicle — consequently reducing the battery-discharging energy.

In contrast with the above design, Figure 5.9(c) shows the tractive effort–speed profile of the drive train, which has a single transmission 1 for the engine and a multispeed transmission 2 for the electric motor. This configuration is considered to be an unfavorable design, because it does not use the advantages of both powerplants.

Figure 5.9(d) shows the tractive effort–speed profile of the drive train, which has two single-gear transmissions. This arrangement results in simple configuration and control. The limitation to the application of this drive train is the maximum tractive effort of the drive train. When power of the engine, electric motor, batteries, and transmission parameters are properly designed, this drive train would serve the vehicle with satisfactory performance and efficiency.

Another configuration of the two-shaft parallel hybrid drive train is shown in Figure 5.10, in which the transmission is located between the torque coupling and drive shaft. The transmission functions to enhance the torques of both engine and electric motor with the same scale. Designing the constant k_1 and k_2 in the torque coupling allows the electric motor to have a

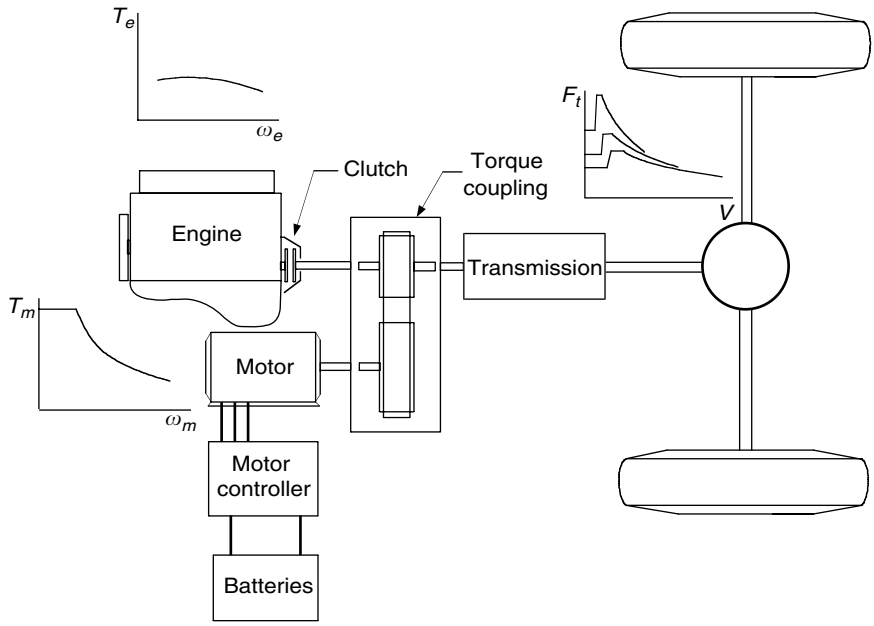

FIGURE 5.10
Two-shaft configuration

different speed range than the engine; therefore, a high-speed motor can be used. This configuration would be suitable in the case when a relatively small engine and electric motor are used, and where a multigear transmission is needed to enhance the tractive effort at low speeds.

The simple and compact architecture of the torque coupling parallel hybrid is the single-shaft configuration where the rotor of the electric motor functions as the torque coupling (k_1=1 and k_2=1 in [5.1] and [5.2]), as shown in Figure 5.11 and Figure 5.12. A transmission may be either placed behind an electric motor that is connected to the engine through a clutch or between the engine and the electric motor. The former configuration is referred to as "pretransmission" (the motor is ahead of the transmission, Figure 5.11) and the latter is referred to as "posttransmission" (the motor is behind the transmission, Figure 5.12).

In the pretransmission configuration, both the engine torque and motor torque are modified by the transmission. The engine and motor must have the same speed range. This configuration is usually used in the case of a small motor, referred to as a mild hybrid drive train, in which the electric motor functions as an engine starter, electrical generator, engine power assistant, and regenerative braking.

However, in the posttransmission configuration as shown in Figure 5.12, the transmission can only modify the engine torque while the motor torque is directly delivered to the driven wheels. This configuration may be used in the drive train where a large electric motor with a long constant power

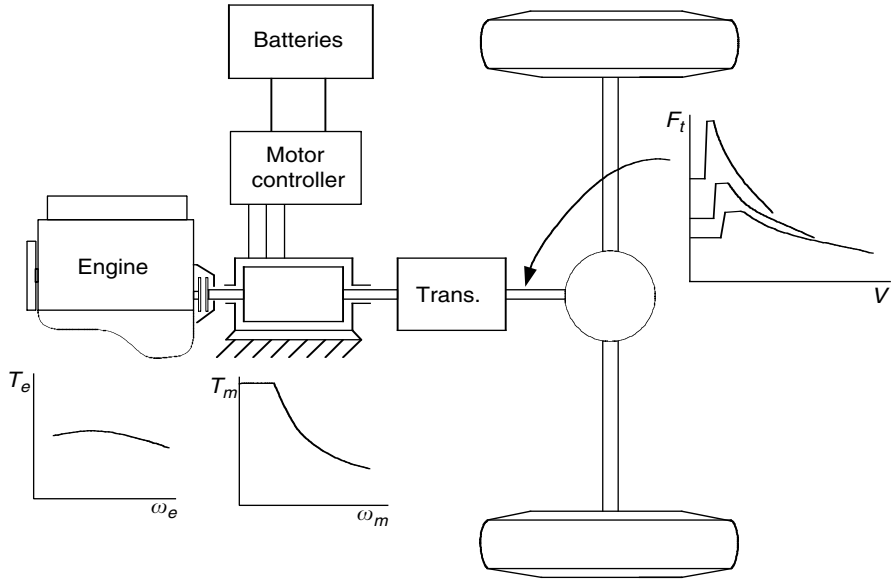

FIGURE 5.11
Pretransmission single-shaft torque combination parallel hybrid electric drive train

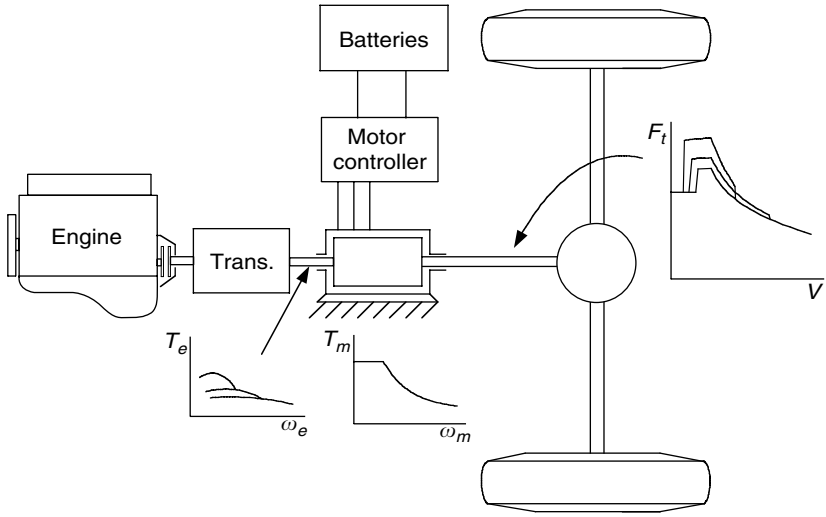

FIGURE 5.12
Posttransmission single-shaft torque combination parallel hybrid electric drive train

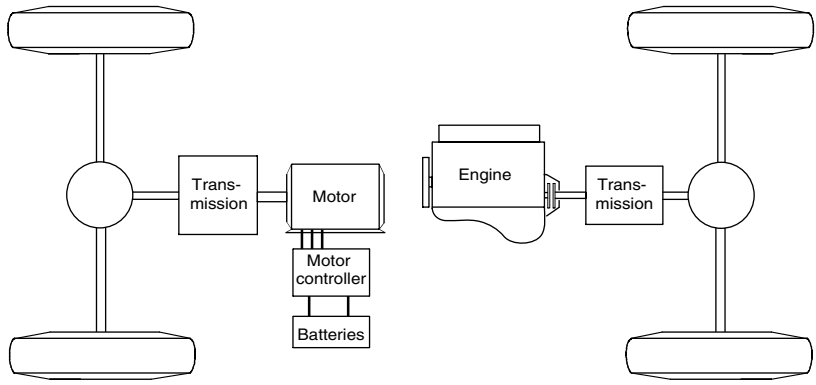

FIGURE 5.13
Separated axle torque combination parallel hybrid electric drive train

region is used. The transmission is only used to change the engine operating points to improve the vehicle performance and engine operating efficiency. It should be noted that the batteries cannot be charged from the engine by running the electric motor as a generator when the vehicle is at a standstill and the motor is rigidly connected to the driven wheels.

Another torque coupling parallel hybrid drive train is the separated axle architecture, in which one axle is powered by the engine and another is powered by the electric motor (Figure 5.13). The tractive efforts from the two power trains are added through the vehicle chassis and the road. The operating principle is similar to the two-shaft configuration shown in Figure 5.8.

Both transmissions for the engine and electric motor may be either single or multigear. This configuration has similar tractive effort characteristics, as shown in Figure 5.9.

The separated axle architecture offers some of the advantages of a conventional vehicle. It keeps the original engine and transmission unaltered and adds an electrical traction system on the other axle. It also has four-wheel drive, which optimizes traction on slippery roads and reduces the tractive effort on a single tire.

However, the electric machines and the eventual differential gear system occupy considerable space and may reduce the available passenger and luggage space. This problem may be solved if the motor transmission is single gear and the electric motor is replaced by two small-sized electric motors that can be placed within two driven wheels. It should be noted that the batteries cannot be charged from the engine when the vehicle is at a standstill.

5.2.2.2 Speed-Coupling Parallel Hybrid Electric Drive Trains

The powers from two powerplants may be coupled together by coupling their speeds, as shown in Figure 5.14. The characteristics of a speed coupling can be described by

$$\omega_{out} = k_1\omega_{in1} + k_2\omega_{in2} \tag{5.3}$$

and

$$T_{out} = \frac{T_{in1}}{k_1} = \frac{T_{in2}}{k_2}, \tag{5.4}$$

where k_1 and k_2 are constants associated with the actual design.

Figure 5.15 shows two typical speed-coupling devices: one is a planetary gear unit and the other is an electric motor with a floating stator, called a transmotor in this book. A planetary gear unit is a three-port unit consisting of the sun gear, the ring gear, and the yoke labeled 1, 2, and 3, respectively. The speed and torque relationship between the three ports indicates that the unit is a speed-coupling device, in which the speed, the sun gear, and the ring gear are added together and output through the yoke. The constants k_1 and k_2 depend only on the radius of each gear or the number of teeth of each gear.

Another interesting device used in speed coupling is an electric motor (called a transmotor in this book), in which the stator, generally fixed to a stationary frame, is released as a power-input port. The other two ports are the rotor and the airgap through which electric energy is converted into

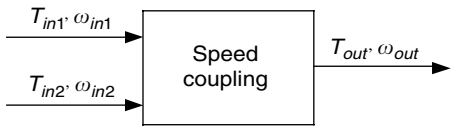

FIGURE 5.14
Speed coupling

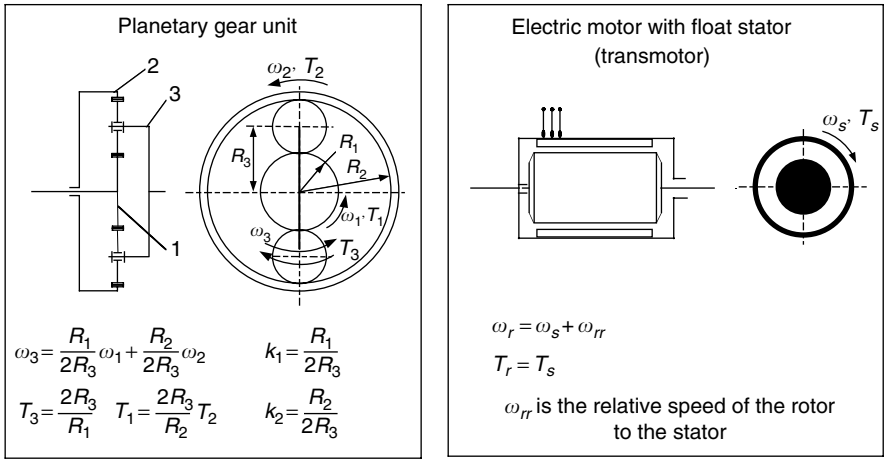

FIGURE 5.15
Typical speed-coupling devices

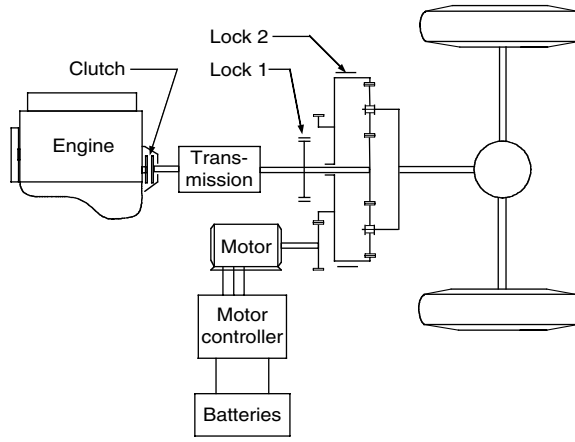

FIGURE 5.16
Hybrid electric drive train with speed coupling of planetary gear unit

mechanical energy. The motor speed, in common terms, is the relative speed of the rotor to the stator. Because of action and reaction effects, the torque action on the stator and rotor is always the same and results in the constants $k_1 = 1$ and $k_2 = 1$.

Just like the torque-coupling device, the speed-coupling units can be used to constitute various hybrid drive trains. Figure 5.16 and Figure 5.17 show two examples of hybrid drive trains with speed coupling of the planetary gear unit and an electric transmotor. In Figure 5.16, the engine supplies its power to the sun gear through a clutch and transmission. The transmission

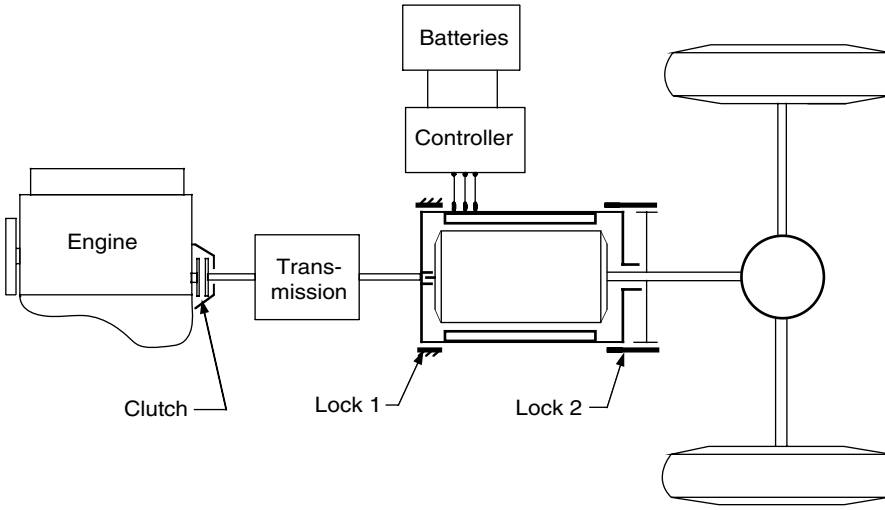

FIGURE 5.17
Hybrid electric drive train with speed coupling of electric transmotor

is used to modify the speed–torque characteristics of the engine so as to match the traction requirements. The electric motor supplies its power to the ring gear through a pair of gears. Locks 1 and 2 are used to lock the sun gear and ring gear to the standstill frame of the vehicle in order to satisfy the different operation mode requirements. The following operation modes can be satisfied:

1. Hybrid traction: When locks 1 and 2 are released the sun gear and ring gear can rotate and both the engine and electric machine supply positive speed and torque (positive power) to the driven wheels.
2. Engine-alone traction: When lock 2 locks the ring gear to the vehicle frame and lock 1 is released only the engine supplies power to the driven wheels.
3. Motor-alone traction: When lock 1 locks the sun gear to the vehicle frame (engine is shut off or clutch is disengaged) and lock 2 is released only the electric motor supplies its power to the driven wheels.
4. Regenerative braking: Lock 1 is set in locking state, the engine is shut off or clutch is disengaged, and the electric machine is controlled in regenerating operation (negative torque). The kinetic or potential energy of the vehicle can be absorbed by the electric system.
5. Battery charging from the engine: When the controller sets a negative speed for the electric machine, the electric machine absorbs energy from the engine.

The drive train, consisting of the transmotor as shown in Figure 5.17, has a structure similar to that in Figure 5.16. Locks 1 and 2 are used to lock the stator to the vehicle frame and the stator to the rotor, respectively. This drive train can fulfill all the operation modes mentioned above. The operating modes analysis is left to the readers.

The main advantage of the hybrid drive train with speed coupling is that the speeds of the two powerplants are decoupled; therefore, the speed of both the powerplants can be chosen freely. This advantage is important to powerplants such as the Stirling engine and the gas turbine engine, in which their efficiencies are sensitive to speed and less sensitive to torque.

5.2.2.3 Torque-Coupling and Speed-Coupling Parallel Hybrid Electric Drive Trains

By combining torque and speed coupling together, one may constitute a hybrid drive train in which torque and speed coupling states can be alternatively chosen. Figure 5.18[9] shows such an example. When the torque coupling operation mode is chosen as the current mode, lock 2 locks the ring gear of the planetary unit to the vehicle frame, while clutches 1 and 3 are engaged and clutch 2 is disengaged. The powers of the engine and the electric motor are added together by adding their torques together (refer to equation [5.1]), and then delivered to the driven wheels. In this case, the engine torque and the electric motor are decoupled, but their speeds have a fixed relationship as described by equation (5.2). When the speed-coupling mode is chosen as the current operating mode, clutch 1 is engaged, whereas clutches 2 and 3 are disengaged, and locks 1 and 2 release the sun gear and the ring gear. The speed of the yoke, connected to the drive wheels, is the combination of engine speed and motor speed (refer to equation [5.3]). But

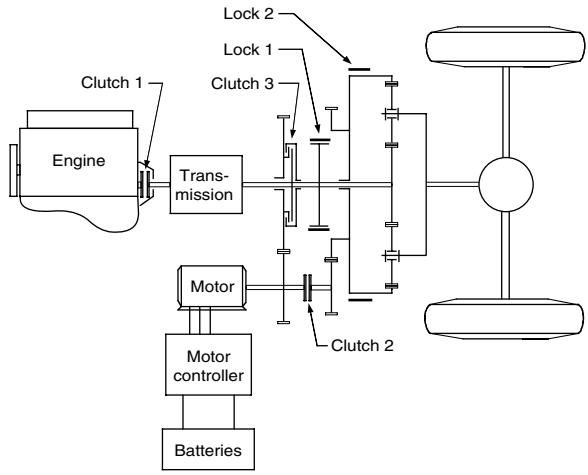

FIGURE 5.18
Alternative torque and speed hybrid electric drive train with a planetary gear unit

the engine torque, the electric motor torque, and the torque on the driven wheels are kept in a fixed relationship as described by equation (5.4).

With the option to choose between torque coupling and speed coupling, the powerplants have more opportunities to determine their operation manner and operation region so as to optimize their performance. For instance, at low vehicle speeds, the torque combination operation mode would be suitable for high acceleration or hill climbing. On the other hand, at high vehicle speeds, the speed-combination mode should be used to keep the engine speed at its optimum region.

The planetary gear unit traction motor in Figure 5.18 can be replaced by a transmotor to constitute a similar drive train as shown in Figure 5.19.[12] When clutch 1 is engaged to couple the engine shaft to the rotor shaft of the transmotor, clutch 2 is disengaged to release the engine shaft from the rotor of the transmotor and the lock is activated to set the stator of the transmotor to the vehicle frame. The drive train then works in the torque-coupling mode. On the other hand, when clutch 1 is disengaged and clutch 2 is engaged and the lock is released, the drive train works in the speed-coupling mode.

Another good example that uses both torque coupling and speed coupling on a drive train is the one developed and implemented in the Toyota Prius by the Toyota Motor Company.[10] This drive train is schematically illustrated in Figure 5.20. A small motor or generator (few kilowatts) is connected through a planetary gear unit (speed coupling). The planetary gear unit splits the engine speed into two speeds (refer to equation [5.3]). One sends output to the small motor through its sun gear, and the other to the driven wheels through its ring gear and an axle-fixed gear unit (torque coupling). A large traction motor (few to ten kilowatts) is also connected to this gear unit to constitute a torque coupling parallel driveline. At low vehicle speeds, the small motor runs with a positive speed and absorbs part of the engine power. As the vehicle speed increases and the engine speed is fixed at a given value, the motor speed decreases to zero. This is called synchronous

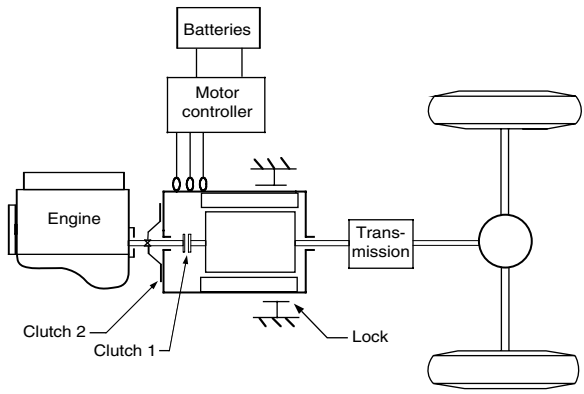

FIGURE 5.19
Alternative torque- and speed-coupling hybrid electric drive train with transmotor

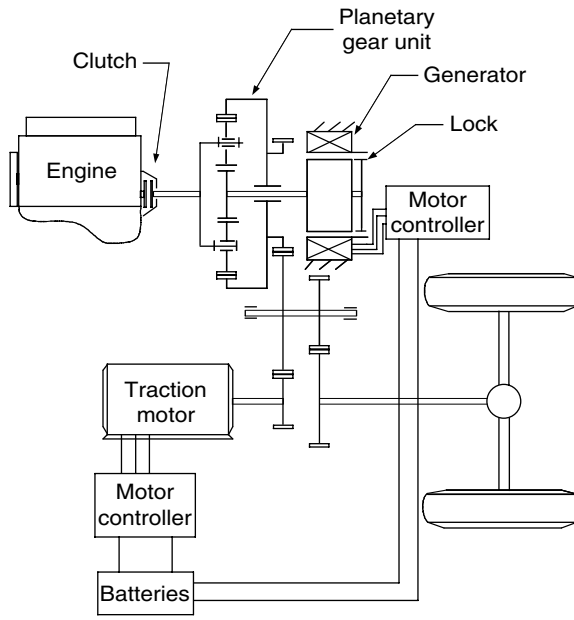

FIGURE 5.20
Integrated speed- and torque-coupling hybrid electric drive train (Toyota Prius)

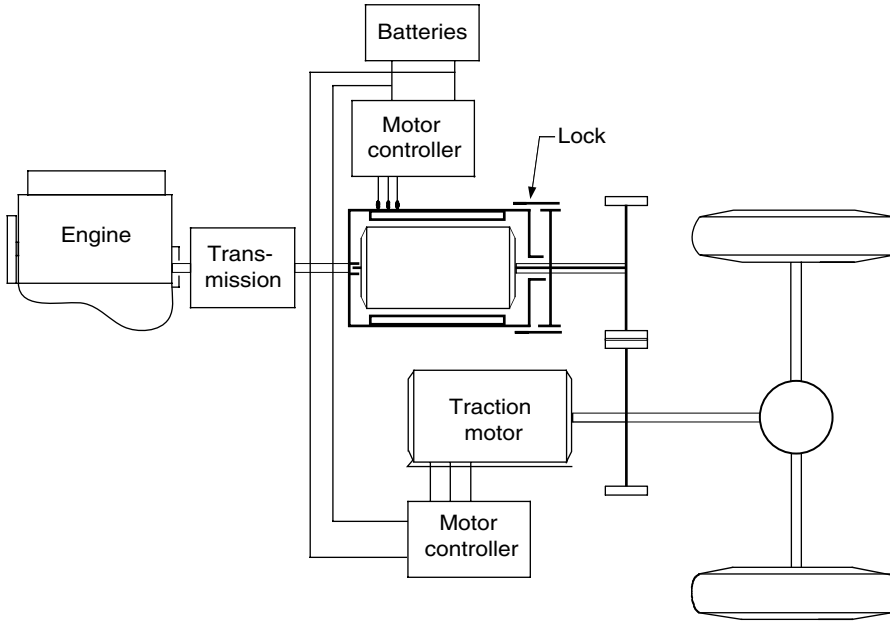

FIGURE 5.21
Integrated speed- and torque-coupling hybrid electric drive train with a transmotor

speed. At this speed, the lock will be activated to lock the rotor and stator together. The drive train is then a parallel drive train. When the vehicle is running at a high speed, in order to avoid too high an engine speed, which leads to high fuel consumption, the small motor can be operated with a negative speed and so that it delivers power to the drive train. A high fuel economy can be achieved when the planetary gear and the small motor are used to adjust the engine speed in order to operate at the optimum speed range.

The small motor and the planetary gear unit in Figure 5.20 can be replaced by an individual transmotor, as shown in Figure 5.21.[11] This drive train has characteristics similar to the drive train in Figure 5.20. The reader would do well to analyze its operating mode.

References

[1] M. Ehsani, K.L. Butler, Y. Gao, K.M. Rahman, and D. Burke, Toward a sustainable transportation without sacrifice of range, performance, or air quality: the ELPH car concept, *Automotive Congress,* International Federation of Automotive Engineering Society, Paris, France, Sept./Oct. 1998.

[2] M. Ehsani, K.L. Butler, Y. Gao, and K.M. Rahman, Next generation passenger cars with better range, performance, and emissions: the ELPH car concept, *Horizon in Engineering Symposium,* Texas A&M University Engineering Program Office, College Station, TX, Sept. 1998.

[3] M. Ehsani, *The Electrically Peaking Hybrid System and Method,* U.S. patent no. 5,586,613, December 1996.

[4] C.C. Chan and K.T. Chau, *Modern Electric Vehicle Technology,* Oxford University Press, New York, 2001.

[5] K. Yamaguchi, S. Moroto, K. Kobayashi, M. Kawamoto, and Y. Miyaishi, Development of a new hybrid system-duel system, *Society of Automotive Engineers (SAE) Journal,* Paper No. 960231, Warrendale, PA, 1997.

[6] Y. Gao, K.M. Rahman, and M. Ehsani, The energy flow management and battery energy capacity determination for the drive train of electrically peaking hybrid, *Society of Automotive Engineers (SAE) Journal,* Paper No. 972647, Warrendale, PA, 1997.

[7] Y. Gao, K.M. Rahman, and M. Ehsani, Parametric design of the drive train of an electrically peaking hybrid (ELPH) vehicle, *Society of Automotive Engineers (SAE) Journal,* Paper No. 970294, Warrendale, PA, 1997.

[8] Y. Gao, L. Chen, and M. Ehsani, Investigation of the effectiveness of regenerative braking for EV and HEV, *Society of Automotive Engineers (SAE) Journal,* Paper No. 1999-01-2901, Warrendale, PA, 1999.

[9] Y. Gao and M. Ehsani, *New Type of Transmission for Hybrid Vehicle with Speed and Torque Summation,* U.S. patent pending.

[10] http://www.toyota.com, Toyota Motor Company, visited in September 2003.

[11] Y. Gao and M. Ehsani, *Series–Parallel Hybrid Drive Train with an Electric Motor of Floating Stator and Rotor,* U.S. Patent pending.

[12] S. Moore and M. Ehsani, A charge-sustaining parallel HEV application of the transmotor, *Society of Automotive Engineers (SAE) Journal,* Paper No. 1999-01-0919, Warrendale, PA, 1997.

6

Electric Propulsion Systems

CONTENTS

6.1 DC Motor Drives 142
6.1.1 Principle of Operation and Performance 142
6.1.2 Combined Armature Voltage and Field Control 146
6.1.3 Chopper Control of DC Motors 146
6.1.4 Multiquadrant Control of Chopper-Fed DC Motor Drives 151
6.1.4.1 Two-Quadrant Control of Forward Motoring and Regenerative Braking 151
6.1.4.1.1 Single Chopper with a Reverse Switch 151
6.1.4.1.2 Class C Two-Quadrant Chopper 152
6.1.4.2 Four-Quadrant Operation 154
6.2 Induction Motor Drives 155
6.2.1 Basic Operation Principles of Induction Motors 156
6.2.2 Steady-State Performance 159
6.2.3 Constant Volt/Hertz Control 162
6.2.4 Power Electronic Control 163
6.2.5 Field Orientation Control 166
6.2.5.1 Field Orientation Principles 166
6.2.5.2 Control 173
6.2.5.3 Direction Rotor Flux Orientation Scheme 175
6.2.5.4 Indirect Rotor Flux Orientation Scheme 178
6.2.6 Voltage Source Inverter for FOC 180
6.2.6.1 Voltage Control in Voltage Source Inverter 182
6.2.6.2 Current Control in Voltage Source Inverter 185
6.3 Permanent Magnetic Brush-Less DC Motor Drives 187
6.3.1 Basic Principles of BLDC Motor Drives 190
6.3.2 BLDC Machine Construction and Classification 190
6.3.3 Properties of PM Materials 193
6.3.3.1 Alnico 194
6.3.3.2 Ferrites 195
6.3.3.3 Rare-Earth PMs 195

6.3.4 Performance Analysis and Control of BLDC Machines.....196
6.3.4.1 Performance Analysis 196
6.3.4.2 Control of BLDC Motor Drives 198
6.3.5 Extension of Speed Technology 199
6.3.6 Sensorless Techniques 200
6.3.6.1 Methods Using Measurables and Math 201
6.3.6.2 Methods Using Observers 201
6.3.6.3 Methods Using Back EMF Sensing 202
6.3.6.4 Unique Sensorless Techniques 203
6.4 Switched Reluctance Motor Drives 204
6.4.1 Basic Magnetic Structure 204
6.4.2 Torque Production 207
6.4.3 SRM Drive Converter 210
6.4.4 Modes of Operation.....213
6.4.5 Generating Mode of Operation (Regenerative Braking) 214
6.4.6 Sensorless Control 216
6.4.6.1 Phase Flux Linkage-Based Method 218
6.4.6.2 Phase Inductance-Based Method.....218
6.4.6.2.1 Sensorless Control Based on Phase Bulk Inductance.....218
6.4.6.2.2 Sensorless Control Based on Phase Incremental Inductance 219
6.4.6.3 Modulated Signal Injection Methods 220
6.4.6.3.1 Frequency Modulation Method 220
6.4.6.3.2 AM and PM Methods 221
6.4.6.3.3 Diagnostic Pulse-Based Method.....221
6.4.6.4 Mutually Induced Voltage-Based Method 222
6.4.6.5 Observer-Based Methods 222
6.4.7 Self-Tuning Techniques of SRM Drives 222
6.4.7.1 Self-Tuning with the Arithmetic Method 223
6.4.7.1.1 Optimization with Balanced Inductance Profiles 223
6.4.7.1.2 Optimization in the Presence of Parameter Variations 224
6.4.7.2 Self-Tuning Using an Artificial Neural Network 224
6.4.8 Vibration and Acoustic Noise in SRM 226
6.4.9 SRM Design 228
6.4.9.1 Number of Stator and Rotor Poles 228
6.4.9.2 Stator Outer Diameter.....229
6.4.9.3 Rotor Outer Diameter 230
6.4.9.4 Air gap.....230
6.4.9.5 Stator Arc.....231
6.4.9.6 Stator Back-Iron 231
6.4.9.7 Performance Prediction.....231
References 232

Electric propulsion systems are at the heart of electric vehicles (EVs) and hybrid electric vehicles (HEVs). They consist of electric motors, power converters, and electronic controllers. The electric motor converts the electric energy into mechanical energy to propel the vehicle, or, vice versa, to enable regenerative braking and/or to generate electricity for the purpose of charging the onboard energy storage. The power converter is used to supply the electric motor with proper voltage and current. The electronic controller commands the power converter by providing control signals to it, and then controls the operation of the electric motor to produce proper torque and speed, according to the command from the drive. The electronic controller can be further divided into three functional units — sensor, interface circuitry, and processor. The sensor is used to translate measurable quantities such as current, voltage, temperature, speed, torque, and flux into electric signals through the interface circuitry. These signals are conditioned to the appropriate level before being fed into the processor. The processor output signals are usually amplified via the interface circuitry to drive power semiconductor devices of the power converter. The functional block diagram of an electric propulsion system is illustrated in Figure 6.1.

The choice of electric propulsion systems for EVs and HEVs mainly depends on a number of factors, including driver expectation, vehicle constraints, and energy source. Driver expectation is defined by a driving profile, which includes the acceleration, maximum speed, climbing capability, braking, and range. Vehicle constraints, including volume and weight, depend on vehicle type, vehicle weight, and payload. The energy source relates to batteries, fuel cells, ultracapacitors, flywheels, and various hybrid sources. Thus, the process of identifying the preferred feature and package options for electric

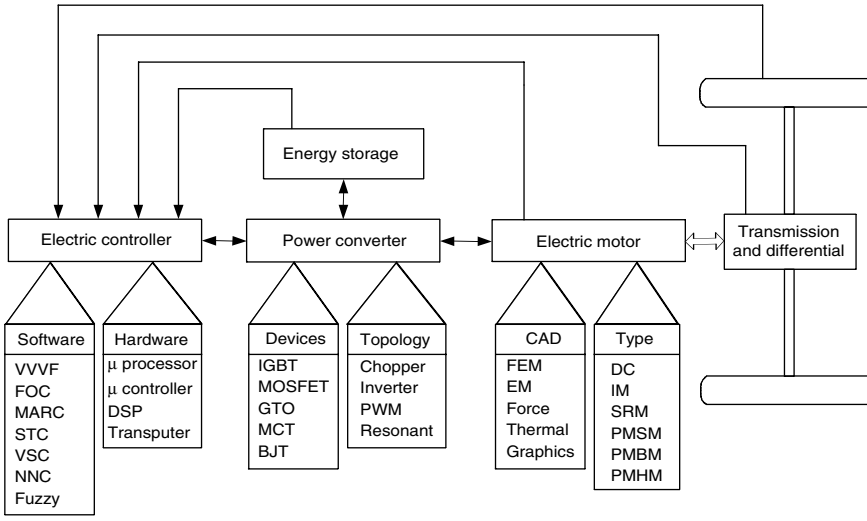

FIGURE 6.1
Functional block diagram of a typical electric propulsion system

propulsion has to be carried out at the system level. The interaction of subsystems and the likely impacts of system trade-offs must be examined.

Differing from the industrial applications of motors, the motors used in EVs and HEVs usually require frequent starts and stops, high rates of acceleration/deceleration, high torque and low-speed hill climbing, low torque and high-speed cruising, and a very wide speed range of operation. The motor drives for EVs and HEVs can be classified into two main groups, namely the commutator motors and commutatorless motors as illustrated in Figure 6.2. Commutator motors mainly are the traditional DC motors, which include series excited, shunt excited, compound excited, separately excited, and permanent magnet (PM) excited motors. DC motors need commutators and brushes to feed current into the armature, thus making them less reliable and unsuitable for maintenance-free operation and high speed. In addition, winding excited DC motors have low specific power density. Nevertheless, because of their mature technology and simple control, DC motor drives have been prominent in electric propulsion systems.

Technological developments have recently pushed commutatorless electric motors into a new era. Advantages include higher efficiency, higher power density, lower operating cost. They are also more reliable and maintenance-free compared to commutator DC motors. Thus, commutatorless electric motors have now become more attractive.

Induction motors are widely accepted as a commutatorless motor type for EV and HEV propulsion. This is because of their low cost, high reliability, and maintenance-free operation. However, conventional control of induction motors such as variable-voltage variable-frequency (VVVF) cannot provide the desired performance. With the advent of the power electronics and microcomputer era, the principle of field-oriented control (FOC) or vector control of induction motors has been accepted to overcome their control complexity due to their nonlinearity.[4] However, these EV and HEV motors using FOC still suffer from low efficiency at low light loads and limited constant-power operating range.

By replacing the field winding of conventional synchronous motors with PMs, PM synchronous motors can eliminate conventional brushes, slip rings, and field copper losses.[7] Actually, these PM synchronous motors are

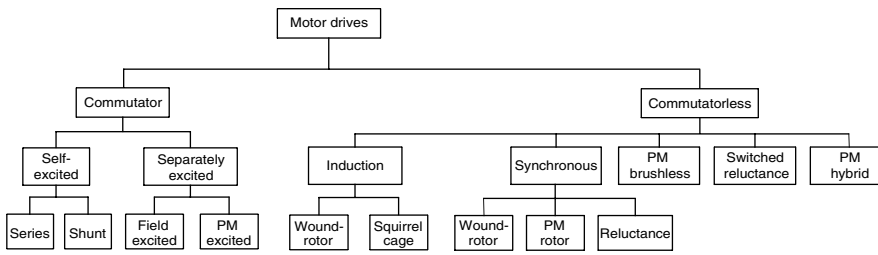

FIGURE 6.2
Classification of electric motor drives for EV and HEV applications

also called PM brushless AC motors, or sinusoidal-fed PM brushless motors, because of their sinusoidal AC current and brushless configuration. Since these motors are essentially synchronous motors, they can run from a sinusoidal or pulsed waveform modulation supply (PWM supply) without electronic commutation. When PMs are mounted on the rotor surface, they behave as nonsalient synchronous motors because the permeability of PMs is similar to that of air. By burying those PMs inside the magnetic circuit of the rotor, the saliency causes an additional reluctance torque, which leads to facilitating a wider speed range at constant power operation. On the other hand, by abandoning the field winding or PMs while purposely making use of the rotor saliency, synchronous reluctance motors are generated. These motors are generally simple and inexpensive, but with relatively low output power. Similar to induction motors, these PM synchronous motors usually use FOC for high-performance applications.[4] Because of their inherently high power density and high efficiency, they have been accepted as having great potential to compete with induction motors for EV and HEV applications.

By virtually inverting the stator and rotor of PM DC motors (commutator), PM brushless DC motors are generated. It should be noted that the term "DC" may be misleading, since it does not refer to a DC current motor. Actually, these motors are fed by rectangular AC current, and are hence also known as rectangular-fed PM brushless motors.[40] The most obvious advantage of these motors is the removal of brushes. Another advantage is the ability to produce a large torque because of the rectangular interaction between current and flux. Moreover, the brushless configuration allows more cross-sectional area for the armature windings. Since the conduction of heat through the frame is improved, an increase in electric loading causes higher power density. Different from PM synchronous motors, these PM brushless DC motors generally operate with shaft position sensors. Recently, sensorless control technologies have been developed in the Power Electronics and Motor Drive Laboratory at Texas A&M University.

Switched reluctance (SR) motors have been recognized to have considerable potential for EV and HEV applications. Basically, they are direct derivatives of single-stack variable-reluctance stepping motors. SR motors have the definite advantages of simple construction, low manufacturing cost, and outstanding torque–speed characteristics for EV and HEV applications. Although they possess simplicity in construction, this does not imply any simplicity of their design and control. Because of the heavy saturation of pole tips and the fringe effect of pole and slots, their design and control are difficult and subtle. Traditionally, SR motors operate with shaft sensors to detect the relative position of the rotor to the stator. These sensors are usually vulnerable to mechanical shock and sensitive to temperature and dust. Therefore, the presence of the position sensor reduces the reliability of SR motors and constrains some applications. Recently, sensorless technologies have been developed in the Power Electronics and Motor Drive Laboratory — again at Texas A&M University. These technologies can ensure smooth operation from zero speed to maximum speed.[65] This will be discussed in detail in the following sections.

6.1 DC Motor Drives

DC motor drives have been widely used in applications requiring adjustable speed, good speed regulation, and frequent starting, braking and reversing. Various DC motor drives have been widely applied to different electric traction applications because of their technological maturity and control simplicity.

6.1.1 Principle of Operation and Performance

The operation principle of a DC motor is straightforward. When a wire carrying electric current is placed in a magnetic field, a magnetic force acting on the wire is produced. The force is perpendicular to the wire and the magnetic field as shown in Figure 6.3. The magnetic force is proportional to the wire length, magnitude of the electric current, and the density of the magnetic field; that is,

$$F = BIL. \tag{6.1}$$

When the wire is shaped into a coil, as shown in Figure 6.3, the magnetic forces acting on both sides produce a torque, which is expressed as

$$T = BIL \cos \alpha, \tag{6.2}$$

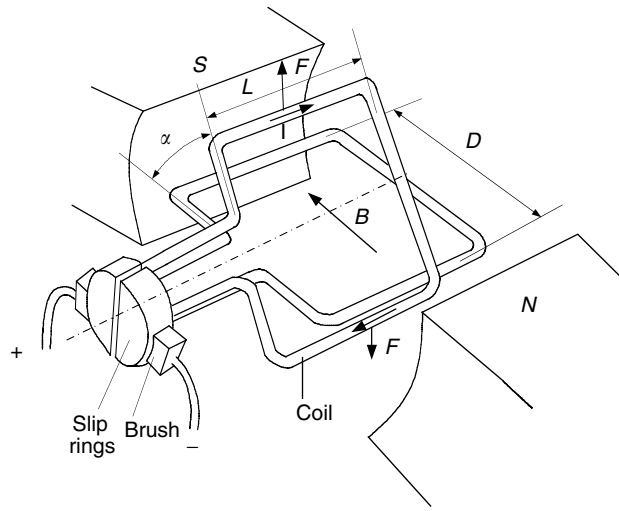

FIGURE 6.3
Operation principle of a DC motor

where α is the angle between the coil plane and magnetic field as shown in Figure 6.3. The magnetic field may be produced by a set of windings or permanent magnets. The former is called wound-field DC motor and the latter is called the PM DC motor. The coil carrying the electric current is called the armature. In practice, the armature consists of a number of coils. In order to obtain continuous and maximum torque, slip rings and brushes are used to conduct each coil at the position of $\alpha = 0$.

Practically, the performance of DC motors can be described by the armature voltage, back electromotive force (EMF), and field flux.

Typically, there are four types of wound-field DC motors, depending on the mutual interconnection between the field and armature windings. They are separately excited, shunt excited, series excited, and compound excited as shown in Figure 6.4. In the case of a separately excited motor, the field and armature voltage can be controlled independently of one another. In a shunt motor, the field and armature are connected in parallel to a common source. Therefore, an independent control of field current and armature or armature voltage can be achieved by inserting a resistance into the appropriate circuit. This is an inefficient method of control. The efficient method is to use power electronics-based DC–DC converters in the appropriate circuit to replace the resistance. The DC–DC converters can be actively controlled to produce proper armature and field voltage. In the case of a series motor, the field current is the same as the armature current; therefore, field flux is a function of armature current. In a cumulative compound motor, the magnetomotive force (mmf) of a series field is a function of the armature current and is in the same direction as the mmf of the shunt field.[2]

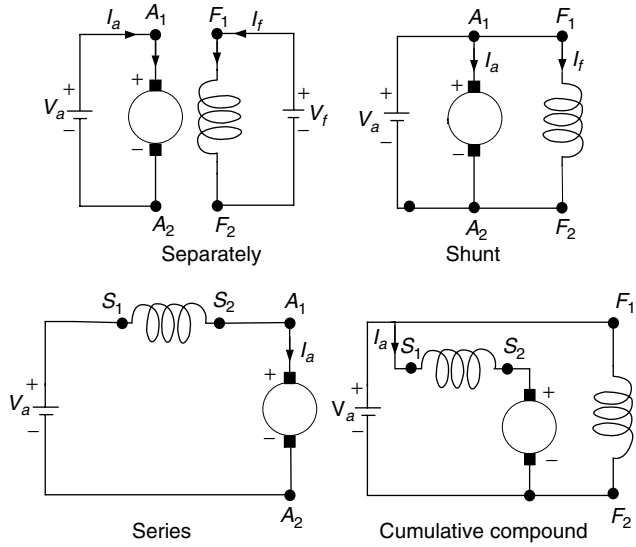

FIGURE 6.4
Wound-field DC motors

The steady-state equivalent circuit of the armature of a DC motor is shown in Figure 6.5. The resistor R_a is the resistance of the armature circuit. For separately excited and shunt DC motors, it is equal to the resistance of the armature windings; for the series and compound motors, it is the sum of armature and series field winding resistances. Basic equations of a DC motor are

$$V_a = E + R_a I_a,\ E = K_e \phi \omega_m, \tag{6.3}$$

$$T = K_e \phi I_a, \tag{6.4}$$

where ϕ is the flux per pole in Webers, I_a is the armature current in A, V_a is the armature voltage in volt, R_a is the resistance of the armature circuit in ohms, ω_m is the speed of the armature in rad/sec, T is the torque developed by the motor in Nm, and K_e is constant.

From equations (6.3)–(6.4), one can obtain

$$T = \frac{K_e \phi}{R_a} V - \frac{(K_e \phi)^2}{R_a} \omega_m. \tag{6.5}$$

Equations (6.3)–(6.5) are applicable to all the DC motors, namely, separately (or shunt) excited, series, and compound motors. In the case of separately excited motors, if the field voltage is maintained as constant, one can assume the flux to be practically constant as the torque changes. In this case, the speed–torque characteristic of a separately excited motor is a straight line, as shown in Figure 6.6. The nonload speed ω_{m0} is determined by the values of the armature voltage and the field excitation. Speed decreases as torque increases, and speed regulation depends on the armature circuit resistance. Separately excited motors are used in applications requiring good speed regulation and proper adjustable speed.

In the case of series motors, the flux is a function of armature current. In an unsaturated region of the magnetization characteristic, ϕ can be assumed to be proportional to I_a. Thus,

$$\phi = K_f I_a. \tag{6.6}$$

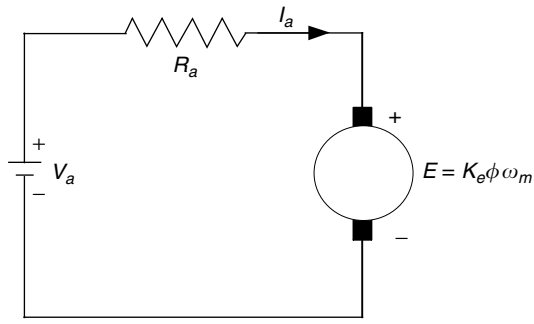

FIGURE 6.5
Steady-state equivalent circuit of the armature circuit of a DC motor

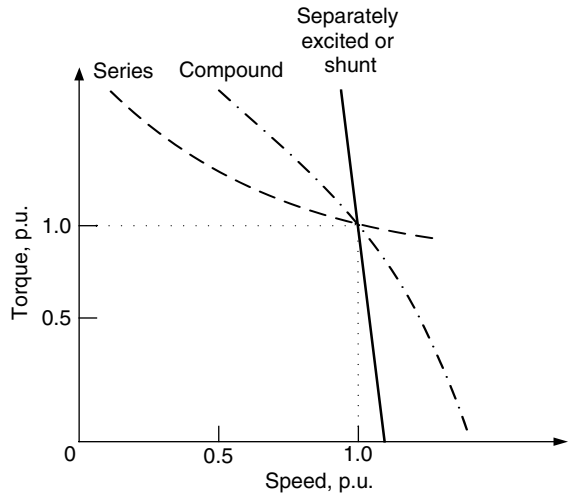

FIGURE 6.6
Speed characteristics of DC motors

By equations (6.4)–(6.6), the torque for series excited DC motors can obtained as

$$T = \frac{K_e K_f V_a^2}{(R_a + K_e K_f \omega_m)^2}, \tag{6.7}$$

where the armature circuit resistance R_a is now the sum of armature and field winding resistance.

A speed–torque characteristic of a series DC motor is shown in Figure 6.6. In the case of series, any increase in torque is accompanied by an increase in the armature current and, therefore, an increase in magnetic flux. Because flux increases with the torque, the speed drops to maintain a balance between the induced voltage and the supply voltage. The characteristic, therefore, shows a dramatic drop. A motor of standard design works at the knee point of the magnetization curve at the rated torque. At heavy torque (large current) overload, the magnetic circuit saturates and the speed–torque curve approaches a straight line.

Series DC motors are suitable for applications requiring high starting torque and heavy torque overload, such as traction. This was just the case for electric traction before the power electronics and microcontrol era. However, series DC motors for traction application have some disadvantages. They are not allowed to operate without load torque with full supply voltage. Otherwise, their speed will quickly increase up to a very high value (refer to equation [6.7]). Another disadvantage is the difficulty in regenerative braking.

Performance equations for cumulative compound DC motors can be derived from equations (6.3) to (6.4). The speed–torque characteristics are between series and separately excited (shunt) motors, as shown in Figure 6.6.

6.1.2 Combined Armature Voltage and Field Control

The independence of armature voltage and field provides more flexible control of the speed and torque than other types of DC motors. In EV and HEV applications, the most desirable speed–torque characteristic is to have a constant torque below a certain speed (base speed), with the torque dropping parabolically with the increase of speed (constant power) in the range above the base speed, as shown in Figure 6.7. In the range of lower than base speed, the armature current and field are set at their rated values, producing the rated torque. From equations (6.3) to (6.4), it is clear that the armature voltage must be increased proportionally with the increase of the speed. At the base speed, the armature voltage reaches its rated value (equal to the source voltage) and cannot be increased further. In order to further increase the speed, the field must be weakened with the increase of the speed, and then the back EMF E and armature current must be maintained constant. The torque produced drops parabolically with the increase in the speed and the output power remains constant, as shown in Figure 6.7.

6.1.3 Chopper Control of DC Motors

Choppers are used for the control of DC motors because of a number of advantages such as high efficiency, flexibility in control, light weight, small size, quick response, and regeneration down to very low speeds. Presently, the separately excited DC motors are usually used in traction, due to the control flexibility of armature voltage and field.

For a DC motor control in open-loop and closed-loop configurations, the chopper offers a number of advantages due to its high operation frequency.

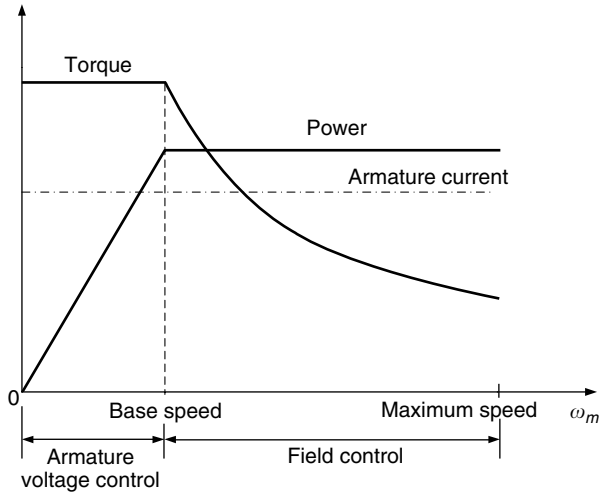

FIGURE 6.7
Torque and power limitations in combined armature voltage and field control

High operation frequency results in high-frequency output voltage ripple and, therefore, less ripples in the motor armature current and a smaller region of discontinuous conduction in the speed–torque plane. A reduction in the armature current ripple reduces the armature losses. A reduction or elimination of the discontinuous conduction region improves speed regulation and the transient response of the drive.

The power electronic circuit and the steady-state waveform of a DC chopper drive are shown in Figure 6.8. A DC voltage source, V, supplies an inductive load through a self-commutated semiconductor switch S. The symbol of a self-commutated semiconductor switch has been used because a chopper can be built using any device among thyristors with a forced commutation circuit: GTO, power transistor, MOSFET, and IGBT. The diode shows the direction in which the device can carry current. A diode D_F is connected in parallel with the load. The semiconductor switch S is operated periodically over a period T and remains closed for a time $t_{on} = \delta T$ with $0 < \delta < 1$. The variable $\delta = t_{on}/T$ is called the duty ratio or duty cycle of a chopper. Figure 6.8 also shows the waveform of control signal i_c. Control signal i_c will be the base current for a transistor chopper, and a gate current for the GTO of a GTO

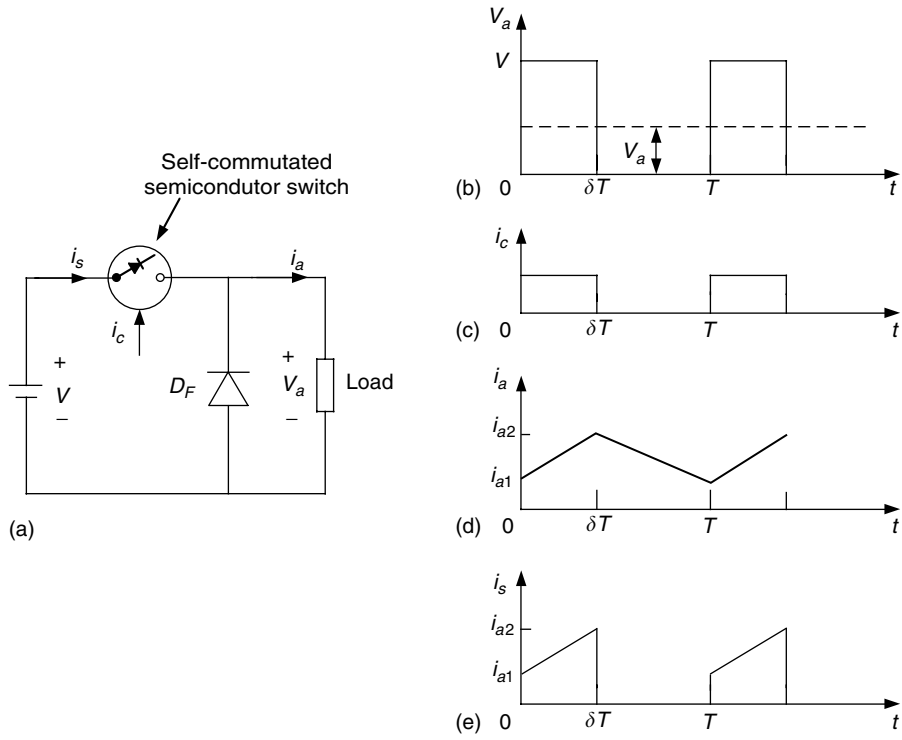

FIGURE 6.8
Principle of operation of a step down (or class A) chopper: (a) basic chopper circuit; (b) to (e) waveforms

chopper or the main thyristor of a thyristor chopper. If a power MOSFET is used, it will be a gate to the source voltage. When the control signal is present, the semiconductor switch S will conduct, if forward biased. It is assumed that the circuit operation has been arranged such that the removal of i_c will turn off the switch.

During the on interval of the switch ($0 \le t \le \delta T$), the load is subjected to a voltage V and the load current increases from i_{a1} to i_{a2}. The switch is opened at $t = \delta T$. During the off period of the switch ($\delta T \le t \le 1$), the load inductance maintains the flow of current through diode D_F. The load terminal voltage remains zero (if the voltage drop on the diode is ignored in comparison to V) and the current decreases from i_{a2} to i_{a1}. The internal $0 \le t \le \delta T$ is called the duty interval and the interval $\delta T \le t \le T$ is known as the freewheeling interval. Diode D_F provides a path for the load current to flow when switch S is off, and thus improves the load current waveform. Furthermore, by maintaining the continuity of the load current at turn off, it prevents transient voltage from appearing across switch S, due to the sudden change of the load current. The source current waveform is also shown in Figure 6.8e. The source current flows only during the duty interval and is equal to the load current.

The direct component or average value of the load voltage V_a is given by

$$V_a = \frac{1}{T}\int_0^T v_a \, dt = \frac{1}{T}\int_0^{\delta T} V \, dt = \delta t. \tag{6.8}$$

By controlling δ between 0 and 1, the load voltage can be varied from 0 to V; thus, a chopper allows a variable DC voltage to be obtained from a fixed voltage DC source.

The switch S can be controlled in various ways for varying the duty ratio δ. The control technologies can be divided into the following categories:

1. Time ratio control (TRC).
2. Current limit control (CLC).

In TRC, also known as pulse width control, the ratio of on time to chopper period is controlled. The TRC can be further divided as follows:

1. Constant frequency TRC: The chopper period T is kept fixed and the on period of the switch is varied to control the duty ratio δ.
2. Varied frequency TRC: Here, δ is varied either by keeping t_{on} constant and varying T or by varying both t_{on} and T.

In variable frequency control with constant on-time, low-output voltage is obtained at very low values of chopper frequencies. The operation of a chopper at low frequencies adversely affects the motor performance. Furthermore, the operation of a chopper with variable frequencies makes the design of an input filter very difficult. Thus, variable frequency control is rarely used.

In current limit control, also known as point-by-point control, δ is controlled indirectly by controlling the load current between certain specified maximum and minimum values. When the load current reaches a specified maximum value, the switch disconnects the load from the source and reconnects it when the current reaches a specified minimum value. For a DC motor load, this type of control is, in effect, a variable frequency variable on time control.

The following important points can be noted from the waveform of Figure 6.8:

1. The source current is not continuous but flows in pulses. The pulsed current makes the peak input power demand high and may cause fluctuation in the source voltage. The source current waveform can be resolved into DC and AC harmonics. The fundamental AC harmonic frequency is the same as the chopper frequency. The AC harmonics are undesirable because they interfere with other loads connected to the DC source and cause radio frequency interference through conduction and electromagnetic radiation. Therefore, an L-C filter is usually incorporated between the chopper and the DC source. At higher chopper frequencies, harmonics can be reduced to a tolerable level by a cheaper filter. From this point, a chopper should be operated at the highest possible frequency.
2. The load terminal voltage is not a perfect direct voltage. In addition to a direct component, it has harmonics of the chopping frequency and its multiples. The load current also has an AC ripple.

The chopper of Figure 6.8 is called a class A chopper. It is one of a number of chopper circuits that are used for the control of DC motors. This chopper is capable of providing only a positive voltage and a positive current. It is therefore called a single-quadrant chopper, capable of providing DC separately excited motor control in the first quadrant, positive speed, and positive torque. Since it can vary the output voltage from V to 0, it is also a step-down chopper or a DC to DC buck converter. The basic principle involved can also be used to realize a step-up chopper or DC to DC boost converter.

The circuit diagram and steady-state waveforms of a step-up chopper are shown in Figure 6.9. This chopper is known as a class B chopper. The presence of control signal i_c indicates the duration for which the switch can conduct if forward-biased. During a chopping period T, it remains closed for an interval $0 \leq t \leq \delta T$ and remains open for an interval $\delta T \leq t \leq T$. During the on period, i_S increases from i_{S1} to i_{S2}, thus increasing the magnitude of energy stored in inductance L. When the switch is opened, current flows through the parallel combination of the load and capacitor C. Since the current is forced against the higher voltage, the rate of change of the current is negative. It decreases from i_{S2} to i_{S1} in the switch's off period. The energy stored in the inductance L and the energy supplied by the low-voltage source are given to the load. The capacitor C serves two purposes. At the instant of

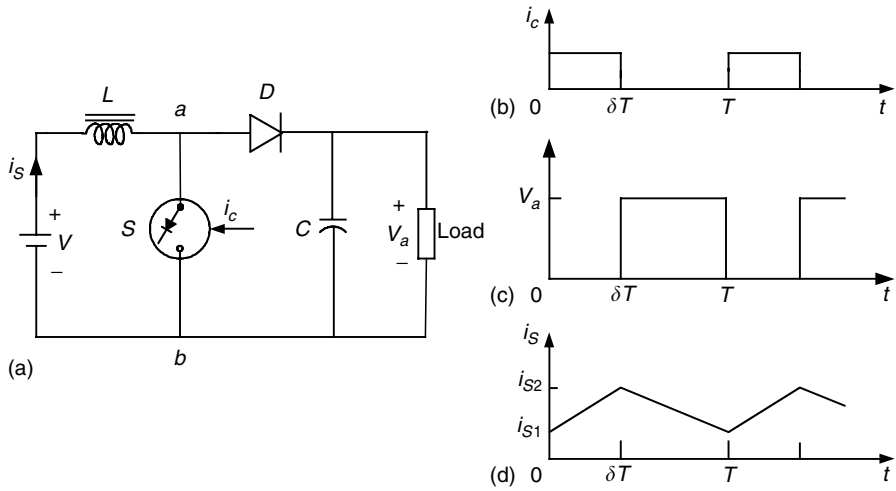

FIGURE 6.9
Principle of operation of a step-up (or class B) chopper: (a) basic chopper circuit; (b) to (d) waveforms

opening of switch S, the source current, i_S, and load current, i_a, are not the same. In the absence of C, the turn off of S will force the two currents to have the same values. This will cause high induced voltage in the inductance L and the load inductance. Another reason for using capacitor C is to reduce the load voltage ripple. The purpose of the diode D is to prevent any flow of current from the load into switch S or source V.

For understanding the step-up operation, capacitor C is assumed to be large enough to maintain a constant voltage V_a across the load. The average voltage across the terminal a, b is given as

$$V_{ab} = \frac{1}{T}\int_0^T v_{ab}\, dt = V_a(1-\delta). \tag{6.9}$$

The average voltage across the inductance L is

$$V_L = \frac{1}{T}\int_0^T \left(L\frac{di}{dt}\right) dt = \frac{1}{T}\int_{i_{s1}}^{i_{s2}} L\, di = 0. \tag{6.10}$$

The source voltage is

$$V = V_L + V_{ab}. \tag{6.11}$$

Substituting from equations (6.9) and (6.10) into (6.11) gives

$$V = V_a(1-\delta) \text{ or } V_a = \frac{V}{1-\delta}. \tag{6.12}$$

According to (6.12), theoretically the output voltage V_a can be changed from V to ∞ by controlling δ from 0 to 1. In practice, V_a can be controlled from V

to a higher voltage, which depends on the capacitor C, and the parameters of the load and chopper.

The main advantage of a step-up chopper is the low ripple in the source current. While most applications require a step-down chopper, the step-up chopper finds application in low-power battery-driven vehicles. The principle of the step-up chopper is also used in the regenerative braking of DC motor drives.

6.1.4 Multiquadrant Control of Chopper-Fed DC Motor Drives

The application of DC motors on EVs and HEVs requires the motors to operate in multiquadrants, including forward motoring, forward braking, backward motoring, and backward braking, as shown in Figure 6.10. For vehicles with reverse mechanical gears, two-quadrant operation (forward motoring and forward braking, or quadrant I and quadrant IV) is required. However, for vehicles without reverse mechanical gears, four-quadrant operation is needed. Multiquadrant operation of a separately excited DC motor is implemented by controlling the voltage poles and magnitude through power electronics-based choppers.

6.1.4.1 Two-Quadrant Control of Forward Motoring and Regenerative Braking

A two-quadrant operation consisting of forward motoring and forward regenerative braking requires a chopper capable of giving a positive voltage and current in either direction. This two-quadrant operation can be realized in the following two schemes.[2]

6.1.4.1.1 Single Chopper with a Reverse Switch

The chopper circuit used for forward motoring and forward regenerative braking is shown in Figure 6.11, where S is a self-commutated semiconductor switch, operated periodically such that it remains closed for a duration of δT and remains open for a duration of $(1-\delta)T$. C is the manual switch. When C is closed and S is in operation, the circuit is similar to that of

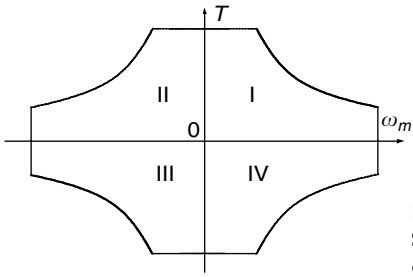

FIGURE 6.10
Speed–torque profiles of multiquadrant operation

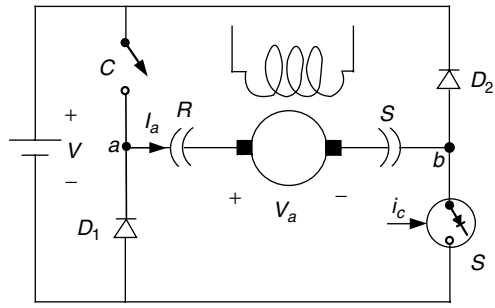

FIGURE 6.11
Forward motoring and regenerative braking control with a single chopper

Figure 6.6, permitting the forward motoring operation. Under these conditions, terminal *a* is positive and terminal *b* is negative.

Regenerative braking in the forward direction is obtained when *C* is opened and the armature connection is reversed with the help of the reversing switch *RS*, making terminal *b* positive and terminal *a* negative. During the on-period of the switch *S*, the motor current flows through a path consisting of the motor armature, switch *S*, and diode D_1, and increases the energy stored in the armature circuit inductance. When *S* is opened, the current flows through the armature diode D_2, source *V*, diode D_1 and back to the armature, thus feeding energy into the source.

During motoring, the changeover to regeneration is done in the following steps. Switch *S* is deactivated and switch *C* is opened. This forces the armature current to flow through diode D_2, source *V*, and diode D_1. The energy stored in the armature circuit is fed back to the source and the armature current falls to zero. After an adequate delay to ensure that the current has indeed become zero, the armature connection is reversed and switch *S* is reactivated with a suitable value of *d* to start regeneration.

6.1.4.1.2 Class C Two-Quadrant Chopper

In some applications, a smooth transition from motoring to braking and vice versa is required. For such applications, the class C chopper is used as shown in Figure 6.12. The self-commutated semiconductor switch S_1 and diode D_1 constitute one chopper and the self-commutator switch S_2 and diode D_2 form another chopper. Both the choppers are controlled simultaneously, both for motoring and regenerative braking. The switches S_1 and S_2 are closed alternately. In the chopping period *T*, S_1 is kept on for a duration δT, and S_2 is kept on from δT to *T*. To avoid a direct short-circuit across the source, care is taken to ensure that S_1 and S_2 do not conduct at the same time. This is generally achieved by providing some delay between the turn off of one switch and the turn on of another switch.

The waveforms of the control signals v_a i_a, and i_s and the devices under conducting during different intervals of a chopping period are shown in

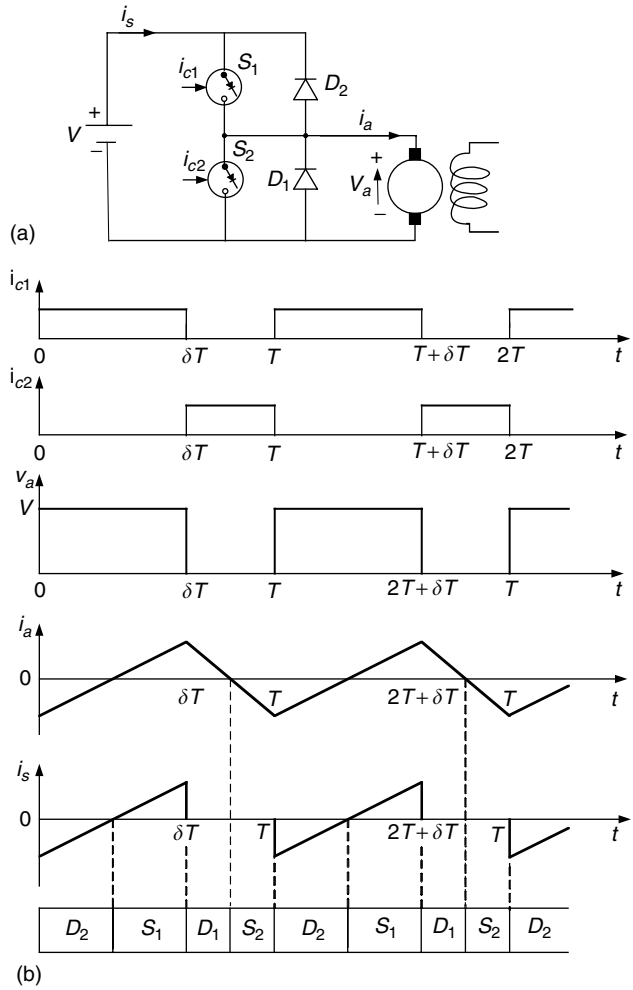

FIGURE 6.12
Forward motoring and regenerative braking control using class C two-quadrant chopper: (a) chopper circuit and (b) waveforms

Figure 6.12(b). In drawing these waveforms, the delay between the turn off of one switch and the turn on of another switch has been ignored because it is usually very small. The control signals for the switches S_1 and S_2 are denoted by i_{c1} and i_{c2}, respectively. It is assumed that a switch conducts only when the control signal is present and the switch is forward biased.

The following points are helpful in understanding the operation of this two-quadrant circuit:

1. In this circuit, discontinuous conduction does not occur, irrespective of its frequency of operation. Discontinuous conduction occurs

when the armature current falls to zero and remains zero for a finite interval of time. The current may become zero either during the freewheeling interval or in the energy transfer interval. In this circuit, freewheeling will occur when S_1 is off and the current is flowing through D_1. This will happen in interval $\delta T \le t \le T$, which is also the interval for which S_2 receives the control signal. If i_a falls to zero in the freewheeling interval, the back EMF will immediately drive a current through S_2 in the reverse direction, thus preventing the armature current from remaining zero for a finite interval of time. Similarly, energy transfer will be present when S_2 is off and D_2 is conducting — that is, during the interval $0 \le t \le \delta T$. If the current falls to zero during this interval, S_1 will conduct immediately because i_c is present and $V > E$. The armature current will flow, preventing discontinuous conduction.

2. Since discontinuous conditions are absent, the motor current will be flowing all the time. Thus, during the interval $0 \le t \le \delta T$, the motor armature will be connected either through S_1 or D_2. Consequently, the motor terminal voltage will be V and the rate of change of i_a will be positive because $V > E$. Similarly, during the interval $\delta T \le t \le T$, the motor armature will be shorted either through D_1 or S_2. Consequently, the motor voltage will be zero and the rate of change of i_a will be negative.
3. During the interval $0 \le t \le \delta T$, the positive armature current is carried by S_1 and the negative armature current is carried by D_2. The source current flows only during this interval and it is equal to i_a. During the interval $\delta T \le t \le T$, the positive current is carried by D_1 and the negative current is carried by S_2.
4. From the motor terminal voltage waveform of Figure 6.12(b), $V_a = \delta V$. Hence,

$$I_a = \frac{\delta V - E}{R_a}. \tag{6.13}$$

Equation (6.13) suggests that the motoring operation takes place when $\delta > E/V$, and that regenerative braking occurs when $\delta < E/V$. The no-load operation is obtained when $\delta = E/V$.

6.1.4.2 Four-Quadrant Operation

The four-quadrant operation can be obtained by combining two class C choppers (Figure 6.12[a]) as shown in Figure 6.13, which is referred to as a class E chopper. In this chopper, if S_2 is kept closed continuously and S_1 and S_4 are controlled, a two-quadrant chopper is obtained, which provides positive terminal voltage (positive speed) and the armature current in either direction (positive or negative torque), giving a motor control in quadrants I and IV. Now if S_3 is kept closed continuously and S_1 and S_4 are controlled, one obtains a two-quadrant chopper, which can supply a variable negative terminal voltage (negative

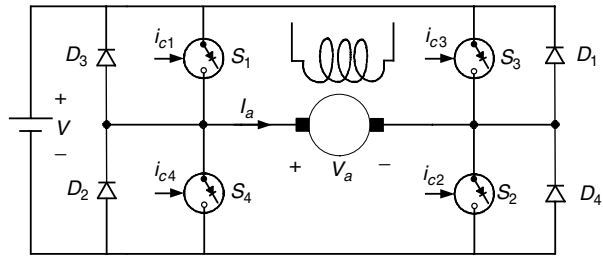

FIGURE 6.13
Class E four-quadrant chopper

speed) and the armature current can be in either direction (positive or negative torque), giving a motor control in quadrants II and III.

This control method has the following features: the utilization factor of the switches is low due to the asymmetry in the circuit operation. Switches S_3 and S_2 should remain on for a long period. This can create commutation problems when the switches use thyristors. The minimum output voltage depends directly on the minimum time for which the switch can be closed, since there is always a restriction on the minimum time for which the switch can be closed, particularly in thyristor choppers.[47] The minimum available output voltage, and therefore the minimum available motor speed, is restricted.

To ensure that switches S_1 and S_4, or S_2 and S_3 are not on at the same time, some fixed time interval must elapse between the turn off for one switch and the turn on of another switch. This restricts the maximum permissible frequency of operation. It also requires two switching operations during a cycle of the output voltage.

Reference[2] provides other control methods to solve the problems mentioned above.

6.2 Induction Motor Drives

Commutatorless motor drives offer a number of advantages over conventional DC commutator motor drives for the electric propulsion of EVs and HEVs. At present, induction motor drives are the mature technology among commutatorless motor drives. Compared with DC motor drives, the AC induction motor drive has additional advantages such as lightweight nature, small volume, low cost, and high efficiency. These advantages are particularly important for EV and HEV applications.

There are two types of induction motors, namely, wound-rotor and squirrel-cage motors. Because of the high cost, need for maintenance, and lack of sturdiness, wound-rotor induction motors are less attractive than their squirrel-cage counterparts, especially for electric propulsion in EVs and HEVs. Hence, squirrel-cage induction motors are loosely termed as induction motors.

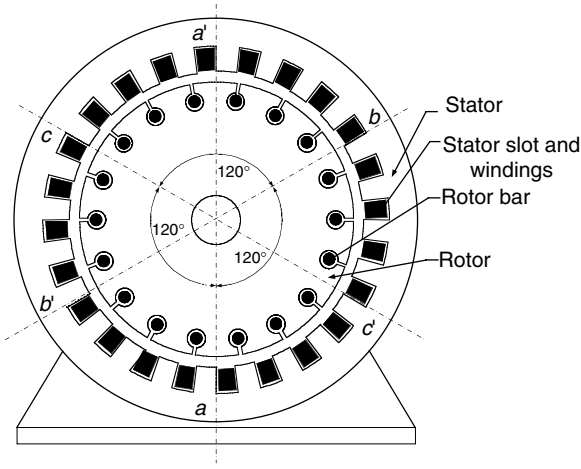

FIGURE 6.14
Cross-section of an induction motor

A cross section of a two-pole induction motor is shown in Figure 6.14. Slots in the inner periphery of the stator are inserted with three phase windings, a–a', b–b', and c–c'. The turns of each winding are distributed such that the current in the winding produces an approximate sinusoidally distributed flux density around the periphery of the air gap. The three windings are spatially arranged by 120° as shown in Figure 6.14.

The most common types of induction motor rotors are the squirrel cage in which aluminum bars are cast into slots in the outer periphery of the rotor. The aluminum bars are short-circuited together at both ends of the rotor by cast aluminum end rings, which can also be shaped into fans.

6.2.1 Basic Operation Principles of Induction Motors

Figure 6.15 shows, schematically, a cross section of the stator of a three-phase, two-pole induction motor. Each phase is fed with a sinusoidal AC current, which has a frequency of ω and a 120° phase difference between each other as shown in Figure 6.15. Current i_{as}, i_{bs}, and i_{cs} in the three stator coils a–a', b–b', and c–c' produce alternative mmfs, $\boldsymbol{F}_{as}$, $\boldsymbol{F}_{bs}$, and $\boldsymbol{F}_{cs}$, which are space vectors. The resultant stator mmf vector $\boldsymbol{F}_s^s$, constitutes a vector sum of the phase mmf vectors.

The mmfs produced by the phase currents can be written as

$$\boldsymbol{F}_{as} = F_{as} \sin \omega t, \tag{6.14}$$

$$\boldsymbol{F}_{bs} = F_{bs} \sin (\omega t - 120^\circ), \tag{6.15}$$

$$\boldsymbol{F}_{cs} = F_{cs} \sin (\omega t - 240^\circ). \tag{6.16}$$

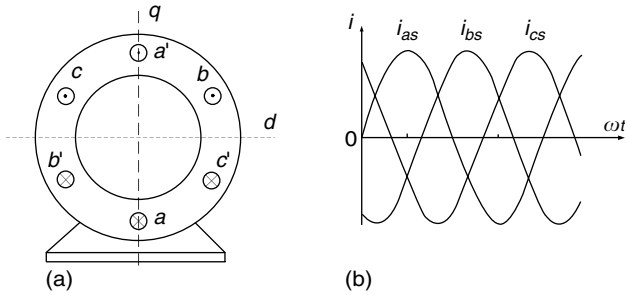

FIGURE 6.15
Induction motor stator and stator winding current: (a) spatially symmetric three-phase stator windings; (b) phase currents

The resultant stator mmf vector, $\boldsymbol{F}_s^s$, is expressed as

$$\boldsymbol{F}_s^s = \boldsymbol{F}_{as}e^{j0^\circ} + \boldsymbol{F}_{bs}e^{j120^\circ} + \boldsymbol{F}_{cs}e^{j240^\circ}. \tag{6.17}$$

Assuming that the magnitude of the three phase mmfs are identical, equal to F_s, equation (6.17) can be further expressed as

$$\boldsymbol{F}_s^s = \tfrac{3}{2}F_s e^{(\omega t - 90^\circ)}. \tag{6.18}$$

Equation (6.18) indicates that the resultant stator mmf vector is rotating with a frequency of the angle velocity of ω, and its magnitude is $(3/2)F_s$. Figure 6.16 graphically shows the stator mmf vectors at $\omega t = 0$ and $\omega t = 90^\circ$; here, ωt is the angle in (6.12) to (6.18), rather than the resultant stator mmf vector relative to the d-axis. Actually, if the ωt in equations (6.14) to (6.16) is taken as the reference, the resultant stator mmf vector is a 90° delay to the phase a–a' mmf.

The reaction between the rotating stator mmf and the rotor conductors induces a voltage in the rotor, and hence electric current in the rotor. In turn, the rotating mmf produces a torque on the rotor, which is carrying the induced current. It is clear that the induced current in the rotor is essential for producing the torque, and in turn the induced current depends on the relative movements between the stator mmf and the rotor. This is why there must exist a difference between the angular velocity of the rotating stator mmf and the angular velocity of the rotor.

The frequency ω, or angular velocity of the rotating stator mmf in the equation depends only on the frequency of the alternative current of the stator; thus, it is referred to as electrical angular velocity. For a machine with two poles, the electrical angular velocity is identical to the mechanical angular velocity of the rotating stator mmf. However, for a machine with more than two poles, the mechanical angular velocity differs from the electrical one, which can be expressed as

$$\omega_{ms} = \frac{2}{p}\omega = \frac{4\pi f}{p}\text{rad/sec}, \tag{6.19}$$

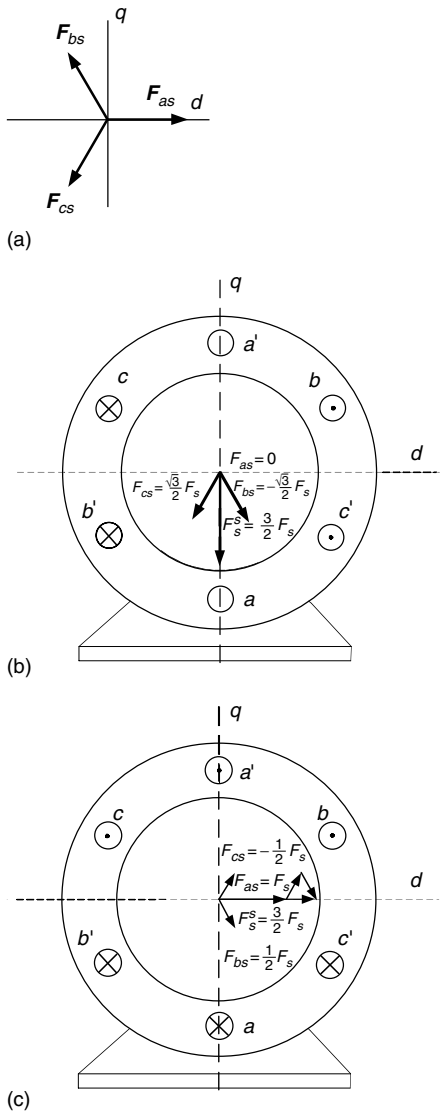

FIGURE 6.16
Stator mmf vectors: (a) positive direction of each phase (b) stator mmf vectors at $\omega t = 0$ and (c) stator mmf vectors at $\omega t = 90^{\circ}$

where f is the frequency of the alternative current or angular velocity of the rotating stator mmf in cycles/sec. When the angular velocity of the rotor is equal to the mechanical angular velocity of the rotating stator mmf, there will be no induced current in the rotor, and then no torque is produced. Thus, the mechanical angular velocity of the rotating stator mmf is also called synchronous speed.

If the rotor speed is ω_m rad/sec, then the relative speed between the stator rotating field and the rotor is given by

$$\omega_{sl} = \omega_{ms} - \omega_m = s\omega_{ms}, \tag{6.20}$$

where ω_{sl} is called slip speed. The parameter s, known as slip, is given by

$$s = \frac{\omega_{ms} - \omega_m}{\omega_{ms}} = \frac{\omega_{sl}}{\omega_{ms}}. \tag{6.21}$$

Because of the relative speed between the stator field and the rotor, balanced three-phase voltages are induced in the rotor mentioned before. The frequency of these voltages is proportional to the slip speed. Hence,

$$\omega_r = \frac{\omega_{sl}}{\omega_{ms}}\omega = s\omega, \tag{6.22}$$

where ω_r is the frequency of the rotor voltage induced.

For $\omega_m < \omega_{ms}$, the relative speed is positive; consequently, the rotor-induced voltages have the same phase sequence as the stator voltages. The three-phase current flowing through the rotor produces a magnetic field that moves with respect to the rotor at the slip speed in the same direction as the rotor speed. Consequently, the rotor field moves in space at the same speed as the stator, and a steady torque is produced. For $\omega_m = \omega_{ms}$, the relative speed between the rotor and stator field becomes zero. Consequently, no voltages are induced and no torque is produced by the motor. For $\omega_m < \omega_{ms}$, the relative speed between the stator field and the rotor speed reverses. Consequently, the rotor-induced voltages and currents also reverse and have a phase sequence opposite to that of the stator. Moreover, the developed torque has a negative sign, suggesting generator operation. (The generator is used to produce regenerative braking.)

6.2.2 Steady-State Performance

A per phase equivalent circuit of an induction motor is shown in Figure 6.15(a). The fields produced by the stator and rotor are linked together by an ideal transformer. a_{T1} is the transformer factor, which is equal to n_s/n_r, where n_s and n_r are the number of turns of stator and rotor windings, respectively. For a squirrel-cage rotor, $n_r = 1$. The equivalent circuit can be simplified by referring the rotor quantities to the stator frequency and number of turns. The resultant equivalent circuit is shown in Figure 6.15(b) where R_r' and X_r' are the rotor resistance and reactance refer to the stator and are given by the following equations:

$$R_r' = a_{T1}^2 R_r \quad \text{and} \quad X_r' = a_{T1}^2 X_r. \tag{6.23}$$

The stator reactance, mutual reactance, and rotor reactance referred to the stator can be expressed by the stator frequency and their inductances, L_s, L_m, and L_r, as shown in Figure 6.17. The impedances of stator, field, and rotor can be expressed as

$$Z_s = R_s + jL_s\omega, \tag{6.24}$$

$$Z_m = jL_m\omega, \tag{6.25}$$

$$Z_r = \frac{R_r'}{s} + jL_r\omega. \tag{6.26}$$

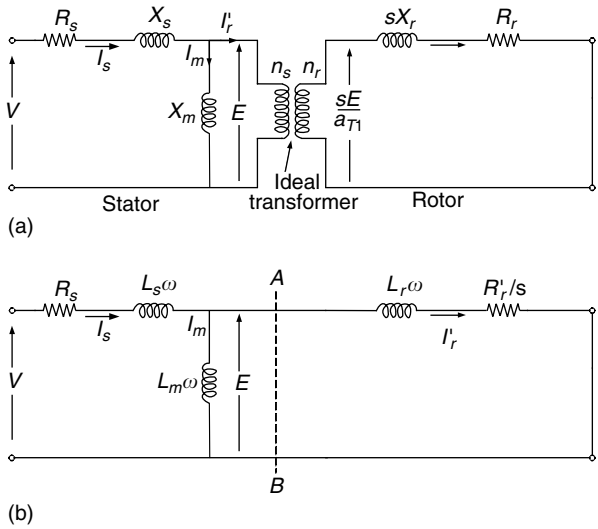

FIGURE 6.17
Per phase equivalent circuit of an induction motor: (a) per phase equivalent circuit and (b) per phase equivalent circuit refer to the stator

The driving-point impedance of the circuit is

$$Z = Z_s + \frac{Z_m Z_r}{Z_m + Z_r}. \tag{6.27}$$

Hence, the current I_s and I'_r can be calculated as

$$I_s = \frac{V}{Z} \tag{6.28}$$

and

$$I'_r = \frac{Z_m}{Z_m + Z_r} I_s. \tag{6.29}$$

The total electrical power supplied to the motor for three phase is

$$P_{elec} = 3I'^2_r \frac{R'_r}{\mathrm{s}}. \tag{6.30}$$

The mechanical power of the rotor can be obtained by subtracting the total power loss in the stator as

$$P_{mech} = P_{elec} - 3I'^2_r R'_r. \tag{6.31}$$

The angular velocity of the rotor, ω_m, is

$$\omega_m = \frac{2}{P}\omega(1-s). \tag{6.32}$$

The torque developed by the motor can be determined by

$$T = \frac{P_{mech}}{\omega_m}. \tag{6.33}$$

Figure 6.18 shows the torque–slip characteristics of an induction motor, which has fixed voltage and frequency. In the region of $0 < s < s_m$, where s_m is the rated slip of the motor, the torque increases approximately linearly with the increase of slip until reaching its maximum at $s = s_m$; then it decreases as the slip further increases. At $s = 1$, the rotor speed is zero and the corresponding torque is the starting torque, which is less than its torque at $s = s_m$. The region of $0 < s < 1$ is the forward motoring region. In the region of $s > 1$, the rotor torque further decreases with the increase of slip, and rotor speed is negative, according to (6.21). Thus, in this region, the operation of the motor is reverse braking. In the region of $s < 0$, that is, when the rotor speed is greater than the synchronous speed, the motor produces a negative torque.

It is clear that the speed–torque characteristics of a fixed voltage and frequency induction motor are not appropriate to vehicle traction applications. This is due to the low starting torque, limited speed range, and unstable operation in the range of $s > s_m$, in which any additional disturbing torque in the load will lead the machine to stop as the torque decreases with the speed-decreasing characteristics. High slip also results in high current, which may cause damage to the stator windings. Actually, the operation of the fixed voltage and frequency induction motor are usually operated in the narrow slip range of $0 < s < s_m$. Thus, for traction application, an induction motor must be controlled to provide proper speed–torque characteristics as mentioned in Chapters 2 to 4.

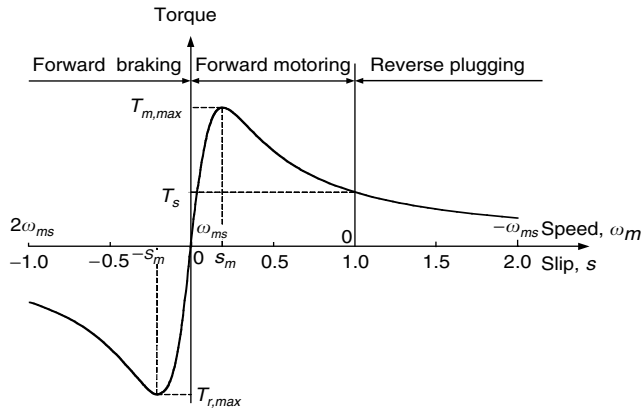

FIGURE 6.18
Torque–slip characteristics of an induction motor with fixed stator frequency and voltage

6.2.3 Constant Volt/Hertz Control

For traction application, the torque–speed characteristic of an induction motor can be varied by simultaneously controlling the voltage and frequency, which is known as constant volt/hertz control. By emulating a DC motor at low speed, the flux may be kept constant. According to Figure 6.17(b), the field current I_m should be kept constant and equal to its rated value. That is,

$$I_{mr} = \frac{E}{X_m} = \frac{E_{rated}}{\omega_r L_m}, \tag{6.34}$$

where I_{mr} is the rated field current, and E_{rated} and ω_r are the rated mmf and frequency of the stator, respectively. To maintain the flux at constant, E/ω should be kept constant and equal to E_{rated}/ω_r. Ignoring the voltage drop in the stator impedance Z_s results in a constant V/ω until the frequency and voltage reach their rated values. This approach is known as constant volt/hertz control.[2]

From Figure 6.17(b), the rotor current can be calculated as

$$I'_r = \frac{(\omega/\omega_r)E_{rated}}{jL_r\omega + R'_r/s}. \tag{6.35}$$

The torque produced can be obtained as

$$T = \frac{3}{\omega} I'^2_r R'_r/s = \frac{3}{\omega}\left[\frac{(\omega/\omega_r)^2 E^2_{rated} R'_r/s}{(R'_r/s)^2 + (L_r\omega)^2}\right]. \tag{6.36}$$

The slip s_m corresponding to the maximum torque is

$$s_m = \pm \frac{R'_r}{L_r\omega}. \tag{6.37}$$

And then, the maximum torque is

$$T_{max} = \frac{3}{2}\frac{E^2_{rated}}{L_r\omega_r^2}. \tag{6.38}$$

Equation (6.38) indicates that with the constant E/ω, the maximum torque is constant with varying frequency. Equation (6.37) indicates that $s_m\omega$ is constant, resulting in constant slip speed, ω_{sl}. In practice, due to the presence of stator impedance and the voltage drop, the voltage should be somewhat higher than that determined by constant E/ω, as shown in Figure 6.19.

When motor speed is beyond its rated speed, the voltage reaches its rated value and cannot be increased with the frequency. In this case, the voltage is fixed to its rated value and the frequency continuously increases with the motor speed. The motor goes into the field weakening operation. The slip s is fixed to its rated value corresponding to the rated frequency, and the slip speed ω_{sl} increases linearly with motor speed. This control approach results in constant power operation as shown in Figure 6.19.

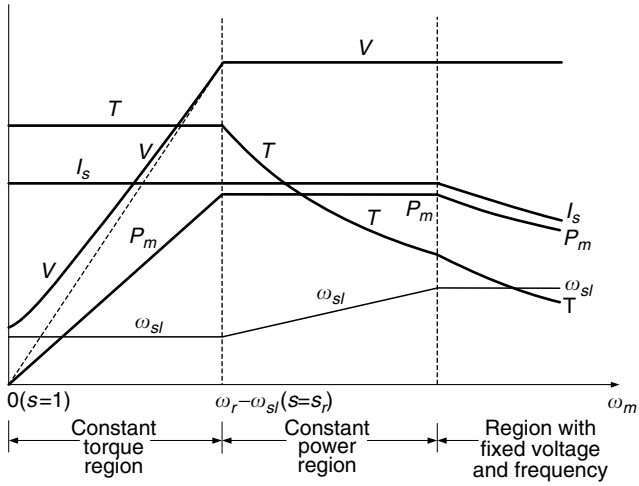

FIGURE 6.19
Operating variables varying with motor speed

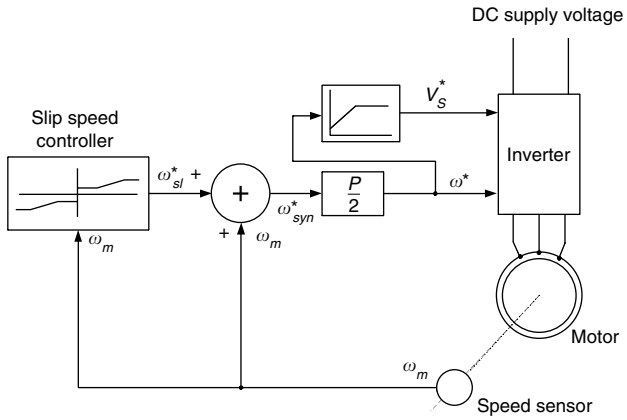

FIGURE 6.20
General configuration of constant *V/f* control

In traction application, speed control in a wide range is usually required and the torque demand in the high-speed range is low. Control beyond constant power range is required. To prevent the torque from exceeding the breakdown torque, the machine is operated at a constant slip speed and the machine current and power are allowed to decrease as shown in Figure 6.19. Figure 6.20 shows a general block diagram where constant *V/f* control is implemented.

6.2.4 Power Electronic Control

As EV and HEV propulsion, an induction motor drive is usually fed with a DC source (battery, fuel cell, etc.), which has approximately constant

terminal voltage. Thus, a variable frequency and variable voltage DC/AC inverter is needed to feed the induction motor. The general DC/AC inverter is constituted by power electronic switches and power diodes. The commonly used topology of a DC/AC inverter is shown in Figure 6.21(a), which has three legs (S_1 and S_4, S_3 and S_6, and S_5 and S_2), feeding phase *a*, phase *b*, and phase *c* of the induction motor, as shown in Figure 6.19(a). When switches S_1, S_3, and S_5 are closed, S_4, S_6, and S_2 are opened, and phases *a, b*, and *c* are supplied with a positive voltage ($V_d/2$). Similarly, when S_1, S_3, and S_5 are opened and S_4, S_6, and S_2 are closed, phases *a, b*, and *c* are supplied with a negative voltage. All the diodes provide a path for the reverse current of each phase.

For constant volt/hertz control of an induction motor, sinusoidal pulse-width modulation (PWM) is used exclusively. Three-phase reference voltages V_a, V_b, and V_c of variable amplitudes A_a, A_b, and A_c are compared with a common isosceles triangular carrier wave V_{tr} of a fixed amplitude A_m as shown in Figure 6.21(c). The outputs of comparators 1, 2, and 3 form the control signals for the three legs of the inverter. When the sinusoidal reference voltage V_a, V_b, and V_c at a time *t* is greater than the triangular waved voltage, turn-on signals are sent to the switches S_1, S_3, and S_5 and turn-off signals are sent to S_4, S_6, and S_2. Thus, the three phases of the induction motor have a positive voltage. On the other hand, when the reference sinusoidal voltage is smaller than the triangular wave voltage, turn-on signals are sent to the switches S_1, S_3, and S_5 and turn-off signals are sent to S_4, S_6, and S_2. The three phases of the induction motor then have a negative voltage. The voltages of the three phases are shown in Figure 6.21(d) to (f).

The frequency of the fundamental component of the motor terminal voltage is the same as that of the reference sinusoidal voltage. Hence, the frequency of the motor voltage can be changed by the frequency of the reference voltage. The ratio of the amplitude of the reference wave to that of the triangular carrier wave, *m*, is called the modulation index; therefore,

$$m = \frac{A}{A_m}, \tag{6.39}$$

where *A* is the multitude of the reference sinusoidal voltage, V_a, V_b, or V_c, and A_m is the multitude of angular carrier voltage. The fundamental (rms) component in the phase waveform, V_{ao}, V_{bo}, or V_{co}, is given by

$$V_f = \frac{mV_d}{2\sqrt{2}}. \tag{6.40}$$

Thus, the fundamental voltage increases linearly with *m* until $m = 1$ (that is, when the amplitude of the reference wave becomes equal to that of the carrier wave). For $m > 1$, the number of pulses in V_{ao}, V_{bo}, or V_{co} becomes less and the modulation ceases to be sinusoidal.[2]

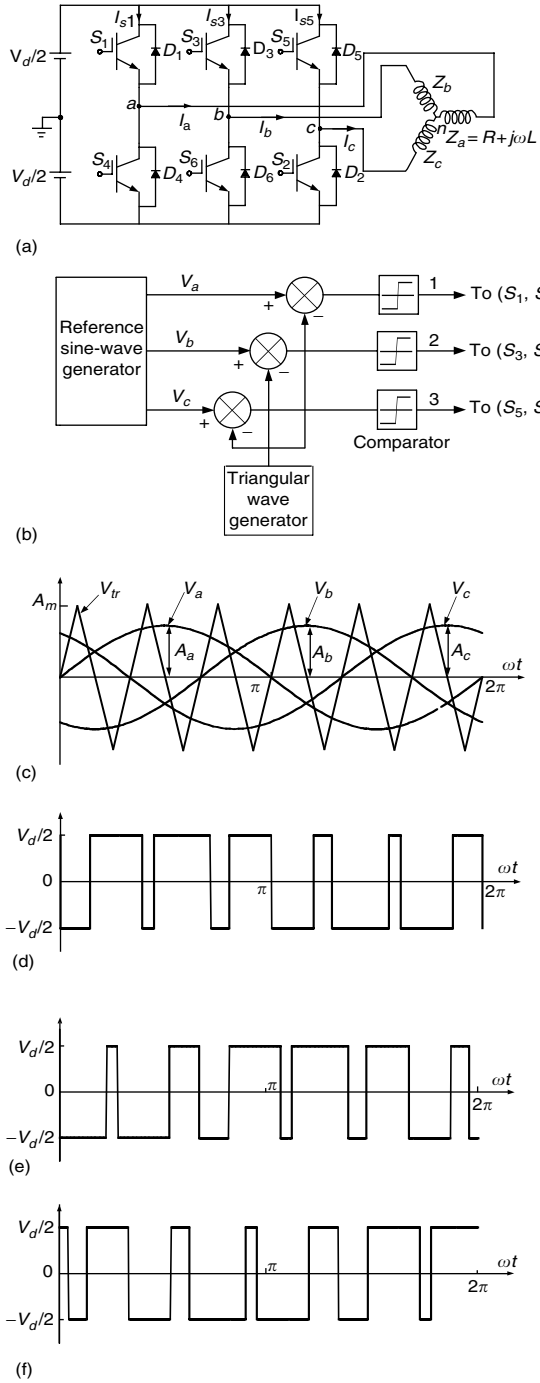

FIGURE 6.21
DC/AC inverter with sinusoidal PWM: (a) inverter topology; (b) control signals; (c) three phase reference voltage and a common isosceles triangular carrier wave; (d) voltage of phase *a*; (e) voltage of phase *b*; and (f) voltage of phase *c*

6.2.5 Field Orientation Control

The constant volt/hertz control of the induction motor is more suitably applied to motors that operate with a relatively slow speed regulation. However, this approach shows poor response to frequent and fast speed varying, and also results in poor operation efficiency due to the poor power factor. In the last two decades, field orientation control (FOC) or vector control technology has been successfully developed. This technology mostly overcomes the disadvantages of the constant volt/hertz control in AC motor drives.

6.2.5.1 Field Orientation Principles

The aim of FOC is to maintain the stator field perpendicular to the rotor field so as to always produce the maximum torque as in DC motors. However, for induction motors, phase voltages are the only accesses for the purpose of control.

As mentioned in Section 6.2.1, when balanced three-phase sinusoidal currents flow through the three phases of the stator of an induction motor, the rotating field is developed; current is induced in the rotor. In turn, the current induced in the rotor is also three-phase and produces a field, which rotates with the same angular velocity of the stator rotating field. The rotating fields of both stator and rotor can be described by two retorting vectors, referring to a common, stationary reference frame, d–q, as shown in Figure 6.16. The mmf of the stator field is expressed by equation (6.17). For convenience, it is repeated as follows:

$$\boldsymbol{F}_s^s = \boldsymbol{F}_{as} e^{j0^\circ} + \boldsymbol{F}_{bs} e^{j120^\circ} + \boldsymbol{F}_{cs} e^{j240^\circ}. \tag{6.41}$$

Similarly, the stator voltage, stator current, and stator flux can be expressed as vectors in the same way. That is,

$$\boldsymbol{v}_s^s = v_{as}^s e^{j0^\circ} + v_{bs}^s e^{j120^\circ} + v_{cs}^s e^{j240^\circ}, \tag{6.42}$$

$$\boldsymbol{i}_s^s = i_{as}^s e^{j0^\circ} + v_{bs}^s e^{j120^\circ} + v_{cs}^s e^{j240^\circ}, \tag{6.43}$$

$$\boldsymbol{\lambda}_s^s = \boldsymbol{\lambda}_{as}^s e^{j0^\circ} + \boldsymbol{\lambda} v_{bs}^s e^{j120^\circ} + \boldsymbol{\lambda}_{cs}^s e^{j240^\circ}. \tag{6.44}$$

The subscript s refers to the stator and as, bs, and cs refer to phases a, b, and c of the stator. The superscript s refers to the variable that is referred to the stator fixed frame. Bold symbols stand for vector variables. The vectors of stator voltage, current, and flux can also be described by its components in d and q axes as follows:

$$\begin{bmatrix} v_{ds}^s \\ v_{qs}^s \end{bmatrix} = \begin{bmatrix} 1 & -\frac{1}{2} & -\frac{1}{2} \\ 0 & \frac{\sqrt{3}}{2} & -\frac{\sqrt{3}}{2} \end{bmatrix} \begin{bmatrix} v_{as} \\ v_{bs} \\ v_{cs} \end{bmatrix}, \tag{6.45}$$

$$\begin{bmatrix} i_{ds}^s \\ i_{qs}^s \end{bmatrix} = \begin{bmatrix} 1 & -\frac{1}{2} & -\frac{1}{2} \\ 0 & \frac{\sqrt{3}}{2} & -\frac{\sqrt{3}}{2} \end{bmatrix} \begin{bmatrix} i_{as} \\ i_{bs} \\ i_{cs} \end{bmatrix}, \tag{6.46}$$

$$\begin{bmatrix} \lambda_{ds}^s \\ \lambda_{qs}^s \end{bmatrix} = \begin{bmatrix} 1 & -\frac{1}{2} & -\frac{1}{2} \\ 0 & \frac{\sqrt{3}}{2} & -\frac{\sqrt{3}}{2} \end{bmatrix} \begin{bmatrix} \lambda_{as} \\ \lambda_{bs} \\ \lambda_{cs} \end{bmatrix}. \tag{6.47}$$

In a real induction motor, the rotor winding differs from the stator winding, that is, the effective number of turns per phase of the rotor winding, N_r, is not equal to that of the stator winding, N_s. Therefore, the turns ratio, $v = N_s/N_r$, must be taken into account. The vectors of rotor current, voltage, and magnetic flux can be described by $\boldsymbol{i}_r^r$, $\boldsymbol{v}_r^r$, and $\boldsymbol{\lambda}_r^r$ in the rotor frame. However, it is necessary to transform the vectors from the rotor frame to the stator frame for the purpose of easy analysis. The transformations of these vectors (refer to Figure 6.22) are described by

$$\boldsymbol{i}_r^s = \frac{e^{j\theta_0}}{v} \boldsymbol{i}_r^r, \tag{6.48}$$

$$\boldsymbol{v}_r^s = v e^{j\theta_0} \boldsymbol{v}_r^r, \tag{6.49}$$

$$\boldsymbol{\lambda}_r^s = v e^{j\theta_0} \boldsymbol{\lambda}_r^r. \tag{6.50}$$

Using vector notation, either the stator or rotor windings can be represented by a simple resistive-plus-inductive circuit, using current, voltage, and magnetic flux space vector as illustrated in Figure 6.23.

Using the vector version of Kirchhoff's voltage law, the equation of the stator winding can be written as

$$\boldsymbol{v}_s^s = R_s \boldsymbol{i}_s^s + \frac{d\boldsymbol{\lambda}_s^s}{dt} \tag{6.51}$$

and that of rotor winding as

$$\boldsymbol{v}_r^r = R_r^r \boldsymbol{i}_r^r + \frac{d\boldsymbol{\lambda}_r^r}{dt}, \tag{6.52}$$

where R_s and R_r^r are the actual stator and rotor resistances per phase, respectively. As is known from the steady-state theory of induction machines, the relation between R_r^r and the rotor resistance referred to the stator is

$$R_r^r = \frac{1}{v^2} R_r. \tag{6.53}$$

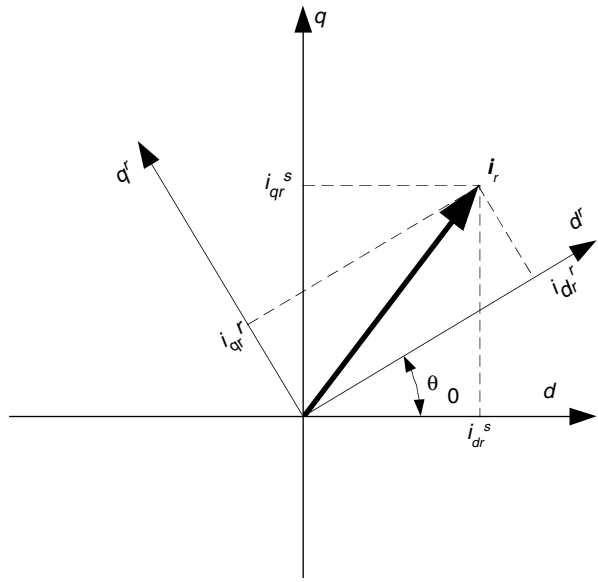

FIGURE 6.22
Transformation of rotor current vector from rotor frame to stator frame

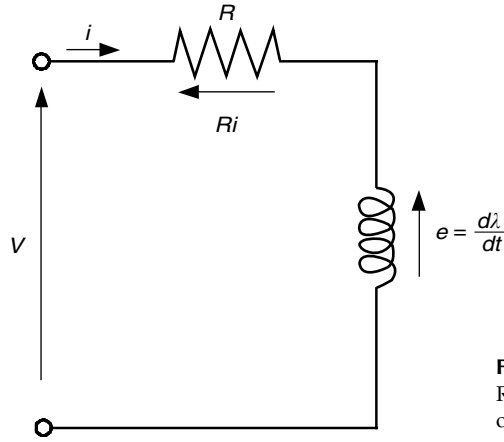

FIGURE 6.23
Resistive-plus-inductive equivalent circuit of either the stator or rotor windings

Hence, from (6.48) and (6.53), the first term of (6.52) is

$$R_r^r \boldsymbol{i}_r^r = \frac{e^{-j\theta_0}}{v} R_r \boldsymbol{i}_r^s. \tag{6.54}$$

The second term, from (6.50), gives

$$\frac{d\boldsymbol{\lambda}_r^r}{dt} = \frac{e^{j\theta_0}}{v}\left(\frac{d\boldsymbol{\lambda}_r^s}{dt} - j\omega_0\right). \tag{6.55}$$

Finally, substituting (6.54) and (6.55) into (6.52) gives

$$\boldsymbol{v}_r^s = R_r \boldsymbol{i}_r^s + \frac{d\boldsymbol{\lambda}_r^s}{dt} - j\omega_0 \boldsymbol{\lambda}_r^s. \tag{6.56}$$

Introducing a differentiation operator $p \equiv d/dt$, the voltage equation of an induction motor can be written as

$$\boldsymbol{v}_s^s = R_s \boldsymbol{i}_s^s + p\boldsymbol{\lambda}_s^s, \tag{6.57}$$

$$\boldsymbol{v}_r^s = R_r \boldsymbol{i}_r^s + (p - j\omega_0)\boldsymbol{\lambda}_r^s. \tag{6.58}$$

The flux vector $\boldsymbol{\lambda}_s^s$ and $\boldsymbol{\lambda}_r^s$ can then be expressed in terms of current vector $\boldsymbol{i}_s^s$ and $\boldsymbol{i}_r^s$, and the motor inductances as

$$\begin{bmatrix} \boldsymbol{\lambda}_s^s \\ \boldsymbol{\lambda}_r^s \end{bmatrix} = \begin{bmatrix} L_s & L_m \\ L_m & L_r \end{bmatrix} \begin{bmatrix} \boldsymbol{i}_s^s \\ \boldsymbol{i}_r^s \end{bmatrix}, \tag{6.59}$$

where L_m is mutual inductance, L_s is stator inductance calculated as the sum of the stator leakage inductance L_{ls} and mutual inductance L_m, and L_r is rotor inductance, calculated as the sum of rotor leakage inductance L_{lr} and mutual inductance L_m.

Finally, the voltage equation can be written in matrix format as

$$\begin{bmatrix} v_{ds}^s \\ v_{qs}^s \\ v_{dr}^s \\ v_{qr}^s \end{bmatrix} = \begin{bmatrix} R_s & 0 & 0 & 0 \\ 0 & R_s & 0 & 0 \\ 0 & \omega_0 L_m & R_r & \omega_0 L_r \\ -\omega_0 L_m & 0 & -\omega_0 L_r & R_r \end{bmatrix} \begin{bmatrix} i_{ds}^s \\ i_{qs}^s \\ i_{dr}^s \\ i_{qr}^s \end{bmatrix} + \begin{bmatrix} L_s & 0 & L_m & 0 \\ 0 & L_s & 0 & L_m \\ L_m & 0 & L_r & 0 \\ 0 & L_m & 0 & L_r \end{bmatrix} \frac{d}{dt} \begin{bmatrix} i_{ds}^s \\ i_{qs}^s \\ i_{dr}^s \\ i_{qr}^s \end{bmatrix}. \tag{6.60}$$

Because the rotor circuit of the induction motor is shorted, v_{dr}^s and v_{qr}^s are zero. At a given rotor speed, ω_0, the stator and rotor currents can be obtained by solving equation (6.60). The torque developed by the motor can be expressed as

$$T = \frac{P}{3} L_m (i_{qs}^s i_{dr}^s - i_{ds}^s i_{qr}^s) = \frac{P}{3} L_m \mathrm{Im}(\boldsymbol{i}_s^s \boldsymbol{i}_r^{s*}), \tag{6.61}$$

where Im stands for the imaginary part of the production of vector $\boldsymbol{i}_s^s$ and conjugate vector of $\boldsymbol{i}_r^{s*}$.

Transferring three phase variables (voltage, current, flux) into a stationary stator-based dq frame does not change the alternate characteristics of the variable with time. AC quantities are somewhat inconvenient for control purposes. For instance, control systems are usually represented by block diagrams in which the variables are time-varying DC signals. Therefore, another transformation is necessary, which allows conversion of the AC dq components of the motor vectors into DC variables. To do this, a transformation is conducted from a stationary stator reference frame dq to the so-called excitation reference frame DQ which rotates with the angular speed w in the same direction as does mmf, $\boldsymbol{F}_s^s$. As a result, in the steady state,

coordinates of motor vectors in the new reference frame do not vary in time. This is illustrated in Figure 6.24, which shows the stator mmf vector in both reference frames.

The voltage vector of the stator in the excitation reference frame can be expressed as

$$\boldsymbol{v}_S^e = \boldsymbol{v}_s^s e^{-j\omega t} \tag{6.62}$$

Considering $e^{-j\omega t} = \cos(\omega t) - \sin(\omega t)$, the components of stator voltage on the DQ frame are

$$\begin{bmatrix} v_{DS}^e \\ v_{QS}^e \end{bmatrix} = \begin{bmatrix} \cos(\omega t) & \sin(\omega t) \\ \sin(\omega t) & \cos(\omega t) \end{bmatrix} \begin{bmatrix} v_{ds}^s \\ v_{qs}^s \end{bmatrix}. \tag{6.63}$$

Thus, the motor equation in the excitation reference frame can be expressed as

$$\boldsymbol{v}_S^e = R_s \boldsymbol{i}_S^e + (p + j\omega)\boldsymbol{\lambda}_s^e, \tag{6.64}$$

$$\boldsymbol{v}_R^e = R_r \boldsymbol{i}_R^e + (p + j\omega - j\omega_0)\boldsymbol{\lambda}_R^e = R_r \boldsymbol{i}_R^e + (p + j\omega_r)\boldsymbol{\lambda}_R^e, \tag{6.65}$$

with $\omega_r = \omega - \omega_0$ as the slip speed, and

$$\begin{bmatrix} \boldsymbol{\lambda}_S^e \\ \boldsymbol{\lambda}_R^e \end{bmatrix} = \begin{bmatrix} L_s & L_m \\ L_m & L_r \end{bmatrix} \begin{bmatrix} \boldsymbol{i}_S^e \\ \boldsymbol{i}_R^e \end{bmatrix}. \tag{6.66}$$

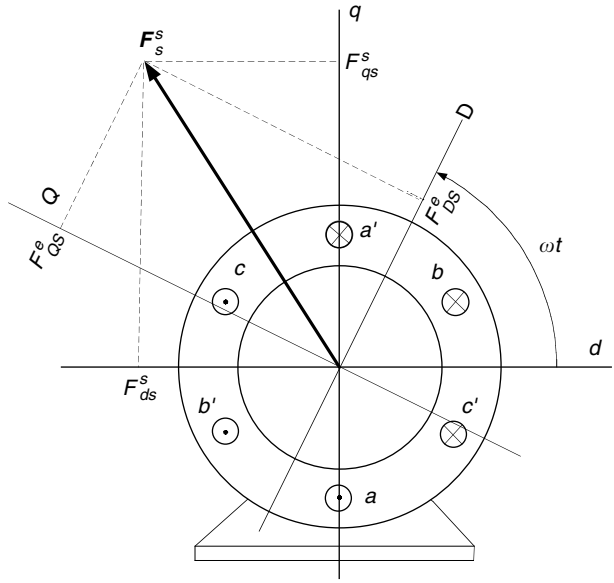

FIGURE 6.24
Stator mmf vector in the stator and excitation reference frames

Again, the rotor voltage vector is normally assumed to be zero because of the shorted rotor winding.

The torque equation in the excitation reference frame is similar to that in the stator frame as

$$T=\frac{P}{3}L_m(i^e_{QS}i^e_{Dr}-i^e_{DS}i^e_{QR})=\frac{P}{3}L_m\mathrm{Im}(\boldsymbol{i}^e_S\boldsymbol{i}^{e*}_R). \tag{6.67}$$

In general, accurate control of instantaneous torque produced by a motor is required in high-performance drive systems, such as EV and HEV propulsions. The torque developed in the motor is a result of the interaction between current in the armature winding and the magnetic field produced in the stator field of the motor. The field should be maintained at a certain optimal level, sufficiently high to yield a high torque per unit of ampere, but not too high to result in excessive saturation of the magnetic circuit of the motor. With a fixed field, the torque is proportional to the armature current.

Independent control of the field and armature currents is desirable. In a manner similar to that of a DC motor, the armature winding in induction motors is also on the rotor, while the field is generated by currents in the stator winding. However, the rotor current is not directly derived from an external source, but results from the EMF induced in the winding as a result of the relative motion of the rotor conductors with respect to the stator field. In the most commonly used, squirrel-cage motors, only the stator current can be directly controlled, since the rotor winding is not accessible. Optimal torque production conditions are not inherent due to the absence of a fixed physical disposition between the stator and rotor fields, and the torque equation is nonlinear. FOC or vector control can realize the optimal control for transient operation of an induction drive. FOC can decouple the field control from the torque control. A field-oriented induction motor emulates a separately excited DC motor in two aspects:

1. Both the magnetic field and the torque developed in the motor can be controlled independently.
2. Optimal conditions for torque production, resulting in the maximum torque per unit ampere, occur in the motor both in the steady state and in transient conditions of the operations.

As mentioned in Section 6.1.1, the optimal torque production conditions are inherently satisfied in a DC motor (refer to Figure 6.3). The armature current i_a, supplied through brushes, is always orthogonal to the flux vector (field flux), λ_f, produced in the stator and linking the rotor winding. In effect, the developed torque, T, is proportional both to the armature current and the field flux, that is,

$$T=K_T i_a \lambda_f, \tag{6.68}$$

where K_T is a constant depending on the physical parameters of the motor. Thus, the torque of separately excited DC motors can be controlled by

independently controlling the armature current and flux as mentioned in Section 6.1.2.

To emulate this independent armature and field control characteristic of a DC motor, the torque equation (6.67) can be rearranged so that the torque is expressed in terms of the stator current and rotor flux. From (6.66), the following equation can be obtained:

$$\boldsymbol{i}_R^e = \frac{1}{L_r}(\boldsymbol{\lambda}_R^e - L_m \boldsymbol{i}_S^e). \tag{6.69}$$

Torque equation (6.67) can be rewritten as

$$T = \frac{P}{3R_r}\frac{L_m}{\tau_r}(i_{QS}^e \lambda_{DR}^e - i_{DS}^e \lambda_{QR}^e), \tag{6.70}$$

where $\tau_r = L_r / R_r$ is the rotor time constant.

In equation (6.70), if

$$\lambda_{QR}^e = 0, \tag{6.71}$$

then

$$T = \frac{P}{3R_r}\frac{L_m}{\tau_r}\lambda_{DR}^e i_{QS}^e. \tag{6.72}$$

Clearly, (6.72) is analogous to (6.68), describing a separately excited DC motor.

As $\boldsymbol{v}_R^e = 0$ (shorted rotor winding), equation (6.65) yields

$$R_r \boldsymbol{i}_R^e + (p + j\omega_w)\boldsymbol{\lambda}_R^e = 0, \tag{6.73}$$

and substituting equation (6.69) into equation (6.73) yields

$$p\boldsymbol{\lambda}_R^e = \frac{1}{\tau_r}[L_m \boldsymbol{i}_S^e - (1 + j\omega_r \tau_r)\boldsymbol{\lambda}_R^e]. \tag{6.74}$$

Thus,

$$p\lambda_{DR}^e = \frac{L_m}{\tau_r} i_{DS}^e - \frac{1}{\tau_r}\lambda_{DR}^e. \tag{6.75}$$

Equation (6.75) indicates that the flux λ_{DR}^e is produced by the current i_{DS}^e. Thus, the torque produced can be represented by the block diagram as shown in Figure 6.25.

Furthermore, equation (6.75) can be expressed in a transfer function as

$$G(p) = \frac{\lambda_{DR}^e}{i_{DS}^e} = \frac{L_m}{\tau_r p + 1}. \tag{6.76}$$

Thus, the block diagram in Figure 6.25 can be further reduced as shown in Figure 6.26.

If conditions (6.71) and $\lambda_{DR}^e = constant$ are satisfied, that is, $\lambda_{QR}^e = 0$ and $p\lambda_{DR}^e = 0$, then equation (6.64) yields $i_{DR}^e = 0$, that is, $\boldsymbol{i}_R^e = j i_{QR}^e$. At the same time,

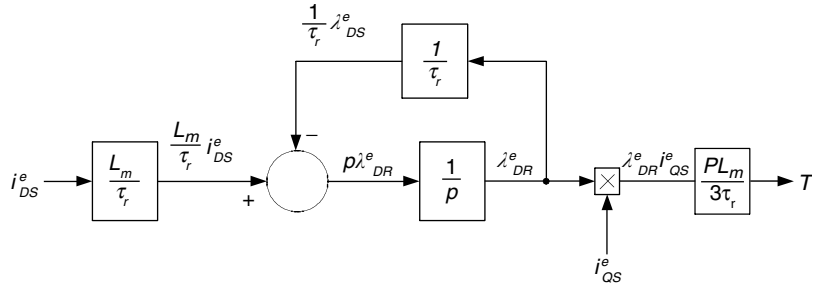

FIGURE 6.25
Block diagram of an induction motor with $\lambda^e_{QR}=0$

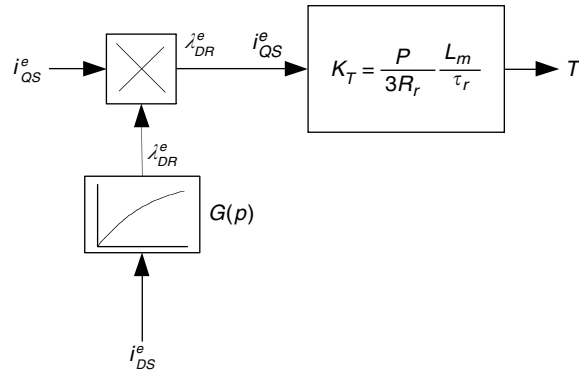

FIGURE 6.26
Block diagram of a field-orientated induction motor

$\boldsymbol{\lambda}^e_R=\lambda^e_{DR}$. Consequently, vectors $\boldsymbol{i}^e_R$ and $\boldsymbol{\lambda}^e_R$ are orthogonal and represent the optimal conditions for torque production, analogous to a DC motor. In an induction motor, the optimal torque-production conditions are always satisfied in the steady state. However, in transient operation, the motor needs delicate control to achieve this optimal torque production.

6.2.5.2 Control

As demonstrated in the above section, the field orientation principle defines the conditions of optimal torque production. Orthogonality of the rotor current and flux vectors must be maintained at all times. This is inherently satisfied in the steady state when the rotor settles down to such a speed that the developed torque matches the load torque. Under transient conditions, however, in order to meet the field orientation principle conditions, special techniques are required to provide an algorithmic equivalent of the actual physical disposition between the stator and rotor fields of the emulated DC motor.

The general block diagram of a vector control system for an induction motor drive is shown in Figure 6.27. A field orientation system produces reference signals i_{as}^*, i_{bs}^*, and i_{cs}^* of the stator currents, based on the input reference values, λ_r^* and T^*, of the rotor flux and motor torque, respectively, and the signals corresponding to selected variables of the motor. An inverter supplies the motor currents, i_{as}, i_{bs}, and i_{cs}, such that their waveforms follow the reference waveform, i_{as}^*, i_{bs}^*, and i_{cs}^*.

As shown in Figure 6.26, in a field-orientated induction motor, the i_{DS}^e and i_{QS}^e components of the stator current vector, $\boldsymbol{i}_s^e$, in the excitation frame can be used for independent control of the motor field and torque, respectively. Hence, the field orientation system as shown in Figure 6.27 first converts λ_r^* and T^* into the corresponding reference signals, i_{DS}^{e*} and i_{QS}^{e*}, of the vector of the stator current, and then transfers these into the reference signals, i_{as}^*, i_{bs}^*, and i_{cs}^*, of the stator phase current, which is to be produced by the inverter. The stator phase currents, i_{as}^*, i_{bs}^*, and i_{cs}^*, can be calculated using *dq* to *abc* transformation (see equation [6.46]) if the corresponding reference signals, $i_{ds}^{s^*}$ and $i_{qs}^{s^*}$, in the stator reference frame are known. This is a simple scalar, or static, transformation, since the elements of the transformation matrix used to perform this operation are constant.

However, it can be seen from equation (6.63) that a dynamic transformation, that is, one involving time, is required to determine $i_{ds}^{s^*}$ and $i_{qs}^{s^*}$ from i_{DS}^{e*} and i_{QS}^{e*}. In Figure 6.24, it does not indicate which vector the excitation reference frame

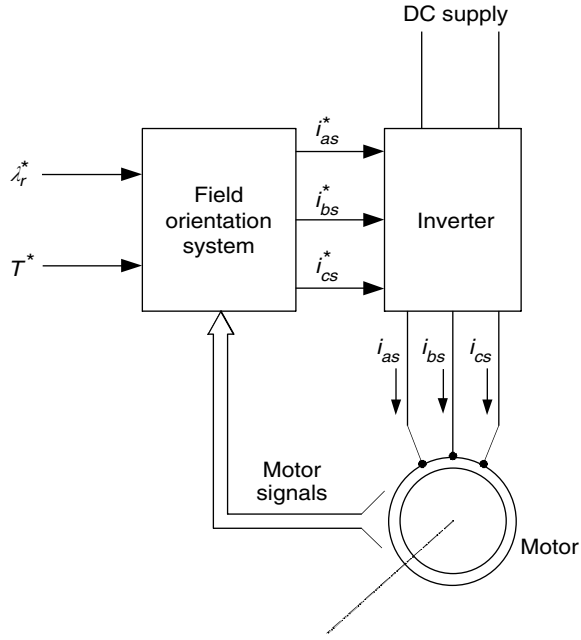

FIGURE 6.27
General block diagram of a vector control system for an induction motor

DQ aligns with. Clearly, any one of the vectors can be used as a reference with which the excitation frame is to be aligned. Usually, it is the rotor flux vector, λ_r^s, along which the excitation frame is orientated. This method is usually referred to as the rotor flux orientation scheme,[55] as shown in Figure 6.28.

If the angular position of the rotor flux vector in the stator reference frame is denoted by θ_r, the *DQ* to *dq* transformation in the described scheme is expressed as

$$\begin{bmatrix} i_{ds}^{s*} \\ i_{qs}^{s*} \end{bmatrix} = \begin{bmatrix} \cos(\theta_r) & -\sin(\theta_r) \\ \sin(\theta_r) & \cos(\theta_r) \end{bmatrix} \begin{bmatrix} i_{DS}^{e*} \\ i_{QS}^{e*} \end{bmatrix}. \tag{6.77}$$

It can be observed that this orientation of the orientation frame inherently satisfies the field orientation principle condition in equation (6.71). The rotor flux is controlled by adjusting the i_{DS}^e component of the stator current vector — independently from the torque control, which is realized by means of the i_{QS}^e component. The only requirement for this scheme is an accurate identification of angle θ_r, that is, the position of λ_r^s. This can be done in either a direct or indirect way.

6.2.5.3 Direction Rotor Flux Orientation Scheme

In direct field orientation systems, the magnitude and angular position (phase) of the reference flux vector $\boldsymbol{\lambda}_r^e$ are either measured or estimated from the stator voltage and currents using flux observers. For example, Hall sensors can be used to measure magnetic fields. Placing the sensors in the

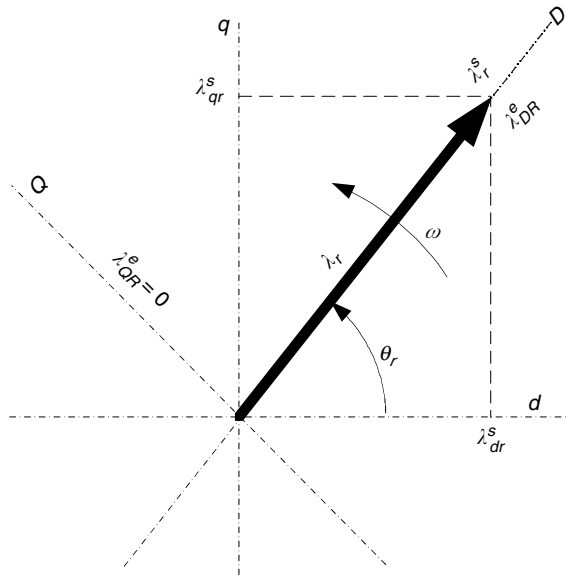

FIGURE 6.28
Orientation of the excitation reference frame along the rotor flux vector

air gap of the motor, on the d and q axes, allows determination of the corresponding components of vector $\boldsymbol{\lambda}^s_m$ of the mutual flux (air gap flux). However, this air gap flux differs from the rotor flux, which is taken as the reference flux vector and needs derivation from the air gap flux $\boldsymbol{\lambda}^s_m$. Referring to the dynamic T equivalent circuit shown in Figure 6.29, the flux appearing across the mutual inductance, L_m, is

$$\boldsymbol{\lambda}^s_m = L_m \boldsymbol{i}^s_m - L_m(\boldsymbol{i}^s_s + \boldsymbol{i}^s_r). \tag{6.78}$$

or

$$\boldsymbol{i}^s_r = \frac{1}{L_m}\boldsymbol{\lambda}^s_m - \boldsymbol{i}^s_s. \tag{6.79}$$

Since $\boldsymbol{\lambda}^s_r$ differs from the $\boldsymbol{\lambda}^s_m$ by only the leakage flux in the rotor, then

$$\boldsymbol{\lambda}^s_r = \boldsymbol{\lambda}^s_m + L_{lr}\boldsymbol{i}^s_r = \boldsymbol{\lambda}^s_m + L_{lr}\left(\frac{1}{L_m}\boldsymbol{\lambda}^s_m - \boldsymbol{\lambda}^s_s\right)\frac{L_r}{L_m}\boldsymbol{\lambda}^s_m - L_{lr}\boldsymbol{i}^s_s. \tag{6.80}$$

A microprocessor-based rotor flux calculator is shown in Figure 6.30. It performs the algebraic operations as follows:

1. Signals i^s_{ds} and i^s_{qs} are calculated from the actual stator phase current, i_{as}, i_{bs}, and i_{cs}, using the *abc* to *dq* transformation expressed in equation (6.46).
2. Using equation (6.80), signals λ^s_{dr} and λ^s_{qr} are calculated.
3. Magnitude λ_r and phase θ_r of the rotor flux vector are determined using the rectangular to polar coordinate transformation.

It must be pointed out that the orthogonal spacing of the flux sensors in Figure 6.30 applies to only two-pole machines. In a P-pole machine, the sensors must be placed $180/P$ from each other.

Since $\lambda^s_{DR} = \lambda_r$ (see Figure 6.28), the output variable, λ_r, of the rotor flux calculator can be used as a feedback signal in the field control loop. The same

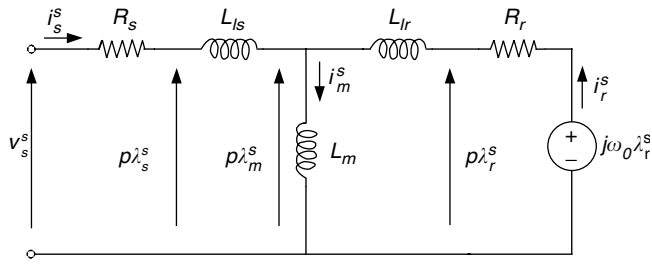

FIGURE 6.29
Dynamic T equivalent circuit of an induction motor

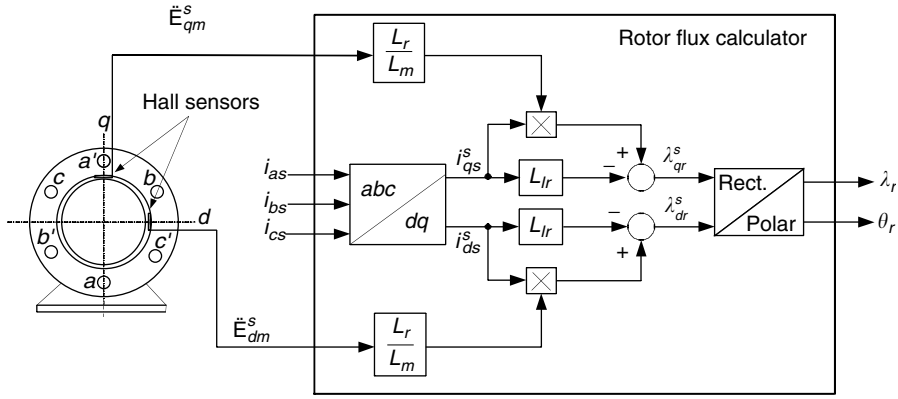

FIGURE 6.30
Determination of the magnitude and position of the rotor flux vector using Hall sensor and a rotor flux calculator[3]

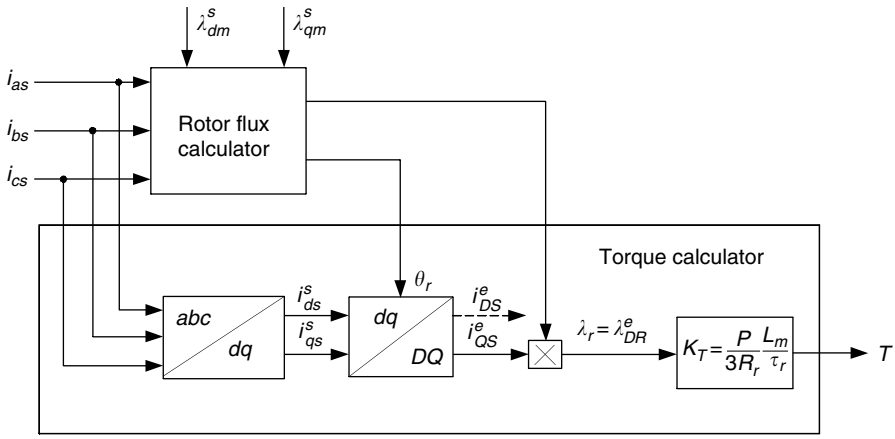

FIGURE 6.31
Torque calculator

variables can also be used for calculation of the developed torque as shown in Figure 6.31. The torque calculator computes torque in the following steps:

1. The static *abc* to *dq* transformation is performed on the stator currents, i_{as}, i_{bs}, and i_{cs}, to obtain i^s_{ds} and i^s_{qs}.
2. Angle θ_r supplied by the rotor flux calculator is substituted into equation (6.63) for ωt in order to transfer signals i^s_{ds} and i^s_{qs} into i^e_{DS} and i^e_{QS} components of the stator current vector in the excitation frame.
3. Magnitude λ_r of the rotor flux, also supplied by the rotor flux calculator and presumed equal to λ^e_{DS}, is multiplied by i^e_{QS} and by the torque constant K_T to calculate the developed torque.

Figure 6.31 shows the torque calculation process block diagram.

Figure 6.32 illustrates an independent flux and torque control block diagram, based on the vector control of an induction motor with direct rotor flux orientation. In the system, proportional-plus integral (PI)-based field and torque controllers are used to generate the control signals i_{DS}^{e*} and i_{QS}^{e*} in the excitation frame by comparing the target rotor flux, λ_r^*, and target torque, T^*, with the actual rotor flux, λ_r, and torque, T. Then, i_{DS}^{e*} and i_{QS}^{e*} in excitation frame are transferred into i_{ds}^{s*} and i_{qs}^{s*} in stator reference frame using rotor flux angle (see equation [6.63]). Furthermore, i_{ds}^{s*} and i_{qs}^{s*} in stator reference frame are transferred into phase current signals i_{as}^*, i_{bs}^*, and i_{cs}^* through static transformation (see equation [6.46]). The phase current signals, as the reference signals, are used to control the power electronics of the inverter to generate corresponding phase current i_{as}, i_{bs}, and i_{cs}.

In practice, the ratio of L_r to L_m, and the rotor leakage inductance, L_{ls}, which are used in the rotor flux calculator (see Figure 6.30) are not significantly affected by changes in the operation conditions of the motor, such as the winding temperature or saturation of the magnetic circuit. Therefore, the field orientation techniques described are considered to be the most robust and accurate. However, they require the placement of vulnerable Hall sensors in the air gap of the motor, to the detriment of the cost and reliability of the drive system.

6.2.5.4 *Indirect Rotor Flux Orientation Scheme*

The presence of vulnerable Hall sensors in vector control with direct rotor flux orientation would weaken the reliability and enhance the cost of the motor drive. The indirect approach is to obtain the rotor flux position by the calculation of the slip speed, ω_r, required for correct field orientation, and the imposition of this speed on the motor.

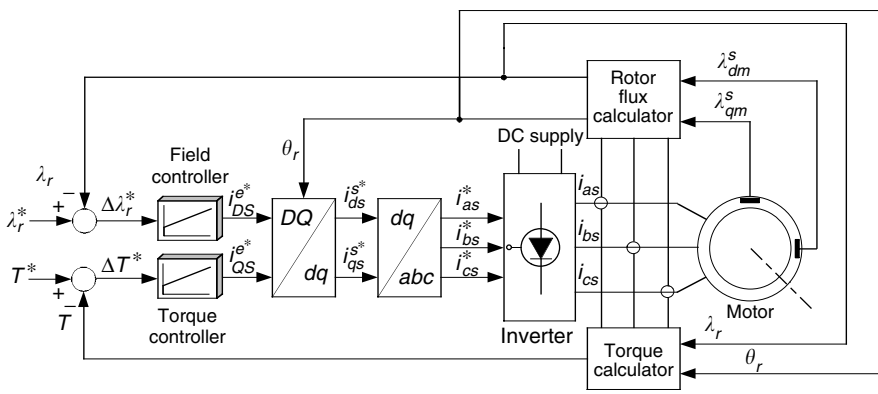

FIGURE 6.32
Vector control system for an induction motor with direct rotor flux orientation

If the synchronous speed necessary to maintain the orthogonal orientation of vectors $\boldsymbol{\lambda}_R^e$ and $\boldsymbol{i}_R^e$ in the given operating conditions of the motor is denoted by ω^*, the θ_r angle can be expressed as

$$\theta_r = \int_0^t \omega^* \, dt = \int_0^t \omega_r^* \, dt + \int_0^t \omega_0 \, dt = \int_0^t \omega_r^* \, dt + \theta_0, \tag{6.81}$$

where ω^*, ω_r^* and ω_0 are the synchronous speed, slip speed, and rotor speed, respectively, and θ_0 is the angular displacement of the rotor, which is easy to measure using a shaft position sensor.

The required value of the slip speed ω_r^* can be computed from equation (6.69). Since $\boldsymbol{\lambda}_R^e = \lambda_{DR}^e$, equation (6.69) becomes

$$\boldsymbol{i}_R^e = \frac{1}{L_r}(\lambda_{DR}^e - L_m \boldsymbol{i}_S^e). \tag{6.82}$$

Substituting (6.82) into (6.73) gives the real and imaginary parts as

$$\lambda_{DR}^e = (1 + \tau_r p) = L_m i_{DS}^e \tag{6.83}$$

and

$$\omega_r \tau_r \lambda_{DR}^e = L_m i_{QS}^e. \tag{6.84}$$

Replacing ω_r, λ_{DR}^e, and i_{QS}^e with ω_r^*, λ_r^*, and i_{QS}^{e*}, respectively, in equation (6.84) yields

$$\omega_r^* = \frac{L_m}{\tau_r} \frac{i_{QS}^{e*}}{\lambda_r^*}. \tag{6.85}$$

Replacing λ_{Dr}^e and i_{DS}^e in equation (6.83) with λ_r^* and i_{DR}^{e*} yields

$$i_{DS}^{e*} = \frac{1 + \tau_r p}{L_m} \lambda_R^*. \tag{6.86}$$

Form torque equation (6.68), the signal i_{QS}^{e*} can be obtained as

$$i_{QS}^{e*} = \frac{T^*}{K_T \lambda_r^*}. \tag{6.87}$$

A vector control system for an induction motor based on the indirect rotor flux orientation scheme is shown in Figure 6.33. The rotor flux and developed torque are controlled in a feedforward. As a consequence of this, performance of the system strongly depends on an accurate knowledge of motor parameters, a requirement that is difficult to satisfy in practical applications. On the other hand, a major advantage of such a system is that a standard motor can be used, whose rotor position is easily measurable by an external sensor. Since the control scheme presented here constitutes an extension of the scalar torque control methods, the reference flux and torque values must satisfy the safe operation area (SOAR) condition described.[3]

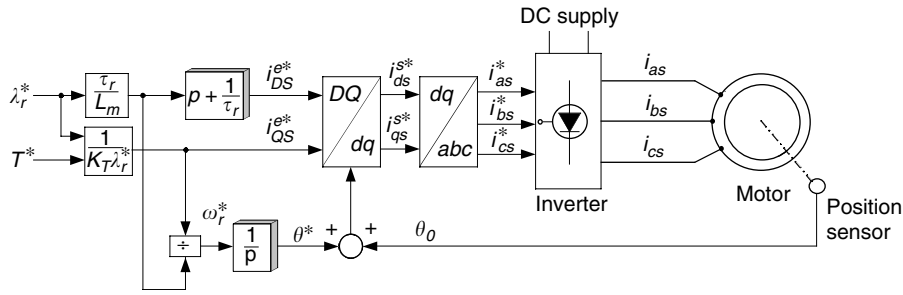

FIGURE 6.33
Vector control system for an induction motor with indirect rotor flux orientation

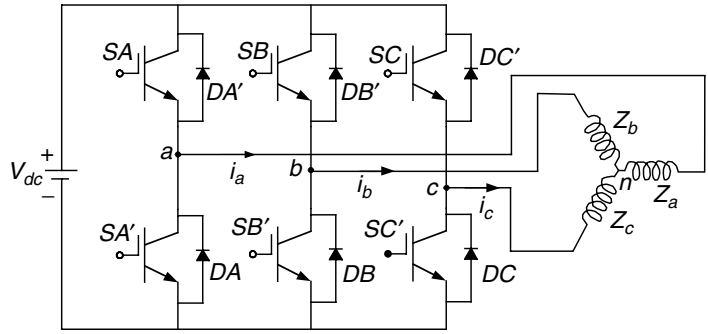

FIGURE 6.34
Circuit diagram of a three-phase voltage source inverter

6.2.6 Voltage Source Inverter for FOC

The power electronic inverter for FOC of induction motor drives has the same topology as shown in Figure 6.21(a), which is illustrated again in Figure 6.34. The power switches in a given leg (*a*, *b*, or *c*) must never both be in ON-state, since this would cause a short circuit. On the other hand, if both the switches on the same leg are in OFF-state, then the potential of the corresponding output terminal is unknown to the control system of the inverter. The circuit can be completed through either the upper or lower diode and, consequently, the potential can be equal to that of either positive bus (+) or negative bus (−). Therefore, the inverter is controlled in such a way that, in a given leg, either the upper switch (*SA*, *SB*, or *SC*) is ON and the lower switch (*SA*′, *SB*′, or *SC*′) is OFF or, vice versa, the upper switch is OFF and the lower switch is ON.

Since only two combinations of states of the switches in each leg are allowed, a switching variable can be assigned to each phase of the inverter. In effect, only eight logic states are permitted for the whole power circuit.

Defining the switching variables as

$$a=\begin{cases}0 \text{ if } SA \text{ is OFF and } SA' \text{ is ON,}\\ 1 \text{ if } SA \text{ is ON and } SA' \text{ is OFF,}\end{cases} \tag{6.88}$$

$$b=\begin{cases}0 \text{ if } SB \text{ is OFF and } SB' \text{ is ON,}\\ 1 \text{ if } SB \text{ is ON and } SB' \text{ is OFF,}\end{cases} \tag{6.89}$$

$$c=\begin{cases}0 \text{ if } SC \text{ is OFF and } SC' \text{ is ON,}\\ 1 \text{ if } SC \text{ is ON and } SC' \text{ is OFF,}\end{cases} \tag{6.90}$$

the instantaneous values of the line-to-line output voltage of the inverter are given by

$$v_{ab} = V_{dc}(a-b), \tag{6.91}$$

$$v_{bc} = V_{dc}(b-c), \tag{6.92}$$

$$v_{ca} = V_{dc}(c-a), \tag{6.93}$$

where V_{dc} is the voltage of the DC supply of the inverter.

In a balanced three-phase system, the line-to-neutral voltage can be calculated from the line-to-line voltages as[3]

$$v_a = \frac{1}{3}(v_{ab}-v_{ca}), \tag{6.94}$$

$$v_b = \frac{1}{3}(v_{bc}-v_{ab}), \tag{6.95}$$

$$v_c = \frac{1}{3}(v_{ca}-v_{bc}). \tag{6.96}$$

Hence, after substituting equations (6.88) to (6.90) into equations (6.94) to (6.96), the line-to-neutral voltages are given by

$$v_a = \frac{V_{dc}}{3}(2a-b-c), \tag{6.97}$$

$$v_b = \frac{V_{dc}}{3}(2b-c-a), \tag{6.98}$$

$$v_c = \frac{V_{dc}}{3}(2c-a-b). \tag{6.99}$$

From (6.91) to (6.93), the line-to-line voltages can assume only three values: $-V_{dc}$, 0, and V_{dc}. However, equations (6.97) through (6.99) give five line-to-neutral voltage values: $(-2/3)V_{dc}$, $-(1/3)V_{dc}$, 0, $(1/3)V_{dc}$, and $(2/3)V_{dc}$. The eight logic states of the inverter can be numbered from 0 to 7 using the

decimal equivalent of binary number abc_2. For example, if $a=1$, $b=0$, and $c=1$, then $abc_2=101_2=5_{10}$ and the inverter is said to be in state 5. Taking V_{dc} as the base voltage, and at state 5, the per-unit output voltages are $v_{ab}=1$, $v_{bc}=-1$, $v_{ca}=0$, $v_a=1/3$, $v_b=-2/3$, *and* $v_c=1/3$.

Performing the *abc* to *dq* transformation, the output voltage can be represented as space vectors, the stator reference frame, each vector corresponding to a given state of the inverter. The space vector diagrams of line-to-line voltages (identified by the superscript *LTL*) and line-to-neutral voltages (identified by the superscript *LTN*) of the voltage source inverter are shown in Figure 6.35. The vectors are presented in the per-unit format.

6.2.6.1 Voltage Control in Voltage Source Inverter

A large number of different PWM technologies have been developed and implemented in practical inverters. Currently, one of the most popular methods is based on the concept of space vectors of the inverter voltages, as shown in Figure 6.35. This method is more suitable for application with the field orientation control of induction motor drives.

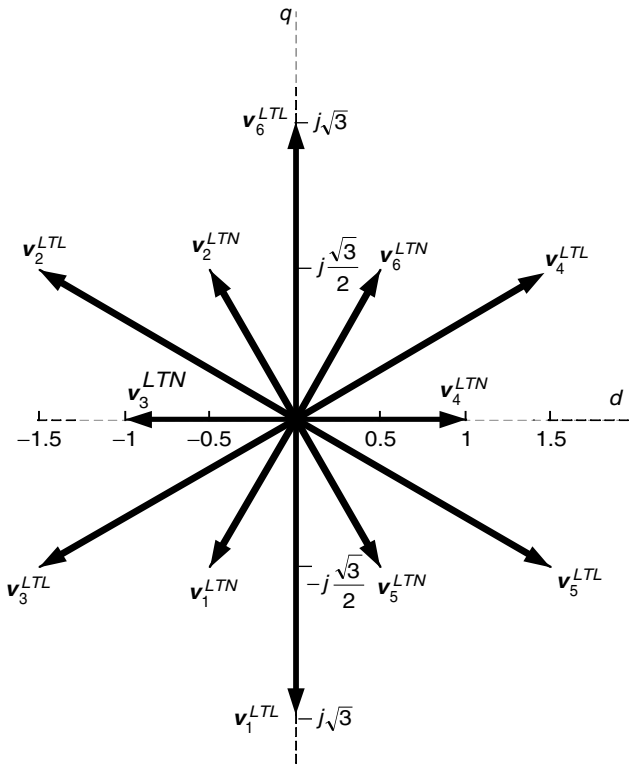

FIGURE 6.35
Space vectors of output voltage of a voltage source inverter

For a wye-connected induction motor, the load currents are generated by the line-to-neutral voltages of the inverter. Thus, the motor operation is controlled by the line-to-neutral voltage inverter voltages.

Space vectors of the line-to-neutral voltages are shown in Figure 6.36, together with an arbitrary vector v^*, to be generated by the inverter. In addition to showing six nonzero vectors (states 1 to 6), another two zero vectors, corresponding to states 0 and 7, are also shown. Clearly, only vectors v_0 to v_7, further referred to as base vectors, can be produced at a given instant of time. Therefore, vector v^* represents an average rather than an instantaneous value, the average being taken over a period of switching, or sampling, interval, which, in practice, constitute a small fraction of the cycle of the output frequency. The switching interval, at the center of which the reference vector is located, is shown in Figure 6.36 as the shaded segment.

The nonzero base vectors divide the cycle into six, 60°-wide sectors. The desired voltage vector v^*, located in a given sector, can be synthesized as a linear combination of the two adjacent base vectors, v_x and v_y, which are framing the sector, and either one of the two zero vectors. That is,

$$v^* = d_x v_x + d_y v_y + d_z v_z, \tag{6.100}$$

where v_z is the zero vector and d_x, d_y, and d_z denote the duty ratios of the states of x, y, and z within the switching interval, respectively. For instance, the reference voltage vector v^*, in Figure 6.36, is located within the first

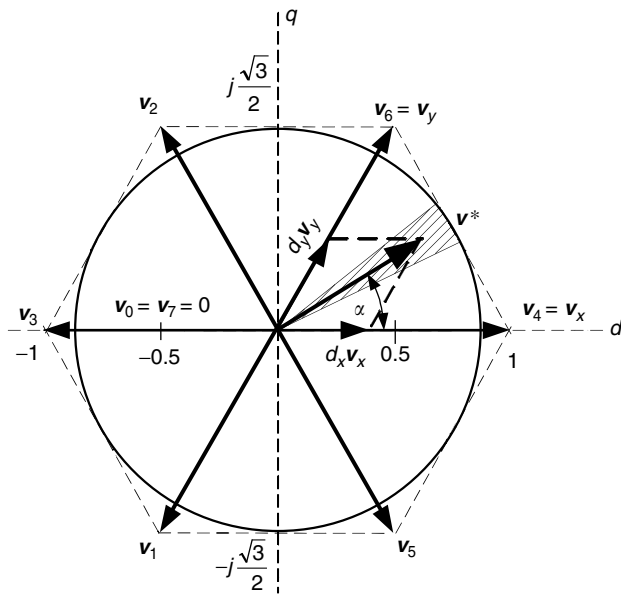

FIGURE 6.36
Illustration of the space vector PWM strategy

sector in which $v_x = v_4$ and $v_y = v_6$; hence, it can be produced by an appropriately timed sequence of states 4, 6, and 0 or 7 of the inverter.

The state duty ratio is defined as the ratio of the duration of the state to the duration of the switching interval. Therefore,

$$d_x + d_y + d_z = 1. \tag{6.101}$$

It can be seen that under this condition the locus of the maximum available vectors v^* constitutes the hexagonal envelop of the base vectors, as shown in Figure 6.36. To avoid low-order voltage harmonics, resulting from the noncircular shape of the envelope, the locus of the synthesized voltage vectors is, in practice, limited to the circle as shown in Figure 6.36. Consequently, the maximum available magnitude, V_{max}, of the resulting voltage is $(\sqrt{3}/2)V_{dc}$. With respect to vector v^*, in Figure 6.36, equation (6.100) can be written as

$$\boldsymbol{v}^* = MV_{max}e^{j\alpha} = d_x\boldsymbol{v}_4 + d_y\boldsymbol{v}_6 + d_z\boldsymbol{v}_z, \tag{6.102}$$

where M is the modulation index, adjustable within the 0 to 1 range and α denotes the angular position of the vector v^* inside the sector, that is, the angular distance between vectors v^* and v_x. As seen in Figure 6.36, $v_x = v_4 = 1 + j0$ p.u., $v_y = v_6 = 1/2 + j\sqrt{3}/2$ p.u., and v_z (either v_0 or v_7) is zero, and $V_{max} = \sqrt{3}/2V_{dc}$; equation (6.100) can be rewritten as

$$\frac{\sqrt{3}}{2}M\cos(\alpha) = d_x + \frac{1}{2}d_y \tag{6.103}$$

and

$$\frac{\sqrt{3}}{2}M\sin(\alpha) = \frac{\sqrt{3}}{2}d_y. \tag{6.104}$$

Thus, d_x and d_y can be expressed as

$$d_x = M\sin(60^\circ - \alpha), \tag{6.105}$$

$$d_x = M\sin(\alpha), \tag{6.106}$$

and

$$d_z = 1 - d_x - d_y. \tag{6.107}$$

The same equations can be applied to the other sectors.

The simple algebraic formulas (6.105) to (6.107) allow duty ratios of the consecutive logic states of an inverter to be computed in real time. Due to the freedom of choice of the zero vectors, various state sequences can be enforced in a given sector. Particularly efficient operation of the inverter is obtained when the state sequences in consecutive switching interval are

$$|x-y-z|z-y-x|\ldots, \tag{6.108}$$

where $z = 0$ in sectors $v_6 - v_2$, $v_3 - v_1$, *and* $v_5 - v_4$, and $z = 7$ in the remaining sectors. Figure 6.37 shows an example of switching signals and output voltages for a voltage source inverter in the previously described PWM mode with $M = 0.7$ and 20° width of the switching interval.[3]

6.2.6.2 Current Control in Voltage Source Inverter

Since the output currents of an inverter depend on load, feed forward current control is not feasible and a feedback from current sensors is required. There exist a number of different control technologies. The simplest one is the controller, based on the so-called "hysteretic" or "bang–bang."

The block diagram of a current control voltage source inverter is shown in Figure 6.38. The output currents, i_a, i_b, and i_c, of the inverter are sensed and compared with the reference current signals, i_a^*, i_b^*, and i_c^*. Current error signals, Δi_a, Δi_b, and Δi_c, are then applied to the hysteresis current controller, which generates switching signals, *a b*, and *c*, for the inverter switches.

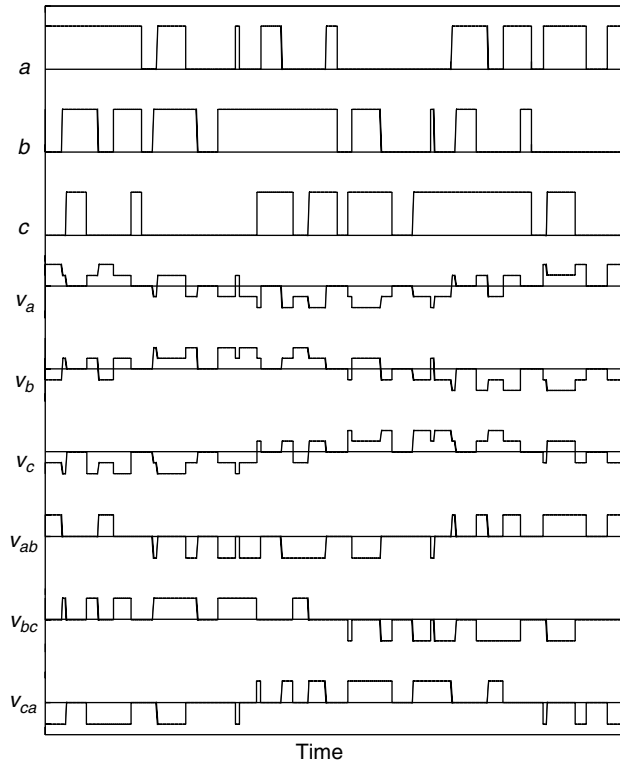

FIGURE 6.37
Example switching signals and output voltage for voltage source inverter in the PWM operation mode

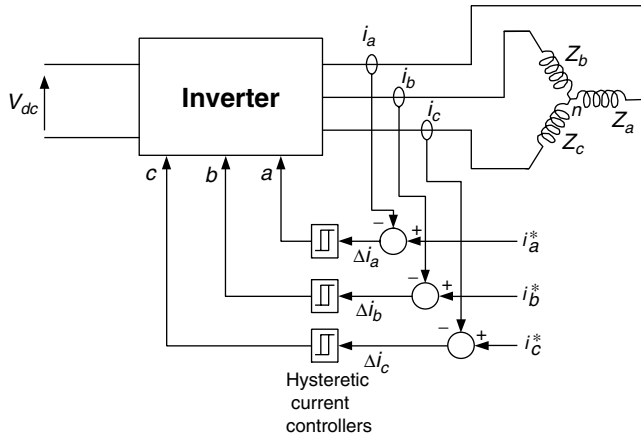

FIGURE 6.38
Block diagram of a current-controlled voltage source inverter

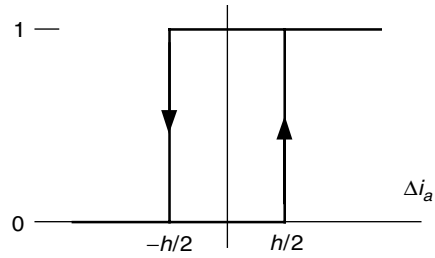

FIGURE 6.39
Input–output characteristics of a hysteresis current controller

The input–output characteristic of the phase-*a* hysteretic current controller is shown in Figure 6.39. The width of the hysteretic loop, denoted by h, represents the tolerance bandwidth for the controlled current. If the current error, Δi_a, is greater than $h/2$, that is, i_a is unacceptably lower than the reference current, i_a^*, then the corresponding line-to-neutral voltage, v_a, must be increased. From equation (6.97), this voltage is most strongly affected by the switch variable a; hence, it is this variable that is regulated by the controller, and is set to a 1 in the described situation. Conversely, an error less than $-h/2$ results in $a = 0$, in order to decrease the current i_a to stay within the tolerance band. The other two controllers operate in a similar manner.

The width, h, of the tolerance band affects the switching frequency of the inverter. The narrower the band, the more frequent the switching takes place and the higher the quality of the current s. This is illustrated in Figure 6.40 and Figure 6.41, in which the switching variables, line-to-neutral voltages, and currents for an inverter supply a resistive-plus-inductive load at values of $h = 10$

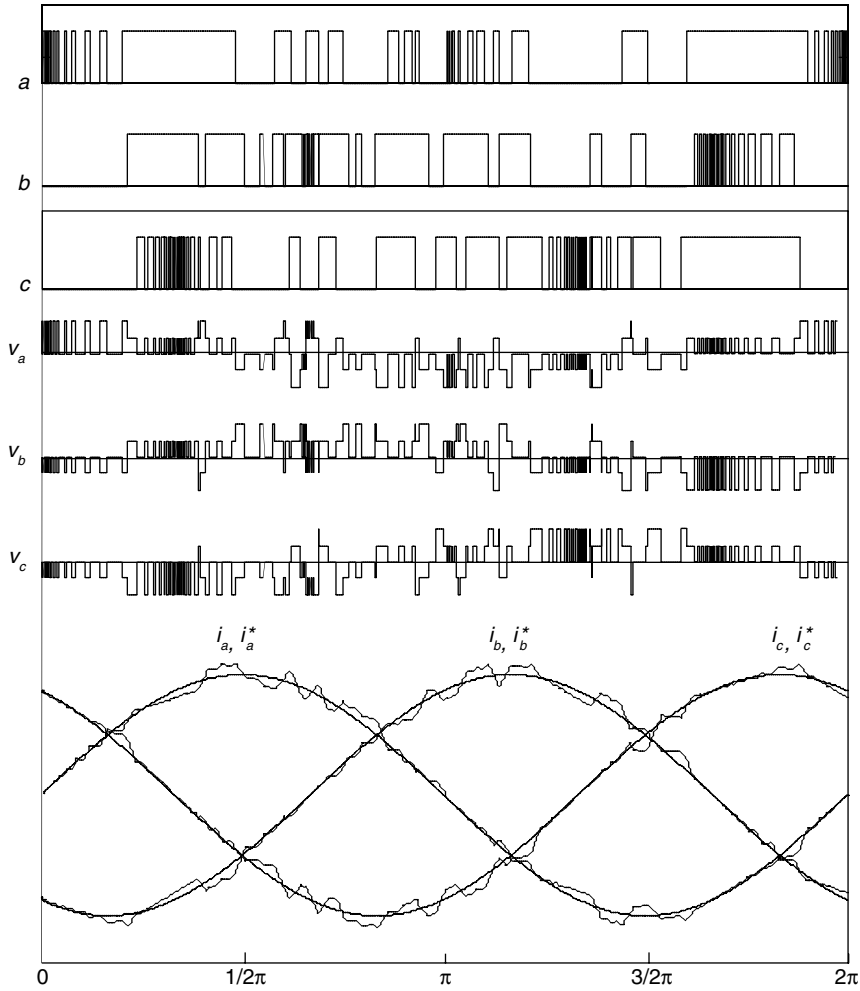

FIGURE 6.40
Current-controlled voltage source inverter (10% tolerance bandwidth)

and 5% of the amplitude of the reference current, respectively. In practice, the tolerance bandwidth should be set to a value that represents an optimal trade-off between the quality of the currents and the efficiency of the inverter.

6.3 Permanent Magnetic Brush-Less DC Motor Drives

By using high-energy permanent magnets as the field excitation mechanism, a permanent magnet motor drive can be potentially designed with high power

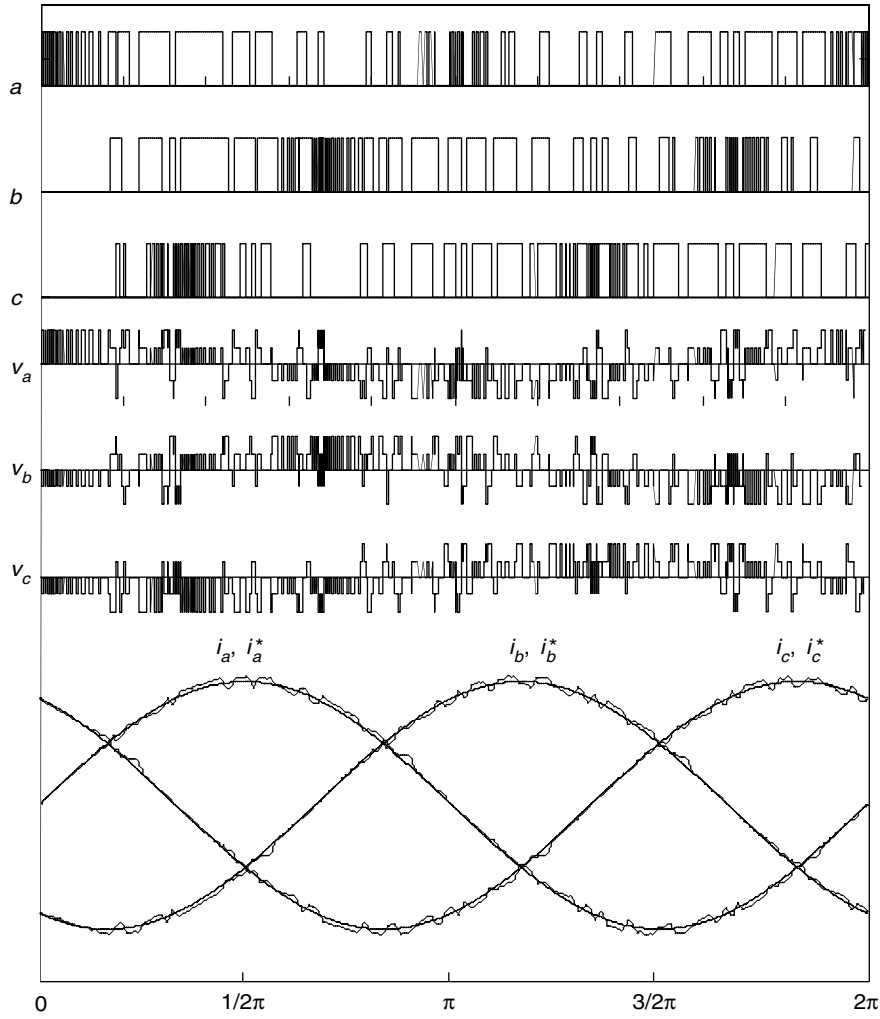

FIGURE 6.41
Current-controlled voltage source inverter (5% tolerance bandwidth)

density, high speed, and high operation efficiency. These prominent advantages are quite attractive to the application on electric and hybrid electric vehicles. Of the family of permanent magnetic motors, the brush-less DC (BLDC) motor drive is the most promising candidate for EV and HEV application.[40]

The major advantages of BLDC motor include:

- High efficiency: BLDC motors are the most efficient of all electric motors. This is due to the use of permanent magnets for the excitation, which consume no power. The absence of a mechanical commutator and brushes means low mechanical friction losses and therefore higher efficiency.

- Compactness: The recent introduction of high-energy density magnets (rare-earth magnets) has allowed achieving very high flux densities in the BLDC motor. This makes it possible to achieve accordingly high torques, which in turns allows making the motor small and light.
- Ease of control: The BLDC motor can be controlled as easily as a DC motor because the control variables are easily accessible and constant throughout the operation of the motor.
- Ease of cooling: There is no current circulation in the rotor. Therefore, the rotor of a BLDC motor does not heat up. The only heat production is on the stator, which is easier to cool than the rotor because it is static and on the periphery of the motor.
- Low maintenance, great longevity, and reliability: The absence of brushes and mechanical commutators suppresses the need for associated regular maintenance and suppresses the risk of failure associated with these elements. The longevity is therefore only a function of the winding insulation, bearings, and magnet life-length.
- Low noise emissions: There is no noise associated with the commutation because it is electronic and not mechanical. The driving converter switching frequency is high enough so that the harmonics are not audible.

However, BLDC motor drives also suffer from some disadvantages such as:

- Cost: Rare-earth magnets are much more expensive than other magnets and result in an increased motor cost.
- Limited constant power range: A large constant power range is crucial to achieving high vehicle efficiencies. The permanent magnet BLDC motor is incapable of achieving a maximum speed greater than twice the base speed.
- Safety: Large rare-earth permanent magnets are dangerous during the construction of the motor because they may attract flying metallic objects toward them. In case of vehicle wreck, if the wheel is spinning freely, the motor is still excited by its magnets and high voltage is present at the motor terminals that can possibly endanger the passengers or rescuers.
- Magnet demagnetization: Magnets can be demagnetized by large opposing mmfs and high temperatures. The critical demagnetization force is different for each magnet material. Great care must be exercised when cooling the motor, especially if it is built compact.
- High-speed capability: The surface-mounted permanent magnet motors cannot reach high speeds because of the limited mechanical strength of the assembly between the rotor yoke and the permanent magnets.
- Inverter failures in BLDC motor drives: Because of the permanent magnets on the rotor, BLDC motors present major risks in case of

short circuit failures of the inverter. Indeed, the rotating rotor is always energized and constantly induces an EMF in the short-circuited windings. A very large current circulates in those windings and an accordingly large torque tends to block the rotor. The dangers of blocking one or several wheels of a vehicle are nonnegligible. If the rear wheels are blocked while the front wheels are spinning, the vehicle will spin uncontrollably. If the front wheels are blocked, the driver has no directional control over the vehicle. If only one wheel is blocked, it will induce a yaw torque that will tend to spin the vehicle, which will be difficult to control. In addition to the dangers to the vehicle, it should be noted that the large current resulting from an inverter short circuit poses a risk of demagnetizing and destroying the permanent magnets.

Open circuit faults in BLDC motor drives are no direct threat to vehicle stability. The impossibility of controlling a motor due to an open circuit may, however, pose problems in terms of controlling the vehicle. Because the magnets are always energized and cannot be controlled, it is difficult to control a BLDC motor in order to minimize the fault. This is a particularly important issue when the BLDC motor operates in its constant power region. Indeed, in this region, a flux is generated by the stator to oppose the magnet flux and allow the motor to rotate at higher speeds. If the stator flux disappears, the magnet flux will induce a large EMF in the windings, which can be harmful to the electronics or passengers.

6.3.1 Basic Principles of BLDC Motor Drives

A BDLC motor drive consists mainly of the brush-less DC machine, a DSP-based controller, and a power electronics-based power converter, as shown in Figure 6.42. Position sensors $H1$, $H2$, and $H3$ sense the position of the machine rotor. The rotor position information is fed to the DSP-based controller, which, in turn, supplies gating signals to the power converter by turning on and turning off the proper stator pole windings of the machine. In this way, the torque and speed of the machines are controlled.

6.3.2 BLDC Machine Construction and Classification

BLDC machines can be categorized by the position of the rotor permanent magnet, the way in which the magnets are mounted on the rotor. The magnets can either be surface-mounted or interior-mounted.

Figure 6.43(a) shows the surface-mounted permanent magnet rotor. Each permanent magnet is mounted on the surface of the rotor. It is easy to build, and specially skewed poles are easily magnetized on this surface-mounted type to minimize cogging torque. But there is a possibility that it will fly apart during high-speed operations.

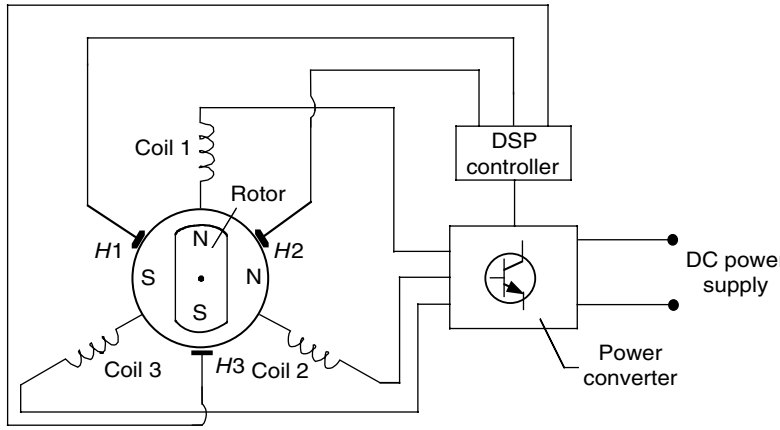

FIGURE 6.42
BLDC motor

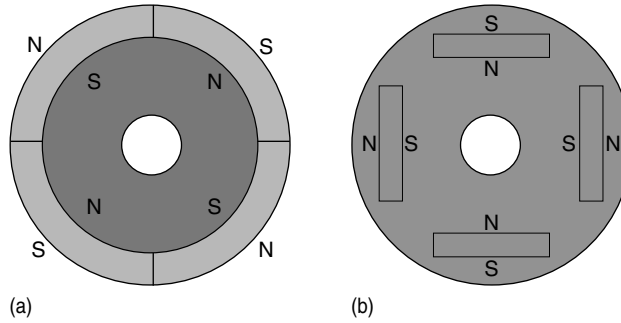

FIGURE 6.43
Cross-sectional view of the permanent magnet rotor: (a) surface-mounted PM rotor and (b) interior-mounted PM rotor

Figure 6.43(b) shows the interior-mounted permanent magnet rotor. Each permanent magnet is mounted inside the rotor. It is not as common as the surface-mounted type but it is a good candidate for high-speed operations. Note that there is inductance variation for this type of rotor because the permanent magnet part is equivalent to air in the magnetic circuit calculation.

In the case of the stator windings, there are two major classes of BLDC motor drives, both of which can be characterized by the shapes of their respective back EMF waveforms: trapezoidal and sinusoidal.

The trapezoidal-shaped back EMF BLDC motor is designed to develop trapezoidal back EMF waveforms. It has the following ideal characteristics:

1. Rectangular distribution of magnet flux in the air gap
2. Rectangular current waveform
3. Concentrated stator windings.

Excitation waveforms take the form of quasisquare current waveforms with two 60° electrical intervals of zero current excitation per cycle. The nature of the excitation waveforms for trapezoidal back EMF permits some important system simplifications compared to sinusoidal back EMF machines. In particular, the resolution requirements for the rotor position sensor are much lower since only six commutation instants are necessary per electrical cycle. Figure 6.44 shows the winding configuration of the trapezoidal-shaped back EMF BLDC machine.

Figure 6.45(a) shows an equivalent circuit and (b) shows trapezoidal back EMF, current profiles, and Hall sensor signals of the three-phase BLDC motor drive. The voltages seen in this figure, e_a, e_b, and e_c, are the line-to-neutral back EMF voltages, the result of the permanent-magnet flux crossing the air gap in a radial direction and cutting the coils of the stator at a rate proportional to the rotor speed. The coils of the stator are positioned in the standard three-phase full-pitch, concentrated arrangement, and thus the phase trapezoidal back EMF waveforms are displaced by 120° electrical degrees. The current pulse generation is a "120° on and 60° off" type, meaning each phase current is flowing for two thirds of an electrical 360° period, 120° positively and 120° negatively. To drive the motor with maximum and constant torque/ampere, it is desired that the line current pulses be synchronized with the line-neutral back EMF voltages of the particular phase.

A sinusoidal-shaped back EMF BLDC motor is designed to develop sinusoidal back EMF waveforms. It has the following ideal characteristics:

1. Sinusoidal distribution of magnet flux in the air gap
2. Sinusoidal current waveforms
3. Sinusoidal distribution of stator conductors.

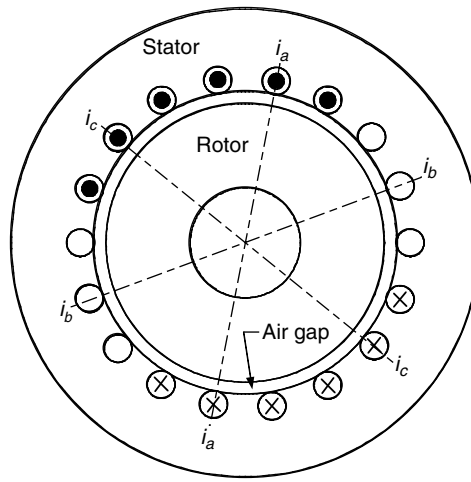

FIGURE 6.44
Winding configuration of the trapezoidal-shaped back EMF BLDC

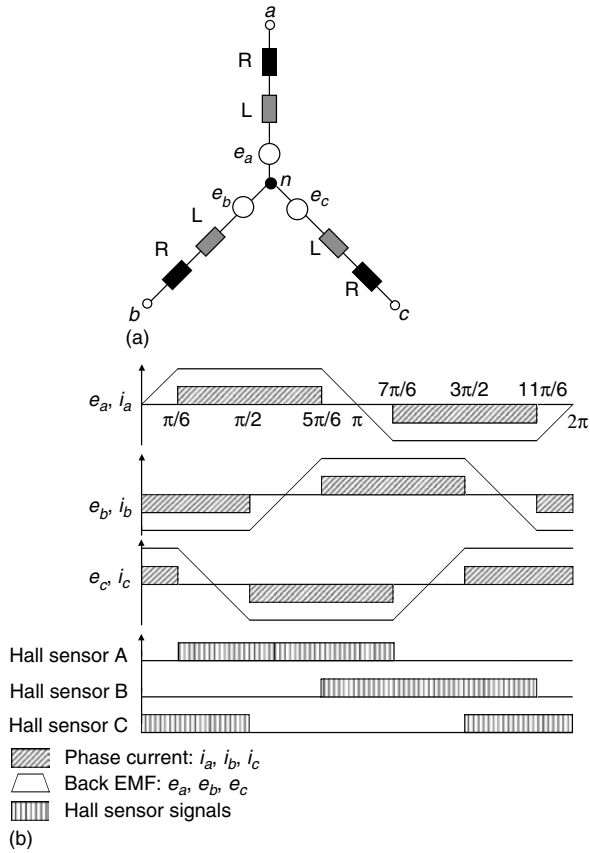

FIGURE 6.45
(a) Three-phase equivalent circuit and (b) back EMFs, currents, and Hall sensor signals of a BLDC motor

The most fundamental aspect of the sinusoidal-shaped back EMF motor is that the back EMF generated in each phase winding by the rotation of the magnet should be a sinusoidal wave function of rotor angle. The drive operation of the sinusoidal-shaped back EMF BLDC machine is similar to the AC synchronous motor. It has a rotating stator MMF wave like a synchronous motor and therefore can be analyzed with a phasor diagram. Figure 6.46 shows the winding configuration of the sinusoidal-shaped back EMF BLDC machine.

6.3.3 Properties of PM Materials

There are three classes of permanent magnet materials currently used for electric motors:

1. Alnicos (Al, Ni, Co, Fe)
2. Ceramics (ferrites), for example, barium ferrets $BaO \times 6Fe_2O_3$ and strontium ferrite $SrO \times 6Fe_2O_3$

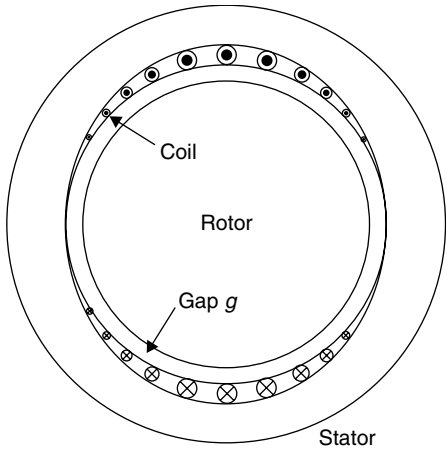

FIGURE 6.46
Winging configuration of sinusoidal-shaped back EMF BLDC

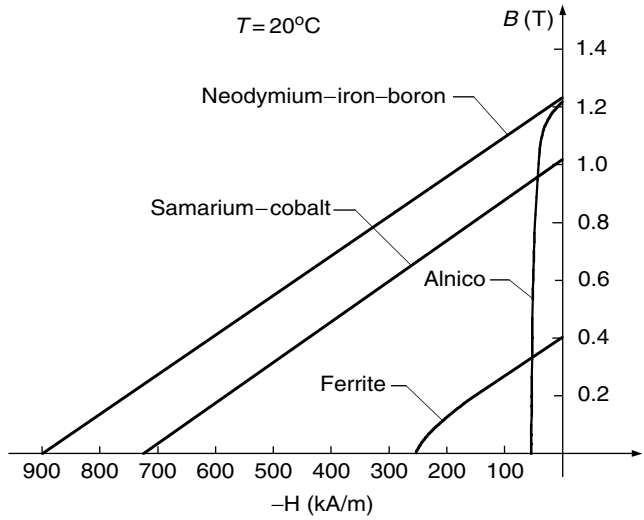

FIGURE 6.47
Demagnetization curves for different PM materials

3. Rare-earth materials, that is, samarium–cobalt SmCO and neodymium–iron–boron NdFeB.

Demagnetization curves of the above PM materials are shown in Figure 6.47.[6]

6.3.3.1 Alnico

The main advantages of Alnico are its high magnetic remanent flux density and low-temperature coefficients. The temperature coefficient of its remanent magnetic flux density B_r, or remanence, is 0.02%/°C and the maximum

service temperature is 520ºC. These advantages allow quite a high airgap flux density and high operating temperature. Unfortunately, coercive force is very low and the demagnetization curve is extremely nonlinear. Therefore, it is very easy not only to magnetize but also to demagnetize Alnico. Alnico magnets have been used in motors having ratings in the range of a few watts to 150 kW. Alnicos dominated the PM industry from the mid-1940s to about 1970, when ferrites became the most widely used materials.[6]

6.3.3.2 Ferrites

Barium and strontium ferrites were invented in the 1950s. A ferrite has a higher coercive force than that of Alnico, but at the same time has a lower remanent magnetic flux density. Temperature coefficients are relatively high, that is, the coefficient of B_r is 0.20%/ºC and the coefficient of coercive field strength, H_c, or coercivity is 0.27%/ºC. The maximum service temperature is 400ºC. The main advantages of ferrites are their low cost and very high electric resistance, which means that there are no eddy-current losses in the PM volume.

6.3.3.3 Rare-Earth PMs

During the last three decades, great progress regarding available energy density $(BH)_{max}$ has been achieved with the development of rare-earth PMs. The first generation of the rare-earth PMs based on the composition of samarium–cobalt ($SmCo_5$) was invented in the 1960s and has been produced commercially since the early 1970s. Today, it is a well-established hard magnetic material. $SmCo_5$ has the advantages of high remanent flux density, high coercive force, high-energy production, linear demagnetization curve, and low temperature coefficient. The temperature coefficient of B_r is 0.03 to 0.045%/ºC and the temperature coefficient of H_c is 0.14 to 0.40%/ºC. The maximum service temperature is 250 to 300ºC. It is well suited for building motors with low volume and, consequently with, high specific power and low moment of inertia. The cost is the only drawback. Both Sm and Co are relatively expensive due to their supply restriction.

With the discovery of a second generation of rare-earth magnets based on inexpensive neodymium (Nd) and iron in the recent years, remarkable progress with regard to lowering raw material cost has been achieved. NdFeB magnets, which are now produced in increasing quantities, have better magnetic properties than those of SmCo, but only at room temperature. The demagnetization curves, especially the coercive force, are strongly temperature dependent. The temperature coefficient of B_r is 0.095 to 0.15%/ºC and the temperature coefficient of H_c is 0.40 to 0.7%/ºC. The maximum service temperature is 150ºC and Curie temperature is 310ºC.

The latest grades of NdFeB have better thermal stability, enabling an increase in working temperature by 50ºC, and offer greatly improved resistance to corrosion.[6]

6.3.4 Performance Analysis and Control of BLDC Machines

Speed–torque performance is most important for traction and other applications. As in any other electric machine, the torque is produced by the interaction of magnetic field and current. The magnetic field is produced in BLDC by the permanent magnet and the current depends on the source voltage, control, and the back EMF, which is determined by the magnetic field and speed of the machine. To obtain the desired torque and speed at a given load, the current needs to be controlled.

6.3.4.1 Performance Analysis

The performance analysis of the BLDC machines is based on the following assumptions:

1. The motor is not saturated
2. Stator resistances of all the windings are equal and self and mutual inductances are constant
3. Power semiconductor devices in the inverter are ideal
4. Iron losses are negligible.

A simplified equivalent circuit of one phase is shown in Figure 6.48, where V_t is the voltage of the power supply, R_s is the resistance of the winding, L_s is leakage inductance ($L_s = L - M$, where L is the self-inductance of the winding and M is mutual inductance), and E_s is the back EMF induced in the winding by the rotating rotor.

Based on the equivalent circuit of Figure 6.47, the performance of the BLDC motor can be described by

$$V_t = R_s I_s + L_s \frac{dI_s}{dt} + E_s, \tag{6.109}$$

$$E_s = k_E \omega_r, \tag{6.110}$$

$$T_e = k_T I_s, \tag{6.111}$$

$$T_e = T_L + J\frac{d\omega_r}{dt} + B\omega_r, \tag{6.112}$$

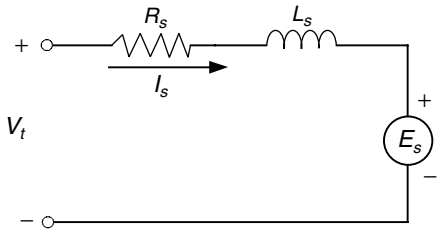

FIGURE 6.48
Simplified equivalent circuit of BLDC motor

where k_E is the back EMF constant, which is associated with the PMs and rotor structure, ω_r is the angular velocity of the rotor, k_T is the torque constant, T_L is load torque, and B is the viscous resistance coefficient. For steady-state operation, (6.109) to (6.111) can be simply reduced to

$$T_e = \frac{(V_t - k_E\omega_r)k_T}{R_s}. \tag{6.113}$$

The speed–torque performance with constant voltage supply is shown in Figure 6.49. It can be seen from Figure 6.48 that at low speed, especially while starting, very high torque is produced, which results in very high current due to the low back EMF. This very high current could damage the stator windings.

With variable voltage supply, the winding current can be restricted to its maximum by actively controlling the voltage; thus, a maximum constant torque can be produced as shown in Figure 6.50.

For dynamic or transient operations, the performance of the BLDC machine is described by (6.109) to (6.112). However, Laplace transform helps to simplify the analysis. Equations (6.109) to (6.112) can be expressed by their

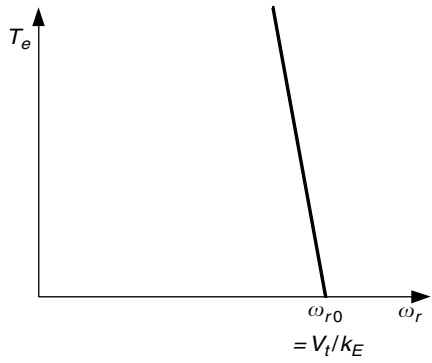

FIGURE 6.49
Speed–torque curve at steady state with constant voltage

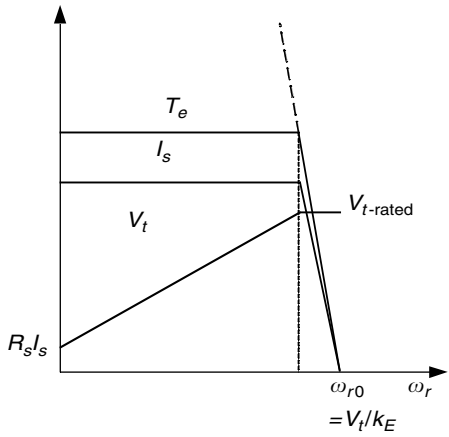

FIGURE 6.50
Speed–torque curve at steady state with variable voltage supply

Laplace forms as

$$V_t(s) = E_s(s) + (R_s + sL_s)I_s(s), \tag{6.114}$$

$$E_s(s) = k_E\omega_r(s), \tag{6.115}$$

$$T_e(s) = k_T I_s(s), \tag{6.116}$$

$$T_e(s) = T_L(s) + (B + sJ)\omega_r(s). \tag{6.117}$$

Thus, the transfer function of the BLDC motor drive system is

$$\omega_r(s) = \frac{k_T}{(R_s + sL_s)(sJ + B) + k_T k_E} V_t(s) - \frac{R_s + sL_s}{(R_s + sL_s)(sJ + B) + k_T k_E} T_L(s). \tag{6.118}$$

L_s and J in (6.118) stand for the electrical and mechanical delay in transient operations. L_s determines how quickly the armature current builds up in response to a step change in the terminal voltage, where the rotor speed is assumed to be constant. J determines how quickly the speed builds up in response to a step change in the terminal voltage.

6.3.4.2 Control of BLDC Motor Drives

In vehicle traction application, the torque produced is required to follow the torque desired by the driver and commanded through the accelerator and brake pedals. Thus, torque control is the basic requirement.

Figure 6.51 shows a block diagram of a torque control scheme for a BLDC motor drive. The desired current I^* is derived from the commanded torque T^* through a torque controller. The current controller and commutation sequencer receive the desired current I^* position information from the position sensors, and perhaps the current feedback through current transducers, and then produces gating signals. These gating signals are sent to the three-phase inverter (power converter) to produce the phase current desired by the BLDC machine.

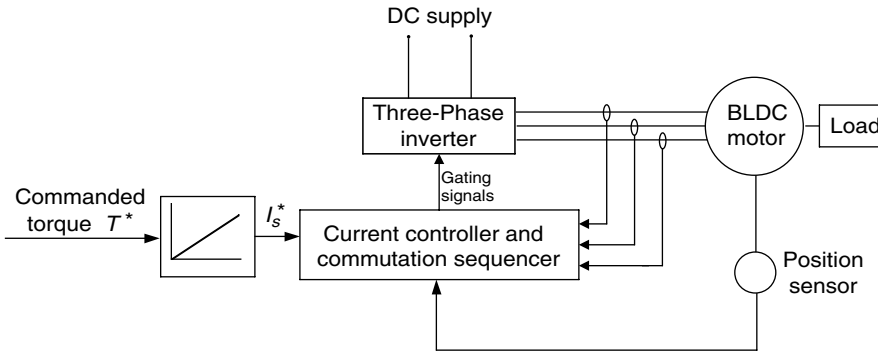

FIGURE 6.51
Block diagram of the torque control of the BLDC motor

In traction application, speed control may be required, cruising control operation, for example (see Figure 6.52). Many high-performance applications include current feedback for torque control. At the minimum, a DC bus current feedback is required to protect the drive and machine from overcurrents. The controller blocks, "speed controller" may be any type of classical controller such as a PI controller, or a more advanced controller such as an artificial intelligence control. The "current controller and commutation sequencer" provides the properly sequenced gating signals to the "three-phase inverter" while comparing sensed currents to a reference to maintain a constant peak current control by hysteresis (current chopping) or with a voltage source (PWM)-type current control. Using position information, the commutation sequencer causes the inverter to "electronically commutate," acting as the mechanical commutator of a conventional DC machine. The commutation angle associated with a brush-less motor is normally set so that the motor will commutate around the peak of the torque angle curve. Considering a three-phase motor, connected in delta or wye, commutation occurs at electrical angles, which are $\pm 30^{o}$ (electrical) from the peaks of the torque–angle curves. When the motor position moves beyond the peaks by an amount equal to 30^{o} (electrical), then the commutation sensors cause the stator phase excitation to switch to move the motor suddenly to -30^{o} relative to the peak of the next torque–angle curve.[77]

6.3.5 Extension of Speed Technology

As discussed above, PM BLDC machines inherently have a short constant power range due to their rather limited field weakening capability. This is a result of the presence of the PM field, which can only be weakened through the production of a stator field component that opposes the rotor magnetic field. The speed ratio, x, is usually less than 2.[8]

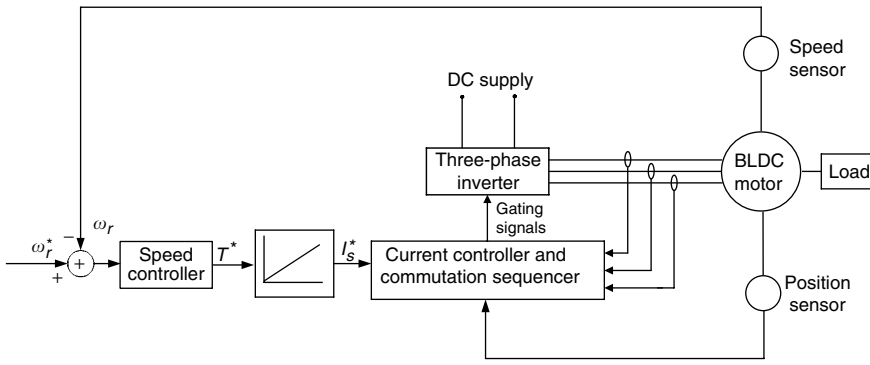

FIGURE 6.52
Block diagram of the speed control of the BLDC motor

Recently, the use of additional field windings to extend the speed range of PM BLDC motors has been developed.[1] The key is to control the field current in such a way that the air gap field provided by PMs can be weakened during high-speed constant-power operation. Due to the presence of both PMs and the field windings, these motors are called PM hybrid motors. The PM hybrid motor can achieve a speed ratio of around 4. The optimal efficiency profiles of a PM hybrid motor drive are shown in Figure 6.53.[1] However, the PM hybrid motors have the drawback of a relatively complex structure. The speed ratio is still not enough to meet the vehicle performance requirement, especially in an off-road vehicle. Thus, a multigear transmission is required.

6.3.6 Sensorless Techniques

As mentioned above, the operation of the BLDC motor drives relies mostly on position sensors for obtaining the rotor position information so as to perform the turn on or turn off of each phase properly.[55] The position sensor is usually either a three-element Hall-effect sensor or an optical encoder. These position sensors are high-cost, fragile elements. Thus, their presence not only enhances the cost of the motor drive but also seriously lowers its reliability and limits its application in some environments, such as a military one. Position sensorless technology can effectively continue the operation of the system in case the position sensors lose their function. This is crucial in some applications, such as in military vehicles.

Several sensorless technologies have been developed. The majority of them are based on voltage, current, and back EMF detection. These techniques can be primarily grouped into four categories:

1. Those using measured currents, voltages, fundamental machine equations, and algebraic manipulations
2. Those using observers

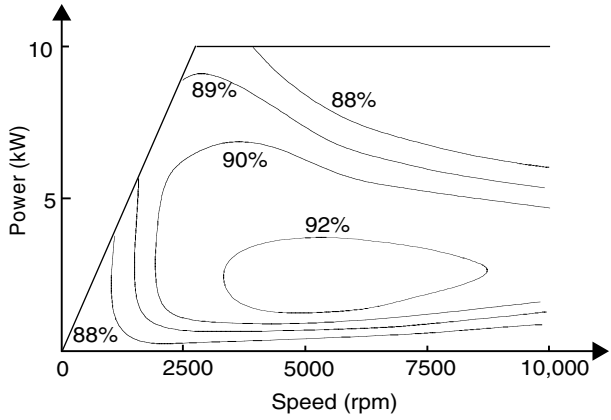

FIGURE 6.53
Optimal efficiency profiles of a PM hybrid motor drive[1]

3. Those using back EMF methods
4. Those with novel techniques not falling into the previous three categories.

6.3.6.1 Methods Using Measurables and Math

This method consists of two subtypes: (1) those that calculate the flux linkages using measured voltages and currents and (2) those that utilize a model's prediction of a measurable voltage or current, compare the model's value with the actual measured voltage or current, and calculate the change in position, proportional to the difference between the measured and actual voltage or current.

The first subtype is seen in references.[9–16] The fundamental idea is to calculate the flux linkage from the measured voltage and current:

$$\Psi = \int_0^t (V - Ri)\, d\tau. \tag{6.119}$$

With a knowledge of initial position, machine parameters, and the flux linkages' relationship with rotor position, the rotor position can be determined. By determining the rate of change of the flux linkage from the integration results, the speed can also be determined. An advantage of the flux-calculating method is that line–line voltages may be used in the calculations and thus no motor neutral is required.[55] This is beneficial, as the most common BLDC configuration is Y-connected with no neutral.

The second subtype is shown in references.[17–20] This method consists of first developing an accurate *d–q* model of the machine. Utilizing the measured currents and a *d–q* transformation, the output voltages of the model are compared to the measured and transformed voltages. The difference is proportional to the difference in angular reference between the model's coordinate system and the actual coordinate system, which is the rotor position with reference to the actual coordinate system's reference. Conversely, they have also used the measured voltages and found the differences in the currents. In either case, the difference between the measured (and transformed) and the calculated is used as the multiplier in an updated equation for the rotor position.

6.3.6.2 Methods Using Observers

These methods determine the rotor position and/or speed using observers. The first of these considered are those utilizing the well-known Kalman filter as a position estimator.[21–26] One of the first of these to appear in the printed literature was by M. Schroedl in 1988. In his many publications, Schroedl utilized various methods of measuring system voltages and currents, which could produce rough estimates of the angular rotor position. The Kalman filtering added additional refinements to the first estimates of

position and speed. Other observer-based systems include those utilizing nonlinear,[27–29] full-order,[9,30,31] and sliding-mode [11,18,32] observers.

6.3.6.3 Methods Using Back EMF Sensing

Using back EMF sensing is the majority approach in sensorless control technology of the BLDC motor drive. This approach consists of several methods, such as (1) terminal voltage sensing method, (2) third-harmonic back EMF sensing method, (3) freewheeling diode conduction, and (4) back EMF integration.

Terminal voltage sensing: In normal operation of the BLDC motors, the flat part of a phase back EMF is aligned with the phase current. The switching instants of the converter can be obtained by knowing the zero crossing of the back EMF and a speed-dependent period of time delay.[33]

Since the back EMF is zero at rest and proportional to speed, it is not possible to use the terminal voltage sensing method to obtain a switching pattern at low speeds. As the speed increases, the average terminal voltage increases, and the frequency of excitation increases. The capacitive reactance in the filters varies with the frequency of excitation, introducing a speed-dependent delay in switching instants. This speed-dependent reactance disturbs current alignment with the back EMF and field orientation, which causes problems at higher speeds. In this method, a reduced speed operating range is normally used, typically around 1000 to 6000 rpm. This method is a good method for steady state; however, phase differences in the circuits used due to speed variations do not allow optimal torque/amp over a wide speed range.

Third-harmonic back EMF sensing: Rather than using the fundamental of the phase back EMF waveform as in the previous technique, the third harmonic of the back EMF can be used in the determination of switching instants in the wye connected 120° current conduction operating mode of the BLDC motor.[34] This method is not as sensitive to phase delay as the zero voltage crossing method, since the frequency to be filtered is three times as high. The reactance of the filter capacitor in this case dominates the phase angle output of the filter more so than at the lower frequency. This method provides a wider speed range than the zero-crossing method, does not introduce as much phase delay as the zero-crossing method, and requires less filtering.

Freewheeling diode conduction: This method uses the indirect sensing of the zero crossing of the phase back EMF to obtain the switching instants of the BLDC motor.[35] In the 120° conducting Y-connected BLDC motor, one of the phases is always open-circuited. For a short period after opening the phase, there phase current remains flowing, via a freewheeling diode, due to the inductance of the windings. This open-phase current becomes zero in the middle of the commutation interval, which corresponds to the point where the back EMF of the open phase crosses zero. The largest downfall of this method is the requirement of six additional isolated power supplies for the comparator circuitry of each freewheeling diode.

Back EMF integration: In this method, position information is extracted by integrating the back EMF of the unexcited phase.[36–39] The integration is based on the absolute value of the open phase's back EMF. Integration of the voltage divider scaled-down back EMF starts when the open phase's back EMF crosses zero. A threshold is set to stop the integration, which corresponds to a commutation instant. As the back EMF is assumed to vary linearly from positive to negative (trapezoidal back EMF assumed), and this linear slope is assumed to be speed-insensitive, the threshold voltage is kept constant throughout the speed range. If desired, current advance can be implemented by changing the threshold. Once the integrated value reaches the threshold voltage, a reset signal is asserted to zero the integrator output.

This approach is less sensitive to switching noise and automatically adjusts to speed changes, but the low-speed operation is poor. With this type of sensorless operation scheme, up to 3600 rpm has been reported.[39]

6.3.6.4 Unique Sensorless Techniques

The following sensorless methods are completely original and unique. These range from artificial intelligence methods to variations in the machine structure. The first of the novel methods to be considered are those utilizing artificial intelligence, that is, artificial neural networks (ANN) and fuzzy logic. In reference,[39] they utilized a neural network using the back-propagation training algorithm (BPN) to act as a nonlinear function implementation between measured phase voltages and currents, which were inputs, and rotor position, which was the output. Using the equations in the above method, the flux linkage can be calculated using the measured voltages, currents, and system parameters.

Utilizing fuzzy logic[41] proposes two fuzzy logic subsystems in an application. Using the conventional equations of phase voltages and currents, the rotor position can be calculated.[55] With a knowledge of the relationships between these measurables and the rotor position, a fuzzy Mamdami-type system was developed to produce rotor position estimates. It was noted that this could have been accomplished just as easily with look-up tables; however, for the desired resolution the size of the look-up tables becomes unmanageably large. The second fuzzy system took as input the estimated rotor position and produced reference current values for two different drive strategies: unity power factor and maximum torque per amp.

In reference,[42] an additional stator lamination with equally spaced slots around the periphery is added to the end of the machine. Each of the slots contains a small sensing coil. The local magnetic circuit variations for each of the sensing coils is affected by the PM rotor's position. A 20 kHz signal is injected through the coils. The signal distortions are analyzed at the terminals of the sensing coils, the second harmonic yielding position information. An artificial saliency was created in reference[42] by attaching small pieces of aluminum to the surface of the permanent magnets. The flow of eddy currents in the aluminum acts to increase the reluctance of the various

windings' magnetic circuits, thus causing changes in the winding's inductances with rotor position.

6.4 Switched Reluctance Motor Drives

The switched reluctance motor (SRM) drive is considered to be an attractive candidate for variable speed motor drives due to its low cost, rugged structure, reliable converter topology, high efficiency over a wide speed range, and simplicity in control.[43,44] These drives are suitable for EVs, electric traction applications, automotive applications, aircraft starter/generator systems, mining drives, washing machines, door actuators, etc.[48,50,51]

The SRM has a simple, rugged, and low-cost structure. It has no PM or winding on the rotor. This structure not only reduces the cost of the SRM but also offers high-speed operation capability for this motor. Unlike the induction and PM machines, the SRM is capable of high-speed operation without the concern of mechanical failures that result from the high-level centrifugal force. In addition, the inverter of the SRM drive has a reliable topology. The stator windings are connected in series with the upper and lower switches of the inverter. This topology can prevent the shoot-through fault that exists in the induction and permanent motor drive inverter. Moreover, high efficiency over a wide speed range and control simplicity are known merits of the SRM drive.[43,47]

A conventional SRM drive system consists of the switched reluctance motor, power inverter, sensors such as voltage, current, and position sensors, and control circuitry such as the DSP controller and its peripherals, as shown in Figure 6.54. Through proper control, high performance can be achieved in the SRM drive system.[43,44]

The SRM drive inverter is connected to a DC power supply, which can be derived from the utility lines through a front-end diode rectifier or from batteries. The phase windings of the SRM are connected to the power inverter, as shown in Figure 6.55. The control circuit provides a gating signal to the switches of the inverter according to particular control strategies and the signals from various sensors.

6.4.1 Basic Magnetic Structure

The SRM has salient poles on both the stator and rotor. It has concentrated windings on the stator and no winding or PM on the rotor. There are several configurations for SRM depending on the number and size of the rotor and stator poles. The configurations of the 8/6 and 6/4 SRM, which are more common, are shown in Figure 6.56.

Due to its double saliency structure, the reluctance of the flux path for a phase winding varies with the rotor position. Also, since the SRM is

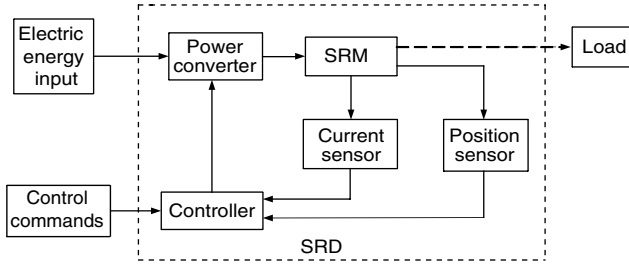

FIGURE 6.54
SRM drive system

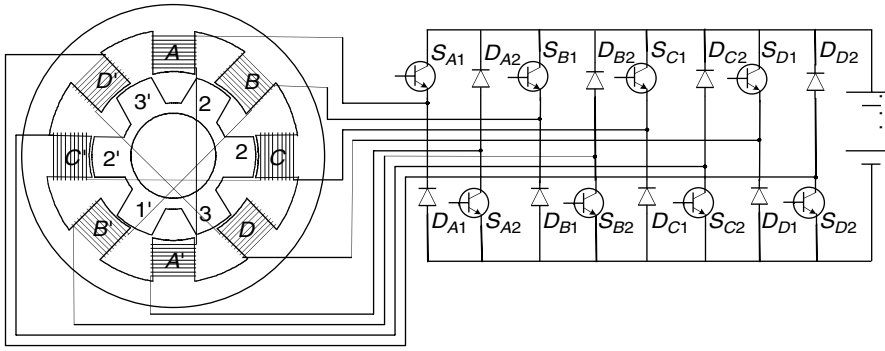

FIGURE 6.55
SRM and its power supply

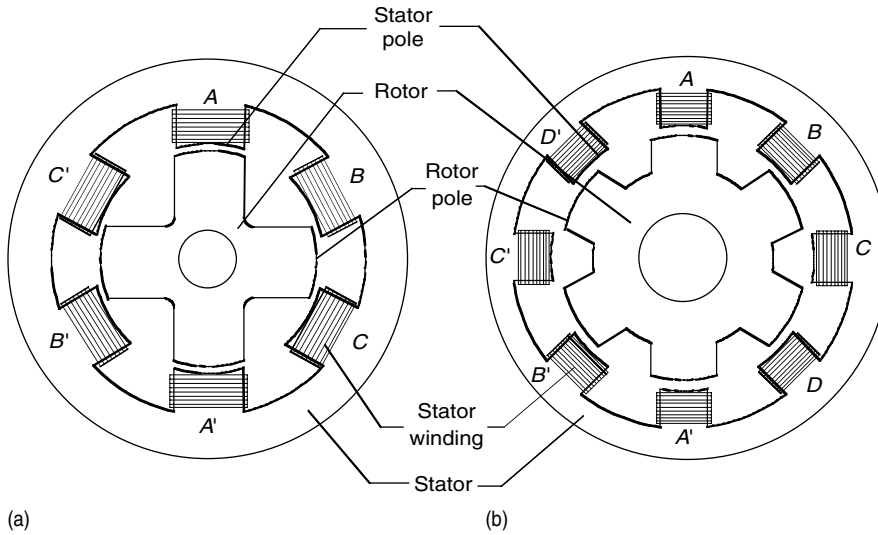

FIGURE 6.56
Cross-section of common SRM configurations: (a) a 6/4 SRM and (b) a 8/6 SRM

commonly designed for high degree saturation at high phase current, the reluctance of the flux path also varies with the phase current. As a result, the stator flux linkage, phase bulk inductance, and phase incremental inductance all vary with the rotor position and phase current.

The phase voltage equation of the SRM (Figure 6.55) is given by

$$V_j = Ri_j + \frac{d}{dt}\sum_{k=1}^{m}\lambda_{jk}, \tag{6.120}$$

where m is the total number of phases, V_j is the applied voltage to phase j, i_j is the current in phase j, R is the winding resistance per phase, λ_{jk} is the flux linkage of phase j due to the current of phase k, and t is the time. The phase flux linkage, λ_{jk}, is given by

$$\lambda_{jk} = L_{jk}(i_{k,\theta},\theta)i_k, \tag{6.121}$$

where L_{jk} is the mutual inductance between phase k and phase j. Mutual inductance between phases is usually small compared to the bulk inductance and is neglected in equations.

At a fixed phase current, as the rotor moves from the unaligned to the aligned position, the reluctance of the flux path reduces due to the reduction in the air gap. As a result, the phase inductance and flux linkage increase as the rotor moves. At a fixed rotor position, as the phase current increases, the flux path becomes more and more saturated. Hence, the reluctance of the flux path reduces as the phase current increases. As a result, the phase bulk inductance drops with an increase in the phase current. But the phase flux linkage still increases as the phase current increases due to enhancement in the excitation. The variations of the phase bulk inductance and flux linkage with respect to the phase current and rotor position for an 8/6 SRM are shown in Figure 6.50 and Figure 6.51, respectively. In these figures, $\theta = -30^{\circ}$ and 0° represent the unaligned and aligned rotor position of the referred SRM, respectively.

Substituting (6.121) into (6.120), one can have

$$\begin{aligned} V_j &= Ri_j + \frac{d}{dt}\sum_{k=1}^{m}\lambda_{jk} = Ri_j + \sum_{k=1}^{m}\left\{\frac{\partial\lambda_{jk}}{\partial i_k}\frac{di_k}{dt} + \frac{\partial\lambda_{jk}}{\partial\theta}\frac{d\theta}{dt}\right\} \\ &= Ri_j + \sum_{k=1}^{m}\left\{\frac{\partial(L_{jk}i_k)}{\partial i_k}\frac{di_k}{dt} + \frac{\partial(L_{jk}i_k)}{\partial\theta}\omega\right\} \\ &= Ri_j + \sum_{k=1}^{m}\left\{\left(L_{jk} + i_k\frac{\partial L_{jk}}{\partial i_k}\right)\frac{di_k}{dt} + i_k\frac{\partial L_{jk}}{\partial\theta}\omega\right\}. \end{aligned} \tag{6.122}$$

When only one phase is energized in the operation, equation (6.122) can be written as

$$V_j = Ri_j + \left(L_{jj} + i_j\frac{\partial L_{jj}}{\partial i_j}\right)\frac{di_j}{dt} + i_J\frac{\partial L_{jj}}{\partial\theta}\omega. \tag{6.123}$$

The third term in equation (6.123) is the back EMF. The phase incremental inductance is defined as the derivative of the phase flux linkage against the phase current as

$$l_{jj} = \frac{\partial \lambda_{jj}}{\partial i_j} = L_{jj} + i_j \frac{\partial L_{jj}}{\partial i_j}, \tag{6.124}$$

where $l_{jj}(i,\theta)$ and $L_{jj}(i,\theta)$ are the phase incremental inductance and bulk inductance, respectively. Figure 6.57 shows a typical example of flux linkage varying with rotor position, θ, and phase current i of an SRM. Figure 6.58 shows typical variation of phase bulk inductance with rotor position and phase current.

When the magnetic flux is not saturated, the flux linkage varies linearly with the phase current. The incremental inductance can be viewed as equal to the phase bulk inductance. However, if the machine is saturated at a certain phase current and rotor position, the phase incremental inductance does not equal the phase bulk inductance any more. The variation of the phase incremental inductance with respect to the phase current and rotor position can be derived from the variation of the phase linkage with respect to the phase current and rotor position. The variation of the phase incremental inductance with respect to the phase current and rotor position for an 8/6 SRM is shown in Figure 6.59.

6.4.2 Torque Production

Torque in SRM is produced by the tendency of the rotor to get into alignment with the excited stator poles. The analytical expression of the torque can be derived using the derivative of the coenergy against the rotor position at a given current.

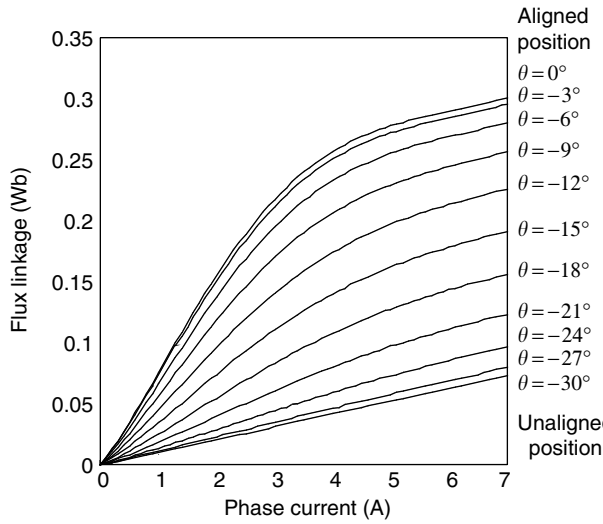

FIGURE 6.57
Variation of phase flux linkage with rotor position and phase current

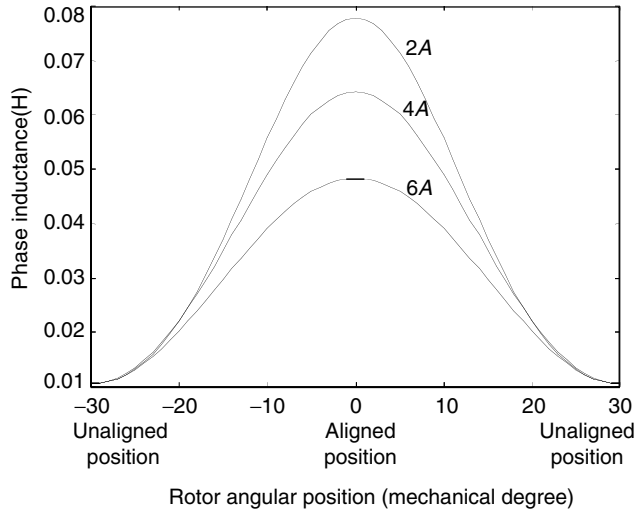

FIGURE 6.58
Variation of phase bulk inductance with rotor position and phase current

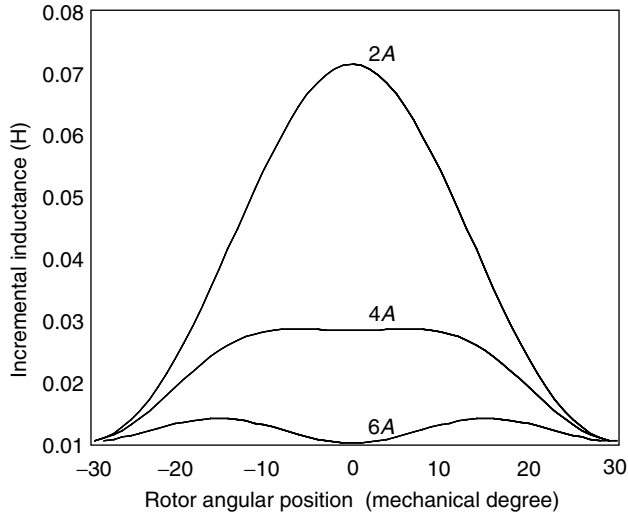

FIGURE 6.59
Variation of phase incremental inductance with rotor position and phase current for a typical 8/6 SRM

For a phase coil with current i linking a flux λ, the stored field energy W_f and the coenergy W'_f are indicated as shaded regions as shown in Figure 6.60. Coenergy can be found from the definite integral:

$$W'_f = \int_0^i \lambda \, di. \tag{6.125}$$

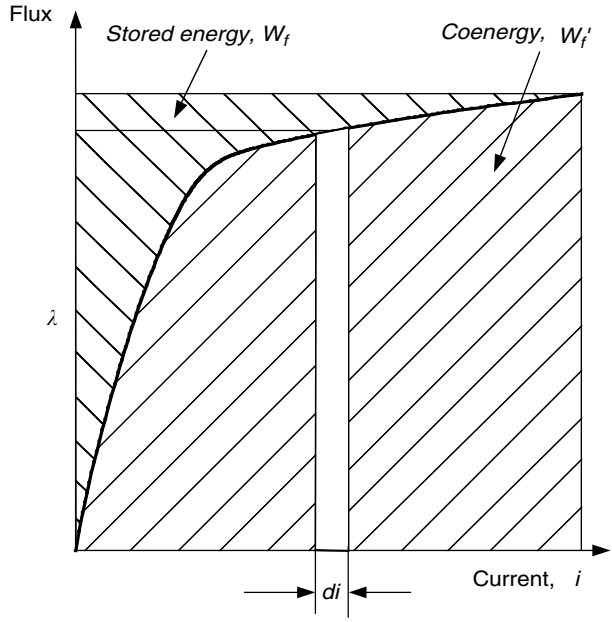

FIGURE 6.60
Stored field energy and coenergy

The torque produced by one phase coil at any rotor position is given by

$$T = \left[\frac{\partial W_f'}{\partial \theta}\right]_{i=constant}. \tag{6.126}$$

In the case of flux being linear with current, for example, in an unsaturated field, the magnetization curve in Figure 6.60 would be a straight line and the coenergy would be equal to the stored field energy. The instantaneous torque can be given as

$$T = \frac{1}{2} i^2 \frac{dL(\theta)}{d\theta}, \tag{6.127}$$

where L is the unsaturated phase bulk inductance.

In the case of a saturated phase, the torque cannot be calculated by a simple algebra equation; instead, an integral equation such as

$$T = \int_0^i \frac{\partial L(\theta, i)}{\partial \theta} i \, di \tag{6.128}$$

is used.

From (6.127) and (6.128), it can be seen that in order to produce positive torque (motoring torque) in SRM, the phase has to be excited when the phase bulk inductance increases as the rotor rotates. It can also be observed from

(6.127) and (6.128) that the phase current can be unidirectional for motoring torque production. Hence, low cost and reliable inverter topology introduced in the later section can be used for the SRM drive. Figure 6.61 shows the ideal phase inductance, current, and torque of the SRM. Positive (motoring) torque is produced if the phase is excited when the phase inductance is increasing as the rotor rotates. Negative torque is generated if the phase is excited when the phase inductance is dropping as the rotor moves.[64,77] This implies that the position information is necessary for control of the SRM drive.

The output torque of an SRM is the summation of torque of all the phases:

$$T_m = \sum_{i=1}^{N} T(i, \theta), \tag{6.129}$$

where T_m and N are the output torque and phase number of motor. The relation between the motor torque and mechanical load is usually given by

$$T_m - T_l = J\frac{d\omega}{dt} + B\omega, \tag{6.130}$$

where J, B, and T_l are the moment of inertia, viscous friction, and load torque, respectively. The relation between position and speed is given by

$$\omega = \frac{d\theta}{dt}. \tag{6.131}$$

6.4.3 SRM Drive Converter

It can be seen from Figure 6.61 that the torque developed by the motor can be controlled by varying the amplitude and the timing of the current pulses

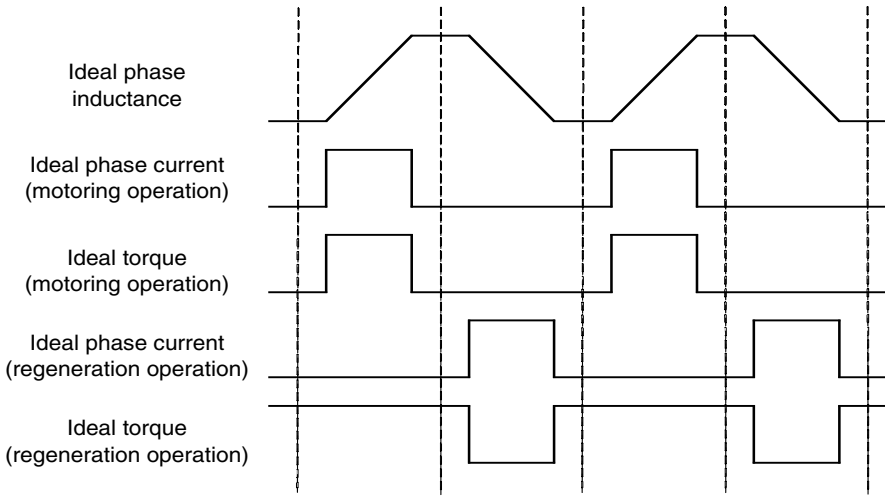

FIGURE 6.61
Idealized inductance, current, and torque profiles of the SRM

in synchronism with the rotor position. In order to control the amplitude and pulse width of the phase current, a certain type of inverter should be used.

The input to the SRM drive is DC voltage, which is usually derived from the utility through a front-end diode rectifier or from batteries. Unlike other AC machines, the currents in SR motors can be unidirectional. Hence, conventional bridge inverters used in AC motor drives are not used in SRM drives. Several configurations have been proposed for an SRM inverter in the literature;[45,46] some of the most commonly used ones are shown in Figure 6.62.

The most commonly used inverter uses two switches and two freewheeling diodes per phase and is called the classic converter. The configuration of the classic converter is shown in Figure 6.62(a). The main advantage of the classic converter is its flexibility in control. All the phases can be controlled independently, which is essential for very high-speed operations where there will be a considerable overlap between the adjacent phase currents.[5]

The operation of the classic converter is shown in Figure 6.63 by taking phase-1 as an example. When the two switches S_1 and S_2 are turned on as in

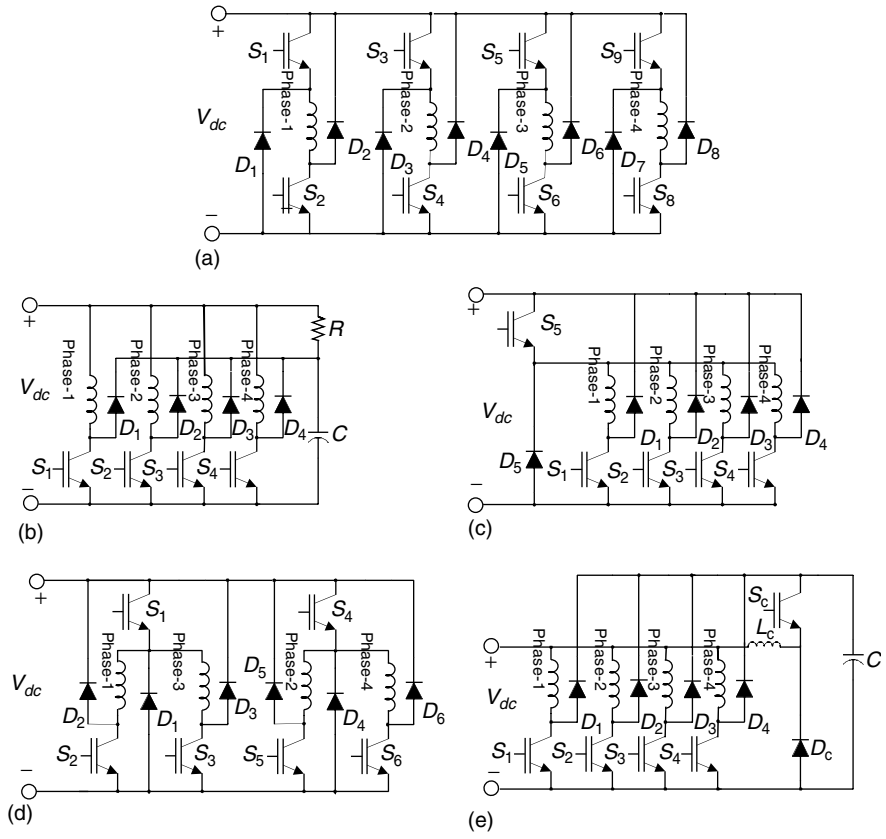

FIGURE 6.62
Different inverter topologies for SRM drives: (a) classical half bridge converter; (b) R-dump; (c) n+1 switch (Miller converter); (d) 1.5n switch converter; and (e) C-dump

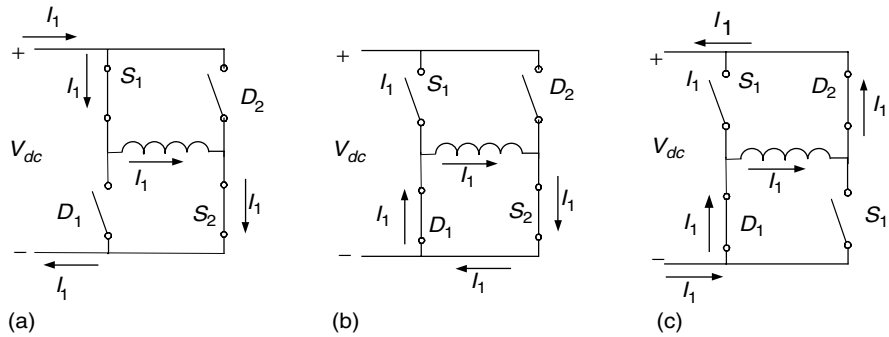

FIGURE 6.63
Modes of operation for the classic converter: (a) turning on phase mode; (b) zero voltage mode; and (c) turning off mode

Figure 6.63(a), the DC bus voltage, V_{dc}, will be applied to the phase-1 winding. Phase-1 current will increase as it flows through the path consisting of V_{dc} positive terminal, S_1, phase-1 winding, S_2, and V_{dc} negative terminal. By turning off S_1 and holding on S_2 (i.e., Figure 6.63[b]), when the phase is energized, the current freewheels through S_2 and D_1. In this mode, phase-1 is not getting or giving energy to the power supply. When S_1 and S_2 are turned off (Figure 6.63[c]), the phase-1 current will flow through D_2, V_{dc} positive terminal, V_{dc} negative terminal, D_1, and phase-1 winding. During this time, the motor phase is subjected to negative DC bus voltage through the freewheeling diodes. The energy trapped in the magnetic circuit is returned to the DC link. The phase current drops due to the negative applied phase voltage. By turning S_1 and S_2 on and off, the phase-1 current can be regulated.

The half bridge converter uses $2n$ switches and $2n$ diodes for an n-phase machine. There are several configurations that use fewer switches: for example, the R-dump-type inverter (Figure 6.62[b]) uses one switch and one diode per phase. This drive is not efficient; during turn off, the stored energy of the phase is charging capacitor C to the bus voltage and dissipating in resistor R. Also, zero voltage mode does not exist in this configuration.

An alternative configuration is an $(n+1)$ switch inverter. In this inverter, all the phases are sharing a switch and diode so that overlapping operation between phases is not possible, which is inevitable in the high-speed operation of this motor. This problem has been solved by sharing switches of each couple of nonadjacent phases, as shown in Figure 6.62(d). This configuration is limited to an even number of phases of switched reluctance motor drives.

One of the popular inverter configurations is C-dump (Figure 6.62[e]), which has the advantage of less switches and of allowing independent phase current control. In this configuration, during the turn-off time, the stored magnetic energy is charging capacitor C, and if the voltage of the capacitor reaches a certain value, for example V_c, it is transferred to the supply through switch S_c. The main disadvantage of this configuration is that the

negative voltage across the phase coil is limited to the difference between the voltage across the capacitor V_c and the system power supply voltage.

6.4.4 Modes of Operation

For SRM, there is a speed at which the back EMF is equal to the DC bus voltage. This speed is defined as the base speed. Below the base speed, the back EMF is lower than the DC bus voltage. From equation (6.125), it can be seen that when the converter switches are turned on or off to energize or de-energize the phase, the phase current will rise or drop accordingly. The phase current amplitude can be regulated from 0 to the rated value by turning the switches on or off. Maximum torque is available in this case when the phase is turned on at an unaligned position and turned off at the aligned position, and the phase current is regulated at the rated value by hysteresis or PWM control. The typical waveforms of the phase current, voltage, and flux linkage of the SRM below base speed are shown in Figure 6.64.

Above the base speed, the back EMF is higher than the DC-bus voltage. At the rotor position — where the phase has a positive inductance slope with respect to the rotor position — the phase current may drop even if the switches of the power inverter are turned on. The phase current is limited by the back EMF. In order to build high current and therefore produce high motoring torque in the SRM, the phase is usually excited ahead of the unaligned position, and the turn-on position is gradually advanced as the rotor speed increases. The back EMF increases with the rotor speed. This leads to a decrease in the phase current and hence the torque drops. If the turn-on position is advanced for building as high as possible a current in the SRM phase, the maximum SRM torque almost drops as a linear function of the reciprocal of the rotor speed. The maximum power of the SRM drive is

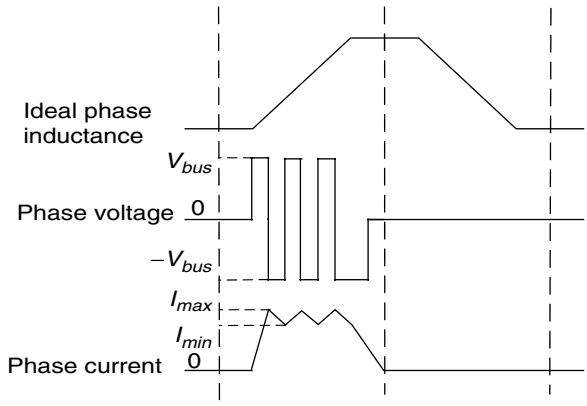

FIGURE 6.64
Low-speed (below the base speed) operation of SRM

almost constant. The typical waveforms at high-speed operations are shown in Figure 6.65.

The advancing of the phase turn-on position is limited to the position at which the phase inductance has a negative slope with respect to the rotor position. If the speed rotor further increases, no phase advancing is available for building higher current in the phase, and the torque of the SRM will drop significantly.[77] The mode is referred to as the natural mode operation. The torque–speed characteristic of the SRM is shown in Figure 6.66.

6.4.5 Generating Mode of Operation (Regenerative Braking)

Torque in the SR machines is created based on the principle of reaching the minimum reluctance for the excited phase. Therefore, if the rotor pole is approaching the excited phase, which means the bulk inductance is increasing, the torque produced is in the direction of the rotor and it is in motoring mode. But if the rotor pole is leaving the stator phase — which means the negative slope of the bulk inductance — the stator tries to keep it in alignment; the torque produced is then in the opposite direction of the movement of the rotor, and the SSR works in generating mode.

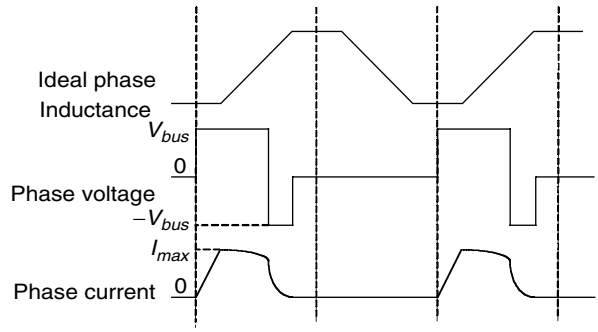

FIGURE 6.65
High-speed (above the base speed) operation of SRM

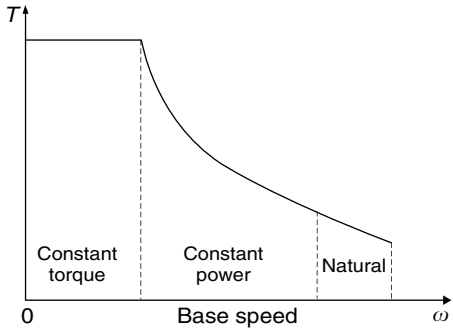

FIGURE 6.66
Torque–speed characteristic of SRM

Regenerative braking is an important issue in the propulsion drive of EVs and HEVs. There is a duality in operation of generating and motoring modes and the current waveforms in the generating modes are simply the mirror images of the waveforms in the motoring region around the alignment rotor position.[52] The SRG is a singly excited machine; thus, in order to obtain power from it, it should be excited near the rotor aligned position and then turned off before the unaligned region (Figure 6.67).

As in motoring operations, the current can be controlled by changing the turn-on and turn-off angles and current level while in low speed. Alternatively, in speeds higher than the base speed, only the turn-on and turn-off angles can be used for control.

The driving circuit for SRG is similar to the SRM's; one of the common configurations is shown in Figure 6.68. When the switches are turned on, the phase gets energy from the supply and capacitor. During the turn-off period, the freewheeling current from the motor charges up the capacitor and delivers energy to the load. Since there is no PM in this motor, during the start-up and initial condition, it needs an external source such as a battery to deliver energy to the phase; after taking transient time, the capacitor is then charged up to the output voltage. Depending on the output voltage during phase on time, both the capacitor and external source or just the capacitor provide the current to the load and the phase coil. The external source can be designed

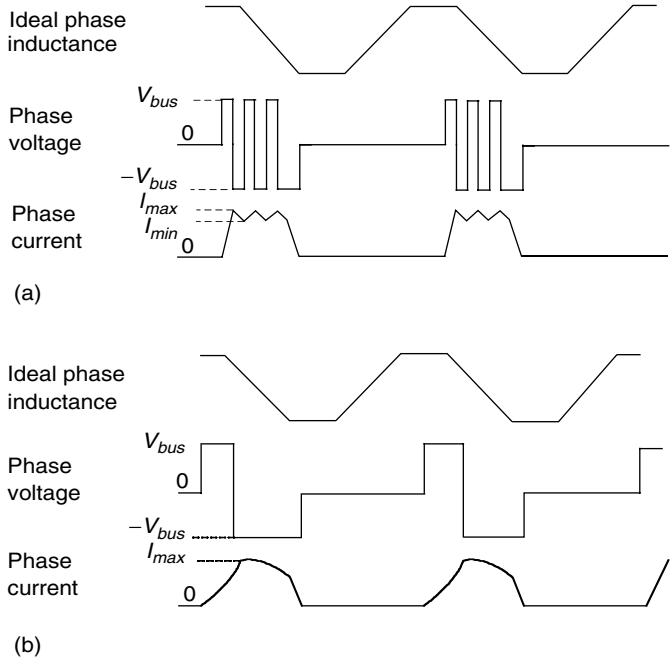

FIGURE 6.67
Low- and high-speed operation in generating mode: (a) low-speed operation in generating mode and (b) high-speed operation in generating mode

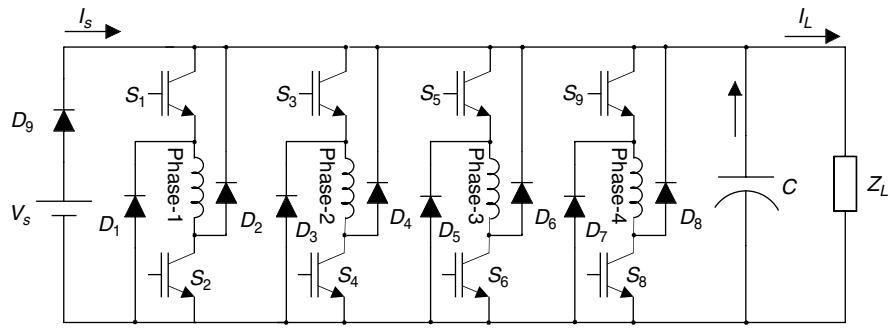

FIGURE 6.68
A driving circuit example for switched reluctance generator

to be charged, or can be disconnected from the system after the system reaches its operating point.

In the generating region, the back EMF is negative and thus it helps the phase to be charged very fast; then, during turn-off, the back EMF opposes the negative supply voltage and decreases slowly.

$$V_C - e = L\frac{di}{dt} + Ri,\ e > 0 \ \text{(during phase on period)}, \tag{6.132}$$

$$-V_C - e = L\frac{di}{dt} + Ri,\ e > 0 \ \text{(during phase off period)}. \tag{6.133}$$

In (6.132) and (6.133), V_c is the bus voltage of the inverter or, equivalently, the voltage of the bus capacitor and e is back EMF voltage.

In certain conditions such as high speed and high loads, the back EMF voltage is greater than the bus supply voltage; thus, the current increases even after turning off the phase. In addition to uncontrollable torque, this necessitates an oversized converter, thereby adding to the cost and overall size of the system. Due to variations in speed of the prime mover, the power electronic converter should be designed for the worst possible case. This will magnify the additional cost and size issues. By properly selecting the turn-off angle, this maximum generating current can be coaxed into the safe region.[49] Figure 6.69 shows the effect of turn-off angle in the maximum generating current.

6.4.6 Sensorless Control

Excitation of the SRM phases needs to be properly synchronized with the rotor position for effective control of speed, torque, and torque pulsation. A shaft position sensor is usually used to provide the rotor position. However, these discrete position sensors not only add complexity and cost to the system but

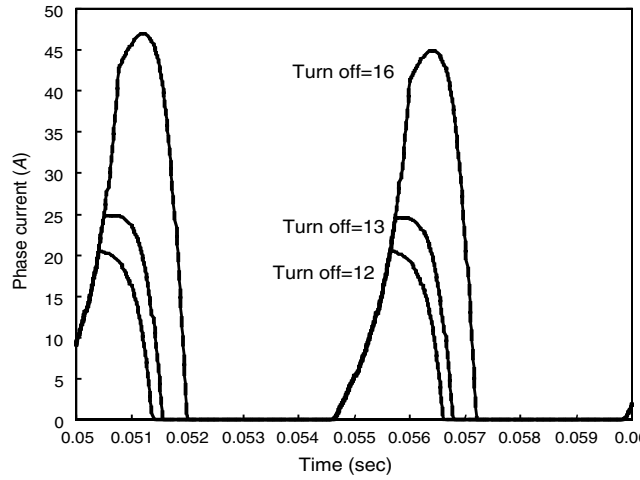

FIGURE 6.69
Effect of the turn-off angle in maximum current level in generating mode in an 8/6 switched reluctance machine

also tend to reduce the reliability of the drive system and restrict their application on some specific environment, such as military applications. Position sensorless technology can effectively continue the operation of the system, in case the position sensors lose their function. This is crucial in some applications, such as military vehicles.

Several sensorless control methods have been reported in the literature over the past two decades.[11–24] Most of these techniques are based on the fact that the magnetic status of the SRM is a function of the angular rotor position. As the rotor moves from the unaligned position toward the aligned position, the phase inductance increases from the minimum value to the maximum value. It is obvious that if the phase bulk inductance can be measured and the functional relation between the phase bulk inductance and the rotor position is known, the rotor position can be estimated according to the measured phase bulk inductance.[66]

Some sensorless techniques do not use the magnetic characteristic and voltage equation of the SRM directly to sense the rotor position. Instead, these sensorless control methods are based on the observer theory or synchronous operation method similar to that applied to conventional AC synchronous machines.

Generally, the existing sensorless control methods can be classified as:[55]

1. Phase flux linkage-based method
2. Phase inductance-based method
3. Modulated signal injected methods
4. Mutual-induced voltage-based method
5. Observer-based methods.

6.4.6.1 Phase Flux Linkage-Based Method[53]

This method uses the phase voltage and current data of the active phases to estimate the rotor position. The basic principle of this method is to use the functional relation between the phase flux linkage, phase current, and rotor position for rotor position detection. From Figure 6.57, it can be observed that if the flux linkage and phase current are known, the rotor position can be estimated accordingly, as shown in Figure 6.70.

The problem with this sensorless control method is the inaccurate estimation of the phase flux linkage at low speed. At high speed (above the base speed), the phase voltage retains its positive polarity until the phase is turned off. The V term dominates in $V-Ri$, and integration of $V-Ri$ in a relatively short period will not lead to a huge error in flux estimation. However, at low speed (below the base speed), the phase voltage changes its polarity from one hysteresis cycle to the next hysteresis cycle. When $V-Ri$ is integrated in a relatively long period, the phase voltage term cancels itself due to the excursions while the Ri term retains its polarity during the integration period — and becomes significant after a long time of integration. The error in R or i may lead to a huge error in the flux estimation in this case. Therefore, this sensorless control method is only suitable for the high-speed operation of SRM.

6.4.6.2 Phase Inductance-Based Method

Similar to the phase flux linkage, the phase bulk and incremental inductances are both functions of the phase current and rotor position. Hence, they can also be used for rotor position estimation.

6.4.6.2.1 Sensorless Control Based on Phase Bulk Inductance[56]

Using the phase flux linkage obtained as shown in Figure 6.70, the phase inductance can be obtained as

$$L_{jj}=\frac{\lambda_{jj}}{i_j}. \tag{6.134}$$

The estimated phase bulk inductance and measured phase current can be input to a prestored look-up table storing the functional relation between the phase bulk inductance and phase current and rotor position, to find the corresponding rotor position. Instead of using a look-up table, one can also use an analytical model to represent the functional relation between phase bulk inductance, phase current, and rotor position.[56]

Like the flux linkage-based method, since integration of $V-Ri$ is used for phase inductance estimation, this method is only suitable for high-speed operation. Some sensorless control methods that can work both at a standstill and at low speed, such as the open-loop method, have to be used to start the SRM and bring the rotor speed to a certain level. After the rotor speed has reached a threshold, the phase flux linkage and/or inductance are calculated using the integration method and the rotor position is estimated according to the calculated phase flux linkage and inductance.

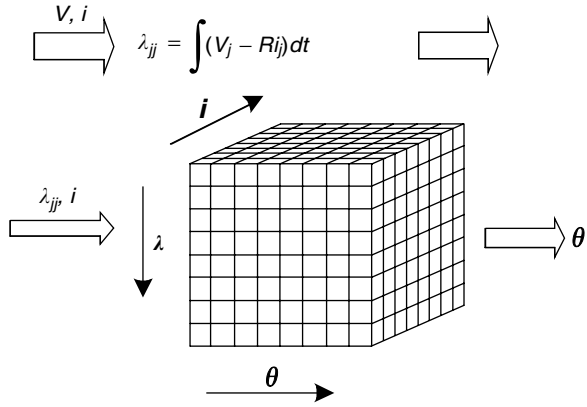

FIGURE 6.70
Flux linkage-based rotor position estimation method

6.4.6.2.2 Sensorless Control Based on Phase Incremental Inductance

The position estimation method using the phase incremental inductance utilizes the current and voltage data of the active phase for estimation of the incremental inductance of this phase, and consequently of the rotor position.

Neglecting the mutual couplings and at very low speeds (neglectable motional-EMF term $i_j[\partial L_{jj}/\partial\theta]\omega$), the incremental inductance can be obtained from (6.123) and (6.124) as

$$\ell_{jj} = \frac{V_j - Ri_j}{di_j/dt}. \tag{6.135}$$

Thus, the phase incremental inductance can be measured from the phase voltage and current. If the relation between the phase incremental inductance and rotor position is known, the rotor position can be estimated according to the estimated phase incremental inductance.

At low phase current — and therefore unsaturated phase — the phase incremental inductance can be viewed as equal to the phase bulk inductance, and monotonically increases as the rotor moves from the unaligned position to the aligned position. The incremental inductance has a one-to-one relation with the rotor position in this case. However, at high phase current, and therefore saturated phase, when the rotor moves from the unaligned position to the aligned position, the phase incremental inductance may be the same value at two or more rotor positions.[57]

Even though the phase incremental inductance does not have a one-to-one relation with the rotor position at high phase current, it can still be used for rotor position estimation. Some switched reluctance motors are designed with high degree saturation such that the phase incremental inductance at the aligned position has the minimum value at high current. In this case, the phase incremental inductance at the aligned position is unique; hence, it can

be used to detect the aligned rotor position. This rotor position estimation technique will give one rotor position at one electrical cycle.

This method does not require any extra sensing circuitry. However, it is applicable only for very low speeds, less than 10% of the base speed, because the back EMF term is neglected for calculation of the phase incremental inductance.

6.4.6.3 Modulated Signal Injection Methods

These methods are to apply a voltage to the idle phase winding and measure the resultant phase current to detect the phase inductance. This derived phase inductance will provide the rotor position information. Both an extra-low amplitude voltage source and a power converter can be used to apply a voltage to the phase winding. When an extra voltage source is used, a sinusoidal voltage is usually used for sensing the phase inductance. The phase angle and the amplitude of the resultant phase current contain the phase inductance; hence, the rotor position information can be obtained. This is the idea behind the amplitude modulation (AM) and phase modulation (PM) methods. When the power converter is used for sensing purposes, a short period voltage pulse is usually applied to the idle phase and a triangular current is induced in the corresponding phase. The changing rate of the phase current contains the phase inductance, and hence the rotor position information. This is the basic idea of the diagnostic pulse-based method.

6.4.6.3.1 Frequency Modulation Method[58,59]

This method is used to first generate a train of square wave voltage whose frequency is in reverse proportion to the instantaneous inductance of the idle phase. The circuitry used for generating a square wave voltage train whose frequency is in reverse proportion to the inductance is referred to as an *L–F* converter.

To detect the frequency of this square wave voltage train, and hence the phase inductance, the timer of a microcontroller can be used to count the frequency of the square wave voltage train. Another approach is to use a frequency to voltage converter (*F–V* converter) to obtain a voltage proportional to the frequency of the square wave voltage train, and sample this voltage using an A/D converter. In order to connect the phase winding, which is in the power circuit, to the sensing circuitry, which is in the control circuit, two photovoltaic BOSFET switches are used for each phase.

Since the signal used for position estimation in this method is an inductance-encoded frequency signal, this method is referred to as the frequency modulation (FM) method. This method is easy to implement and is robust. However, at high-speed operation the phase energizing current exists — even when the phase inductance is decreasing as the rotor moves. This restricts the signal injection to the SRM phases. Another problem with this method is that it requires additional circuitry for implementation. The cost associated with this additional circuitry may be a concern in some applications. Furthermore, it is very sensitive to mutual coupling since the current in the active phase

induces voltage in the unenergized phases, which strongly distorts the probing pulses.

6.4.6.3.2 AM and PM Methods[60]

The AM and PM techniques are based on the phase and amplitude variations, respectively, of the phase current due to the time-varying inductance when a sinusoidal voltage is applied to the phase winding in series with a resistance *R*. The current flowing through the circuit in response to the applied voltage is a function of the circuit impedance. Since the coil inductance varies periodically, the phase angle between the current and the applied voltage also varies in a periodic manner. With a large inductance, the lagging angle of the current wave behind the voltage wave is large and the peak current is small. The PM encoder technique measures the instantaneous phase angle on a continuous basis, while the AM encoder technique measures the amplitude. These instantaneous measurements contain the phase inductance information that can be obtained after passing the signals through a demodulator. The demodulator generates a signal that represents the phase inductance as a function of the rotor position. Using an inverse function or a conversion table, the rotor position can be estimated.

Since the AM and PM methods need the injection of a low-amplitude signal to one of the idle phases, the photovoltaic BOSFET switches are needed to connect the phase winding to the sensing circuitry.

Like the FM method, signal injection to one of the idle phases is restricted at high-speed operations where the torque-producing current occupies most of the electrical cycle and makes the signal injection impossible. Another disadvantage of these methods is that they require additional hardware for indirect position sensing. As stated before, they are very sensitive to mutual coupling.

6.4.6.3.3 Diagnostic Pulse-Based Method[61]

Instead of using an additional voltage source to inject the sensing signal to the idle phase, the power converter of the SRM drive can be used to provide a short period voltage pulse to the idle phase, and low-amplitude current is produced. Therefore, the back EMF, saturation effect, and the voltage drop on the winding resistance can all be neglected. From (6.123) and (6.124), the changing rate of the phase current is given as

$$\frac{di_j}{dt} = \frac{V}{L_{jj}}. \tag{6.136}$$

Equation (6.136) indicates that the phase current changing rate contains the phase inductance, and hence the rotor position information.

Similar to the case of switches being turned on, when the switches connected to the phase are turned off, the phase current freewheels through the diodes. The phase voltage equals the negative DC-bus voltage; the change rate of the current has the same expression as (6.136), but with a negative sign.

Either the current growing rate or dropping rate can be used for sensing the phase inductance. When the current changing rate is found to exceed a

threshold that is dedicated by the phase inductance at the commutation position, the phase can be commutated. This method does not require additional hardware for indirect rotor position sensing. However, at high-speed operation, the phase excitation current occupies the majority of one electrical cycle and restricts the injection of the testing signal. And like FM, AM, and PM methods, it is very sensitive to mutual coupling.

6.4.6.4 Mutually Induced Voltage-Based Method[62]

The idea of this method is based on measuring the mutually induced voltage in an idle phase, which is either adjacent or opposite to the energized phase of an SRM. The mutual voltage in the "off" phase, induced due to the current in the active phase, varies significantly with respect to the rotor position. This mutually induced voltage variation can be sensed by a simple electronic circuit. If the functional relation between the mutually induced voltage in the inactive phase due to the current in the active phase and the rotor position is known, the rotor position information can be extracted from the mutually measured induced voltage in the inactive phase. This method is only suitable for low-speed operation. Furthermore, it is very sensitive to noise since the ratio between induced voltage and system noise is small.

6.4.6.5 Observer-Based Methods[63]

In this method, state-space equations are used to describe the dynamic behavior of the SRM drive. An observer is then developed based on these nonlinear state-space differential equations for estimation of the rotor position. The input and output of this observer are phase voltage and phase current, respectively. The state variables of this observer are stator flux linkage, rotor position angle, and rotor speed. The phase current, flux linkage, rotor position, and rotor speed can be estimated using this observer. The phase current estimated by this observer is compared to the actual phase current of the SRM, and the resultant current errors are used to adjust the parameters of the observer. When the current estimated by the observer matches the actual current, the observer is considered as a correct representation of the dynamic behavior of the actual SRM drive and the rotor position estimated by the observer is used to represent the actual rotor position.

The main disadvantages of these methods are real-time implementation of complex algorithms, which require a high-speed DSP, and a significant amount of stored data. This increases the cost and speed limitations by the DSP. However, high resolution in detecting rotor position and applicability to whole speed range are some merits of these methods.

6.4.7 Self-Tuning Techniques of SRM Drives

As discussed in previous sections, the SRM drive has a simple and rugged construction — favorable characteristics for traction application. But its control is very complicated due to the nonlinearity of its magnetic circuit and

the fact that the control heavily depends on the mechanical and electrical parameters, such as air gap, resistance, etc.[67] In mass production and real-world operation, it is impossible for these parameters to have exact values and remain unchanged. For example, the air gap would be changed due to mechanical vibration wearing, and the resistance in windings and inductance would vary with temperature. These parameter variations would cause significant degradation of the drive performance if the control system cannot "know" these variations and implement corresponding corrections in the control process. Self-tuning techniques are referred to as methods of updating the control strategy in a control system.

The major purpose of self-tuning control for the SRM drive is to update the control variables in the presence of motor parameters' variations, so as to optimize the torque per ampere.[70] There are two approaches to this problem: arithmetic mean method and neural network-based method.

6.4.7.1 Self-Tuning with the Arithmetic Method

To optimize the SRM drive performance, it is necessary to maximize torque per amp through real-time optimization. The SRM drive control variables are phase current, turn-on angle, and turn-off angle. In a low-speed region, hysteresis-type current control is used to keep the commanded current constant. The chopping current band has to be optimally chosen, as there is a trade-off between the width of the band and the chopping frequency. Assuming the selected band is optimal, maximum torque per amp can be obtained by aptly tuning the turn-on angle (θ_{on}) and the turn-off angle (θ_{off}) of the phase current excitation. Computer simulations, based on a simple mathematical model, have been performed to prove the existence of a unique (θ_{on},θ_{off}) optimal pair, which gives the maximum torque per amp for a given current and speed.[27] It has been shown that the optimal values of θ_{on} and θ_{off} are bounded within the following limits:

$$\theta_{on}^{min} < \theta_{on} < 0^{\circ}, \tag{6.137}$$

$$\theta_{off}^{max} < \theta_{off} < 180^{\circ}, \tag{6.138}$$

where θ_{on}^{min} is the turn-on angle such that the current reaches the desired value at 0°and θ_{off}^{max} is the turn-off angle such that the current reduces to zero at 180°.

The intuitive selections for control angles are such as to turn on each phase exactly at its unaligned position and turn off the phase just before its aligned position. The optimal θ_{on} is not very susceptible to the change in inductance due to the parameter variations because of the large air gap at the unaligned position.[43] Hence, optimal θ_{on} calculated off-line based on the linear model is sufficient to give the optimal torque per ampere. Therefore, the optimization problem reduces to calculation of θ_{off} on-line that gives maximum torque per ampere.

6.4.7.1.1 Optimization with Balanced Inductance Profiles

To minimize the phase current for a given torque and speed, a heuristic search algorithm for finding the optimum turn-off angle[68] can be used in

which both the reference current and the turn-off angle are varied, while the PI controller maintains the speed.

The optimization algorithm is explained as follows. Initially, the default turn-off angle is used to reach the commanded speed. Then, the turn-off angle is reduced in steps. With the turn-off angle variation, the torque will either decrease or increase, and the PI controller adjusts the phase reference current according to a new value so that the speed remains at its set value. If the current reduces with change in the turn-off angle, then the direction of search is correct and is continued till the current starts increasing with further change in the turn-off angle. The step size for the turn-off angle can be a function of the operating point itself.

Once the optimization is completed for a given operating point, the optimum values of control variables — that is, the reference current and the control angles — can be stored in look-up tables so that the controller can directly pick up these values if the same operating point is to be reached in the future. This will save some amount of time and effort.

6.4.7.1.2 Optimization in the Presence of Parameter Variations

Initially, when optimization is performed, the reference currents for all the phases are kept the same, assuming that the phase inductances are balanced. If there are parameter variations, then different phases will have different optimal reference currents and turn-off angles. In order to take care of this problem, once the general optimization is complete, the control variables for the individual phases are tuned separately, that is, the reference current and turn-off angle for only one of the phases are varied at a time, while these parameters for the other phases are kept fixed. Finally, when all the phases are tuned, the optimum reference current and turn-off angle for different phases will be different if there is any parameter variation. The main advantage of using this method is that the optimization algorithm does not require any information about the degree of imbalance present in the inductance profile, which may change considerably over a period of time.

Figure 6.71 shows the current waveform of the SRM phase with default values of turn-on and turn-off angles, and Figure 6.72 shows the current waveform after applying the self-tune algorithm, which is running almost at the same operating point. By comparing the two figures, it can be seen that there is a considerable reduction in both the amplitude and the width of the phase current and hence its RMS value. The operating speeds are also the same before and after optimization for both the cases.

6.4.7.2 Self-Tuning Using an Artificial Neural Network

ANNs with highly nonlinear and adaptive structure have been used in many applications. ANNs have inherent interpolation property; hence, they are an ideal candidate for storing turn-on and turn-off angles instead of storing them in look-up tables. Figure 6.73 shows a three-layer feedforward neural

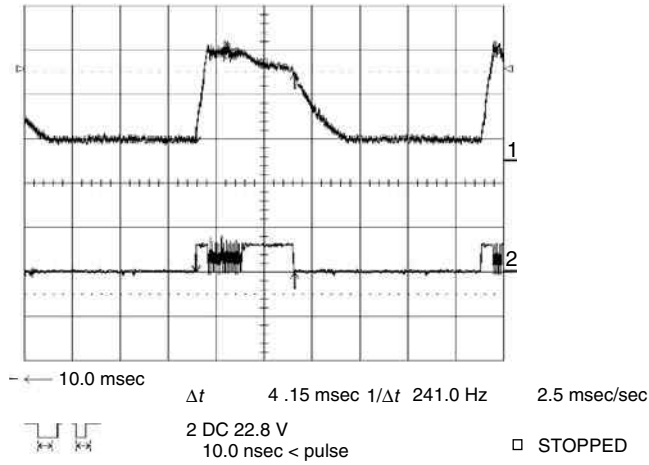

FIGURE 6.71
Phase current and gating pulse without optimization: terminal voltage, 50 V; load, 120 W; reference current, 5.5 A; speed, 1200 rpm; conduction angle, 30°

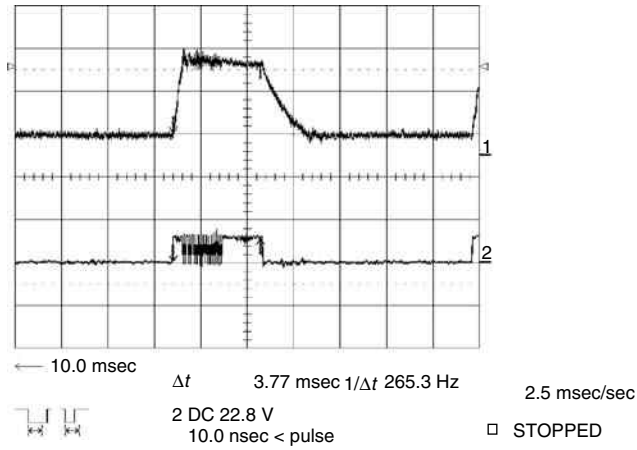

FIGURE 6.72
Phase current and gating pulse with optimization: terminal voltage, 50 V; load, 120 W; reference current, 4.7 A; speed, 1200 rpm; conduction angle, 27.25°

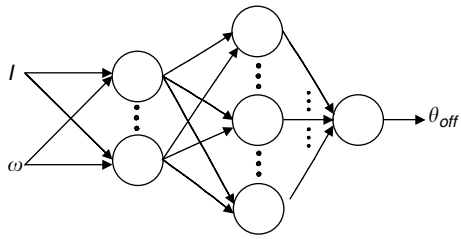

FIGURE 6.73
A three-layer feedforward ANN for holding optimal turn-off angles

network with two inputs — current and speed — and one output — the optimum turn-off angle.[69]

The proposed self-tuning control technique incorporates a heuristic search method along with an adaptive type ANN-based method. The weights of ANNs are initially set to default values. The control technique incorporates a periodic heuristic search of optimal θ_{off} to verify the accuracy of the θ_{off} obtained from the ANN. If there is a variation in the inductance profile due to parameter drift, the optimal θ_{off} obtained from the ANN will no longer be valid. This prompts the controller to activate the heuristic search by modifying the θ_{off} in small steps until the current reaches the minimum value. This new optimal θ_{off} at that particular operating point is now used to adapt the weights of the ANN. Hence, this novel ANN-based control technique coupled with the heuristic search learns and adapts to any parameter drift to give the optimal θ_{off}.

ANNs have been successfully used for many applications in control systems. But the ANN learning algorithm gives a great performance when used off-line. This means that the ANNs have to be fully trained before being applied. Neural networks with incremental learning capability and stable adaptation of network parameters are essential for on-line adaptive control. Adaptive learning is based on the assumption that the ANN is well trained in such a way that it can perform input/output mapping for the initial training set with a high degree of accuracy. This can be achieved by training the ANN with a sufficient amount of data at a very low error rate. In this application, this training can be done off-line as it may require more time.

Now when new training data are obtained, the already-trained ANN is used to generate additional examples. These additional examples with the newly obtained training data are then used to retrain the current ANN. This ensures that the original ANN mapping is retained with only a change localized around the neighborhood of the new training data. This makes the network gradually adapt to the new data. The above method ensures the stability of the network weight variations by slow adaptation as the new optimal θ_{off} will be in the neighborhood of the old value.

Some simulation results[69] that show the ability of this algorithm are shown in Figure 6.74. These results belongs to an 8/6, 12 V, 0.6 kW SRM. This plot clearly shows the improvement in torque per amp with optimization, which is about 13.6%.

6.4.8 Vibration and Acoustic Noise in SRM

Despite the excellent attributes, SRM drives exhibit high levels of torque ripple and audible noise. Indeed, in some noise-sensitive applications like domestic products, the problem of acoustic noise and vibration appears to be particularly important. The acoustic noise in SRM is due mainly to the varying radial magnetic force between the stator and rotor poles, as shown in Figure 6.75 and Figure 6.76.[71,72] This varying magnetic force causes the deformation of the stator and, therefore, radial vibrations of the stator and acoustic noise.

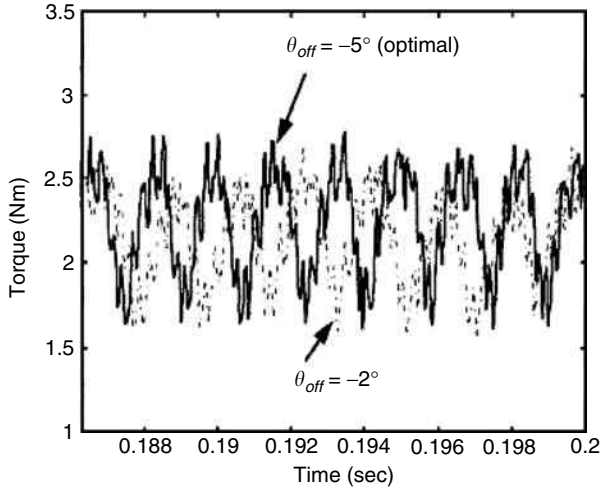

FIGURE 6.74
Developed torque before and after optimization

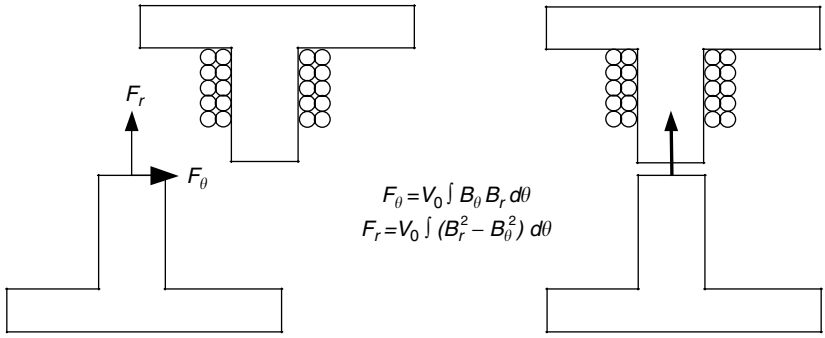

FIGURE 6.75
Static profile of the radial component of the force

The results of the structural study of SRM show that the back-iron is the most significant parameter in the dynamic behavior of the stator deformations.[53,54] Increasing the back-iron length results in larger natural frequencies and smaller deformation, which consequently reduce the chance of mechanical resonance even at high speeds.

Increasing the air gap length will reduce the radial forces.[74] However, it will vitiate the performance of the SRM.

Radial vibration of the stator experiences a severe acceleration during the turn-off process. This is due to the large magnitude of the attraction forces and their fast rate of change. This is effectively the point of impact of a hammer on the stator structure. Smoothing of the radial force during the turn-off process has been found to be the most direct method for reducing the vibration.[76]

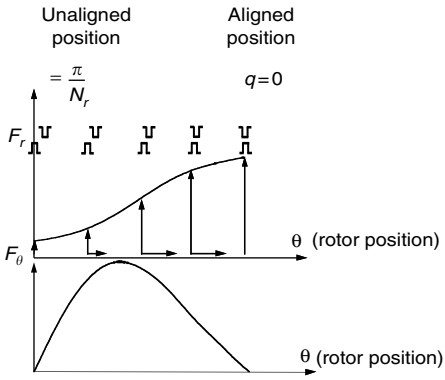

FIGURE 6.76
Distribution of radial (F_r) and tangential (F_θ) forces

The current profiling algorithm has to make sure that negative torque will not be generated. In other words, the phase current has to be completely removed at or before the aligned position. Also, it must be noted that a large number of steps in controlling the tail current will increase the switching losses. Moreover, unconstrained reduction of vibration using this method will vitiate the performance of the machine. Therefore, the study of other objectives such as efficiency and torque ripple under the proposed control method is an essential step.[71]

In reference,[75] it has been shown that for practical implementation two levels of current will provide a smooth variation in radial force. Therefore, turn-off instant, the position at which the second current limit is assigned and the position at which the final hard chopping of the phase current occurs, is considered a controlled variable. These parameters are computed at various operating points using the analytical model of the SRM drive.[81]

6.4.9 SRM Design

SRM has a simple construction. However, this does not mean its design is simple. Actually, due to the double salient structure, continuously varying inductance and high saturation of pole tips and the fringing effect of pole and slots, the design of SRM has great difficulty in using the magnetic circuit approach. In most cases, the electromagnetic finite element analysis is used to determine the motor parameters and performances. Typical electromagnetic field distributions of an 8/6 SRM are shown in Figure 6.77. Nevertheless, there are some basic criteria to initialize the design process of SRM for EVs and HEVs.[73,80]

6.4.9.1 Number of Stator and Rotor Poles

For continuous rotating, the stator and rotor poles should satisfy some special conditions, that is, stator poles and rotor poles must be equally distributed on the circumferences, and pole numbers of stator and rotor must

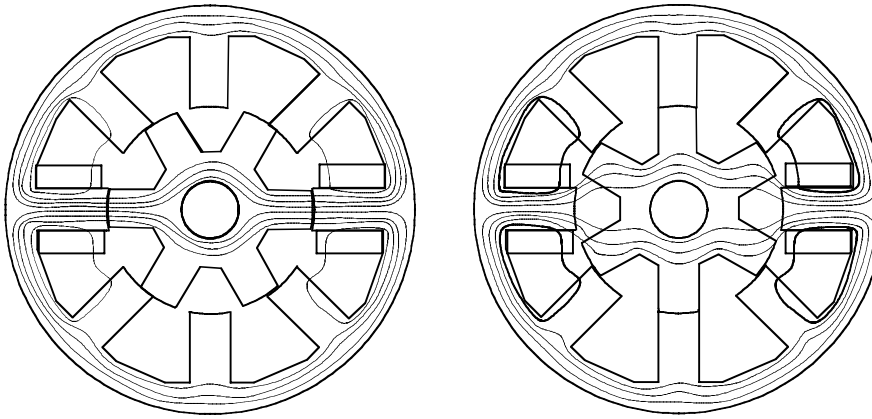

FIGURE 6.77
Typical electromagnetic field distribution of an 8/6 SRM: (a) aligned position and (b) unaligned position

satisfy the relationship as

$$N_s = 2mq,$$

$$N_r = 2(mq \pm 1), \tag{6.139}$$

where N_s and N_r are the pole numbers of stator and rotor, respectively, q is the phase number of the machine, and m is equal to 1 or 2. In order to reduce the switch frequency and the minimum inductance, the rotor pole number is less than the stator pole number, that is, a minus sign is used in (6.138). The most common combination of q, m, N_s, and N_r is listed in Table 6.1.

Four-phase 8/6 and three-phase 6/4 configurations are the most commonly used SRM structures. A three-phase 6/4 configuration has the advantage of having more room for phase advancing in high-speed application. In addition, compared to an 8/6 configuration, this structure will minimize the effects of mutual coupling between adjacent phases. However, it results in more torque pulsation due to its torque–angle characteristics, which contain large dead zones. Furthermore, starting torque can be a problem with this configuration. On the other hand, an 8/6 structure can be used to reduce the torque ripple and improve the starting torque.[77] However, by selecting an 8/6 machine, the cost of the silicon will increase. By increasing the number of poles per phase (12/8, 16/12 configuration), one can minimize the demerits of a 6/4 machine while maintaining the same cost of silicon. In this design study, an 8/6 configuration has been selected.

6.4.9.2 Stator Outer Diameter

Stator outer diameter is mainly designed based on the available space given in the desired specifications. In fact, the main compromise has to be made

TABLE 6.1

Common Combination of q, N_s, and N_r

	m = 1			m = 2		
		N_r			N_r	
q	N_s	"−"	"+"	N_s	"−"	"+"
3	6	4	8	12	10	14
4	8	6	10	16	14	18
5	10	8	12	20	18	22

between the length of the machine and its outer diameter. A pancake (the length of the machine is less than stator outer radius) type of the design is subject to three-dimensional effects of coils' endings,[78] whereas a very long structure will face cooling and rotor bending issues that are of particular importance for large machines.

6.4.9.3 Rotor Outer Diameter

The relationship between the developed torque by SRM and machine parameters can be represented by the following equation:

$$T \propto D_r^2 l (N_i)^2, \tag{6.140}$$

where D_r, N_i, and l are the outer diameter of the rotor, equivalent ampere-turn of one phase, and the length of the machine. Once the outer diameter of the SRM is fixed, any increase in rotor outer diameter will result in a reduction of N_i, thereby reducing the torque developed by SRM. Because of this and considering the fact that SRM is highly saturated, rotor boring should be equal to or slightly larger than stator outer radius. It must be noted that rotor geometry enhances the moment of inertia and vibrational modes of the machine.

6.4.9.4 Air gap

Air gap has an important impact on the generated torque and dynamic behavior of the SRM. In fact, by reducing the air gap, inductance at the aligned position will increase, resulting in a higher torque density. On the other hand, a very small air gap will cause severe saturation in the stator and rotor pole areas.[74] In addition, mechanical manufacturing of a very small air gap might not be feasible. The following empirical formula can be used as a reference for selecting the air gap in large machines:[79]

$$\delta(\text{mm}) = 1 + \frac{D_s}{1000}, \tag{6.141}$$

where δ and D_s are the air gap and the stator outer boring in (mm) and (m), respectively. By investigating the value of the flux density (B) in the

stator and rotor poles, the level of saturation and consequently the air gap can be finalized.

6.4.9.5 Stator Arc

Since the developed torque depends on the area available for the coils, it is important to design the stator arc in such a way that maximum space for inserting the coils is provided. A very narrow stator arc will result in tangential vibration of the stator pole. Moreover, it reduces the effective region in the torque–angle characteristics, which increases the torque ripple and reduces the average torque. An optimal value for the stator arc can be chosen using the following equation:[81]

$$0.3\frac{\pi D_R}{N_S} \leqslant \lambda_s \leqslant 0.35\frac{\pi D_R}{N_S}, \tag{6.142}$$

where D_R, N_S, and λ_S are, respectively, the rotor diameter, number of stator poles, and stator arc.

6.4.9.6 Stator Back-Iron

For designing the back-iron, the following constraints have to be considered:

1. Radial vibration of the stator body has to be minimized.
2. There should be enough space for the cooling of the stator.
3. The back-iron should be capable of carrying half of the flux existing in the stator poles without getting saturated.
4. The area available for inserting the coils should not be reduced.

6.4.9.7 Performance Prediction

Clearly, most of the performance requirements are related to the dynamic performance of the drive and hence call for an overall modeling of the drive system including control and power electronics considerations. However, in order to predict the dynamic performance of the drive, static characteristics of the machine (phase inductance and torque–angle profiles) should be available.

The improved magnetic equivalent circuit approach (IMEC)[82] is a shortcut method that gives an approximation of the steady-state parameters of the SRM. Indeed, by replacing all the magnetomotive sources (ampere-turn) with voltage sources and various parts of the magnetic structure with their equivalent reluctances, one can perform a magnetic analysis. Furthermore, by dividing the stator and rotor poles into several smaller portions, the accuracy of this method can be arbitrarily improved. It must be noted that FE analysis of SRM is a time-consuming procedure. Therefore, the IMEC method is more appropriate for developing first design examples.

Figure 6.78 depicts a general design strategy for the SRM drive.

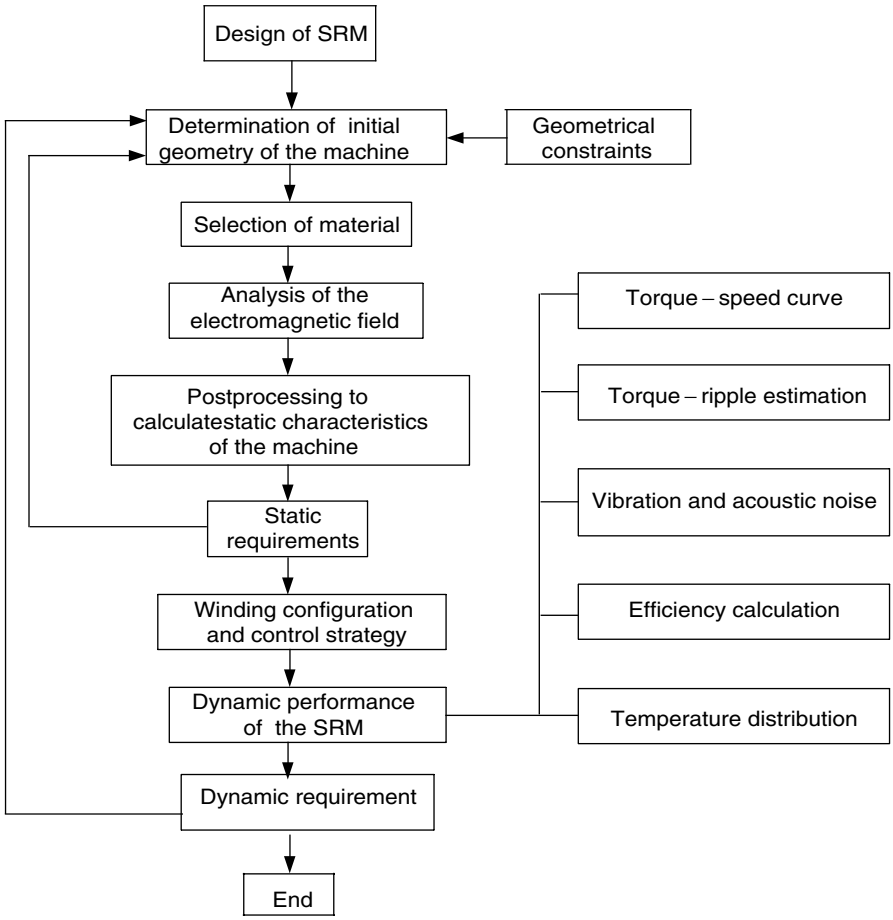

FIGURE 6.78
Basic design strategy

References

[1] C.C. Chan and K.T. Chau, *Modern Electric Vehicle Technology*, Oxford University Press, Oxford, 2001.
[2] G.K. Dubey, *Power Semiconductor Controlled Drives*, Prentice-Hall Inc., Englewood Cliffs, NJ, 1989.
[3] A.M. Trzynadlowski, *The Field Orientation Principle in Control of Induction Motor*, Kluwer Academic Publishers, Dordrecht, 1994.
[4] D.W. Novotny and T.A. Lipo, *Vector Control and Dynamics of AC Drives*, Oxford Science Publications, London, 1996.
[5] N. Mohan, T.M. Undeland, and W.P. Robbins, *Power Electronics — Converters, Applications, and Design*, John Wiley & Sons, New York, 1995.

[6] J.F. Gieras and M. Wing, *Permanent Magnet Motor Technology, Design and Applications*, Marcel Dekker, Inc., New York, 1997.
[7] D.C. Hanselman, *Brushless Permanent-Magnet Motor Design*, McGraw-Hill Inc., New York, 1994.
[8] K.M. Rahman and M. Ehsani, Performance analysis of electric motor drives for electric and hybrid electric vehicle application, *IEEE Power Electronics in Transportation*, 49–56, Nov. 1996.
[9] T. Senjyu and K. Uezato, Adjustable speed control of brushless DC motors without position and speed sensors, in *Proceedings of the IEEE/IAS Conf. on Industrial Automation and Control: Emerging Technologies*, pp. 160–164, 1995.
[10] A. Consoli, S. Musumeci, A. Raciti, and A. Testa, Sensorless vector and speed control of brushless motor drives, *IEEE Transactions on Industrial Electronics*, 41, 91–96, 1994.
[11] P. Acarnley, Sensorless position detection in permanent magnet drives, *IEE Colloquium on Permanent Magnet Machines and Drives*, 1, 10/1–10/4, 1993.
[12] T. Liu and C. Cheng, Adaptive control for a sensorless permanent-magnet synchronous motor drive, *IEEE Transactions on Aerospace and Electronic Systems*, 30, 900–909, 1994.
[13] R.Wu and G.R. Slemon, A Permanent magnet motor drive without a shaft sensor, *IEEE Transactions on Industry Applications*, 27, 1005–1011, 1991.
[14] T. Liu and C. Cheng, Controller design for a sensorless permanent magnet synchronous drive system, *IEE Proc.-B*, 140, 369–378, 1993.
[15] N. Ertugrul, P.P. Acarnley, and C.D. French, Real-time estimation of rotor position in PM motors during transient operation, *IEE 5th European Conference on Power Electronics and Applications*, pp. 311–316, 1993.
[16] N. Ertugrul and P. Acarnley, A new algorithm for sensorless operation of permanent magnet motors, *IEEE Transactions on Industry Applications*, 30, 126–133, 1994.
[17] T. Takeshita and N. Matsui, Sensorless brushless DC motor drive with EMF constant identifier, *IEEE International Conference on Industrial Electronics, Control, and Instrumentation*, Vol. 1, pp. 14–19, 1994.
[18] N. Matsui and M. Shigyo, Brushless DC motor control without position and speed sensors, *IEEE Transactions on Industry Applications*, 28, 120–127, 1992.
[19] N. Matsui, Sensorless operation of brushless DC motor drives, *Proceedings of the IEEE International Conference on Industrial Electronics, Control, and Instrumentation*, Vol. 2, pp. 739–744, Nov. 1993.
[20] N. Matsui, Sensorless PM brushless DC motor drives, *IEEE Transactions on Industrial Electronics*, 43, 300–308, 1996.
[21] M. Schrodl, Digital implementation of a sensorless control algorithm for permanent magnet synchronous motors, *Proceedings of the International Conference "SM 100,"* ETH Zurich, Switzerland, pp. 430–435, 1991.
[22] M. Schrodl, Operation of the permanent magnet synchronous machine without a mechanical sensor, *IEE Proceedings of the International Conference on Power Electronics and Variable Speed Drives*, pp. 51–56, July 1990.
[23] M. Schrodl, Sensorless control of permanent magnet synchronous motors, *Electric Machines and Power Systems*, 22, 173–185, 1994.
[24] B.J. Brunsbach, G. Henneberger, and T. Klepsch, Position controlled permanent magnet excited synchronous motor without mechanical sensors, *IEE Conference on Power Electronics and Applications*, Vol. 6, pp. 38–43, 1993.

[25] R. Dhaouadi, N. Mohan, and L. Norum, Design and implementation of an extended Kalman filter for the state estimation of a permanent magnet synchronous motor, *IEEE Transactions on Power Electronics*, 6, 491–497, 1991.
[26] A. Bado, S. Bolognani, and M. Zigliotto, Effective estimation of speed and rotor position of a PM synchronous motor drive by a Kalman filtering technique, in *Proceedings of the 23rd IEEE Power Electronics Specialist Conference*, Vol. 2, pp. 951–957, 1992.
[27] K.R. Shouse and D.G. Taylor, Sensorless velocity control of permanent-magnet synchronous motors, in *Proceedings of 33rd Conference on Decision and Control*, pp. 1844–1849, Dec. 1994.
[28] J. Hu, D.M. Dawson, and K. Anderson, Position control of a brushless DC motor without velocity measurements, *IEE Proceedings on Electronic Power Applications*, Vol. 142, pp. 113–119, Mar. 1995.
[29] J. Solsona, M.I. Valla, and C. Muravchik, A nonlinear reduced order observer for permanent magnet synchronous motors, *IEEE Transactions on Industrial Electronics*, Vol. 43, pp. 38–43, Aug. 1996.
[30] R.B. Sepe and J.H. Lang, Real-time observer-based (adaptive) control of a permanent-magnet synchronous motor without mechanical sensors, *IEEE Transactions on Industry Applications*, Vol. 28, pp. 1345–1352, Nov./Dec. 1992.
[31] L. Sicot, S. Siala, K. Debusschere, and C. Bergmann, Brushless DC motor control without mechanical sensors, in *Proceedings of the IEEE Power Electronics Specialist Conference*, pp. 375–381, 1996.
[32] T. Senjyu, M. Tomita, S. Doki, and S. Okuma, Sensorless vector control of brushless DC motors using disturbance observer, in *Proceedings of the 26th IEEE Power Electronics Specialists Conference*, Vol. 2, pp. 772–777, 1995.
[33] K. Iizuka, H. Uzuhashi, and M. Kano, Microcomputer control for sensorless brushless motor, *IEEE Transactions on Industry Applications*, IA-27, 595–601, 1985.
[34] J. Moreira, Indirect sensing for rotor flux position of permanent magnet AC motors operating in a wide speed range, *IEEE Transactions on Industry Applications Society*, 32, 401–407, 1996.
[35] S. Ogasawara and H. Akagi, An approach to position sensorless drive for brushless DC motors, *IEEE Transactions on Industry Applications*, 27, 928–933, 1991.
[36] T.M. Jahns, R.C. Becerra, and M. Ehsani, Integrated current regulation for a brushless ECM drive, *IEEE Transactions on Power Electronics*, 6, 118–126, 1991.
[37] R.C. Becerra, T.M. Jahns, and M. Ehsani, Four-quadrant sensorless brushless ECM drive, in *Proceedings of the IEEE Applied Power Electronics Conference and Exposition*, pp. 202–209, Mar. 1991.
[38] D. Regnier, C. Oudet, and D. Prudham, Starting brushless DC motors utilizing velocity sensors, in *Proceedings of the 14th Annual Symposium on Incremental Motion Control Systems and Devices*, Champaign, Illinois, Incremental Motion Control Systems Society, pp. 99–107, June 1985.
[39] D. Peters and J. Harth, I.C.s provide control for sensorless DC motors, *EDN*, 85–94, 1993.
[40] F. Huang and D. Tien, A neural network approach to position sensorless control of brushless DC motors, in *Proceedings of the IEEE 22nd International Conference on Industrial Electronics, Control, and Instrumentation*, Vol. 2, pp. 1167–1170, Aug. 1996.
[41] M. Hamdi and M. Ghribi, A sensorless control scheme based on fuzzy logic for AC servo drives using a permanent-magnet synchronous motor, *IEEE Canadian Conference on Electrical and Computing Engineering*, pp. 306–309, 1995.

[42] D.E. Hesmondhalgh, D. Tipping, and M. Amrani, Performance and design of an electromagnetic sensor for brushless DC motors, *IEE Proceedings*, 137, 174–183, 1990.
[43] T.J.E. Miller, *Switched Reluctance Motors and their Control*, Oxford Science Publications, London, 1993.
[44] P.J. Lawrenson, J.M. Stephenson, P.T. Blenkinsop, J. Corda, and N.N. Fulton, Variable-speed switched reluctance motors, *Proceedings of IEE*, 127, (Part B), 253–265, 1980.
[45] M. Ehsani, *Switched Reluctance Motor Drive System*, U.S. Patent Pending, Filing Date: January 1997, Serial Number 60/061,087.
[46] R. Krishnan, *Switched Reluctance Motors Drives: Modeling, Simulation Analysis, Design and Applications*, CRC Press, Boca Raton, FL, 2001.
[47] S.R. MacMinn and J.W. Sember, Control of a switched-reluctance aircraft starter-generator over a very wide speed range, in *Proceedings of the Intersociety Energy Conversion Engineering Conference*, 1989, pp. 631–638.
[48] E. Richter, J.P. Lyons, C.A. Ferreira, A.V. Radun, and E. Ruckstatder, Initial testing of a 250 kW starter/generator for aircraft applications, in *Proceedings of the SAE Aerospace Atlantic Conference Expo.*, Dayton, OH, Apr. 18–22, 1994.
[49] B. Fahimi, A switched reluctance machine based starter/generator for more electric cars, in *Proceedings of the IEEE Electric Machines and Drives Conference*, pp. 73–78, 2000.
[50] J.M. Kokernak, D.A. Torrey, and M. Kaplan, A switched reluctance starter/alternator for hybrid electric vehicles, in *Proceedings of the PCIM'99*, pp. 74–80, 1999.
[51] D.A. Torrey, Variable-reluctance generators in wind-energy systems, in *Proceedings of the IEEE PESC'93*, pp. 561–567, 1993.
[52] A. Radun, Generating with the switched-reluctance motor, in *Proceedings IEEE APEC'94*, pp. 41–47, 1994.
[53] J.P. Lyons, S.R. MacMinn, and M.A. Preston, Discrete position estimator for a switched reluctance machine using a flux-current map comparator, U.S. Patent 5140243, 1991.
[54] H. Gao, B. Fahimi, F.R. Salmasi, and M. Ehsani, Sensorless control of the switched reluctance motor drive based on the stiff system control concept and signature detection, in *Proceedings of the 2001 IEEE Industry Applications Society Annual Meeting*, pp. 490–495, 2001.
[55] M. Ehsani, *Method and Apparatus for Sensing the Rotor Position of a Switched Reluctance Motor*, U.S. Patent No. 5, 410, 235, April 1995.
[56] G. Suresh, B. Fahimi, K.M. Rahman, and M. Ehsani, Inductance based position encoding for sensorless SRM drives, in *Proceedings of the 1999 IEEE Power Electronics Specialists Conference*, Vol. 2, pp. 832–837, 1999.
[57] H. Gao, *Sensorless Control of the Switched Reluctance Motor at Standstill and Near-Zero Speed*, Ph.D. Dissertation, Texas A&M University, December 2001.
[58] M. Ehsani, *Position Sensor Elimination Technique for the Switched Reluctance Motor Drive*, U.S. Patent 5072166, 1990.
[59] M. Ehsani, *Phase and Amplitude Modulation Techniques for Rotor Position Sensing in Switched Reluctance Motors*, U.S. Patent No. 5,291,115, March 1994.
[60] M. Ehsani, I. Husain, S. Mahajan, and K.R. Ramani, New modulation encoding techniques for indirect rotor position sensing in switched reluctance motors, *IEEE Transactions on Industry Applications*, 30, 85–91, 1994.

[61] G.R. Dunlop and J.D. Marvelly, Evaluation of a self commuted switched reluctance motor, in *Proceedings of the 1987 Electric Energy Conference*, pp. 317–320, 1987.
[62] M. Ehsani and I. Husain, Rotor position sensing in switched reluctance motor drives by measuring mutually induced voltages, in *Proceedings of the 1992 IEEE Industry Application Society Annual Meeting*, Vol. 1, pp. 422–429, 1992.
[63] A. Lumsdaine and J.H. Lang, State observer for variable reluctance motors, *IEEE Transactions on Industrial Electronics*, 37, 133–142, 1990.
[64] J.T. Bass, M. Ehsani, and T.J.E. Miller, Simplified electronics for torque control of sensorless switched reluctance motor, *IEEE Transactions on Industrial Electronics*, 34, 234–239, 1987.
[65] S. Vukosavic, L. Peric, E. Levi, and V. Vuckovic, Sensorless operation of the SR motor with constant dwell, in *Proc. 1990 IEEE Power Electronics Specialists Conference*, pp. 451–454, 1990.
[66] H. Gao, F.R. Salmasi, and M. Ehsani, Sensorless control of SRM at standstill, in *Proceedings of the 2000 IEEE Applied Power Electronics Conference*, Vol. 2, pp. 850–856, 2000.
[67] M. Ehsani, *Self-Tuning Control of Switched Reluctance Motor Drives System,* U.S. Patent Pending, File Number 017575.0293.
[68] P. Tandon, A. Rajarathnam, and M. Ehsani, Self-tuning of switched reluctance motor drives with shaft position sensor, *IEEE Transactions on Industry Applications*, 33, 1002–1010, 1997.
[69] A. Rajarathnam, B. Fahimi, and M. Ehsani, Neural network based self-tuning control of a switched reluctance motor drive to maximize torque per ampere, in *Proceedings of the IEEE Industry Applications Society Annual Meeting*, Vol. 1, pp. 548–555, 1997.
[70] K. Russa, I. Husain, and M.E. Elbuluk, A self-tuning controller for switched reluctance motors, *IEEE Transactions on Power Electronics,* 15, 545–552, 2000.
[71] B. Fahimi, *Control of Vibration in Switched Reluctance Motor Drive,* Ph.D. Dissertation, Texas A&M University, May 1999.
[72] D.E. Cameron, J.H. Lang, and S.D. Umans, The origin and reduction of acoustic noise an doubly salient variable reluctance motor, *IEEE Transactions on Industry Applications*, IA-28, 1250–1255, 1992.
[73] B. Fahimi, G. Suresh, and M. Ehsani, Design considerations of switched reluctance motors: vibration and control issues, in *Proceedings of the 1999 IEEE Industry Application Society Annual Meeting*, Phoenix, AZ, Oct. 1999.
[74] B. Fahimi and M. Ehsani, Spatial distribution of acoustic noise caused by radial vibration in switched reluctance motors: application to design and control, in *Proceedings of the 2000 IEEE Industry Application Society Annual Meeting*, Rome, Italy, Oct. 2000.
[75] B. Fahimi, G. Suresh, K.M. Rahman, and M. Ehsani, Mitigation of acoustic noise and vibration in switched reluctance motor drive using neural network based current profiling, in *Proceedings of the 1998 IEEE Industry Application Society Annual Meeting*, Vol. 1, pp. 715–722, 1998.
[76] B. Fahimi and M. Ehsani, *Method and Apparatus for Reducing Noise and Vibration in Switched Reluctance Motor Drives*, U.S. Patent Pending.
[77] I. Husain, Minimization of torque ripple in SRM drives, *IEEE Transactions on Industrial Electronics*, 49, 28–39, 2002.

[78] A.M. Michaelides and C. Pollock, Effect of end core flux on the performance of the switched reluctance motor, *IEE Proceedings of the Electrical Power Applications*, 141, 308–316, 1994.
[79] G. Henneberger, *Elektrische Maschinen I, II, III*, RWTH Aachen, Manuscripts at Institut fuer Elektrische Maschinen, 1989.
[80] J. Faiz and J.W. Finch, Aspects of design optimization for switched reluctance motors, *IEEE Transactions on Energy Conversion*, 8, 704–712, 1993.
[81] G.S. Buja and M.I. Valla, Control characteristics of the SRM drives — part I: Operation in the linear region, *IEEE Transactions on Industrial Electronics*, 38, 313–321, 1991.
[82] B. Fahimi, G. Henneberger, and M. Moallem, Prediction of transient behavior of SRM drive using improved equivalent magnetic circuit method, *PCIM Conference Records*, 1995, pp. 285–291.

7

Series Hybrid Electric Drive Train Design

CONTENTS

7.1 Operation Patterns 240
7.2 Control Strategies 242
7.2.1 Max. SOC-of-PPS Control Strategy 243
7.2.2 Thermostat Control Strategy (Engine-On–Off) 244
7.3 Sizing of the Major Components 246
7.3.1 Power Rating Design of the Traction Motor 246
7.3.2 Power Rating Design of the Engine/Generator 247
7.3.3 Design of PPS 249
7.3.3.1 Power Capacity of PPS 249
7.3.3.2 Energy Capacity of PPS 250
7.4 Design Example 251
7.4.1 Design of Traction Motor Size 251
7.4.2 Design of the Gear Ratio 251
7.4.3 Verification of Acceleration Performance 252
7.4.4 Verification of Gradeability 253
7.4.5 Design of Engine/Generator Size 254
7.4.6 Design of the Power Capacity of PPS 255
7.4.7 Design of the Energy Capacity of PPS 255
7.4.8 Fuel Consumption 256
References 257

The concept of a series hybrid electric drive train was developed from the electric vehicle drive train.[1] As mentioned in Chapter 4, electric vehicles, compared with conventional gasoline or diesel-fueled vehicles, have the advantages of zero mobile pollutant emissions, multienergy sources, and high efficiency. However, electric vehicles using present technologies have some disadvantages: a limited drive range due to the shortage of energy storage in the on-board batteries, limited payload and volume capacity due to heavy and bulky batteries, and a longer battery charging time. The initial objective of developing a series hybrid electric vehicle (S-HEV) was aimed at extending the drive range by adding an engine/alternator system to charge the batteries on-board.

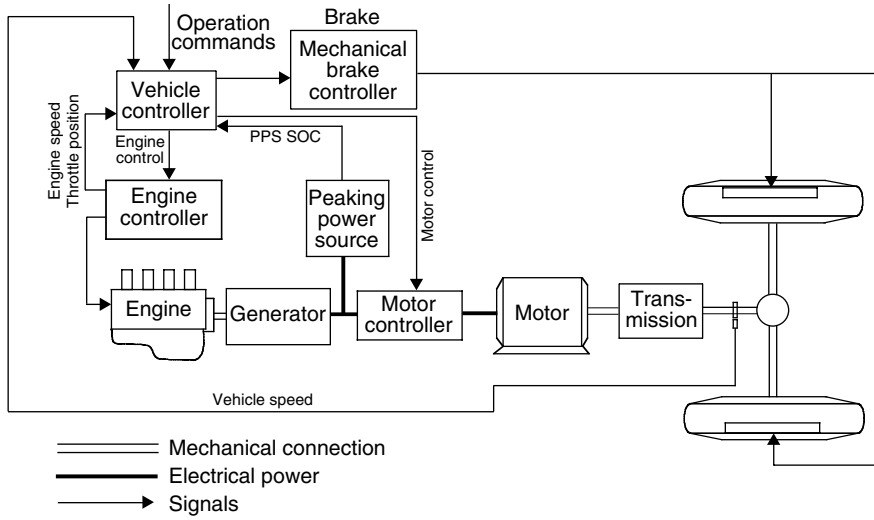

FIGURE 7.1
Configuration of a typical series hybrid electric drive train

A typical series hybrid electric drive train configuration is shown in Figure 7.1. The vehicle is propelled by a traction motor. The traction motor is powered by a battery pack and/or an engine/generator unit. The engine/generator unit either helps the batteries to power the traction motor when load power demand is large or charges the batteries when load power demand is small. The motor controller is to control the traction motor to produce the power required by the vehicle.

Vehicle performance (acceleration, gradeability, and maximum speed) is completely determined by the size and characteristics of the traction motor drive. The determination of the size of the motor drive and gears of transmission is the same as in the electric vehicle design discussed in Chapter 4. However, the drive train control is essentially different from the pure electric drive train due to the involvement of an additional engine/generator unit. This chapter focuses on the design of the engine/alternator system, operation control strategy, and battery size design. Also, the term "peak power source" will replace "battery pack," because, in HEVs, the major function of batteries is to supply peaking power. They can be replaced with other kinds of sources such as ultracapacitors and flywheels.

7.1 Operation Patterns

In series hybrid electric drive trains, the engine/generator system is mechanically decoupled from the driven wheels as shown in Figure 7.1.

The speed and torque of the engine are independent of vehicle speed and traction torque demand, and can be controlled at any operating point on its speed–torque plane.[3,4] Generally, the engine should be controlled in such a way that it always operates in its optimal operation region, where fuel consumption and emissions of the engine are minimized (see Figure 7.2). Due to the mechanical decoupling of the engine from the drive wheels, this optimal engine operation is realizable. However, it heavily depends on the operating modes and control strategies of the drive train.

The drive train has several operating modes, which can be used selectively according to the driving condition and desire of the driver. These operating modes are:

1. Hybrid traction mode: When a large amount of power is demanded, that is, the driver depresses the accelerator pedal deeply, both engine/generator and peaking power source (PPS) supply their powers to the electric motor drive. In this case, the engine should be controlled to operate in its optimal region for efficiency and emission reasons as shown in Figure 7.2. The PPS supplies the additional power to meet the traction power demand. This operation mode can be expressed as

$$P_{demand} = P_{e/g} + P_{pps}, \tag{7.1}$$

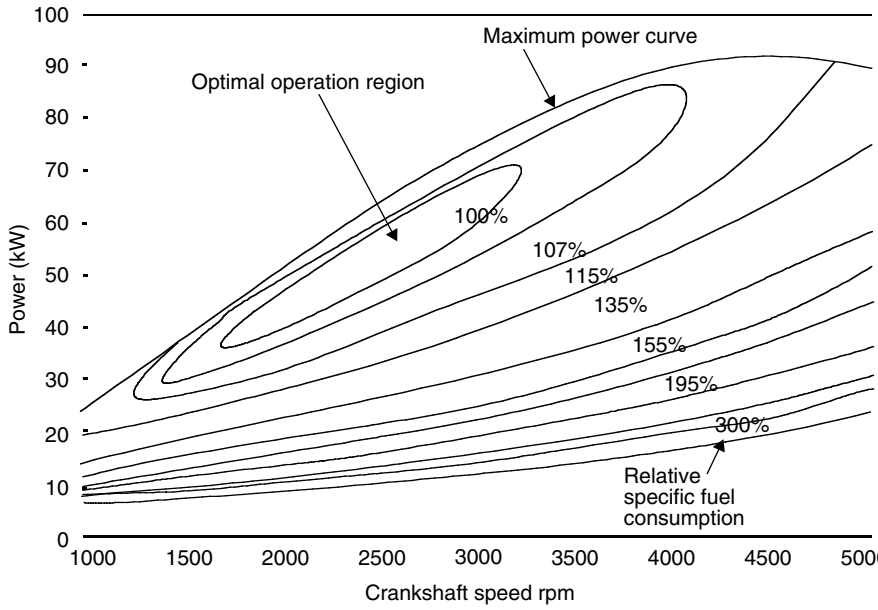

FIGURE 7.2
Example of engine characteristics and optimal operating region

where P_{demand} is the power demanded by the driver, $P_{e/g}$ is the engine/generator power, and P_{pps} is the PPS power.

2. Peak Power Source-Alone Traction Mode: In this operating mode, the peak power source alone supplies its power to meet the power demand, that is,

$$P_{demand} = P_{pps}. \tag{7.2}$$

3. Engine/Generator-Alone Traction Mode: In this operating mode, the engine/generator alone supplies its power to meet the power demand, that is,

$$P_{demand} = P_{e/g}. \tag{7.3}$$

4. PPS Charging from the Engine/Generator: When the energy in the PPS decreases to a bottom line, the PPS must be charged. This can be done by regenerative braking or by the engine/generator. Usually, engine/generator charging is needed, since regenerative braking charging is insufficient. In this case, the engine power is divided into two parts: one is used to propel the vehicle and the other is used to charge the PPS. That is,

$$P_{demand} = P_{e/g} - P_{pps}. \tag{7.4}$$

It should be noticed that the operation mode is only effective when the power of the engine/generator is greater than the load power demand.

5. Regenerative Braking Mode: When the vehicle is braking, the traction motor can be used as a generator, converting part of the kinetic energy of the vehicle mass into electric energy to charge the PPS.

As shown in Figure 7.1, the vehicle controller commands the operation of each component according to the traction power (torque) command from the driver, the feedback from each of the components, and also the drive train and the preset control strategy. The control objectives are to (1) meet the power demand of the driver, (2) operate each component with optimal efficiency, (3) recapture braking energy as much as possible, and (4) maintain the state-of-charge (SOC) of the PPS in a preset window.

7.2 Control Strategies

A control strategy is a control rule that is preset in the vehicle controller and commands the operating of each component. The vehicle controller receives

the operation commands from the driver and the feedback from the drive train and all the components, and then makes the decisions to use proper operation modes. Obviously, the performance of the drive train relies mainly on the control quality, in which the control strategy plays a crucial role.

In practice, there are a number of control strategies that can be used in a drive train for vehicles with different mission requirements. In this chapter, two typical control strategies are introduced: (1) maximum state-of-charge of peaking power source (Max. SOC-of-PPS) and (2) engine turn-on and turn-off (engine-on–off) control strategies.[2]

7.2.1 Max. SOC-of-PPS Control Strategy

The target of this control strategy is to meet the power demand commanded by the driver and, at the same time, maintain the SOC of the PPS at its high level. This control strategy is considered to be the proper design for vehicles for which the performance relies heavily on the peak power source. This includes vehicles with frequent stop–go driving patterns, and military vehicles for which carrying out their mission is the most important. A high SOC level will guarantee the high performance of the vehicles at any time.

The Max. SOC-of-PPS control strategy is depicted in Figure 7.3, in which points A, B, C, and D represent the power demands that the driver commands in either traction mode or braking mode. Point A represents the commanded traction power that is greater than the power that the engine/generator can produce. In this case, the PPS must produce its power to make up the power shortage of the engine/generator. Point B represents the commanded power that is less than the power that the engine/generator produces when operating in its optimal operation region (refer to Figure 7.2). In this case, two operating modes may be used, depending on the SOC level of PPS. If the SOC of the PPS is below its top line, the PPS charging mode is applied — that is, the engine/generator is operated within its optimal operating region and part of its power goes to the traction motor to propel the vehicle and the other part goes to the PPS. On the other hand, if the SOC of the PPS has already reached its top line, the engine/generator traction mode alone is supplied, that is, the engine/generator is controlled to produce power equal to the demanded power, and the PPS is set at idle. Point C represents the commanded braking power that is greater than the braking power that the motor can produce (maximum regenerative braking power). In this case, the hybrid braking mode is used, in which the electric motor produces its maximum braking power and the mechanical braking system produces the remaining braking power. Point D represents the commanded braking power that is less than the maximum braking power that the motor can produce. In this case, only regenerative braking is used. The control flowchart of Max. SOC-of-PPS is illustrated in Figure 7.4.

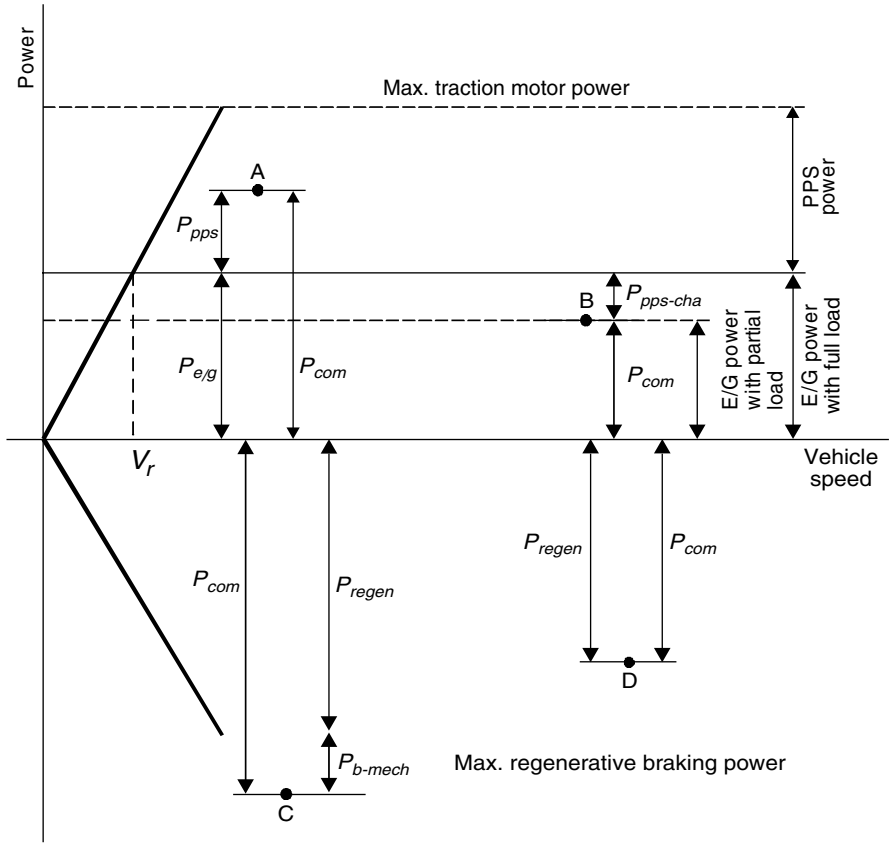

A — Hybrid traction mode
P_{com} — Commanded power
P_{pps} — Power of the peaking power source
$P_{e/g}$ — Power of engine/generator

B — Engine/generator-alone traction mode or PPS charging mode
$P_{pps\text{-}cha}$ — PPS charging power

C — Hybrid braking mode
P_{regen} — Regenerative braking power
$P_{b\text{-}mech}$ — Mechanical braking power

D — Regenerative braking mode

FIGURE 7.3
Illustration of the Max. SOC-of-PPS control strategy

7.2.2 Thermostat Control Strategy (Engine-On–Off)

The Max. SOC-of-PPS control strategy emphasizes maintaining the SOC of the PPS at a high level. However, in some driving conditions such as long

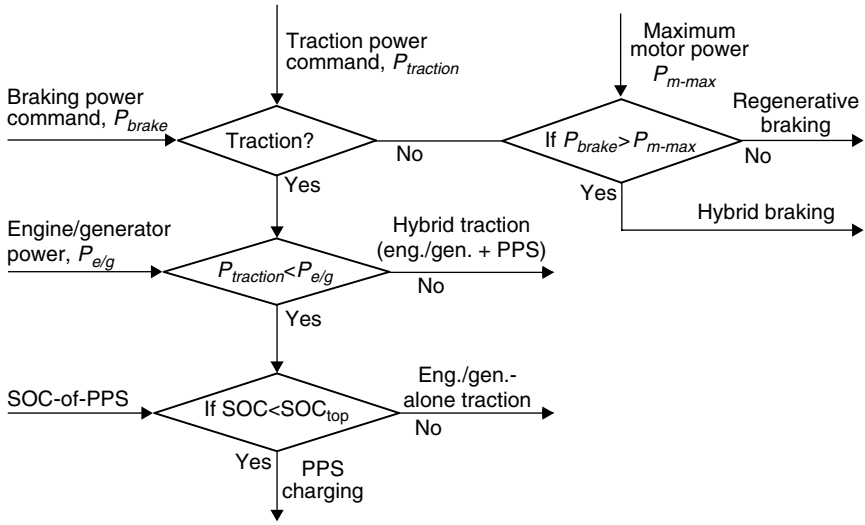

FIGURE 7.4
Control flowchart of the Max. SOC-of-PPS control strategy

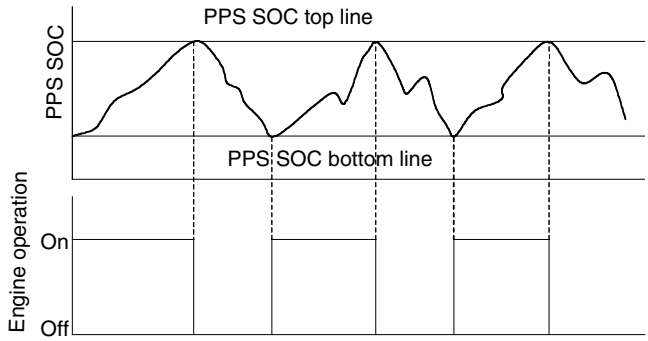

FIGURE 7.5
Illustration of thermostat control

time driving with a low load on a highway at constant speed, the PPS can be easily charged to its full level, and the engine/generator is forced to operate with a power output smaller than its optimum. Hence, the efficiency of the drive train is reduced. In this case, engine-on–off or thermostat control of the engine/generator would be appropriate. This control strategy is illustrated in Figure 7.5. The operation of the engine/generator is completely controlled by the SOC of the PPS. When the SOC of the PPS reaches its preset top line, the engine/generator is turned off and the vehicle is propelled only by the PPS. On the other hand, when the SOC of the PPS reaches its bottom line, the engine/generator is turned on. The PPS gets its charging from the

engine/generator. In this way, the engine can always be operated within its optimal deficiency region.

7.3 Sizing of the Major Components

The major components in a series hybrid drive train include traction motor, engine/generator, and PPS. The design of the power ratings of these components is the first and most important step in the whole system design. In the design of these parameters, some design constraints must be considered, which include (1) acceleration performance, (2) highway driving and urban driving, and (3) energy balance in the PPS.

7.3.1 Power Rating Design of the Traction Motor

Similar to the pure electric vehicle discussed in Chapter 4, the power rating of the electric motor drive in series HEV is completely determined by vehicle acceleration performance requirements, motor characteristics, and transmission characteristics (refer to Chapter 4). At the beginning of the design, the power rating of the motor drive can be estimated, according to the acceleration performance (time used to accelerate the vehicle from zero speed to a given speed), using the following equation:

$$P_t = \frac{\delta M_v}{2t_a}(V_f^2 + V_b^2) + \frac{2}{3}M_v g f_r V_f + \frac{1}{5}\rho_a C_D A_f V_f^3, \tag{7.5}$$

where M_v is the total vehicle mass in kg, t_f is the expected acceleration time in sec, V_b is the vehicle speed in m/s, corresponding to the motor-based speed (see Figure 7.6), V_f is the final speed of the vehicle accelerating in m/s, g is gravity acceleration in 9.80 m/s^2, f_r is the tire rolling resistance coefficient, ρ_a is the air density in 1.202 kg/m^3, A_f is the front area of the vehicle in m^2, and C_D is the aerodynamic drag coefficient. The first term in equation (7.5) represents the power used to accelerate the vehicle mass, and the second and third terms represent the average power for overcoming the tire rolling resistance and aerodynamic drag.

Figure 7.6 shows the tractive effort and traction power vs. vehicle speed with a two-gear transmission. During acceleration, starting from low gear, the tractive effort follows the trace of a–b–d–e and $V_b = V_{b1}$. However, when a single-gear transmission is used, that is, only when a high gear is available, the tractive effort follows the trace of c–d–e and $V_b = V_{b2}$.

Figure 7.7 shows an example of the power rating of motor vs. speed ratio, which is defined as the ratio of maximum speed to the base speed as shown in Figure 7.6.

It should be noted that the rated motor power determined by equation (7.5) is only an estimate for meeting the acceleration performance. In order to accurately determine the rated motor power, verification would be necessary.

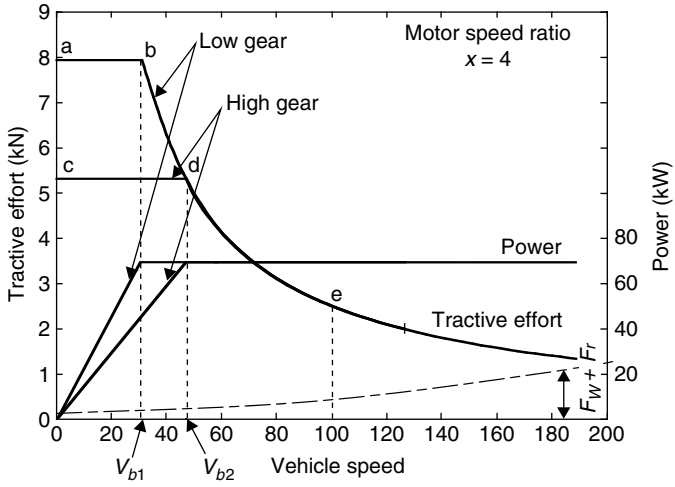

FIGURE 7.6
Speed–torque (power) characteristics of an electric motor

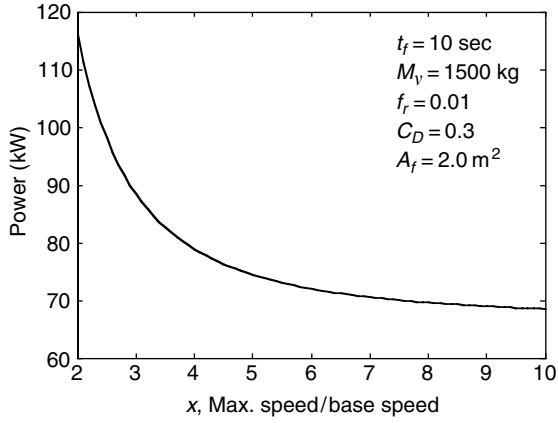

FIGURE 7.7
Power rating of the traction power vs. speed ratio of drive train

The calculation of vehicle performance, such as acceleration time, acceleration distance, and gradeability, is exactly the same as that of a pure electric vehicle (refer to Chapter 4).

7.3.2 Power Rating Design of the Engine/Generator

As discussed in Chapter 5, the engine/generator in a series hybrid drive train is used to supply steady-state power in order to prevent the PPS from being discharged completely. In the design of the engine/generator, two driving conditions should be considered: driving for a long time with constant

speed, such as highway driving between cities, and driving with a frequent stop–go driving pattern, such as driving in cities. With the former driving pattern (long time at a constant speed), the engine/generator and drive train should not rely on the PPS to support the operation at a high speed of, for example, 130 km/h or 80 mph. The engine/generator should be able to produce sufficient power to support this speed. For a frequent stop–go driving pattern, the engine/generator should produce sufficient power to maintain the energy storage of the PPS at a certain level, so that enough power can be drawn to support vehicle acceleration. As mentioned above, the energy consumption in the PPS is closely related to the control strategy.

At a constant speed and on a flat road, the power output from the power source (engine/generator and/or the PPS) can be expressed as

$$P_{e/g}=\frac{V}{1000\eta_t\eta_m}\left(M_v g f_r+\frac{1}{2}\rho_a C_D A_f V^2\right)(\text{kW}), \tag{7.6}$$

where η_t and η_m are the efficiency of transmission and traction motor, respectively. Figure 7.8 shows an example of the load power (not including η_t and η_m, curve vs. vehicle speed) for a 1500 kg passenger car. It indicates that the power demand at constant speed is much less than that for acceleration (refer to Figure 7.8). In this example, about 35 kW are needed at 130 km/h of constant speed driving.

Considering the inefficiency of the motor drive and transmission (η_t and η_m, equation [7.7]), the power output of the engine/generation system is about 20 to 25% more than that shown in Figure 7.7.

When the vehicle is driving in a stop-and-go pattern in urban areas, the power that the engine/generator produces should be equal to or slightly greater than the average load power in order to maintain balanced PPS energy storage. The average load power can be expressed as

$$P_{ave}=\frac{1}{T}\int_0^T\left(M_v g f_r+\frac{1}{2}\rho_a C_D A_f V^2\right)V\,dt+\frac{1}{T}\int_0^T \delta M_v\frac{dV}{dt}\,dt, \tag{7.7}$$

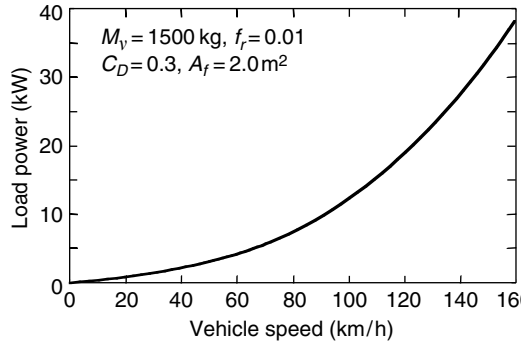

FIGURE 7.8
Load power of a 1500 kg passenger car at constant speed

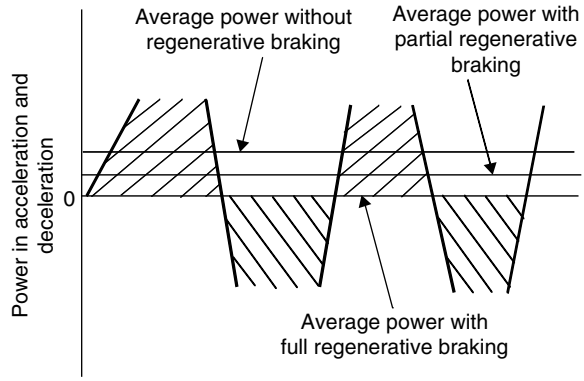

FIGURE 7.9
Average power consumed in acceleration and deceleration with full, partial, and zero regenerative braking

where δ is the vehicle mass factor (refer to Chapter 4) and dV/dt is the acceleration of the vehicle. The first term in equation (7.8) is the average power that is consumed to overcome the tire rolling resistance and aerodynamic drag. The second term is the average power consumed in acceleration and deceleration. When the vehicle has the ability to recover all of the kinetic energy of the vehicle, the average power consumed in acceleration and deceleration is zero. Otherwise, it will be greater than zero, as shown in Figure 7.9.

In the design of an engine/generator system, the power capability should be greater than, or at least not less than, the power that is needed to support the vehicle driving at a constant speed (highway driving) and at average power when driving in urban areas. In actual design, some typical urban drive cycles may be used to predict the average power of the vehicle, as shown in Figure 7.10.

7.3.3 Design of PPS

The PPS must be capable of delivering sufficient power to the traction motor at any time. At the same time, the PPS must store sufficient energy to avoid failure of power delivery due to too-deep discharging.

7.3.3.1 Power Capacity of PPS

To fully utilize the electric motor power capacity, the total power of the engine/generator and PPS should be greater than, or at least equal to, the rated maximum power of the electric motor. Thus, the power capacity of the PPS can be expressed as

$$P_{pps} \geq \frac{P_{m,max}}{\eta_m} - P_{e/g}, \tag{7.8}$$

where $P_{m,max}$ is the maximum rated power of the motor, η_m is the efficiency of the motor, and $P_{e/g}$ is the power of the engine/generator system.

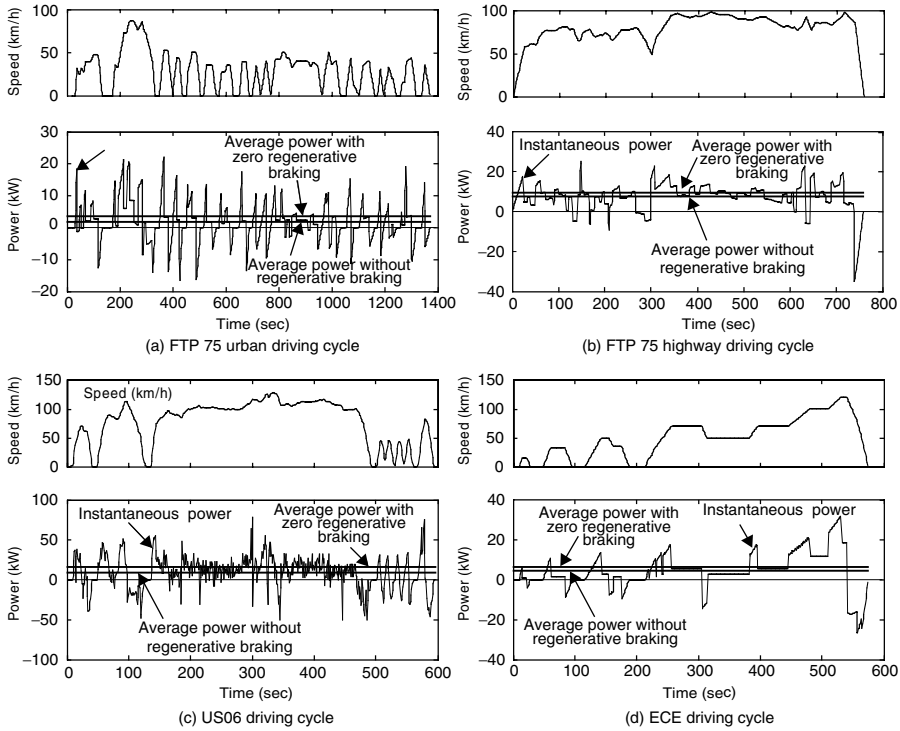

FIGURE 7.10
Instantaneous power and average power with full and zero regenerative braking in typical drive cycles

7.3.3.2 Energy Capacity of PPS

In some driving conditions, a frequent accelerating/decelerating driving pattern would result in a low SOC in the PPS, thus losing its delivery power. In order to properly determine the energy capacity of the PPS, the energy changes in the PPS in some typical drive cycles must be known. The energy changes in the PPS can be expressed as

$$\Delta E = \int_0^T P_{pps}\, dt, \tag{7.9}$$

where P_{pps} is the power of the PPS. Positive P_{pps} represents charging power, and negative P_{pps} represents discharging power. Figure 7.11 shows an example in which the energy changes in the peaking power vary with driving time. Figure 7.11 also shows the maximum amount of energy changes, ΔE_{max}, in the whole drive cycle, if the SOC of the PPS is allowed in the operating range between SOC_{top} and SOC_{bott}. The whole energy capacity of the peaking power can be calculated using equation (7.10). The operating range of PPS SOC depends upon the operating characteristics of the PPS. For example, for efficiency reasons chemical batteries would have an optimal operating range in

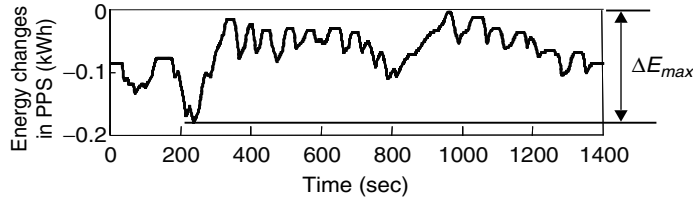

FIGURE 7.11
Energy changes in a typical urban drive cycle with Max. SOC control strategy

the middle (0.4–0.7), and for limited voltage variation reasons, ultracapacitors would only have a very limited energy change range (0.8–1.0).

$$E_{cap} = \frac{\Delta E_{max}}{SOC_{top} - SOC_{bott}}. \tag{7.10}$$

7.4 Design Example

Design specification:
Parameters

Vehicle total mass	1500 kg
Rolling resistance coefficient	0.01
Aerodynamic drag coefficient	0.3
Front area	2.0 m^2
Transmission efficiency (single gear)	0.9

Performance speciation:

Acceleration time (from 0 to 100 km/h)	10±1 sec
Maximum gradeability	>30% at low speed and >5 at 100 km/h
Maximum speed	160 km/h

7.4.1 Design of Traction Motor Size

Using equation (7.5) and supposing the motor drive has a speed ratio of $x = 4$, the motor drive power rating can be obtained as 82.5 kW for the specified acceleration time of 10 sec from zero to 100 km/h. Figure 7.12 shows the speed–torque and speed–power profiles of the motor.

7.4.2 Design of the Gear Ratio

The gear ratio is designed such that the vehicle reaches its maximum speed at the motor maximum speed, that is,

$$i_g = \frac{\pi n_{m,max} r}{30 V_{max}}, \tag{7.11}$$

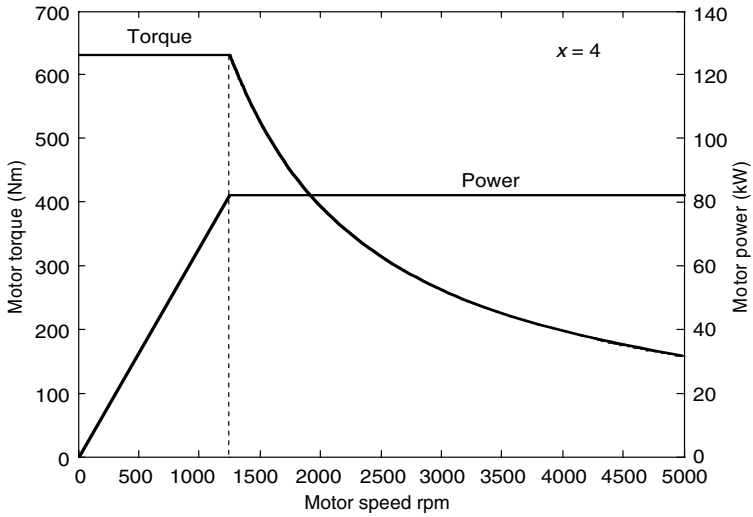

FIGURE 7.12
Characteristics of traction motor vs. motor rpm and vehicle speed

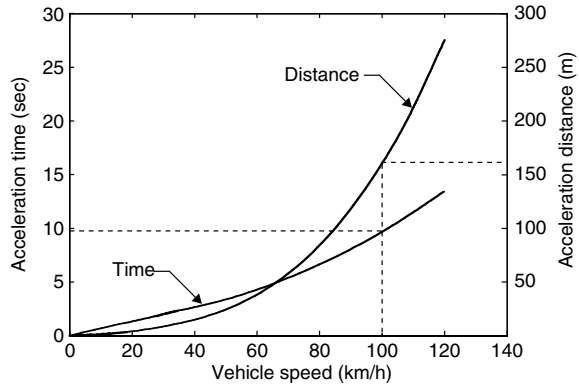

FIGURE 7.13
Accelerating time and distance vs. vehicle speed

where $n_{m,max}$ is the maximum motor rpm and V_{max} is the maximum speed of the vehicle in m/s. Suppose $n_{m,max} = 5000$ rpm, $V_{max} = 44.4$ m/s (160 km/h or 100 mph), and $r = 0.2794$ m (11 in.); $i_g = 3.29$ is obtained.

7.4.3 Verification of Acceleration Performance

Based on the torque–speed profile of the traction motor, gear ratio, and the vehicle parameters, and using the calculation method discussed in Chapters 2 and 4, the vehicle acceleration performance (acceleration time and distance vs. vehicle speed) can be obtained as shown in Figure 7.13. If the acceleration

time obtained does not meet the design specification, the motor power rating should be redesigned.

7.4.4 Verification of Gradeability

Using the motor torque–speed profile, gear ratio and vehicle parameters, and the equations described in Chapters 2 and 4, the tractive effort and resistance vs. vehicle speed can be calculated and drawn in a diagram, as shown in Figure 7.14(a). Further, the gradeability of the vehicle can be calculated as shown in Figure 7.14(b). Figure 7.14 indicates that the gradeability calculated is much greater than that specified in the design specification. This result implies that for a passenger car, the power needed

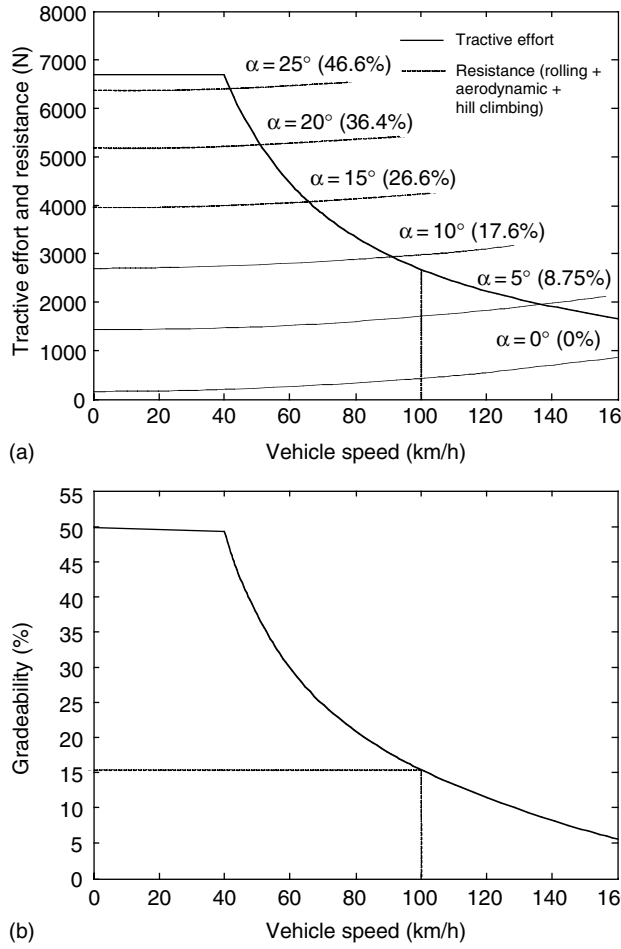

FIGURE 7.14
Traction effort and resistance of the vehicle vs. speed

for acceleration performance is usually larger than that needed for gradeability; the former determines the power rating of the traction motor.

7.4.5 Design of Engine/Generator Size

The power rating of the engine/generator is designed to be capable of supporting the vehicle at a regular highway speed (130 km/h or 81 mph) on a flat road. Figure 7.15 shows that the engine power needed at 130 km/h or 81 mph is 32.5 kW, in which energy losses in transmission (90% of efficiency), motor drive (85% of efficiency), and generator (90% of efficiency) are involved. Figure 7.15 also indicates that 32.5 kW of engine power can be capable of supporting a vehicle driving at 78 km/h (49 mph) on a 5% grade road.

Another consideration in the design of the power rating of the engine/generator is the average power when driving with some typical stop-and-go driving patterns as illustrated in Figure 7.10. The typical data in these drive cycles are listed in Table 7.1.

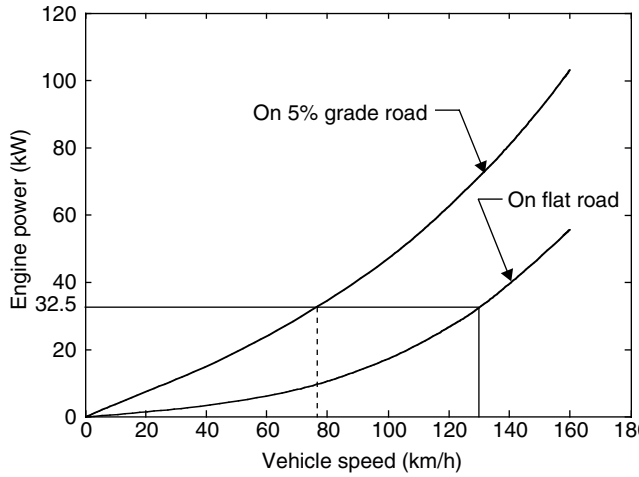

FIGURE 7.15
Engine power vs. vehicle constant speed on a flat road and a 5% grade road

TABLE 7.1

Typical Data of Different Drive Cycles

	Max. Speed (km/h)	Average Speed (km/h)	Average Power with Full Regen. Braking (kW)	Average Power with No Regen. Braking (kW)
FTP 75 urban	86.4	27.9	3.76	4.97
FTP 75 highway	97.7	79.6	12.6	14.1
US06	128	77.4	18.3	23.0
ECE-1	120	49.8	7.89	9.32

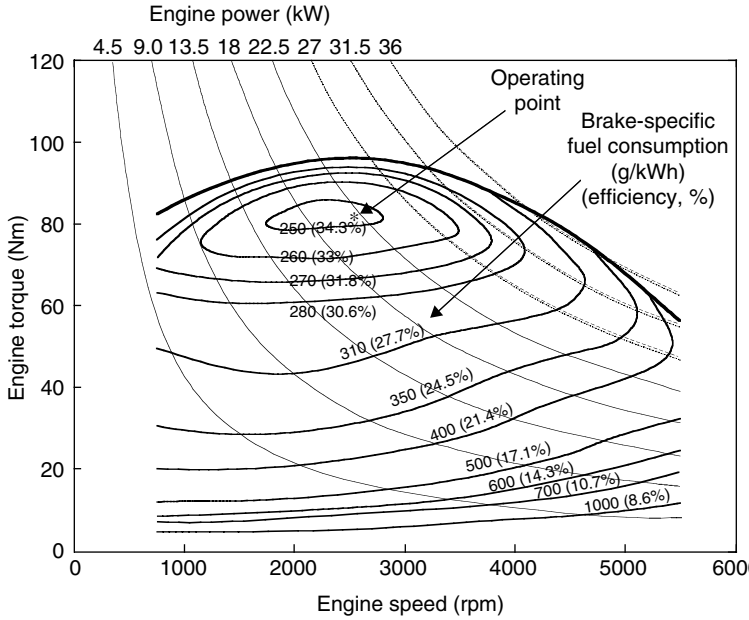

FIGURE 7.16
Engine characteristics and operating points

Compared with the power needed in Figure 7.14, the average power in these drive cycles is smaller. Hence, 32.5 kW of engine power can meet the power requirement in these drive cycles. Figure 7.16 shows the engine characteristics.

7.4.6 Design of the Power Capacity of PPS

The sum of the output power of the engine/generator PPS should be greater than, or at least equal to, the input power of the traction motor. That is,

$$P_{pps} = \frac{P_{motor}}{\eta_{motor}} - P_{e/g} = \frac{82.5}{0.85} - 32.5 \times 0.9 = 67.8 \text{ kW}. \tag{7.12}$$

7.4.7 Design of the Energy Capacity of PPS

The energy capacity of the PPS heavily depends on the drive cycle and overall control strategy. In this design, because the power capacity of the engine/generator is much greater than the average load power and average traction power, the thermostat control strategy (engine-on–off) is considered to be appropriate.

Figure 7.17 shows simulation results of the above vehicle with engine-on–off control strategy in the FTP 75 urban drive cycle. In the simulation,

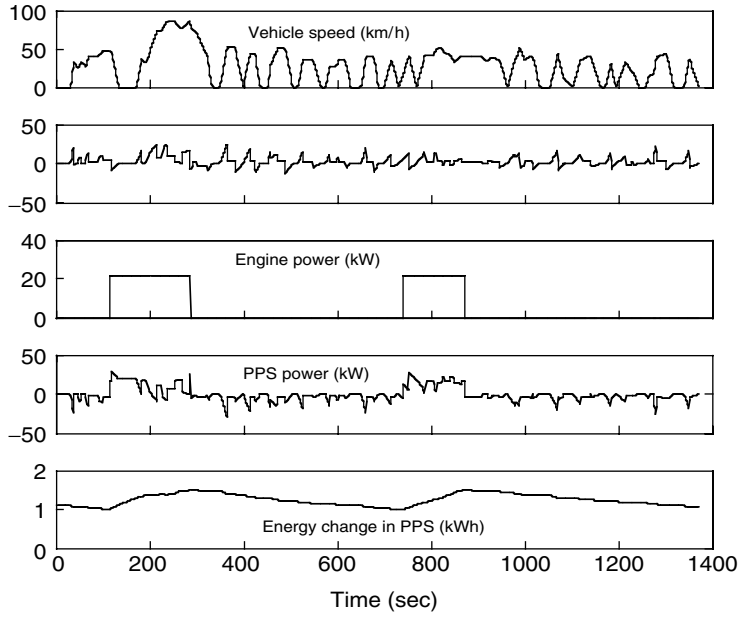

FIGURE 7.17
Simulation results in the FTP 75 urban drive cycle

regenerative braking is involved (see Chapter 11). In the control, the allowed maximum energy variation in the PPS is 0.5 kWh. Suppose that the peaking power allowed to operate in the SOC range is 0.2. Using batteries as the PPS, operating in the range of 0.4 to 0.6 of SOC will have optimal efficiency. Using ultracapacitors, 0.2 variation of SOC will limit the terminal voltage to 10%. The total storage energy in the PPS can be calculated by

$$E_{pps} = \frac{\Delta E_{max}}{\Delta SOC} = \frac{0.5}{0.2} = 2.5 \text{ kWh}. \tag{7.13}$$

7.4.8 Fuel Consumption

The fuel consumption for various drive cycles can be calculated by simulation. In the FTP 75 urban drive cycle (Figure 7.17), the designed drive train has the fuel economy of 17.9 km/l or 42.4 mpg, and in the FTP highway drive cycle (Figure 7.18), it is 18.4 km/l or 43.5 mpg. It is clear that a hybrid vehicle with performance similar to a conventional vehicle is much more efficient, especially in a frequent stop-and-go environment. The main reasons are the high operating efficiency of the engine and the significant amount of braking energy recovered by regenerative braking. Regenerative braking techniques are described in Chapter 11.

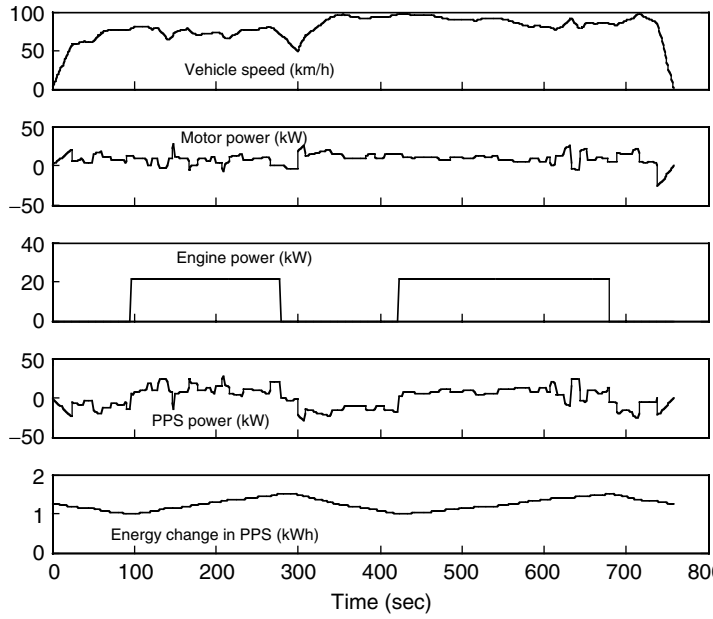

FIGURE 7.18
Simulation results in the FTP 75 highway drive cycle

References

[1] C.C. Chan and K.T. Chau, *Modern Electric Vehicle Technology*, Oxford University Press, New York, 2001.

[2] M. Ehsani, Y. Gao, and K. Butler, Application of electric peaking hybrid (ELPH) propulsion system to a full size passenger car with simulation design verification, *IEEE Transactions on Vehicular Technology*, 48, 1779–1787, 1999.

[3] C.G. Hochgraf, M.J. Ryan, and H.L. Wiegman, Engine control strategy for a series hybrid electric vehicle incorporating load-leveling and computer controlled energy management, *Society of Automotive Engineers (SAE) Journal,* Paper No. 960230, Warrendale, PA, 2002.

[4] M. Ender and P. Dietrich, Duty cycle operation as a possibility to enhance the fuel economy of an SI engine at part load, *Society of Automotive Engineers (SAE) Journal,* Paper No. 960227, Warrendale, PA, 2002.

8

Parallel Hybrid Electric Drive Train Design

CONTENTS

8.1 Control Strategies of Parallel Hybrid Drive Train 261
8.1.1 Maximum State-of-Charge of Peaking Power Source (Max. SOC-of-PPS) Control Strategy 262
8.1.2 Engine Turn-On and Turn-Off (Engine-On–Off) Control Strategy 265
8.2 Design of Drive Train Parameters 266
8.2.1 Design of Engine Power Capacity 266
8.2.2 Design of Electric Motor Drive Power Capacity 268
8.2.3 Transmission Design 271
8.2.4 Energy Storage Design 272
8.3 Simulations 274
References 276

Unlike the series hybrid drive train, the parallel hybrid drive train has features that allow both the engine and traction motor to supply their mechanical power in parallel directly to the driven wheels. The major advantages of parallel configuration over a series configuration are (1) generator is not required, (2) the traction motor is smaller, and (3) multiconversion of the power from the engine to the driven wheels is not necessary. Hence, the overall efficiency can be higher.[5] However, the control of the parallel hybrid drive train is more complex than that of a series hybrid drive train, due to the mechanical coupling between the engine and the driven wheels.

There are several possibilities for configurations in a parallel hybrid drive train, as mentioned in Chapter 5. But the design methodology for one particular configuration may be not applicable to other configurations and the design result for a particular configuration may be applicable for only a given operation environment and mission requirement. This chapter will focus on the design methodology of parallel drive trains with torque coupling, which operate on the electrically peaking principle; that is, the engine supplies its power to meet the base load (operating at a given

constant speed on flat and mild grade roads, or at the average of the load of a stop-and-go driving pattern) and the electrical traction supplies the power to meet the peaking load requirement. Other options, such as a mild hybrid drive train, are discussed in Chapter 9.

The base load is much lower than the peaking load in normal urban and highway driving, as mentioned in Chapter 5. This suggests that the engine power rating is lower than the electrical traction power rating. Due to the better torque–speed characteristics of the traction motor compared to the engine, the single-gear transmission for the traction motor might be the proper option. Thus, this chapter will focus on the design of the drive train as shown in Figure 8.1.

The design objectives are:

1. To satisfy the performance requirements (gradeability, acceleration, and maximum cruising speed)
2. To achieve high overall efficiency
3. To maintain the battery state-of-charge (SOC) at reasonable levels in the whole drive cycle without charging from outside the vehicle
4. To recover the brake energy.

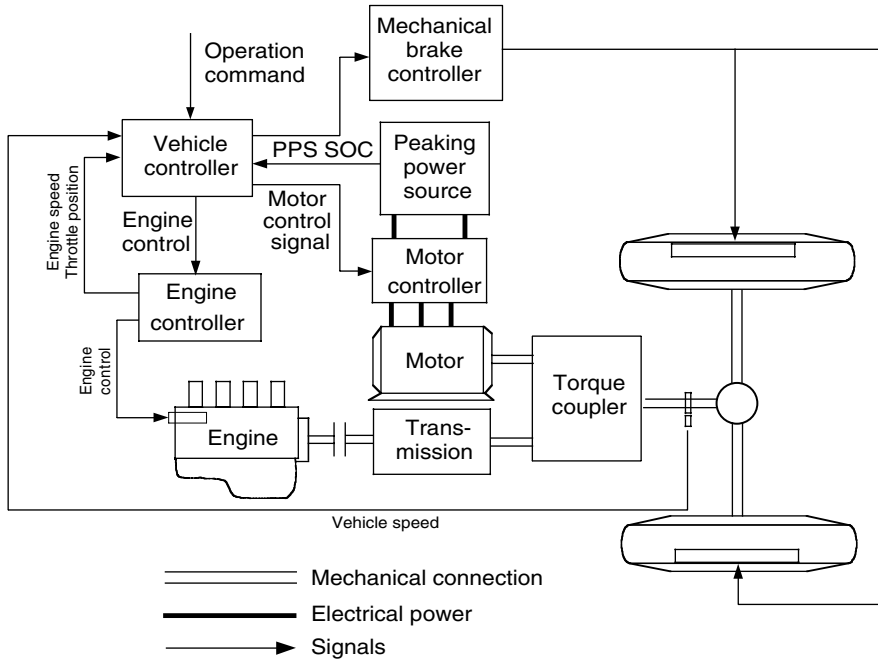

FIGURE 8.1
Configuration of the parallel torque-coupling hybrid drive train

8.1 Control Strategies of Parallel Hybrid Drive Train

The available operation modes in a parallel hybrid drive train, as mentioned in Chapter 5, mainly include (1) engine-alone traction, (2) electric-alone traction, (3) hybrid traction (engine plus motor), (4) regenerative braking, and (5) peaking power source (PPS) charging from the engine. During operation, the proper operation modes should be used so as to meet the traction torque requirement, achieve high overall efficiency, maintain a reasonable level of PPS SOC, and recover braking energy as much as possible.[4]

The overall control scheme consists of two levels. A vehicle system level controller (a high-level controller) functions as a control commander and gives torque commands to low-level controllers (local or component controllers) based on the operator's command, component characteristics, and feedback information from the components. The low-level controllers (local or component controllers), such as the engine controller, motor controller, and transmission controller in a multigear transmission, control the corresponding components to make them operate properly.

The overall control scheme of the parallel hybrid drive train is schematically shown in Figure 8.2. It consists of a vehicle controller, engine controller,

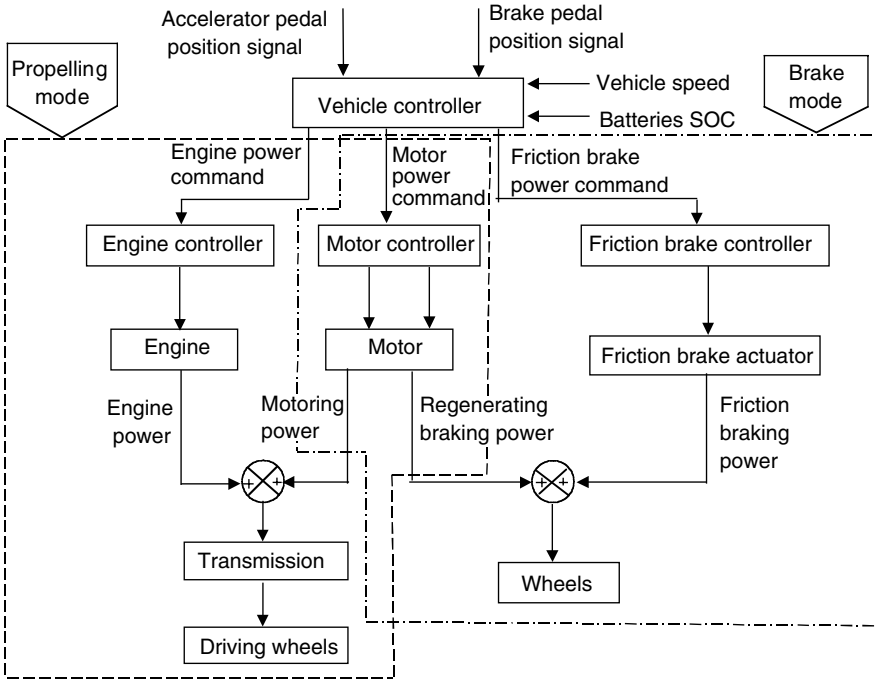

FIGURE 8.2
Overall control scheme of the parallel hybrid drive train

electric motor controller, and mechanical brake controller. The vehicle controller is in the highest position. It collects data from the driver and all the components, such as desired torque, vehicle speed, PPS SOC, engine speed and throttle position, electric motor speed, etc. Based on these data, component characteristics, and preset control strategy, the vehicle controller gives its control signals to each component controller/local controller. Each local controller controls the operation of the corresponding component to meet the requirements of the drive train.

The vehicle controller plays a central role in the operation of the drive train. The vehicle controller should fulfill various operation modes — according to the drive condition and the data collected from components and the driver's command — and should give the correct control command to each component controller. Hence, the preset control strategy is the key to the optimum success of the operation of the drive train.

8.1.1 Maximum State-of-Charge of Peaking Power Source (Max. SOC-of-PPS) Control Strategy

When a vehicle is operating in a stop-and-go driving pattern, the PPS must deliver its power to the drive train frequently. Consequently, the PPS tends to be discharged quickly. In this case, maintaining a high SOC in the PPS is necessary to ensure vehicle performance. Thus, the maximum SOC of the PPS control strategy may be the proper option.[2]

The maximum control strategy can be explained by Figure 8.3. In this figure, the maximum power curves for hybrid traction (engine plus electric motor), engine-alone traction, electric motor-alone traction, and regenerative braking

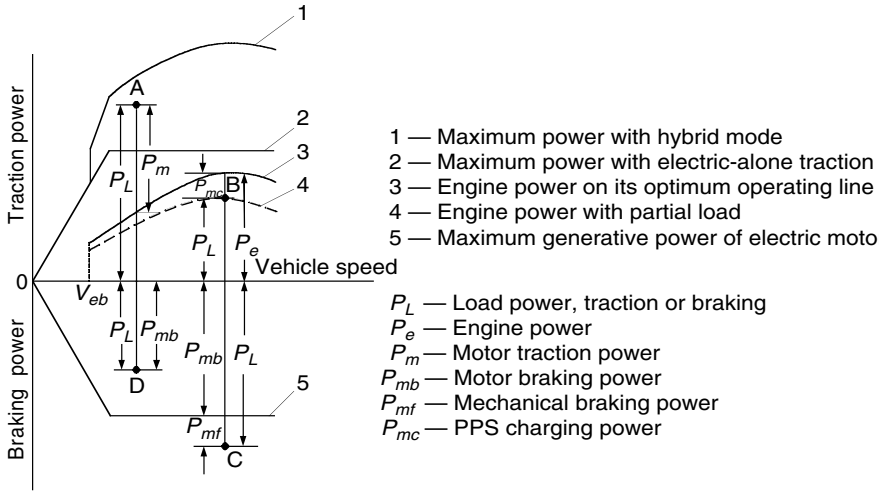

FIGURE 8.3
Demonstration of various operating modes based on power demand

are plotted against vehicle speed. Power demands in different conditions are also plotted, represented by points A, B, C, and D.

The operation modes of the drive train are explained below:

Motor-alone propelling mode: The vehicle speed is less than a preset value V_{eb}, which is considered to be the bottom line of the vehicle speed below which the engine cannot operate steadily. In this case, the electric motor alone delivers its power to the driven wheels, while the engine is shut down or idling. The engine power, electric traction power, and the PPS discharge power can be written as

$$P_e = 0, \tag{8.1}$$

$$P_m = \frac{P_L}{\eta_{t,m}}, \tag{8.2}$$

$$P_{pps\text{-}d} = \frac{P_m}{\eta_m}, \tag{8.3}$$

where P_e is the engine power output, P_L is the load power demand on the drive wheels, $\eta_{t,m}$ is the transmission efficiency from the motor to the driven wheels, P_m is the power output of the electric motor, $P_{pps\text{-}d}$ is the PPS discharge power, and η_m is the motor efficiency.

Hybrid propelling mode: The load power demand, represented by point A in Figure 8.3, is greater than what the engine can produce, both the engine and electric motor must deliver their power to the driven wheels at the same time. This is called hybrid propelling mode. In this case, the engine operation is set on its optimum operation line by controlling the engine throttle to produce power P_e. The remaining power demand is supplied by the electric motor. The motor power output and PPS discharge power are

$$P_m = \frac{P_L - P_e \eta_{t,e}}{\eta_{t,m}}, \tag{8.4}$$

$$P_{pps\text{-}d} = \frac{P_m}{\eta_m}, \tag{8.5}$$

where $\eta_{t,e}$ is the transmission efficiency from the engine to the drive wheels.

PPS charge mode: When the load power demand, represented by point B in Figure 8.3, is less than the power that the engine can produce while operating on its optimum operation line, and the PPS SOC is below its top line, the engine is operated on its optimum operating line, producing its power P_e. In this case, the electric motor is controlled by its controller to function as a generator, powered by the remaining power of the engine. The output power of the electric motor and PPS charge power are

$$P_m = \left(P_e - \frac{P_L}{\eta_{t,e}}\right)\eta_{t,e,m}, \eta_m, \tag{8.6}$$

$$P_{pps\text{-}c} = P_m, \tag{8.7}$$

where $\eta_{t,e,m}$ is the transmission efficiency from the engine to the electric motor.

Engine-alone propelling mode: When the load power demand (represented by point B in Figure 8.3) is less than the power that the engine can produce while operating on its optimum operation line, and the PPS SOC has reached its top line, the engine-alone propelling mode is used. In this case, the electric system is shut down, and the engine is operated to supply the power that meets the load power demand. The power output curve of the engine with a partial load is represented by the dashed line in Figure 8.3. The engine power, electric power, and battery power can be expressed by

$$P_e = \frac{P_L}{\eta_{t,e}}, \tag{8.8}$$

$$P_m = 0, \tag{8.9}$$

$$P_{pps} = 0. \tag{8.10}$$

Regenerative-alone brake mode: When the vehicle experiences braking and the demanded braking power is less than the maximum regenerative braking power that the electric system can supply (as shown in Figure 8.3 by point D), the electric motor is controlled to function as a generator to produce a braking power that equals the commanded braking power. In this case, the engine is shut down or set idling. The motor power output and PPS charge power are

$$P_{mb} = P_L \eta_{t,m} \eta_m, \tag{8.11}$$

$$P_{pps\text{-}c} = P_{mb}. \tag{8.12}$$

Hybrid braking mode: When the demanded braking power is greater than the maximum regenerative braking power that the electric system can supply (as shown in Figure 8.3 by point C), the mechanical brake must be applied. In this case, the electric motor should be controlled to produce its maximum regenerative braking power, and the mechanical brake system should handle the remaining portion. The motor output power, battery charging power, and mechanical braking power are

$$P_{mb} = P_{mb,max} \eta_m, \tag{8.13}$$

$$P_{pps\text{-}c} = P_{mb}. \tag{8.14}$$

It should be noted that for better braking performance, the front forces on the front and rear wheels should be proportional to their normal load on the wheels. Thus, braking power control will not be exactly that mentioned above (for more details, see Chapter 11). The control flowchart of the Max. SCO-of-PPS is illustrated in Figure 8.4.

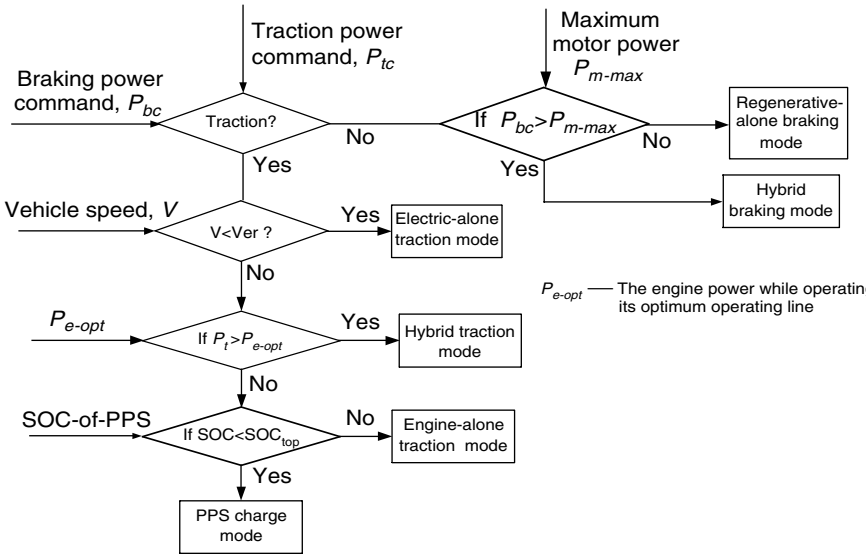

FIGURE 8.4
Flowchart of Max. SOC-of-PPS control strategy

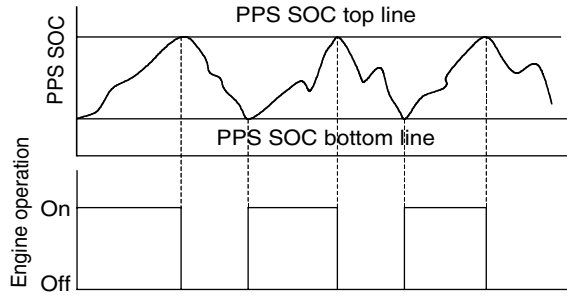

FIGURE 8.5
Illustration of engine-on–off control strategy

8.1.2 Engine Turn-On and Turn-Off (Engine-On–Off) Control Strategy

Similar to that used in a series hybrid drive train, the engine turn-on and turn-off control strategy may be used in some operation conditions with low speed and low acceleration. In an engine-on–off control strategy, the operation of the engine is controlled by the SOC of PPS, as shown in Figure 8.5.

In the engine-on period, the control is Max. SOC-of-PPS strategy. When the SOC of the PPS reaches its top line, the engine is turned off and the vehicle is propelled only by the electric motor. When the SOC of the PPS reaches its bottom line, the engine is turned on and the control again goes into Max. SOC-of-PPS.

8.2 Design of Drive Train Parameters

The parameters of the drive train such as engine power, electric motor power, gear ratios of transmission, and power and energy capacity of the peaking power source are key parameters, and exert a considerable influence on vehicle performance and operation efficiency. However, as initial steps in the design, these parameters should be estimated based on performance requirements. Such parameters should also be refined by more accurate simulations.

In the following sections, the parameters of a passenger car are used in the calculations. These parameters are vehicle mass $M_v = 1500$ kg, rolling resistance coefficient $f_r = 0.01$, air density $\rho_a = 1.205$ kg/m^3, front area $A_f = 2.0$ m^2, aerodynamic drag coefficient $C_D = 0.3$, radius of driven wheels $r = 0.2794$ m, and transmission efficiency from engine to drive wheels $\eta_{t,e} = 0.9$, and from motor to drive wheels $\eta_{t,m} = 0.95$.

8.2.1 Design of Engine Power Capacity

The engine should be able to supply sufficient power to support the vehicle operation at normal constant speeds both on a flat and a mild grade road without the help of the PPS. At the same time, the engine should be able to produce an average power that is larger than the average load power when the vehicle operates with a stop-and-go operating pattern.

As a requirement of normal highway driving at constant speed on a flat or a mild grade road, the power needed is expressed as

$$P_e = \frac{V}{1000\eta_{t,e}}\left(M_v g f_r + \frac{1}{2}\rho_a C_D A_f V^2 + M_v g\, i\right)(\text{kW}). \tag{8.15}$$

Figure 8.6 shows the load powers of a 1500 kg example passenger car, along with vehicle speed, on a flat road and a road with 5% grade. It is seen that on a flat road, a speed of 160 km/h (100 mph) needs a power of 42 kW. For a comprehensive analysis, the power curves of a 42 kW engine with a multigear transmission are also plotted in Figure 8.6. From Figure 8.6, it can also be seen that on a 5% grade road, the vehicle can reach a maximum speed of about 92 and 110 km/h with the fourth gear and third gear, respectively.

The above-designed engine power should be evaluated so that it meets the average power requirement while driving in a stop-and-go pattern. In a drive cycle, the average load power of a vehicle can be calculated by

$$P_{ave} = \frac{1}{T}\int_0^T \left(M_v g f_r V + \frac{1}{2}\rho_a C_D A_f V^3 + \delta M_v V \frac{dV}{dt}\right) dt. \tag{8.16}$$

The average power varies with the degree of regenerative braking. The two extreme cases are the full and zero regenerative braking cases. Full regenerative braking recovers all the energy consumed in braking and the average power is calculated by (8.16). However, when the vehicle has no regenerative

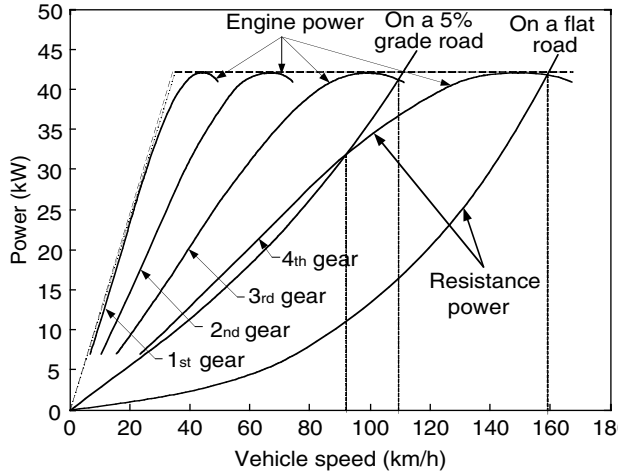

FIGURE 8.6
Engine power required at constant speed on a flat road and a 5% grade road

braking, the average power is larger than that with full regenerative braking, which can be calculated from (8.16) in such a way that when the instantaneous power is less than zero, it is given a zero.

Figure 8.7 shows the vehicle speed, instantaneous load power, and average powers with full regenerative braking and zero regenerative braking, in some typical drive cycles for a 1500 kg passenger car.

In the engine power design, the average power that the engine can produce must be greater than the average load power. In a parallel drive train, the engine is mechanically coupled to the driven wheels. Hence, the engine rotating speed varies with the vehicle speed. On the other hand, the engine power with full throttle varies with engine rotating speed. Thus, the determination of the engine power to meet the average power in a drive cycle is not as straightforward as in a series hybrid, in which the engine operating can be fixed. The average power that the engine can produce with full throttle can be calculated as

$$P_{max\text{-}ave} = \frac{1}{T}\int_0^T P_e(v)\, dt, \tag{8.17}$$

where T is the total time in drive cycles and $P_e(v)$ is the engine power with full throttle, which is a function of vehicle speed when the gear ratio of the transmission is given, as shown in Figure 8.6.

The possible operating points of the engine with full throttle and the maximum possible average powers in some typical drive cycles are shown in Figure 8.8, in which the maximum engine power is 42 kW and transmission is single gear (fourth gear only in Figure 8.6). Comparing these maximum possible average powers to the load average powers, as shown in Figure 8.7, it is concluded that the engine power is sufficient to support a vehicle operating in these typical drive cycles.

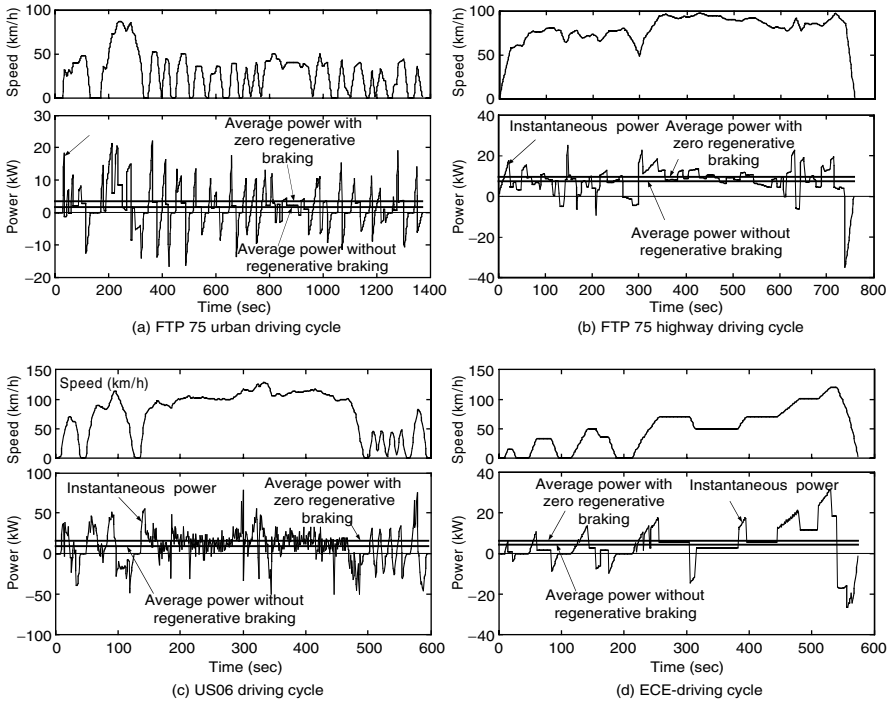

FIGURE 8.7
Instantaneous power and average power with full and zero regenerative braking in typical drive cycles

8.2.2 Design of Electric Motor Drive Power Capacity

In HEV, the major function of the electric motor is to supply peak power to the drive train. In the motor power design, acceleration performance and peak load power in typical drive cycles are the major concerns.[3]

It is difficult to directly design the motor power from the acceleration performance specified. It is necessary to make a good estimate based on specified acceleration requirements, and then make a final design through accurate simulation. As an initial estimate, one can make the assumption that the steady-state load (rolling resistance and aerodynamic drag) is handled by the engine and the dynamic load (inertial load in acceleration) is handled by the motor. With this assumption, acceleration is directly related to the torque output of an electric motor by

$$\frac{T_m i_{t,m} \eta_{t,m}}{r} = \delta_m M_v \frac{dV}{dt}, \tag{8.18}$$

where T_m is the motor torque and δ_m is the mass factor associated with the electric motor (refer to Chapter 2).

Using the output characteristics of the electric motor shown in Figure 8.5, and a specified acceleration time, t_a, from zero speed to final high speed, V_f,

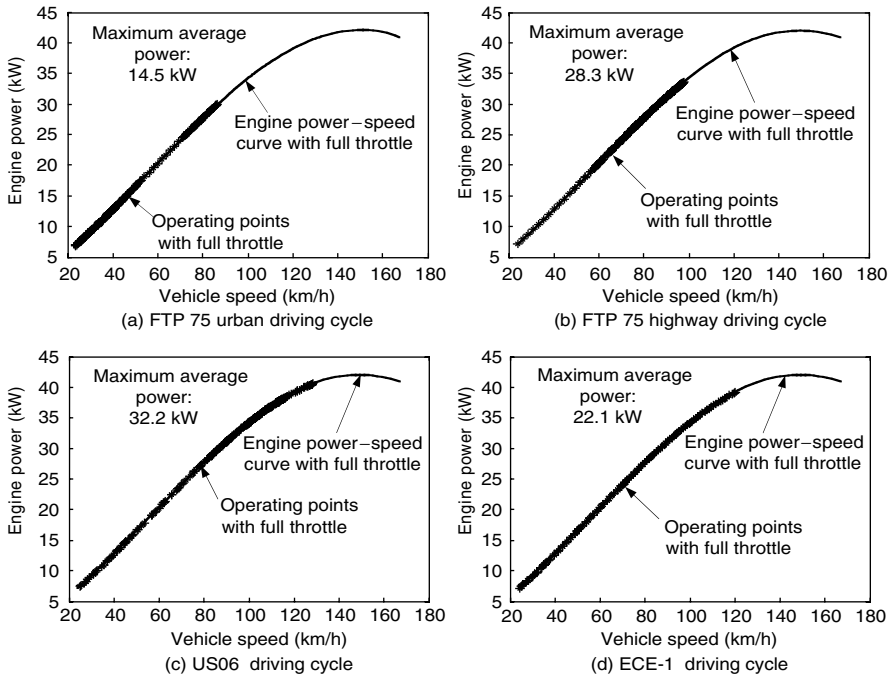

FIGURE 8.8
Maximum possible operating points of the engine and the maximum average power in typical drive cycles

and referring to Chapter 4, the motor power rating is expressed as

$$P_m = \frac{\delta_m M_v}{2\eta_{t,m} t_a}(V_f^2 + V_b^2). \tag{8.19}$$

For a 1500 kg passenger car with a maximum speed of 160 km/h, a base speed of 50 km/h, a final acceleration speed of 100 km/h, acceleration time $t_a = 10$ sec, and $\delta_m = 1.04$, the power rating of the electric motor is 74 kW (Figure 8.9).

It should be noted that the motor power obtained above is somewhat overestimated. Actually, the engine has some remaining power to help the electric motor to accelerate the vehicle as shown in Figure 8.6. This fact is also shown in Figure 8.10, in which vehicle speed, engine power with full throttle, resistance power (rolling resistance, aerodynamic drag, and power losses in transmission), and single-gear transition are plotted along the acceleration time. The average remaining power of the engine, used to accelerate the vehicle, can be expressed as

$$P_{e,a} = \frac{1}{t_a - t_i}\int_{t_i}^{t_a}(P_e - P_r)\,dt, \tag{8.20}$$

where P_e and P_r are the engine power and resistance power, respectively. It should be noted that the engine power transmitted to the driven wheels is

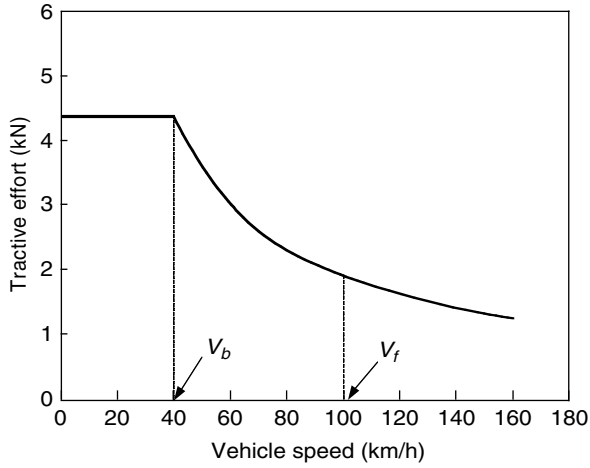

FIGURE 8.9
Tractive effort vs. vehicle speed of an electric motor-driven vehicle

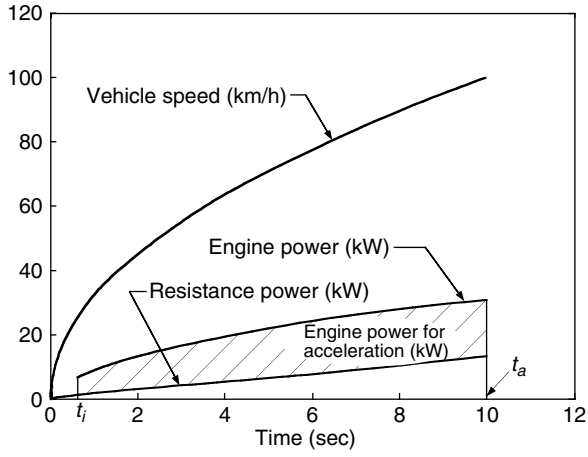

FIGURE 8.10
Vehicle speed, engine power, and resistance power vs. acceleration time

associated with the transmission, that is, the gear number and gear ratios. It is clear from Figure 8.6 that a multigear transmission will effectively increase the remaining power at the driven wheels, thus reducing the motor power required for acceleration.

Using the numbers of engine power and vehicle parameters mentioned above, the engine's remaining power (as shown in Figure 8.10) is obtained as 17 kW. Thus, the motor power is finally estimated as $74-17=57$ kW.

When the power ratings of the engine and electric motor are initially designed, a more accurate calculation needs to be performed to evaluate the

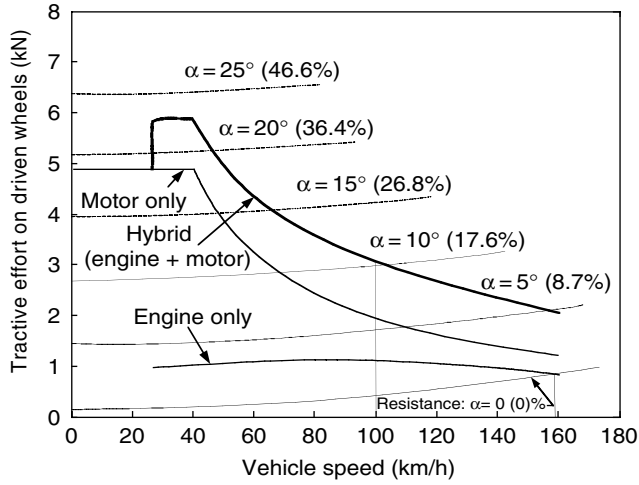

FIGURE 8.11
Tractive effort and resistance on slope road vs. vehicle speed

vehicle performance, mainly maximum speed, gradeability, and acceleration. The maximum speed and gradeability can be obtained from the diagram of tractive effort and resistance vs. vehicle speed. This diagram can be made by using the methods discussed in Chapter 2.

The diagram (as shown in Figure 8.11) shows the design results of an example passenger car. It indicates that the vehicle at 100 km/h has a gradeability of 4.6% (2.65°) for the engine-alone mode, 10.36% (5.91°) for the motor-alone mode, and 18.14% (10.28°) for the hybrid mode (engine plus motor).

Figure 8.12 shows the acceleration performance for the passenger car example. It indicates that 10.7 sec are used and 167 m are covered for accelerating the vehicle from zero speed to 100 km/h.

8.2.3 Transmission Design

Since the electric motor supplies the peak power and has high torque at low speed, single-gear transmission between the electric motor and the driven wheels can produce sufficient torque for hill climbing and acceleration (refer to Figure 8.11). However, a multigear transmission between the engine and driven wheels can indeed enhance the vehicle performance.

The use of multigear transmission, as shown in Figure 8.6, can effectively increase the remaining power of the engine. Consequently, the vehicle performance (acceleration and gradeability) can be improved. On the other hand, the energy storage can be charged with the large power of the engine. The vehicle fuel economy can also be improved, since the use of proper gears of the multigear transmission allows the engine to operate closer to its optimal speed region. Furthermore, the large remaining power of the engine can quickly charge the energy storage from low SOC to high SOC.[1]

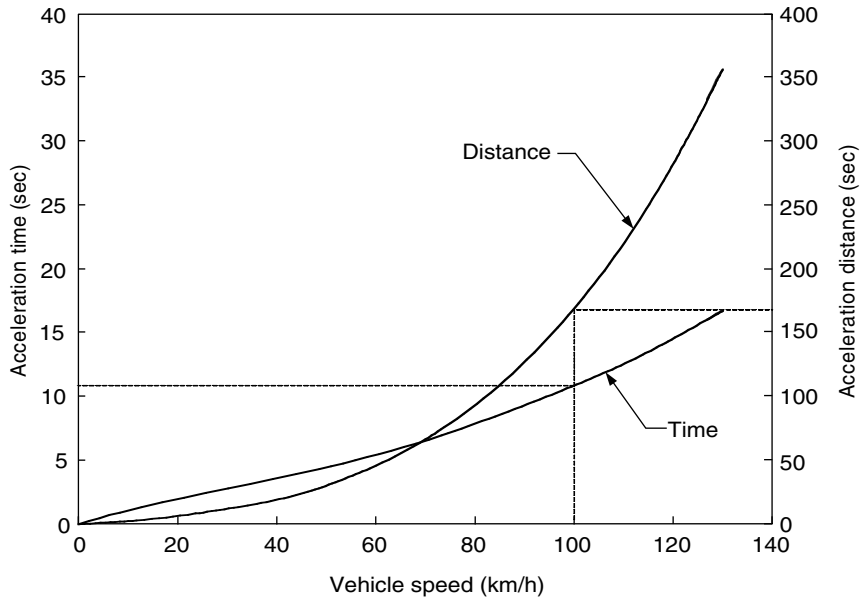

FIGURE 8.12
Acceleration time and distance vs. vehicle speed

However, multigear transmission is much more complex, heavier, and larger than single-gear transmission. Moreover, it also needs a complicated gear shifting control. Thus, in the design of parallel HEV, some trade-offs must be made.

8.2.4 Energy Storage Design

The energy storage design mainly includes the design for the power and energy capacity. The power capacity design is somewhat straightforward. The terminal power of the energy storage must be greater than the input electric power of the electric motor, that is,

$$P_s \geqslant \frac{P_m}{\eta_m}, \tag{8.21}$$

where P_m and η_m are the motor power rating and efficiency.

The energy capacity design of the energy storage is closely associated with the energy consumption in various driving patterns — mainly the full load acceleration and in typical drive cycles.

During the acceleration period, the energies drawn from energy storage and the engine can be calculated along with the calculation of the acceleration time and distance by

$$E_s = \int_0^{t_a} \frac{P_m}{\eta_m}\, dt \tag{8.22}$$

and

$$E_{eng} = \int_0^{t_a} P_e dt, \tag{8.23}$$

where E_s and E_{eng} are the energy drawn from the energy storage and the engine, respectively, and P_m and P_e are the powers drawn from the motor and engine, respectively. Figure 8.13 shows the energies drawn from the energy storage and the engine in the period of acceleration along the vehicle speed for the example passenger car. At an end speed of 120 km/h, about 0.3 kWh energy is drawn from the energy storage.

The energy capacity of the energy storage must also meet the requirement while driving in a stop-and-go pattern in typical drive cycles. The energy changes of the energy storage can be obtained by

$$E_c = \int_0^t (P_{sc} - P_{sd})\, dt, \tag{8.24}$$

where P_{sc} and P_{sd} are the charging and discharging power of the energy storage. With a given control strategy, the charging and discharging power of the energy storage can be obtained by drive train simulation.

Figure 8.14 shows the simulation results of the example passenger car in an FTP 75 urban drive cycle with maximum SOC control strategy. It can be seen that the maximum energy change in the energy storage is about 0.11 kWh, which is less than that in full load acceleration (0.3 kWh). Thus, the energy consumption in fuel load acceleration determines the energy capacity of the energy storage.

Actually, not all the energy stored in the energy storage can be fully used to deliver sufficient power to the drive train. In the case of batteries used as the energy storage, low SOC will limit their power output, and will at the same time lead to a low efficiency, due to an increase of internal resistance. In the case of ultracapacitors used as the energy storage, low SOC will result in low terminal voltage that will affect the performance of the traction motor.

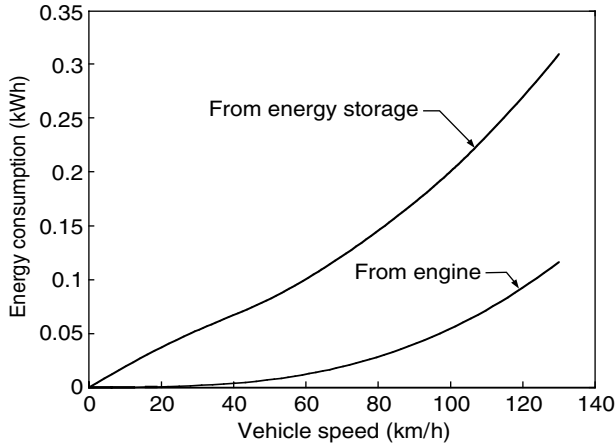

FIGURE 8.13
Energies drawn from the energy storage and engine in the acceleration period

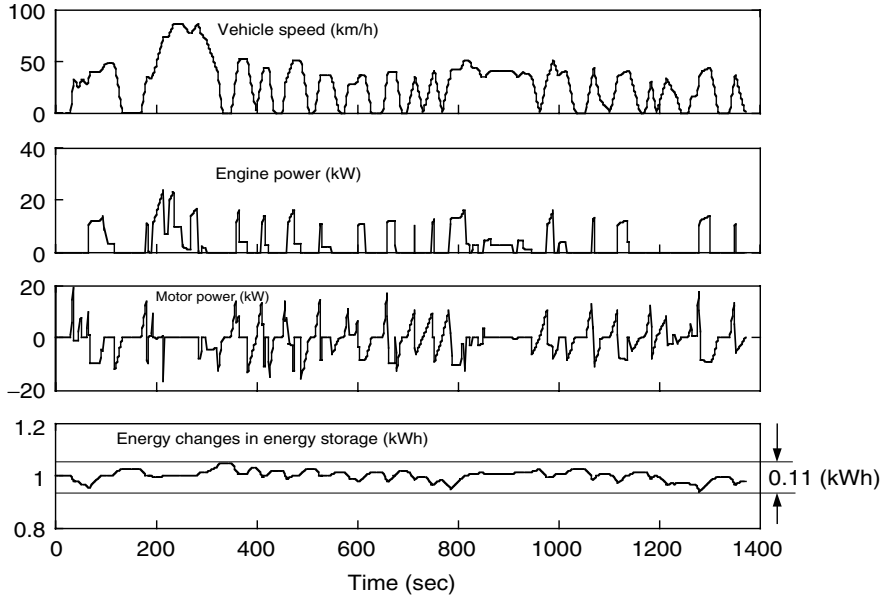

FIGURE 8.14
Vehicle speed, engine power, electric motor power, and energy changes in energy storage in an FTP 75 urban drive cycle with maximum SOC control strategy

Similarly, when a flywheel is used, low SOC means the low flywheel speed at which the terminal voltage of the electric machine, functioning as the energy exchange port, is low. Thus, only part of the energy stored in the energy storage can be available for use, which can be presented by the percentage of its SOC. Thus, the energy capacity of the energy storage can be obtained as

$$E_{cs} = \frac{E_D}{SOC_t - SOC_b}, \tag{8.25}$$

where E_d is the energy discharged from the energy storage, and SOC_t and SOC_b are the top line and bottom line of the SOC of the energy storage. In the example, $E_d = 0.3$ kW and, assuming that 30% of the total energy of the energy storage is allowed to be used, the minimum energy capacity of the energy storage is 1 kWh.

8.3 Simulations

When all the major components have been designed, the drive train should be simulated by using a simulation program. The simulation in typical drive cycles can produce plenty of useful information about the drive train, such

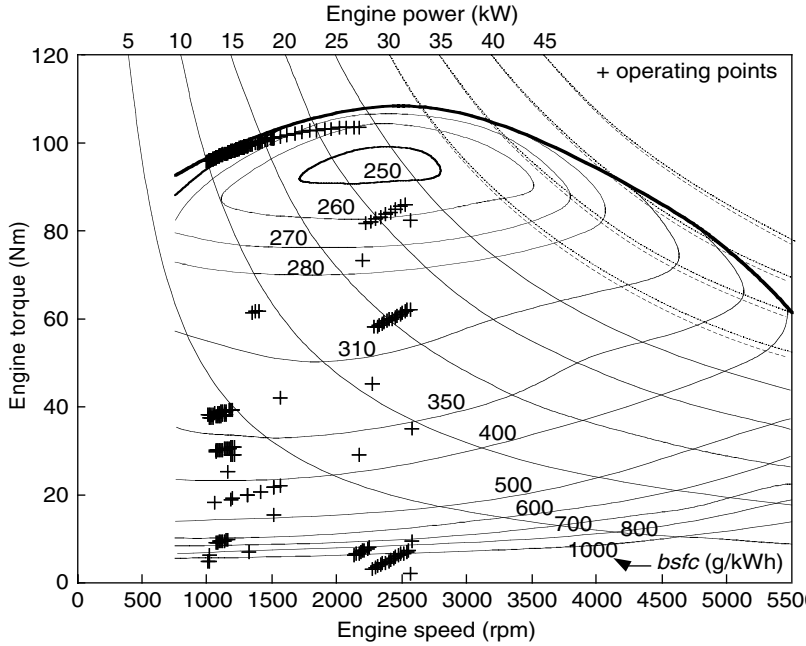

FIGURE 8.15
Engine operating points overlap its fuel consumption map in an FTP 75 urban drive cycle with maximum SOC control strategy

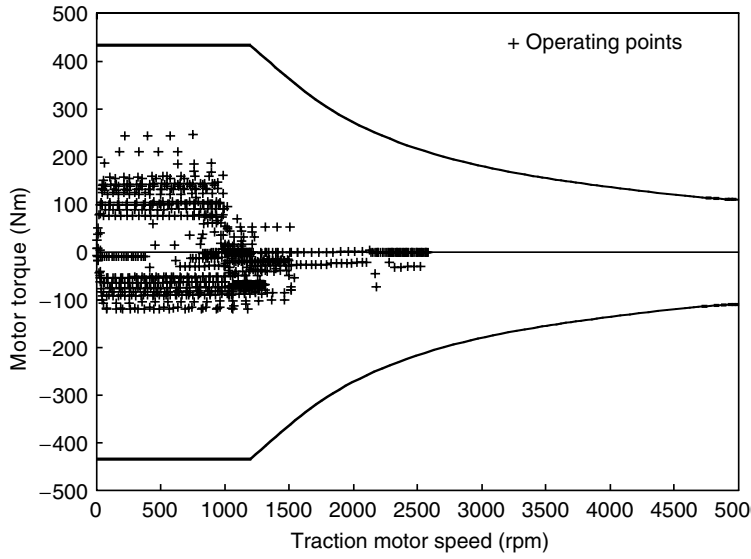

FIGURE 8.16
Motor operating points in an FTP 75 urban drive cycle with maximum SOC control strategy

as engine power, electric motor power, energy changes in the energy storage, engine operating points, motor operating points, fuel consumption, etc.

Figure 8.14 shows the vehicle speed, engine power, motor power, and energy changes in the energy storage along with the driving time for the example passenger car in the FTP 75 urban drive cycle. Figure 8.15 and Figure 8.16 show the engine and motor operating points, respectively. The simulation results in the fuel economy of the example passenger car as 4.66 l per 100 km or 50.7 mi per gallon when the engine is turned off during the period of standstill and braking, and 5.32 l per 100 km or 44.4 mi per gallon when the engine is set at idle during the period of standstill and braking.

References

[1] Y. Gao, K.M. Rahman, and M. Ehsani, Parametric design of the drive train of an electrically peaking hybrid (ELPH) vehicle, *Society of Automotive Engineers (SAE) Journal,* Paper No. 970294, Warrendale, PA, 1997.

[2] Y. Gao, K.M. Rahman, and M. Ehsani, The energy flow management and battery energy capacity determination for the drive train of electrically peaking hybrid, *Society of Automotive Engineers (SAE) Journal,* Paper No. 972647, Warrendale, PA, 1997.

[3] Y. Gao, H. Moghbelli, and M. Ehsani, Investigation of proper motor drive characteristics for military vehicle propulsion, *Society of Automotive Engineers (SAE) Journal,* Paper No. 2003-01-2296, Warrendale, PA, 2003.

[4] M. Ehsani, Y. Gao, and K. Butler, Application of electric peaking hybrid (ELPH) propulsion system to a full size passenger car with simulation design verification, *IEEE Transactions on Vehicular Technology,* 48, 6, 1999.

[5] M. Ehsani, K.L. Butler, Y. Gao, K.M. Rahman, and D. Burke, Toward a sustainable transportation without sacrifice of range, performance, or air quality: the ELPH car concept, *International Federation of Automotive Engineering Society Automotive Congress,* Paris, France, Sept./Oct. 1998.

9

Mild Hybrid Electric Drive Train Design

CONTENTS

9.1 Energy Consumed in Braking and Transmission 278
9.2 Parallel Mild Hybrid Electric Drive Train.....280
9.2.1 Configuration 280
9.2.2 Operating Modes and Control Strategy 281
9.2.3 Drive Train Design.....283
9.2.4 Performance 285
9.3 Series–Parallel Mild Hybrid Electric Drive Train 287
9.3.1 Configuration of the Drive Train with a Planetary Gear Unit.....287
9.3.2 Operating Modes and Control.....291
9.3.2.1 Speed-Coupling Operating Mode 291
9.3.2.2 Torque-Coupling Operating Mode 293
9.3.2.3 Engine-Alone Traction Mode 294
9.3.2.4 Regenerative Braking Mode.....294
9.3.2.5 Engine Starting.....295
9.3.3 Control Strategy 295
9.3.4 Drive Train with Floating-Stator Motor 296
References 298

Full hybrid electric vehicles with parallel or series configurations can significantly reduce fuel consumption by operating the engine optimally and using effective regenerative braking.[6,7] However, a high electric power demand requires a bulky and heavy energy storage pack. This means that energy loss in tire rolling will increase, packing the drive train under the hood will be difficult, and the loading capacity of the vehicle will be reduced. Full hybrid drive trains have structures totally different from conventional drive trains. To turn totally from conventional drive trains to full hybrids, a huge investment of time and money is needed. A compromise is to develop an intermediate product that is easier to convert from the current products, and yet is more efficient than those products. One solution is to put a small electric motor behind the engine to constitute the so-called mild or soft hybrid electric

drive train. This small electric motor can operate as an engine starter as well as electrical generator. It can also add additional power to the drive train when high power is demanded and can convert part of the braking energy into electric energy. This small motor can potentially replace the clutch or the torque converter, which is inefficient when operating with a high slip ratio.

A mild hybrid electric drive train does not need high power energy storage due to the small power rating of the electric motor. A 42 V electrical system may be able to meet the requirements. Other subsystems of conventional vehicles, such as engine, transmission (gear box), and brake do not need many changes.

This chapter introduces two typical configurations of the mild hybrid drive trains. Their control and parametric design are explained along with a design example.

9.1 Energy Consumed in Braking and Transmission

As indicated in Chapter 11, a significant amount of energy, is consumed in braking, especially when driving in urban areas. Chapter 11 also indicates that the braking power in normal driving is not large (refer to Figure 11.5).[5,8] Thus, a small motor would be able to recover most of the braking energy.

Another source of energy loss in conventional vehicles is the transmission. Conventional vehicles are usually equipped with automatic transmissions, especially in North America. In the automatic transmission, the dynamic hydraulic torque converter is the basic element, and has low efficiency when operating with a low speed ratio (high speed slip), as shown in Figure 9.1.

When the vehicle is operating with a stop-and-go driving pattern in urban areas, the frequent accelerating of the vehicle leads to a low speed ratio in the torque converter, thus resulting in low operation efficiency. Figure 9.2 shows the operating efficiency of a typical automatic transmission in an FTP 75 urban drive cycle. In this drive cycle, the average efficiency is around 0.5.[1,2]

In addition, when driving in urban areas, the engine idling time in standstill and braking is significant. In an FTP 75 drive cycle, the percentage of engine idling time reaches 44%, and in New York City it reaches about 57%. When the engine is idling, not only does the engine itself consume energy, but energy is also needed to drive the transmission. For instance, about 1.7 kW of engine power is needed to drive the automatic transmission when the vehicle is at a standstill.

Using a small electric motor to replace the torque converter and then constitute a mild hybrid electric drive train is considered to be an effective approach to saving the energy losses in an automatic transmission, and also during braking and engine idling operations.

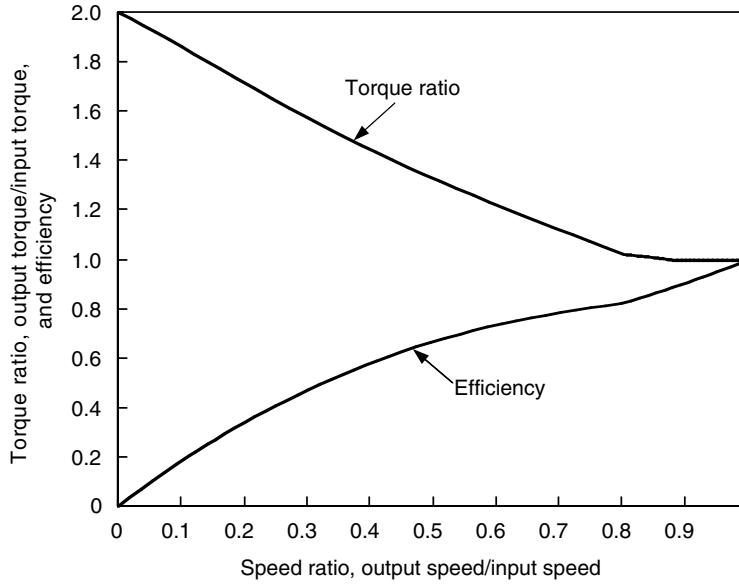

FIGURE 9.1
Characteristics of a typical dynamic hydraulic torque converter

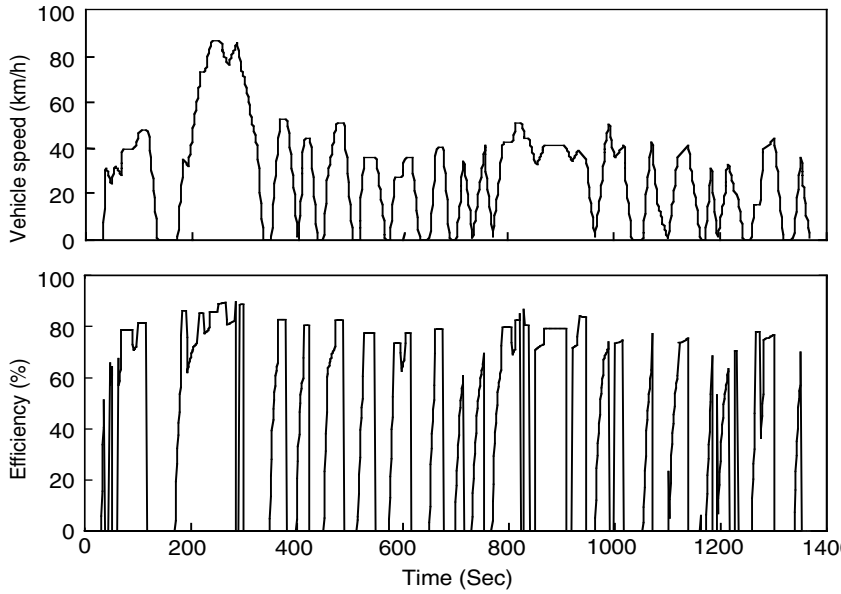

FIGURE 9.2
Vehicle speed and operating efficiency of an automatic transmission while driving in an FTP 75 urban drive cycle

9.2 Parallel Mild Hybrid Electric Drive Train

9.2.1 Configuration

A parallel connected mild hybrid electric drive train is shown in Figure 9.3. A small electric motor, which can function as an engine starter, generator, and traction motor, is placed between the engine and the automatically shifted multigear transmission (gearbox). The clutch is used to disconnect the gearbox from the engine when needed, such as during gear shifting and

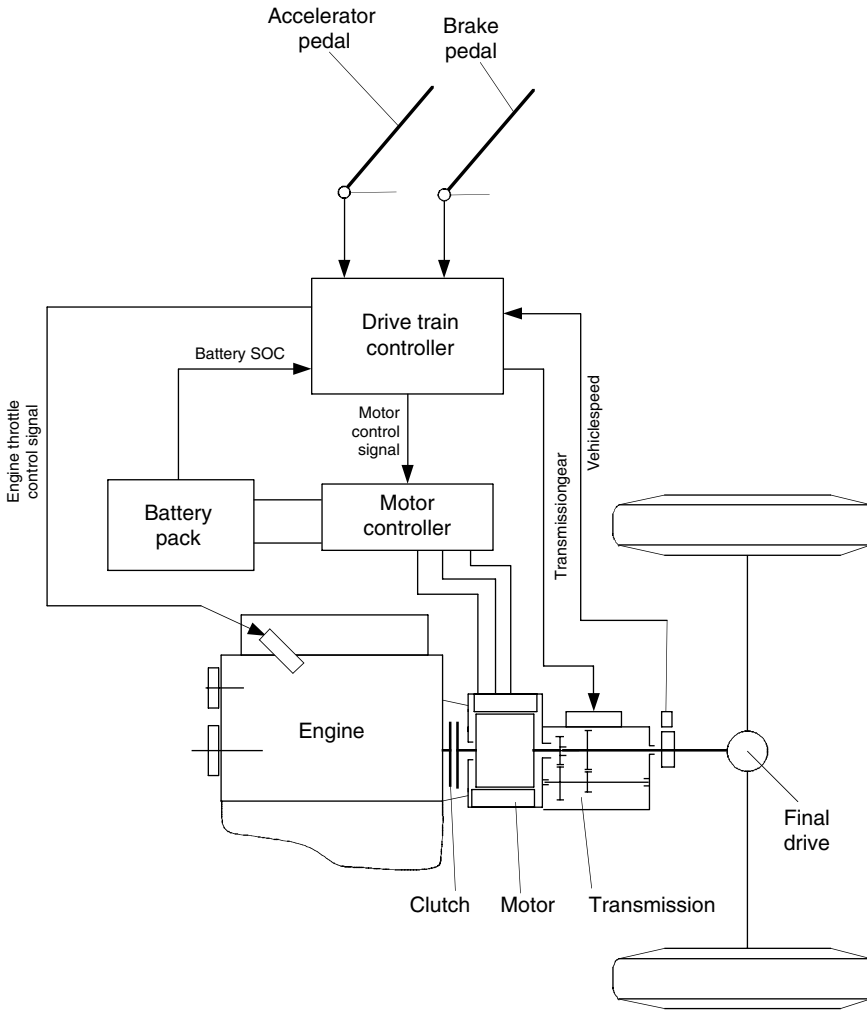

FIGURE 9.3
Configuration of the parallel connected mild hybrid electric drive train

low vehicle speed. The power rating of the electric motor may be in the range of about 10% of the engine power rating. The electric motor can be smoothly controlled to operate at any speed and torque; thus, isolation between the electric motor and transmission is not necessary. The operation of the drive train and each individual component is controlled by the drive train controller and component controllers.

9.2.2 Operating Modes and Control Strategy

The drive train has several operating modes, depending on the operation of the engine and electric motor.

Engine-alone traction mode. In this mode, the electric motor is de-energized, and the vehicle is propelled by the engine alone. This mode may be used when the state-of-charge (SOC) of the batteries is in the high region, and the engine alone can handle the power demand.

Motor-alone traction mode. In this mode, the engine is shut down and the clutch is disengaged (open). The vehicle is propelled by the electric motor alone. This operating mode may be used at low vehicle speed: less than 10 km/h, for example.

Battery charge mode. In this mode, the electric motor operates as a generator and is driven by the engine to charge the batteries.

Regenerative braking mode. In this mode, the engine is shut down and the clutch is disengaged. The electric motor is operated to produce a braking torque to the drive train. Part of the kinetic energy of the vehicle mass is converted into electric energy and stored in the batteries.

Hybrid traction mode. In this mode, both the engine and electric motor deliver traction power to the drive train.

Which of the above operating modes is used in real operation depends on the power demand, which is commanded by the driver through the accelerator or brake pedal, the SOC of the batteries, and vehicle speed.

Control strategy is the preset control logic in the drive train controller. The drive train controller receives the real-time signals from the driver and each individual component (refer to Figure 9.3), and then commands the operation of each component, according to the preset control logic. A proposed control logic is illustrated in Table 9.1 and Figure 9.4.[1]

TABLE 9.1

Illustration of the Control Logic

Driving Condition	Control Operation
Standstill	Both engine and motor are shut down
Low speed (<10 km/h)	Electric motor-alone traction
Braking	Regenerative braking
High power demand (greater than the power that the engine can produce)	Hybrid traction
Middle and low power demand	Battery charge mode or engine-alone traction mode, depending on the battery SOC (see Figure 9.5)

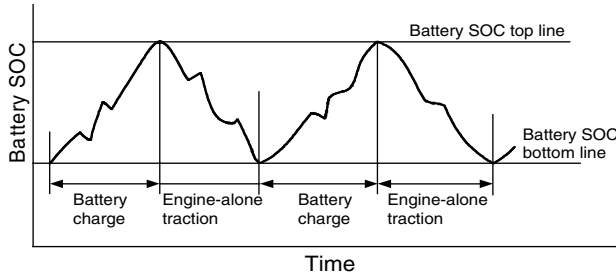

FIGURE 9.4
Battery charge and engine-alone traction, depending on the battery SOC

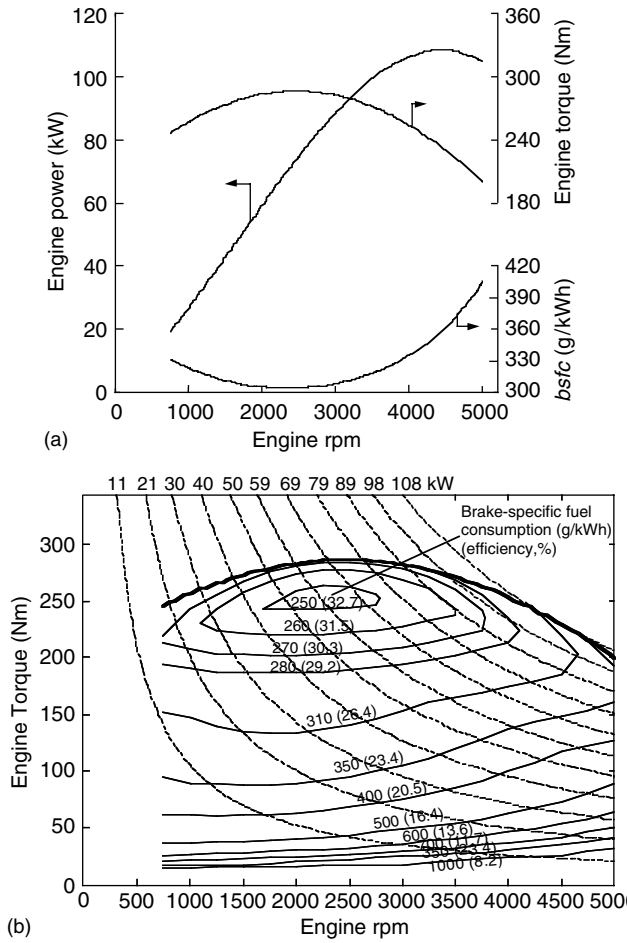

FIGURE 9.5
Performance of the engine: (a) performance with full throttle and (b) fuel consumption map

9.2.3 Drive Train Design

The design of the mild hybrid electric drive train is very similar to the design of the conventional drive train, because the mild hybrid drive train is very close to the conventional drive train. The following is an example of the systematic design of a 1500 kg passenger car drive train. The major parameters of the vehicle are listed in Table 9.2.

Referring to the similar conventional drive train, the engine is designed to have a peak power of 108 kW. The engine characteristics of performance are shown in Figure 9.5.

In this design, a small motor with 7 kW rating power is used, which can operate as an engine starter, alternator, and assist regenerative braking. Figure 9.6 shows the torque and power characteristics vs. the speed of this motor.

TABLE 9.2

Major Parameters of the Mild Hybrid Electric Drive Train

Vehicle mass	1500 kg
Rolling resistance coefficient	0.01
Aerodynamic drag coefficient	0.28
Front area of the vehicle	2.25 m^2
Four-gear transmission	
Gear ratio:	
1st gear	2.25
2nd gear	1.40
3rd gear	1.00
4th gear	0.82
Final gear ratio	3.50

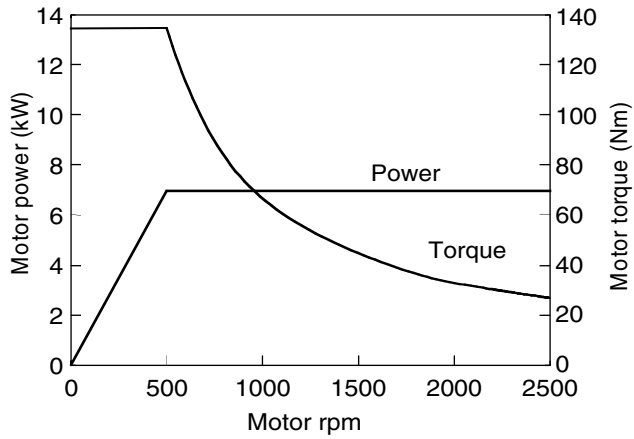

FIGURE 9.6.
Power and torque of electric motor vs. motor speed

The batteries in this design example are lead-acid batteries. Lead-acid batteries are popularly used in automobiles and are expected to be used more widely in the near future due to their mature technology and low cost. They have a relatively high power density, compared with other kinds of common batteries.[4] Thus, they are considered to be the right choice for hybrid electric vehicles, in which power density is more important than energy density.

A cell of a lead-acid battery has the characteristics as shown in Figure 9.7. The terminal voltage varies with discharging current and time, which represent in turn, the SOC of the battery. These characteristics can be modeled simply as shown in Figure 9.8.

In the discharging process, the battery's terminal voltage can be expressed as

$$V_t = V_0(SOC) - (R_i(SOC) + R_c)I, \tag{9.1}$$

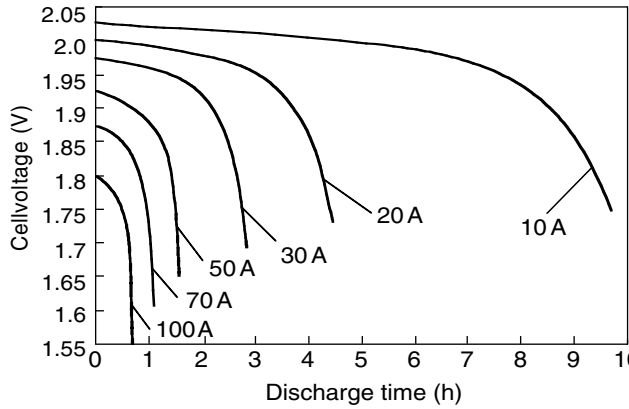

FIGURE 9.7
Discharge characteristics of the lead-acid battery

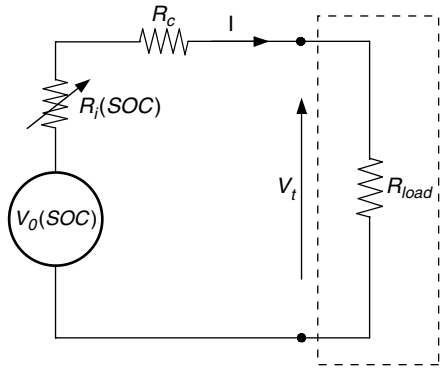

FIGURE 9.8
Battery model

where $V_0(SOC)$ and $R_i(SOC)$ are the open circuit voltage and internal resistance of the battery respectively, which are functions of battery *SOC*, and R_c is the conductor resistance. The discharging power at the terminals can be expressed as

$$P_t = I\,V_0(SOC) - (R_i(SOC) + R_c)I^2. \tag{9.2}$$

The maximum power that the load can obtain at the terminals is expressed as

$$P_{t\,max} = \frac{V_0^2(SOC)}{4(R_i(SOC)+R_c)}. \tag{9.3}$$

This maximum power is obtained when the discharging current is

$$I = \frac{V_0}{2(R_i(SOC)+R_c)}. \tag{9.4}$$

Figure 9.9(a) shows the terminal voltages and currents of 36 and 12 V batteries with a current capacity of 100 A h vs. load power (discharge power). It indicates that for the 36 V battery, the maximum power that the battery can supply is about 8.5 kW. But for the 12 V battery, it is less than 3 kW. Figure 9.9(b) shows that the 36 V battery has a discharge efficiency of over 70% at power less than 7 kW. For the 12 V voltage battery, it is less than 2.5 kW. Thus, for the mild hybrid electric drive train proposed in this chapter, a 42 V electric system (36 V battery) can support the operation of the electric motor (rated power of 7 kW).

9.2.4 Performance

Because there are few differences from the conventional drive train (engine, transmission, etc.), the mild hybrid electric drive train is expected to have similar acceleration and gradeability performance. Figure 9.10 shows the performance of a 1500 kg mild hybrid passenger car.

Figure 9.11 shows the simulation results of a 1500 kg hybrid passenger car in an FTP 75 urban drive cycle. Figure 9.11(b) indicates that a mild hybrid electric drive train with a small motor cannot significantly improve engine operating efficiency because most of the time, the engine still operates in a low load region. However, because of the elimination of engine idling and an inefficient torque converter, and the utilization of regenerative braking, the fuel economy in urban driving is significantly improved. The simulation shows that for the 1500 kg passenger car mentioned above, the fuel consumption is 14.2 km/l (33.2 miles per gallon [mpg]). Simulated fuel consumption for a similar conventional vehicle is 9.3 km/l (22 mpg), whereas Toyota Camry (1445 kg curb weight, four-cyclinder, 2.4 l, 157 hp or 117 kW maximum engine power, automatic transmission) has a fuel economy of about 9.7 km/l (23 mpg).[3] With mild hybrid technology, fuel consumption can be reduced by more than 30%. Figure 9.11(c) shows the motor efficiency map and operating points. They indicate that the electric motor operates as a generator more than a traction motor, to support the electric load of auxiliaries and maintain the battery SOC balance.

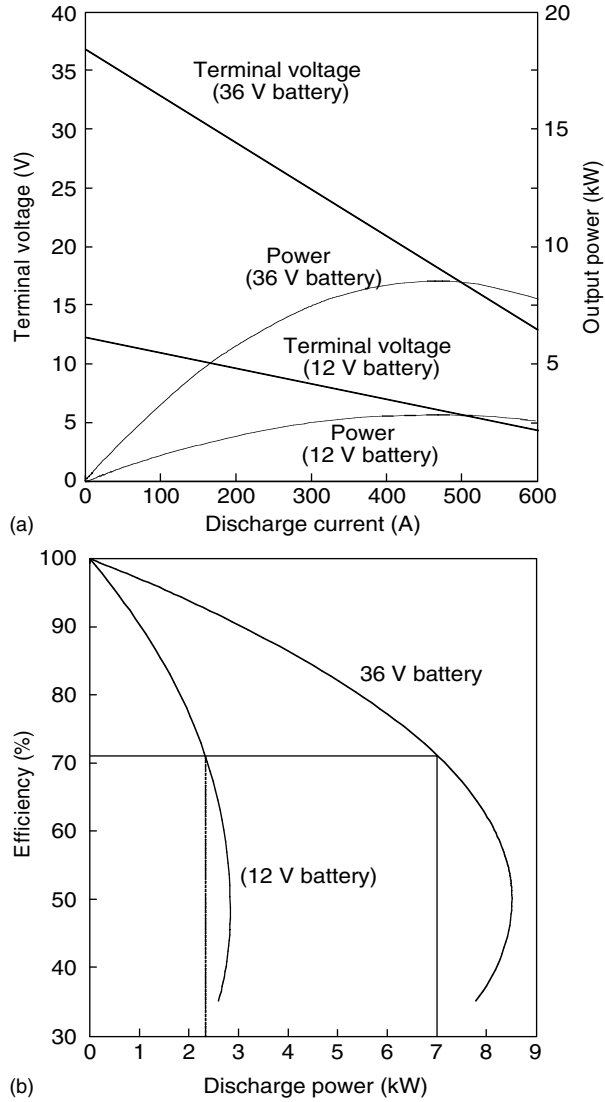

FIGURE 9.9
Battery performance with 36 and 12 V rated voltages: (a) battery power and terminal voltage vs. discharge current and (b) battery discharge efficiency

Figure 9.12 shows the simulation results of the same vehicle on an FTP 75 highway drive cycle. Compared to urban driving, the speeds of both engine and motor are higher, due to higher vehicle speed. The fuel consumption is 13.1 km/l (31 mpg) (Toyota Camry: 13.5 km/l or 32 mpg[3]). The fuel economy when compared to that of conventional vehicles has not improved. The reason is that the highway vehicle faces fewer energy losses in engine idling, braking,

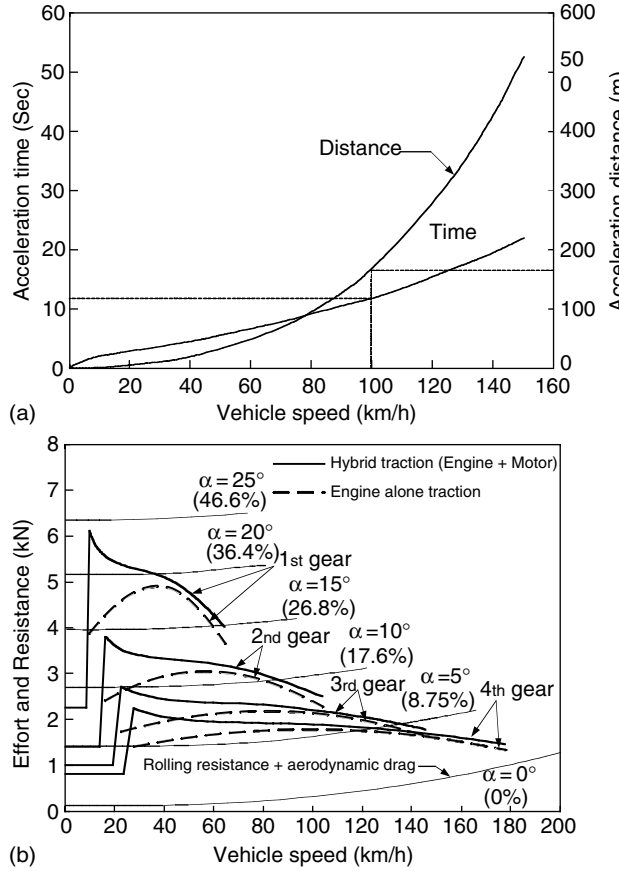

FIGURE 9.10
Performance of the hybrid electric drive train: (a) acceleration and (b) tractive effort vs. vehicle speed

and transmission than during urban driving, and not much room exists for fuel economy improvement by using mild hybrid technology.

9.3 Series–Parallel Mild Hybrid Electric Drive Train

9.3.1 Configuration of the Drive Train with a Planetary Gear Unit

Figure 9.13 shows the configuration of a series–parallel mild hybrid electric drive train, which uses a planetary gear unit to connect the engine, motor, and transmission (gear box) together. The engine is connected to the ring gear of the planetary gear unit through clutch 1, which is used to couple or

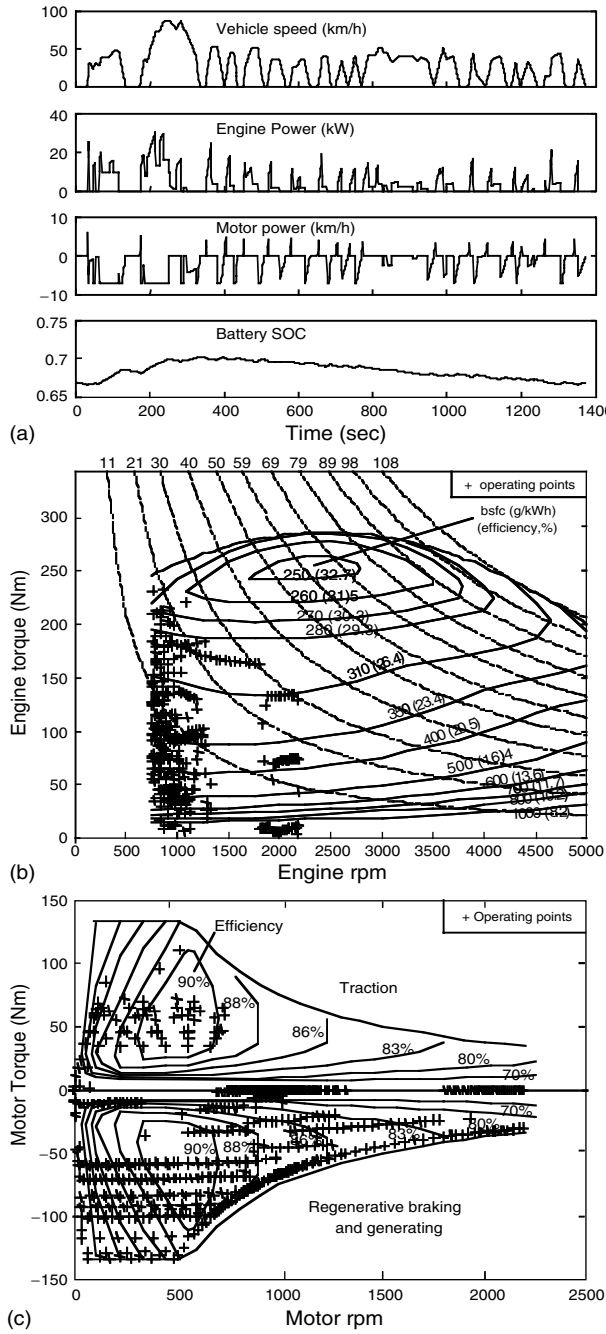

FIGURE 9.11
Simulation in an FTP 75 urban drive cycle: (a) vehicle speed, engine power, motor power, and battery SOC, (b) engine fuel consumption map and operating points, and (c) motor efficiency map and operating points

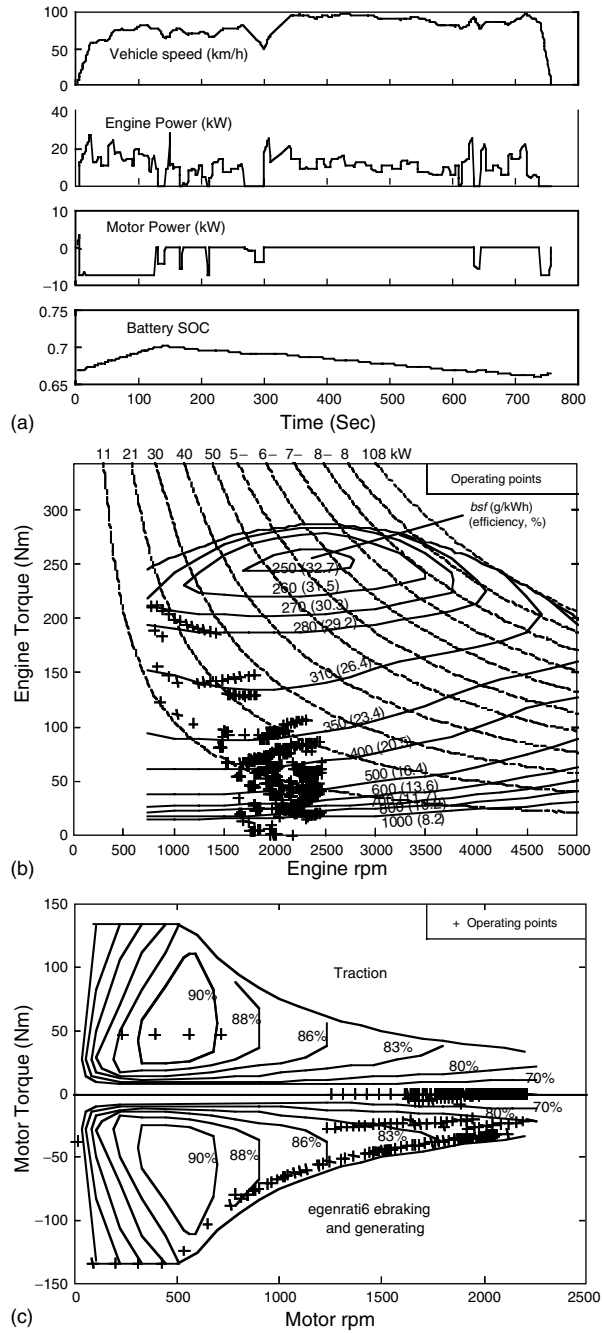

FIGURE 9.12
Simulation in an FTP 75 highway drive cycle: (a) vehicle speed, engine power, motor power, and battery SOC, (b) engine fuel consumption map and operating points, and (c) motor efficiency map and operating points

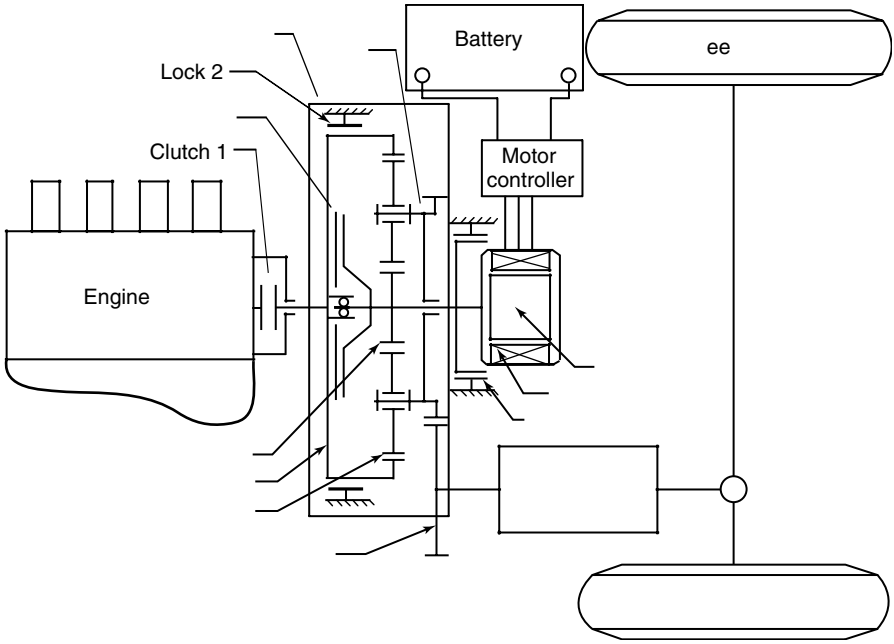

FIGURE 9.13
Series–parallel mild hybrid electric drive train with a planetary gear unit

decouple the engine from the ring gear. The electric motor is connected to the sun gear. Lock 1 is used to lock the sun gear and the rotor of the electric motor to the vehicle frame. Lock 2 is used to lock the ring gear to the vehicle frame. Clutch 2 is used to couple or decouple the sun gear to or from the ring gear. The transmission (gear box) is driven by the carrier of the planetary gear unit through a gear.

The planetary gear unit is a speed-summing unit (as mentioned in Chapter 5), which is a three-port unit. These three ports are sun gear, ring gear, and carrier. The angular velocities of these three elements are related as

$$\omega_c = \frac{\omega_s}{(1+R)} + \frac{R\omega_r}{(1+R)}, \tag{9.5}$$

where $R = r_r/r_s > 1$ is defined as the gear ratio and ω_s, ω_r, and ω_c are the angular velocities of the sun gear, ring gear, and carrier, respectively. By ignoring the loss in the planetary gear unit, the torques acting on the sun gear, ring gear, and carrier have the following relationship:

$$T_c = (1+R)T_s = \frac{1+R}{R}T_r, \tag{9.6}$$

where T_s, T_r, and T_c are the torque acting on the sun gear, ring gear, and carrier, respectively, as shown in Figure 9.14.

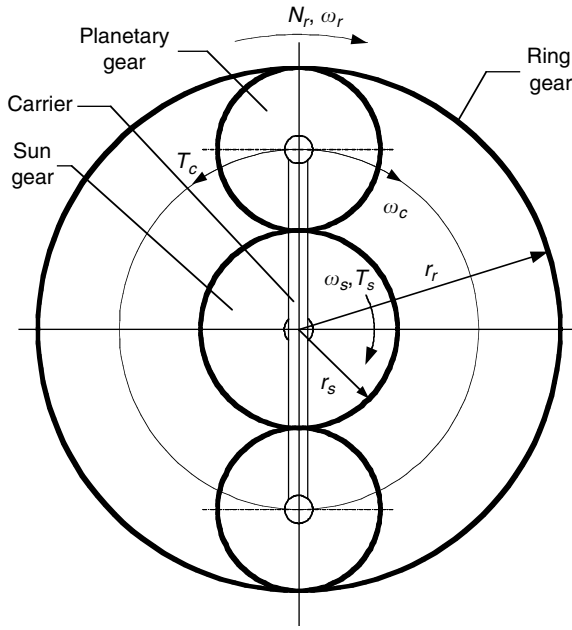

FIGURE 9.14
Planetary gear unit

As indicated by (9.5), the angular velocity of the carrier is the summation of the angular velocities of the sun gear and ring gear. Equation (9.6) indicates that the torque on the sun gear is the smallest, the torque on the carrier is the largest, and the torque on the ring gear is in between, since $R>1$. In the mild hybrid electric drive train shown in Figure 9.13, the motor carries the smallest torque, and the largest torque is transmitted to the transmission. At a given motor torque, the larger gear ratio will result in larger torque to the transmission, and at the same time will need a larger engine torque, as shown in Figure 9.15. However, at a given angular velocity of the carrier, which is proportional to the vehicle speed, a larger gear ratio, R, will result in high engine and motor speed (refer to equation [9.5]).

9.3.2 Operating Modes and Control

As suggested by the configuration of the drive trains, there are two distinct basic operating modes: speed coupling and torque coupling between the engine and gearbox, depending on the engagement or disengagement of the clutches and the lock.

9.3.2.1 Speed-Coupling Operating Mode

When the vehicle is starting from zero speed, the engine cannot run at zero speed and the transmission has only a finite gear ratio. Therefore, slip must

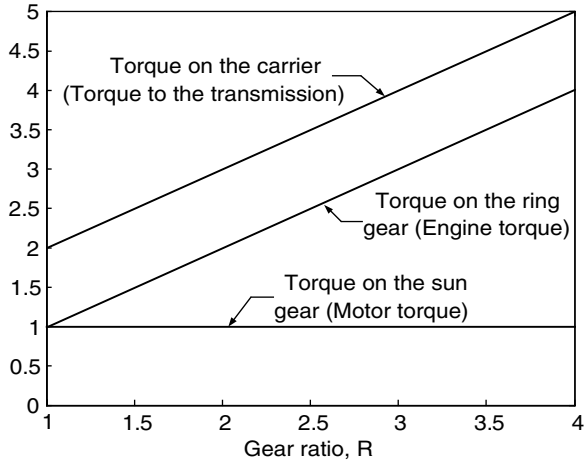

FIGURE 9.15
Torque on the ring gear and carrier (engine torque and the torque to the transmission) varying with gear ratio, *R*, at a given torque on the sun gear (motor torque)

exist between the input shaft and output shaft of the transmission. The slip usually occurs in a clutch for manual transmission or in a hydrodynamic torque converter for an automatic transmission. Thus, a certain amount of energy is lost in this slip. However, in the case of the drive train shown in Figure 9.12, this slip is performed between the engine and the electric motor (ring gear and sun gear). In this case, clutch 1 connects the engine shaft to the ring gear, clutch 2 releases the sun gear from the ring gear, and locks 1 and 2 release the sun gear (motor) and ring gear (engine) from the vehicle frame. At a given engine and carrier velocity, proportional to the vehicle speed and according to equation (15.5), the motor speed is

$$\omega_s = (1 + R)\omega_c - R\omega_r. \tag{9.7}$$

When the first term on the right-hand side of equation (9.7) is smaller than the second term — that is, at low vehicle speed — the motor velocity is negative. However, from equation (9.6), it is known that the motor torque must be positive. Thus, the motor power is negative, that is, operating as a generator, and can be expressed as

$$P_m = T_s\omega_s = T_c\omega_c - T_r\omega_r = P_t - P_e, \tag{9.8}$$

where P_m is motor power, P_t is the power to transmission, and P_e is engine power. When vehicle speed increases to the value at which the first term on the right-hand side of equation (9.7) is equal to the second term and when the sun gear velocity ω_s becomes zero, the electric motor power becomes zero. This speed is defined as synchronous speed, which depends on engine

speed. With a further increase in vehicle speed, ω_s becomes positive and the electric motor goes into a motoring state.

In the speed-coupling operating mode, the engine speed is decoupled from the vehicle speed and the engine speed can be controlled by the motor torque and engine throttle. In equation (9.6), it is known that the engine torque is proportional to the motor torque as

$$T_r = RT_s. \tag{9.9}$$

The engine speed is a function of engine torque and throttle angle. Thus, the engine speed can be controlled by the motor torque and engine throttle, as shown in Figure 9.16. At a given motor torque, the engine speed can be changed by changing the engine throttle angle. At a given engine throttle angle, the engine speed can be changed by changing the motor torque.

9.3.2.2 Torque-Coupling Operating Mode

When clutch 1 is engaged and lock 2 releases the ring gear, the sun gear (motor) and ring gear (engine) are locked together and the velocities of sun gear and ring gear are forced to be the same. From equation (9.5), it is seen that the velocity of the carrier is also equal to the velocity of the sun and ring gear, and the spinning of the planetary gears around their axle stops. In this

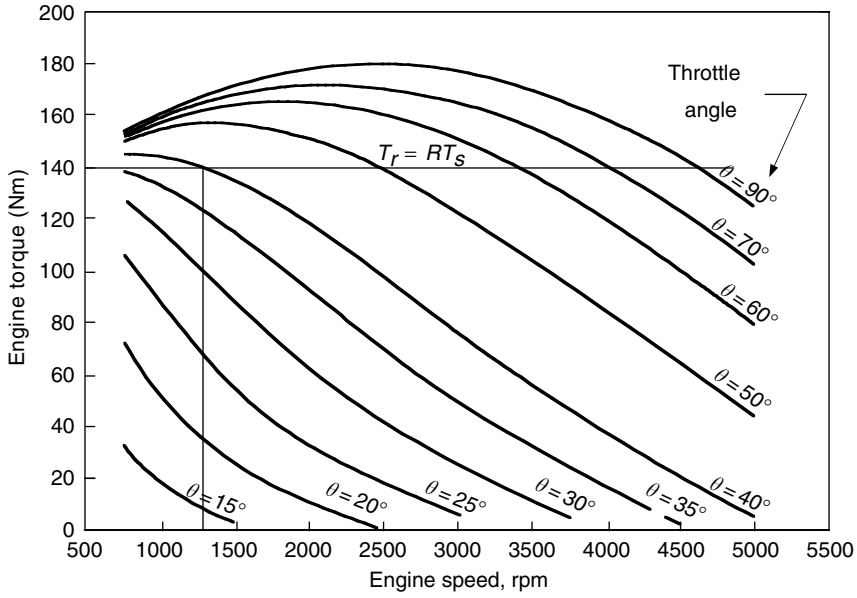

FIGURE 9.16
Engine speed controlled by engine throttle and motor torque

case, the torque on the carrier is the summation of the torque's input through sun gear and ring gear; that is,

$$T_c = T_s + T_r. \tag{9.10}$$

The drive train operates with torque summing pattern.

9.3.2.3 Engine-Alone Traction Mode

The engine-alone traction mode can be realized with both the speed summing and torque summing operation pattern. In the speed summing operation, lock 1 locks the electric motor, thus the sun gear, to the vehicle frame, and clutch 2 releases the sun gear from the ring gear. From equations (9.5) and (9.6), the carrier velocity and torque can be expressed as

$$\omega_c = \frac{R}{1+R}\,\omega_r \tag{9.11}$$

and

$$T_c = \frac{1+R}{R}\,T_r. \tag{9.12}$$

Equations (9.11) and (9.12) indicate that there is a gear ratio of $(1+R)/R$ between the ring gear (engine) and the carrier. This gear ratio is greater than 1.

In the torque summing operation, the engine-alone traction mode can be realized by de-energizing the electric motor. In this case, the velocity and torque on the carrier are equal to the velocity and torque of the engine. The gear ratio is equal to 1.

It is known from the above discussion that the planetary gear unit functions as a two-gear transmission. The speed summing mode gets a low gear (gear ratio, $R/(1+R)$) and torque summing gets high gear (gear ratio, 1).

9.3.2.4 Regenerative Braking Mode

During braking, clutch 1 is disengaged and the engine is decoupled from the ring gear. The engine can be shut down or set at idling. The electric motor is controlled to operate as a generator to produce negative torque. Similar to the engine-alone traction mode, this operation can be performed by either speed or torque summing. During the speed summing operation, the ring gear is locked to the vehicle frame by lock 2, and the sun gear (motor) is released from the ring gear by disengaging clutch 2. From (9.5) and (9.6), the velocity and torque of the electric motor associate with the velocity and torque of the carrier by

$$\omega_c = \frac{\omega_s}{1+R} \tag{9.13}$$

and

$$T_c = (1+R)T_s. \tag{9.14}$$

When the electric motor is controlled to produce negative torque, the carrier obtains a negative (braking) torque. Equations (9.13) and (9.14) indicate that a gear ratio, $1+R$, is introduced between the motor (sun gear) and the carrier.

In the torque summing mode, clutch 2 is engaged to couple the sun gear (motor) to the ring gear and lock 2 releases the ring gear from the vehicle frame. In this case, the velocity and torque of the motor are equal to the velocity and torque of the carrier. The gear ratio between the motor (sun gear) and carrier is 1.

Again, the planetary gear unit functions as a two-gear transmission. The speed summing mode gets a low gear (gear ratio, $1+R$) and torque summing gets a high gear (gear ratio, 1).

9.3.2.5 Engine Starting

The engine can be started by the electric motor with either a speed summing mode or a torque summing mode when the vehicle is at a standstill. In the speed summing mode, clutch 1 is engaged to couple the engine shaft to the ring gear; clutch 2 releases the sun gear (motor) from the ring gear, and both locks 1 and 2 are disengaged. From (9.5) and (9.6), the velocity and torque of the engine are associated with the velocity and torque of the electric motor by

$$\omega_r = -\frac{1}{R}\omega_s \tag{9.15}$$

and

$$T_r = RT_s. \tag{9.16}$$

To start the engine, the electric motor must rotate with a negative velocity, that is, in an opposite direction. Again, a gear ratio, R, is introduced between the engine (ring gear) and the motor (sun gear). Thus, a small motor torque is required to start the engine.

Actually, equation (9.6) indicates that a positive motor torque always results in a positive engine torque whether the vehicle is at a standstill or running. This implies that the engine can be started even when the vehicle is running.

In the torque summing operation mode, the engine can be started directly by the electric motor. In this case, the transmission (gear box) must be set at neutral gear. The velocity and torque that the engine obtains are equal to the velocity and torque that the motor develops.

9.3.3 Control Strategy

When the vehicle speed is lower than the synchronous speed, the speed summing operation mode is used. As explained in Section 9.2.1.1, the electric motor operates with a negative speed and negative power. Part of the engine power is used to charge the batteries and part to propel the vehicle.

The torque of the carrier of the planetary gear unit (propelling torque) is determined by the smaller one of $(1 + R)T_s$ and $((1 + R)/R)T_r$, as described in equation (9.6).

When the vehicle speed is higher, it uses its synchronous, torque summing operation mode. The drive train control strategy is:

1. When the traction power demand is greater than the power that the engine can develop with full throttle, hybrid traction mode is used. In this case, the engine is operated with full throttle and an electric motor supplies extra power to meet the traction power demand.
2. When the traction power demand is less than the power the engine can develop with full throttle, the operations of the engine and electric motor are determined by the SOC of the batteries, as shown in Figure 9.17. In the battery charge mode, the battery charging power may be determined by the maximum power of the electric power, or by the maximum engine power and demanded traction power.

9.3.4 Drive Train with Floating-Stator Motor

An alternative mild hybrid electric drive train, which has characteristics similar to the drive train discussed above, is shown in Figure 9.18.[2] This drive train uses an electric motor, which has a floating stator, to replace the planetary gear unit and electric motor.

As mentioned in Chapter 5, the angular velocity of the rotor is the summation of the angular velocity of the stator and the relative angular velocity between the stator and rotor, that is,

$$\omega_r = \omega_s + \omega_{rr}. \tag{9.17}$$

Due to the action and reaction effect, the torques acting on the stator and rotor are always equal to the electromagnetic torque produced in the air gap

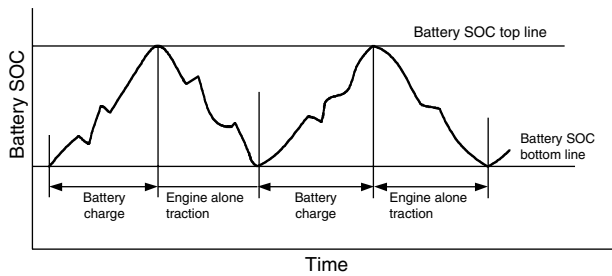

FIGURE 9.17
Battery charge and engine-alone traction, depending on battery SOC

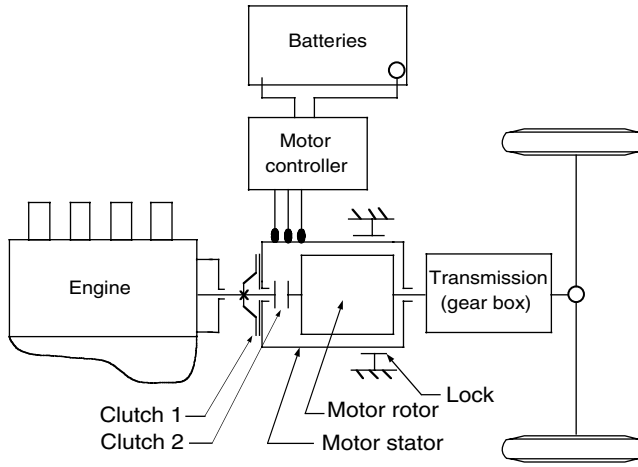

FIGURE 9.18
Series–parallel mild hybrid electric drive train with a floating stator motor

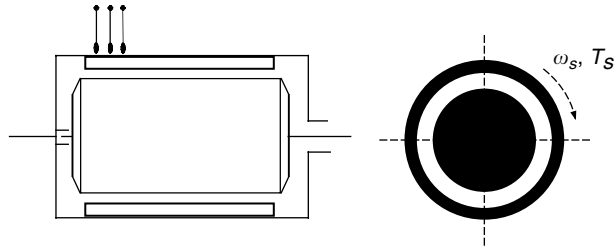

FIGURE 9.19
An electric motor with a floating stator

(refer to Figure 9.19), which is, in a general sense, the electric motor torque. This relationship is described as

$$T_r = T_s = T_m, \tag{9.18}$$

where T_m is the electromagnetic torque in the air gap.

Comparing (9.17) and (9.18) with (9.5) and (9.6), it is known that both the planetary gear unit and the floating stator motor bear the same operating characteristics. Therefore, the mild hybrid electric drive trains as shown in Figure 9.13 and Figure 9.18 have the same operating principle and use the same control strategy. However, the design of the drive train with a planetary gear unit is more flexible since the gear ratio, R, is selectable. Furthermore, the gear ratio can increase the motor torque. Therefore, a low torque motor is required to start the engine and deliver a large torque to the transmission.

References

[1] Y. Gao and M. Ehsani, A mild hybrid drive train for 42V automotive power system — design, control, and simulation, *Society of Automotive Engineers (SAE) World Congress,* Paper No. 2002-02-1082, Detroit, MI, 2002.

[2] Y. Gao and M. Ehsani, A mild hybrid vehicle drive train with a floating stator motor — configuration, control strategy, design, and simulation verification, *Society of Automotive Engineers (SAE) Future Car Congress,* Paper No. 2002-01-1878, Crystal City, VA, June 2002.

[3] Y. Gao and M. Ehsani, Electronic braking system of EV and HEV — integration of regenerative braking, automatic braking force control and ABS, *Society of Automotive Engineers (SAE) Future Transportation Technology Conference,* Paper No. 2001-01-2478, Costa Mesa, CA, Aug. 2001.

[4] Y. Gao and M. Ehsani, Investigation of battery technologies for the Army's hybrid vehicle application, in *Proceedings of the IEEE 56th Vehicular Technology Conference,* Vancouver, British Columbia, Canada, Sept. 2002.

[5] Y. Gao, L. Chen, and M. Ehsani, Investigation of the effectiveness of regenerative braking for EV and HEV, *Society of Automotive Engineers (SAE) Journal,* SP-1466, Paper No. 1999-01-2901, 1999.

[6] Y. Gao, K.M. Rahman, and M. Ehsani, The energy flow management and battery energy capacity determination for the drive train of electrically peaking hybrid, *Society of Automotive Engineers (SAE) Journal,* SP-1284, Paper No. 972647, 1997.

[7] Y. Gao, K.M. Rahman, and M. Ehsani, Parametric design of the drive train of an electrically peaking hybrid (ELPH) vehicle, *Society of Automotive Engineers (SAE) Journal,* SP-1243, Paper No. 970294, 1997.

[8] H. Gao, Y. Gao and M. Ehsani Design issues of the switched reluctance motor drive for propulsion and regenerative braking in EV and HEV, *Society of Automotive Engineers (SAE) Future Transportation Technology Conference,* Costa Mesa, CA, Paper No. 2001-01-2526, Aug. 2001.

10

Energy Storages

CONTENTS

10.1 Electrochemical Batteries 300
10.1.1 Electrochemical Reactions 302
10.1.2 Thermodynamic Voltage 304
10.1.3 Specific Energy 304
10.1.4 Specific Power 306
10.1.5 Energy Efficiency 309
10.1.6 Battery Technologies 309
10.1.6.1 Lead-Acid Batteries 310
10.1.6.2 Nickel-based Batteries 311
10.1.6.2.1 Nickel/Iron System 311
10.1.6.2.2 Nickel/Cadmium System 311
10.1.6.2.3 Nickel–Metal Hydride (Ni–MH) Battery 312
10.1.6.3 Lithium-Based Batteries 313
10.1.6.3.1 Lithium–Polymer (Li–P) Battery 313
10.1.6.3.2 Lithium-Ion (Li-Ion) Battery 313
10.2 Ultracapacitors 314
10.2.1 Features of Ultracapacitors 315
10.2.2 Basic Principles of Ultracapacitors 315
10.2.3 Performance of Ultracapacitors 317
10.2.4 Ultracapacitor Technologies 320
10.3 Ultrahigh-Speed Flywheels 322
10.3.1 Operation Principles of Flywheels 322
10.3.2 Power Capacity of Flywheel Systems 324
10.3.3 Flywheel Technologies 326
10.4 Hybridization of Energy Storages 328
References 332

"Energy storages" are defined in this book as the devices that store energy, deliver energy outside (discharge), and accept energy from outside (charge). There are several types of energy storages that have been proposed for electric

vehicle (EV) and hybrid electric vehicle (HEV) applications. These energy storages, so far, mainly include chemical batteries, ultracapacitors or supercapacitors, and ultrahigh-speed flywheels. The fuel cell, which essentially is a kind of energy converter, will be discussed in Chapter 12.

There are a number of requirements for energy storage applied in an automotive application, such as specific energy, specific power, efficiency, maintenance requirement, management, cost, environmental adaptation and friendliness, and safety. For allocation on an EV, specific energy is the first consideration since it limits the vehicle range. On the other hand, for HEV applications, specific energy becomes less important and specific power is the first consideration, because all the energy is from the energy source (engine or fuel cell) and sufficient power is needed to ensure vehicle performance, particularly during acceleration, hill climbing, and regenerative braking. Of course, other requirements should be fully considered in vehicle drive train development.

10.1 Electrochemical Batteries

Electrochemical batteries, more commonly referred to as "batteries," are electrochemical devices that convert electrical energy into potential chemical energy during charging, and convert chemical energy into electric energy during discharging. A "battery" is composed of several cells stacked together. A cell is an independent and complete unit that possesses all the electrochemical properties. Basically, a battery cell consists of three primary elements: two electrodes (positive and negative) immersed into an electrolyte as shown in Figure 10.1.

Battery manufacturers usually specify the battery with coulometric capacity (amp-hours), which is defined as the number of amp-hours gained when discharging the battery from a fully charged state until the terminal voltage drops to its cut-off voltage, as shown in Figure 10.2. It should be noted that the same battery usually has a different number of amp-hours at different discharging current rates. Generally, the capacity will become smaller with a large discharge current rate, as shown in Figure 10.3. Battery manufacturers usually specify a battery with a number of amp-hours along with a current rate. For example, a battery labeled 100 Ah at C5 rate has a 100 amp-hour capacity at 5 hours discharge rate (discharging current=100/5=20 A).

Another important parameter of a battery is the state-of-charge (SOC). SOC is defined as the ratio of the remaining capacity to the fully charged capacity. With this definition, a fully charged battery has an SOC of 100% and a fully discharged battery has an SOC of 0%. However, the term "fully discharged" sometimes causes confusion because of the different capacity at different discharge rates and different cut-off voltage (refer to

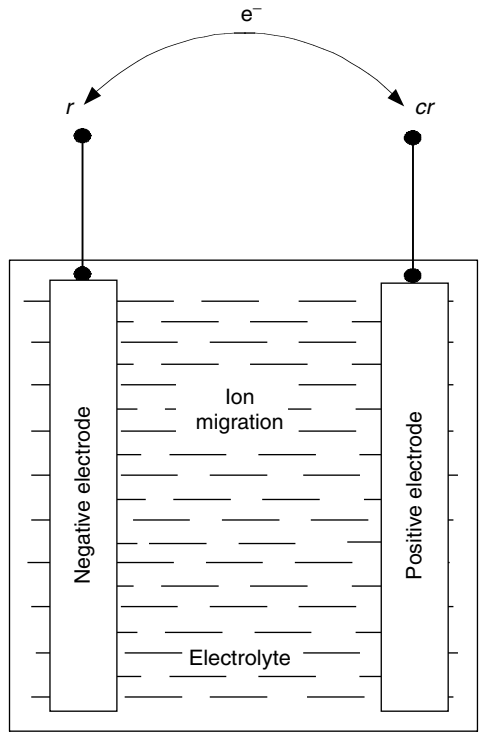

FIGURE 10.1
A typical electrochemical battery cell

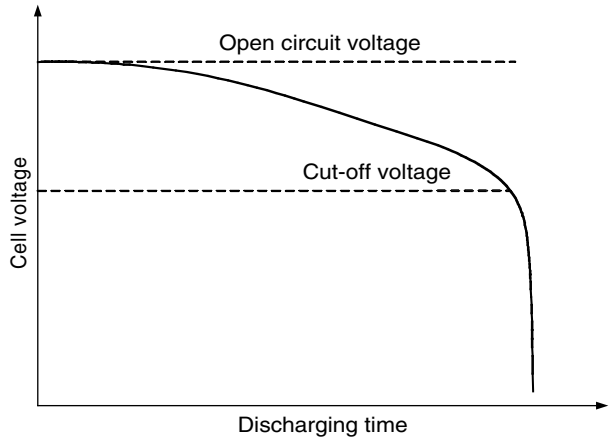

FIGURE 10.2
Cut-off voltage of a typical battery

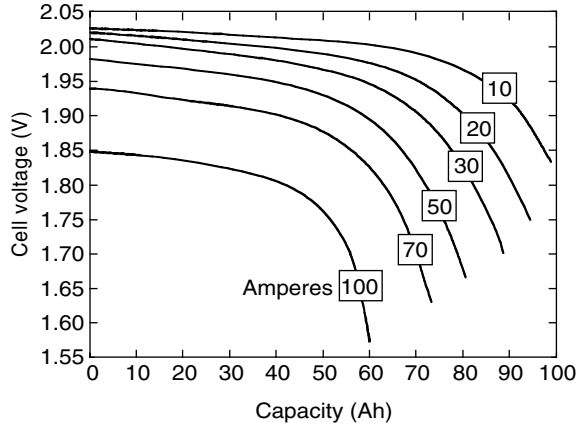

FIGURE 10.3
Discharge characteristics of a lead-acid battery

Figure 10.3). The change in SOC in a time interval, dt, with discharging or charging current i may be expressed as

$$\Delta SOC = \frac{i\,dt}{Q(i)}, \tag{10.1}$$

where $Q(i)$ is amp-hour capacity of the battery at current rate i. For discharging, i is positive, and for charging, i is negative. Thus, the SOC of the battery can be expressed as

$$SOC = SOC_0 - \int \frac{i\,dt}{Q(i)}, \tag{10.2}$$

where SOC_0 is the initial value of the SOC.

For EVs and HEVs, the energy capacity is considered to be more important than the coulometric capacity (Ahs), because it is directly associated with the vehicle operation. The energy delivered from the battery can be expressed as

$$EC = \int_0^t V(i, SOC)\, i(t)\, dt, \tag{10.3}$$

where $V(i, SOC)$ is the voltage at the battery terminals, which is a function of the battery current and SOC.

10.1.1 Electrochemical Reactions

For simplicity, and because it is the most widespread battery technology in today's automotive applications, the lead-acid battery case is used as an example to explain the operating principle theory of electrochemical batteries. A lead-acid battery uses an aqueous solution of sulfuric acid ($2H^+ + SO_4^{2-}$)

as the electrolyte. The electrodes are made of porous lead (Pb, anode, electrically negative) and porous lead oxide (PbO_2, cathode, electrically positive). The processes taking place during discharging are shown in Figure 10.4(a), where lead is consumed and lead sulfate is formed. The chemical reaction on the anode can be written as

$$Pb + SO_4^{2-} \rightarrow PbSO_4 + 2e^-. \tag{10.4}$$

This reaction releases two electrons and, thereby, gives rise to an excess negative charge on the electrode that is relieved by a flow of electrons through the external circuit to the positive (cathode) electrode. At the positive electrode, the lead of PbO_2 is also converted to $PbSO_4$ and, at the same time, water is formed. The reaction can be expressed as

$$PbO_2 + 4H^+ + SO_4^{2-} + 2e^- \rightarrow PbSO_4 + 2H_2O. \tag{10.5}$$

During charging, the reactions on the anode and cathode are reversed as shown in Figure 10.4(b) that can be expressed by:

anode: $$PbSO_4 + 2e^- \rightarrow Pb + SO_4^{2-} \tag{10.6}$$

and

cathode: $$PbSO_4 + 2H_2O \rightarrow PbO_2 + 4H^+ + SO_4^{2-} + 2e^- \tag{10.7}$$

The overall reaction in a lead-acid battery cell can be expressed as

overall: $$Pb + PbO_2 + 2H_2SO_4 \underset{\text{charge}}{\overset{\text{discharge}}{\rightleftharpoons}} 2PbSO_4 + 2H_2O. \tag{10.8}$$

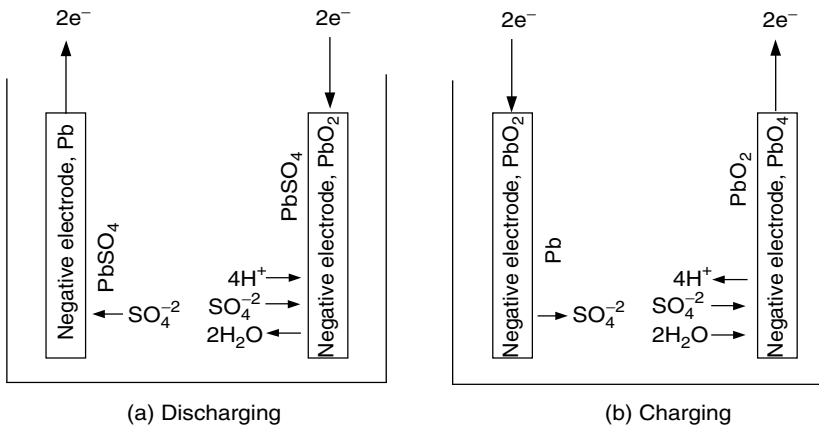

FIGURE 10.4
Electrochemical processes during the discharge and charge of a lead-acid battery cell

The lead-acid battery has a cell voltage of about 2.03 V at standard condition, which is affected by the concentration of the electrolyte.

10.1.2 Thermodynamic Voltage

The thermodynamic voltage of a battery cell is closely associated with the energy released and the number of electrons transferred in the reaction. The energy released by the battery cell reaction is given by the change in Gibbs free energy, ΔG, usually expressed in per mole quantities. The change in Gibbs free energy in a chemical reaction can be expressed as

$$\Delta G = \sum_{Products} G_i - \sum_{Reactants} G_j, \tag{10.9}$$

where G_i and G_j are the free energy in species i of products and species j of reactants. In a reversible process, ΔG is completely converted into electric energy, that is,

$$\Delta G = -nFV_r, \tag{10.10}$$

where n is the number of electrons transferred in the reaction, $F = 96{,}495$ is the Faraday constant in coulombs per mole, and V_r is the reversible voltage of the cell. At standard condition (25°C temperature and 1 atm pressure), the open circuit (reversible) voltage of a battery cell can be expressed as

$$V_r^0 = -\frac{\Delta G^0}{nF}, \tag{10.11}$$

where ΔG^0 is the change in Gibbs free energy at standard conditions.

The change of free energy, and thus the cell voltage, in a chemical reaction is a function of the activities of the solution species. From equation (10.10) and the dependence of ΔG on the reactant activities, the *Nernst relationship* is derived as

$$V_r = V_r^0 - \frac{RT}{nF} \ln\left[\frac{\Pi(activities\ of\ products)}{\Pi(activities\ of\ reactants)}\right], \tag{10.12}$$

where R is the universal gas constant, 8.31J/mol K, and T is absolute temperature in K.

10.1.3 Specific Energy

Specific energy is defined as the energy capacity per unit battery weight (Wh/kg). The theoretical specific energy is the maximum energy that can be generated per unit total mass of the cell reactant. As discussed above, the energy in a battery cell can be expressed by the Gibbs free energy ΔG. With respect to theoretical specific energy, only the effective weights (molecular weight of reactants and products) are involved; then

$$E_{spe,theo} = -\frac{\Delta G}{3.6\sum M_i} = \frac{nFV_r}{3.6\sum M_i}(\text{Wh/kg}), \tag{10.13}$$

where ΣM_i is the sum of the molecular weight of the individual species involved in the battery reaction. Taking the lead-acid battery as an example, $V_r = 2.03$ V, $n = 2$, and $\Sigma M_i = 642$ g; then $E_{spe,the} = 170$ Wh/kg. From (10.13), it is clear that the "ideal" couple would be derived from a highly electronegative element and a highly electropositive element, both of low atomic weight. Hydrogen, lithium, or sodium would be the best choice for the negative reactants, and the lighter halogens, oxygen, or sulfur would be the best choice for the positive. To put such couples together in a battery requires electrode designs for effective utilization of the contained active materials, as well as electrolytes of high conductivity compatible with the materials in both electrodes. These constraints result in oxygen and sulfur being used in some systems as oxides and sulfides rather than as the elements themselves. For operation at ambient temperature, aqueous electrolytes are advantageous because of their high conductivities. Here, alkali-group metals cannot be used as electrodes since these elements react with water. It is necessary to choose other metals, which have a reasonable degree of electropositivity, such as zinc, iron, or aluminum. When considering electrode couples, it is preferable to exclude those elements that have a low abundance in the earth's crust, are expensive to produce, or are unacceptable from a health or environmental point of view.

Examination of possible electrode couples has resulted in the study of more than 30 different battery systems with a view of developing a reliable, high-performance, inexpensive high-power energy source for electric traction. The theoretical specific energies of the systems championed for EVs and HEVs are presented in Table 10.1. Practical specific energies, however, are well below the theoretical maxima. Apart from electrode kinetic and other restrictions that serve to reduce the cell voltage and prevent full utilization of the reactants, there is a need for construction materials which add to the battery weight but which are not involved in the energy-producing reaction.

In order to appreciate the extent to which the practical value of the specific energy is likely to differ from the theoretical values, it is instructive to consider the situation of the well-established lead-acid battery. A breakdown of the various components of a lead-acid battery designed to give a practical specific energy of 45 Wh/kg is shown in Figure 10.5.[1] It shows that only about 26% of the total weight of the battery is directly involved in producing electrical energy. The remainder is made up of (1) potential call reactants that are not discharged at the rates required for EV operation, (2) water used as the solvent for the electrolyte (sulfuric acid alone is not suitable), (3) lead grids for current collection, (4) "top lead", that is, terminals, straps and intercell connectors, and (5) cover, connector, and separators.

A similar ratio of practical-to-theoretical specific energy is expected for each of the candidate systems listed in Table 10.1. The present values realized by experimental cells and prototype batteries are listed in Table 10.2[1].

TABLE 10.1

Theoretical Specific Energies of Candidate Batteries for EVs and HEVs[1]

Battery		Cell Reaction		Specific Energy (Wh/kg)
⊕	⊖	Charge ⇐	Discharge ⇒	
Acidic aqueous solution				
PbO_2	Pb	$PbO_2+2H_2SO_4+Pb$	$\Leftrightarrow 2PbSO_4+2H_2O$	170
Alkaline aqueous solution				
NiOOH	Cd	$2NiOOH+2H_2O+Cd$	$\Leftrightarrow 2Ni(OH)_2+Cd(OH)_2$	217
NiOOH	Fe	$2NiOOH+2H_2O+Fe$	$\Leftrightarrow 2Ni(OH)_2+Fe(OH)_2$	267
NiOOH	Zn	$2NiOOH+2H_2O+Zn$	$\Leftrightarrow 2Ni(OH)_2+Zn(OH)_2$	341
NiOOH	H_2	$2NiOOH+H_2$	$\Leftrightarrow 2Ni(OH)_2$	387
MnO_2	Zn	$2MnO2+H_2O+Zn$	$\Leftrightarrow 2MnOOH+ZnO$	317
O_2	Al	$4Al+6H_2O+3O_2$	$\Leftrightarrow 4Al(OH)_3$	2815
O_2	Fe	$2Fe+2H_2O+O_2$	$\Leftrightarrow 2Fe(OH)_2$	764
O_2	Zn	$2Zn+2H_2O+O_2$	$\Leftrightarrow 2Zn(OH)_2$	888
Flow				
Br_2	Zn	$Zn+Br_2$	$\Leftrightarrow ZnBr_2$	436
Cl_2	Zn	$Zn+Cl_2$	$\Leftrightarrow ZnCl_2$	833
$(VO_2)_2SO_4$	VSO_4	$(VO_2)_2SO_4+2HVSO_4+2H_2SO_4$	$\Leftrightarrow 2VOSO_4+V_2(SO_4)_3+2H_2O$	114
Molten salt				
S	Na	$2Na+3S$	$\Leftrightarrow Na_2S_3$	760
$NiCl_2$	Na	$2Na+NiCl_2$	$\Leftrightarrow 2NaCl$	790
FeS_2	LiA1	$4LiA1+FeS_2$	$\Leftrightarrow 2Li_2S+4Al+Fe$	650
Organic lithium				
$LiCoO_2$	Li-C	$Li_{(y+x)}C_6+Li_{(1-(y-x))}CoO_2$	$\Leftrightarrow Li_yC6+Li_{(1-y)}CoO_2$	320[a]

[a]For a maximum value of $x-0.5$ and $y=0$.

10.1.4 Specific Power

Specific power is defined as the maximum power of per unit battery weight that the battery can produce in a short period. Specific power is important in the reduction of battery weight, especially in high power demand applications, such as HEVs. The specific power of a chemical battery depends mostly on the battery's internal resistance. With the battery model as shown in Figure 10.6, the maximum power that the battery can supply to the load is

$$P_{peak}=\frac{V_0^2}{4(R_c+R_{int})}, \tag{10.14}$$

where R_{ohm} is the conductor resistance (ohmic resistance) and R_{int} is the internal resistance caused by chemical reaction.

Internal resistance, R_{int}, represents the voltage drop, ΔV, which is associated with the battery current. The voltage drop ΔV, termed overpotential in

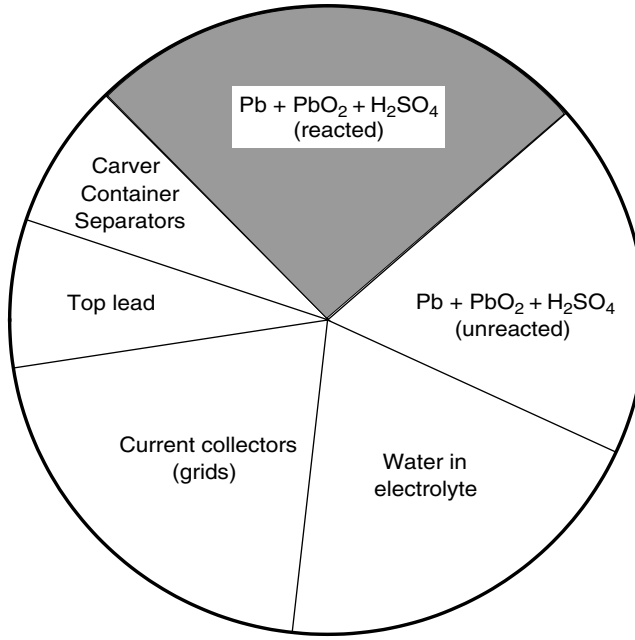

FIGURE 10.5
Weight distribution of the components of a lead-acid EV battery with a specific energy of 45 Wh/kg at the C5/5 rate[1]

battery terminology, includes two components: one is caused by reaction activity ΔV_A, and the other by electrolyte concentration ΔV_C. General expressions of ΔV_A and ΔV_C are[2]

$$\Delta V_A = a + b \log I \tag{10.15}$$

and

$$\Delta V_C = -\frac{RT}{nF}\ln\left(1-\frac{I}{I_L}\right), \tag{10.16}$$

where a and b are constants, R is the gas constant, 8.314 J/K mol, T is the absolute temperature, n is the number of electrons transferred in the reaction, F is the Faraday constant — 96,495 ampere-seconds per mole — and I_L is the limit current. Accurate determination of battery resistance or voltage drop by analysis is difficult and is usually obtained by measurement.[1] The voltage drop increases with increasing discharging current, decreasing the stored energy in it (refer to Figure 10.3).

Table 10.2 also shows the status of battery systems potentially available for EV. It can be seen that although specific energies are high in advanced batteries, the specific powers have to improve. About 300 W/kg might be

TABLE 10.2

Status of Battery Systems for Automotive Applications

System	Specific Energy (Wh/kg)	Peak Power (W/kg)	Energy Efficiency (%)	Cycle Life	Self-Discharge (% per 48 h)	Cost (US$/kWh)
Acidic aqueous solution						
Lead/acid	35–50	150–400	>80	500–1000	0.6	120–150
Alkaline aqueous solution						
Nickel/cadmium	50–60	80–150	75	800	1	250–350
Nickel/iron	50–60	80–150	75	1500–2000	3	200–400
Nickel/zinc	55–75	170–260	65	300	1.6	100–300
Nickel/metal hydride	70–95	200–300	70	750–1200+	6	200–350
Aluminum/air	200–300	160	<50	?	?	?
Iron/air	80–120	90	60	500+	?	50
Zinc/air	100–220	30–80	60	600+	?	90–120
Flow						
Zinc/bromine	70–85	90–110	65–70	500–2000	?	200–250
Vanadium redox	20–30	110	75–85	—	—	400–450
Molten salt						
Sodium/sulfur	150–240	230	80	800+	0[a]	250–450
Sodium/nickel chloride	90–120	130–160	80	1200+	0[a]	230–345
Lithium/iron sulfide (FeS)	100–130	150–250	80	1000+	?	110
Organic/lithium						
Lithium-ion	80–130	200–300	>95	1000+	0.7	200

[a]No self-discharge, but some energy loss by cooling.

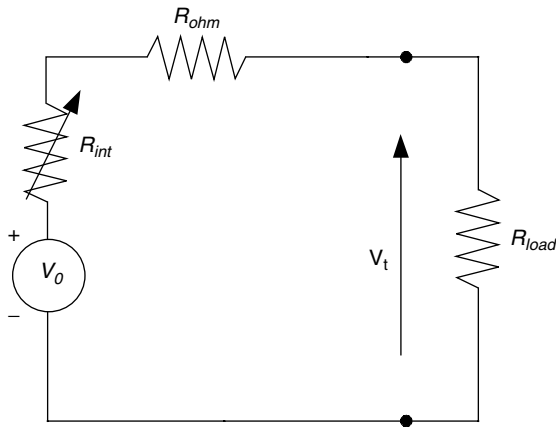

FIGURE 10.6
Battery circuit model

the optimistic estimate. However, SAFT has reported their Li-ion high-power for HEV application with a specific energy of 85 Wh/kg and a specific power of 1350 W/kg and their high-energy batteries for EV application with about 150 Wh/kg and 420 W/kg (at 80% SOC, 150 A current and 30 sec), respectively.[4]

10.1.5 Energy Efficiency

The energy or power losses during battery discharging and charging appear in the form of voltage loss. Thus, the efficiency of the battery during discharging and charging can be defined at any operating point as the ratio of the cell operating voltage to the thermodynamic voltage, that is:

during discharging: $$\eta = \frac{V}{V_0} \tag{10.17}$$

and

during charging: $$\eta = \frac{V_0}{V}. \tag{10.18}$$

The terminal voltage, as a function of battery current and energy stored in it or SOC, is lower in discharging and higher in charging than the electrical potential produced by a chemical reaction. Figure 10.7 shows the efficiency of the lead-acid battery during discharging and charging. The battery has a high discharging efficiency with high SOC and a high charging efficiency with low SOC. The net cycle efficiency has a maximum in the middle range of the SOC. Therefore, the battery operation control unit of an HEV should control the battery SOC in its middle range so as to enhance the operating efficiency and depress the temperature rise caused by energy loss. High temperature would damage the battery.

10.1.6 Battery Technologies

The viable EV and HEV batteries consist of the lead-acid battery, nickel-based batteries such as nickel/iron, nickel/cadmium, and nickel–metal hydride batteries, and lithium-based batteries such as lithium polymer and lithium-ion batteries.[3] In the near term, it seems that lead-acid batteries will still be the major type due to its many advantages. However, in the middle and long term, it seems that cadmium- and lithium-based batteries will be major candidates for EVs and HEVs.

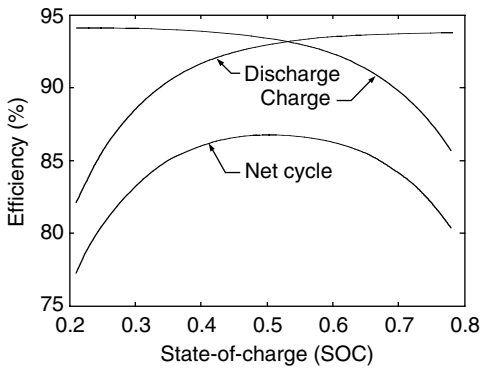

FIGURE 10.7
Typical battery charge and discharge efficiency

10.1.6.1 Lead-Acid Batteries

The lead-acid battery has been a successful commercial product for over a century and is still widely used as electrical energy storage in the automotive field and other applications. Its advantages are its low cost, mature technology, relative high power capability, and good cycle. These advantages are attractive for its application in HEVs where high power is the first consideration. The materials involved (lead, lead oxide, sulfuric acid) are rather low in cost when compared to their more advanced counterparts. Lead-acid batteries also have several disadvantages. The energy density of lead-acid batteries is low, mostly because of the high molecular weight of lead. The temperature characteristics are poor.[2] Below 10°C, its specific power and specific energy are greatly reduced. This aspect severely limits the application of lead-acid batteries for the traction of vehicles operating in cold climates.

The presence of highly corrosive sulfuric acid is a potential safety hazard for vehicle occupants. Hydrogen released by the self-discharge reactions is another potential danger, since this gas is extremely flammable even in tiny concentrations. Hydrogen emission is also a problem for hermetically sealed batteries. Indeed, in order to provide a good level of protection against acid spills, it is necessary to seal the battery, thus trapping the parasitic gases in the casing. As a result, pressure may build up in the battery, causing swelling and mechanical constraints on the casing and sealing. The lead in the electrodes is an environmental problem because of its toxicity. The emission of lead consecutive to the use of lead-acid batteries may occur during the fabrication of the batteries, in case of vehicle wreck (spill of electrolyte through cracks), or during their disposal at the end of battery life.

Different lead-acid batteries with improved performance are being developed for EVs and HEVs. Improvements of the sealed lead-acid batteries in specific energy over 40 Wh/kg, with the possibility of rapid charge, have been attained. One of these advanced sealed lead-acid batteries is Electrosource's Horizon battery. It adopts the lead wire woven horizontal plate and hence offers the competitive advantages of high specific energy (43 Wh/kg), high specific power (285 W/kg), long cycle life (over 600 cycles for on-road EV application), rapid recharge capability (50% capacity in 8 min and 100% in less than 30 min), low cost (US$2000–3000 an EV), mechanical ruggedness (robust structure of horizontal plate), maintenance-free conditions (sealed battery technology), and environmental friendliness. Other advanced lead-acid battery technologies include bipolar designs and microtubular grid designs.

Advanced lead-acid batteries have been developed to remedy these disadvantages. The specific energy has been increased through the reduction of inactive materials such as the casing, current collector, separators, etc. The lifetime has been increased by over 50% — at the expense of cost, however. The safety issue has been addressed and improved, with

electrochemical processes designed to absorb the parasitic releases of hydrogen and oxygen.

10.1.6.2 Nickel-based Batteries

Nickel is a lighter metal than lead and has very good electrochemical properties desirable for battery applications. There are four different nickel-based battery technologies: nickel–iron, nickel–zinc, nickel–cadmium, and nickel–metal hydride.

10.1.6.2.1 Nickel/Iron System

The nickel/iron system was commercialized during the early years of the 20th century. Applications included fork-lift trucks, mine locomotives, shuttle vehicles, railway locomotives, and motorized hand-trucks.[1] The system comprises a nickel (III) hydroxy-oxide (NiOOH) positive electrode and a metallic iron negative electrode. The electrolyte is a concentrated solution of potassium hydroxide (typically 240 g/l) containing lithium hydroxide (50 g/l). The cell reaction is given in Table 10.1 and its nominal open-circuit voltage is 1.37 V.

Nickel/iron batteries suffer from gassing, corrosion, and self-discharge problems. These problems have been partially or totally solved in prototypes that have yet to reach the market. These batteries are complex due to the need to maintain the water level and the safe disposal of the hydrogen and oxygen released during the discharge process. Nickel–iron batteries also suffer from low temperatures, although less than lead-acid batteries. Finally, the cost of nickel is significantly higher than that of lead. Their greatest advantages are high power density compared with lead-acid batteries, and a capability of withstanding 2000 deep discharges.

10.1.6.2.2 Nickel/Cadmium System

The nickel/cadmium system uses the same positive electrodes and electrolyte as the nickel/iron system, in combination with metallic cadmium negative electrodes. The cell reaction is given in Table 10.1 and its nominal open-circuit voltage is 1.3 V. Historically, the development of the battery has coincided with that of nickel/iron and they have a similar performance.

Nickel/cadmium technology has seen enormous technical improvement because of the advantages of high specific power (over 220 W/kg), long cycle life (up to 2000 cycles), a high tolerance of electric and mechanical abuse, a small voltage drop over a wide range of discharge currents, rapid charge capability (about 40 to 80% in 18 min), wide operating temperature (-40 to 85°C), low self-discharge rate ($<0.5\%$ per day), excellent long-term storage due to negligible corrosion, and availability in a variety of size designs. However, the nickel/cadmium battery has some disadvantages, including high initial cost, relatively low cell voltage, and the carcinogenicity and environmental hazard of cadmium.

The nickel/cadmium battery can be generally divided into two major categories, namely the vented and sealed types. The vented type consists of many alternatives. The vented sintered-plate is a more recent development, which has a high specific energy but is more expensive. It is characterized by a flat discharge voltage profile, and superior high current rate and low-temperature performance. A sealed nickel/cadmium battery incorporates a specific cell design feature to prevent a build-up of pressure in the cell caused by gassing during overcharge. As a result, the battery requires no maintenance.

The major manufacturers of the nickel/cadmium battery for EV and HEV allocation are SAFT and VARTA. Recent EVs powered by the nickel/cadmium battery have included the Chrysler TE Van, Citroën AX, Mazda Roadster, Mitsubishi EV, Peugeot 106, and Renault Clio.[3,6]

10.1.6.2.3 Nickel–Metal Hydride (Ni–MH) Battery

The Nickel-metal hydride battery has been on the market since 1992. Its characteristics are similar to those of the nickel/cadmium battery. The principal difference between them is the use of hydrogen, absorbed in a metal hydride, for the active negative electrode material in place of cadmium. Because of its superior specific energy when compared to the Ni–Cd and its freedom from toxicity or carcinogenicity, the Ni–MH battery is superseding the Ni–Cd battery.

The overall reaction in a Ni–MH battery is

$$\mathrm{MH} + \mathrm{NiOOH} \leftrightarrow \mathrm{M} + \mathrm{Ni(OH)_2}. \tag{10.19}$$

When the battery is discharged, the metal hydride in the negative electrode is oxidized to form metal alloy, and nickel oxyhydroxide in the positive electrode is reduced to nickel hydroxide. During charging, the reverse reaction occurs.

At present, Ni–MH battery technology has a nominal voltage of 1.2 V and attains a specific energy of 65 Wh/kg and a specific power of 200 W/kg. A key component of the Ni–MH battery is the hydrogen storage metal alloy, which is formulated to obtain a material that is stable over a large number of cycles. There are two major types of these metal alloys being used. These are the rare-earth alloys based around lanthanum nickel, known as AB_5, and alloys consisting of titanium and zirconium, known as AB_2. The AB_2 alloys have a higher capacity than the AB_5 alloys. However, the trend is to use AB_5 alloys because of better charge retention and stability characteristics.

Since the Ni–MH battery is still under development, its advantages based on present technology are summarized as follows: it has the highest specific energy (70 to 95 Wh/kg) and highest specific power (200 to 300 W/kg) of nickel-based batteries, environmental friendliness (cadmium free), a flat discharge profile (smaller voltage drop), and rapid recharge capability. However, this battery still suffers from its high initial cost. Also, it may have a memory effect and may be exothermic on charge.

The Ni–MH battery has been considered as an important near-term choice for EV and HEV applications. A number of battery manufacturers, such as GM Ovonic, GP, GS, Panasonic, SAFT, VARTA, and YUASA, have actively engaged in the development of this battery technology, especially for powering EVs and HEVs. Since 1993, Ovonic battery has installed its Ni–MH battery in the Solectric GT Force EV for testing and demonstration. A 19-kWh battery has delivered over 65 Wh kg, 134 km/h, acceleration from zero to 80 km/h in 14 sec, and a city driving range of 206 km. Toyota and Honda have used the Ni–MH battery in their HEVs — Prius and Insight, respectively.[3,6]

10.1.6.3 Lithium-Based Batteries

Lithium is the lightest of all metals and presents very interesting characteristics from an electrochemical point of view. Indeed, it allows a very high thermodynamic voltage, which results in a very high specific energy and specific power. There are two major technologies of lithium-based batteries: lithium–polymer and lithium-ion.

10.1.6.3.1 Lithium–Polymer (Li–P) Battery

Lithium–polymer batteries use lithium metal and a transition metal intercalation oxide (M_yO_z) for the negative and positive electrodes, respectively. This M_yO_z possesses a layered structure into which lithium ions can be inserted, or from where they can be removed on discharge and charge, respectively. A thin solid polymer electrolyte (SPE) is used, which offers the merits of improved safety and flexibility in design. The general electrochemical reactions are

$$x\mathrm{Li} + \mathrm{M}_y\mathrm{O}_z \leftrightarrow \mathrm{Li}_x\mathrm{M}_y\mathrm{O}_z. \tag{10.20}$$

On discharge, lithium ions formed at the negative electrode migrate through the SPE, and are inserted into the crystal structure at the positive electrode. On charge, the process is reversed. By using a lithium foil negative electrode and vanadium oxide (V_6O_{13}) positive electrode, the Li/SPE/V_6O_{13} cell is the most attractive one within the family of Li–polymer. It operates at a nominal voltage of 3 V and has a specific energy of 155 Wh/kg and a specific power of 315 W/kg. The corresponding advantages are a very low self-discharge rate (about 0.5% per month), capability of fabrication in a variety of shapes and sizes, and safe design (reduced activity of lithium with solid electrolyte). However, it has the drawback of a relatively weak low-temperature performance due to the temperature dependence of ionic conductivity.[6]

10.1.6.3.2 Lithium-Ion (Li-Ion) Battery

Since the first announcement of the Li-ion battery in 1991, Li-ion battery technology has seen an unprecedented rise to what is now considered to be the most promising rechargeable battery of the future. Although still at the

development stage, the Li-ion battery has already gained acceptance for EV and HEV applications.

The Li-ion battery uses a lithiated carbon intercalation material (Li_xC) for the negative electrode instead of metallic lithium, a lithiated transition metal intercalation oxide ($Li_{1-x}M_yO_z$) for the positive electrode, and a liquid organic solution or a solid polymer for the electrolyte. Lithium ions swing through the electrolyte between the positive and negative electrodes during discharge and charge. The general electrochemical reaction is described as

$$Li_xC + Li_{1-x}M_yO_z \leftrightarrow C + LiM_yO_z. \tag{10.21}$$

On discharge, lithium ions are released from the negative electrode, migrate via the electrolyte, and are taken up by the positive electrode. On charge, the process is reversed. Possible positive electrode materials include $Li_{1-x}CoO_2$, $Li_{1-x}NiO_2$, and $Li_{1-x}Mn_2O_4$, which have the advantages of stability in air, high voltage, and reversibility for the lithium intercalation reaction.

The $Li_xC/Li_{1-x}NiO_2$ type, loosely written as $C/LiNiO_2$ or simply called the nickel-based Li-ion battery, has a nominal voltage of 4 V, a specific energy of 120 Wh/kg, an energy density of 200 Wh/l, and a specific power of 260 W/kg. The cobalt-based type has a higher specific energy and energy density, but at a higher cost and significant increase in the self-discharge rate. The manganese-based type has the lowest cost and its specific energy and energy density lie between those of the cobalt- and nickel-based types. It is anticipated that the development of the Li-ion battery will ultimately move to the manganese-based type because of the low cost, abundance, and environmental friendliness of the manganese-based materials.

Many battery manufacturers, such as SAFT, GS Hitachi, Panasonic, SONY, and VARTA, have actively engaged in the development of the Li-ion battery. Starting in 1993, SAFT focused on the nickel-based Li-ion battery. Recently, SAFT reported the development of Li-ion high-power batteries for HEV applications with a specific energy of 85 Wh/kg and a specific power of 1350 W/kg. They also announced high-energy batteries for EV applications with about 150 Wh/kg and 420 W/kg (at 80% SOC, 150 A current, and 30 sec), respectively.[4]

10.2 Ultracapacitors

Because of the frequent stop/go operation of EVs and HEVs, the discharging and charging profile of the energy storage is highly varied. The average power required from the energy storage is much lower than the peak power of relatively short duration required for acceleration and hill climbing. The ratio of the peak power to the average power can be over 10:1 (Chapter 2).

In fact, the energy involved in the acceleration and deceleration transients is roughly two thirds of the total amount of energy over the entire vehicle mission in urban driving (Chapters 8 and 9). In HEV design, the peak power capacity of the energy storage is more important than its energy capacity, and usually constrains its size reduction. Based on present battery technology, battery design has to carry out the trade-off among the specific energy and specific power and cycle life. The difficulty in simultaneously obtaining high values of specific energy, specific power, and cycle life has led to some suggestions that the energy storage system of EV and HEV should be a hybridization of an energy source and a power source. The energy source, mainly batteries and fuel cells, has high specific energy whereas the power source has high specific power. The power sources can be recharged from the energy source during less demanding driving or regenerative braking. The power source that has received wide attention is the ultracapacitor.

10.2.1 Features of Ultracapacitors

The ultracapacitor is characterized by much higher specific power, but much lower specific energy compared to the chemical batteries. Its specific energy is in the range of a few watt-hours per kilogram. However, its specific power can reach up to 3 kW/kg, much higher than any type of battery. Due to their low specific energy density and the dependence of voltage on the SOC, it is difficult to use ultracapacitors alone as an energy storage for EVs and HEVs. Nevertheless, there are a number of advantages that can result from using the ultracapacitor as an auxiliary power source. One promising application is the so-called battery and ultracapacitor hybrid energy storage system for EVs and HEVs.[6,7] Specific energy and specific power requirements can be decoupled, thus affording an opportunity to design a battery that is optimized for the specific energy and cycle life with little attention being paid to the specific power. Due to the load leveling effect of the ultracapacitor, the high-current discharging from the battery and the high-current charging to the battery by regenerative braking is minimized so that the available energy, endurance, and life of the battery can be significantly increased.

10.2.2 Basic Principles of Ultracapacitors

Double-layer capacitor technology is the major approach to achieving the ultracapacitor concept. The basic principle of a double-layer capacitor is illustrated in Figure 10.8. When two carbon rods are immersed in a thin sulfuric acid solution, separated from each other and charged with voltage increasing from zero to 1.5 V, almost nothing happens up to 1 V; then at a little over 1.2 V, a small bubble will appear on the surface of both the electrodes. Those bubbles at a voltage above 1 V indicate electrical decomposition of water. Below the decomposition voltage, while the current does not

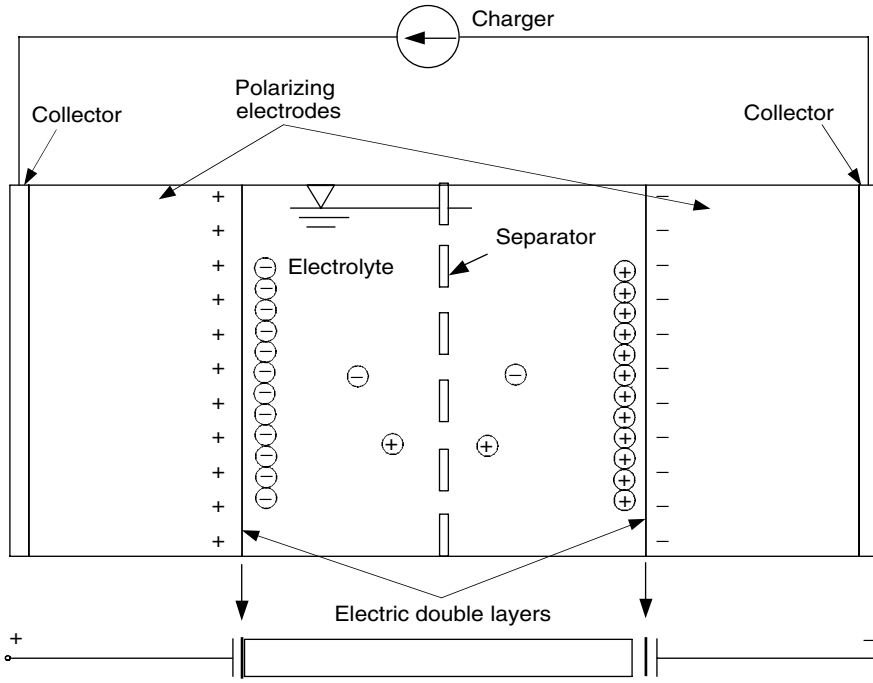

FIGURE 10.8
Basic principles of a typical electric double-layer capacitor

flow, an "electric double layer" then occurs at the boundary of electrode and electrolyte. The electrons are charged across the double layer and for a capacitor.

An electrical double layer works as an insulator only below the decomposing voltage. The stored energy, E_{cap}, is expressed as

$$E_{cap} = \frac{1}{2} CV^2, \tag{10.22}$$

where C is the capacitance in Faraday and V is the usable voltage in volt. This equation indicates that the higher rated voltage V is desirable for larger energy density capacitors. Up to now, capacitors' rated voltage with an aqueous electrolyte has been about 0.9 V per cell, and 2.3 to 3.3 V for each cell with a nonaqueous electrolyte.

There is great merit in using an electric double layer in place of plastic or aluminum oxide films in a capacitor, since the double layer is very thin — as thin as one molecule with no pin holes — and the capacity per area is quite large, at 2.5 to 5 $\mu F/cm^2$.

Even if a few $\mu F/cm^2$ are obtainable, the energy density of capacitors is not large when using aluminum foil. For increasing capacitance, electrodes are made from specific materials that have a very large area, such as activated carbons, which are famous for their surface areas of 1,000 to 3,000 m^2/g.

To those surfaces, ions are adsorbed and result in 50 F/g (1,000 $m^2/g \times 5$ $F/cm^2 \times 10{,}000$ $cm^2/m^2 = 50$ F/g). Assuming that the same weight of electrolyte is added, 25 F/g is quite a large capacity density. Nevertheless, the energy density of these capacitors is far smaller than secondary batteries; the typical specific energy of ultracapacitors at present is about 2 Wh/kg, only 1/20 of 40 Wh/kg, which is the available value of typical lead-acid batteries.

10.2.3 Performance of Ultracapacitors

The performance of an ultracapacitor may be represented by terminal voltages during discharge and charge with different current rates. There are three parameters in a capacitor: the capacitance itself (its electric potential V_C), the series resistance R_S, and the dielectric leakage resistance, R_L, as shown in Figure 10.9. The terminal voltage of the ultracapacitor during discharge can be expressed as

$$V_t = V_C - iR_S. \tag{10.23}$$

The electric potential of a capacitor can be expressed by

$$\frac{dV_C}{dt} = -\left(\frac{i+i_L}{C}\right), \tag{10.24}$$

where C is the capacitance of the ultracapacitor. On the other hand, the leakage current i_L can be expressed as

$$i_L = \frac{V_c}{R_L}. \tag{10.25}$$

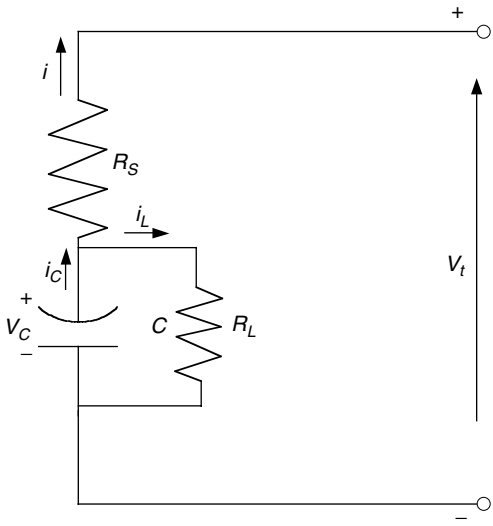

FIGURE 10.9
Ultracapacitor equivalent circuit

Substituting (10.22) into (10.21), one can obtain

$$\frac{dV_C}{dt} = \frac{V_c}{CR_L} - \frac{i}{C}. \tag{10.26}$$

The terminal voltage of the ultracapacitor cell can be represented by the diagram as shown in Figure 10.10. The analytical solution of (10.26) is

$$V_C = \left[V_{C0} \int_0^t \frac{i}{C} e^{t/CR_L}\, dt \right] e^{t/CR_L}, \tag{10.27}$$

where i is the discharge current, which is a function of time in real operation. The discharge characteristics of the Maxwell 2600 F ultracapacitor are shown in Figure 10.11. At different discharge current rates, the voltage decreases linearly with discharge time. At a large discharge current rate, the voltage decreases much faster than at a small current rate.

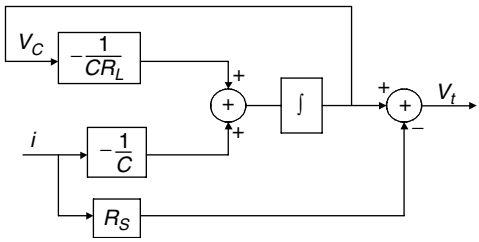

FIGURE 10.10
Block diagram of the ultracapacitor model

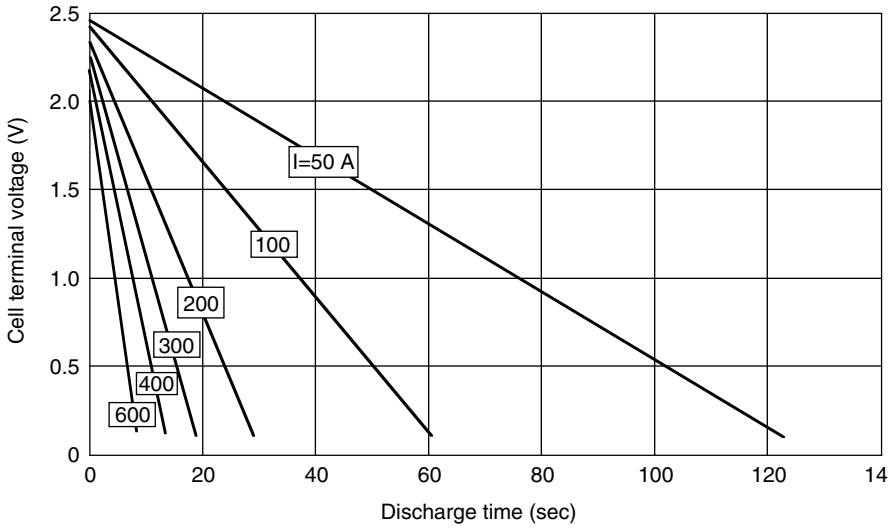

FIGURE 10.11
Discharge characteristics of the 2600 F Maxwell Technologies ultracapacitor

A similar model can be used to describe the charging characteristics of an ultracapacitor, and readers who are interested may do their own analysis and simulation.

The operation efficiency in discharging and charging can be expressed as:

discharging:
$$\eta_d = \frac{V_t I_t}{V_C I_C} = \frac{(V_C - I_t R_S) I_t}{V_C (I_t + I_L)} \tag{10.28}$$

and

charging:
$$\eta_c = \frac{V_C I_C}{V_t I_t} = \frac{V_C (I_t - I_L)}{(V_C + I_t R_s) I_t}, \tag{10.29}$$

where V_t is the terminal voltage and I_t is the current input to or output from the terminal. In actual operation, the leakage current I_L is usually very small (few mA) and can be ignored. Thus, equations (10.28) and (10.29) can be rewritten as:

discharging:
$$\eta_d = \frac{V_C - R_S I_t}{V_C} = \frac{V_t}{V_C} \tag{10.30}$$

and

charging:
$$\eta_c = \frac{V_C}{V_C + R_s I_t} = \frac{V_C}{V_t}. \tag{10.31}$$

The above equations indicate that the energy loss in an ultracapacitor is caused by the presence of series resistance. The efficiency decreases at a high current rate and low cell voltage, as shown in Figure 10.12. Thus, in actual

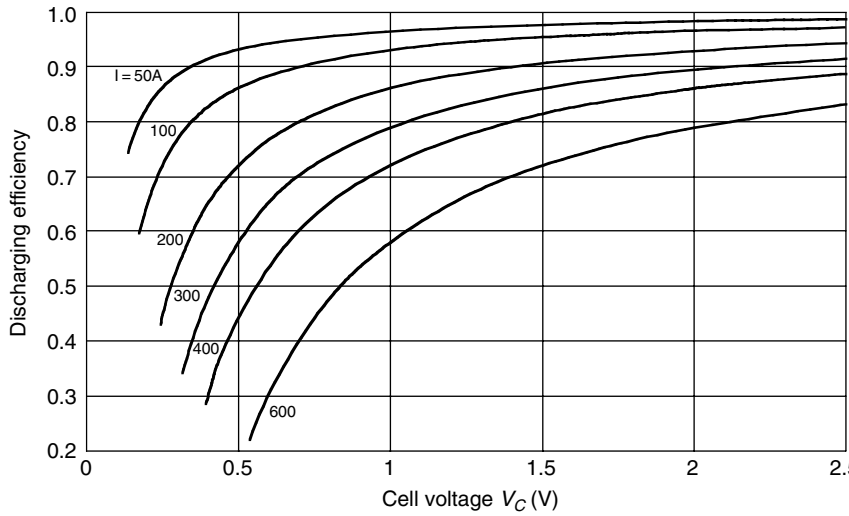

FIGURE 10.12
Discharge efficiency of the 2600 F Maxwell Technologies ultracapacitor

operation, the ultracapacitor should be maintained at its high voltage region, for more than 60% of its rated voltage.

The energy stored in an ultracapacitor can be obtained through the energy needed to charge it to a certain voltage level, that is,

$$E_C = \int_0^t V_C I_C \, dt = \int_0^v C V_C \, dV_C = \frac{1}{2} C V_C^2, \tag{10.32}$$

where V_C is the cell voltage in volts. At its rated voltage, the energy stored in the ultracapacitor reaches its maxima. Equation (10.31) indicates that increasing the rated voltage can significantly increase the stored energy since the energy increases with the voltage squared. In real operation, it is impossible to utilize the stored energy completely because of the low power in the low SOC (low voltage). Thus, an ultracapacitor is usually given a bottom voltage, V_{Cb}, below which the ultracapacitor will stop delivering energy. Consequently, the available or useful energy for use is less than its fully charged energy, which can be expressed as

$$E_u = \frac{1}{2} C\left(V_{CR}^2 - V_{Cb}^2\right), \tag{10.33}$$

where V_{CR} is the rated voltage of the ultracapacitor. At its bottom voltage, the SOC can be written as

$$SOC = \frac{0.5\, C V_{Cb}^2}{0.5\, C V_{CR}^2} = \frac{V_{Cb}^2}{V_{CR}^2}. \tag{10.34}$$

For example, when the cell voltage drops from rated voltage to 60% of the rated voltage, 64% of the total energy is available for use, as shown in Figure 10.13.

10.2.4 Ultracapacitor Technologies

According to the goals set by the U.S. Department of Energy for the inclusion of ultracapacitors in EVs and HEVs, the near-term specific energy and specific power should be better than 5 Wh/kg and 500 W/kg, respectively, while the advanced performance values should be over 15 Wh/kg and 1600 W/kg. So far, none of the available ultracapacitors can fully satisfy these goals. Nevertheless, some companies are actively engaged in the research and development of ultracapacitors for EV and EHV applications. Maxwell Technologies has claimed that its power BOOSTCAP® ultracapacitor cells (2600 F at 2.5 V) and integrated modules (145 F at 42 V and 435 F at 14 V) are in production. The technical specifications are listed in Table 10.3.

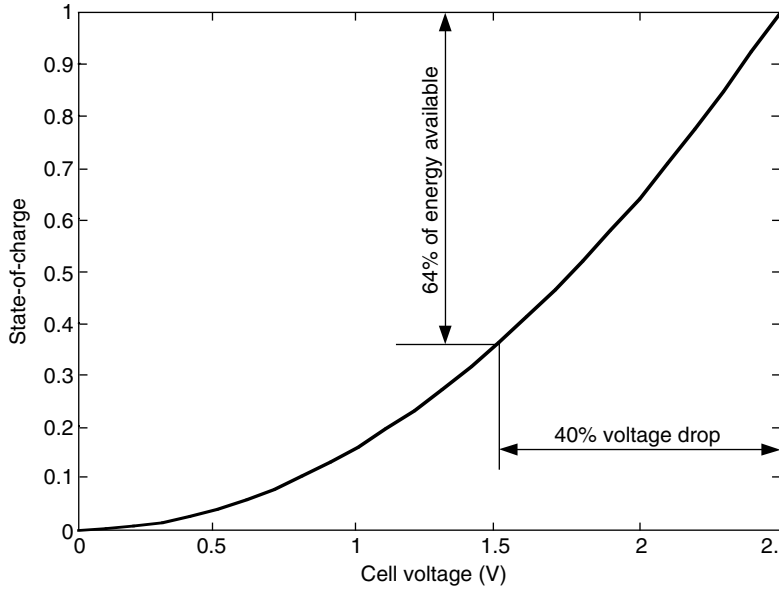

FIGURE 10.13
SOC vs. cell voltage

TABLE 10.3

Technical Specifications of the Maxwell Technologies Ultracapacitor Cell and Integrated Modules[5]

	BCAP0010 (Cell)	BMOD0115 (Module)	BMOD0117 (Module)
Capacitance (farads, −20%/+20%)	2600	145	435
maximum series resistance ESR at 25°C (mΩ)	0.7	10	4
Voltage (V), continuous (peak)	2.5 (2.8)	42 (50)	14 (17)
Specific power at rated voltage (W/kg)	4300	2900	1900
Specific energy at rated voltage (Wh/kg)	4.3	2.22	1.82
Maximum current (A)	600	600	600
Dimensions (mm) (reference only)	60 × 172 (Cylinder)	195 × 165 × 415 (Box)	195 × 265 × 145 (Box)
Weight (kg)	0.525	16	6.5
Volume (l)	0.42	22	7.5
Operating temperature[a] (°C)	−35 to +65	−35 to +65	−35 to +65
Storage temperature (°C)	−35 to +65	−35 to +65	−35 to +65
Leakage current (mA) 12 h, 25°C	5	10	10

[a]Steady-state case temperature.

10.3 Ultrahigh-Speed Flywheels

The use of flywheels for storing energy in mechanical form is not a new concept. More than 25 years ago, the Oerlikon Engineering Company in Switzerland made the first passenger bus solely powered by a massive flywheel. This flywheel, which weighed 1500 kg and operated at 3000 rpm, was recharged by electricity at each bus stop. The traditional flywheel is a massive steel rotor with hundreds of kilograms that spins on the order of ten hundreds of rpm. On the contrary, the advanced flywheel is a lightweight composite rotor with tens of kilograms and rotates on the order of 10,000 rpm; it is the so-called ultrahigh-speed flywheel.

The concept of ultrahigh-speed flywheels appears to be a feasible means for fulfilling the stringent energy storage requirements for EV and HEV applications, namely high specific energy, high specific power, long cycle life, high-energy efficiency, quick recharge, maintenance free characteristics, cost effectivenees, and environmental friendliness.

10.3.1 Operation Principles of Flywheels

A rotating flywheel stores energy in the kinetic form as

$$E_f = \frac{1}{2} J_f \omega_f^2 \tag{10.35}$$

where J_f is the moment of inertia of the flywheel in kgm^2/sec and ω_f is the angular velocity of the flywheel in rad/sec. Equation (10.32) indicates that enhancing the angular velocity of the flywheel is the key method of increasing its energy capacity and reducing its weight and volume. At present, a speed of over 60,000 rpm has been achieved in some prototypes.

With current technology, it is difficult to directly use the mechanical energy stored in a flywheel to propel a vehicle, due to the need for continuous variation transmission (CVT) with a wide gear ratio variation range. The commonly used approach is to couple an electric machine to the flywheel directly or through a transmission to constitute a so-called mechanical battery. The electric machine, functioning as the energy input and output port, converts the mechanical energy into electric energy or vice versa, as shown in Figure 10.14.

Equation (10.35) indicates that the energy stored in a flywheel is proportional to the moment of inertia of the flywheel and flywheel rotating speed squared. A lightweight flywheel should be designed to achieve moment of inertia per unit mass and per unit volume by properly designing its geometric shape. The moment of inertia of a flywheel can be calculated by

$$J_f = 2\pi\rho \int_{R_1}^{R_2} W(r) r^3 \, dr, \tag{10.36}$$

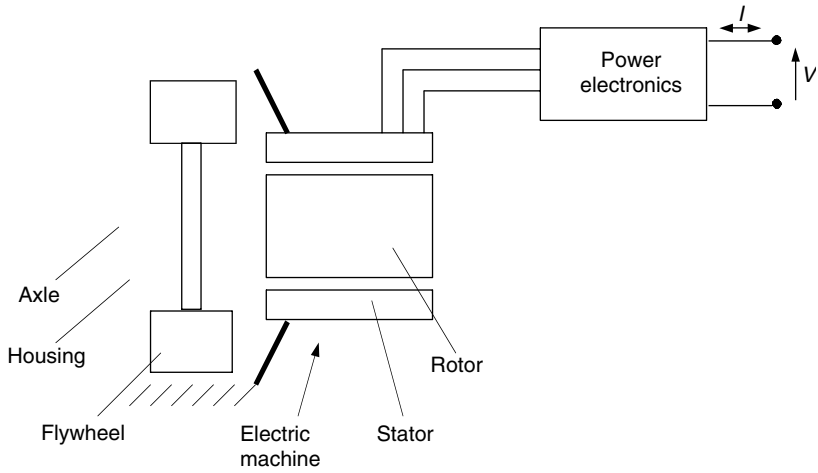

FIGURE 10.14
Basic structure of a typical flywheel system (mechanical battery)

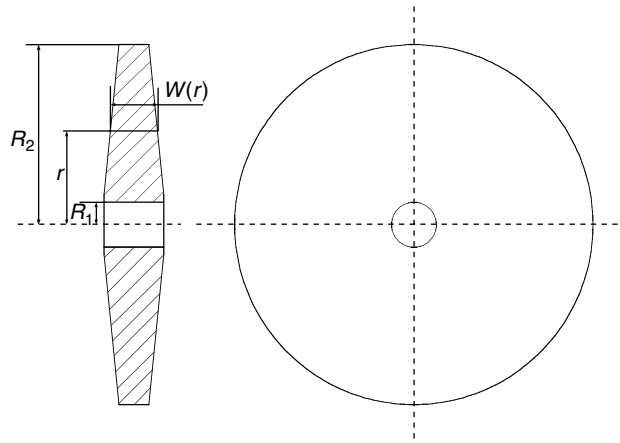

FIGURE 10.15
Geometry of a typical flywheel

where ρ is the material mass density and $W(r)$ is the width of the flywheel corresponding to the radius r, as shown in Figure 10.15. The mass of the flywheel can be calculated by

$$M_f = 2\pi\rho\int_{R_1}^{R_2} W(r) r \, dr. \tag{10.37}$$

Thus, the specific moment of inertia of a flywheel, defined as the moment of inertia per unit mass, can be expressed as

$$J_{fs} = \frac{\int_{R_1}^{R_2} W(r) r^3 \, dr}{\int_{R_1}^{R_2} W(r) r \, dr}. \tag{10.38}$$

Equation (10.35) indicates that the specific moment of inertia of a flywheel is independent of its material mass density and dependent solely on its geometric shape $W(r)$.

For a flywheel with equal width, the moment of inertia is

$$J_f = 2\pi\rho\left(R_2^4 - R_1^4\right) = 2\pi\rho\left(R_2^2 + R_1^2\right)\left(R_2^2 - R_1^2\right). \tag{10.39}$$

The specific moment of inertia is

$$J_{fs} = R_2^2 + R_1^2. \tag{10.40}$$

The volume density of the moment of inertia, defined as the moment of inertia per unit volume, is, indeed, associated with the mass density of the material. The volume of the flywheel can be obtained by

$$V_f = 2\pi \int_{R_2}^{R_2} W(r) r \, dr. \tag{10.41}$$

The volume density of the moment of inertia can be expressed as

$$J_{fV} = \frac{\rho \int_{R_1}^{R_2} W(r) r^3 \, dr}{\int_{R_1}^{R_2} W(r) r \, dr}. \tag{10.42}$$

For a flywheel with equal width, the volume density of the moment of inertia is

$$J_{fV} = \rho\left(R_2^2 + R_1^2\right). \tag{10.43}$$

Equations (10.42) and (10.43) indicate that heavy material can, indeed, reduce the volume of the flywheel with a given moment of inertia.

10.3.2 Power Capacity of Flywheel Systems

The power that a flywheel delivers or obtains can be obtained by differentiating equation (10.35) with respect to time, that is,

$$P_f = \frac{dE_f}{dt} = J_f \omega_f \frac{d\omega_f}{dt} = \omega_f T_f, \tag{10.44}$$

where T_f is the torque acting on the flywheel by the electric machine. When the flywheel discharges its energy, the electric machine acts as a generator and converts the mechanical energy of the flywheel into electric energy. On the other hand, when the flywheel is charged, the electric machine acts as a motor and converts electric energy into mechanical energy stored in the flywheel. Equation (10.44) indicates that the power capacity of a flywheel system depends completely on the power capacity of the electric machine.

An electric machine usually has the characteristics as shown in Figure 10.16, which has two distinct operating regions — constant torque and constant power region. In the constant torque region, the voltage of the electric machine is proportional to its angular velocity, and the magnetic flux in the air gap is constant. However, in the constant power region, the voltage is constant and the magnetic field is weakened with increasing machine angular velocity.

In charge of the flywheel, that is, accelerating the flywheel from a low speed, ω_0, to a high speed, maximum speed, ω_{max}, for example, the torque delivered from the electric machine is

$$T_m = J_f \frac{d\omega_f}{dt}, \tag{10.45}$$

where it is supposed that the electric machine is directly connected to the flywheel. The time, t, needed can be expressed as

$$t = \int_{\omega_0}^{\omega_{max}} \frac{J_f}{T_m} d\omega = \int_{\omega_0}^{\omega_b} \frac{J_f}{p_m/\omega_b} \omega + \int_{\omega_b}^{\omega_{max}} \frac{J_f}{p_m/\omega} d\omega. \tag{10.46}$$

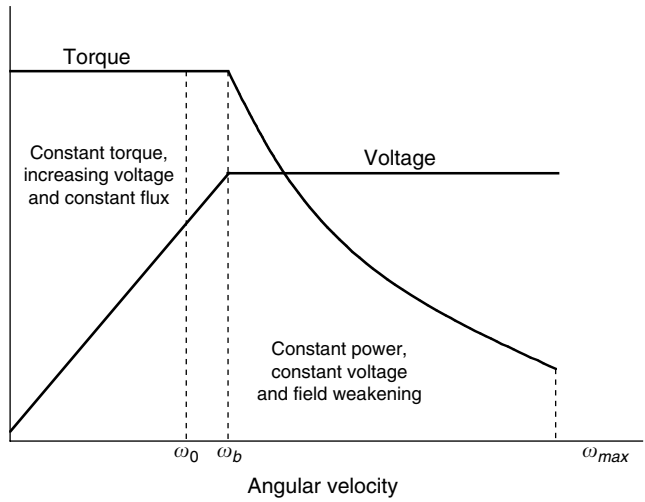

FIGURE 10.16
Typical torque and voltage profile vs. rotational speed

With the given accelerating time, t, the maximum power of the electric machine can be obtained from (10.46) as

$$P_m = \frac{J_f}{2_t}\left(\omega_b^2 - 2\omega_0\omega_b + \omega_{max}^2\right). \tag{10.47}$$

Equation (10.47) indicates that the power of the electric machine can be minimized by the design of its corner speed or base speed, ω_b, equal to the bottom speed of the flywheel, ω_0. This conclusion implies that the effective operating speed range of the flywheel should coincide with the constant speed region of the electric machine. The power of the electric machine can be minimized as

$$P_m = \frac{J_f}{2_t}\left(\omega_0^2 + \omega_{max}^2\right). \tag{10.48}$$

Another advantage achieved by coinciding the operating speed range of the flywheel with the constant power speed range is that the voltage of the electric machine is always constant (refer to Figure 10.16), therefore significantly simplifying the power management system, such as DC/DC converters and their controls.

10.3.3 Flywheel Technologies

Although higher rotational speed can significantly increase the stored energy (equation [10.35]), there is a limit to which the tensile strength σ of the material constituting the flywheel cannot withstand the stress resulting from the centrifugal force. The maximum stress acting on the flywheel depends on its geometry, specific density ρ, and rotational speed. The maximum benefit can be obtained by adopting flywheel materials that have a maximum ratio of σ/ρ. Notice that if the speed of the flywheel is limited by the material strength, the theoretical specific energy is proportional to the ratio of σ/ρ. Table 10.4 summarizes the characteristics of some composite materials for ultrahigh-speed flywheels.

A constant-stress principle may be employed for the design of ultrahigh-speed flywheels. To achieve the maximum energy storage, every element in the rotor should be stressed equally to its maximum limit. This results in a

TABLE 10.4
Composite Materials for an Ultrahigh-Speed Flywheel[6]

	Tensile Strength s (MPa)	Specific Energy ρ (kg/m^3)	Ratio σ/ρ (Wh/kg)
E-glass	1379	1900	202
Graphite epoxy	1586	1500	294
S-glass	2069	1900	303
Kevlar epoxy	1930	1400	383

shape of gradually decreasing thickness that theoretically approaches zero as the radius approaches infinity, as shown in Figure 10.17.[6]

Due to the extremely high rotating speed and in order to reduce the aerodynamic loss and frictional loss, the housing inside the flywheel in spinning is always highly vacuumed, and noncontact, magnetic bearings are employed.

The electric machine is one of the most important components in the flywheel system, since it has critical impact on the performance of the system. At present, permanent magnet (PM) brushless DC motors are usually accepted in the flywheel system. Apart from possessing high power density and high efficiency, the PM brushless DC motor has a unique advantage that no heat is generated inside the PM rotor, which is particularly essential for the rotor to work in a vacuum environment to minimize the windage loss.

A switched reluctance machine (SRM) is also a very promising candidate for the application in a flywheel system. SRM has a very simple structure and can operate efficiently at very high speed. In addition, SRM presents a large extended constant power speed region, which allows more energy in the flywheel that can be delivered (refer to Section 10.3.2). In this extended speed region, only the machine excitation flux is varied, and is easily realized. On the contrary, the PM brushless motor shows some difficulty in weakening the field flux induced by the PM.

In contrast to applying the ultrahigh-speed flywheel for energy storage in stationary plants, its application to EVs and HEVs suffers from two specific problems. First, gyroscopic forces occur whenever a vehicle departs from its straight-line course, such as in turning and in pitching upward or downward

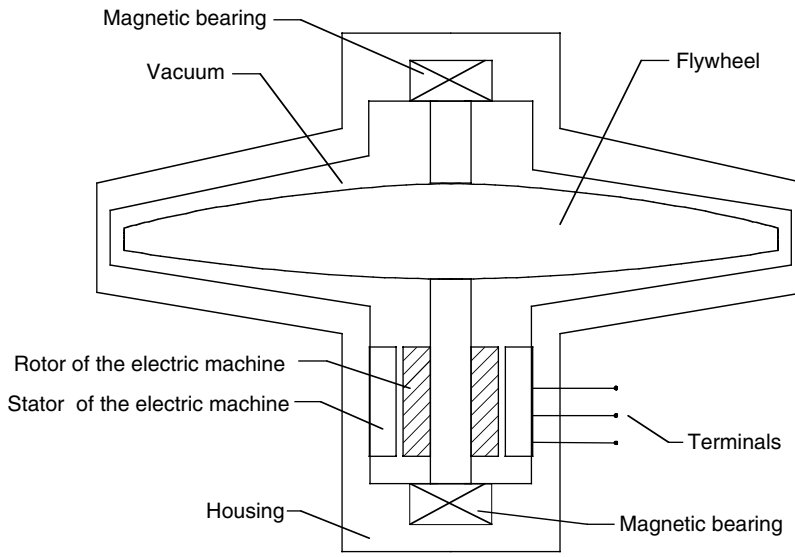

FIGURE 10.17
Basic structure of a typical flywheel system

from road grades. These forces essentially reduce the maneuverability of the vehicle. Secondly, if the flywheel is damaged, its stored energy in mechanical form will be released in a very short period of time. The corresponding power released will be very high, which can cause severe damage to the vehicle. For example, if a 1-kWh flywheel breaks apart in 1 to 5 sec, it will generate a huge power output of 720 to 3600 kW. Thus, containment in case of failure is presently the most significant obstacle to implementing the ultrahigh-speed flywheel in EVs and HEVs.

The simplest way to reduce the gyroscopic forces is to use multiple smaller flywheels. By operating them in a pair (one half spinning in one direction and another in the opposite direction), the net gyroscopic effect becomes theoretically zero. Practically, it still has some problems related to the distribution and coordination of these flywheels. Also, the overall specific energy and specific power of all flywheels may be smaller than a single one. Similarly, the simplest way to minimize the damage due to the breakage of the ultrahigh-speed flywheel is to adopt multiple small modules, but this means that vehicle performance suffers from the possible reduction of specific energy and specific power. Recently, a new failure containment has been proposed. Instead of diminishing the thickness of the rotor's rim to zero based on the maximum stress principle, the rim thickness is purposely enlarged. Hence, the neck area just before the rim (virtually a mechanical fuse) will break first at the instant that the rotor suffers from a failure. Due to the use of this mechanical fuse, only the mechanical energy stored in the rim needs to be released or dissipated in the casing upon failure.[6]

Many companies and research agencies have engaged in the development of ultrahigh-speed flywheels as the energy storages of EVs and HEVs, such as Lawrence Livermore National Laboratory (LLNL) in the U.S., Ashman Technology, AVCON, Northrop Grumman, Power R&D, Rocketdyne/Rockwell Trinity Flywheel US Flywheel Systems, Power Center at UT Austin, etc. However, technologies of ultrahigh-speed flywheel are still in their infancy. Typically, the whole ultrahigh-speed flywheel system can achieve a specific energy of 10 to 150 Wh/kg and a specific power of 2 to 10 kW. LLIL has built a prototype (20 cm diameter and 30 cm height) that can achieve 60,000 rpm, 1 kWh, and 100 kW.

10.4 Hybridization of Energy Storages

The hybridization of energy storage is to combine two or more energy storages together so that the advantages of each one can be brought out and the disadvantages can be compensated by others. For instance, the hybridization of a chemical battery with an ultracapacitor can overcome such problems as low specific power of electrochemical batteries and low specific energy of ultracapacitors, therefore achieving high specific energy and high specific power.

Basically, the hybridized energy storage consists of two basic energy storages: one with high specific energy and the other with high specific power. The basic operation of this system is illustrated in Figure 10.18. In high power demand operations, such as acceleration and hill climbing, both basic energy storages deliver their power to the load as shown in Figure 10.18(a). On the other hand, in low power demand operation, such as constant speed cruising operations, the high specific energy storage will deliver its power to the load and charge the high specific power storage to recover its charge lost during high power demand operation, as shown in Figure 10.18(b). In regenerative braking operations, the peak power will be absorbed by the high specific

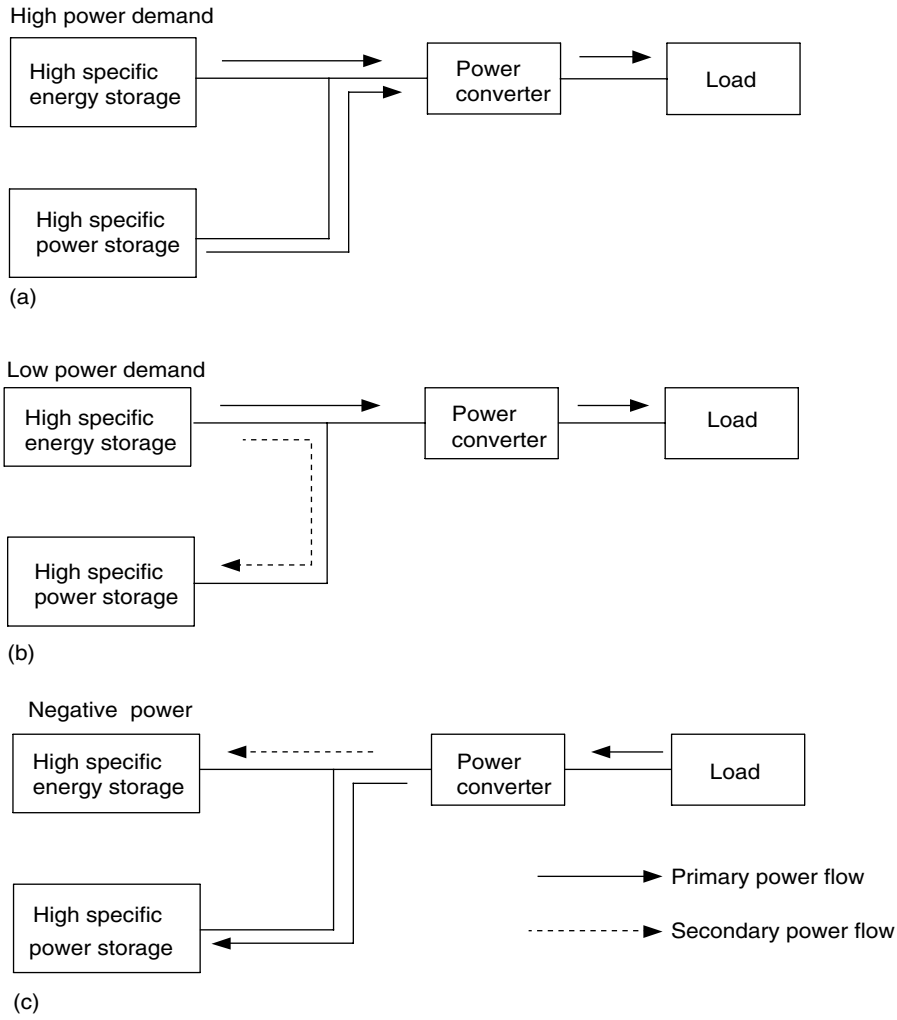

FIGURE 10.18
Concept of a hybrid energy storage operation

power storage, and only a limited part is absorbed by the high specific energy storage. In this way, the whole system would be much smaller in weight and size than if any one of them alone was the energy storage.

Based on the available technologies of various energy storages, there are several viable hybridization schemes for EVs and HEVs, typically, battery and battery hybrids, and battery and ultracapacitor hybrids. The latter is more natural since the ultracapacitor can offer much higher power than batteries, and it collaborates with various batteries to form the battery and ultracapacitor hybrids. During hybridization, the simplest way is to connect the ultracapacitors to the batteries directly and in parallel, as shown in Figure 10.19.

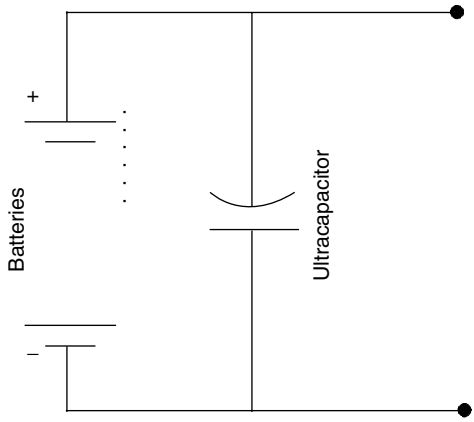

FIGURE 10.19
Direct and parallel connection of batteries and ultracapacitors

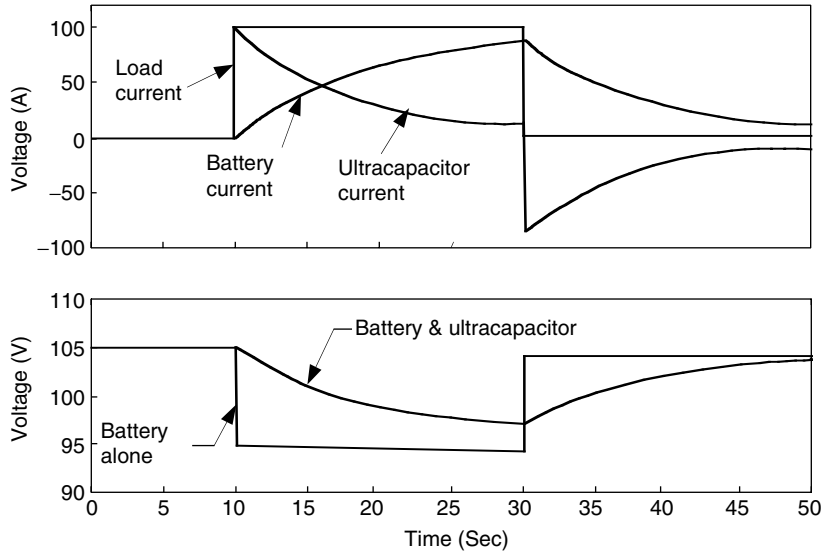

FIGURE 10.20
Variation of battery and ultracapacitor currents and voltages with a step current output change

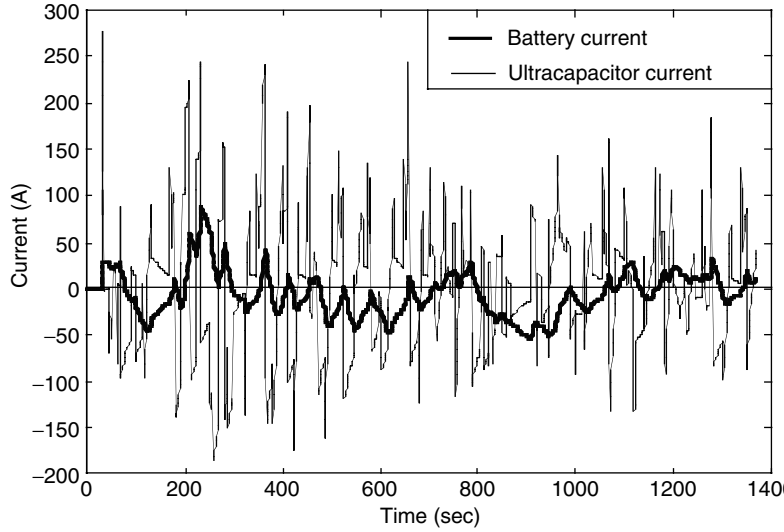

FIGURE 10.21
Battery and ultracapacitor currents during operation of HEV in an FTP 75 urban drive cycle

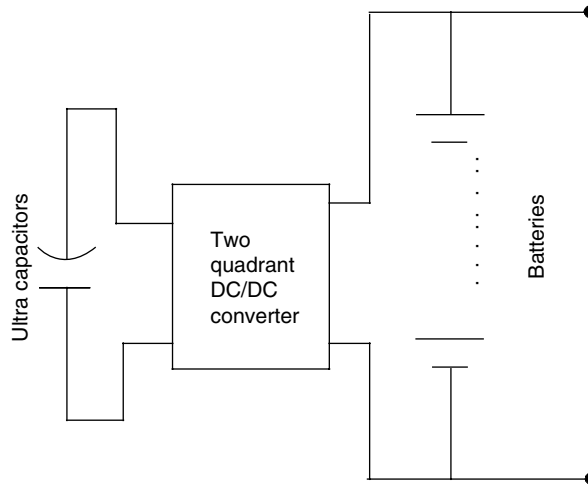

FIGURE 10.22
Actively controlled hybrid battery/ultracapacitor energy storage

In this configuration, the ultracapacitors simply act as a current filter, which can significantly level the peak current of the batteries and reduce the battery voltage drop as shown in Figure 10.20 and Figure 10.21. The major disadvantages of this configuration are that the power flow cannot be actively controlled and the ultracapacitor energy cannot be fully used.

Figure 10.22 shows a configuration in which a two-quadrant DC/DC converter is placed between the batteries and ultracapacitors. This design allows

the batteries and the ultracapacitors to have a different voltage, the power flow between them can be actively controlled, and the energy in the ultracapacitors can be fully used. In the long term, an ultrahigh-speed flywheel would replace the batteries in hybrid energy storage to obtain a high-efficiency, compact, and long-life storage system for EVs and HEVs.

References

[1] D.A.J. Rand, R. Woods, and R.M. Dell, *Batteries for Electric Vehicles*, Society of Automotive Engineers (SAE), Warrendale, PA, 1988.
[2] T.R. Crompton, *Battery Reference Book*, Society of Automotive Engineers (SAE), Warrendale, PA, 1996.
[3] Y. Gao and M. Ehsani, Investigation of battery technologies for the army's hybrid vehicle application, in Proceedings of the IEEE 56th *Vehicular Technology Conference*, Fall 2002, pp. 1505–1509.
[4] http://www.saftbatteries.com, SAFT, The Battery Company, 2003.
[5] http://www.maxwell.com, Maxwell Technologies, 2003.
[6] C.C. Chan and K.T. Chau, *Modern Electric Vehicle Technology*, Oxford University Press, Oxford, 2001.
[7] Y. Gao, H. Moghbelli, M. Ehsani, G. Frazier, J. Kajs, and S. Bayne, Investigation of high-energy and high-power hybrid energy storage systems for military vehicle application, *Society of Automotive Engineers (SAE) Journal*, Paper No. 2003-01-2287, Warrendale, PA, 2003.

11

Fundamentals of Regenerative Braking

CONTENTS

11.1 Energy Consumption in Braking 334
11.2 Braking Power and Energy on Front and Rear Wheels 334
11.3 Brake System of EVs and HEVs 338
11.3.1 Series Brake — Optimal Feel 338
11.3.2 Series Brake — Optimal Energy Recovery.....339
11.3.3 Parallel Brake 341
11.4 Antilock Brake System (ABS) 343
References 345

One of the most important features of electric vehicles (EVs) and hybrid electric vehicles (HEVs) is their ability to recover significant amounts of braking energy. The electric motors in EVs and HEVs can be controlled to operate as generators to convert the kinetic or potential energy of the vehicle mass into electric energy that can be stored in the energy storage and reused.

The braking performance of a vehicle is undoubtedly one of the important factors to affect vehicle safety. A successfully designed braking system for a vehicle must always meet two distinct demands. Firstly, in emergency braking, it must bring the vehicle to rest in the shortest possible distance. Secondly, it must maintain control over the vehicle's direction. The former requires that the braking system be able to supply sufficient braking torque on all the wheels. The latter requires braking force to be distributed on all the wheels equally.

Generally, the braking torque required is much larger than the torque that an electric motor can produce. In EVs and HEVs, mechanically frictional braking systems must coexist with electrically regenerative braking. Thus, the proper design and control of both mechanical and electrical braking systems are major concerns.

11.1 Energy Consumption in Braking

A significant amount of energy is consumed by braking. Braking a 1500 kg vehicle from 100 km/h to zero speed consumes about 0.16 kWh of energy ($0.5 \times M_v \times V^2$) in a few tens of meters. If this amount of energy is consumed in coasting by only overcoming the drags (rolling resistance and aerodynamic drag) without braking, the vehicle will travel about 2 km, as shown in Figure 11.1.

When vehicles are driving with a stop-and-go pattern in urban areas, a significant amount of energy is consumed by frequent braking, which results in high fuel consumption. Figure 11.2 shows the total traction energy on driven wheels, energies consumed by drags (rolling resistance and aerodynamic drag), and braking of a 1500 kg passenger car. Table 11.1 lists the maximum speed, average speed, total traction energy on driven wheels, and total energies consumed by drags and braking per 100 km traveling distance of the 1500 kg passenger car.

Figure 11.2 and Table 11.1 indicate that the braking energy in typical urban areas may reach up to more than 25% of the total traction energy. In large cities, such as New York, it may reach up to 70%. It is concluded that effective regenerative braking can significantly improve the fuel economy of EVs and HEVs.[1]

11.2 Braking Power and Energy on Front and Rear Wheels

Braking power and braking energy consumed by the front and rear wheels are closely related to the braking forces on the front and rear wheels. A full understanding of the braking force, braking power, and braking energy consumed

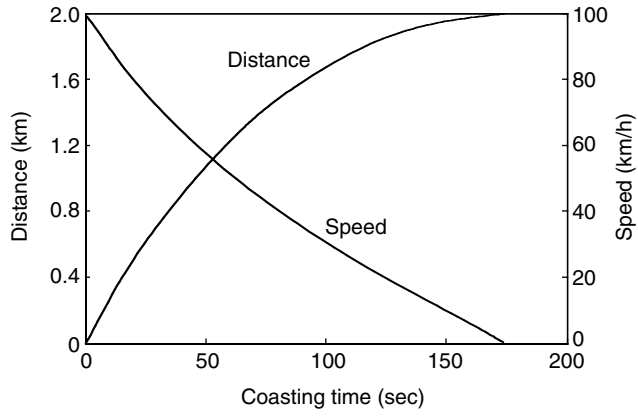

FIGURE 11.1
Coasting speed and distance

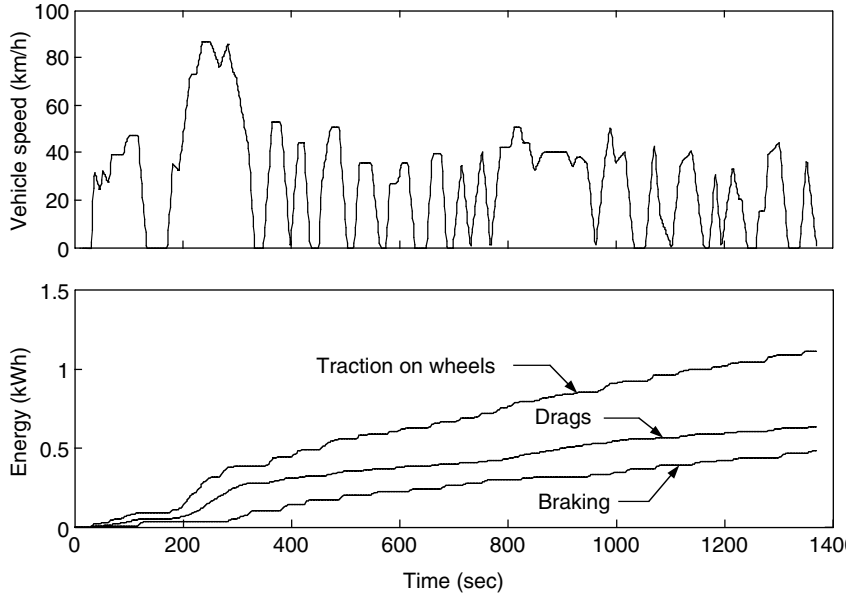

FIGURE 11.2
Total traction energy and energies consumed by drags and braking in an FTP 75 urban drive cycle

TABLE 11.1

Maximum Speed, Average Speed, Total Traction Energy, and Energies Consumed by Drags and Braking per 100 km Traveling Distance in Different Drive Cycles

	FTP 75 Urban	FTP 75 Highway	US06	ECE-1	New York City
Maximum speed (km/h)	86.4	97.7	128.5	120	44.6
Average speed (km/h)	27.9	79.3	77.5	49.9	12.2
Total traction energy[a] (kWh)	10.47	10.45	17.03	11.79	15.51
Total energy consumed by drags[a] (kWh)	5.95	9.47	11.73	8.74	4.69
Total energy consumed by braking[a] (kWh)	4.52	0.98	5.30	3.05	10.82
Percentage of braking energy to total traction energy (%)	43.17	9.38	31.12	25.87	69.76

[a]Measured on driven wheels.

by the front and rear wheels in typical drive cycles is helpful in the design of regenerative braking systems.

Initially, assuming that the braking distribution on the front and rear wheels follows the curve *I* (refer to Chapter 2), ignoring vehicle drags, the braking forces on the front and rear wheels can be expressed as:

$$F_{bf} = \frac{jM_v}{L}\left(L_b + \frac{h_g}{g}j\right) \tag{11.1}$$

and

$$F_{br} = \frac{jM_v}{L}\left(L_a - \frac{h_g}{g}j\right), \tag{11.2}$$

where j is the deceleration of the vehicle in m/s^2, L is the wheel base of the vehicle, L_a and L_b are the horizontal distances between the vehicle gravity center to the center of the front and rear wheels, respectively, and h_g is the height of the gravity center of the vehicle to the ground (refer to Chapter 2). Figure 11.3 shows vehicle speed and acceleration/deceleration in an FTP 75 urban drive cycle.

Figures 11.4–11.6 show the braking force, braking power, and braking energy of a 1500 kg passenger car in an FTP 75 urban drive cycle. This example has parameters of $L = 2.7m$, $L_a = 0.4L$, $L_b = 0.6L$, and $h_g = 0.55m$.

Figures 11.4–11.6 indicate that: (1) The front wheels consume about 65% of the total braking power and energy. Thus, regenerative braking on front wheels, if available only on one axle, is more effective than on rear wheels. (2) The braking force is almost constant in the speed range of less than 50 km/h and decreases when the speed is greater than 40 km/h. This characteristic naturally matches that of an electric motor that has a constant torque at the low-speed region and a constant power at the high-speed region. Further, Figure 11.6 indicates that most braking energy is consumed in the speed range of 10 to 50 km/h.

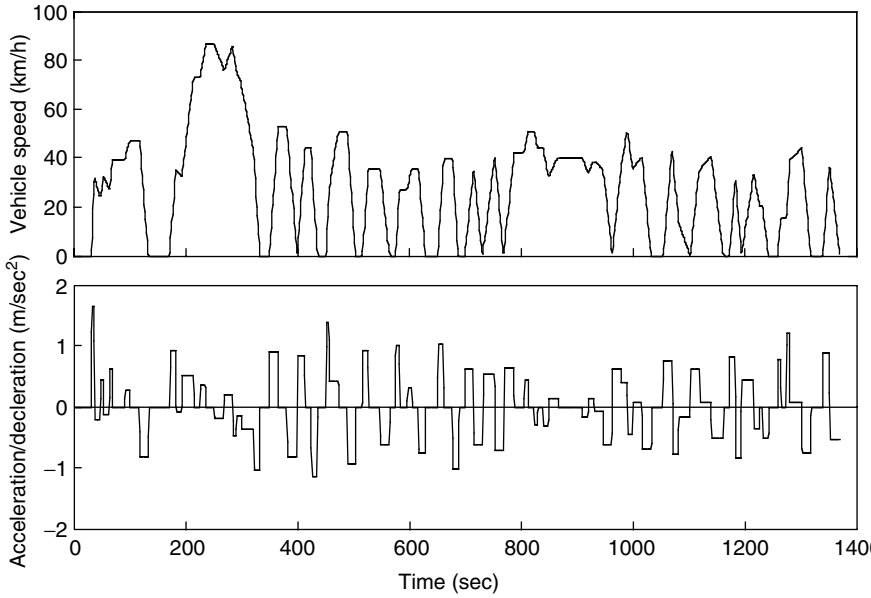

FIGURE 11.3
Vehicle speed and acceleration/deceleration in an FTP urban drive cycle

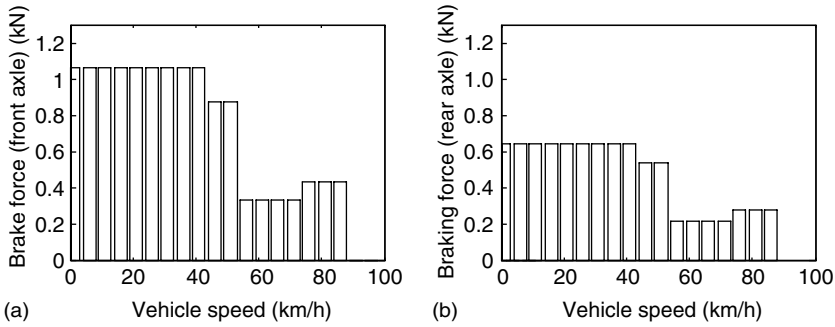

FIGURE 11.4
Braking force vs. vehicle speed in an FTP 75 urban drive cycle: (a) on front wheels and (b) on rear wheels

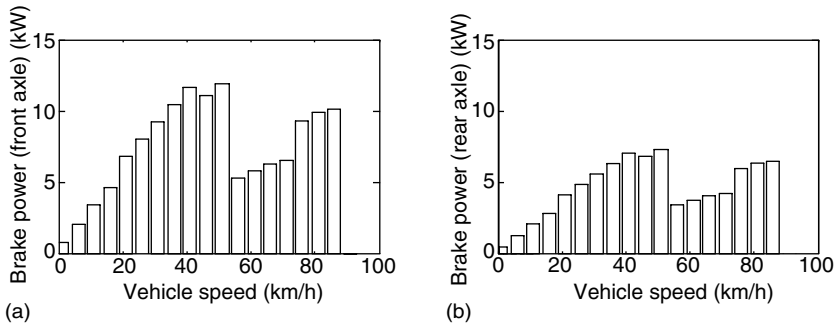

FIGURE 11.5
Braking power vs. vehicle speed in an FTP 75 urban drive cycle: (a) on front wheels and (b) on rear wheels

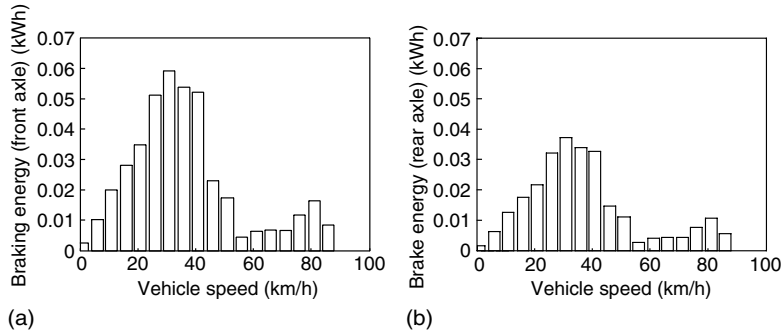

FIGURE 11.6
Braking energy vs. vehicle speed in an FTP 75 urban drive cycle: (a) on front wheels and (b) on rear wheels

From Chapter 2, we know that for passenger cars, in order to prevent the rear wheels from becoming locked before the front wheels, resulting in unstable braking, the actual braking force on the front wheels is usually greater than that

dictated by the ideal distribution curve *I*. Consequently, the braking power and braking energy on the front wheels are even more than those shown in Figure 11.5 and Figure 11.6. In the following sections, the discussion will focus on the configuration in which only front wheels are available for regenerative braking.

11.3 Brake System of EVs and HEVs

Regenerative braking in EVs and HEVs adds some complexity to the braking system design. Two basic questions arise: one is how to distribute the total braking forces required between the regenerative brake and the mechanical friction brake so as to recover the kinetic energy of the vehicle as much as possible; the other is how to distribute the total braking forces on the front and rear axles so as to achieve a steady-state braking.[3] Usually, regenerative braking is effective only for the driven axle.[1] The traction motor must be controlled to produce the proper amount of braking force for recovering the kinetic energy as much as possible and, at the same time, the mechanical brake must be controlled to meet the braking force command from the driver. Basically, there are three different brake control strategies: series braking with optimal braking feel; series braking with optimal energy recovery; and parallel braking.

11.3.1 Series Brake — Optimal Feel

The series braking system with optimal feel consists of a braking controller that controls the braking forces on the front and rear wheels. The control objective is to minimize the stopping distance and optimize the driver's feel. As mentioned in Section 2.9 of Chapter 2, the shortest braking distance and good braking feel require the braking forces on the front and rear wheels to follow the ideal braking force distribution curve *I*.

Figure 11.7 illustrates the principle of this braking control strategy. When the commanded deceleration (represented by the braking pedal position) is less than 0.2 g, only the regenerative braking on the front wheels is applied, which emulates the engine retarding function in conventional vehicles. When the commanded deceleration is greater than 0.2 g, the braking forces on the front and rear wheels follow the ideal braking forces distribution curve *I*, as shown in Figure 11.7 by the thick solid line.

The braking force on the front wheels (driven axle) is divided into two parts: regenerative braking force and mechanically frictional braking force. When the braking force demanded is less than the maximum braking force that the electric motor can produce, only electrically regenerative braking will apply. When the commanded braking force is greater than the available regenerative braking force, the electric motor will operate to produce its maximum braking torque, and the remaining braking force is met by the mechanical brake system.

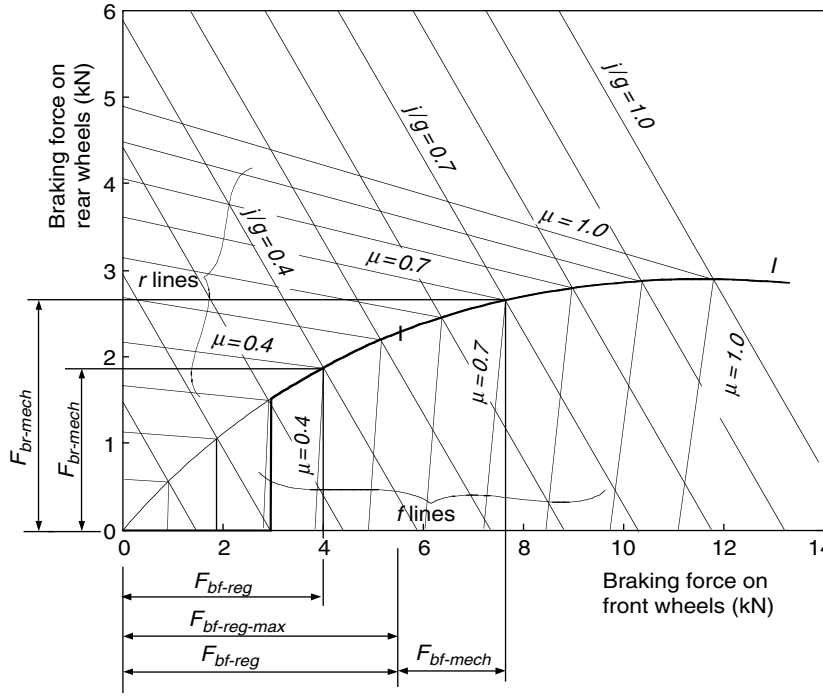

FIGURE 11.7
Illustration of braking forces on the front and rear axle for series braking — optimal feel

It should be noted that the maximum regenerative braking force produced by an electric motor is closely related to the electric motor's speed. At low speed (lower than its base speed), the maximum torque is constant. However, at high speed (higher than its base speed), the maximum torque decreases hyperbolically with its speed. Therefore, the mechanical brake torque at a given vehicle deceleration varies with vehicle speed.

11.3.2 Series Brake — Optimal Energy Recovery

The principle of the series braking system with optimal energy recovery is to recover the braking energy as much as possible in the condition of meeting the total braking force demanded for the given deceleration. This principle is illustrated in Figure 11.8.

When the vehicle is braked with an acceleration rate of $j/g < \mu$, the braking forces on the front and rear wheels can be varied in a certain range, as long as the $F_{bf} + F_{br} = M_v j$ is satisfied. This variation range of the front and rear axles is shown in Figure 11.8 by the thick solid line ab, where $\mu = 0.9$ and $j/g = 0.7$. In this case, regenerative braking should be used in priority. If the available regenerative braking force (maximum braking force produced

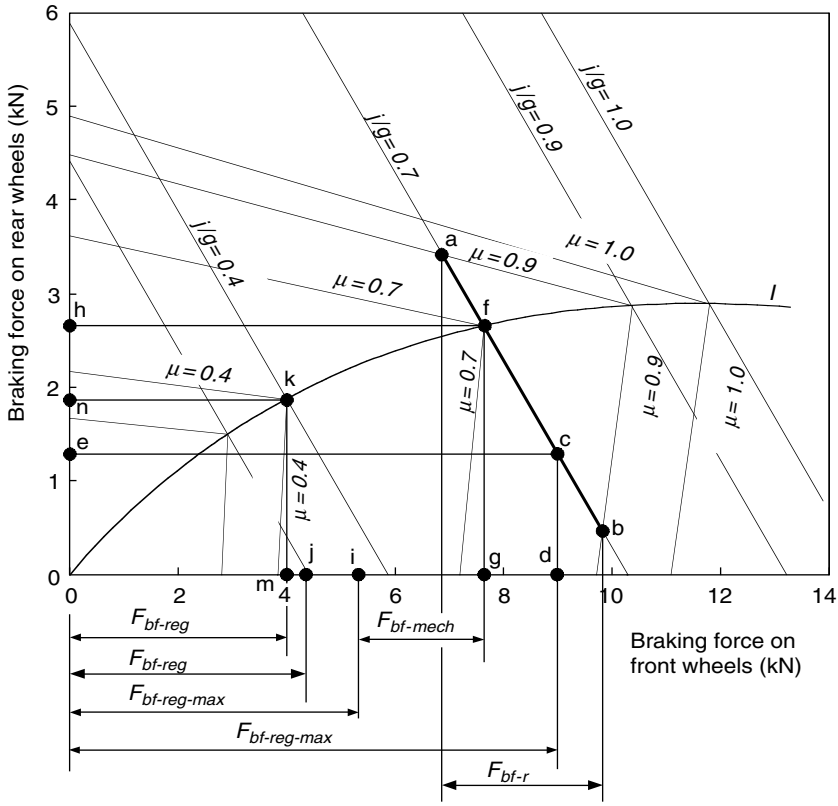

FIGURE 11.8
Demonstration of series braking — optimal energy recovery

by the electric motor) is in this range (point c in Figure 11.8, for example), the braking force on the front wheels should be developed only by regenerative braking without mechanical braking. The braking force on the rear wheels, represented by point e, should be developed in order to meet the total braking force requirement. If, on the same road, the available regenerative braking force is less than the value corresponding to point a (e.g., point i in Figure 11.8), the electric motor should be controlled to produce its maximum regenerative braking force. The front and rear braking forces should be controlled at point f so as to optimize the driver feel and reduce braking distance. In this case, additional braking force on the front wheels must be developed by mechanical braking by the amount represented by $F_{bf\text{-}mech}$, and the braking force on the rear axle is represented by point h.

When the commanded deceleration rate, j/g, is much smaller than the road adhesive coefficient ($j/g = 0.3$ in Figure 11.8 for example), and the regenerative braking force can meet the total braking force demand, only regenerative braking is used without mechanical braking on the front and rear wheels (point j in Figure 11.8).

When the commanded deceleration rate, j/g, is equal to the road adhesive coefficient μ, the operating point of the front and rear braking forces must be on the curve *I*. On a road with a high adhesive coefficient ($\mu = 0.7$, operating point f, in Figure 11.8, for example), the maximum regenerative braking force is applied and the remaining is supplied by the mechanical brake. On a road with a low adhesive coefficient ($\mu = 0.4$, operating point k, in Figure 11.8, for example), regenerative braking alone is used to develop the front braking force.

When the commanded deceleration rate, j/g, is greater than the road adhesive coefficient μ, this commanded deceleration rate will never be reached due to the limitation of the road adhesion. The maximum deceleration that the vehicle can obtain is $(a/g)_{max} = \mu$. The operating point of the front and rear braking forces is on the curve *I*, corresponding to μ ($\mu = 0.4$ and $j/g > 0.4$ in Figure 11.8, for example); the operating point is point k and the maximum deceleration rate is $j/g = 0.4$.

It should be noted that the series brake with both optimal feel and energy recovery needed active control of both electric regenerative braking and mechanical braking forces on the front and rear wheels. At present, such a braking system is under research and development.

11.3.3 Parallel Brake

The parallel brake system includes both an electrical (regenerative) brake and a mechanical brake, which produce braking forces is parallel and simultaneously. The operating principle is illustrated in Figure 11.9, in which regenerative braking is applied only to the front wheels.

The parallel brake system has a conventional mechanical brake which has a fixed ratio of braking force distribution on the front and rear wheels. Regenerative braking adds additional braking force to the front wheels, resulting in the total braking force distribution curve. The mechanical braking forces on the front and rear axles are proportional to the hydraulic pressure in the master cylinder. The regenerative braking force developed by the electric motor is a function of the hydraulic pressure of the master cylinder, and therefore a function of vehicle deceleration. Because the regenerative braking force available is a function of motor speed and because almost no kinetic energy can be recovered at low motor speed, the regenerative braking force at high vehicle deceleration (e.g., $a/g = 0.9$) is designed to be zero so as to maintain braking balance. When the demanded deceleration is less than this deceleration, regenerative braking is effective. When the braking deceleration commanded is less than a given value, say 0.15 g, only regenerative braking is applied. This emulates the engine retarding in a conventional vehicle. In Figure 11.9, the regenerative braking force, $F_{bf\text{-}regen}$, and mechanical braking forces on the front and rear wheels, $F_{bf\text{-}mech}$ and F_{br}, are illustrated.

Figure 11.10 shows the total braking force, regenerative braking force, and mechanical braking force on the front wheels as well as the braking force on the rear wheels in the parallel braking system of a passenger car.

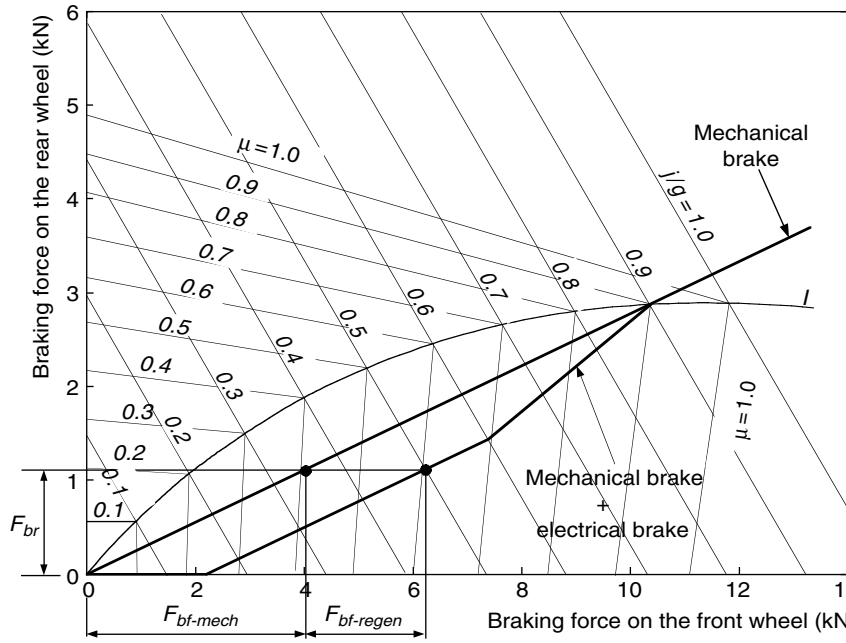

FIGURE 11.9
Illustration of parallel braking strategy

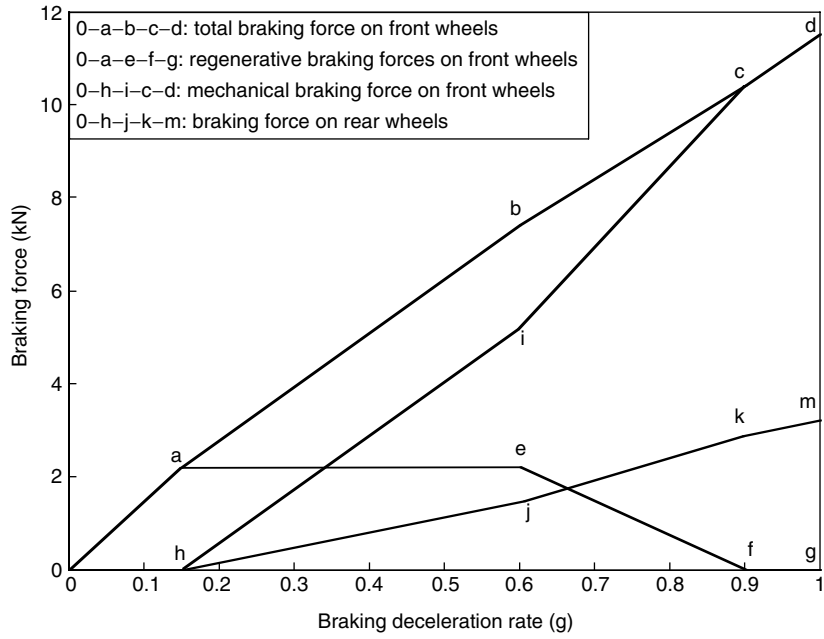

FIGURE 11.10
Braking forces varying with deceleration rate

The parallel braking system does not need an electronically controlled mechanical brake system. A pressure sensor senses the hydraulic pressure in the master cylinder, which represents the deceleration demand. The pressure signal is regulated and sent to the electric motor controller to control the electric motor to produce the demanded braking torque. Compared with the series braking of both optimal feel and energy recovery, the parallel braking system has a much simpler construction and control system.[4] However, the driver's feeling, and amount of energy recovered are compromised.

11.4 Antilock Brake System (ABS)

Active control of the braking force (torque) of the electric motor is easier than the control of the mechanical braking force. Thus, antilock in braking with an electric brake in EVs and HEVs is another inherent advantage, especially for a vehicle with an electric motor on four wheels. Figure 11.11 conceptually illustrates a scheme of regenerative braking, which can potentially function as an ABS.[2]

The main components of this braking system are the brake pedal, master cylinder, electrically powered and electronically controlled brake actuators, electronically controlled three-port switches (common mode: port 1 open, port 2 close, and port 3 open), fluid accumulator, pressure sensor, and an overall controller unit. The pressure sensor measures the fluid pressure,

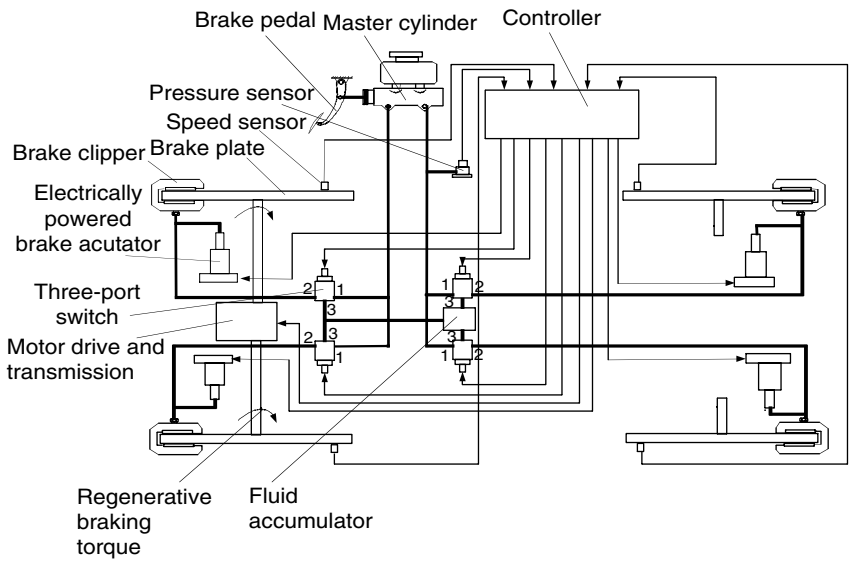

FIGURE 11.11
Electronically controlled regenerative braking system functioning as an ABS

which represents the driver's desirable braking strength. The fluid is discharged into the fluid accumulator through the electronically controlled three-port switches. This emulates the braking feeling of a conventional braking system. After receiving a braking pressure signal, the overall controller unit determines the braking torques of the front and rear wheels, regenerative braking torque, and mechanical braking torque, according to the traction motor characteristics and control rule. The motor controller (not shown in Figure 11.11) commands the motor to produce correct braking torque, and the mechanical braking controller commands the electrically powered braking actuator to produce correct braking torques for each wheel. The braking actuators are also controlled to function as an antilock system to prevent the wheels from being locked completely. If an electrically powered braking actuator is detected to be a failure, the corresponding three-port switch closes port 3 and opens port 2, and then fluid is directly discharged to the wheel cylinder to produce braking torque. The control strategy is crucial for energy recovery and braking performance.

Figure 11.12 shows the simulation results of a passenger car, which is experiencing a sudden strong braking on a road with varying road adhesive coefficients.[2] When the commanded braking force is less than the maximum braking force that the ground surface can support without the wheel being locked, the actual braking force follows the commanded braking force. However, when the commanded braking force is greater than the maximum

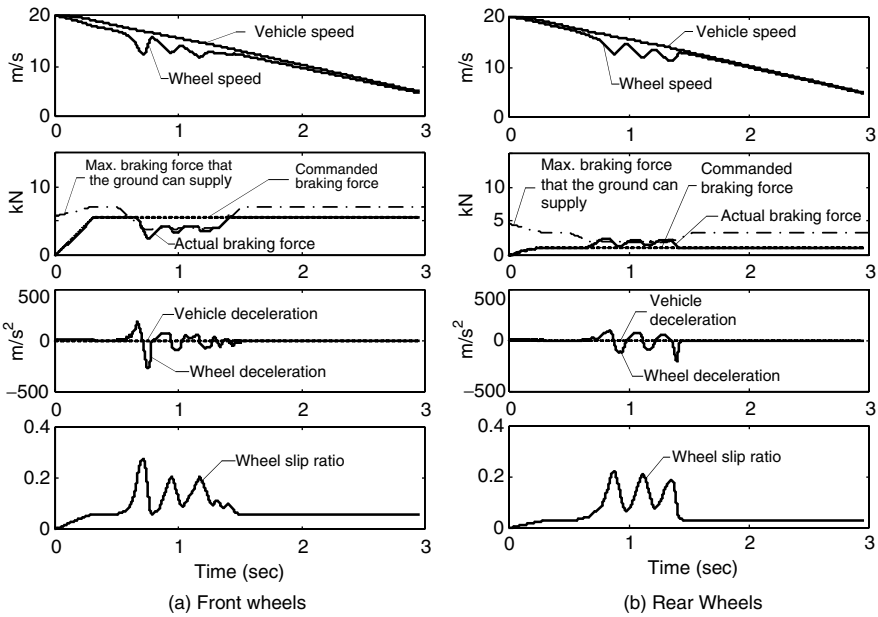

FIGURE 11.12
Braking with ABS

braking force that the ground can support, the actual braking force follows the maximum ground braking force (in a period of 0.5 to 1.5 sec in Figure 11.12). Then, the wheel slip ratios can be controlled in a proper range (usually <25%). The vehicle will have directional stability and short braking distance.

References

[1] Y. Gao, L. Chen, and M. Ehsani, Investigation of the effectiveness of regenerative braking for EV and HEV, *Society of Automotive Engineers (SAE) Journal*, SP-1466, Paper No. 1999-01-2901, 1999.

[2] Y. Gao and M. Ehsani, Electronic braking system of EV and HEV — integration of regenerative braking, automatic braking force control and ABS, in *Proceedings of the SAE 2001 Future Transportation Technology Conference*, Paper No. 2001-01-2478, Costa Mesa, CA, Aug. 2001.

[3] H. Gao, Y. Gao, and M. Ehsani, Design issues of the switched reluctance motor drive for propulsion and regenerative braking in EV and HEV, in *Proceedings of the SAE 2001 Future Transportation Technology Conference*, Paper No. 2001-01-2526, Costa Mesa, CA, Aug. 2001.

[4] S.R. Cikanek and K.E. Bailey, Energy recovery comparison between series and parallel braking system for electric vehicles using various drive cycles, *Advanced Automotive Technologies, American Society of Mechanical Engineers (ASME)*, DSC-vol. 56/DE-vol. 86, pp. 17–31, 1995.

12

Fuel Cell Vehicles

CONTENTS

12.1 Operating Principles of Fuel Cells 348
12.2 Electrode Potential and Current–Voltage Curve 350
12.3 Fuel and Oxidant Consumption....354
12.4 Fuel Cell System Characteristics 355
12.5 Fuel Cell Technologies 357
12.5.1 Proton Exchange Membrane Fuel Cells 357
12.5.2 Alkaline Fuel Cells....359
12.5.3 Phosphoric Acid Fuel Cells1 361
12.5.4 Molten Carbonate Fuel Cells 361
12.5.5 Solid Oxide Fuel Cells....362
12.5.6 Direct Methanol Fuel Cells....363
12.6 Fuel Supply 364
12.6.1 Hydrogen Storage 364
12.6.1.1 Compressed Hydrogen....364
12.6.1.2 Cryogenic Liquid Hydrogen 366
12.6.1.3 Metal Hydrides 367
12.6.2 Hydrogen Production 368
12.6.2.1 Steam Reforming 369
12.6.2.2 POX Reforming 370
12.6.2.3 Autothermal Reforming 370
12.6.3 Ammonia as Hydrogen Carrier....371
12.7 Nonhydrogen Fuel Cells 371
References 372

In recent decades, the application of fuel cells in vehicles has been the focus of increased attention. In contrast to a chemical battery, the fuel cell generates electric energy rather than storing it and continues to do so as long as a fuel supply is maintained. Compared with the battery-powered electric vehicles (EVs), the fuel cell-powered vehicle has the advantages of a longer driving range without a long battery charging time. Compared with the internal combustion engine (ICE) vehicles, it has the advantages of high

energy efficiency and much lower emissions due to the direct conversion of free energy in the fuel into electric energy, without undergoing combustion.

12.1 Operating Principles of Fuel Cells

A fuel cell is a galvanic cell in which the chemical energy of a fuel is converted directly into electrical energy by means of electrochemical processes. The fuel and oxidizing agents are continuously and separately supplied to the two electrodes of the cell, where they undergo a reaction. An electrolyte is necessary to conduct the ions from one electrode to the other as shown in Figure 12.1. The fuel is supplied to the anode or positive electrode, where electrons are released from the fuel under catalyst. The electrons, under the potential difference between these two electrodes, flow through the external circuit to the cathode electrode or negative electrode, where, in combination with positive ions and oxygen, reaction products, or exhaust, are produced.

The chemical reaction in a fuel cell is similar to that in a chemical battery. The thermodynamic voltage of a fuel cell is closely associated with the energy released and the number of electrons transferred in the reaction.[4,5] The energy released by the battery cell reaction is given by the change in Gibbs free energy, ΔG, usually expressed in per mole quantities. The change in Gibbs free energy in a chemical reaction can be expressed as

$$\Delta G = \sum_{Products} G_i - \sum_{Reactants} G_j, \tag{12.1}$$

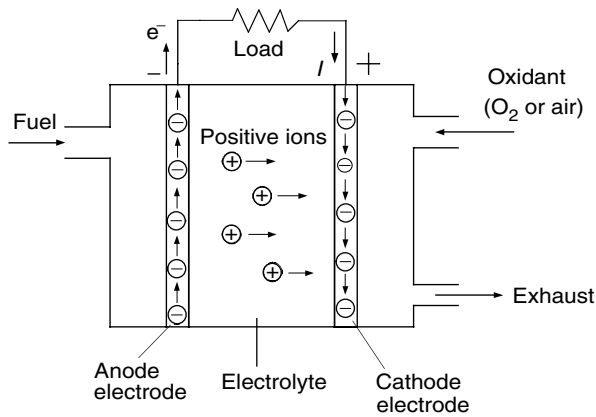

FIGURE 12.1
Basic operation of a fuel cell

where G_i and G_j are the free energies in species i of products and species j of reactants. In a reversible process, ΔG is completely converted into electric energy, that is,

$$\Delta G = -nFV_r, \tag{12.2}$$

where n is the number of electrons transferred in the reaction, $F = 96{,}495$ is the Faraday constant in coulombs per mole, and V_r is the reversible voltage of the cell. At standard conditions (25°C temperature and 1 atm pressure), the open circuit (reversible) voltage of a battery cell can be expressed as

$$V_r^0 = -\frac{\Delta G^0}{nF}, \tag{12.3}$$

where ΔG^0 is the change in Gibbs free energy at standard condition. ΔG is expressed as

$$\Delta G = \Delta H - T\Delta S, \tag{12.4}$$

where ΔH and ΔS are the enthalpy and entropy of the reaction at the absolute temperature T, respectively. Table 12.1 shows the values of standard enthalpy, entropy, and Gibbs free energy of some typical substances. Table 12.2 shows the thermodynamic data for some reactions in a fuel cell at 25°C and 1 atm pressure.

The "ideal" efficiency of a reversible galvanic cell is related to the enthalpy for the cell reaction by

$$\eta_{id} = \frac{\Delta G}{\Delta H} = 1 - \frac{\Delta S}{\Delta H}T. \tag{12.5}$$

η_{id} will be 100% if the electrochemical reaction involves no change in the number of gas moles, that is, when ΔS is zero. This is the case of, for example,

TABLE 12.1

Standard Enthalpy of Formation and Gibbs Free Energy for Typical Fuels

Substance	Formula	ΔH°_{298} (kJ/mol)	ΔS°_{298} (kJ/mol K)	ΔG°_{298} (kJ/mol)
Oxygen	O(g)	0	0	0
Hydrogen	H(g)	0	0	0
Carbon	C(s)	0	0	0
Water	H_2O(l)	−286.2	−0.1641	−237.3
Water	H_2O(g)	−242	−0.045	−228.7
Methane	CH_4(g)	−74.9	−0.081	−50.8
Methanol	CH_3OH(l)	−238.7	−0.243	−166.3
Ethanol	C_2H_5OH(l)	−277.7	−0.345	−174.8
Carbon monoxide	CO(g)	−111.6	0.087	−137.4
Carbon dioxide	CO_2	−393.8	0.0044	−394.6
Ammonia	NH_3 (g)	−46.05	−0.099	−16.7

TABLE 12.2

Thermodynamic Data for Different Reactions at 25°C and 1 atm Pressure

	ΔH°_{298} (kJ/mol)	ΔS°_{298} (kJ/mol K)	ΔG°_{298} (kJ/mol)	n	E° (V)	η_{id} (%)
$H_2+\frac{1}{2}O_2\rightarrow H_2O(l)$	−286.2	−0.1641	−237.3	2	1.23	83
$H_2+\frac{1}{2}O_2\rightarrow H_2O(g)$	−242	−0.045	−228.7	2	1.19	94
$C+\frac{1}{2}O_2\rightarrow CO(g)$	−116.6	0.087	−137.4	2	0.71	124
$C+O_2\rightarrow CO_2(g)$	−393.8	0.003	−394.6	4	1.02	100
$CO+\frac{1}{2}O_2\rightarrow CO_2(g)$	−279.2	−0.087	−253.3	2	1.33	91

reactions $C+O_2=CO_2$. However, if the entropy change ΔS, of a reaction is positive, then the cell — in which this reaction proceeds isothermally and reversibly — has at its disposal not only the chemical energy, ΔH, but also (in analogy to a heat pump) a quantity of heat, $T\Delta S$, absorbed from the surroundings for conversion into electrical energy (see Table 12.2).

The change of free energy, and thus the cell voltage, in a chemical reaction is a function of the activities of the solution species. The dependence of cell voltage on the reactant activities is expressed as

$$V_r = V_r^0 - \frac{RT}{nF}\ln\left[\frac{\Pi(\textit{activities of products})}{\Pi(\textit{activities of reactants})}\right], \tag{12.6}$$

where R is the universal gas constant, 8.31 J/mol K, and T is the absolute temperature in K. For gaseous reactants and products, equation (12.5) can be expressed as

$$V_r = V_r^0 - \frac{RT}{nF}\sum_i V_i \ln\left(\frac{p_i}{p_i^o}\right), \tag{12.7}$$

where V_r is the voltage of the cell in which the reaction proceeds with gaseous participants at nonstandard pressure p_i, V_r^0 is the corresponding cell voltage with all gases at the standard pressure p_i^0 (normally 1 atm), and v_i is the number of moles of species i accounted as positive for products and negative for reactants. Figure 12.2 shows the temperature dependence of the cell voltage and ideal reversible efficiency.

12.2 Electrode Potential and Current–Voltage Curve

Experiments have shown that the rest voltage, V, is usually lower than the reversible voltage, V_r^0 calculated from the ΔG value. The voltage drop is called rest-voltage drop, ΔV_0. The reason may be the existence of a significant kinetic hindrance to the electrode process, or else that the process does not take place in the manner assumed in the thermodynamic calculation of V_r^0.

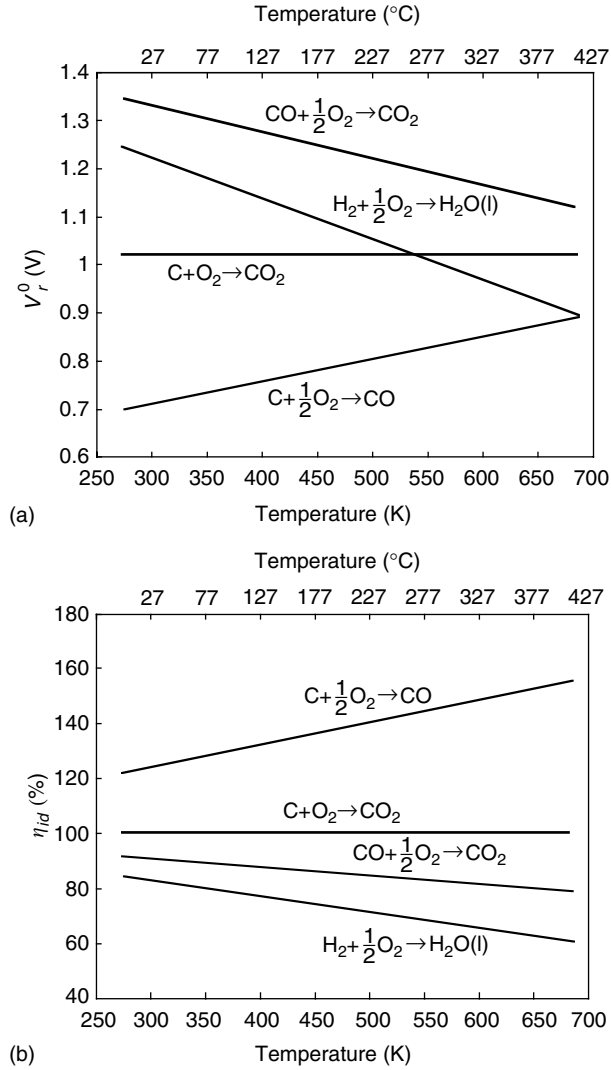

FIGURE 12.2
Temperature dependence of cell voltage and reversible efficiency: (a) voltage and (b) reversible efficiency

This rest-voltage drop depends, in general, on the electrode materials and the kind of electrolyte being used.

When current is drawn from a cell, the voltage drop is caused by the existence of ohmic resistance in the electrode and electrolyte, which increases in direct proportion to the current density, that is,

$$\Delta V_{\Omega} = R_e i, \tag{12.8}$$

where R_e is the equivalent ohmic resistance per area and i is the current density.

In a fuel cell, part of the generated energy is lost in pushing the species to react, due to the fact that extra energy is required to overcome the activation barriers. These losses are called activation losses, and are represented by an activation voltage drop, ΔV_a. This voltage drop is closely related to the materials of electrodes and the catalysts. The Tafel equation is most commonly used to describe this behavior, by which the voltage drop is expressed as[2]

$$\Delta V_a = \frac{RT}{\beta nF} \ln\left(\frac{i}{i_0}\right). \tag{12.9}$$

Or more conveniently, it is written as

$$\Delta V_a = a + b \ln(i), \tag{12.10}$$

where $a = -(RT/\beta nF) \ln(i_0)$ and $b = RT/\beta nF$, and i_0 is the exchange current at equilibrium state and b is constant depending on the process. For a more detailed theoretical description, refer to pp. 230–236 of Messerle.[2]

When current flows, ions are discharged near the negative electrode and, as a result, the concentration of ions in this region tends to decrease. If the current is to be maintained, ions must be transported to the electrode. This takes place naturally by the diffusion of ions from the bulk electrolyte and by direct transport due to fields caused by concentration gradients. Bulk movement of the electrolyte by convection or stirring also helps to bring the ions up.

The voltage drop caused by the lack of ions is called concentration voltage drop, since it is associated with a decrease in the concentration of the electrolyte in the immediate vicinity of the electrode. For small current densities, the concentration voltage drop is generally small. However, as the current density increases, it reaches a limit, when the maximum possible rate of transport of ions to the electrode is approached and as the concentration at the electrode surface falls to zero.

The voltage drop caused by the concentration at the electrode where the ions are removed (cathode electrode in fuel cell) can be expressed as[2]

$$\Delta V_{c1} = \frac{RT}{nF} \ln\left(\frac{i_L}{i_L - i}\right), \tag{12.11}$$

and at the electrode where the ions are formed (anode electrode in fuel cell):

$$\Delta V_{c2} = \frac{RT}{nF} \ln\left(\frac{i_L + i}{i_L}\right), \tag{12.12}$$

where i_L is the limiting current density.

Voltage drop caused by concentration is not only restricted to the electrolyte. When either the reactant or product is gaseous, a change in partial pressure in the reacting zones also represents a change in concentration. For example, in a hydrogen–oxygen fuel cell, the oxygen may be introduced in air. When the reaction takes place, oxygen is removed near the electrode surface in the pores of the electrode and the partial pressure of oxygen must drop

there compared to that in the bulk air. The change in partial pressure must cause a voltage drop, which is determined by

$$\Delta V_{cg} = \frac{RT}{nF} \ln\left(\frac{p_s}{p_0}\right), \tag{12.13}$$

where p_s is the partial pressure at the surface and p_0 is the partial pressure in the bulk feed. For more details, see pp. 236–238 of Messerle.[2]

Figure 12.3 shows the voltage–current curves of a hydrogen–oxygen fuel cell at a temperature of 80°C. It can be seen that the drop caused by the chemical reaction, including activation and concentration, is the source of the voltage drop. This also indicates that improving the electrode materials and manufacturing, using advanced technology, such as nanotechnology, and advanced catalysts, will significantly reduce the voltage drop and will consequently improve the efficiency of the fuel cell.

Energy loss in a fuel cell is represented by the voltage drop. Thus, the efficiency of a fuel cell can be written as

$$\eta_{fc} = \frac{V}{V_r^0}, \tag{12.14}$$

where V_r^0 is the cell reversible voltage at standard conditions ($T = 298$ K and $p = 1$ atm). The efficiency curve is strictly homothetic to the voltage curve. An efficiency–current curve for a hydrogen–oxygen fuel cell (refer to Figure 12.3) is shown in Figure 12.4. Figure 12.4 indicates that the efficiency decreases, and power increases, with an increase in current. Therefore, operating a fuel cell at its low current, and then at low power, achieves high operating efficiency. However, in taking into account energy consumed by its auxil-

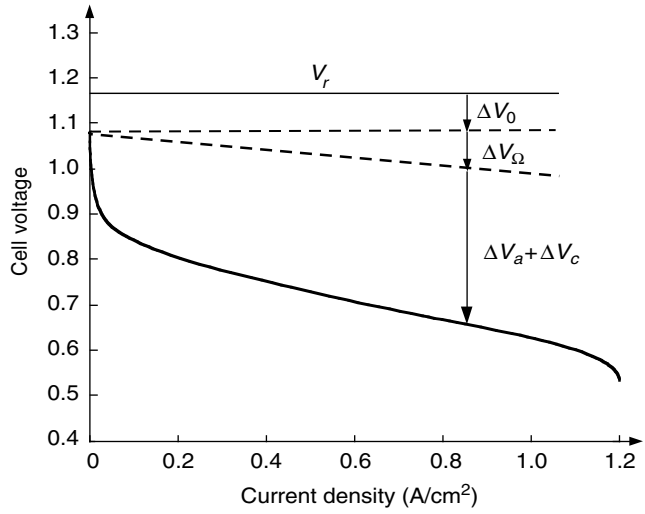

FIGURE 12.3
Current–voltage curves for a hydrogen–oxygen fuel cell at $T = 80$°C

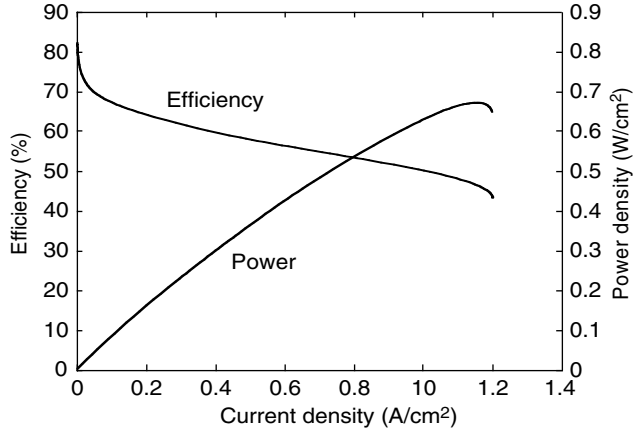

FIGURE 12.4
Operating efficiency and power density along with the current density in a hydrogen–oxygen fuel cell

iaries, such as the air circulating pump, cooling water circulating pump, etc., very low power (<10% of its maximum power) results in low operating efficiency, due to the larger percentage of power consumption in the auxiliary. This will be discussed in more detail later.

12.3 Fuel and Oxidant Consumption

The fuel and oxidant consumptions in a fuel cell are proportional to the current drawn from the fuel cell. Chemical reaction in a fuel cell can be generally described by (12.15), where A is the fuel, B is the oxidant, C and D are the products, and n electrons are transferred.

$$A + x_B B \rightarrow x_c C + x_D D. \tag{12.15}$$

The mass flow of the fuel, associated with the current drawn from the fuel cell, can be expressed as

$$\dot{m}_A = \frac{W_A I}{1000nF}(\text{kg/sec}), \tag{12.16}$$

where W_A is the molecular weight, I is the fuel cell current, and $F = 96.495$ C/mol is the Faraday constant. The stoichiometric ratio of the oxidant mass flow to the fuel mass flow can be expressed as

$$\frac{\dot{m}_B}{\dot{m}_A} = \frac{x_B W_B}{W_A}. \tag{12.17}$$

For a hydrogen–oxygen fuel cell (see Table 12.2 for the reaction), the stoichiometric ratio of hydrogen to oxygen is

$$\left(\frac{\dot{m}_{\mathrm{H}}}{\dot{m}_{\mathrm{O}}}\right)_{stoi} = \frac{0.5W_{\mathrm{O}}}{W_{\mathrm{H}}} = \frac{0.5\times 32}{2.016} = 7.937. \tag{12.18}$$

The equivalent ratio of oxidant to fuel is defined as the ratio of the actual oxidant–fuel ratio to the stoichiometric ratio, that is,

$$\lambda = \frac{(\dot{m}_B/\dot{m}_A)_{actual}}{(\dot{m}_B/\dot{m}_A)_{stoi}}. \tag{12.19}$$

When $\lambda < 1$, the reaction is fuel rich; when $\lambda = 1$, the reaction is stoichiometric; and when $\lambda > 1$, the reaction is fuel lean. In practice, fuel cells are always operated with $\lambda >$, that is, excessive air over the stoichiometric value is supplied in order to reduce the voltage drop caused by concentration. For the fuel cells, using O_2 as oxidant, air is usually used, rather than pure oxygen. In this case, the stoichiometric ratio of fuel to air can be expressed as

$$\frac{\dot{m}_{air}}{\dot{m}_a} = \frac{(x_O W_O)/0.232}{W_A}, \tag{12.20}$$

where it is supposed that oxygen mass takes 23.2% of the air mass. For hydrogen–air fuel cells, equation (12.19) becomes

$$\left(\frac{\dot{m}_{air}}{\dot{m}_{\mathrm{H}}}\right)_{stoi} = \frac{(0.5W_{\mathrm{O}})/0.232}{W_{\mathrm{H}}} = \frac{(0.5\times 32)/0.232}{2.016} = 34.21 \tag{12.21}$$

12.4 Fuel Cell System Characteristics

In practice, fuel cells need auxiliaries to support their operation. The auxiliaries mainly include an air circulating pump, a coolant circulating pump, a ventilation fan, a fuel supply pump, and electrical control devices as shown in Figure 12.5. Among the auxiliaries, the air circulating pump is the largest energy consumer. The power consumed by the air circulating pump (including its drive motor) may take about 10% of the total power output of the fuel cell stack. The other auxiliaries consume much less energy compared with the air circulating pump.

In a fuel cell, the air pressure on the electrode surface, p, is usually higher than the atmospheric pressure, p_0, in order to reduce the voltage drop (see [12.13]). According to thermodynamics, the power needed to compress air from low-pressure p_0 to high-pressure p with a mass flow $\dot{m}_{air}$ can be calculated by[4,5]

$$P_{air\text{-}comp} = \frac{\gamma}{\gamma - 1}\dot{m}_{air}RT\left[\left(\frac{p}{p_0}\right)^{(\gamma-1)/\gamma} - 1\right] (\mathrm{W}), \tag{12.22}$$

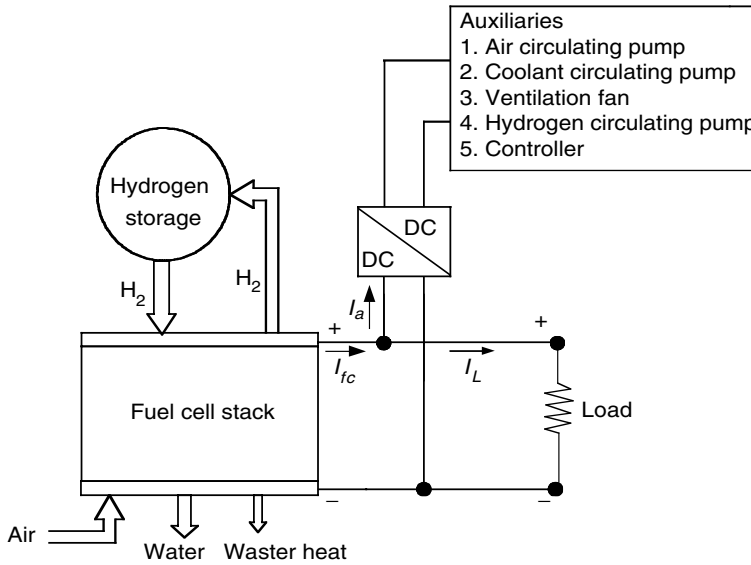

FIGURE 12.5
A hydrogen–air fuel cell system

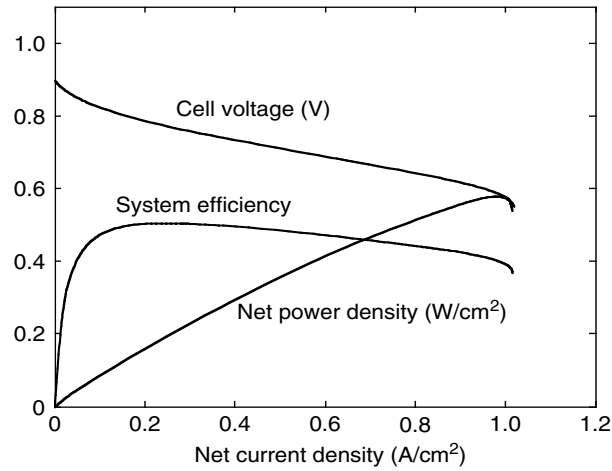

FIGURE 12.6
Cell voltage, system efficiency, and net power density varying with net current density of a hydrogen–air fuel cell

where γ is the ratio of specific heats of air (=1.4), R is the gas constant of air (=287.1 J/kg K), and T is the temperature at the inlet of the compressor in K. When calculating the power consumed by the air-circulating pump, the

energy losses in the air pump and motor drive must be taken into account. Thus, the total power consumed is

$$P_{air\text{-}cir} = \frac{P_{air\text{-}comp}}{\eta_{ap}}, \tag{12.23}$$

where η_{ap} is the efficiency of the air pump plus motor drive.

Figure 12.6 shows an example of the operation characteristics of the hydrogen–air fuel cell system, where $\lambda = 2$, $p/p_0 = 3$ *and* $\eta_{ap} = 0.8$, and the net current and net power are the current and power that flow to the load (see Figure 12.5). This figure indicates that the optimal operation region of the fuel cell system is in the middle region of the current range, say, 7 to 50% of the maximum current. A large current leads to low efficiency due to the large voltage drop in the fuel cell stack and, on the other hand, a very small current leads to low efficiency due to the increase in the percentage of the auxiliaries' energy consumption.

12.5 Fuel Cell Technologies

It is possible to distinguish six major types of fuel cells depending on the type of their electrolyte.[11,16] They are proton exchange membrane (PEM) or polymer exchange membrane fuel cells (PEMFCs), alkaline fuel cells (AFCs), phosphoric acid fuel cells (PAFCs), molten carbonate fuel cells (MCFCs), solid oxide fuel cells (SOFCs), and direct methanol fuel cells (DMFCs). Table 12.3 lists their normal operation temperature and the state of electrolyte.

12.5.1 Proton Exchange Membrane Fuel Cells

The PEMFCs use solid polymer membranes as the electrolyte. The polymer membrane is perfluorosulfonic acid, which is also referred to as Nafion (®Dupont). This polymer membrane is acidic; therefore, the ions transported are hydrogen ions (H^+) or protons. The PEMFC is fueled with pure hydrogen and oxygen or air as oxidant.

TABLE 12.3

Operating Data of Various Fuel Cell Systems[11,16]

Cell system	Temperature °C	Electrolyte state
Proton exchange fuel cells	60–100	Solid
Alkaline fuel cells	100	Liquid
Phosphoric acid fuel cells	60–200	Liquid
Molten carbonate fuel cells	500–800	Liquid
Solid oxide fuel cells	1000–1200	Solid
Direct methanol fuel cells	100	Solid

The polymer electrolyte membrane is coated with a carbon-supported catalyst. The catalyst is in direct contact with both the diffusion layer and the electrolyte for a maximized interface. The catalyst constitutes the electrode. Directly above the catalyst layer is the diffusion layer. The assembly of the electrolyte, catalyst layers, and gas diffusion layers is referred to as the membrane–electrode assembly.

The catalyst is a critical issue in PEM fuel cells. In early realizations, very high loadings of platinum were required for the fuel cell to operate properly. Tremendous improvements in catalyst technology have made it possible to reduce the loading from 28 to 0.2 mg/cm^2. Because of the low operating temperature of the fuel cell and the acidic nature of the electrolyte, noble metals are required for the catalyst layer. The cathode is the most critical electrode because the catalytic reduction of oxygen is more difficult than the catalytic oxidation of hydrogen.

Another critical issue in PEM fuel cells is water management. In order to operate properly, the polymer membrane needs to be kept humid. Indeed, the conduction of ions in polymer membranes requires humidity. If the membrane is too dry, there will not be enough acid ions to carry the protons. If it is too wet (flooded), the pores of the diffusion layer will be blocked and the reactant gases will not be able to reach the catalyst.

In PEM fuel cells, water is formed on the cathode. It can be removed by keeping the fuel cell at a certain temperature and flowing enough to evaporate the water and carry it out of the fuel cell as a vapor. However, this approach is difficult because the margin of error is narrow. Some fuel cell stacks run on a large excess of air that would normally dry the fuel cell, and use an external humidifier to supply water by the anode.

The last major critical issue in PEM fuel cells is poisoning. The platinum catalyst is extremely active and thus provides great performance. The trade-off of this great activity is a greater affinity for carbon monoxide (CO) and sulfur products than oxygen. The poisons bind strongly to the catalyst and prevent hydrogen or oxygen from reaching it. The electrode reactions cannot take place on the poisoned sites and the fuel cell performance is diminished. If hydrogen is fed from a reformer (see Section "12.3 Fuel and oxidant consumption"), the stream will contain some carbon monoxide. The carbon monoxide may also enter the fuel cell in the air stream if the air is pumped from the atmosphere of a polluted city. Poisoning by carbon monoxide is reversible but it comes at a cost and requires the individual treatment of each cell.

The first PEM fuel cells were developed in the 1960s for the needs of the U.S. manned space program. It is now the most investigated fuel cell technology for automotive applications by such manufacturers as Ballard. It is operated at 60 to 100°C and can offer a power density of 0.35 to 0.6W/cm^2. The PEM fuel cell has some definite advantages in its favor for EV and hybrid electric vehicle (HEV) applications.[10] First, its low-temperature operation and hence its fast start-up are desirable for an EV and HEV. Second, the power density is the highest among all the available types of fuel cells. The higher the power density, the smaller the size of the fuel cell that needs to be

installed for the desired power demand. Third, its solid electrolyte does not change, move, or vaporize from the cell. Finally, since the only liquid in the cell is water, the possibility of any corrosion is essentially delimited. However, it also has some disadvantages, such as the expensive noble metal needed, expensive membrane, and easily poisoned catalyst and membrane.[3]

12.5.2 Alkaline Fuel Cells

AFCs use an aqueous solution of potassium hydroxide (KOH) as the electrolyte to conduct ions between electrodes. Potassium hydroxide is alkaline. Because the electrolyte is alkaline, the ion conduction mechanism is different from PEM fuel cells. The ion carried by the alkaline electrolyte is a hydroxide ion (OH^-). This affects several other aspects of the fuel cell. The half reactions are:

$$\textit{anode}: \quad 2H_2 + 4OH^- \rightarrow 4H_2O + 4e^-$$

$$\textit{cathode}: \quad O_2 + 4e^- + 2H_2O \rightarrow 4OH^-.$$

Unlike in acidic fuel cells, water is formed on the hydrogen electrode. In addition, water is needed at the cathode by the oxygen reduction. Water management becomes an issue, which is sometimes resolved by making the electrodes waterproof and keeping the water in the electrolyte. The cathode reaction consumes water from the electrolyte where the anode reaction rejects its product water. The excess water (2 mol per reaction) is evaporated outside the stack.

AFCs are capable of operating over a wide range of temperatures and pressures[2] from 80 to 230°C and 2.2 to 45 atm. High-temperature AFCs also make use of a highly concentrated electrolyte, so highly concentrated that the ion transport mechanism changes from aqueous solution to molten salt.

AFCs are capable of achieving very high efficiencies because of the fast kinetics allowed by the hydroxide electrolyte. The oxygen reaction ($O_2 \rightarrow OH^-$) in particular is much easier than the oxygen reduction in acidic fuel cells. As a result, the activation losses are very low. The fast kinetics in AFCs allow using silver or nickel as catalysts instead of platinum. The cost of the fuel cell stack is thus greatly reduced.

The AFC kinetics is further improved by the eventual circulation of the electrolyte. When the electrolyte is circulated, the fuel cell is said to be a "mobile electrolyte fuel cell." The advantages of such an architecture are: an easy thermal management because the electrolyte is used as coolant; more homogeneous electrolyte concentration, which solves problems of concentration around the cathode; the possibility of using the electrolyte for water management; the possibility of replacing the electrolyte if it has been too polluted by carbon dioxide; and finally there is the possibility of removing the electrolyte from the fuel cell when it is turned off, which has the potential to greatly lengthen the lifetime of the stack.

The use of a circulated electrolyte, however, poses some difficult problems. The greatest problem is the increased risk of leakage: potassium

hydroxide is highly corrosive and has a natural tendency to leak even through the tightest seals. The construction of the circulation pump and heat exchanger and eventual evaporator is further complicated. Another problem is the risk of internal electrolytic short-circuit between two cells if the electrolyte is circulated too violently or if the cells are not isolated enough. A circulating electrolyte alkaline fuel cell is pictured in Figure 12.7.[1]

The greatest problem with AFCs is the poisoning by carbon dioxide. The alkaline electrolyte has a great affinity for carbon dioxide and together they form carbonate ions (CO_3^{2-}). These ions do not participate in the fuel cell reaction and diminish its performance. There is also a risk that the carbonate will precipitate and obstruct the electrodes. This last issue may be taken care

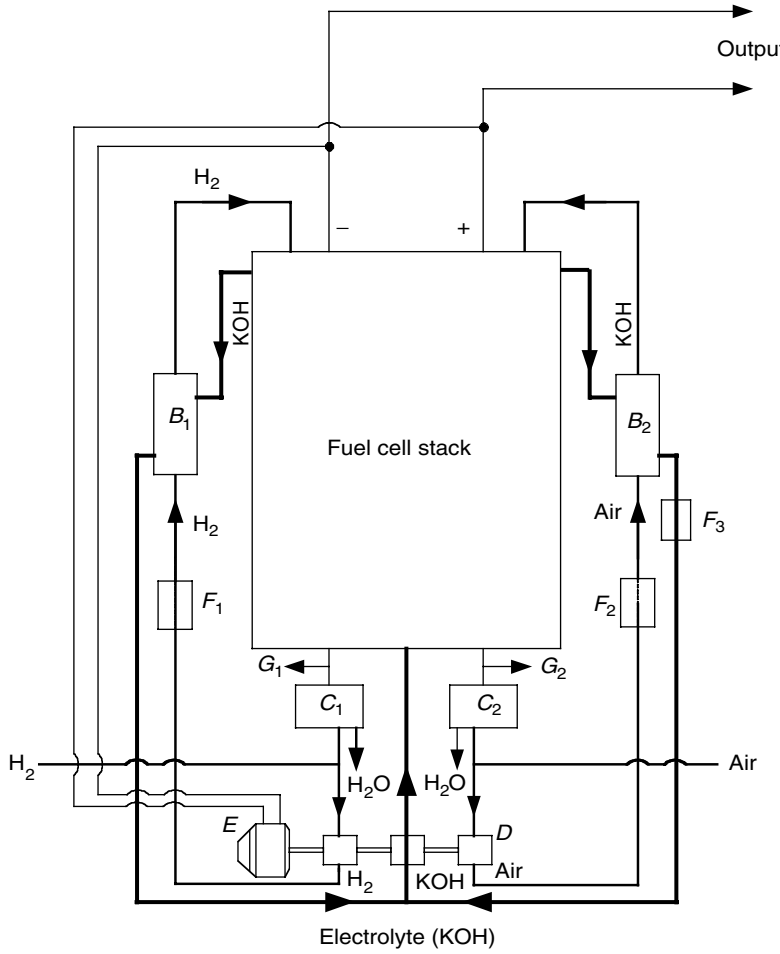

FIGURE 12.7
Circulating electrolyte and supplies of hydrogen and air in an AFC: B_1, B_2, heater exchangers; C_1, C_2, condensers; D, pampers; E, motor; F_1, F_2, F_3, controls; G_1, G_2, outlets[1]

of by circulating the electrolyte. The solution, which adds to the cost and complexity, is to use a carbon dioxide scrubber that will remove the gas from the air stream.

The advantages of AFCs are that they require cheap catalysts, cheap electrolytes, high efficiency, and low-temperature operation. However, they also have some disadvantages such as impaired durability due to corrosive electrolyte, water produced on fuel electrode, and poisoning by carbon dioxides.

12.5.3 Phosphoric Acid Fuel Cells[1]

PAFCs rely on an acidic electrolyte, like PEM fuel cells, to conduct hydrogen ions. The anode and cathode reactions are the same as PEM fuel cell reactions. Phosphoric acid (H_3PO_4) is a viscous liquid that is contained by capillarity in the fuel cell in a porous silicon carbide matrix.

PAFC is the first fuel cell technology to be marketed. Many hospitals, hotels, and military bases make use of a PAFC to cover part or a totality of their electricity and heat needs. Very little work has been done to apply this technology to vehicles, probably because of temperature problems.

The phosphoric acid electrolyte temperature must be kept above 42°C, which is its freezing point. Freezing and rethawing the acid unacceptably stresses the stack. Keeping the stack above this temperature requires extra hardware, which adds to its cost, complexity, weight, and volume. Most of these issues are minor in the case of a stationary application but are incompatible with a vehicular application. Another problem arising from the high operating temperature (above 150°C) is the energy consumption associated with warming up the stack. Every time the fuel cell is started, some energy (i.e., fuel) must be spent to heat it up to operating temperature and every time the fuel cell is turned off, the heat (i.e., energy) is wasted. The loss is significant for short travel time, which is a common occurrence for city drivers. However, this issue seems to be minor in the case of mass transportation such as buses.

The advantages of PAFC are its use of a cheap electrolyte, low operating temperature, and reasonable start-up time. The disadvantages are expensive catalyst (platinum), corrosion by acidic electrolyte, CO_2 poisoning, and low efficiency.

12.5.4 Molten Carbonate Fuel Cells

MCFCs are high-temperature fuel cells (500 to 800°C). They rely on a molten carbonate salt to conduct ions, usually lithium–potassium carbonate or lithium–sodium carbonate. The ions conducted are carbonate ions (CO_3^{2-}). The ion conduction mechanism is that of a molten salt like in PAFC or highly concentrated alkaline fuel cells.

The electrode reactions are different from other fuel cells:

$$\textit{anode}: \quad H_2 + CO_3^{2-} \rightarrow H_2O + CO_2 + 2e^-$$

and

$$\textit{cathode}: \quad \frac{1}{2}O_2 + CO_2 + 2e^- \rightarrow CO_3^{2-}.$$

The major difference from other fuel cells is the necessity to provide carbon dioxide at the cathode. It is not necessary to have an external source since it can be recycled from the anode. MCFCs are never used with pure hydrogen but rather with hydrocarbons. Indeed, the major advantage of high-temperature fuel cells is their capability to, almost, directly process hydrocarbon fuels because the high temperature allows decomposing them to hydrogen on the electrodes. This would be a tremendous advantage for automotive applications because of the present availability of hydrocarbon fuels. In addition, the high temperatures enhance the kinetics to the point that cheap catalysts may be used.

MCFCs, however, pose many problems due to the nature of their electrolytes and the operating temperatures that they require. The carbonate is an alkali, and is extremely corrosive especially at high temperatures. Not only is this unsafe, there is also the problem of corrosion on the electrodes. It is unsafe to have a large device at 500 to 800°C under the hood of a vehicle. While it is true that temperatures in internal combustion engines do reach above 1000°C, these temperatures are restricted to the gases themselves and most parts of the engine are kept cool (around 100°C) by the cooling system. The fuel consumption associated with heating up the fuel cell is also a problem, worsened by the very high operating temperature, and latent heat necessary to melt the electrolyte. These problems are likely to confine molten carbonate fuel cells to stationary or steady power applications such as ships.

The major advantages of MCFCs are that they are fueled with hydrocarbon fuels, require a low-cost catalyst, have improved efficiency due to fast kinetics, and low sensitivity to poisoning. The major disadvantages are slow start-up and reduced material choice due to high temperature, complex fuel cell system due to CO_2 cycling, corrosive electrolyte, and slow power response.

12.5.5 Solid Oxide Fuel Cells

SOFCs conduct ions in a ceramic membrane at high temperature (1000 to 1200°C). Usually, the ceramic is a yttrium stabilized zirconia (YSZ) that will conduct oxygen ions (O^{2-}), but other ceramics conduct hydrogen ions. The conduction mechanism is similar to that observed in semiconductors, often called solid-state devices. The name of the fuel cell is derived from that similarity. The half reactions are as follows:

$$\textit{anode}: \quad H_2 + O^{2-} \rightarrow H_2O + 2e^-$$

and

$$\textit{cathode}: \quad \frac{1}{2}O_2 + 2e^- \rightarrow O^{2-}$$

Here again, water is produced at the fuel electrode. The greatest advantage of SOFCs is this static electrolyte. There is no moving part, except perhaps in the ancillaries. The very high operating temperature allows the use of hydrocarbon fuels as in MCFCs. It should also be noted that SOFCs are not poisoned by carbon monoxide and that they process it about as efficiently as hydrogen. The anode reaction is then

$$CO + O^{2-} \rightarrow CO_2 + 2e^{-}.$$

SOFCs also benefit from reduced activation losses due to their high operating temperature. The losses are dominated by the ohmic component. SOFCs may be of two kinds: planar or tubular. The planar type is a bipolar stack similar to other fuel cell technologies. A tubular solid oxide fuel cell is described in Figure 12.8. The major advantages of tubular technologies include easier sealing and reduced constraints on the ceramics. Disadvantages include lower efficiency and power density.

Like MCFCs, the disadvantages of SOFCs are mostly associated with their high operating temperature (safety, fuel economy). Supplementary problems arise because the ceramic electrolyte and electrodes are extremely brittle. This is a major disadvantage for vehicular applications where vibrations are a common occurrence. Thermal cycling further stresses the ceramics and is a major concern for planar fuel cells.

12.5.6 Direct Methanol Fuel Cells

Instead of using hydrogen, methanol can be directly used as the fuel for a fuel cell; this is the so-called DMFC. There are some definite motivations for applying DMFC to vehicles. First, methanol is a liquid fuel that can be stored easily, distributed, and marketed for vehicle application; hence, the current

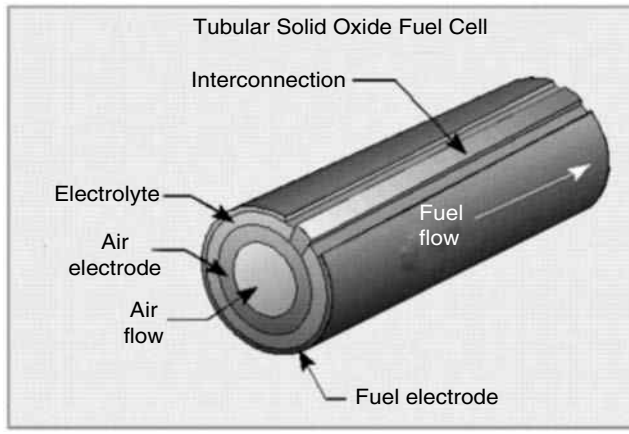

FIGURE 12.8
Tubular solid oxide fuel cell

infrastructure of fuel supply can be used without too much further investment. Second, methanol is the simplest organic fuel, which can be most economically and efficiently produced on a large scale from relatively abundant fossil fuel, namely coal and natural gas. Furthermore, methanol can be produced from agriculture products, such as sugar cane.[8]

In the DMFC, both the anode and cathode adopt platinum or platinum alloys as electrocatalyst. The electrolyte can be trifluoromethane sulfonic acid or PEM. The chemical reaction in a DMFC is:

$$\textit{anode}: \quad CH_3OH + H_2O \rightarrow CO_2 + 6H^+ + 6e^-,$$

$$\textit{cathode}: \quad \frac{3}{2}O_2 + 6H^+ + 6e^- \rightarrow 3H_2O,$$

and

$$\textit{overall}: \quad CH_3OH + \frac{3}{2}O_2 \rightarrow CO_2 + 2H_2O.$$

The DMFC is relatively immature among the aforementioned fuel cells. At the present status of DMFC technology, it generally operates at 50 to 100°C. Compared with direct hydrogen fuel cells, DMFC has low power density, slow power response, and low efficiency.[6,7,8]

12.6 Fuel Supply

Fuel supply to the on-board fuel cells is the major challenge for fuel cell vehicle applications. As mentioned before, hydrogen is the ideal fuel for fuel cell-powered vehicles.[11,16] Hence, hydrogen production and storage on-board are the major concern. Generally, there are two ways to supply fuel to fuel cells. One is to produce hydrogen in ground stations and store pure hydrogen on-board. The other is to produce hydrogen on-board from an easy-carrying hydrogen carrier and directly feed the fuel cells.

12.6.1 Hydrogen Storage

So far, there are three methods for storage of hydrogen on-board. They are compressed hydrogen in a container at ambient temperature, cryogenic liquid hydrogen at low temperature, and the metal hydride method. All these methods have their advantages and disadvantages.

12.6.1.1 Compressed Hydrogen

Pure hydrogen may be stored on-board the vehicle under pressure in a tank. The ideal gas equation can be used to calculate the mass of hydrogen stored in a container with volume V and pressure, p, that is,

$$m_H = \frac{pV}{RT} W_H, \tag{12.24}$$

where p and V are the pressure and volume of the container, R is the gas constant (8.31 J/mol K), T is the absolute temperature, and W_H is the molecular weight of hydrogen (2.016 g/mol). The energy stored in hydrogen can be calculated as

$$E_H = m_H HV, \tag{12.25}$$

where HV is the heating value of hydrogen. The heating value is either the high heating value ($HHV_H = 144$ MJ/kg) or the lower heating value ($LHV_H = 120$ MJ/kg), depending on whether or not the produced water condensation energy can be recuperated. For a convenient comparison with ICEs, the lower heating value is most often used.

Figure 12.9 shows the mass and energy in 1 l of hydrogen and the equivalent liters of gasoline under different pressure and at room temperature (25°C). The equivalent liters of gasoline are defined as the number of liters of gasoline in which the same amount of energy is contained as that in 1 l of hydrogen. Figure 12.9 also indicates that at a pressure of 350 bar, the energy per liter of hydrogen is less than 1 kWh and is equivalent to about 0.1 l of gasoline. Even if the pressure is increased to 700 bar, which is believed to be the maximum pressure that can be reached, the energy per liter of hydrogen is still less than 2.0 kWh and about 0.2 of equivalent liters of gasoline.

In addition, a certain amount of energy is needed to compress hydrogen from low pressure to high pressure. The process in hydrogen compression may be assumed to be an adiabatic process, that is, no heat exchange occurs during the process. The energy consumed can be expressed as

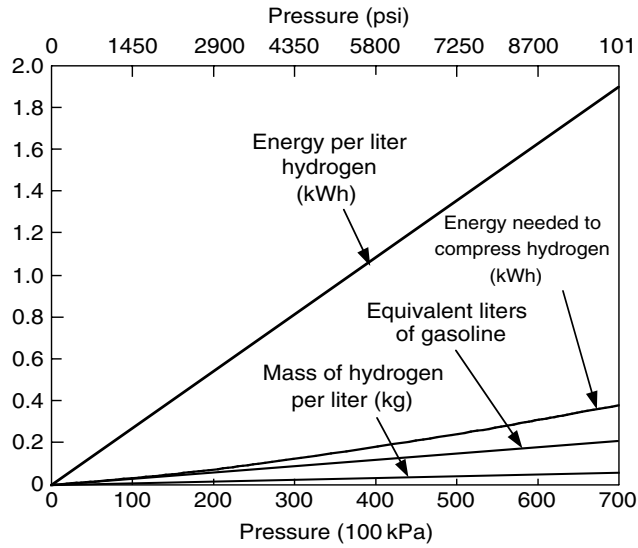

FIGURE 12.9
Energy per liter of hydrogen and equivalent liters of gasoline vs. pressure

$$E_{com} = \frac{\gamma}{\gamma - 1} \frac{m}{W_{\mathrm{H}}} RT \left[\left(\frac{p}{p_0} \right)^{(\gamma-1)/\gamma} - 1 \right], \tag{12.26}$$

where m is mass of hydrogen, W_{H} is the molecular weight of hydrogen, γ is the ratio of the specific heat ($\gamma = 1.4$), p is pressure of hydrogen, and p_0 is atmospheric pressure. This energy consumption is also shown in Figure 12.9. It shows that about 20% of the hydrogen energy must be consumed to compress it to high pressure. Taking account of the inefficiency of the compressor and electric motor, it is estimated that about 25% of hydrogen energy is consumed.

Containing a gas at several hundred atmospheres requires a very strong tank. In order to keep the weight as low as possible and the volume reasonable, today's hydrogen tanks for automotive applications use composite materials such as carbon fiber. The cost of a compressed hydrogen tank is thus likely to be high.

The hazards of compressed hydrogen on-board a vehicle must be taken into consideration. Besides the risk of leakages through cracks in the tank walls, seals, etc., there is the problem of permeation of hydrogen through the material of the wall. The dihydrogen molecule is so small that it can diffuse through some materials.

In addition, a compressed gas tank is a potential bomb in case of a wreck. The dangers are even greater in the case of hydrogen, which has a very wide explosive range in air from 4 to 77%[14] and is capable of mixing very quickly with air. This is to be compared to gasoline, which has an explosive range from only 1 to 6% and is a liquid. It should be noted that hydrogen has a high autoignition temperature of 571°C, whereas gasoline autoignites at around 220°C but must be vaporized first.

So far, the technology of compressed hydrogen storage on-board is still a huge challenge for vehicle application.

12.6.1.2 Cryogenic Liquid Hydrogen

Another alternative solution to storing hydrogen on-board a vehicle is to liquefy the gas at cryogenic temperatures (−259.2°C). The thus stored hydrogen is commonly referred to as "LH_2". LH_2 storage is affected by the same density problems that affect compressed hydrogen. Indeed, the density of liquid hydrogen is very low and 1 l of liquid hydrogen only weighs 71×10^{-3} kg. This low density results in an energy content of about 8.52×10^6 J per liter of liquid hydrogen.

Containing a liquid at such a low temperature as −259.2°C is technically challenging. It requires a heavily insulated tank to minimize the heat transfer from the ambient air to the cryogenic liquid and thus prevent it from boiling. The approach usually taken is to build a significantly insulated tank and to make it strong enough to withstand some of the pressure resulting from the boil-off. The excess pressure is then released to the atmosphere by means of a safety valve. The tank insulation, strength, and safety devices also add significantly to the weight and cost of LH_2 storage.

The boil-off is a problematic phenomenon: if the vehicle is parked in a closed area (garage, underground parking), there is the risk that hydrogen will build up in the confined atmosphere and that the explosive mixture thus formed will explode at the first spark (light switch, lighter, etc.). The refueling of a tank with liquid hydrogen requires specific precautions: air must be kept out of the circuit. The commonly used solution is to fill the tank with nitrogen prior to fueling in order to evacuate the residual gas in the tank. It is also necessary to use specialized equipment, designed to handle the explosion and the cryogenic hazards. Indeed, a cryogenic liquid is a dangerous compound for living beings, as it burn-freezes the skin and organs. It may well be, however, that the ambient temperature would evaporate the cryogenic hydrogen fast enough to limit or eliminate this risk.

12.6.1.3 Metal Hydrides

Some metals are capable of combining with hydrogen to form stable compounds that can later be decomposed under particular pressure and temperature conditions. These metals may be iron, titanium, manganese, nickel, lithium, and some alloys of these metals. Metal hydrides are stable under normal temperature and pressure conditions and are capable of releasing hydrogen only when required.

The hydrogen storage metals and metal alloys are Mg, Mg_2Ni, FeTi, and $LaNi_5$. These metals and metal alloys absorb hydrogen to form Mg–H_2, Mg_2Ni–H_4, FeTi–H_2, and $LaNi_5$–H_6. Theoretically, metal and metal alloys store hydrogen at a higher density than pure hydrogen, as shown in Table 12.4. In practice, the hydrogen storage capacity depends heavily on the surface area of the material on which the hydrogen molecules are absorbed. A large surface area per unit weight of material can be obtained by fine porous modules made of the finely ground powder of the metals or metal alloys. Figure 12.10 shows the practical mass and volume needed to store 6 kg of hydrogen (22 l of gasoline equivalent). This figure indicates that Mg–H_2 is the promising technology.

TABLE 12.4

Theoretical Hydrogen Storage Densities in Compressed, Liquid, and Metal Hydride Approaches[14]

Material	H-atoms per cm^3 ($\times 10^{22}$)	% of weight that is hydrogen
H_2 gas, 200 bar (2900 psi)	0.99	100
H_2 liquid, 20 K (−253°C)	4.2	100
H_2 solid, 4.2 K (−269°C)	5.3	100
Mg–H_2	6.5	7.6
Mg_2Ni–H_2	5.9	3.6
FeTi–H_2	6.0	1.89
$LaNiH_6$	5.5	1.37

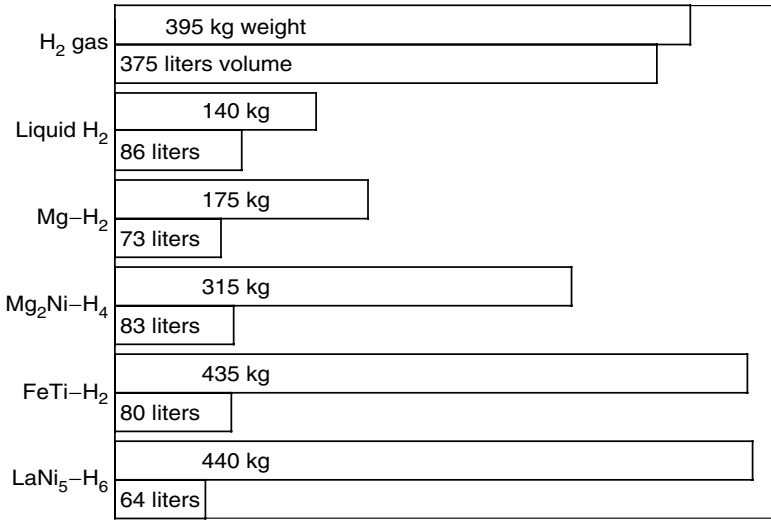

FIGURE 12.10
Current mass and volume needed to store 6 kg of hydrogen (22 l of gasoline equivalent) in various hydrogen storage devices[14]

Alkaline metal hydrides are possible alternatives to metal hydride absorption. These hydrides react, violently, with water to release hydrogen and a hydroxide. The example of sodium hydride is shown below.

$$NaH + H_2O \rightarrow NaOH + H_2.$$

The major disadvantage is the necessity to carry a highly reactive hydride and a corrosive solution of hydroxide in the same vehicle. The storage density is decent in comparison to many other hydrogen storage techniques, but shy in comparison to gasoline. The manufacturing of these hydrides and their recycling is also challenging.

Carbon nanotubes, discovered in 1991, would be a prospective method for hydrogen storage systems, due to their potential high hydrogen absorbing capability and light weight. However, carbon nanotube technology is in its infancy and has a long way to go before its practical utility can be assessed.

12.6.2 Hydrogen Production

At present, hydrogen is mostly produced from hydrocarbon fuels through reforming. Reforming is a chemical operation that extracts hydrogen from hydrocarbons. During this reaction, the energy content of the fuel is transferred

from the carbon–hydrogen bonds to the hydrogen gas. Hydrocarbons such as gasoline, methane, or methanol are the most likely candidates due to the ease with which they reform.

There are three major methods of reforming: steam reforming (SR), autothermal reforming (ATR), and partial oxidation (POX). Steam reforming may be used indifferently with methanol, methane, or gasoline, while autothermal and partial oxidation reforming are most commonly used for processing gasoline.

12.6.2.1 Steam Reforming

Steam reforming (SR) is a chemical process in which hydrogen is produced through the chemical reaction between hydrocarbon fuels and water steam at high temperature. The following chemical equations describe the reforming, using methane (CH_4), methanol (CH_3OH), and gasoline (iso-octane C_8H_{18}) as the fuels:

$$\begin{array}{lccccccccc} & CH_4 & + & 2H_2O & + & 258\ \text{kJ/mol}\ CH_4 & \rightarrow & 4H_2 & + & CO_2 \\ \Delta H^\circ & -79.4 & & 2\times(-286.2) & & & & 0 & & -393.8 \end{array}$$

$$\begin{array}{lccccccccc} & CH_3OH & + & H_2O & + & 131\ \text{kJ/mol}\ CH_3OH & \rightarrow & 3H_2 & + & CO_2 \\ \Delta H^\circ & -238.7 & & -286.2 & & & & 0 & & -393.8 \end{array}$$

$$\begin{array}{lccccccccc} & C_8H_{18} & + & 16H_2O & + & 1652.9\ \text{kJ/mol}\ C_8H_{18} & \rightarrow & 25H_2 & + & 8CO_2 \\ \Delta H^\circ & -224.1 & & 16\times(-286.2) & & & & & & 8\times(-393.8) \end{array}$$

The above reactions are highly endothermic and need to be powered by the burning of some fuels. Also, these reactions yield some carbon monoxide in their product, which is a poison to electrolytes such as PEMFCs, AFCs, and PAFCs. The carbon monoxide can be further converted to hydrogen and carbon dioxide by means of a water-gas shift reaction:

$$\begin{array}{lccccccccc} & CO & + & H_2O & + & 4\ \text{kJ/mol}\ CO & \rightarrow & H_2 & + & CO_2 \\ \Delta H^\circ & -111.6 & & -286.2 & & & & 0 & & -393.8 \end{array}$$

In steam reforming, it is particularly preferred to use methanol as the fuel, since there is no theoretical need for a water-gas shift reaction and since the processing temperature is low (250°C). The hydrogen yield is also particularly high. Among its disadvantages, the most significant are the poisoning of the reformer catalysts by impurities in methanol and the need for an external heat input for the endothermic reaction. The heat requirements slow the reaction down and impose a slow start-up time of between 30 and 45 min.[15] The methanol steam reformer also has slow output dynamics. Although feasible, the steam reforming of gasoline is not commonly used.

12.6.2.2 POX Reforming

POX reforming combines fuel with oxygen to produce hydrogen and carbon monoxide. This approach generally uses air as the oxidant, and results in a reformate that is diluted with nitrogen. Then, the carbon monoxide further reacts with water steam to yield hydrogen and carbon dioxide (CO_2), as mentioned above. Partial oxidation reforming usually uses gasoline (iso-octane) as its fuel. The reaction is expressed as:

$$\begin{array}{lccccccccc} & C_8H_{18} & + & 4O_2 & + & 16N_2 & \rightarrow & 8CO & + & 9H_2 & + & 16N_2 & + & 668.7\ \text{kJ/mol}\ C_8H_{18} \\ \Delta H^\circ & -224.1 & & 0 & & 0 & & 8\times(-111.6) & & 0 & & 0 & & \end{array}$$

$$\begin{array}{lccccccc} & 8CO & + & 8H_2O & + & 32\ \text{kJ/mol}\ 8CO & \rightarrow & 8H_2 & + & 8CO_2 \\ \Delta H^\circ & 8\times(-111.6) & & 8\times(-286.2) & & & & 0 & & 8\times(-393.8) \end{array}$$

The POX reforming is highly exothermic, which thus has the advantage of very fast response to transients capable of very fast start-ups. POX reformers are also fuel flexible, and are capable of treating a wide variety of fuels. The disadvantages include a high operating temperature (800 to 1000°C) and a difficult construction due to heat-integration problems between the different steps of the reaction.[15] In addition, it can be seen from the above chemical equation that the heat produced from the first reaction is much more than that in the second reaction, and hence partial oxidation reforming is somewhat less efficient than the steam reforming of methanol.

Figure 12.11 shows a fuel processing system developed by Epyx Cooperation.[15]

12.6.2.3 Autothermal Reforming

Autothermal reforming combines fuel with both water and steam so that the exothermic heat from the POX reaction is balanced by the

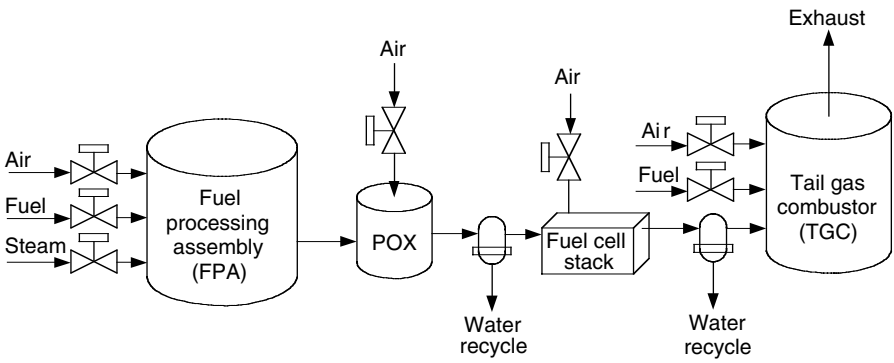

FIGURE 12.11
Fuel processing diagram[15]

endothermic heat of the steam reforming reaction. The chemical equation in this reaction is

$$\begin{array}{lccccccc} & C_8H_{18} & + & nO_2 & + & (8-2n)H_2O & \rightarrow & 8CO + (17-2n)H_2 \\ \Delta H^\circ & -224.1 & & & & (8-2n)\times(-286.2) & & 8\times(-111.6) \end{array}$$

Zero heat produced in the above equation yields $n = 2.83$. The CO produced in the above reaction can further react with water steam to produce hydrogen by the water-shift reaction mentioned above.

ATR yields a more concentrated hydrogen stream than POX reforming, but less than steam reforming. The heat integration is easier than for POX reforming, but a catalyst is required. ATR is potentially more efficient than POX reforming.

12.6.3 Ammonia as Hydrogen Carrier

Ammonia is a noncarbon-based chemical that presents interesting characteristics as a hydrogen source. The extraction of hydrogen from ammonia, called "cracking," is shown below:

$$2NH_3 \rightarrow N_2 + 3H_2.$$

The above reaction is easily achieved by heating ammonia, either alone or over a catalyst bed, which has the advantage of lowering the reaction temperature. The energy requirement for this reaction is minimal because it is reversible. Ammonia presents great advantages in terms of storage as it is easily liquefied at low pressure (about 10 atm) or mildly low temperatures (−33°C). Other advantages include a very high autoignition temperature (651°C) and a limited explosive range in air (15 to 28%).

Despite its many advantages, ammonia has a major disadvantage: it is toxic. Ammonia is an alkali that has an extreme affinity for water and thus strongly attacks the eyes and lungs and causes severe burns. This causticity makes it challenging to conceive of ammonia as a fuel for fuel cell-powered automobiles.

12.7 Nonhydrogen Fuel Cells

Some fuel cells technologies can directly process fuels other than hydrogen.[11,16] Some likely couples are listed below

- Direct methanol PEM fuel cell
- Ammonia alkaline fuel cell
- Direct hydrocarbon molten carbonate or solid oxide fuel cells.

Like their hydrogen counterparts, direct methanol PEM fuel cells (DMFCs) are actively studied and present many advantages such as the absence of a reformer, the handling of a liquid fuel, and the absence of high temperatures in the system. The major disadvantages are the necessity of diluting the methanol in liquid water to feed the fuel electrode, and a strong crossover of methanol — due to its absorption in the polymer membrane, but due mostly to its slow kinetics.

Ammonia AFCs[13] are possible alternatives to the thermal cracking of ammonia. Ammonia gas is directly fed to the fuel cell and is catalytically cracked on the anode. The ammonia fuel cell reaction yields a slightly lower thermodynamic voltage and higher activation losses than hydrogen AFCs. The activation losses may be reduced by improving the catalyst layer. Interestingly, it would be possible to use ammonia directly with other fuel cell technologies if it were not for the fact that the acidic nature of their electrolyte would be destroyed by the alkaline ammonia.

MCFCs and SOFCs have the capability of directly cracking hydrocarbons because of their high operating temperature. Therefore, they are not directly consuming the hydrocarbons, but are internally extracting the hydrogen from them. This option obviously has all the disadvantages of high-temperature fuel cells as discussed in the section on fuel cell technologies.

References

[1] W. Vielstich, *Fuel Cells — Modern Processes for Electrochemical production of Energy*, John Wiley & Sons, New York, 1970.
[2] H.K. Messerle, *Energy Conversion Statics*, Academic Press, New York, 1969.
[3] J. Larminie and A. Dicks, *Fuel Cell Systems Explained*, John Wiley & Sons, New York, 2000.
[4] J. Bevan Ott and J. Boerio-Goates, *Chemical Thermodynamics — Advanced Applications*, Academic Press, New York, 2000.
[5] S.I. Sandler, *Chemical and Engineering Thermodynamics*, 3rd ed., John Wiley & Sons, New York, 1999.
[6] N.Q. Minh and T. Takahashi, *Science and Technology of Ceramic Fuel Cells*, Elsevier, Amsterdam, 1995.
[7] M. Baldauf and W. Preidel, Status of the development of a direct methanol fuel cell, *Fuel Cell Technology for Vehicles*, Society of Automotive Engineers (SAE), Warrendale, PA, 2001.
[8] R.M. Moore, Direct methanol fuel cells for automotive power system *Fuel Cell Technology for Vehicles*, Society of Automotive Engineers (SAE), Warrendale, PA, 2001.
[9] T. Simmons, P. Erickson, M. Heckwolf, and V Roan, The effects of start-up and shutdown of a fuel cell transit bus on the drive cycle, *Society of Automotive Engineers (SAE) Journal*, Paper No. 2002-01-0101, Warrendale, PA, 2002.
[10] F. Michalak, J. Beretta, and J.-P. Lisse, Second generation proton exchange membrane fuel cell working with hydrogen stored at high pressure for fuel cell

electric vehicle, *Society of Automotive Engineers (SAE) Journal*, Paper No. 2002-01-0408, Warrendale, PA, 2002.

[11] P.J. Berlowitz and C.P. Darnell, Fuel choices for fuel cell powered vehicles, *Society of Automotive Engineers (SAE) Journal*, Paper No. 2000-01-0003, Warrendale, PA, 2002.

[12] D. Tran, M. Cummins, E. Stamos, J. Buelow, and C. Mohrdieck, Development of the Jeep Commander 2 fuel cell hybrid electric vehicle, *Society of Automotive Engineers (SAE) Journal*, Paper No. 2001-01-2508, Warrendale, PA, 2002.

[13] C.E. Thomas, B.D. James, F.D. Lomax Jr, and I.F. Kuhn Jr, Societal impacts of fuel options for fuel cell vehicles, *Society of Automotive Engineers (SAE) Journal*, Paper No. 982496, Warrendale, PA, 2002.

[14] S.E. Gay, J.Y. Routex, M. Ehsani, and M. Holtzapple, Investigation of hydrogen carriers for fuel cell based transportation, *Society of Automotive Engineers (SAE) Journal*, Paper No. 2002–01–0097, Warrendale, PA, 2002.

[15] Hydrogen at GKSS: Storage Alternative, http://www.gkss.de/, last visited in May 2003.

[16] P.J. Berlowitz and C.P. Darnell, Fuel choices for fuel cell powered vehicles, *Society of Automotive Engineers (SAE) Journal*, Paper No. 2001-01-0003, Warrendale, PA, 2002.

13

Fuel Cell Hybrid Electric Drive Train Design

CONTENTS

13.1 Configuration 376
13.2 Control Strategy 377
13.3 Parametric Design....379
13.3.1 Motor Power Design 379
13.3.2 Power Design of the Fuel Cell System 381
13.3.3 Design of the Power and Energy Capacity of the PPS....381
13.3.3.1 Power Capacity of the PPS....381
13.3.3.2 Energy Capacity of the PPS 381
13.4 Design Example 383
References 385

Fuel cells, as discussed in Chapter 12, are considered to be one of the advanced power sources for applications in transportation. Compared with the internal combustion engines (ICE), fuel cells have the advantages of high energy efficiency and much lower emissions. This is due to their directly converting the free energy in fuel into electrical energy, without it undergoing combustion. However, vehicles powered solely by fuel cells have some disadvantages, such as a heavy and bulky power unit caused by the low power density of the fuel cell system, long start-up time, and slow power response. Furthermore, in propulsion applications, the extremely large power output in sharp acceleration and the extremely low power output in low-speed driving lead to low efficiency, as shown in Figure 13.1.

Hybridization of the fuel cell system with a peaking power source is an effective technology to overcome the disadvantages of the fuel cell-alone-powered vehicles. The fuel cell hybrid electric vehicle is totally different from the conventional ICE-powered vehicles and ICE-based hybrid drive trains. Therefore, a totally new design methodology is necessary.[1] In this chapter, a general systematic design methodology as well as a control strategy for the fuel cell hybrid electric drive trains are discussed. Along

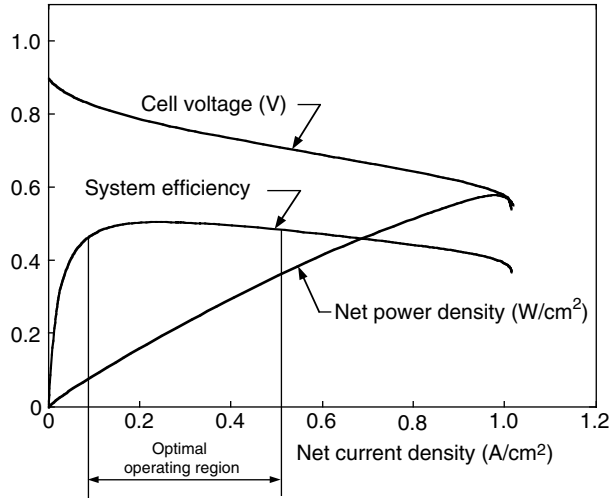

FIGURE 13.1
Typical operating characteristics of a fuel cell system

with this discussion, a design example for a passenger car drive train is introduced.

13.1 Configuration

The fuel cell-powered hybrid drive train is constructed as shown in Figure 13.2. It mainly consists of a fuel cell system as the primary power source, peaking power source (PPS), electric motor drive (motor and its controller), vehicle controller, and an electronic interface between the fuel cell system and the PPS.[1] According to the power or torque command received from the accelerator or the brake pedal and other operating signals, the vehicle controller controls the motor power or torque output and the energy flows between the fuel cell system, PPS, and the drive train. For peak power demand, for instance, in a sharp acceleration, both the fuel cell system and the PPS supply propulsion power to the electric motor drive. In braking, the electric motor, working as a generator, converts part of the braking energy into electric energy and stores it in the PPS. The PPS can also restore its energy from the fuel cell system, when the load power is less than the rated power of the fuel cell system. Thus, with a proper design and control strategy, the PPS will never need to be charged from outside the vehicle.

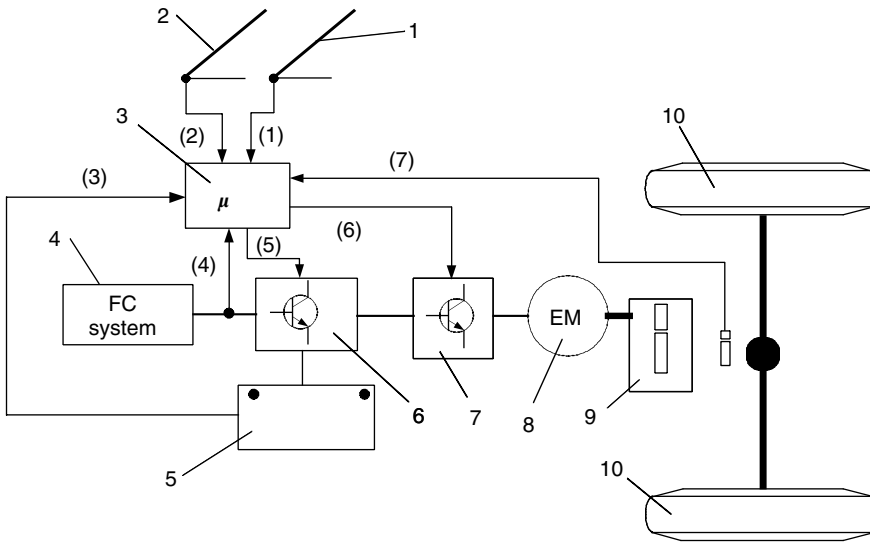

1: accelerator pedal; 2: brake pedal; 3: vehicle controller; 4: fuel cell system; 5: peaking power sound; 6: electronic interface; 7: motor controller; 8: traction motor; 9: transmission; 10: wheels. (1): traction command signal; (2): braking command signal; (3): energy signal of peaking power sour; (4): fuel cell power signal; (5): electronic interface control signal; (6): motor control signal; (7): speed

FIGURE 13.2
Configuration of a typical fuel cell hybrid drive train

13.2 Control Strategy

The control strategy that is preset in the vehicle controller controls the power flow between the fuel cell system, the peaking power system (PPS), and the drive train. The control strategy should ensure that:

1. The power output of the electric motor always meets the power demand
2. The energy level in PPS is always maintained within its optimal region
3. The fuel cell system operates within its optimal operating region.

The driver gives a traction command or brake command through the accelerator pedal or brake pedal (refer to Figure 13.3), which is represented by a power command, P_{comm}, that the motor is expected to produce. Thus, in traction mode, the electric power input to the motor drive can be expressed as

$$P_{m\text{-}in} = \frac{P_{comm}}{\eta_m}, \tag{13.1}$$

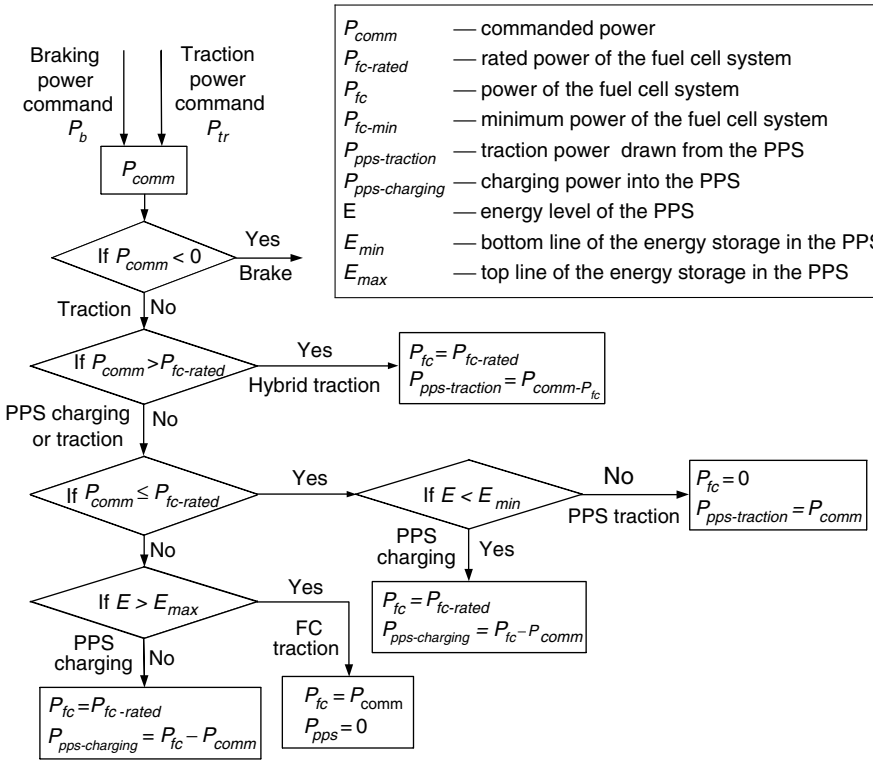

FIGURE 13.3
Flow chart of the control strategy

where η_m is the efficiency of the motor drive. However, in braking, the motor drive functions as a generator, and the electric power output from the motor is expressed as

$$P_{m\text{-}out} = P_{mb\text{-}comm}\eta_m, \tag{13.2}$$

where $P_{mb\text{-}comm}$ is the braking power command to the motor, which may be different from the power command, P_{comm}, coming from the brake pedal, since not all the braking power, P_{comm}, may be supplied by regenerative braking, as discussed in Chapter 11.

According to the motor power command and other vehicle information, such as energy level in PPS and minimum operating power of the fuel cell system — below which the efficiency of the fuel cell will decrease significantly (see Figure 13.1) — the fuel cell system and PPS are controlled to produce corresponding power. Various operating modes of the drive train and the corresponding power control strategy are described in detail below.

Standstill mode: Neither the fuel cell system nor the PPS supplies power to the drive train. The fuel cell system may operate at idle.

Braking mode: The fuel cell system operates at idle, and the PPS absorbs the regenerative braking energy, according to the brake system operating characteristics.

Traction mode:

1. If the commanded motor input power is greater than the rated power of the fuel cell system, the hybrid traction mode is used, in which the fuel cell system operates with its rated power, and the remaining power demanded is supplied by the PPS. The rated power of the fuel cell system may be set as the top line of the optimal operating region of the fuel cell.
2. If the commanded motor input power is smaller than the preset minimum power of the fuel cell system, and the PPS needs charging (the energy level is less than the minimum value), the fuel cell system operates with its rated power — part of which goes to the drive train while the other part goes to the PPS. Otherwise, if the PPS does not need charging (the energy level is close to its maximum value), the fuel cell system operates at idle and the PPS alone drives the vehicle. In the latter case, the peak power that the PPS can produce is greater than the commanded motor input power.
3. If the load power is greater than the preset minimum power and less than the rated power of the fuel cell, and the PPS does not need charging, the fuel cell system alone drives the vehicle. Otherwise, if the PPS does need charging, the fuel cell system operates with its rated power — part of which goes to the drive train to drive the vehicle, while the other part is used to charge the PPS.

13.3 Parametric Design

Similar to the design of the engine-based hybrid drive train, the parametric design of the fuel cell-powered hybrid drive train includes the design of the traction motor power, the fuel cell system power, and the PPS power and energy capacity.

13.3.1 Motor Power Design

The motor power is required to meet the acceleration performance of the vehicle as discussed in previous chapters. Figure 13.4 shows the motor power for a 1500 kg passenger car, with respect to the acceleration time from zero to 100 km/h and a constant speed on a flat road and a 5% grade road. The parameters used in this example are: vehicle mass is 1500 kg, rolling resistance coefficient is 0.01, aerodynamic drag coefficient is 0.3, and front area is 2 m^2. It can be seen that accelerating the vehicle from zero speed to

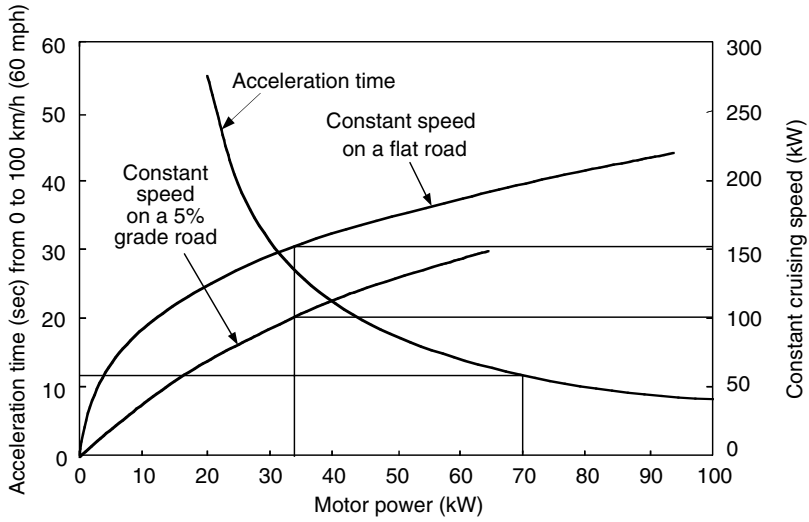

FIGURE 13.4
Motor power vs. acceleration time and vehicle cruising speed

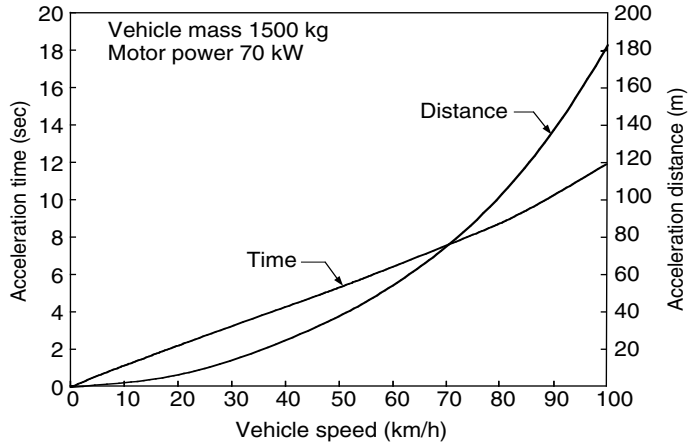

FIGURE 13.5
Acceleration time and distance vs. vehicle speed of the passenger car example

100 km/h in 12 sec needs about 70 kW of motor power. Figure 13.4 also shows the required power while driving at a constant speed on a flat road and a 5% grade road. It can be seen that 33 kW of motor power can support the vehicle driving at around 150 and 100 km/h on a flat road and a 5% grade road, respectively. Thus, 70 kW of traction motor power is considered to be the proper design for this vehicle example. Figure 13.5 shows the acceleration time and distance covered by the vehicle during acceleration driving.

13.3.2 Power Design of the Fuel Cell System

The PPS, as discussed in previous chapters, is only used to supply peak power in short time periods and has a limited amount of energy in it. Thus, the fuel cell system must be able to supply sufficient power to support the vehicle while it drives at high constant speeds on a long trip (e.g., highway driving between cities), and to support the vehicle to overcome a mild grade at a specified speed without the help of the PPS.

For the 1500 kg example passenger car, as indicated in Figure 13.4, 33 kW of motor power is sufficient to meet the power demand with about 150 km/h of constant speed on a flat road and 100 km/h on a 5% grade road.[3] Considering the inefficiency of the motor drive, a fuel cell system of about 40 kW power will be needed to support long trip driving. (In the fuel cell system design, the maximum power may be designed slightly larger than that dictated by the constant speed driving.)[1]

13.3.3 Design of the Power and Energy Capacity of the PPS

13.3.3.1 Power Capacity of the PPS

Based on the maximum power of the motor determined by the specified acceleration performance, and the rated power of the fuel cell system determined by the constant speed driving, the rated power of the peaking power source can be determined by

$$P_{pps} = \frac{P_{motor}}{\eta_{motor}} - P_{fc}, \tag{13.3}$$

where P_{pps} is the rated power of the peaking power source, P_{motor} is the maximum motor power, η_{motor} is the efficiency of the motor drive, and P_{fc} is the rated power of the fuel cell system. The rated power of the PPS in the passenger car example is about 43 kW.

13.3.3.2 Energy Capacity of the PPS

The PPS supplies its energy to the drive train while peaking power is needed, and restores its energy storage from regenerative braking or from the fuel cell system. The energy changes in the PPS in a driving cycle can be expressed as

$$E = \int_t (P_{pps\text{-}charge} - P_{pps\text{-}discharge})\, dt, \tag{13.4}$$

where $P_{pps\text{-}charge}$ and $P_{pps\text{-}discharge}$ are the charge and discharge power of the PPS, respectively. The energy changes, E, in the PPS depend on the size of the fuel cell system, vehicle control strategy, and the load power profile along with time. Figure 13.6 shows the time profiles of the vehicle speed, the power of the fuel cell system, PPS power, and energy change in the PPS for a 1500 kg passenger car with a 40 kW rated power fuel cell system, driving

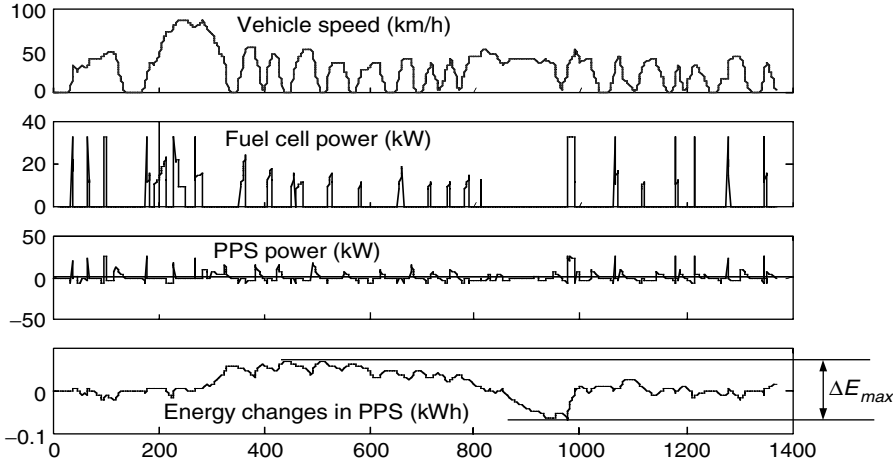

FIGURE 13.6
Vehicle speed, fuel cell power, power of the PPS, and energy changes in the PPS

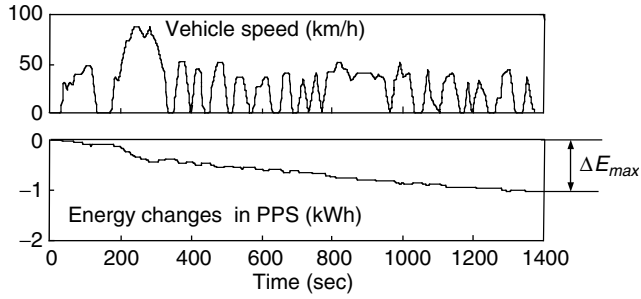

FIGURE 13.7
Energy changes in the PPS while powered by PPS alone in an FTP 75 urban drive cycle

in an FTP 75 urban driving cycle and using the control strategy mentioned above. Figure 13.6 indicates that the maximum energy change, ΔE_{max}, in PPS is quite small (about 0.1 kWh). This result implies that the PPS does not need much stored energy to support the vehicle driving in this driving cycle.

It should be noted that the power-producing capability of the fuel cell system is limited before the fuel cell system is warmed up, and the propulsion of the vehicle relies on the PPS. In this case, the energy in the PPS will be delivered quickly. Figure 13.7 shows the energy changes in the PPS in an FTP 75 urban driving cycle for a 1500 kg passenger car, while PPS alone propels the vehicle. It indicates that about 1 kWh of energy in the PPS is needed to complete the driving cycle (approximately 10.62 km (6.64 mi) in 23 min), and about 43.5 Wh of energy from the PPS will be discharged each minute.

Assuming that 10 min are needed to warm up the fuel cell system, about 435 Wh of energy in the PPS will be discharged.[2]

Based on the maximum discharged energy in the PPS discussed above, the energy capacity of the PPS can be determined by

$$C_E = \frac{\Delta E_{max}}{C_p}, \tag{13.5}$$

where C_E is the total energy capacity of the PPS and C_p is the percentage of the total energy capacity that is allowed to be used, according to the characteristics of the PPS.

13.4 Design Example

Using the design methodology developed in previous sections, a fuel cell-powered hybrid drive train for a passenger car has been designed.[1] For comparison, a fuel cell system-alone-powered passenger car with the same size has also been simulated. The simulation results are shown in Table 13.1, Figure 13.8, and Figure 13.9. The design and simulation results indicate that the hybrid vehicle has a much higher fuel efficiency and the same performance when compared with the fuel cell system-alone-powered vehicle.

TABLE 13.1

Simulation Results for the 1500 kg Hybrid and Fuel Cell-Alone-Powered Passenger Cars

		Hybrid	**Fuel cell**
Vehicle mass (kg)		1500	1500
Rated motor power (kW)		70	70
Rated power of fuel cell system (kW)		40	83
Maximum power of PPS (kW)		43	—
Maximum energy storage in PPS (kWh)		1.5	—
Acceleration time (0 to 100 km/h or 60 mph) (sec)		12	12
Gradeability (at 100 km/h or 60 mph) (%)		5	5
Fuel economy	Constant speed, at 100 km/h or 60 mph	1.81 l/100 km or 130 mpg (gas. equi.) 0.475 kg H_2/100 km or 131 mi/kg H_2	1.91 l/100 km or 123 mpg (gas. equi.) 0.512 kg H_2/100 km 124 mi/kg H_2
	FTP 75 urban driving cycle	2.93 l/100 km or 80 mpg (gas. equi.) 0.769 kg H_2/100 km or 80.4 mi/kg H_2	4.4 l/100 km or 53.4 mpg (gas. equi.) 1.155 kg H_2/100 km or 53.7 mi/kg H_2
	FTP 75 highway driving cycle	2.65 l/100 km or 88.7 mpg (gas. equi.) 0.695 kg H_2/100 km or 89.1 mi/kg H_2	2.9 l/100 km or 81 mpg (gas. equi.) 0.762 kg H_2/100 km or 81.4 mi/kg H_2

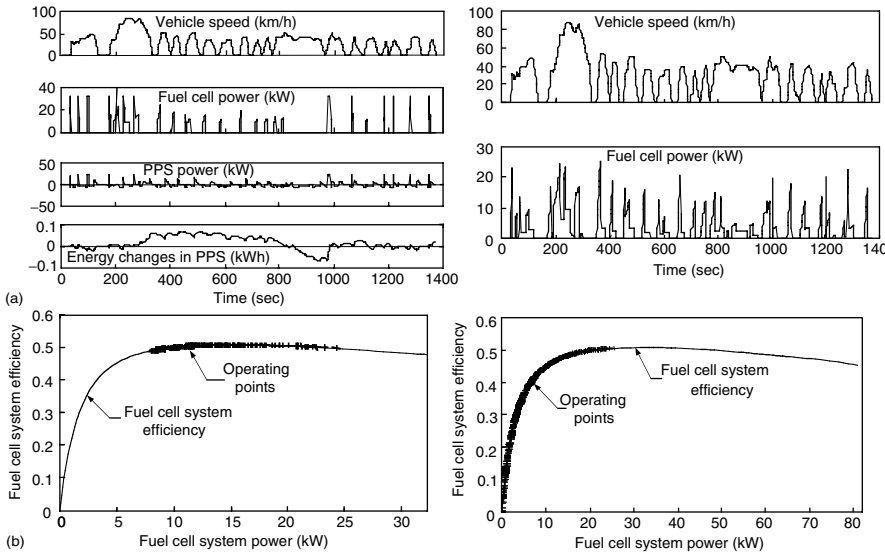

FIGURE 13.8
Operating simulation of the fuel cell hybrid and fuel cell-alone-powered passenger car in an FTP 75 urban drive cycle. (a) hybrid drive train and (b) fuel cell-alone-powered drive train

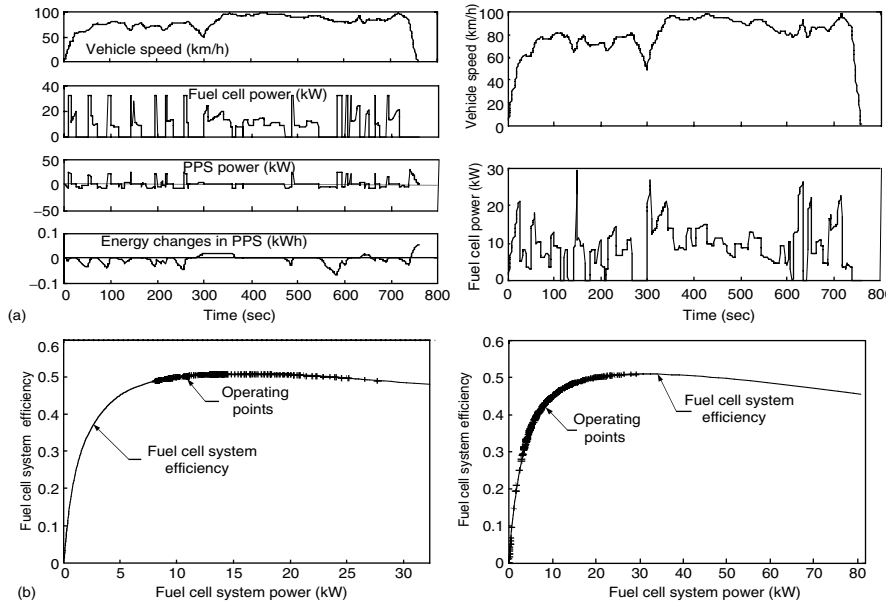

FIGURE 13.9
Operating simulation of the fuel cell hybrid and fuel cell-alone-powered passenger car in an FTP 75 highway drive cycle. (a) Hybrid drive train and (b) fuel cell-alone-powered drive train

References

[1] Y. Gao and M. Ehsani, Systematic design of FC powered hybrid vehicle drive trains, *Society of Automotive Engineers (SAE) Journal*, Paper No. 2001-01-2532, Warrendale, PA, 2001.

[2] T. Simmons, P. Erickson, M. Heckwolf, and V. Roan, The effects of start-up and shutdown of a FC transit bus on the drive cycle, *Society of Automotive Engineers (SAE) Journal,* Paper No. 2002-01-0101, Warrendale, PA, 2002.

[3] D. Tran, M. Cummins, E. Stamos, J. Buelow, and C. Mohrdieck, Development of the Jeep Commander 2 FC hybrid electric vehicle, *Society of Automotive Engineers (SAE) Journal,* Paper No. 2001-01-2508, Warrendale, PA, 2001.

Index

ABS. *See* antilock braking system
acceleration performance
  electric vehicles (EVs) 105–109
  hybrid electric vehicles (HEVs) 252
acid rain 2, 3, 8
aerodynamic drag 25–26. *See also* resistance
AFCs. *See* alkaline fuel cells
air gap
  switched reluctance motor (SRM) drives 230–231
air mass flow ratio 68
air pollution 2–4
air pumping device
  two-stroke engine 85
air/fuel ratio 68–69
alkaline fuel cells (AFCs) 359–361
Alnico 194–195
ammonia
  hydrogen carrier 371
ammonia alkaline fuel cells (AFCs) 372
ANNs. *See* artificial neural networks
anodes
alkaline fuel cells (AFCs) 359
  chemical reaction 303
  direct methanol fuel cells (DMFCs) 364
  fuel cells 348
  molten carbonate fuel cells (MCFCs) 361
  solid oxide fuel cells (SOFCs) 362–363
antilock braking system (ABS) 60, 343–345
armature 143, 144, 146
armature winding 171
artificial intelligence 203
artificial neural networks (ANNs) 203, 224–226
ATR. *See* autothermal reforming
automatic gearbox 39
autothermal reforming (ATR) 370–371. *See also* reforming
auxiliary power source
  ultracapacitor as 315
auxiliary subsystem
  electric vehicles (EVs) 100–101

back EMF integration sensing 203
Bacon, F. 17–18
base speed operation
  switched reluctance motor (SRM) drives 213–214
  batteries 273. *See also* electrochemical batteries; lead-acid batteries
  and ultracapacitators 330
  efficiency during charge/discharge 309
  electrochemical reactions 302–304
  energy efficiency 309
  internal resistance 306–307
  performance 285–286
  specific energy 304–306
  specific power 306–309
  systems for automotive applications 308
  technologies 14, 309–313
  thermodynamic voltage 304
battery charge mode
  parallel mild hybrid electric vehicles (HEVs) 281
  series hybrid electric vehicles (HEVs) 122
BLDC. *See* brush-less DC motor drives
blowdown 83
bmep. *See* brake mean effective pressure
brake control strategies 338
brake mean effective pressure (*bmep*) 66, 67, 71
brake power 66, 71, 337
brake torque 72
brake-specific fuel consumption (*bsfc*) 67
braking 54–60, 333. *See also* regenerative braking
  actuator 344
  distribution 55–60
  energy 334–336, 337
  force 54–55, 56–58, 334–336, 337

power 264, 334–336
series 338–339, 339–341
braking mode
fuel cell hybrid electric vehicles (HEVs) 379
braking torque 333
brush-less DC (BLDC) motor drives
advantages 188–189
basic principles 190
construction and classification 190–193
control 198–199
cooling 189
disadvantages 189–190
inverter failure 189–190
open circuit faults 190
performance analysis 196–198
reliability 189
sensorless techniques 200–203
speed control 199–200
torque control scheme 198–199
bsfc. *See* brake-specific fuel consumption

capacitor 317
capacity factor 41–42
Carnot cycle 92
carrier 290–291
catalytic converter 78
cathodes
alkaline fuel cells (AFCs) 359
chemical reaction 303
direct methanol fuel cells (DMFCs) 364
fuel cells 348
molten carbonate fuel cells (MCFCs) 362
solid oxide fuel cells (SOFCs) 362
choppers 146–151
class A 149
class B 149
class C 152–154
class E 154–155
thyristor 155
CLC. *See* current limit control
combustion quality 34
commanded deceleration rate 340–341
commutator motors 140
commutatorless motors 140, 155
compression-ignition IC engines 81–82
compression stroke 62
concentration voltage drop 352
constant frequency time ratio control (TRC) 148
continuous combustion 93
continuous external combustion engines 89
continuous internal combustion (IC) engines 94
continuous variation transmission (CVT) 322. *See also* transmission
control strategies 242
engine-on-off 244–246, 265
max. SOC-of-PPS 243–244, 262, 265
parallel hybrid drive trains 261–262
converter, classic 211–212
coulometric capacity 300
cryogenic liquid hydrogen 366–367
current control
hysteretic 185–186
current limit control (CLC) 148
CVT. *See* continuous variation transmission
cycles, Stirling engine 90–91

Darracq, M.A. 13
DC motor drives 142–155
chopper control 146–151
combined armature voltage and field control 146
four-quadrant operation 154–155
multiquadrant control 151–154
performance 142–146
permenant magnetic brush-less 187–204
principles of operation 142–146
speed/torque characteristics 145
two-quadrant control 151–154
DC source
induction motor drives 163–164
DC/AC inverter
induction motor drives 164
topology 164–165
diesel engines 81–82
direct methanol fuel cells (DMFCs) 363–364
direct methanol proton exchange membrane (PEM) fuel cells (DMFCs) 372
DMFCs. *See* direct methanol fuel cells
double-layer capacitor technology 315–316
drive cycles 278, 335
electric vehicles (EVs) 110–114
and fuel economy 51–52
highway 289, 384
urban 279, 288, 382, 384
drive trains 54
architectures 120–136
concept 118–120
electric vehicles (EVs) 100
hybrid electric 117, 118–135
parallel 123–136
patterns of combining power flows 119–120
series 121–123
dynamic equation 27–29
dynamic power
hybrid electric vehicles (HEVs) 120
dynamometer 66

efficiency, mechanical 66–67
  dimensionless 67
  fuel conversion 67
  techniques to improve 78–81
EGR. *See* exhaust gas recirculation
EI. *See* emissions index
electric motor 34, 35–36
electric motor drive power capacity
  parallel hybrid electric vehicles (HEVs) 268–271
electric propulsion subsystems 100
electric propulsion systems 139
electric vehicles (EVs) 99–116
  configurations 99–102
  energy consumption 114–116
  history 13–15
  performance 102–109
  subsystems 100
Electroboat 13
electrochemical batteries 300–314
electrode couples 305
electrodes 303
electronic controller 139
emissions
  after-treatment 78
  characteristics, techniques to improve 78–81
  compression ignition engines 81–82
  control 76–78
  global warming 4–5
  internal combustion (IC) engines 68
  pollution 2–4
  Stirling engines 93
  two-stroke engines 86
  Wankel rotary engines 88
emissions index (EI) 68
energy consumption
  electric vehicles (EVs) 114–116
  mild hybrid electric vehicles (HEVs) 278–280
energy loss
  conventional vehicles 278
energy source subsystem
  electric vehicles (EVs) 100
energy storage
  defined 299
  hybridization 328–332
  parallel hybrid electric vehicles (HEVs) 272–274
  requirements, automotive application 300
engine efficiency
  spark-ignited (SI) engines 74
engine performance
  internal combustion (IC) engines 69
  parameters 64, 70
  spark-ignited (SI) engines 74
engine power capacity
  parallel hybrid electric vehicles (HEVs) 266–267
engine rating values 64
engine, supercharged 65
engine traction and battery charging mode
  series hybrid electric vehicles (HEVs) 122
engine/generator
  power rating design 247–249
  size for hybrid electric vehicles (HEVs) 254–255
engine/generator-alone traction mode
  series hybrid electric vehicles (HEVs) 242
engine-alone propelling mode
  parallel hybrid electric vehicle 264
engine-alone traction mode
  parallel mild hybrid electric vehicles (HEVs) 281
EVs. *See* electric vehicles
exhaust
  after-treatment 78
  recycled 76
exhaust gas recirculation (EGR) 80
exhaust stroke 64
expansion stroke 62
exterior air intake 78
externalities. *See* induced costs

Faraday constant 307, 349
ferrites 195
field orientation control (FOC)
  control 173–175
  indirect rotor flux orientation scheme 178–180
  induction motor drives 166–180
  principles 166–173
  rotor flux orientation scheme 175–178
  voltage source inverter 180–185
flywheels 274
  basic structure 327
  electric machine characteristics 325
  geometry 323
  mass 323
  moment of inertia 324
  operating principles 322
  operating speed range 326
  power capacity 324–326
  technologies 326–326
  volume 324
  ultra-high speed 322–326
FOC. *See* field orientation control
forced induction 78
Ford Hybrid Electric Vehicle Challenge 17
fossil fuels 6. *See also* petroleum resources
freewheeling diode conduction sensing 202

friction power 66
fuel 364–371
fuel cell hybrid electric vehicles (HEVs) 375, 376–384
  configuration 376–377
  control strategy 376–379
  design example 383–385
  design of the power and energy capacity of the peak power source (PPS) 381–383
  drive trains 376–377
  operating modes 378–379
  parametric design 379
  power design of the fuel cell system 381
  power requirements 381
  simulation results 383
fuel cell hybrid electric vehicle motors
  power design 379–380
fuel cells 375
  air pressure on the electrode surface 355–356
  auxiliaries 355–356
  chemical reactions 348–350, 354
  electrode potential and current–voltage curve 350–354
  energy loss 353–354
  enthalpy 349
  fuel and oxidant consumption 354–355
  fuel supply 364–371
  generated energy 352
  Gibbs free energy 349
  hydrogen-air 356–357
  hydrogen–oxygen 353, 355
  operating principles 348–350
  system characteristics 355–357
  thermodynamic data 350
  types 357–363
  voltage drop 352–353
  fuel cell vehicles 11, 347, 348–371. *See also* fuel cells; fuel cell hybrid electric vehicles (HEVs)
  history 17–18
fuel consumption 67, 334
  gas turbines 96
  hybrid electric vehicles (HEVs) 256
  internal combustion (IC) engines 72
  parallel mild hybrid electric vehicles (HEVs) 285
  spark-ignited (SI) engines 73
fuel conversion efficiency 71, 76
fuel economy 37, 117
  calculation 50–52
  gas turbine engines 94
  internal combustion engines (ICEs) 49–50
  parallel hybrid electric vehicles (HEVs) 271, 276
  Stirling engines 93
  techniques to improve 52–54
  Wankel rotary engines 88
fuel injection system 77
fuel mass flow rate 68
fuel/air mixture 74–77
fuel/air ratio 68–69, 76–77, 81
fuzzy logic 203

galvanic cells 349. *See also* fuel cells
gas turbine engines 94–97
gasoline direct injection 79–80
gasoline vehicles 13
gear ratio 37–38
  fuel economy 50
  hybrid electric vehicles (HEVs) 251–252
gear transmission 51
Gibbs free energy 304, 348–350
global warming 4–5, 9
gradeability 46
  electric vehicles (EVs) 105–109
  hybrid electric vehicles (HEVs) 253–254
  parallel hybrid electric vehicles (HEVs) 271
greenhouse effect 4
gross indicated work 64–65
ground reaction force 23–24
Grove, W. 17
gyroscopic force 327–328

Hall sensors 178, 192–193
Hall-effect sensors 200
heat transfer processes, Stirling engine 92
HEVs. *See* hybrid electric vehicles
high-energy density magnets 189
Holtzapple, M. 97
hybrid battery charging mode
  series hybrid electric vehicles (HEVs) 122
hybrid braking mode
  parallel hybrid electric vehicles (HEVs) 264
hybrid electric vehicles (HEVs) 11, 117, 118–135, 139
  architectures 120–136
  concept 118–120
  history 15–17
  parallel 123–136
  series 121–123
hybrid mode
  series hybrid electric vehicles (HEVs) 122
hybrid propelling mode
  parallel hybrid electric vehicles (HEVs) 263
hybrid traction mode
  parallel mild hybrid electric vehicles (HEVs) 281
  series hybrid electric vehicles (HEVs) 241

hydrogen
  ammonia as carrier 371
  compressed 364–366
  cryogenic liquid 366–367
  energy stored 365
  hazards 366
  production 368–371
  storage methods 364–367
hydrogen storage metals 367–368
hysteresis, in tire material 23

ICEs. *See* internal combustion engines
Ihrig, H.K. 18
IMEC. *See* improved magnetic equivalent circuit
imep. *See* indicated mean effective pressure
improved magnetic equivalent circuit (IMEC) 231
indicated mean effective pressure (*imep*) 66
indicated power 66, 71
induced costs 7–9
induction motor drives 140, 155–187
  basic operation principles 156–159
  cross section 156
  field orientation control (FOC) 166–180
  power electronic control 163–166
  squirrelcage 155–156
  steady-state performance 159–162
  torque/slip characteristics 161–162
  wound-rotor 155
induction stroke 62
intelligent ignition 80
internal combustion engines (ICEs) 11, 34–35, 62–98, 117
  four-stroke compression-ignition IC engines 81–82
  four-stroke spark-ignited IC engines 62–81
  gas turbine engines 94–97
  quasi-isothermal brayton cycle engines 97–98
  Stirling engines 89–94
  two-stroke engines 82–86
  Wankel rotary engines 86–89

Jenatzy, C. 13, 15

Kalman filter 201
Kirchhoff's voltage law 167
knock 79
knocking 74
Krieger, H. 15

Langer, C. 17, 18
Laplace 197–198
lead-acid batteries 310–311. *See also* batteries
  discharging process 284–285
  electrochemical processes 302–304
lean-burn engines 79–80
lithium-based batteries. *See also* batteries
  lithium-ion (Li-Ion) battery 313–314
  lithium-polymer batteries 313
load power 120, 248, 263, 264
load voltage ripple 150
Lunar Roving Vehicle 14

magnetomotive force (*mmf*) 143
magnets
  high-energy density 189
  permanent 193–195
mass factor 47
max. SOC-of-PPS. *See* maximum state-of-charge of peaking power source
maximum brake torque (MBT) 74–75
maximum cruising speed
  electric vehicles (EVs) 105–109
maximum speed
  parallel hybrid electric vehicles (HEVs) 271
maximum state-of-charge of peaking power source (Max. SOC-of-PPS) 243–244, 245, 262, 265
Maxwell Technologies cell 321
MBT. *See* maximum brake torque
MCFCs. *See* molten carbonate fuel cells
mean effective pressure (*mep*) 65–66, 70
mechanical efficiency 66–67
mechanically frictional braking force 338
mep. *See* mean effective pressure
Messerle, H.K. 352
metal hydrides 367–368
methyl tertiary-butyl ether (MTBE) 78
mild hybrid electric drive trains
  major parameters 283
mmf. *See* magnetomotive force
mobile electrolyte fuel cells. *See* alkaline fuel cells (AFCs)
modulation index 164, 184
molten carbonate fuel cells (MCFCs) 361–362, 372
Mond, L. 17, 18
motor-alone propelling mode
  parallel hybrid electric vehicles (HEVs) 263
motor-alone traction mode
  parallel mild hybrid electric vehicles (HEVs) 281
movement, general vehicle 22
MTBE. *See* methyl tertiary-butyl ether
multivalve timing 80

NASA 18
negative reactants 305
new engine materials 81
nickel-based batteries. *See also* batteries
  nickel/cadmium system 311–312
  nickel/iron system 311
  nickel-metal hydride systems 312–313
noise emissions 189
nonhydrogen fuel cells 371–372

oil consumption 8, 10, 11–12. *See also* petroleum resources
oil reserves 7, 9, 10. *See also* petroleum resources
operating modes
  parallel hybrid electric vehicles (HEVs) 262

PAFCs. *See* phosphoric acid fuel cells
parallel brakes 341–343. *See also* regenerative braking
parallel hybrid electric drive trains
  advantages 259
  configuration 124
  design objectives 260
  speed-coupling 130–133, 133–136
  torque-coupling 124–130, 133–136
parallel mild hybrid electric vehicles (HEVs)
  configuration 280–281
  drive train design 283–285
  operating modes and control strategy 281
performance 285–287
partial oxidation (POX) 369. *See also* reforming
Partnership for a New Generation of Vehicles (PNGV) 17
peak power source (PPS) 240, 242, 243, 248, 376, 377, 378. *See also* control strategies, max SOC-of-PPS
  energy capacity 250–251, 255–256, 381–383
  energy changes 381
  power capacity 249, 255, 381–382
peak power source (PPS) alone traction mode
  series hybrid electric vehicles (HEVs) 242
peak power source (PPS) charge mode
  parallel hybrid electric vehicles (HEVs) 263
peak power source (PPS) charging from the engine/generator
  series hybrid electric vehicles (HEVs) 242
PEM. *See* proton exchange membrane
PEMFCs. *See* polymer exchange membrane fuel cells
performance
  acceleration 46–49
  electric vehicles (EVs) 102–109
  general vehicles 44–49
  techniques to improve 78–81
permanent magnet brush-less AC motors 141
permanent magnet brush-less DC motors 141, 327
permanent magnet DC motors 143
permanent magnet hybrid motors 200
permanent magnet synchronous motors 140–141
permanent magnets 193–195
petroleum resources 5–7, 9
phosphoric acid fuel cells (PAFCs) 361
Pieper vehicle 15
piston knocking 74
pistons 70
planetary gear 130, 133–134
  series-parallel mild hybrid electric vehicles (HEVs) 287–291, 295, 297
planetary gear unit 290–291
PM. *See* permanent magnet
PNGV. *See* Partnership for a New Generation of Vehicles
polymer exchange membrane fuel cells (PEMFCs) 357–359
positive reactants 305
posttransmission
  hybrid electric vehicles (HEVs) 128–129
power converter 139
power plant 34
POX. *See* partial oxidation
PPS. *See* peak power source
pretransmission
  hybrid electric vehicles (HEVs) 128
proton exchange membrane (PEM) 357–359
proton exchange membrane (PEM) fuel cells 358–359. See also polymer exchange membrane fuel cells (PEMFCs)
pulse-width modulation (PWM) 164
pure electric mode
  series hybrid electric vehicles (HEVs) 122
pure engine mode
  series hybrid electric vehicles (HEVs) 122
PWM. *See* pulse-width modulation

quasi-isothermal brayton cycle engine (QIBCE) 97–98

rare-earth magnets 195
rated speed 162
rated value
  voltage 162
reforming 368–370
  autothermal (ATR) 370–371
  partial oxidation (POX) 370
  steam 369–370

reformulated gasoline 78
regenerative braking 13, 242, 256, 329, 333, 334–345
  antilock braking system (ABS) 343–345
  DC motor drives 151–152
  energy consumption 334
  force 338
  hybrid electric vehicles (HEVs) 132
  induction motor drives 159
  parallel hybrid electric vehicles (HEVs) 266–267
  series-parallel mild hybrid electric vehicles (HEVs) 294–295
  switched reluctance motor (SRM) drives 214–216
  systems 338–343
regenerative braking mode
  electric vehicles (EVs) 101, 115
  hybrid electric vehicles (HEVs) 119
  parallel mild hybrid electric vehicles (HEVs) 281
  series hybrid electric vehicles (HEVs) 122, 242
regenerative-alone brake mode
  parallel hybrid electric vehicles (HEVs) 264
regenerator, Stirling engine 89, 91
resistance 23–26, 52–53
  aerodynamic drag 25–26
  equilibrium 45, 46
  grading 26–27
  rolling 23–25, 27
rest-voltage drop 350–351
ring gear 290–291
road adhesive coefficient 340, 344
road resistance 27. *See also* resistance
rolling resistance 23–25, 27. *See also* resistance
rotary-piston engine 86. *See* Wankel rotary engine
rotor
  induction motor drives 156, 159–160, 166–169
  switched reluctance motor (SRM) drives 228–229, 230
rotor flux calculator 176–177

scavenge process 83
Schroedl, M. 201
sensorless control 216–222
  amplitude modulation (AM) 220, 221
  diagnostic pulse-based method 221
  frequency modulation method 220
  modulated signal injection method 220–222
  mutually induced voltage-based method 222
  observer-based method 222
  phase bulk inductance 218
  phase flux linkage-based method 218
  phase incremental inductance 219–220
  phase inductance-based method 218–220
  phase modulation (PM) 220, 221
sensorless technologies 200–203
series braking. *See also* braking; regenerative braking
  optimal energy recovery 339–341
  optimal feel 338–339
series DC motors 145
series hybrid electric drive trains
  advantages 123
  configuration 240
  design example 251–257
  disadvantages 123
  major components 246–251
  operating modes 122, 241–242
series-parallel mild hybrid electric vehicles (HEVs)
  control strategy 295–296
  drive train configuration 287–291
  engine starting 295
  engine-alone traction mode 294
  operating modes and control 291
  speed-coupling operating mode 291–293
sfc. *See* specific fuel consumption
shape drag 25. *See also* resistance
short-circuiting 83
SI. *See* spark-ignited engines
simulations
  parallel hybrid electric vehicle 274–276
skin friction 25. *See also* resistance
slip 159, 162
slip speed 179
slip speed controller 163
smog 2, 3
SOC. *See* state-of-charge
Society of Automotive Engineers in the U.S.A 110
SOFCs. *See* solid oxide fuel cells
solid oxide fuel cells (SOFCs) 362–363, 372
spark advance 74
spark advance angle 75
spark-ignited (SI) engines 62–81
  emission control 77–78
  engine operation characteristics 70–73
  parameters 64–69, 69–70
  principles 62–64
  techniques to improve performance 78–81
  variables affecting performance 74–77
spark timing 74
specific energy
  ratio of practical to theoretical 305–306
specific fuel consumption (*sfc*) 67

speed
  fuel economy 50
  maximum 45–46
  power plant 34–36
  synchronous 134–136
  and tractive effort 31–33
speed coupling 130–133, 133–136, 293
speed/torque 145, 197
speed-summing unit 290–291
squirrelcage 155–156
SR. *See* steam reforming
SRM. *See* switched reluctance motor drives
standstill mode
  fuel cell hybrid electric vehicles (HEVs) 378
state-of-charge (SOC) 300–302, 309
stator
  floating 296–297
  induction motor drives 156, 159–160, 166–169
  radial vibration 227–228
  switched reluctance motor (SRM) drives 228–230
stator arc 231
stator back-iron 231
stator phase current 174
steady (average) power
  hybrid electric vehicles (HEVs) 120
steady-state theory of induction machines 167
steam reforming (SR) 369. *See also* reforming
Stirling engines 89–94
stoichiometric fuel/air ratio 68
stoichiometry 76
stratified charge 88
stroke cycle
  four-stroke spark-ignited IC engines 62–64
  Wankel rotary engines 87
sun gear 290–291, 294
supercharged engine 65
supercharging 79
switched reluctance motor (SRM) drives 141, 204–232, 327
  arithmetic method 223–224
  artificial neural networks (ANNs) 224–226
  basic magnetic structure 204–207
  configurations 205
  design 228–232
  drive converter 210–213
  generating mode of operation 214–216
  inverter topology 211–212
  modes of operation 213–214
  output torque 210
  phase voltage equation 206
  self-tuning techniques 222–226
  sensorless control 216–222
  stator and rotor 228–230
  torque production 207–210
  torque/speed characteristics 214
  vibration and acoustic noise 226–228

Tafel equation 352
terminal voltage sensing 202
Texas A&M University, Power Electronics and Motor Drive Laboratory 141
thermodynamic sponge 89, 91
thermostat control strategy (engine-on–off) 255–256. *See also* control strategies
third-harmonic back EMF sensing 202
throttle position
  mechanical efficiency 66
throttle-less torque control 80
thyristor 14
time ratio control (TRC) 148
tire slip 30. *See also* tire-ground adhesion
tire-ground adhesion 29–31
torque 34–36, 65, 66, 70, 74, 80
  braking 54–55
  characteristics 72
  engine performance 69
  induction motor drives 157, 161, 162, 171
  performance 64–65
  propelling 296
  series-parallel mild hybrid electric (HEVs) 291, 292, 295
  switched reluctance motor (SRM) drives 207–210, 230
torque calculator 177–178
torque converter 39–41, 279
torque coupling 124–130, 133–136
  one-shaft design 124, 128–129
  seperated axle architecture 129–130
  two-shaft design 124, 125–128
torque equation 169, 171, 172
torque ratio range 41
torque/speed
  electric vehicles (EVs) 103–104
  Stirling engines 92–93
torque-coupling 260
  series-parallel mild hybrid electric vehicles (HEVs) 293–294
Toyota Motor Company, Prius 134–136
traction mode
  fuel cell hybrid electric vehicles (HEVs) 379
traction motor
  characteristics in electric vehicles (EVs) 103–104
  power rating design 246–247
  size in hybrid electric vehicles (HEVs) 251

tractive effort, 22, 28–31, 37, 43, 44, 45, 46, 125–126, 246, 253, 270
  electric vehicles (EVs) 104, 106, 107, 109–114
  hybrid electric vehicles (HEVs) 127
  power train 31–33
tractive effort coefficient 30, 31
tractive power rating
  electric vehicles (EVs) 108
transfer function
  brush-less DC (BLDC) motor drive system 198
transistor 14
transmission
  characteristics 36–44
  continuously variable transmission (CVT) 43–44
  fuel economy 54
  hydrodynamic 39–43
  manual gear 37–39
  mechanical efficiency 33
  parallel hybrid electric vehicles (HEVs) 271–272
  power losses in electric vehicles (EVs) 114–115
  requirement in electric vehicles (EVs) 104–105
transmotor 130–131
transportation development strategies 9
trapezoidal brush-less DC (BLDC) motor drives 191–192
trapping point
  two-stroke engine 84
TRC. *See* time ratio control
Trouvé, G. 13
turbocharging 79
two-stroke cycle 82–84
two-stroke engines 82–86

ultracapacitors 273, 314–320
  and batteries 330
  charging characteristics 319–320
  discharge characteristics 318
  energy storage 320
  features 315
  Maxwell Technologies cell 321
  performance 317–320
  principles 315–317
  technologies 320–322
  terminal voltage 317–318
uniflow scavenging
  two-stroke engine 84
universal gas constant 350

valves, two-stroke engine 84–85
variable compression ratio 80
variable intake manifold 79
variable valve timing 80
varied frequency time ratio control (TRC) 148
vector control system 174, 178–179
Vendovelli and Priestly Electric Carriage Company 15, 16
voltage source inverter
  current control 185–187
  tolerance band 186–187
  voltage control 182–185
volumetric efficiency 69, 71

Wakefield, E.H. 16
Wankel rotary engines 86–88
wheel lockup 58–60
wheel slip ratio 345
Wouk, V. 16
wound-field DC motors 143

yttrium stabilized zirconia (YSZ) 362